D 3715

[02]

EurJIC

European Journal of Inorganic Chemistry

2/2012
2nd January Issue

Eur. J. Inorg. Chem. 2012, 165–336

Cover Picture

Yuji Mikata et al.

Rhenium(I) Tricarbonyl Complexes

Microreview

Isaac Garcia-Bosch, Xavi Ribas, and Miquel Costas

M_2O_2 Complexes Arising from O_2 Binding and Activation

A Journal of ChemPubSoc Europe

WILEY-VCH

www.eurjic.org

EJICFK (2) 165–336 (2012) · ISSN 1434-1948 · No. 2/2012

EurJIC
European Journal of Inorganic Chemistry

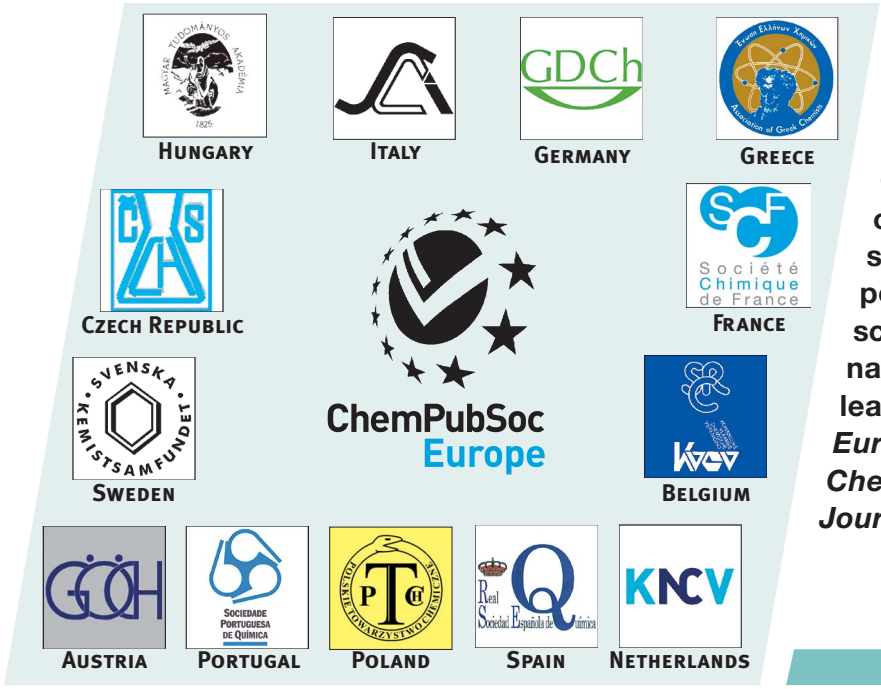

EurJIC is a journal of ChemPubSoc Europe, a union of 16 European chemical societies formed for the purpose of publishing high-quality science. All owners merged their national journals to form two leading chemistry journals, the *European Journal of Inorganic Chemistry* and the *European Journal of Organic Chemistry*.

Other ChemPubSoc Europe journals are *Chemistry – A European Journal*, *ChemBioChem*, *ChemPhysChem*, *ChemMedChem*, *ChemSusChem*, *ChemCatChem*, *ChemPlusChem* and *ChemistryOpen*.

COVER PICTURE

The cover picture shows the cellular uptake of $[Re^{I}\mathbf{L}(CO)_3]^{n+}$ (**L** = ligand; n = 1 or 0) complexes with carbohydrate-pendant ligands. The ligand library includes (i) glucose/galactose as a carbohydrate, (ii) bis(2-pyridylmethyl)amine (DPA)/bis(2-quinolylmethyl)amine (DQA)/*N*-(2-pyridylmethyl)glycine (NPG) as the metal-binding component, and (iii) an ethylene chain as a linker between the metal-binding site and the *O*/*C*-glycosides. Microscopic analysis by using the fluorescent Re complex reveals that the complex stays in the cytosol and cannot penetrate into the nucleus. Details are discussed in the article by Y. Mikata et al. on p. 217ff.

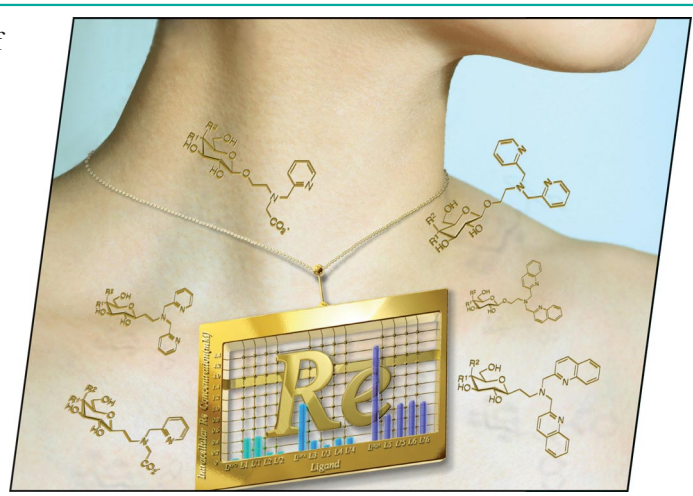

EurJIC
European Journal of Inorganic Chemistry

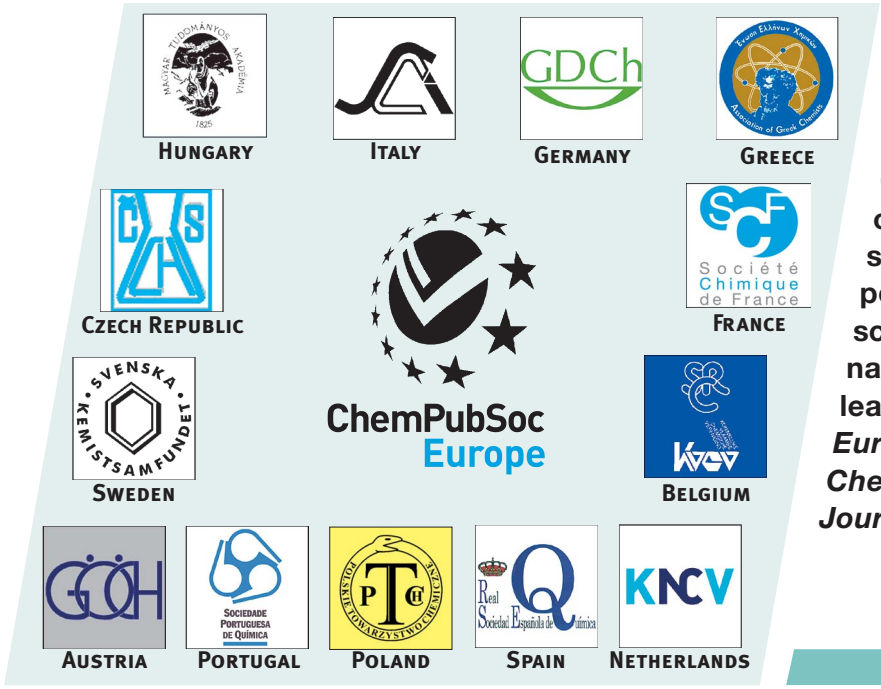

EurJIC is a journal of ChemPubSoc Europe, a union of 16 European chemical societies formed for the purpose of publishing high-quality science. All owners merged their national journals to form two leading chemistry journals, the *European Journal of Inorganic Chemistry* and the *European Journal of Organic Chemistry*.

Other ChemPubSoc Europe journals are *Chemistry – A European Journal*, *ChemBioChem*, *ChemPhysChem*, *ChemMedChem*, *ChemSusChem*, *ChemCatChem*, *ChemPlusChem* and *ChemistryOpen*.

COVER PICTURE

The cover picture shows the cellular uptake of $[Re^{I}\mathbf{L}(CO)_3]^{n+}$ (**L** = ligand; n = 1 or 0) complexes with carbohydrate-pendant ligands. The ligand library includes (i) glucose/galactose as a carbohydrate, (ii) bis(2-pyridylmethyl)amine (DPA)/bis(2-quinolylmethyl)amine (DQA)/*N*-(2-pyridylmethyl)glycine (NPG) as the metal-binding component, and (iii) an ethylene chain as a linker between the metal-binding site and the *O*/*C*-glycosides. Microscopic analysis by using the fluorescent Re complex reveals that the complex stays in the cytosol and cannot penetrate into the nucleus. Details are discussed in the article by Y. Mikata et al. on p. 217ff.

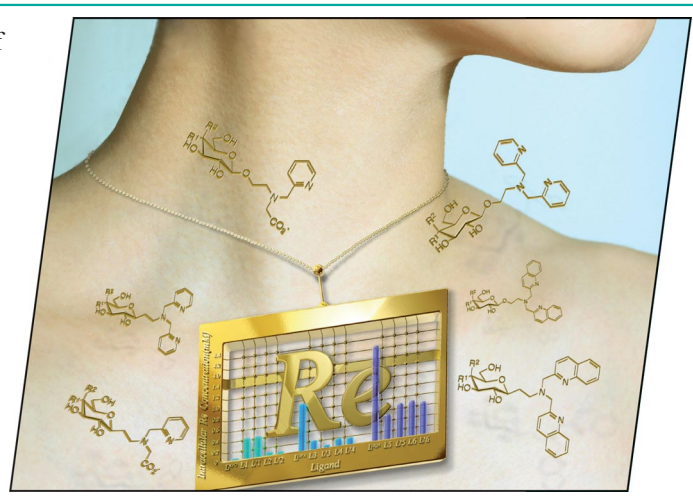

CONTENTS

MICROREVIEW

SHORT COMMUNICATIONS

Synthesis of Co Nanoparticles

Keywords: Cobalt / Nanoparticles / Synthetic methods / Surfactants / Magnetic properties

The thermal decomposition of $Co_2(CO)_8$ in the presence of ionic compounds leads exclusively to ε-Co nanocubes. The ionic species can be added directly or generated in situ. An additional weak magnetic field leads exclusively to ε-Co nanodiscs, which assemble to chains.

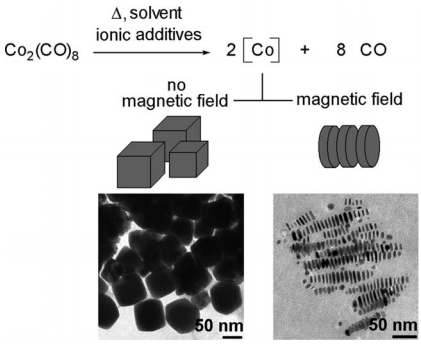

Spin-Canted Antiferromagnetism

Keywords: Cobalt / Bridging ligands / N ligands / Spin canting / Magnetic properties

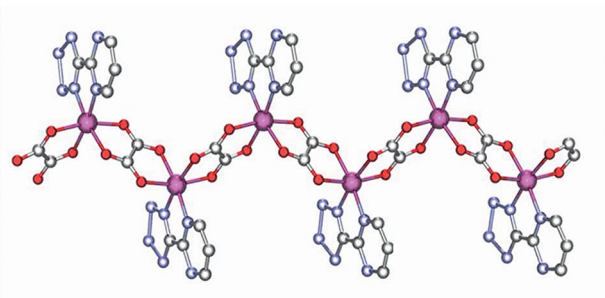

The neutral zig-zag oxalate bridged cobalt(II) chain complex [Co(μ-ox)(Hpmtz)] has been synthesized by hydrothermal techniques. Magnetic susceptibility measurements indicate that this compound shows a strong intrachain antiferromagnetic interaction and 3D weak ferromagnetic ordering at T_C = 6.5 K.

Acid Waves

Keywords: Water / Boron / Structure elucidation / Thermal analysis / Hydrogen bonds

The structure of $(H_3O)_2B_{12}F_{12}·nH_2O$ (n = 6) consists of a CCP array of $B_{12}F_{12}^{2-}$ anions intercalated with nonplanar networks of O_6 rings of H_3O^+ ions and H_2O molecules. The n = 6 compound rapidly and reversibly desorbs water in discrete stages to form n = 4, 2, and 0 phases, which demonstrate latent porosity.

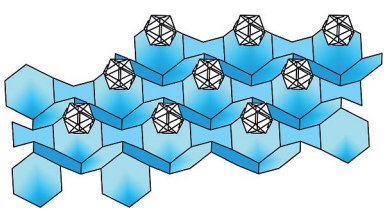

Thermal Decomposition of POMs

Keywords: In situ spectroscopy / Thermochemistry / Structure elucidation / Tungsten / Polyoxometalates

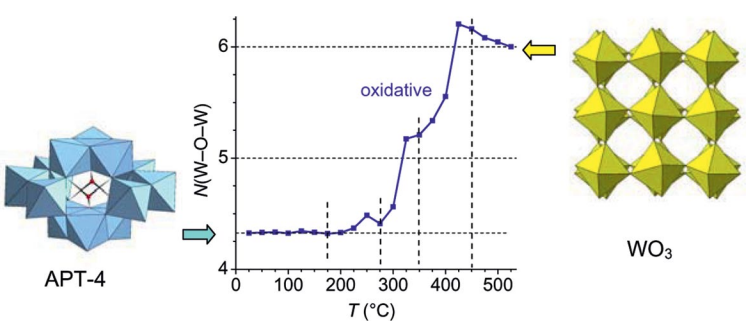

The graphic illustrates the stepwise increasing number of nearest tungsten ions due to thermally induced condensation of WO_6 octahedra, which was calculated from the edge energies of the ligand-to-metal charge transfer transitions of tungsten ions. These optical transitions, in turn, were determined from the in situ UV/Vis diffuse reflectance spectra while heating in oxidative and reductive atmospheres.

CONTENTS

FULL PAPERS

Rhenium Complexes

Keywords: Sugar–metal hybrid material / Carbohydrates / Glycosides / Rhenium / Ligand effects

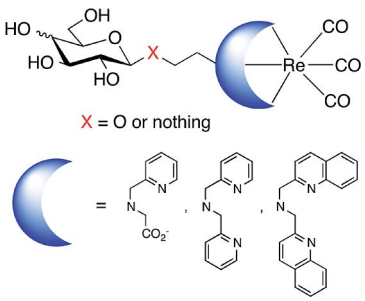

Twelve $[Re^{I}L(CO)_3]^{n+}$ (**L** = carbohydrate-pendant ligand; n = 1 or 0) complexes have been prepared. All complexes were incorporated into HeLa S3 cells. With respect to the corresponding Re^{I} complexes without the pendant carbohydrate functions, *N*-(2-pyridylmethyl)glycine complexes exhibited carbohydrate enhanced cellular uptake. The complexes stay in the cytosol and cannot penetrate into nucleus.

Photoactive Nanocrystallites

Keywords: Titania / Sol–gel processes / Heterogeneous catalysis / Nanoparticles / Self cleaning

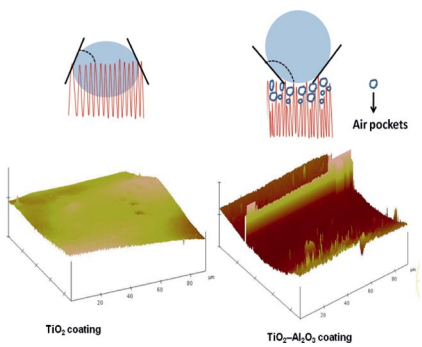

Titania–alumina nanocomposites were synthesized by an aqueous sol–gel route starting from titanyl sulfate. The titania–alumina composition containing 5 mol-% Al_2O_3 (TA-5), annealed at 700 °C, shows the highest photocatalytic activity. Nanocoatings developed over glazed ceramic surfaces indicated preferentially hydrophobic character.

Multifunctional Materials

Keywords: Redox chemistry / Materials science / Schiff bases / N ligands / Tetrathiafulvalene

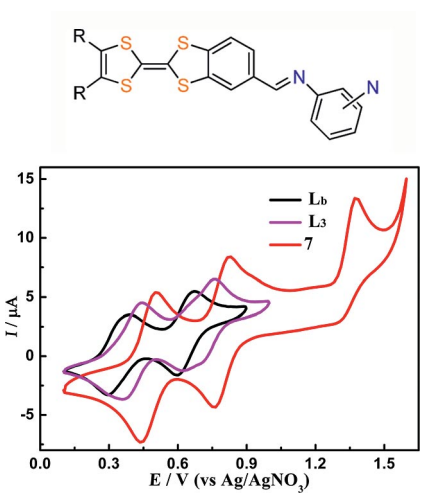

A series of π-extended tetrathiafulvalene (TTF) Schiff base ligands has been prepared. Four complexes have been prepared with these redox active ligands, and the electrochemical and spectroscopic behavior of these compounds have been studied. These new imine-bridged TTF ligands with diverse substitution patterns are useful for the syntheses and design of new metal complexes.

Organocadmium Compounds

Keywords: Cadmium / Hydrazine / Hydrazide / X-ray diffraction / NMR spectroscopy

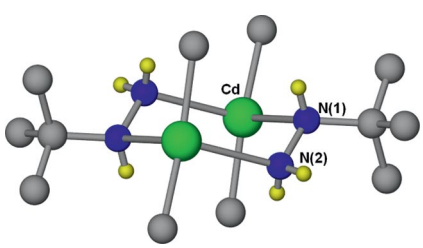

Hydrazine adducts $(Me_2CdL)_n$ [L = $H_2NN(H)tBu$, n = 2 (**1**); L = $H_2NN(CH_2CH_2)_2NMe$, n = ∞ (**2**)] with new structural motifs are reported, along with the conversion of **2** to the tetrameric hydrazide $[MeCdN(H)N(CH_2CH_2)_2NMe]_4$ (**4**), which forms a Cd_4N_8 cage.

Supported Catalysts

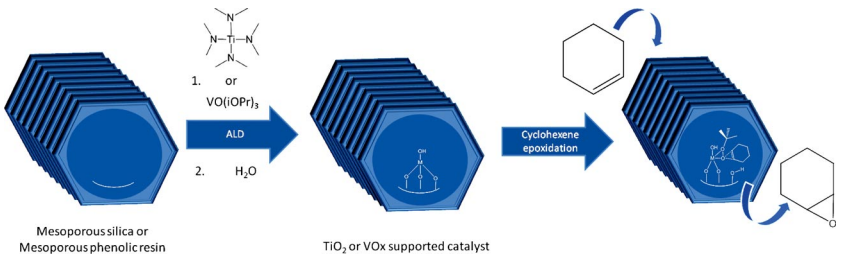

Keywords: Mesoporous materials / Heterogeneous catalysis / Epoxidation / Atomic layer deposition / Supported metal oxides

Supported titanium and vanadium oxide catalysts have been synthesised by atomic layer deposition. The influence of the support type (mesoporous silica vs. mesoporous phenolic resin) on the catalytic activity has been investigated. The support–oxygen–metal bond is assumed to be critical for catalytic behaviour.

Phosphenium Ion Pairs

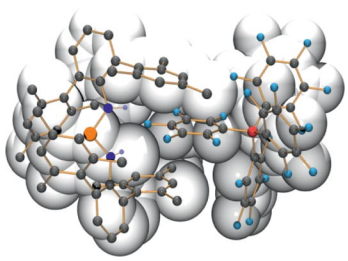

Keywords: Sensors / Cations / Anions / Phosphorus / Weakly coordinating anions / Bonding

The structure in bis(amino)phosphenium salts bearing different anions such as (F^-, Cl^-, $[CF_3CO_2]^-$, $[CF_3SO_3]^-$, $[B(C_6F_5)_4]^-$, $[GaCl_4]^-$, $[SbF_6]^-$, $[Al(OCH(CF_3)_2)_4]^-$ and the carborate $[CHB_{11}H_5Br_6]^-$) has been studied in detail. The bis(amino)phosphenium ion can be used as sensitive probe for the examination of anion properties as well as kind and degree of cation···anion interactions.

Double Bond Cleavage

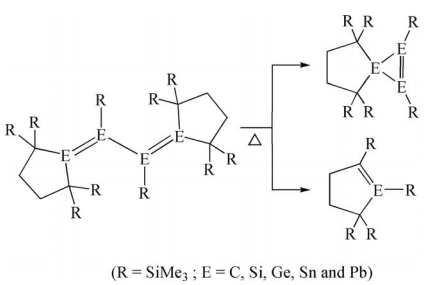

Keywords: Reaction mechanisms / Density functional calculations / Cleavage reactions / Cycloaddition

DFT results suggest that the thermolysis of heavy 1,3-butadienes with sterically overcrowded substituents can lead to two kinds of intramolecular reactions: cycloaddition and 1,2-migration. Our findings indicate that the heavier the group 14 atoms that participate in the intermediate carbene species, the more kinetically stable its intramolecular products.

Thiolate/Thioether Complexes

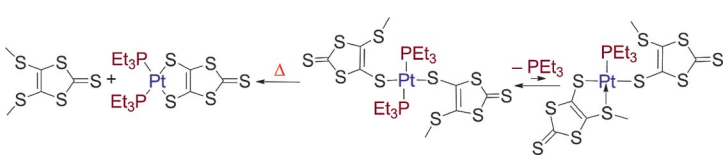

Keywords: Platinum / S ligands / Coordination modes / C–S activation

The thiolate/thioether ligand 4-methylthio-2-thioxo-1,3-dithiole-5-thiolate coordinates to a diphosphane platinum(II) centre by a firm metal–thiolate link and an incipient metal–thioether link. The dative interaction leads to the displacement of a phosphane ligand (hemilabile behaviour) or to the activation of the C–SMe bond on the platinum centre to generate a dithiolene complex.

CONTENTS

A fluorescent, colorimetric chemosensor, **L1**, based on 8-aminoquinoline, has been developed as a sensor for Zn^{2+}. **L1** exhibited high selectivity and sensitivity towards Zn^{2+} over other common metal ions in a physiological pH window with a 1:1 binding mode. Fluorescent imaging of Zn^{2+} in living cells has been successfully demonstrated.

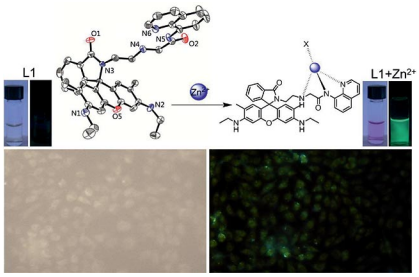

Keywords: Fluorescence / Zinc / N ligands / Colorimetric chemosensor / 8-Aminoquinoline / Cell imaging

* Author to whom correspondence should be addressed.

Supporting information on the WWW (see article for access details).

This article is available online free of charge (Open Access).

If not otherwise indicated in the article, papers in issue 1 were published online on December 23, 2011

On these pages, we feature a selection of the excellent work that has recently been published in our sister journals. If you are reading these pages on a computer, click on any of the items to read the full article. Otherwise please see the DOIs for easy online access through Wiley Online Library.

Facilitated Ion Transfer

T. J. Stockmann, Y. Lu, J. Zhang, H. H. Girault, Z. Ding*

Interfacial Complexation Reactions of Sr^{2+} with Octyl(phenyl)-*N*,*N*-diisobutylcarbamoylmethylphosphine Oxide for Understanding Its Extraction in Reprocessing Spent Nuclear Fuels

The extraction of strontium at a liquid|liquid microinterface, housed at the tip of a pulled capillary is described using "classical" octyl(phenyl)-*N*,*N*-diisobutylcarbamoylmethylphosphine oxide as a ligand. This system has wide applications as a sensor technology; in the recovery of fissile material and radioisotopes for medicinal use from nuclear waste; or in environmental recovery/reclamation projects. The thermodynamics of simple and facilitated ion transfer at the aqueous|ionic liquid interface are discussed.

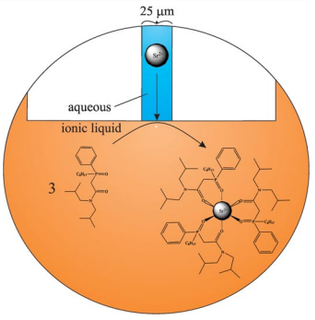

Chem. Eur. J.
DOI: **10.1002/chem.201102491**

Polymers

K. Kano,* T. Ochi, S. Okunaka, Y. Ota, K. Karasugi, T. Ueda, H. Kitagishi

Preparation and Function of Poly(acrylic acid)s Modified by Supramolecular Complex Composed of Porphinatoiron and a Cyclodextrin Dimer That Bind Diatomic Molecules (O_2 and CO) in Aqueous Solution

Finding hemo! Poly(acrylic acid) was functionalized by attaching a supramolecular chromophore composed of a ferrous porphyrin and a per-*O*-methylated β-cyclodextrin dimer with a pyridine linker that can bind diatomic molecules, such as oxygen and carbon monoxide, in aqueous solution.

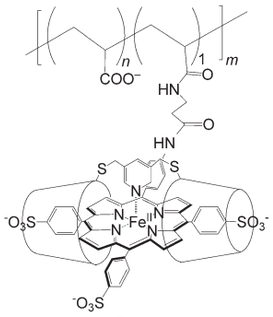

Chem. Asian J.
DOI: **10.1002/asia.201100354**

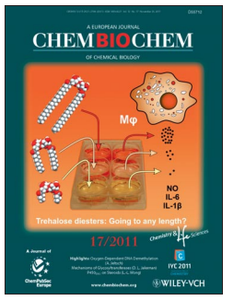

Cyclic Peptides

L. Sando, S. Troeira Henriques, F. Foley, S. M. Simonsen, N. L. Daly, K. N. Hall, K. R. Gustafson, M.-I. Aguilar, D. J. Craik*

A Synthetic Mirror Image of Kalata B1 Reveals that Cyclotide Activity Is Independent of a Protein Receptor

D **activated**: Positive results from hemolysis assays with the all-D isomer imply that the activity of cyclotide kalata B1 is primarily modulated by the lipid-bilayer environment and the self-assembly of cyclotides on the lipid membrane rather than depending on the recognition of chiral receptors.

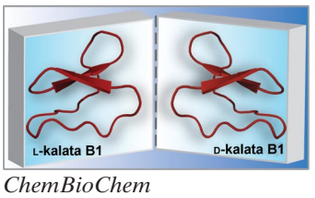

ChemBioChem
DOI: **10.1002/cbic.201100450**

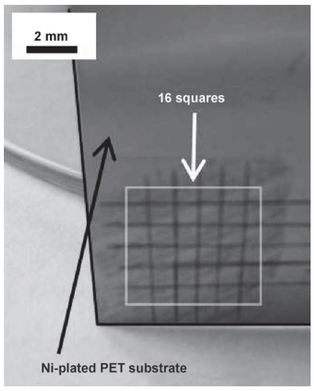

ChemPhysChem
DOI: **10.1002/cphc.201100562**

Metal Plating

A. Garcia, T. Berthelot,* P. Viel, P. Jégou, S. Palacin

3D Amino-Induced Electroless Plating: A Powerful Toolset for Localized Metallization on Polymer Substrates

Patterns on polymers: A cost-effective process based on a versatile one-step technique to graft covalent thin polymer films for localized electroless metal plating on polymers, such as flexible and transparent poly(ethylene terephtalate) sheets, is demonstrated (see picture).

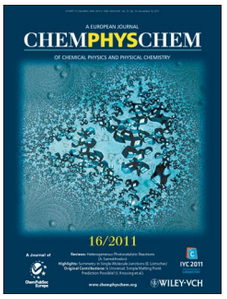

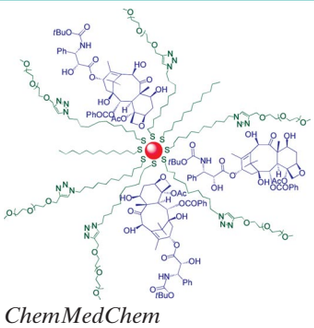

ChemMedChem
DOI: **10.1002/cmdc.201100311**

Antitumor Agents

A. François, A. Laroche, N. Pinaud, L. Salmon, J. Ruiz, J. Robert,* D. Astruc*

Encapsulation of Docetaxel into PEGylated Gold Nanoparticles for Vectorization to Cancer Cells

Right on target: Herein we describe the preparation of *click* PEGylated gold nanoparticles that encapsulate and solubilize docetaxel for specific delivery to cancer cells. These nanovectors were characterized spectroscopically and tested against cultured tumor cells as a preliminary in vitro assessment of their anticancer properties.

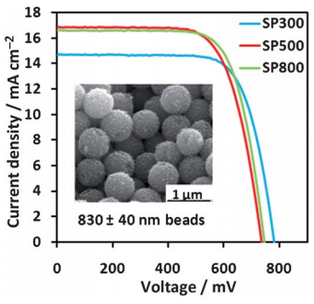

ChemSusChem
DOI: **10.1002/cssc.201100060**

Solar Cells

Y. Chen, F. Huang, D. Chen, L. Cao, X. L. Zhang, R. A. Caruso, Y.-B. Cheng*

Effect of Mesoporous TiO_2 Bead Diameter in Working Electrodes on the Efficiency of Dye-Sensitized Solar Cells

Big beads better: The effect of the diameter of mesoporous TiO_2 beads in dye-sensitized solar cells is studied. Cells with larger beads achieve the highest conversion efficiency, mainly because of their higher electron diffusion coefficient.

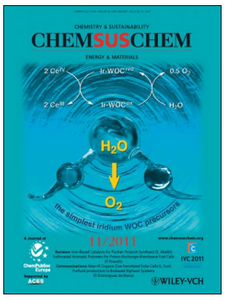

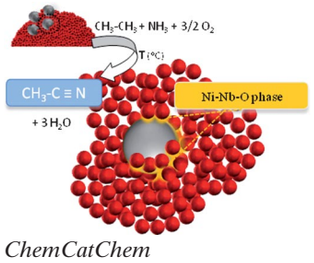

ChemCatChem
DOI: **10.1002/cctc.201100115**

Ammoxidation

F. Rubio-Marcos,* E. Rojas, R. López-Medina, M. O. Guerrero-Pérez, M. A. Bañares, J. F. Fernandez

Tuning of Active Sites in Ni–Nb–O Catalysts for the Direct Conversion of Ethane to Acetonitrile or Ethylene

Spreading the activity: The results of this study demonstrate that NiO nanoparticles are active for ethane activation and that their catalytic performance can be modulated through the use of the appropriate support. These nanoparticles are dispersed on the surface of two different Nb_2O_5 materials by using a novel dry nanodispersion method. The catalysts obtained by the proposed route are promising catalytic materials for the ethane ammoxidation.

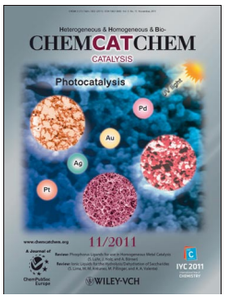

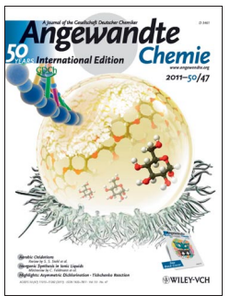

Nanomaterials

M. Böhmler, Z. Wang, A. Myalitsin, A. Mews, A. Hartschuh*

Optical Imaging of CdSe Nanowires with Nanoscale Resolution

Down to the wire: High-resolution photoluminescence (PL) and Raman images of CdSe nanowires were obtained using tip-enhanced near-field optical microscopy. They show that the optical properties of the CdSe nanowires vary significantly within a few nanometers leading to strong spatial fluctuations in both PL intensities and energies (see picture).

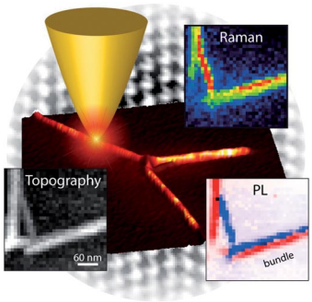

Angew. Chem. Int. Ed.
DOI: **10.1002/anie.201105217**

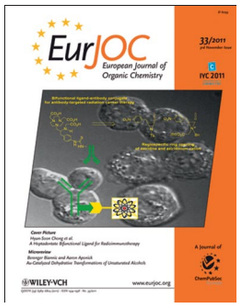

Enzymatic Deprotection

T. Bavaro, M. Filice,* P. Bonomi, Q. Abu alassal, G. Speranza, J. M. Guisan, M. Terreni

Regioselective Deprotection of Peracetylated Disaccharides at the Primary Position Catalyzed by Immobilized Acetyl Xylan Esterase from *Bacillus pumilus*

A novel regioselective deprotection at the C6′ position of peracetylated β-methyl lactoside, β-methyl lactosaminide, and lactal catalyzed by immobilized acetyl xylan esterase from *Bacillus Pumilus* was developed.

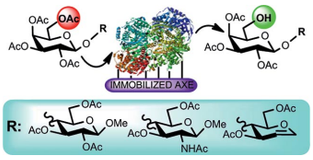

Eur. J. Org. Chem.
DOI: **10.1002/ejoc.201100944**

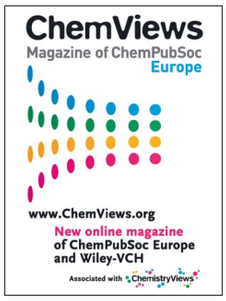

Women in Chemistry – Interview with Supawan Tantayanon

Vera Köster

Women in Chemistry – Interview with Supawan Tantayanon

2011 is the International Year of Chemistry and the centenary of Marie Curie's Nobel prize in Chemistry. Therefore, ChemViews introduces interesting women throughout the year. Professor Supawan Tantayanon, Chulalongkorn University, Thailand, is the first female president of the Federation of Asian Chemical Societies.

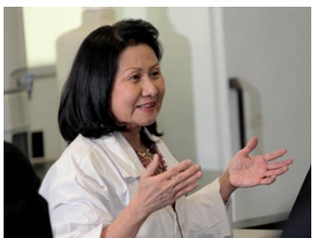

ChemViews magazine
DOI: **10.1002/chemv.201000099**

DOI: 10.1002/ejic.201100957

Well-Defined Heterometallic and Unsymmetric M_2O_2 Complexes Arising from Binding and Activation of O_2

Isaac Garcia-Bosch,[a] Xavi Ribas,*[a] and Miquel Costas*[a]

Keywords: Oxygen / Oxygen binding / Oxygen activation / Bioinorganic chemistry / Coordination modes / Unsymmetric complexes

Oxygen binding and activation reactions at dimetal sites constitute chemical processes of fundamental interest, because of the implication of these reactions in biology, chemical synthesis, and catalysis. This account collects and discusses studies of O_2 binding and/or activation by inequivalent dimetal sites, and it specially focuses on systems in which O_2-bound reaction intermediates have been experimentally characterized. Homometallic unsymmetric systems and heterometallic complexes are reviewed, and their chemistry in oxidative transformations is described. Introduction of asymmetry into M_2O_2 cores poses important challenges to their preparation, and strategies developed to address this problem are discussed. Distinct spectroscopic and chemical properties emerge from these unsymmetric systems.

Introduction

The dioxygen molecule plays key roles in aerobic organisms. On one hand, O_2 is the terminal electron acceptor in cellular respiration.[1–4] On the other hand, dioxygen is used by metalloenzymes as oxidant in metabolic oxidation reactions.[5–10] Because of kinetic barriers associated to spin conservation rules, the reaction of O_2 with closed-shell organic molecules is generally very slow. For these reactions to proceed, the O_2 molecule needs to be activated, most commonly by interacting with redox-active transition metals.[11] A number of enzymes use a dimetallic site to bind and activate O_2.[6,9] This activation involves reduction of the O_2 molecule to form reactive species such as superoxides, peroxides, or metal oxide species. In most of the cases in which two metal centers participate synergistically in the binding and activation of O_2, the two metal sites are not equivalent. This lack of equivalence can have different causes: (a) The metals may be different, such as, for example, in cytochrome *c* oxidases, where a heme–copper dinuclear site performs the $4e^-$ reduction of O_2 as the last step in cellular respiration (Figure 1a),[3,4] or Cu–Zn superoxide dismutases,[12] where the superoxide disproportionation is mediated by a heterometallic Cu–Zn center (Figure 1b). (b) The asymmetry may also arise from a distinct coordination environment, for example, dopamine-β-hydroxylase (DβH),[13,14] peptidylglycine-α-hydroxylating monooxygenase (PHM, Figure 1c)[15,16] and also tyrosinase (Tyr, Figure 1d).[17,18] In the first two cases, the coordination environment of the two copper ions is different. In the case of Tyr, the differences of the second coordination sphere render the two metal ions inequivalent.[17]

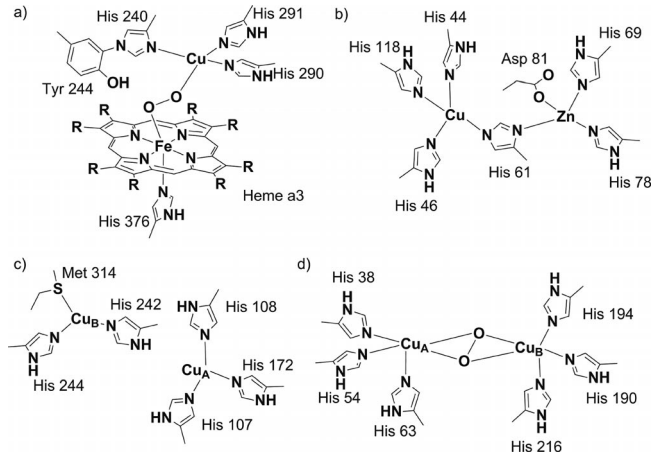

Figure 1. Active centers of: (a) cytochrome *c* oxidase in the O_2-bound form (*Cc*O), (b) CuZn superoxide dismutase (CuZnSOD), (c) peptidylglycine-α-hydroxylating monooxygenase (PHM), and (d) O_2-bound form of tyrosinase (oxy–Tyr).

Because of the biological relevance of O_2-binding and O_2-activation reactions at transition metal ions, and also because of the potential technological interest that these reactions can have in the field of selective oxidation catalysis, the O_2 chemistry of transition metal coordination complexes has been extensively investigated, and particular emphasis has been traditionally placed on examples containing biologically relevant first-row transition metal ions.[19–27]

The immense majority of the biomimetic synthetic dinuclear complexes developed so far contains metal ions with the same coordination geometry, and symmetric binding

[a] QBIS Research Group, Departament de Química, Universitat de Girona, Facultat de Ciències,
Campus de Montilivi, 17071 Girona, Spain
Fax: +34-972-418150
E-mail: miquel.costas@udg.edu
xavi.ribas@udg.edu

modes are adopted by the O_2 molecule when interacting with the complex.[19,20,22,24–28] Oxygen activation at unsymmetric and heterometallic sites remains much less explored. The study of O_2 binding and activation at unsymmetric dimetal cores is interesting, because it can provide a fundamental understanding of enzymatic O_2-binding/activation reactions, but it may also allow the preparation of novel species exhibiting alternative reactivity patterns relative to symmetric species. Such novel oxidation chemistry may also lead to the development of catalytic processes exhibiting hitherto unprecedented selectivities.

The purpose of the present work is to provide a brief collection of well-defined unsymmetric M_2O_2 systems described so far, while paying special attention to those that contain copper ions. Systems that implicate porphyrin units are not covered in this account.

Synthetic Strategies

Preparing unsymmetric [(LM)(LM′O_2] species (L stands for ligand and M for transition metal) is inherently more complicated than synthesizing their symmetric analogues. The most common methodology employed to prepare symmetric M_2O_2 species involves the reaction of O_2 with mononuclear LM synthons, resulting in the spontaneous self-assembly of the dimetallic O_2 core. However, this methodology is unsuitable for unsymmetric systems, because of the possible formation of mixtures of products. In order to address this problem, two main strategies have been pursued, as depicted in Scheme 1.

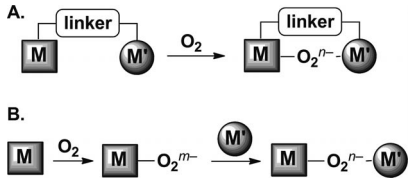

Scheme 1. Two main strategies used in the development of unsymmetric complexes for the activation of O_2.

One of the strategies consists of the design of ligands that have two different binding sites with distinct coordination environments for the two metals (Scheme 1A). In this case, the preparation of the unsymmetric ligand usually constitutes a more significant synthetic challenge. Nevertheless, in the case of heterometallic complexes, the most challenging aspect is to accomplish site-selective metal binding and to avoid the formation of mixtures.

On the other hand, unsymmetric complexes can be obtained by the reaction between a preformed LM–O_2 synthon with a reduced metal complex L′M′, to form a LM–O_2–M′L′ species (Scheme 1B). In this case, the challenge resides in finding complexes that preclude the formation of LM–O_2–ML species. This is generally accomplished by using sterically hindered ligands L.

In Figure 2, LM–O_2–M′L′ complexes are classified on the basis of the strategy employed in their preparation, and this classification is illustrated with examples taken from the literature. For comparative purposes, symmetric systems have also been included (Figure 2a, e).[29,30] As shown in

Isaac Garcia-Bosch obtained his degree in Chemistry at the University of Girona in 2006. He then started his PhD studies in the QBIS group under the supervision of Dr. Miquel Costas and Dr. Xavi Ribas. His research interests include: (i) the design of bioinspired non-porphyrinic manganese complexes as catalysts for the epoxidation of alkenes under environmentally benign conditions, (ii) C–H activation by high-valent non-porphyrinic manganese complexes, and (iii) biomimetic inorganic complexes of copper-based enzymes for the activation of O_2.

Xavi Ribas obtained his PhD degree in Chemistry at the University of Girona in 2001. He then moved to the ICMAB-CSIC laboratories with a postdoctoral fellowship. In 2004 he got a Juan de la Cierva postdoctoral contract and returned to Girona, where he is currently an associate professor since 2006. In early 2011, he received an ICREA Acadèmia Award, and in July 2011 he was awarded an ERC-Starting Grant. His research interests include the design of transition metal catalysts for C–heteroatom cross-coupling reactions, as well as the design of bioinspired Mn and Fe catalysts for alkane and alkene oxidation, and the synthesis of bioinorganic models of copper-based enzymes capable of O_2 activation.

Miquel Costas graduated in chemistry at the University of Girona (UdG) in 1994, where he also pursued PhD studies. Research work during his PhD involved scientific stays at Texas A&M University under the supervision of late Prof. Derek Barton (1996) and in Basel with the group of Prof. Andreas Zuberbühler (1998). After defending his PhD dissertation, he moved to the group of Prof. Lawrence Que Jr. at the University of Minnesota. In September 2002 he returned to Girona with a Ramon I Cajal Fellowship and become professor in April 2003. His research interests involve the fundamental understanding of the mechanisms of O_2 activation and/or substrate oxidation taking place at transition metal ions that have biological relevance, especially Fe, Cu, and Mn, and application of this knowledge to the development of bioinspired oxidation catalysts to carry out selective oxidation reactions under environmentally benign conditions. In 2008 he received the ICREA Acadèmia Award from the Generalitat de Catalunya, and was awarded an ERC Starting Grant.

Figure 2, in both strategies the lack of symmetry can arise from the nature of the metal ion (M ≠ M′, Figure 2c),[31] the first coordination sphere of the metal ions (L ≠ L′, Figures 2b, f),[32,33] or both (LM ≠ L′M′, Figures 2d, g).[27,34]

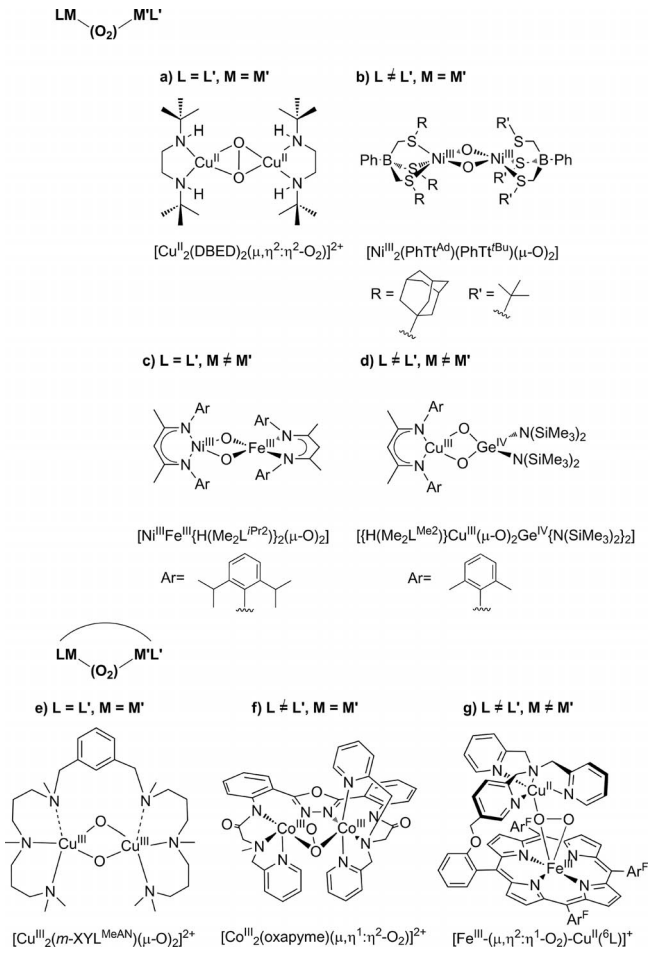

Figure 2. Illustrative examples of symmetric and unsymmetric well-defined LM–(O_2)–M′L′ complexes. Top (a–d): complexes prepared by stepwise combination of O_2 with two LM synthons. Bottom (e–g): complexes prepared from reaction of an unsymmetric dimetallic complex with O_2.

Formation of Unsymmetric Complexes by Reaction between M–O_2 Complexes with Reduced Species M′

Pioneer work in the field was reported by van Koten and co-workers, who described that organometallic complexes $[Pd^{II}L^{N2}(Cl)(R)]$ (L^{N2} is a bidentate N-based ligand, and R is an aryl group) (**1**) reacted with oxidomolybdenum diperoxide complex $[Mo^{VI}O(O_2)_2{\cdot}HMPT{\cdot}H_2O]$ (HMPT = hexamethylphosphoric triamide) (**2**) to form the corresponding aryl halide (R–X).[35] When L^{N2} is a sterically hindered ligand, R–OR′ products form instead in R′OH solvent. The authors proposed that reaction between the molybdenum peroxide and the Pd^{II} complex occurs via a $Pd^{IV}(\mu\text{-}O)_2$-Mo^{VI} (**3**) species (Figure 3) in a formal oxidative addition reaction. This intermediate evolves by reductive elimination forming R–X, unless the Pd ion is bound to a sterically hindered ligand. In the latter case, reductive elimination results in C–O bond formation.

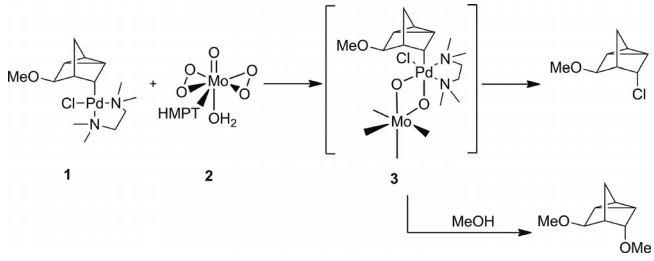

Figure 3. Proposed mechanism for the formation of C–X and C–O bonds via a $Pd^{IV}(\mu\text{-}O)_2Mo$ intermediate.

More recently, Carpenter and co-workers used an isolable complex $[(Ph_3P)_2Pt^{II}(\eta^2\text{-}O_2)]$ (**4a**) to react with $Ge^{II}[N(SiMe_3)_2]_2$ (**5**) to yield heterodimetallic complex $[(Ph_3P)_2Pt^{II}(\mu\text{-}O)_2Ge^{IV}\{N(SiMe_3)_2\}_2]$ (**6a**) (Figure 4, top).[36] The reaction of $[(Ph_3P)_2PtGe^{II}\{N(SiMe_3)_2\}_2]$ (**7a**) with O_2 also affords **6a**. Interestingly, the direct reaction of the complex $[(Et_3P)_2PtGe^{II}\{N(SiMe_3)_2\}_2]$ (**7b**) with O_2 in the absence of light leads to a rare complex $[(Et_3P)_2Pt^{I}(\mu\text{-}\eta^1\text{:}\eta^1\text{-}O_2)Ge^{III}\{N(SiMe_3)_2\}_2]$ (**8**), which was crystallographically characterized. When this complex was exposed to light, O–O bond cleavage occurred to yield the crystallographically characterized complex $[(Et_3P)_2Pt^{II}(\mu\text{-}O)_2Ge^{IV}\text{-}\{N(SiMe_3)_2\}_2]$ (**6b**).

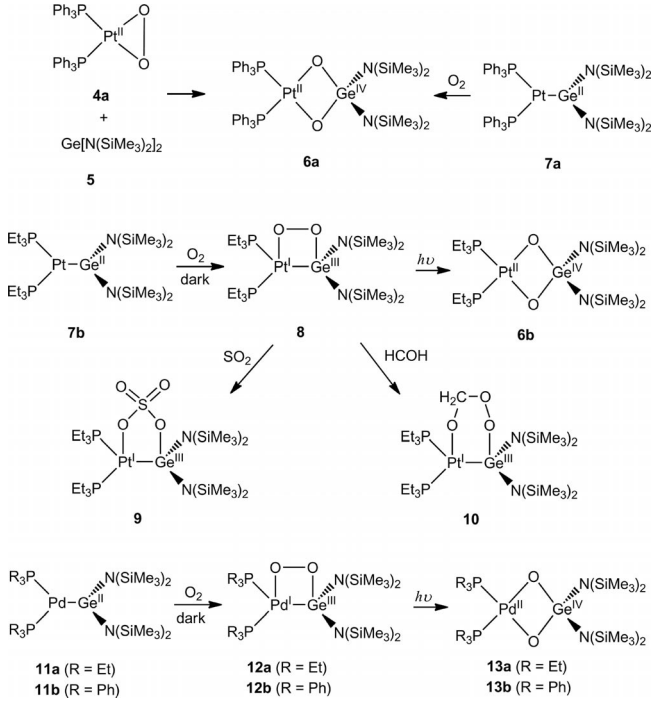

Figure 4. Schematic diagram of O_2 chemistry for heterometallic Pt–Ge complexes.

Peroxide complex $[(Et_3P)_2Pt^{I}(\mu\text{-}\eta^1\text{:}\eta^1\text{-}O_2)Ge^{III}\{N(SiMe_3)_2\}_2]$ (**8**) does not react with CO_2, alkenes, alkynes, alkyl and arylphosphanes, but it reacts with SO_2 and H_2CO.

Reaction with SO_2 results in the oxidation of SO_2 and in the formation of $[(Et_3P)_2Pt^{I}(\mu\text{-}\eta^2\text{-}SO_4)Ge^{III}\{N(SiMe_3)_2\}_2]$ (**9**). Reaction with formaldehyde results in the insertion of formaldehyde into the Pt–O bond to form $[(Et_3P)_2Pt^{I}(\mu\text{-}\eta^2\text{-}OCH_2OO)Ge^{III}\{N(SiMe_3)_2\}_2]$ (**10**). This data is consistent with the nucleophilic character of the peroxide moiety.

Analogous germylene complexes $[(R_3P)_2PdGe^{II}\{N(SiMe_3)_2\}_2]$ (**11a**, R = Et; **11b**, R = Ph) also react with O_2 to produce complexes with $Pd^{I}(\mu\text{-}\eta^1\text{:}\eta^1\text{-}O_2)Ge^{III}$ (**12a**, **12b**) and $Pd^{II}(\mu\text{-}O)_2Ge^{IV}$ (**13a**, **13b**) cores, but both complexes were unstable.[37]

Following the same strategy, Tolman and co-workers used an isolable $LCuO_2$ complex, where L stands for a sterically bulky β-diketiminate ligand, to synthesize unsymmetric $LCu^{III}(\mu\text{-}O)_2Cu^{III}L'$ complexes by reaction with a second mononuclear $L'Cu^{I}$ synthon.[38] A key aspect in this strategy is the use of a bulky β-diketiminate ligand, which allowed the isolation of complexes $[H(Me_2L^{iPr2})Cu^{III}(\eta^2\text{-}O_2)]$ (**14a**) and $[H(Me_2L^{Me2})Cu^{III}(\eta^2\text{-}O_2)]$ (**14b**) (Figure 5). The bulky nature of the β-diketiminate ligand prevents the formation of symmetric $LCu^{III}(\mu\text{-}O)_2Cu^{III}L$ species. In addition, its anionic character likely contributes to the stabilization of the copper(III) oxidation state. Once the monomeric moiety **14** was isolated, it was used as a building block to generate unsymmetric species $[H(Me_2L^{iPr2})Cu^{III}(\mu\text{-}O)_2Cu^{III}L']$ (**15**) {L′ = $H(Me_2L^{Me2})$, Me_3TACN, TMPDA} by reaction with a second $L'Cu^{I}$ complex (Figure 5, top). Moreover, the $[H(Me_2L^{iPr2})Cu^{III}(\eta^2\text{-}O_2)]$ moiety was combined with other metal complexes to generate heterometallic complexes containing $[Cu^{III}(\mu\text{-}O)_2Ni^{III}]$ (**16**)[39] and $[Cu^{III}(\mu\text{-}O)_2Ge^{IV}]$ (**17**) cores.[34] Likewise, $[(PPh_3)_2M^{II}(\eta^2\text{-}O_2)]$ (M = Pt, Pd) (**4a**, **4b**) could be isolated and subsequently were used to obtain complexes $[(PPh_3)_2M^{II}(\mu\text{-}O)_2Cu^{III}H(Me_2L^{Me2})]$ (M = Pt, **18a**; M = Pd, **18b**) (Figure 5, bottom).[40] Furthermore, the use of $[(PPh_3)_2M^{II}(\eta^2\text{-}O_2)]$ allowed the preparation of $[(PPh_3)_2M^{II}(\mu\text{-}O)_2Cu^{III}\text{-}(TMPDA)]$ (M = Pt, **19a**, M = Pd, **19b**) and $[(PPh_3)_2M^{II}(\mu\text{-}O)_2Cu^{III}(iPr_3TACN)]$ (M = Pt, **20a**; M = Pd, **20b**), for which the $LCu^{III}(\eta^2\text{-}O_2)$ moiety is not isolable because it undergoes fast dimerization.

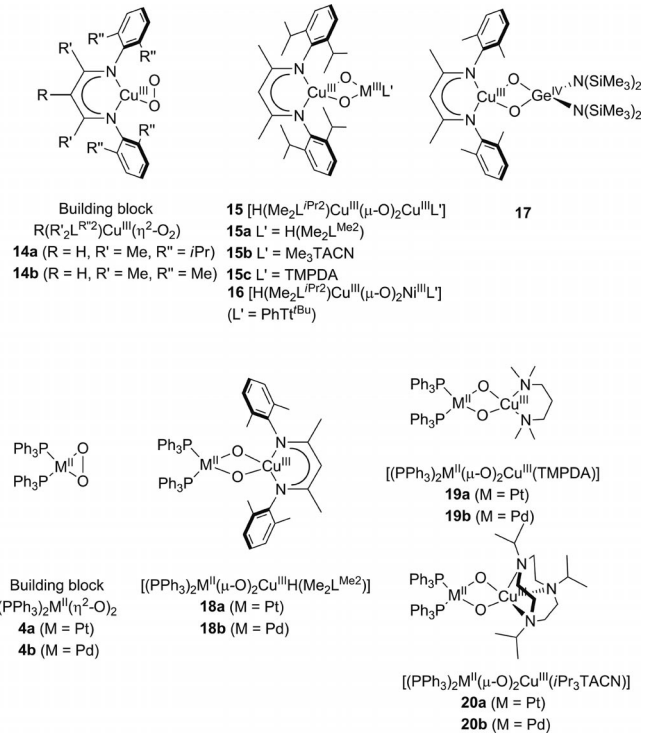

Figure 5. Structural diagram of heterometallic $Cu(\mu\text{-}O)_2M$ complexes.

Access to this set of complexes allows comparison between the reactivity of symmetric and unsymmetric complexes towards exogenous substrates (Figure 6). $[(PPh_3)_2Pt^{II}(\mu\text{-}O)_2Cu^{III}H(Me_2L^{Me2})]$ (**18a**) acted as a nucleophile in the presence of substrates such as $[NH_4](PF_6)$ (weak acid) or CO_2, while symmetric complex $[H(Me_2L^{Me2})_2Cu^{III}{}_2(\mu\text{-}O)_2]$ (**21**) showed no reaction with these substrates. The symmetric $Cu^{III}{}_2(\mu\text{-}O)_2$ complex **21** does not oxidize substrates such as 9,10-dihydroanthracene (9,10-DHA), thioanisole, or 1-decene, which usually undergo electrophilic oxidations by $Cu^{III}{}_2(\mu\text{-}O)_2$ cores. The authors suggested that the low reactivity exhibited by the symmetric $Cu^{III}{}_2(\mu\text{-}O)_2$ core could be due to the inhibition of substrate approach by the bulky β-diketiminate ligand or because the anionic character of one of the ligands quenches the electrophilicity of the Cu_2O_2 core. When the complexes were tested in the oxidation of 2,4-di-*tert*-butylphenol, another interesting behavior was found: while the homometallic complex was not able to oxidize the phenol, the heterometallic complex reacted via hydrogen atom abstraction from the O–H bond, forming the C–C coupling product. It was proposed that the higher basicity of the unsymmetric $Pt^{II}(\mu\text{-}O)_2Cu^{III}$ allowed the deprotonation of the substrate, which preceded the electron transfer from the bound phenolate to the copper center.

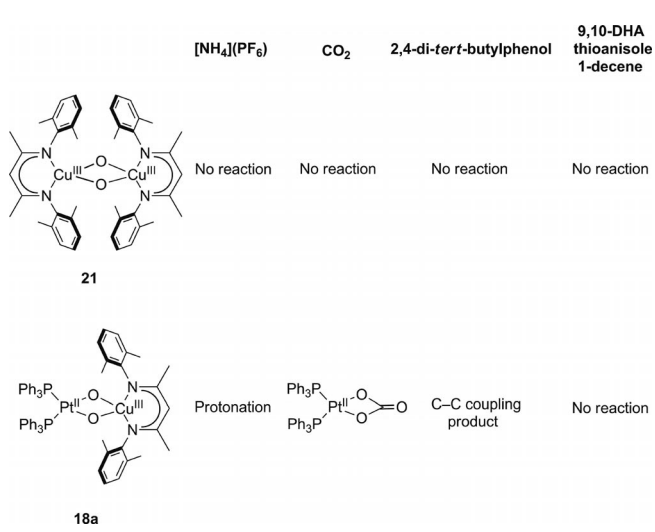

Figure 6. Reactivity of heterometallic complex $[(PPh_3)_2Pt^{II}(\mu\text{-}O)_2\text{-}Cu^{III}H(Me_2L^{Me2})]$ (**18a**) in comparison with that of its homometallic symmetric analog $[\{H(Me_2L^{Me2})\}_2Cu^{III}{}_2(\mu\text{-}O)_2]$ (**21**).

This methodology was extended to nickel by Riordan and co-workers.[32] The isolation of the mononuclear com-

plex $\{[PhTt^{Ad}]Ni^{II}(\eta^2\text{-}O_2)\}^+$ (**22**) provided the possibility to generate a homometallic unsymmetric complex $\{[PhTt^{Ad}]\text{-}Ni^{III}(\mu\text{-}O)_2Ni^{III}[PhTt^{tBu}]\}^{2+}$ (**23**) (Figure 7).

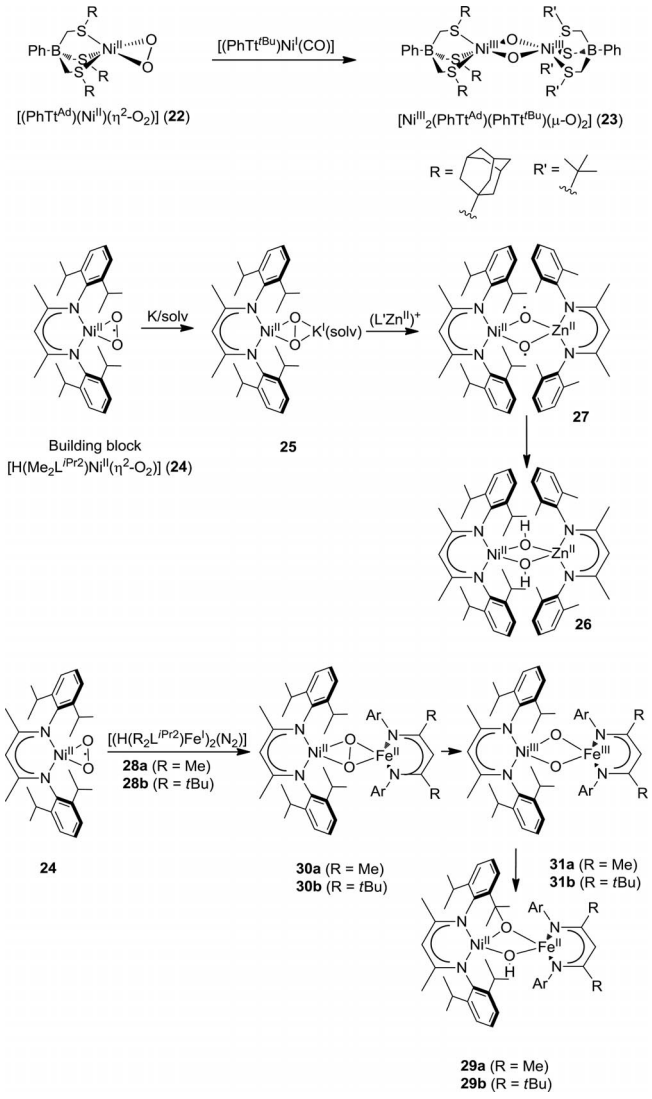

Figure 7. Homometallic unsymmetric Ni^{III}_2 complexes developed by Riordan and co-workers and heterometallic Ni–(O_2)–M complexes developed by Driess, Limberg, and co-workers.

Combining the copper and nickel precedents, Driess, Limberg, and co-workers developed a novel family of Ni–O_2–M complexes. The basic structure of this series of compounds is a mononuclear side-on superoxidonickel compound $[H(Me_2L^{iPr2})Ni^{II}(\eta^2\text{-}O_2)]$ (**24**) bearing a bulky β-diketiminate ligand $H(Me_2L^{iPr2})$ (Figure 7).[41] Similar to the analogous copper complex reported by Tolman, $[H(Me_2\text{-}L^{iPr2})Cu^{III}(\eta^2\text{-}O_2)]$ (**14a**), the bulky nature of the ligand prevents the formation of dimers. However, while **14a** was best formulated as a side-on peroxide compound, **24** was unequivocally described as a side-on superoxide complex on the basis of X-ray diffraction and several spectroscopic (IR, EPR, NMR) and theoretical (DFT calculations) tools. Complex **24** is remarkably stable, and it can be isolated as crystals and handled at room temperature, which makes it a good candidate as a building block for the construction of heterometallic nickel/metal–dioxygen species. Moreover, the cyclic voltammetry of **24** shows a quasireversible redox wave at $E_{1/2}$ = –0.98 V (vs. Fc^+/Fc), which indicates that this compound can be easily reduced by one electron to give the corresponding peroxide compound.[42] Indeed, Driess, Limberg, and co-workers have reported the easy reduction of **24** by low-valent metal complexes to give a series of heterometallic complexes with Ni–(O_2)–K, Ni–(O_2)–Zn, and Ni–(O_2)–Fe cores.[42,43] A clean one-electron chemical reduction of **24** was achieved by reaction with metallic potassium, which led to the formation of a heterometallic peroxide complex with a $Ni^{II}(\mu\text{-}\eta^2\text{:}\eta^2\text{-}O_2)K^I$(solvent) (**25**) moiety. This compound exhibits diamagnetic behavior; it is thermally stable and could be characterized by X-ray analysis.

Surprisingly, substitution of the potassium center by the redox-inactive zinc(II) did not retain the peroxide structure, but instead a diamagnetic heterometallic complex with a $Ni^{II}(OH)_2Zn^{II}$ core (**26**) was formed. Theoretical calculations helped to shed light on this process. While in **25** the singlet ground state is the most stable configuration, the ground state of the hypothetical intermediate species with a $Ni^{II}(\mu\text{-}O_2)Zn^{II}$ moiety corresponds to a triplet configuration defined as a $Ni(\mu\text{-}O^{\cdot})_2Zn$ (**27**) species, containing two oxide moieties with a strong radical character. This biradical compound is highly reactive, and it is responsible for the hydrogen-atom abstraction from an exogenous source (e.g. solvent) to give the isolated bis(hydroxide) compound **26**. Finally, the reaction of superoxidonickel building block **24** with redox-active iron(I) precursor $[\{H(R_2L^{iPr2})\text{-}Fe^I\}_2(N_2)]$ (**28**) yielded compound **29**, in which intramolecular ligand oxidation had occurred. This oxidation process entails the hydroxylation of an unactivated C–H bond, which, in turn, requires the formation of a highly reactive intermediate species. Despite the fact that no transient intermediates could be isolated in this process, DFT calculations suggested the stepwise reduction of the superoxide unit in **24** to the peroxide **30** and bis(μ-oxide) **31** moieties upon reaction with the iron(I) center. Compound **31** with the general formula $[H(Me_2L^{iPr2})Ni^{III}(\mu\text{-}O)_2Fe^{III}H\text{-}(R_2L^{iPr2})]$ was postulated as the highly reactive species responsible for ligand oxidation. Unfortunately, these interesting species could not be directly detected by experimental means.

Very recently, Tolman and co-workers described a new mononuclear anionic copper(II) complex **32**, which led to the formation of an end-on superoxide complex **33** by reaction with KO_2 (Figure 8). Complex **33** is supported by a sterically hindered pyridinedicarboxamide ligand and adopts a tetragonal coordination geometry. Compound **33** can then be used as a building block for the synthesis of other unsymmetric complexes,[44] as illustrated by its reaction with $[Cu^I(tpa)(CH_3CN)](CF_3SO_3)$ (**34**) to yield dicopper complex **35** exhibiting an unsymmetric $Cu^{II}_2(\mu\text{-}\eta^1\text{:}\eta^1\text{-}O_2)$ core.

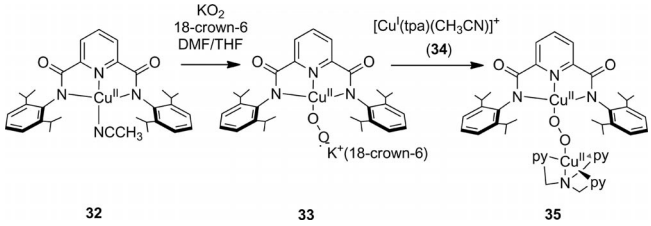

Figure 8. Schematic diagram for the synthesis of an unsymmetric Cu_2O_2 complex with a $Cu^{II}_2(\mu\text{-}\eta^1\text{:}\eta^1\text{-}O_2)$ core assembled from the reaction of a $LCu^{II}O_2$ complex and a second $L'Cu^{I}$.

Formation of Unsymmetric Complexes by Reaction of LMM′L′ Complexes with Molecular Oxygen

A different strategy to build unsymmetric complexes is based on the design of ligands that possess two different coordination environments. A prototypical example is the set of model complexes that have been prepared and studied as models for the enzyme cytochrome *c* oxidase, in which two distinct binding sites are connected by different linkers.[27,45] In this case, one of the two sites is a porphyrin complex, while the second one contains a non-porphyrin, N-based ligand (see Figure 2g). Unsymmetric complexes are relatively common in the literature, but only few reports describe the formation of well-defined M_2O_2 species from O_2 binding/activation reactions or from the reaction with reduced forms of O_2 such as superoxides or peroxides.

Pioneer work done by Karlin and co-workers comprised four different unsymmetric xylyl-type ligands, each of which was used to synthesize the corresponding dicopper(I) complex.[46–48] A rich chemistry was observed when the complexes were exposed to molecular oxygen (Figure 9). In first place, when $[Cu^{I}_2(UN)]^{2+}$ (**36**) reacted with O_2 at low temperatures, a side-on peroxidodicopper complex $[Cu^{II}_2(UN)(\mu\text{-}\eta^2\text{:}\eta^2\text{-}O_2)]^{2+}$ (**37**) was obtained, which subsequently underwent aryl oxidation of the UN ligand to generate hydroxy-bridged dicopper complex **38**. Related behavior was also observed for the analogous $[Cu^{I}_2(UN2)]^{2+}$ complex. In second place, $[Cu^{I}_2(UN\text{–}OH)]^{2+}$ (**39**) (Figure 9) reacted with O_2 at –80 °C to form $[Cu^{II}_2(UN\text{–}O)(OOH)]^{2+}$ (**40**), a hydroperoxidodicopper(II) complex. Thirdly, the oxygenation of the related complex, $[Cu^{I}_2(UN\text{–}O^{-})]^{+}$ (**41**), gave the corresponding $[Cu^{II}_2(UN\text{–}O^{-})(O_2)]^{+}$ (**42**). Interestingly, the latter complex undergoes a one-electron oxidation to produce unsymmetric superoxidodicopper(II) complex **43**. This complex was also obtained by initial chemical oxidation of the $[Cu^{I}_2(UN\text{–}O^{-})]^{+}$ precursor **41** with $[Fe(Cp)_2]^{+}$ to form mixed-valence copper(I)–copper(II) complex **44**, followed by exposure to molecular O_2. Finally, hydroperoxidodicopper(II) complex **40** was also prepared by protonation of $[Cu^{II}_2(UN\text{–}O^{-})(O_2)]^{+}$ (**42**).

The oxidation ability of complexes $[Cu^{II}_2(UN\text{–}O^{-})(O_2)]^{+}$ (**42**) and $[Cu^{II}_2(UN\text{–}O)(OOH)]^{2+}$ (**40**) was tested by using PPh_3 as substrate. Peroxidodicopper(II) complex **42** does not oxidize PPh_3 to phosphane oxide, but instead PPh_3 coordinates the metal, extruding O_2 and forming the corresponding complex $[Cu^{I}_2(UN\text{–}O^{-})(PPh_3)_2]^{+}$ (**45**). This reactivity is consistent with a species exhibiting nucleophilic character. Also consistent with this character is the reaction of **42** with an excess of protons, which quantitatively produces H_2O_2. Moreover, hydroperoxidodicopper(II) complex **40** readily oxidizes PPh_3 to quantitatively form $O{=}PPh_3$ and $[Cu^{II}_2(UN\text{–}O^{-})(OH)]^{2+}$. This reaction can be understood as an electrophilic oxygen-atom transfer to the substrate, and it provides evidence for fundamental differences between the reactivity of copper peroxide complex **42** and copper hydroperoxide **40**.

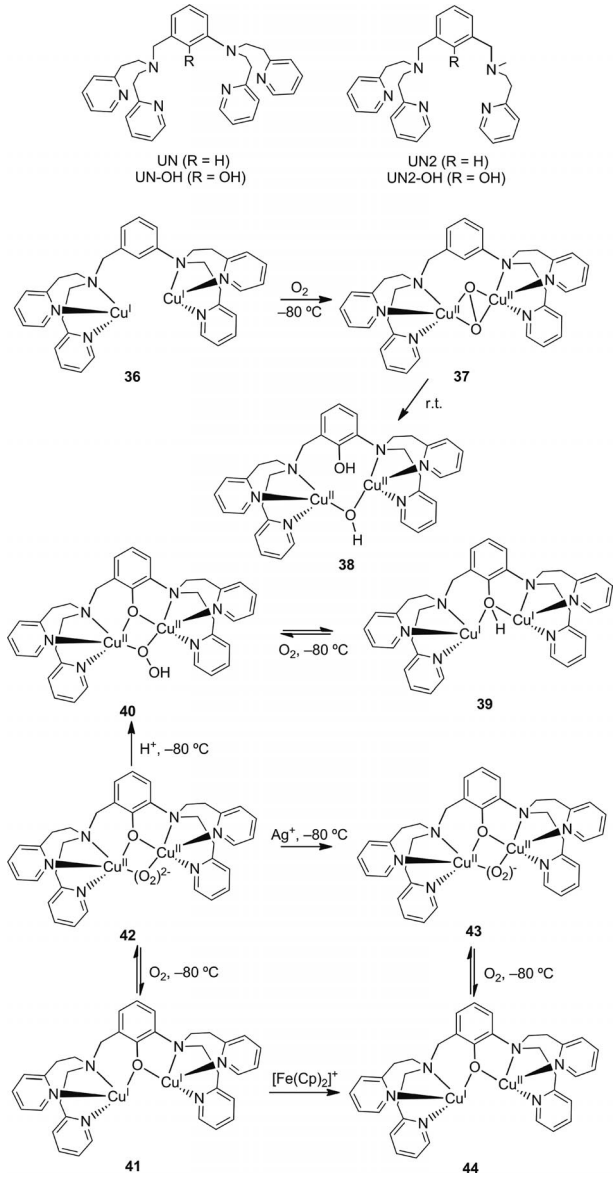

Figure 9. Unsymmetric xylyl-bridged dicopper complexes described by Karlin and co-workers.

Superoxide dismutases catalyze a very fast two-step disproportionation of the superoxide anion (O_2^{-}) to molecular oxygen and hydrogen peroxide.[12] The reaction is essentially different from a O_2-binding/activation process, but the nature of the intermediate species implicated is strongly re-

lated. The heterometallic active site of the copper- and zinc-dependent form of superoxide dismutase (CuZnSOD) also constitutes an attractive target for synthetic bioinorganic chemistry. Fukuzumi and co-workers provided an interesting model by designing heterometallic Cu^{II}–Zn^{II} complex **46** with a bridging imidazolate ring (Figure 10).[49,50] The analogous homometallic Cu^{II}_2 complex **47** was also synthesized. The SOD activity of both complexes was tested, and heterometallic complex **46** showed a higher activity than dicopper complex **47**. Indeed, the activity of the latter complex constitutes the highest reported to date for a dinuclear complex. Furthermore, when **46** reacts with H_2O_2/NEt_3 at low temperatures, metastable $Cu^{II}(OOH)Zn^{II}$ species **48** could be spectroscopically characterized. Such a species is considered an intermediate during CuZnSOD activity. The corresponding homometallic $Cu^{II}_2(OOH)_2$ species **49** could also be characterized when compound **47** was reacted in a similar manner.

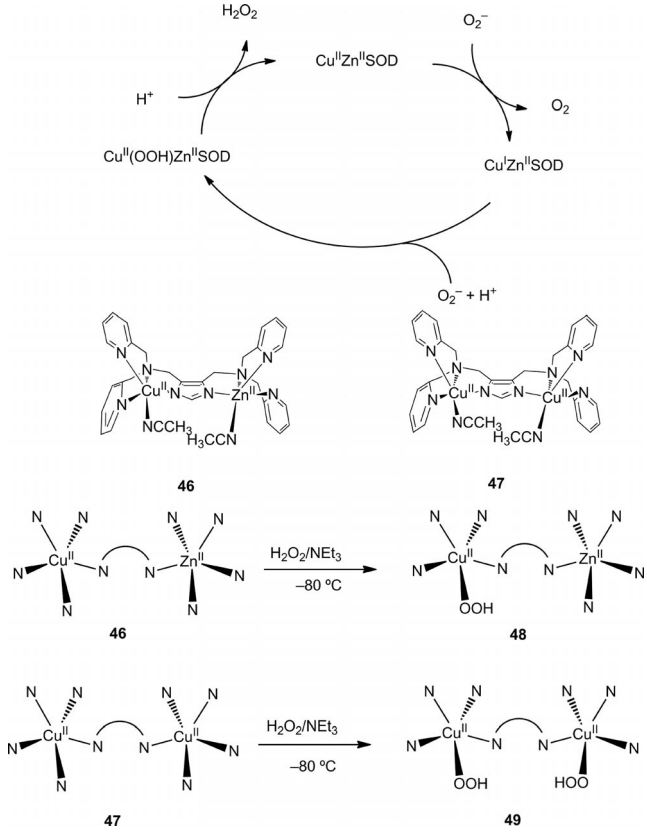

Figure 10. Schematic diagram of SOD activity in CuZnSOD (top), heterometallic complex **46** and homometallic complex **47** (middle), and reaction of heterometallic **46** and homometallic **47** with H_2O_2 at low temperature (bottom).

The design of the ligand oxapyme, which contains two different coordination sites, was used by Bosnich and co-workers to synthesize unsymmetric dinuclear Co^{II} complex **50** (Figure 11).[33] One of the cobalt ions is bound to four N atoms of the dinucleating ligand, and the other is bound to five. A bridging hydroxide moiety connects the two metal ions, and a water molecule fulfils the coordination sphere of the N_4Co site. This dicobalt complex reacted with O_2 at low temperatures to generate end-on dicobalt(III) peroxide **51**, in which the oxygen was exclusively bound to the N_4Co center. Reaction of **51** with protons promoted the release of the hydroxide moiety as a water molecule to generate the unsymmetric complex $[Co^{III}_2(\mu\text{-}\eta^1\text{:}\eta^2\text{-}O_2)(oxapyme)]^{2+}$ (**52**). Remarkably, **52** isomerizes toward a $Co^{III}(\mu\text{-}\eta^1\text{:}\eta^1\text{-}O_2)\text{-}Co^{III}$ complex (compound **53**) when NO_2^- is added.

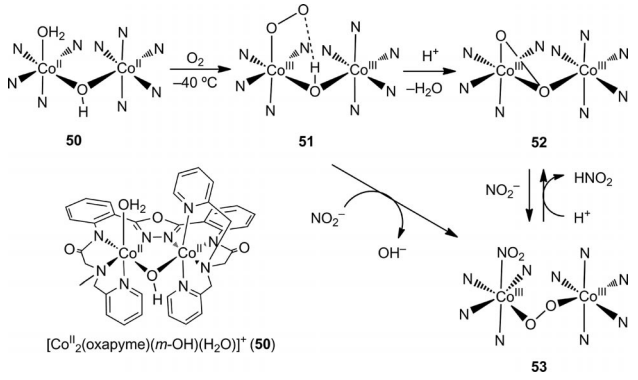

Figure 11. Reactivity of the unsymmetric dicobalt complex described by Bosnich and co-workers.

In another interesting contribution, Itoh and co-workers synthesized a pentapyridine molecule that acted as an unsymmetric dinucleating ligand for copper ions.[51] The reaction of the corresponding dicopper(I) complex **54** with O_2 at low temperatures in acetone resulted in the formation of Cu^{II}_2–O_2 species **55**, which the authors described as the first example of a $Cu^{II}(\mu\text{-}\eta^1\text{:}\eta^2\text{-}O_2)Cu^{II}$ complex (Figure 12). The reactivity of this novel Cu_2O_2 intermediate was studied in some prototypical reactions of peroxidodicopper cores. When it was treated with CF_3SO_3H, the complex underwent protonation, releasing H_2O_2, which suggests that the Cu_2O_2 unit can exhibit nucleophilic character in the presence of protons. However, when the complex was treated with substrates such PPh_3, PhSMe, or 2,4-di-*tert*-butylphenol, products resulting from electrophilic oxidation reactions (Ph_3PO, PhSOMe, and the biphenol coupling product, respectively; see Figure 12) were observed. This rather

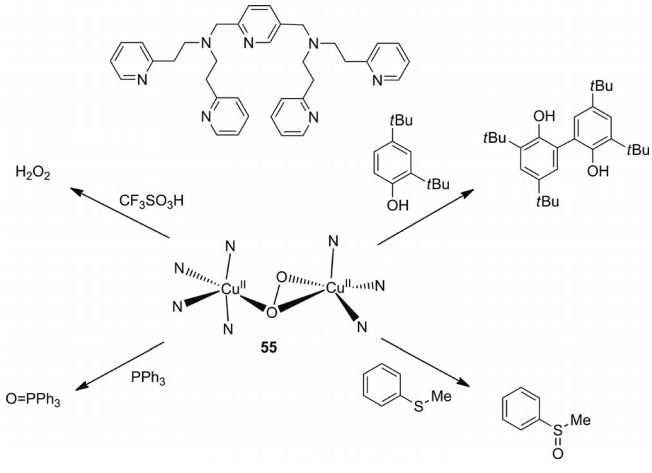

Figure 12. Pentapyridine ligand described by Itoh (top) and reactivity of the corresponding $Cu^{II}(\mu\text{-}\eta^1\text{:}\eta^2\text{-}O_2)Cu^{II}$ complex.

unusual behavior was explained by the chameleonic character of the unsymmetric $Cu^{II}(\mu\text{-}\eta^1\text{:}\eta^2\text{-}O_2)Cu^{II}$ intermediate, which could exhibit nucleophilic reactivity in the presence of good electrophiles, like the majority of $Cu^{II}(\mu\text{-}\eta^1\text{:}\eta^1\text{-}O_2)$ complexes, but it could also engage in electrophilic oxygen-atom-transfer reactions in the presence of oxophilic substrates, as commonly observed in $Cu^{II}(\mu\text{-}\eta^2\text{:}\eta^2\text{-}O_2)Cu^{II}$ centers.[19]

Along a similar path, Garcia-Bosch et al. designed an unsymmetric heptaazadentate ligand based on the combination of two different coordination sites spaced by a xylyl linker (Figure 13).[52] One of the two binding sites is tetradentate and structurally very similar to the Karlin's tpa tripodal ligand. The second site is tridentate and contains two benzylimidazole rings. Structural analysis of $[Cu^I_2(m\text{-}Xyl^{N3N4})]^{2+}$ (**56**) by X-ray diffraction showed that the copper ion at the tetradentate arm adopts a distorted trigonal pyramidal geometry, and a T-shape geometry was established for the tridentate site. For comparative reasons, dicopper complex $[Cu^I_2(m\text{-}Xyl^{N4N4})]^{2+}$ (**57**), which contains the analogous symmetric ligand $m\text{-}Xyl^{N4N4}$ with two tetradentate sites, was also synthesized. The chemistry of the corresponding tridentate symmetric complex, $[Cu^I_2(m\text{-}Xyl^{N3N3})]^{2+}$ (**58**), was previously studied by the group of Casella.[53]

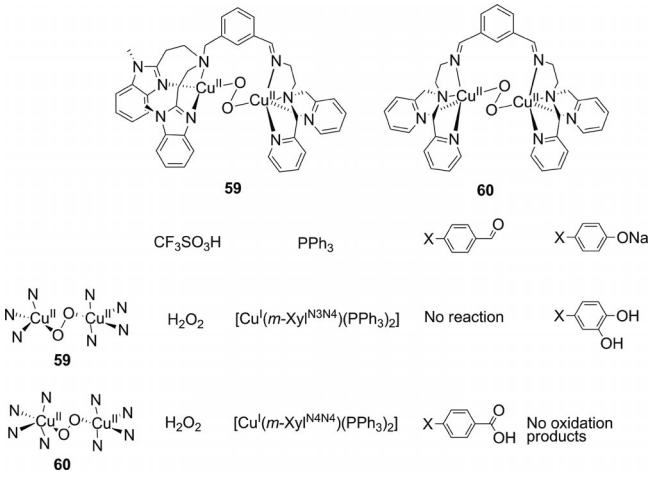

Figure 13. Unsymmetric and symmetric dicopper complexes **59** and **60**, respectively, described by Garcia-Bosch et al. (top). Schematic diagram of the reactivity of the unsymmetric and symmetric $Cu_2(\mu\text{-}\eta^1\text{:}\eta^1\text{-}O_2)$ cores towards prototypical substrate probes (bottom).

As expected from the low coordination numbers of the copper ions, both complexes proved extraordinarily reactive towards O_2. At cryogenic temperatures (–80 °C), in acetone solution, unsymmetric $[Cu^I_2(m\text{-}Xyl^{N3N4})]^{2+}$ (**56**) reacted with O_2 to form a thermally very unstable complex, $[Cu^{II}_2(\mu\text{-}\eta^1\text{:}\eta^1\text{-}O_2)(m\text{-}Xyl^{N3N4})]^{2+}$ (**59**). Analogously, symmetric complex $[Cu^I_2(m\text{-}Xyl^{N4N4})]^{2+}$ (**57**) also reacted with O_2 to form $[Cu^{II}_2(\mu\text{-}\eta^1\text{:}\eta^1\text{-}O_2)(m\text{-}Xyl^{N4N4})]^{2+}$ (**60**). The binding mode of the O_2 molecule in the two complexes was ascertained on the basis of their resonance Raman and UV/Vis spectra. The reactivity of both complexes towards prototypical chemical probes such as H^+, PPh_3, thioanisole, and benzaldehyde was studied. The two complexes react with 2 equiv. of H^+ to afford H_2O_2 quantitatively and with PPh_3 to yield $[Cu^I_2(L)(PPh_3)_2]^{2+}$ {L = $m\text{-}Xyl^{N3N4}$} (**61**) and $m\text{-}Xyl^{N3N4}$ (**62**) and release O_2. None of the two complexes react with thioanisole or dihydroanthracene. Different reactivity was observed towards benzaldehyde: Symmetric complex **60** reacted with this electrophilic substrate quantitatively, yielding benzoic acid. A Hammett plot analysis afforded a negative correlation for this reaction, indicative of a nucleophilic character of the peroxide. In contrast, unsymmetric complex **59** was unable to oxidize benzaldehyde.

On the other hand, a completely different behavior was observed when the complexes were tested in the oxidation of sodium phenolates. While the symmetric complex was unable to oxidize the substrate, unsymmetric complex $[Cu^{II}_2(\mu\text{-}\eta^1\text{:}\eta^1\text{-}O_2)(m\text{-}Xyl^{N3N4})]^{2+}$ (**59**) reacted with sodium phenolates to yield *ortho*-hydroxylated phenols. A Hammett analysis indicated that the reaction had an electrophilic character, and no hydroxylation took place when electron-deficient substrates were employed. No reaction occurred with sterically hindered phenolates, either. Complex **59** constitutes the first example of a *trans*-peroxidodicopper(II) complex showing tyrosinase-like reactivity. Spectroscopic analysis indicated that the reaction with sodium phenolates (NaOPh) occurred via intermediate $[Cu^{II}_2(OPh)(\mu\text{-}\eta^1\text{:}\eta^1\text{-}O_2)(m\text{-}Xyl^{N3N4})]^{2+}$ (**63**), the substrate binding at the tridentate site. Computational analysis indicated that phenolate binding did not trigger isomerization of the Cu_2O_2 core, and that electrophilic attack of a peroxide oxygen atom over the arene ring had a low activation barrier. The ability of the unsymmetric complex to bind a phenolate substrate at the N-tricoordinate copper(II) center was proposed to be essential and was presumably enabled by placing the aromatic ring with the proper orientation and distance to the peroxide oxygen atom.

Conclusions

Oxygen binding and activation at unsymmetric and heterometallic complexes remains a promising field that has been very scarcely explored, especially relative to the corresponding symmetric M_2O_2 species. Studies described so far have provided evidence for a rich and interesting chemistry. Proof of concept that these systems can offer novel spectroscopic properties, electronic structures, and reactivities has been provided in the past years. These pioneer studies hint at a myriad of avenues of novel chemistry waiting to be explored.

Acknowledgments

We thank Dr. A. Company for fruitful discussions. I. G.-B. thanks the Ministerio de Ciencia e Innovación (MICINN) for a PhD grant. M. C. and X. R. acknowledge financial support by Institució Catalana de Recerca i Estudis Avançats (ICREA-Acadèmia), Generalitat de Catalunya (2009-SGR637), Ministerio de Ciencia e Innovación (MICINN), Spain (CTQ2009-08464/BQU), the Euro-

pean Research Council (project ERC-2009-StG-239910), and Consolider Ingenio (CSD2010-00065).

[1] M. Saraste, *Science* **1999**, *283*, 1488–1493.
[2] G. T. Babcock, M. Wikström, *Nature* **1992**, *356*, 301–309.
[3] R. Gennis, S. Ferguson-Miller, *Science* **1995**, *269*, 1063–1064.
[4] V. R. I. Kaila, M. I. Verkhovsky, M. Wikström, *Chem. Rev.* **2010**, *110*, 7062–7081.
[5] M. Sono, M. P. Roach, E. D. Coulter, J. H. Dawson, *Chem. Rev.* **1996**, *96*, 2841–2887.
[6] E. I. Solomon, P. Chen, M. Metz, S.-K. Lee, A. E. Palmer, *Angew. Chem.* **2001**, *113*, 4702; *Angew. Chem. Int. Ed.* **2001**, *40*, 4570–4590.
[7] E. G. Kovaleva, J. D. Lipscomb, *Nat. Chem. Biol.* **2008**, *4*, 186–193.
[8] Y. M. P. Monita, J. D. Lipscomb, E. I. Solomon, *Proc. Natl. Acad. Sci. USA* **2007**, *104*, 18355–18362.
[9] M. H. Sazinsky, S. J. Lippard, *Acc. Chem. Res.* **2006**, *39*, 558–566.
[10] P. R. Ortiz de Montellano, *Cytochrome P450: Structure, Mechanism and Biochemistry*, Kluwer Academic/Plenum Publishers, New York, **2005**.
[11] D. T. Sawyer, *Oxygen Chemistry*, Oxford University Press, New York, **1991**.
[12] J. A. Tainer, E. D. Getzoff, K. M. Beem, J. S. Richardson, D. C. Richardson, *J. Mol. Biol.* **1982**, *160*, 181–217.
[13] N. J. Blackburn, T. M. Pettingill, K. S. Seagraves, R. T. Shigeta, *J. Biol. Chem.* **1990**, *265*, 15383–15386.
[14] J. P. Klinman, *Chem. Rev.* **1996**, *96*, 2541–2561.
[15] P. Chen, E. I. Solomon, *Proc. Natl. Acad. Sci. USA* **2004**, *101*, 13105–13110.
[16] S. T. Prigge, A. S. Kolhekar, B. A. Eipper, R. E. Mains, L. M. Amzel, *Science* **1997**, *278*, 1300–1305.
[17] Y. Matoba, T. Kumagai, A. Yamamoto, H. Yoshitsu, M. Sugiyama, *J. Biol. Chem.* **2006**, *281*, 8981–8990.
[18] H. Decker, T. Schweikardt, F. Tuczek, *Angew. Chem.* **2006**, *118*, 4658; *Angew. Chem. Int. Ed.* **2006**, *45*, 4546–4550.
[19] E. A. Lewis, W. B. Tolman, *Chem. Rev.* **2004**, *114*, 1047–1076.
[20] L. M. Mirica, X. Ottenwaelder, T. D. P. Stack, *Chem. Rev.* **2004**, *114*, 1013–1046.
[21] S. Schindler, *Eur. J. Inorg. Chem.* **2000**, 2311–2326.
[22] M. Rolffe, J. Schottenheim, H. Decker, F. Tuczek, *Chem. Soc. Rev.* **2011**, *40*, 4077–4098.
[23] a) M. Costas, M. P. Mehn, M. P. Jensen, L. Que Jr., *Chem. Rev.* **2004**, *104*, 939–986; b) M. M. Abu-Omar, A. Loaiza, N. Hontzeas, *Chem. Rev.* **2005**, *105*, 2227–2252; c) P. C. A. Bruijnincx, G. van Koten, R. J. M. Klein Gebbink, *Chem. Soc. Rev.* **2008**, *37*, 2716–2744.
[24] a) S. Friedle, E. Reisner, S. J. Lippard, *Chem. Soc. Rev.* **2010**, *39*, 2768–2779; b) I. Siewert, C. Limberg, *Chem. Eur. J.* **2009**, *15*, 10316–10328.
[25] G. Battaini, A. Granata, E. Monzani, M. Gullotti, L. Casella, *Adv. Inorg. Chem.* **2006**, *58*, 185–233.
[26] M. T. Kieber-Emmons, C. G. Riordan, *Acc. Chem. Res.* **2007**, *40*, 618–625.
[27] E. Kim, E. E. Chufan, K. Kamaraj, K. D. Karlin, *Chem. Rev.* **2004**, *104*, 1077–1134.
[28] A. L. Gavrilova, B. Bosnich, *Chem. Rev.* **2004**, *104*, 349–384.
[29] A. Company, S. Palavicini, I. Garcia-Bosch, R. Mas-Ballesté, L. Que Jr., E. V. Rybak-Akimova, L. Casella, X. Ribas, M. Costas, *Chem. Eur. J.* **2008**, *14*, 3535–3538.
[30] L. M. Mirica, M. Vance, D. J. Rudd, B. Hedman, K. O. Hodgson, E. I. Solomon, T. D. P. Stack, *Science* **2005**, *308*, 1890–1892.
[31] S. Yao, M. Driess, *Acc. Chem. Res.* **2011**, DOI: 10.1021/ar200156r.
[32] K. Fujita, R. Schenker, W. Gu, T. C. Brunold, S. P. Cramer, C. G. Riordan, *Inorg. Chem.* **2004**, *43*, 3324–3326.
[33] A. L. Gavrilova, C. J. Qin, R. D. Sommer, A. L. Rheingold, B. Bosnich, *J. Am. Chem. Soc.* **2002**, *124*, 1714–1722.
[34] J. T. York, V. G. Young Jr., W. B. Tolman, *Inorg. Chem.* **2006**, *45*, 4191–4198.
[35] P. Alsters, L. J. Boersma, G. van Koten, *Organometallics* **1993**, *12*, 1629–1638.
[36] K. E. Litz, M. M. B. Holl, J. W. Kampf, G. B. Carpenter, *Inorg. Chem.* **1998**, *37*, 6461–6469.
[37] Z. T. Cygan, J. E. B. IV, K. E. Litz, J. W. Kampf, M. M. B. Holl, *Organometallics* **2002**, *21*, 5373–5381.
[38] N. W. Aboelella, E. A. Lewis, A. M. Reynolds, W. W. Brennessel, C. J. Cramer, W. B. Tolman, *J. Am. Chem. Soc.* **2002**, *124*, 10660–10661.
[39] N. W. Aboelella, J. T. York, A. M. Reynolds, K. Fujita, C. R. Kinsinger, C. J. Cramer, C. G. Riordan, W. B. Tolman, *Chem. Commun.* **2004**, *15*, 1716–1717.
[40] J. T. York, A. Llobet, C. J. Cramer, W. B. Tolman, *J. Am. Chem. Soc.* **2007**, *129*, 7990–7999.
[41] S. Yao, E. Bill, C. Milsmann, K. Wieghardt, M. Driess, *Angew. Chem.* **2008**, *120*, 7218; *Angew. Chem. Int. Ed.* **2008**, *47*, 7110–7113.
[42] S. Yao, Y. Xiong, M. Vogt, H. Grutzmacher, C. Herwig, C. Limberg, M. Driess, *Angew. Chem.* **2009**, *121*, 8251; *Angew. Chem. Int. Ed.* **2009**, *48*, 8107–8110.
[43] S. Yao, C. Herwig, Y. Xiong, A. Company, E. Bill, C. Limberg, M. Driess, *Angew. Chem.* **2010**, *122*, 7208; *Angew. Chem. Int. Ed.* **2010**, *49*, 7054–7058.
[44] P. J. Donoghue, A. K. Gupta, D. W. Boyce, C. J. Cramer, W. B. Tolman, *J. Am. Chem. Soc.* **2010**, *132*, 15869–15871.
[45] T. Chishiro, Y. Shimazaki, F. Tani, Y. Tachi, Y. Naruta, S. Karasawa, S. Hayami, Y. Maeda, *Angew. Chem.* **2003**, *115*, 2894; *Angew. Chem. Int. Ed.* **2003**, *42*, 2788–2791.
[46] M. Mahroof-Tahir, K. D. Karlin, *J. Am. Chem. Soc.* **1992**, *114*, 7599–7601.
[47] M. S. Nasir, K. D. Karlin, D. McGowty, J. Zubieta, *J. Am. Chem. Soc.* **1991**, *113*, 698–700.
[48] N. N. Murthy, M. Mahroof-Tahir, K. D. Karlin, *Inorg. Chem.* **2001**, *40*, 628–635.
[49] H. Ohtsu, Y. Shimazaki, A. Odani, O. Yamauchi, W. Mori, S. Itoh, S. Fukuzumi, *J. Am. Chem. Soc.* **2000**, *122*, 5733–5741.
[50] H. Ohtsu, S. Itoh, S. Nagatomo, T. Kitagawa, S. Ogo, Y. Watanabe, S. Fukuzumi, *Chem. Commun.* **2000**, 1051–1052.
[51] Y. Tachi, K. Aita, S. Teramae, F. Tani, Y. Naruta, S. Fukuzumi, S. Itoh, *Inorg. Chem.* **2004**, *43*, 4558–4560.
[52] I. Garcia-Bosch, A. Company, J. R. Frisch, M. Torrent-Sucarrat, M. Cardellach, I. Gamba, M. Guell, L. Casella, L. Que, X. Ribas, J. M. Luis, M. Costas, *Angew. Chem. Int. Ed.* **2010**, *49*, 2406–2409.
[53] S. Palavicini, A. Granata, E. Monzani, L. Casella, *J. Am. Chem. Soc.* **2005**, *127*, 18031–18036.

Received: September 8, 2011
Published Online: December 9, 2011

DOI: 10.1002/ejic.201101041

Activation of Nitriles by Trichloro[2-(dialkylphosphanyl)imidazol-1-yl]silanes – Synthesis and Characterization of New Dinuclear Pentacoordinate Silicon(IV) Complexes with Bridging Imido-Nitrogen Ligand Atoms

Konstantin Junold,[a] Christian Burschka,[a] and Reinhold Tacke*[a]

Dedicated to Professor Gerhard Bringmann on the occasion of his 60th birthday

Keywords: Coordination chemistry / Nitrile activation / Pentacoordination / Phosphorus / Silicon / N ligands

Trichloro[2-(dialkylphosphanyl)imidazol-1-yl]silanes **3** and **4** react with aceto- or propionitrile to yield the dinuclear pentacoordinate silicon(IV) complexes **5**–**8**, which contain two bridging dianionic N,N-ligands generated by silicon-mediated nitrile activation. Compounds **5**–**8** contain two $SiCl_2N_3$ skeletons, with two imido-nitrogen ligand atoms that bridge the silicon coordination centers. The pentacoordinate silicon(IV) complexes **5**–**8** were characterized by elemental analysis, single-crystal X-ray diffraction, and solid-state NMR spectroscopy.

Introduction

Monodeprotonated 2-(dialkylphosphanyl)imidazoles are common bidentate N,P-chelate ligands.[1] To the best of our knowledge, higher-coordinate silicon(IV) complexes with this particular type of ligands are unknown.[2] Generally, penta- and hexacoordinate silicon compounds with Si–P interactions are very rare,[3–6] and some of these species are not well characterized.[6] In continuation of our systematic studies on higher-coordinate silicon(IV) complexes,[7] we targeted the synthesis of pentacoordinate silicon compounds that contain bidentate monoanionic N,P-ligands derived from 2-(dialkylphosphanyl)imidazoles. Here we report our unsuccessful attempts to synthesize these target compounds and the discovery of a new nitrile activation that led to the formation of dinuclear pentacoordinate silicon(IV) complexes with bridging imido-nitrogen ligand atoms.

Results and Discussion

Tetrachlorosilane was treated with 1 mol-equiv. each of triethylamine and 2-(diethylphosphanyl)imidazole (**1**)[8] or 2-(diisopropylphophanyl)imidazole (**2**)[8] in tetrahydrofuran to furnish the trichloro[2-(dialkylphosphanyl)imidazol-1-yl]-silanes **3** and **4**, respectively (Scheme 1). Compounds **3** and **4** could not be isolated as analytically pure products; however, their identity was established unequivocally by NMR spectroscopy,[9] which showed no Si–P interactions (no pentacoordination of the silicon atom). Attempts to purify **3** and **4** by crystallization from acetonitrile or propionitrile led to a surprising observation: both silanes were found to react with these nitriles to furnish the dinuclear pentacoordinate silicon(IV) complexes **5**–**8** (Scheme 1), which were isolated as colorless solids [55 (**5**), 31 (**6**), 47 (**7**), 27% (**8**)]. As demonstrated for **7**, the yield was increased significantly (→ 84%) by reaction of tetrachlorosilane with triethylamine and **2** with the corresponding nitrile (acetonitrile) as the solvent.

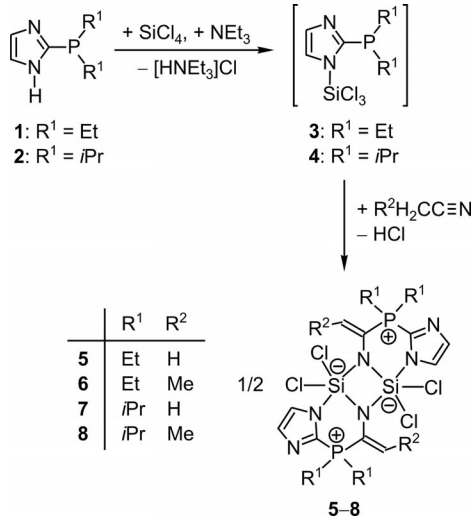

	R^1	R^2
5	Et	H
6	Et	Me
7	*i*Pr	H
8	*i*Pr	Me

Scheme 1. Synthesis of **5**–**8**.

[a] Universität Würzburg, Institut für Anorganische Chemie, Am Hubland, 97074 Würzburg, Germany
Fax: +49-931-31-84609
E-mail: r.tacke@uni-wuerzburg.de

The zwitterionic compounds **5**–**8** contain two pentacoordinate (formally negatively charged) silicon atoms, two tetracoordinate (formally positively charged) phosphorus atoms,[10] and two new bridging dianionic N,N-ligands (generated by nitrile activation) with an imido- and an amido-nitrogen atom.

The identities of **5**–**8** were established by elemental analysis (C, H, N), crystal-structure analysis,[11] and solid-state NMR spectroscopy (^{13}C, ^{15}N, ^{29}Si, ^{31}P). NMR spectroscopic studies in solution failed due to the poor solubility of **5**–**8** in common organic solvents.

The molecular structures of **5**–**8** are characterized by C_i symmetry, with two five- and two six-membered rings and one central four-membered ring (Figures 1, 2, 3, and 4). Compounds **5**–**8** contain two $SiCl_2N_3$ skeletons, with two imido-nitrogen ligand atoms that bridge the silicon coordination centers. The silicon coordination polyhedra are best described as distorted trigonal bipyramids; the Berry distortions (transition trigonal bipyramid → square pyramid) amount to 8.8 (**5**), 23.0 (**6**), 20.2 (**7**), and 21.7% (**8**).[11] As shown in Figure 5, two different coordination modes were observed. In **5**, the two chlorido ligands and one bridging imido-nitrogen ligand atom are found in the equatorial positions, whereas the equatorial sites of **6**–**8** are occupied by one chlorido, one imido-nitrogen, and the amido-nitrogen ligand atom.

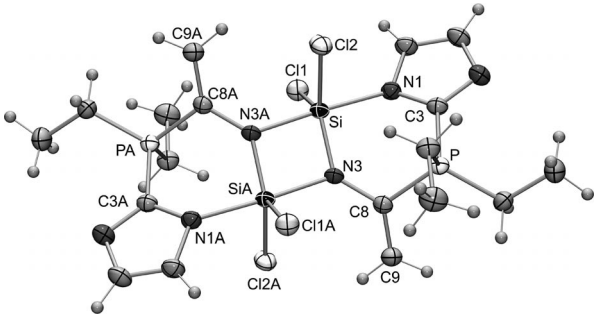

Figure 1. Molecular structure of **5** in the crystal (probability level of displacement ellipsoides 50%). Selected bond lengths [Å] and angles [°]: Si–Cl1 2.1227(7), Si–Cl2 2.1263(7), Si–N1 1.9138(15), Si–N3 1.7282(15), Si–N3A 1.8364(15), P–C3 1.7786(17), P–C8 1.7992(18), N1–C3 1.365(2), N3–C8 1.402(2), C8–C9 1.335(2); Si–N3–SiA 99.19(7), Cl1–Si–Cl2 115.77(3), Cl1–Si–N1 88.86(5), Cl1–Si–N3 122.86(6), Cl1–Si–N3A 92.75(5), Cl2–Si–N1 86.51(5), Cl2–Si–N3 121.34(6), Cl2–Si–N3A 95.16(5), N1–Si–N3 96.10(7), N1–Si–N3A 176.91(6), N3–Si–N3A 80.81(7), Si–N1–C3 126.42(11), Si–N3–C8 132.61(12), SiA–N3–C8 128.06(11), P–C3–N1 120.87(13), P–C8–N3 114.30(12), P–C8–C9 117.45(14), N3–C8–C9 128.07(16).

The axial N–Si–N (**5**) and Cl–Si–N angles (**6**–**8**) are in the range 172.65(5)–176.91(6)°, and the sum of the equatorial bond angles of **5**–**8** range from 359.80 to 359.97°. The central four-membered Si_2N_2 rings are planar, with Si–N–Si angles of 99.19(7)–100.13(7)° and N–Si–N angles of 79.87(7)–80.81(7)°. Despite of their isomeric $SiCl_2N_3$ skeletons (Figure 5), **5**–**8** show very similar lengths of the analogous Si–Cl and Si–N bonds. The axial Si–Cl bond lengths are in the range 2.2291(6)–2.2595(6) Å and are somewhat longer than the equatorial ones [2.1214(7)–2.1446(7) Å]. The axial Si–N(imido) bond lengths [1.8275(15)–1.8364(15) Å] are also longer than the equatorial ones [1.7270(15)–1.7368(16) Å]. The Si–N(amido) bond lengths are somewhat longer than the Si–N(imido) ones [$Si–N(amido)_{ax}$ 1.9138(15) Å, $Si–N(amido)_{eq}$ 1.8327(17)–1.8409(16) Å].

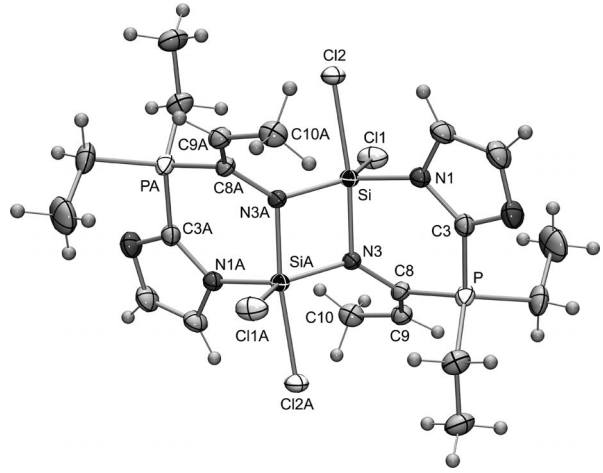

Figure 2. Molecular structure of **6** in the crystal (probability level of displacement ellipsoides 50%). Selected bond lengths [Å] and angles [°]: Si–Cl1 2.1214(7), Si–Cl2 2.2595(6), Si–N1 1.8327(17), Si–N3 1.8320(14), Si–N3A 1.7270(15), P–C3 1.7907(18), P–C8 1.7898(19), N1–C3 1.385(2), N3–C8 1.409(2), C8–C9 1.346(3); Si–N3–SiA 99.83(7), Cl1–Si–Cl2 88.41(3), Cl1–Si–N1 109.67(6), Cl1–Si–N3 92.95(5), Cl1–Si–N3A 128.13(6), Cl2–Si–N1 91.67(5), Cl2–Si–N3 172.65(5), Cl2–Si–N3A 93.31(5), N1–Si–N3 94.67(7), N1–Si–N3A 122.07(8), N3–Si–N3A 80.17(7), Si–N1–C3 126.36(12), Si–N3–C8 125.03(11), SiA–N3–C8 135.14(12), P–C3–N1 127.89(14), P–C8–N3 109.05(12), P–C8–C9 122.45(14), N3–C8–C9 128.47(17), C8–C9–C10 124.66(17).

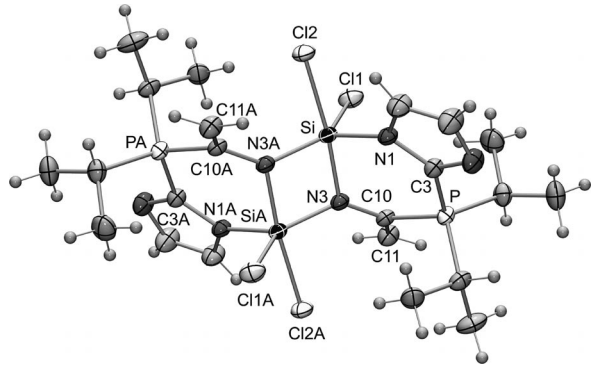

Figure 3. Molecular structure of **7** in the crystal (probability level of displacement ellipsoides 50%). Selected bond lengths [Å] and angles [°]: Si–Cl1 2.1242(7), Si–Cl2 2.2316(8), Si–N1 1.8409(16), Si–N3 1.8341(15), Si–N3A 1.7368(16), P–C3 1.7889(18), P–C10 1.8081(18), N1–C1 1.390(2), N3–C10 1.400(2), C10–C11 1.343(2); Si–N3–SiA 100.13(7), Cl1–Si–Cl2 88.90(3), Cl1–Si–N1 108.19(15), Cl1–Si–N3 92.59(5), Cl1–Si–N3A 125.73(6), Cl2–Si–N1 90.57(5), Cl2–Si–N3 173.83(6), Cl2–Si–N3A 94.40(5), N1–Si–N3 94.65(7), N1–Si–N3A 125.88(7), N3–Si–N3A 79.87(7), Si–N1–C3 126.51(12), Si–N3–C10 125.78(12), SiA–N3–C10 133.92(12), P–C3–N1 127.75(13), P–C10–N3 113.10(12), P–C10–C11 119.24(14), N3–C10–C11 127.62(17).

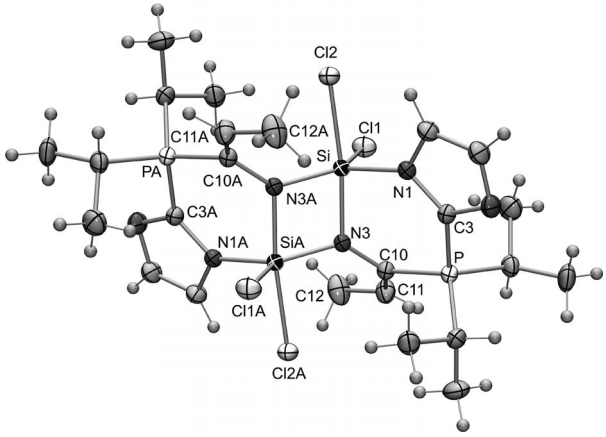

Figure 4. Molecular structure of **8** in the crystal (probability level of displacement ellipsoides 50%). Selected bond lengths [Å] and angles [°]: Si–Cl1 2.1446(7), Si–Cl2 2.2291(6), Si–N1 1.8387(15), Si–N3 1.8275(15), Si–N3A 1.7360(14), P–C3 1.7894(18), P–C10 1.8040(17), N1–C1 1.389(2), N3–C10 1.400(2), C10–C11 1.346(2); Si–N3–SiA 99.97(7), Cl1–Si–Cl2 88.99(3), Cl1–Si–N1 108.45(5), Cl1–Si–N3 92.41(5), Cl1–Si–N3A 126.72(5), Cl2–Si–N1 91.38(5), Cl2–Si–N3 173.04(5), Cl2–Si–N3A 93.67(5), N1–Si–N3 94.64(7), N1–Si–N3A 124.63(7), N3–Si–N3A 80.03(7), Si–N1–C3 126.62(11), Si–N3–C10 125.35(11), SiA–N3–C10 134.64(12), P–C3–N1 128.05(12), P–C10–N3 112.33(12), P–C10–C11 119.63(13), N3–C10–C11 128.01(15), C10–C11–C12 125.25(17).

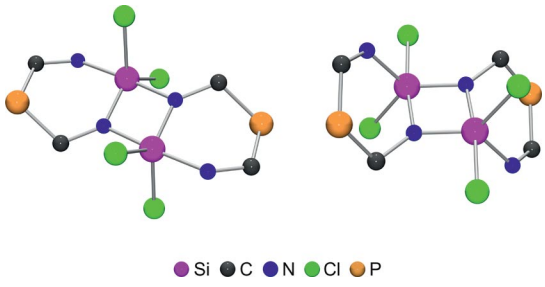

Figure 5. Different coordination modes observed for the $SiCl_2N_3$ skeletons of **5** (left) and **6**–**8** (right).

A hypothetical mechanism for the formation of **5**–**8** is depicted in Scheme 2. We propose the coordination of the acetonitrile or propionitrile molecule to the silicon atom of the silanes **3** and **4** (→ **I**) to be the key step in the nitrile activation, which is followed by nucleophilic attack of the phosphorus atom at the α-carbon atom of the nitrile to generate a P–C bond (→ **II**). Subsequent deprotonation at the β-carbon atom of the nitrile (elimination of hydrogen chloride and formation of a C=C bond) leads to the zwitterionic species **III**, which dimerizes to give **5**–**8**.

Attempts to generate the free bidentate N,N-ligands by hydrolysis of **5**–**8** failed. Treatment of **5**–**8** with water under neutral, acidic, and basic conditions at room temperature led to a rapid hydrolytic decomposition, but we could not isolate the free N,N-ligands. Instead, 1:1 mixtures of **3** and acetamide, **3** and propanamide, **4** and acetamide, or **4** and propanamide were obtained in almost quantitative yield (Scheme 3).

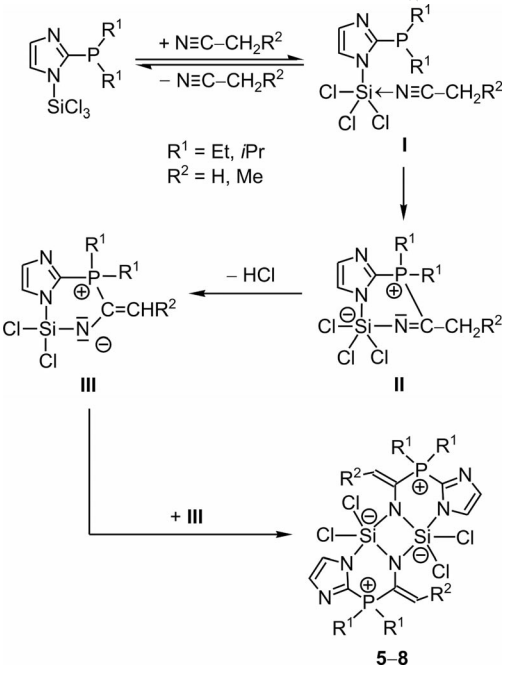

Scheme 2. Proposed mechanism for the formation of **5**–**8**.

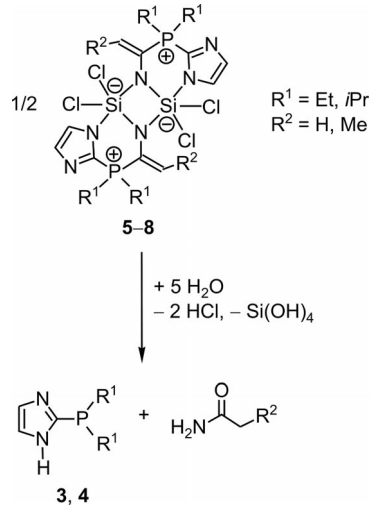

Scheme 3. Reaction of **5**–**8** with water.

Conclusions

We have discovered a new silicon-mediated nitrile activation and studied a new class of dinuclear zwitterionic pentacoordinate silicon(IV) complexes with bridging imido-nitrogen ligand atoms and $SiCl_2N_3$ skeletons. Future studies will explore the scope of this new chemistry.

Experimental Section

General: All syntheses were carried out under dry argon. Organic solvents were dried and purified according to standard procedures and stored under nitrogen. Melting points were determined with a Büchi Melting Point B-540 apparatus by using samples in sealed capillaries. Solid-state ^{13}C, ^{15}N, ^{29}Si, and ^{31}P VACP/MAS NMR

spectra were recorded at 22 °C with a Bruker DSX-400 NMR spectrometer with bottom layer rotors of ZrO_2 (diameter, 7 mm) with ca. 200 mg of sample [^{13}C 100.6, ^{15}N 40.6, ^{29}Si 79.5, ^{31}P 162.0 MHz; external standard: Me_4Si (^{13}C and ^{29}Si, δ = 0 ppm), glycine (^{15}N, δ = –342.0 ppm), or H_3PO_4 (85%, ^{31}P, δ = 0 ppm); contact time, 1 (^{13}C), 3 (^{15}N), 5 (^{29}Si), or 2 ms (^{31}P); 90° ^1H transmitter pulse length, 3.6 μs, repetition time, 4 s].

General Procedure for the Synthesis of 5–8: Triethylamine (4 mmol) and tetrachlorosilane (4 mmol) were added sequentially at 20 °C in single portions to a stirred solution of **1**[8] or **2**[8] (4 mmol) in tetrahydrofuran (20 mL), and the resulting suspension was stirred at this temperature for 24 h. The resulting precipitate was isolated by filtration, washed with tetrahydrofuran (5 mL), and discarded. The solvent of the filtrate (including the wash solution) was removed in vacuo, the corresponding nitrile (10 mL) was added to the residue, and the mixture was stirred at 20 °C for 2 d. The resulting precipitate was isolated by filtration, washed with *n*-pentane (2× 5 mL), and dried in vacuo (0.01 mbar, 20 °C, 6 h) to yield **5**–**8** as colorless solids.

5: Yield: 55%. $C_{18}H_{28}Cl_4N_6P_2Si_2$ (588.39): calcd. C 36.74, H 4.80, N 14.28; found C 37.1, H 5.0, N 14.4. ^{13}C VACP/MAS NMR: δ = 6.8 (CH_2CH_3), 9.5 (CH_2CH_3), 13 (br., CH_2CH_3), 14 (br., CH_2CH_3), 117.5, 129.1 (br.), 131.5 (br.), 132.4 (br.) [C=CH_2, C=CH_2, *C*(imidazol-1-yl)] ppm. ^{15}N VACP/MAS NMR: δ = –254.8 (Si*N*C), –134.0 (C*N*C), –92.3 (Si*N*Si) ppm. ^{29}Si VACP/MAS NMR: δ = –122.2 ppm. ^{31}P VACP/MAS NMR: δ = 7.1 ppm.

6: Yield: 31%. $C_{20}H_{32}Cl_4N_6P_2Si_2$ (616.44): calcd. C 38.97, H 5.23, N 13.63; found C 39.0, H 5.3, N 13.4. ^{13}C VACP/MAS NMR: δ = 3.9 (CH_2CH_3), 4.3 (CH_2CH_3), 11.7 (C=CHCH_3), 18.2 [d, $^1J(^{31}P,^{13}C)$ = 50 Hz CH_2CH_3], 121.3 (br.), 128.9, 132.2, 133.2, 139.7 [C=*C*HCH$_3$, *C*=CHCH$_3$, *C*(imidazol-1-yl)] ppm. ^{15}N VACP/MAS NMR: δ = –265.1 (Si*N*C), –164.4 (C*N*C), –84.1 (Si*N*Si) ppm. ^{29}Si VACP/MAS NMR: δ = –124.6 ppm. ^{31}P VACP/MAS NMR: δ = 17.6 ppm.

7: Yield: 47%. $C_{22}H_{36}Cl_4N_6P_2Si_2$ (644.50): calcd. C 41.00, H 5.63, N 13.04; found C 40.8, H 5.6, N 12.9. ^{13}C VACP/MAS NMR: δ = 14.4 (CHCH_3), 15.4 (CHCH_3), 16.3 (CHCH_3), 16.7 (CHCH_3), 23.6 (br., $CHCH_3$), 26.2 (br., $CHCH_3$), 127.7, 129.1 (br.), 131.3 (br.), 132.9 (br.) [C=CH_2, C=CH_2, *C*(imidazol-1-yl)] ppm. ^{15}N VACP/MAS NMR: δ = –244.9 (Si*N*C), –160.9 (C*N*C), –82.6 (Si*N*Si) ppm. ^{29}Si VACP/MAS NMR: δ = –125.8 ppm. ^{31}P VACP/MAS NMR: δ = –23.4 ppm.

8: Yield: 27%. $C_{24}H_{40}Cl_4N_6P_2Si_2$ (672.55): calcd. C 42.86, H 6.00, N 12.50; found C 43.1, H 6.0, N 12.6. ^{13}C VACP/MAS NMR: δ = 14.3 (CHCH_3), 15.2 (CHCH_3), 16.0 (CHCH_3), 17.3 (CHCH_3, C=CCH_3), 23.9 [d, $^1J(^{31}P,^{13}C)$ = 43 Hz, $CHCH_3$], 25.3 [d, $^1J(^{31}P,^{13}C)$ = 43 Hz, $CHCH_3$], 123.6 (br.), 132.4 (br.), 140.4 (br.) [C=*C*HCH$_3$, *C*=CHCH$_3$, *C*(imidazol-1-yl)] ppm. ^{15}N VACP/MAS NMR: δ = –228.7 (Si*N*C), –162.5 (C*N*C), –84.1 (Si*N*Si) ppm. ^{29}Si VACP/MAS NMR: δ = –125.1 ppm. ^{31}P VACP/MAS NMR: δ = –23.7 ppm.

Alternative Synthesis of 7: Triethylamine (415 mg, 4.10 mmol) and tetrachlorosilane (397 mg, 2.34 mmol) were added sequentially at 20 °C in single portions to a stirred suspension of **2** (375 mg, 2.04 mmol) in acetonitrile (30 mL), and the mixture was stirred at this temperature for 2 d. The resulting precipitate was isolated by filtration, washed with dichloromethane (5 mL), and dried in vacuo (0.01 mbar, 20 °C, 6 h) to yield **7** as a colorless solid. Yield: 553 mg (858 μmol, 84%). The analytical data of the product match with those obtained for the product synthesized according to the general method described above.

Crystal Structure Analyses of 5–8: Suitable single crystals of **5**–**8** were mounted in inert oil (perfluoropolyalkyl ether, ABCR) on a glass fiber and transferred to the cold nitrogen gas stream of the diffractometer (Stoe IPDS; graphite-monochromated Mo-K_α radiation, λ = 0.71073 Å). The structures were solved by direct methods (SHELXS-97) and refined by full-matrix least-squares methods on F^2 for all unique reflections (SHELXL-97).[12] A riding model was employed for the CH hydrogen atoms. Selected data for **5**: Single crystal of dimensions 0.30 × 0.20 × 0.04 mm obtained by crystallization from acetonitrile at 20 °C, $C_{18}H_{28}Cl_4N_6P_2Si_2$, M_r = 588.38, analysis at 173(2) K, triclinic, space group $P\bar{1}$ (no. 2), a = 7.6200(13), b = 9.1276(15), c = 10.5963(17) Å, α = 99.728(3), β = 103.531(3), γ = 113.180(3)°, V = 629.97(18) Å^3, Z = 1, $\rho_{calcd.}$ = 1.551 g cm^{-3}, μ = 0.713 mm^{-1}, $F(000)$ = 304, $2\theta_{max}$ = 56.08°, 8333 collected reflections, 3022 unique reflections (R_{int} = 0.0368), 147 parameters, S = 1.045, R_1 = 0.0346 [$I > 2\sigma(I)$], wR_2 (all data) = 0.0924, max./min. residual electron density = +0.492/–0.242 e Å^{-3}. Selected data for **6**: Single crystal of dimensions 0.40 × 0.30 × 0.20 mm obtained by slow cooling of a saturated solution in propionitrile from 90 to 20 °C, $C_{20}H_{32}Cl_4N_6P_2Si_2$, M_r = 616.44, analysis at 173(2) K, monoclinic, space group $P2_1/n$ (no. 14), a = 7.8083(7), b = 10.5254(13), c = 17.1856(17) Å, β = 92.302(12)°, V = 1411.3(3) Å^3, Z = 2, $\rho_{calcd.}$ = 1.451 g cm^{-3}, μ = 0.640 mm^{-1}, $F(000)$ = 640, $2\theta_{max}$ = 58.10°, 11187 collected reflections, 3647 unique reflections (R_{int} = 0.0475), 157 parameters, S = 1.003, R_1 = 0.0373 [$I > 2\sigma(I)$], wR_2 (all data) = 0.1000, max./min. residual electron density = +0.436/–0.433 e Å^{-3}. Selected data for **7**: Single crystal of dimensions 0.50 × 0.30 × 0.15 mm obtained by crystallization from acetonitrile at 20 °C, $C_{22}H_{36}Cl_4N_6P_2Si_2$, M_r = 644.49, analysis at 173(2) K, monoclinic, space group $C2/c$ (no. 15), a = 16.274(3), b = 12.3909(15), c = 15.676(3) Å, β = 109.74(2)°, V = 2975.4(9) Å^3, Z = 4, $\rho_{calcd.}$ = 1.439 g cm^{-3}, μ = 0.611 mm^{-1}, $F(000)$ = 1344, $2\theta_{max}$ = 58.12°, 20773 collected reflections, 3922 unique reflections (R_{int} = 0.0567), 167 parameters, S = 1.080, R_1 = 0.0402 [$I > 2\sigma(I)$], wR_2 (all data) = 0.1137, max./min. residual electron density = +0.464/–0.380 e Å^{-3}. Selected data for **8**: Single crystal of dimensions 0.50 × 0.30 × 0.20 mm obtained by crystallization from propionitrile at 20 °C, $C_{24}H_{40}Cl_4N_6P_2Si_2$, M_r = 672.54, analysis at 173(2) K, monoclinic, space group $P2_1/c$ (no. 14), a = 9.6854(12), b = 16.2387(14), c = 10.5653(11) Å, β = 106.663(13)°, V = 1591.9(3) Å^3, Z = 2, $\rho_{calcd.}$ = 1.403 g cm^{-3}, μ = 0.574 mm^{-1}, $F(000)$ = 704, $2\theta_{max}$ = 58.28°, 12012 collected reflections, 4249 unique reflections (R_{int} = 0.0358), 177 parameters, S = 1.072, R_1 = 0.0394 [$I > 2\sigma(I)$], wR_2 (all data) = 0.1122, max./min. residual electron density = +0.464/–0.411 e Å^{-3}. CCDC-843678 (for **5**), -843679 (for **6**), -843680 (for **7**), and -843681 (for **8**) contain the supplementary crystallographic data for this paper. These data can be obtained free of charge from The Cambridge Crystallographic Data Centre via www.ccdc.cam.ac.uk/data_request/cif.

[1] a) D. B. Grotjahn, Y. Gong, A. G. DiPasquale, L. N. Zakharov, A. L. Rheingold, *Organometallics* **2006**, *25*, 5693–5695; b) Z. Chen, H. W. Schmalle, T. Fox, O. Blacque, H. Berke, *J. Organomet. Chem.* **2007**, *692*, 4875–4885; c) D. B. Grotjahn, J. E. Kraus, H. Amouri, M.-N. Rager, A. L. Cooksy, A. J. Arita, S. A. Cortes-Llamas, A. A. Mallari, A. G. DiPasquale, C. E. Moore, L. M. Liable-Sands, J. D. Golen, L. N. Zakharov, A. L. Rheingold, *J. Am. Chem. Soc.* **2010**, *132*, 7919–7934.

[2] For selected reviews of higher-coordinate silicon compounds, see: a) R. R. Holmes, *Chem. Rev.* **1996**, *96*, 927–950; b) V. Pestunovich, S. Kirpichenko, M. Voronkov, in *The Chemistry of Organic Silicon Compounds*, vol. 2, part 2 (Eds.: Z. Rappoport, Y. Apeloig), Wiley, Chichester, **1998**, pp. 1447–1537; c) C. Chuit, R. J. P. Corriu, C. Reye, in *Chemistry of Hypervalent Compounds* (Ed.: K.-y. Akiba), Wiley-VCH, New York, **1999**,

pp. 81–146; d) R. Tacke, M. Pülm, B. Wagner, *Adv. Organomet. Chem.* **1999**, *44*, 221–273; e) M. A. Brook, *Silicon in Organic, Organometallic and Polymer Chemistry*, Wiley, New York, **2000**, pp. 97–114; f) R. Tacke, O. Seiler, in *Silicon Chemistry: From the Atom to Extended Systems* (Eds.: P. Jutzi, U. Schubert), Wiley-VCH, Weinheim, **2003**, pp. 324–337; g) D. Kost, I. Kalikhman, *Adv. Organomet. Chem.* **2004**, *5*, 1–106; h) D. Kost, I. Kalikhman, *Acc. Chem. Res.* **2009**, *42*, 303–314; i) E. P. A. Couzijn, J. C. Slootweg, A. W. Ehlers, K. Lammertsma, *Z. Anorg. Allg. Chem.* **2009**, *635*, 1273–1278.

[3] a) H. H. Karsch, R. Richter, E. Witt, *J. Organomet. Chem.* **1996**, *521*, 185–190; b) H. H. Karsch, B. Deubelly, U. Keller, O. Steigelmann, J. Lachmann, G. Müller, *Chem. Ber.* **1996**, *129*, 671–676; c) H. H. Karsch, B. Deubelly, U. Keller, F. Bienlein, R. Richter, P. Bissinger, M. Heckel, G. Müller, *Chem. Ber.* **1996**, *129*, 759–764.

[4] A. Toshimitsu, T. Saeki, K. Tamao, *J. Am. Chem. Soc.* **2001**, *123*, 9210–9211.

[5] D. Gau, R. Rodriguez, T. Kato, N. Saffon-Merceron, F. P. Cossío, A. Baceiredo, *Chem. Eur. J.* **2010**, *16*, 8255–8258.

[6] a) K. Issleib, H. Reinhold, *Z. Anorg. Allg. Chem.* **1962**, *314*, 113–124; b) I. R. Beattie, M. Webster, *J. Chem. Soc.* **1963**, 4285–4287; c) G. Fritz, R. Wiemers, U. Protzer, *Z. Anorg. Allg. Chem.* **1968**, *363*, 225–232; d) G. A. Ozin, *J. Chem. Soc. D* **1969**, 104; e) H. E. Blayden, M. Webster, *Inorg. Nucl. Chem. Lett.* **1970**, *6*, 703–705.

[7] a) S. Cota, M. Beyer, R. Bertermann, C. Burschka, K. Götz, M. Kaupp, R. Tacke, *Chem. Eur. J.* **2010**, *16*, 6582–6589; b) S. Metz, B. Theis, C. Burschka, R. Tacke, *Chem. Eur. J.* **2010**, *16*, 6844–6856; c) K. Junold, C. Burschka, R. Bertermann, R. Tacke, *Dalton Trans.* **2010**, *39*, 9401–9413; d) K. Junold, C. Burschka, R. Bertermann, R. Tacke, *Dalton Trans.* **2011**, *40*, 9844–9857.

[8] Compounds **1** and **2** were synthesized according to a method reported in ref.[1c]

[9] ^{1}H, $^{13}C\{^{1}H\}$, $^{29}Si\{^{1}H\}$, and $^{31}P\{^{1}H\}$ NMR spectra in solution were recorded at 23 °C with a Bruker Avance 500 NMR spectrometer (^{1}H 500.1, ^{13}C 125.8, ^{29}Si 99.4, ^{31}P 202.5 MHz). CD_2Cl_2 was used as the solvent. Chemical shifts were determined relative to internal $CDHCl_2$ (^{1}H, δ = 5.32 ppm), internal CD_2Cl_2 (^{13}C, δ = 53.8 ppm), external Me_4Si (^{29}Si, δ = 0 ppm), or external H_3PO_4 (85%, ^{31}P, δ = 0 ppm). Assignment of the ^{13}C NMR spectroscopic data was supported by DEPT 135 and $^{1}H,^{1}H$, $^{1}H,^{13}C$, $^{1}H,^{29}Si$, and $^{1}H,^{31}P$ correlation experiments. NMR spectroscopic data for **4**: ^{1}H NMR: δ = 0.87 [dd, $^{3}J(^{1}H,^{1}H)$ = 7.1, $^{3}J(^{31}P,^{1}H)$ = 14.3 Hz, 6 H, CH_3], 1.04 [dd, $^{3}J(^{1}H,^{1}H)$ = 7.1, $^{3}J(^{31}P,^{1}H)$ = 14.3 Hz, 6 H, CH_3], 2.14 [dsept, $^{2}J(^{31}P,^{1}H)$ = 3.8, $^{3}J(^{1}H,^{1}H)$ = 7.1 Hz, 2 H, CH_3CHCH_3], 7.26 [d, $^{4}J(^{31}P,^{1}H)$ = 1.5 Hz, 1 H, C*H*], 7.35–7.37 (m, 1 H, C*H*) ppm. $^{13}C\{^{1}H\}$ NMR: δ = 19.5 [d, $^{2}J(^{31}P,^{13}C)$ = 14.8 Hz, *C*H_3], 20.3 [d, $^{2}J(^{31}P,^{13}C)$ = 12.5 Hz, *C*H_3], 25.5 [d, $^{1}J(^{31}P,^{13}C)$ = 8.5 Hz, CH_3CHCH_3], 125.6–125.7 (m, *C*H), 132.0 (*C*H), 153.8 [d, $^{1}J(^{31}P,^{13}C)$ = 22.8 Hz, N_2CP] ppm. $^{29}Si\{^{1}H\}$ NMR: δ = –33.6 ppm. $^{31}P\{^{1}H\}$ NMR: δ = –10.1 ppm.

[10] For other dinuclear higher-coordinate silicon(IV) complexes, see: a) I. D. Kalikhman, B. A. Gostevskii, O. B. Bannikova, M. G. Voronkov, V. A. Pestunovich, *J. Organomet. Chem.* **1989**, *376*, 249–258; b) G. Cerveau, C. Chuit, E. Colomer, R. J. P. Corriu, C. Reyé, *Organometallics* **1990**, *9*, 2415–2417; c) D. A. Loy, J. H. Small, K. J. Shea, *Organometallics* **1993**, *12*, 1484–1488; d) M. Mühleisen, R. Tacke, *Organometallics* **1994**, *13*, 3740–3742; e) R. Tacke, M. Mühleisen, P. G. Jones, *Angew. Chem.* **1994**, *106*, 1250–1252; *Angew. Chem. Int. Ed. Engl.* **1994**, *33*, 1186–1188; f) B. Theis, C. Burschka, R. Tacke, *Chem. Eur. J.* **2008**, *14*, 4618–4630; g) E. Kertsnus-Banchik, B. Gostevskii, M. Botoshansky, I. Kalikhman, D. Kost, *Organometallics* **2010**, *29*, 5435–5445.

[11] The Berry distortions were analyzed with PLATON: A. L. Spek, *Acta Crystallogr., Sect. D* **2009**, *65*, 148–155.

[12] G. M. Sheldrick, *Acta Crystallogr., Sect. A* **2008**, *64*, 112–122.

Received: September 30, 2011
Published Online: December 5, 2011

DOI: 10.1002/ejic.201101192

Unprecedented Bidentate Coordination of the Uranyl Cation by the Chromate Anion in the Structure of $[(CH_3)_2CHNH_3]_2[UO_2(CrO_4)_2]$

Oleg I. Siidra,[a] Evgeny V. Nazarchuk,[a] and Sergey V. Krivovichev*[a]

Keywords: Chromium / Bidentate coordination / Structure elucidation / Uranium / Structural distortions / Actinides

$[(CH_3)_2CHNH_3]_2[UO_2(CrO_4)_2]$ is the first uranyl chromate with a bidentate coordination mode between the uranyl and chromate ions. Although this type of coordination is typical for sulfates, it has not been previously observed for other group VI elements. Statistical analysis of the bidentate coordination geometry parameters in uranyl compounds is given.

Introduction

Uranium compounds with tetrahedral oxoanions have received considerable attention due to their importance as minerals,[1] microporous[2] and nanostructured[3] materials, compounds present in altered spent nuclear fuel and radioactive waste, materials with interesting properties,[4] etc. In these structures, uranium ions may coordinate tetrahedral groups in either monodentate or bidentate coordination modes with the former being by far the most common in uranyl compounds. However, bidentate coordination of uranyl ions by TO_4 tetrahedral oxoanions is frequently observed for compounds with penta- and tetravalent T cations ($T = P^{5+}$, As^{5+}, V^{5+}, Si^{4+}, Ge^{4+}). Among hexavalent group VI elements (S, Cr, Se, Mo, W), bidentate coordination had been described in the crystal structures[5] and aqueous solutions[6] of uranyl sulfates but has so far been unknown for uranyl chromates, selenates, molybdates and tungstates.[7] This observation is striking as the S^{6+} cation is the smallest in the group ($S^{6+} < Cr^{6+} < Se^{6+} < Mo^{6+} < W^{6+}$) and therefore the absence of bidentate coordination cannot be assigned to the repulsive forces between the U^{6+} and T^{6+} cations only. Here we report the structure of $[(CH_3)_2CHNH_3]_2[UO_2(CrO_4)_2]$ (**1**), which is the first uranyl chromate with bidentate coordination of the uranyl cation by the chromate anion. In addition, we have investigated the bonding and structure–geometry trends in uranyl compounds with bidentate coordination of uranyl ions by tetrahedral oxoanions. The most interesting finding is that the U···T distance in bidentate complexes is seemingly independent of the formal oxidation state of T.

Results and Discussion

Orange-yellow crystals of **1** were obtained by a hydrothermal method. The crystal structure of **1** is based on uranyl chromate layers with a unique topology that has not been previously described for uranyl compounds (Figure 1a). There are two symmetrically independent U atoms, which both form linear $[O=U^{6+}=O]^{2+}$ uranyl cations (U–O 1.752–1.773 Å) equatorially coordinated by five O atoms to form pentagonal bipyramids. Four independent Cr positions are each tetrahedrally coordinated by four O atoms. The unique feature of the structure of **1** is that both U sites

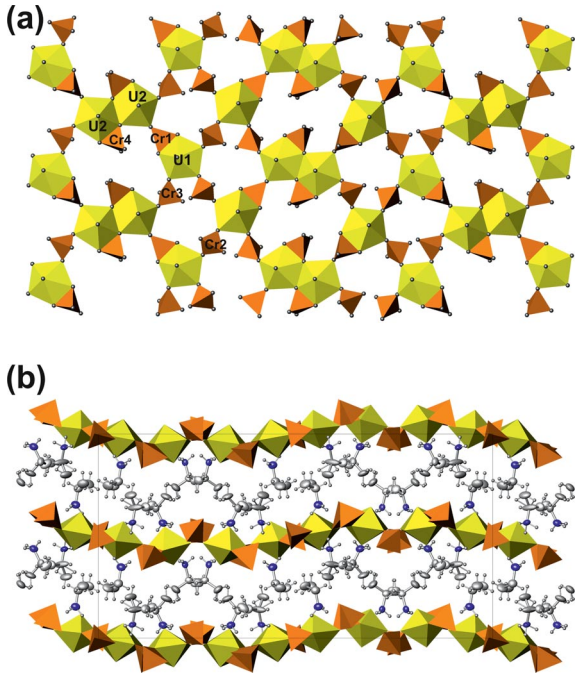

Figure 1. Uranyl chromate layer in the structure of **1** (a) and the structure projected along the *a* axis (b). Yellow and orange denote U and Cr polyhedra, respectively; C and N displacement ellipsoids (drawn at 50% probability level) are shown as grey and blue, respectively; H atoms are shown as small grey spheres.

[a] Department of Crystallography, Faculty of Geology,
St. Petersburg State University,
University Emb. 7/9; 199034 St. Petersburg, Russian Federation
Fax: +7-812-3284418
E-mail: skrivovi@mail.ru

Supporting information for this article is available on the WWW under http://dx.doi.org/10.1002/ejic.201101192.

are coordinated in a bidentate fashion by CrO_4^{2-} tetrahedral anions, which is the first time that this type of coordination has been observed for uranyl chromates. The $U1O_7$ pentagonal bipyramid forms a monomeric unit, in which two equatorial O atoms are involved in a bidentate linkage to the $Cr1O_4$ tetrahedron. Two $U2O_7$ bipyramids share an equatorial edge to form a dimeric moiety, in which each bipyramid is involved in bidentate coordination to the $Cr4O_4$ tetrahedra. The monomers and dimers are linked into layers through $Cr2O_4$ and $Cr3O_4$ tetrahedra, which coordinate uranyl ions in a monodentate fashion. The resulting layers have a $[UO_2(CrO_4)_2]^{2-}$ composition and are oriented parallel to (010) (Figure 1b). The layers are slightly modulated with a modulation vector parallel to the *c* axis of 35.29 Å.

The protonated isopropylamine units, $[(CH_3)_2CHNH_3]^+$, are located between the uranyl chromate layers and pack according to the balance of hydrophobic/hydrophillic interactions. The hydrophobic parts of the organic molecules are packed together into corrugated layers, whereas the amine headgroups are oriented towards the uranyl chromate layers and form N–H···O hydrogen bonds to the O atoms of uranyl ions and chromate tetrahedra.

The bidentate coordination mode in the uranyl chromate layer in **1** is associated with significant distortion of both the U and Cr coordination polyhedra. In order to analyse the distortion degree, O atoms in the layer can be classified into four groups: (i) atoms of the uranyl groups (O_{ur}, not affected by distortion), (ii) atoms of chromate tetrahedra involved in bidentate coordination (bidentate bridging, O_{bb}), (iii) atoms of chromate tetrahedra involved in monodentate coordination (monodentate bridging, O_{mb}) and (iv) terminal atoms of chromate tetrahedra not bonded to U (terminal, O_t). Geometric distortions induced by the bidentate coordination of the uranyl ion by chromate include the following effects: (a) the U–O_{bb} bonds are essentially longer (2.448–2.528 Å) than the average standard U–O bond in a UO_7 pentagonal bipyramid[8] (2.37 Å), (b) the O_{bb}–U–O_{bb} valence angles (ξ_1) are smaller (61.2–63.3°) than the expected ideal value of 72°, (c) the Cr–O_{bb} bond lengths are longer (1.658–1.717 Å; <Cr–O_{bb}> = 1.679 Å) than the average value of 1.647 Å observed for uranyl chromates[9] and (d) the O_{bb}–Cr–O_{bb} bond valence angles (ξ_2) are smaller (99.7–100.6°) than the ideal tetrahedral value of 109.5°. In the chromate tetrahedra, additional distortion is provoked by their monodentate bridging role with the Cr–O_{mb} bonds (1.655–1.697 Å), which are longer than the Cr–O_t bonds (1.572–1.594 Å).

In order to investigate the general effects of bidentate coordination on the structural geometric parameters in uranyl compounds, we have analysed the available literature data on uranyl phosphates, arsenates, vanadates, silicates and sulfates. The only chromate compound taken into account was **1**. For the analysis, only structures with uranium ions with pentagonal bipyramidal coordination were taken into account. The analysis involved the calculation of the U···T interatomic distances, average T–O, T–O_{bb} and U–O_{bb} bond lengths, and O_{bb}–U–O_{bb} (ξ_1) and O_{bb}–T–O_{bb} (ξ_2) valence angles. The results are presented in Table 1 and some representative trends are shown in Figure 2. The U···T interatomic distance positively correlates with the average

Table 1. Geometric parameters of bidentate coordination of uranyl ions by TO_4 tetrahedra tetrahedral oxoanions (T = V, P, As, S, Cr, Si).

T	<T–O> [Å]	<T–O_{bb}> [Å]	<U–O_{bb}> [Å]	<U···T> [Å]	<ξ_1> [°]	<ξ_2> [°]
V	1.710	1.747	2.500	3.270	63.37	97.57
P	1.549	1.537	2.479	3.129	57.98	101.78
As	1.697	1.679	2.504	3.258	60.76	96.62
S	1.495	1.477	2.473	3.103	56.50	102.89
Cr	1.680	1.643	2.489	3.206	62.38	100.09
Si	1.617	1.620	2.464	3.206	60.64	100.59
V	1.710	1.747	2.500	3.270	63.37	97.57

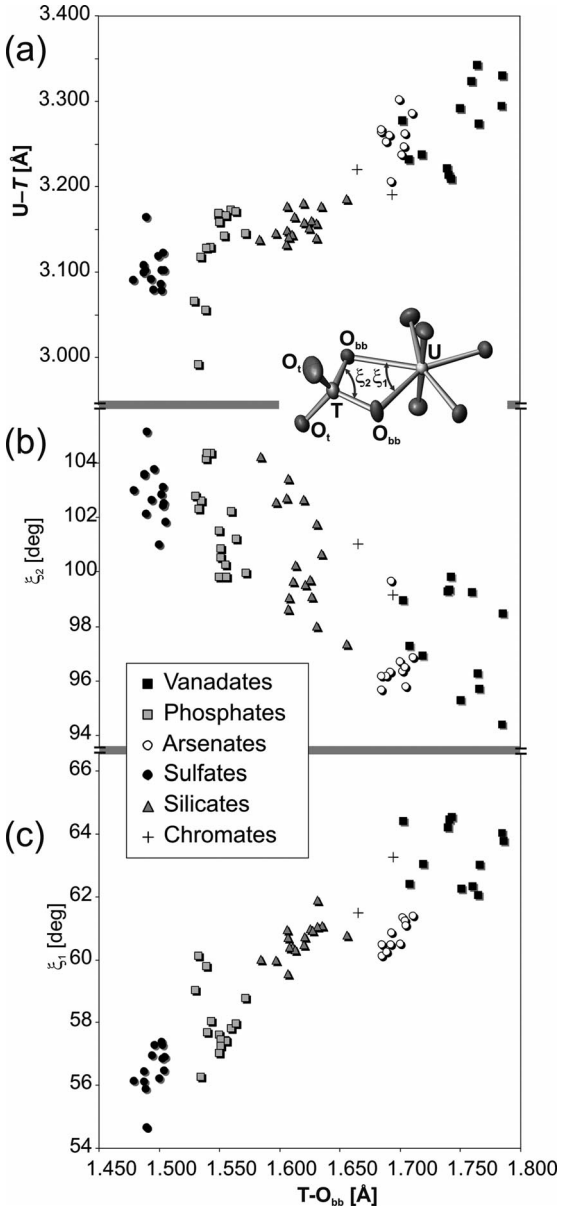

Figure 2. Geometric parameters of bidentate coordination in uranyl oxosalts: (a) the U···T distance vs. T–O_{bb}; (b) and (c) the ξ_1 and ξ_2 valence angles vs. T–O_{bb}, respectively.

<T–O_{bb}> bond length: the larger the tetrahedral oxoanion, the longer the U···T distance (Figure 2a). However, variations in the U···T distances occur in a narrow range (2.99–3.34 Å), owing to the mutual adjustment of the ξ_1 and ξ_2 valence angles (Figure 2b and c). The smaller the tetrahedron, the more rigid its structure and the less deviated the ξ_2 valence angle is from the ideal tetrahedral value of 109.5°. As a result, the U···T distance is adjusted by the essential reduction of the ξ_1 valence angle and its significant deviation from 72°, which is the value for an ideal UO_7 pentagonal bipyramid. With the increasing size of the tetrahedral oxoanion, it becomes more flexible and the appropriate range of the U···T distances is adjusted by both ξ_1 and ξ_2 valence angles; the larger the tetrahedron, the smaller the deviation of the ξ_1 valence angle from 72°. Figure 2 illustrates an interesting observation: the U···T distance is seemingly independent of the formal oxidation state of T, which ranges from 4+ (silicates) to 6+ (sulfates and chromates). The data presented in Table 1 also indicate that, although bidentate coordination has a strong influence on the U–O_{bb} bond length [it appears to be essentially longer than the average U–O bond length in typical pentagonal bipyramidal coordination (2.37 Å)], bond length distortions within the TO_4 tetrahedra are much less sensitive to the bonding interactions with uranyl ions. This observation is, however, somewhat lessened by the participation of the tetrahedra in bonding to other types of cations in the structure.

Conclusions

We have been able to prepare and characterize the first uranyl chromate with a bidentate coordination mode between the uranyl and chromate ions. It is worth noting that, in contrast to uranyl chromates, bidentate coordination is typical for neptunyl chromates[10] and, with the accumulation of structural data, it would be worthwhile to compare the influence of the coordination mode on the structural geometries in uranyl and neptunyl compounds. It would also be of interest to provide a theoretical basis for these trends by quantum chemical computations.

Experimental Section

Single crystals of **1** were obtained by a hydrothermal method from a mixture of CrO_3 (0.1 g), $(UO_2)(NO_3)_2{\cdot}6H_2O$ (0.095 g), $(CH_3)_2CHNH_2$ (1 mL) and distilled H_2O (5 mL). The reactants were placed in a Teflon-lined Parr bomb and heated to 100 °C for six days and then cooled to 25 °C with a cooling rate of 8 °C/h. The products consisted of yellow-orange, transparent, perfectly shaped crystals of **1**. The products were collected by filtration and washed with ultrapure water. IR spectra (Bruker Vertex 70) collected from **1** confirmed the presence of isopropylamine, uranyl ions and chromate groups. Qualitative electron microprobe analysis (LINK AN-10000 EDS) indicated the presence of no elements with an atomic number greater than 11 (Na) except U^{6+} and Cr^{6+}. Crystallographic data for $[(CH_3)_2CHNH_3]_2[UO_2(CrO_4)_2]$: Greenish yellow plate, 0.09 × 0.06 × 0.11 mm^3, orthorhombic, *Pbca*, a = 10.327(3), b = 18.257(5), c = 35.285(10) Å, V = 6653(3) $Å^3$, Z = 16, T = 296(2) K, Mo-K_α radiation (λ = 0.71073 Å), μ = 11.041 mm^{-1}, $R1$ = 0.033, $wR2$ = 0.057, GOF = 0.769 for 5612 unique reflections with $I > 2\sigma I$. CCDC-843100 contains the supplementary crystallographic data for this paper. These data can be obtained free of charge from The Cambridge Crystallographic Data Centre via www.ccdc.cam.ac.uk/data_request/cif.

Supporting Information (see footnote on the first page of this article): IR spectra and SEM images of crystals of **1**.

Acknowledgments

This work was supported by St. Petersburg State University through the internal grant 3.37.84.2011 and the X-ray Diffraction Resource Center.

[1] a) P. C. Burns, *Can. Mineral.* **2001**, *39*, 1139–1146; b) J. M. Jackson, P. C. Burns, *Can. Mineral.* **2001**, *39*, 187–195; c) A. J. Locock, P. C. Burns, *Amer. Mineral.* **2003**, *88*, 240–244; d) A. J. Locock, P. C. Burns, *Can. Mineral.* **2003**, *41*, 91–101; e) J. Brugger, P. C. Burns, N. Meisser, *Amer. Mineral.* **2003**, *88*, 676–685; f) S. J. Mills, W. D. Birch, U. Kolitsch, W. G. Mumme, I. E. Grey, *Amer. Mineral.* **2008**, *93*, 691–697; g) K. Walenta, F. Hatert, T. Theye, F. Lissner, K. Roeller, *Eur. J. Mineral.* **2009**, *21*, 515–520.

[2] a) J. A. Danis, W. H. Runde, B. Scott, J. Fettinger, B. Eichhorn, *Chem. Commun.* **2001**, 2378–2379; b) X. Wang, J. Huang, A. J. Jacobson, *J. Am. Chem. Soc.* **2002**, *124*, 15190–15191; c) M. Doran, A. J. Norquist, D. O'Hare, *Chem. Commun.* **2002**, *8*, 2946–2947; d) S. V. Krivovichev, C. L. Cahill, P. C. Burns, *Inorg. Chem.* **2003**, *42*, 2459–2464; e) M. B. Doran, C. L. Stuart, A. J. Norquist, D. O'Hare, *Chem. Mater.* **2004**, *16*, 565–566; f) S. V. Krivovichev, T. Armbruster, D. Yu. Chernyshov, P. C. Burns, E. V. Nazarchuk, W. Depmeier, *Microporous Mesoporous Mater.* **2005**, *78*, 225–234; g) S. V. Krivovichev, P. C. Burns, T. Armbruster, E. V. Nazarchuk, W. Depmeier, *Microporous Mesoporous Mater.* **2005**, *78*, 217–224; h) S. V. Krivovichev, C. L. Cahill, E. V. Nazarchuk, P. C. Burns, T. Armbruster, W. Depmeier, *Microporous Mesoporous Mater.* **2005**, *78*, 209–215; i) C.-S. Chen, S. F. Lee, K.-H. Li, *J. Am. Chem. Soc.* **2005**, *127*, 12208–12209; j) C. Lin, C. Chen, A. A. Shiryaev, Y. V. Zubavichus, K.-H. Lii, *Inorg. Chem.* **2008**, *47*, 4445–4447; k) C.-S. Lee, S.-L. Wang, K.-H. Lii, *J. Am. Chem. Soc.* **2009**, *131*, 15116–15117; l) Y. Yu, W. Zhan, T. E. Albrecht-Schmitt, *Inorg. Chem.* **2008**, *47*, 9050–9054; m) M. S. Bharara, A. E. V. Gorden, *Dalton Trans.* **2010**, *39*, 3557–3559; n) V. K. Rao, K. Bharathi, R. Prabhu, M. Chandra, S. Natarajan, *Inorg. Chem.* **2010**, *49*, 2931–2947.

[3] a) S. V. Krivovichev, V. Kahlenberg, R. Kaindl, E. Mersdorf, I. G. Tananaev, B. F. Myasoedov, *Angew. Chem.* **2005**, *117*, 1158–1160; *Angew. Chem.* **2005**, *117*, 1158; *Angew. Chem. Int. Ed.* **2005**, *44*, 1134–1136; b) S. V. Krivovichev, V. Kahlenberg, I. G. Tananaev, R. Kaindl, E. Mersdorf, B. F. Myasoedov, *J. Am. Chem. Soc.* **2005**, *127*, 1072–1073; c) E. V. Alekseev, S. V. Krivovichev, W. Depmeier, *Angew. Chem.* **2008**, *120*, 559–561; *Angew. Chem. Int. Ed.* **2008**, *47*, 549–551; d) J. Ling, J. Qiu, G. E. Sigmon, M. Ward, J. E. S. Szymanowski, P. C. Burns, *J. Am. Chem. Soc.* **2010**, *132*, 13395–13402; e) S. V. Krivovichev, *Eur. J. Inorg. Chem.* **2010**, 2594–2603.

[4] a) K. M. Ok, J. Baek, P. S. Halasyamani, D. O'Hare, *Inorg. Chem.* **2006**, *45*, 10207–10214; b) T. Y. Shvareva, J. V. Beitz, E. C. Duin, T. E. Albrecht-Schmitt, *Chem. Mater.* **2005**, *17*, 6219–6222; c) T. Y. Shvareva, T. A. Sullens, T. C. Shehee, T. E. Albrecht-Schmitt, *Inorg. Chem.* **2005**, *44*, 300–305; d) T. Y. Shvareva, T. E. Albrecht-Schmitt, *Inorg. Chem.* **2006**, *45*, 1900–1902.

[5] a) Yu. N. Mikhailov, L. A. Kokh, V. G. Kuznetsov, T. G. Grevtseva, S. K. Sokol, G. V. Ellert, *Koord. Khim.* **1977**, *3*, 508–

513; b) P. C. Burns, L. A. Hayden, *Acta Crystallogr., Sect. C* **2002**, *58*, i121–i123; c) L. A. Hayden, P. C. Burns, *Can. Mineral.* **2002**, *40*, 211–216; d) L. A. Hayden, P. C. Burns, *J. Solid State Chem.* **2002**, *163*, 313–318; e) M. B. Doran, A. J. Norquist, D. O'Hare, *Acta Crystallogr., Sect. E* **2003**, *59*, m765–m767; f) M. B. Doran, A. J. Norquist, D. O'Hare, *Acta Crystallogr., Sect. E* **2003**, *59*, m762–m764; g) A. J. Norquist, M. B. Doran, D. O'Hare, *Inorg. Chem.* **2005**, *44*, 3837–3843; h) A. J. Norquist, M. B. Doran, D. O'Hare, *Acta Crystallogr., Sect. E* **2005**, *61*, m807–m810.

[6] a) H. Moll, T. Reich, C. Henning, A. Rossberg, Z. Szabo, I. Grenthe, *Radiochim. Acta* **2000**, *88*, 559–566; b) J. Neuefeind, S. Skanthakumar, L. Soderholm, *Inorg. Chem.* **2004**, *43*, 2422–2426; c) V. Vallet, I. Grenthe, *C. R. Chim.* **2007**, *10*, 905–915; d) C. Hennig, K. Schmeide, V. Brendler, H. Moll, S. Tsushima, A. C. Scheinost, *Inorg. Chem.* **2007**, *46*, 5882–5892; e) C. Hennig, K. Schmeide, V. Brendler, H. Moll, T. Tsushima, A. C. Scheinost, *AIP. Conf. Proc.* **2007**, *882*, 262–264; f) T. Vercouter, P. Vitorge, B. Amekraz, C. Moulin, *Inorg. Chem.* **2008**, *47*, 2180–2189; g) C. Hennig, W. Kraus, F. Emmerling, A. Ikeda, A. C. Scheinost, *Inorg. Chem.* **2008**, *47*, 1634–1638.

[7] S. V. Krivovichev, P. C. Burns in *Structural Chemistry of Inorganic Actinide Compounds* (Eds: S. V. Krivovichev, P. C. Burns, I. G. Tananaev), Elsevier, Amsterdam, **2007**, pp. 95–182.

[8] P. C. Burns, R. C. Ewing, F. C. Hawthorne, *Can. Mineral.* **1997**, *35*, 1551–1570.

[9] S. V. Krivovichev, *Radiochemistry* **2004**, *46*, 434–437.

[10] a) M. S. Grigor'ev, N. A. Baturin, A. M. Fedoseev, N. A. Budantseva, *Radiochemistry* **1991**, *33*, 53–63; b) M. S. Grigor'ev, T. E. Plotnikova, N. A. Baturin, N. A. Budantseva, A. M. Fedoseev, *Radiochemistry* **1995**, *37*, 102–105.

Received: October 27, 2011
Published Online: December 8, 2011

DOI: 10.1002/ejic.201100947

Ionic Additives and Weak Magnetic Fields in the Thermal Decomposition of Octacarbonyldicobalt – Tools To Control the Morphology of Cobalt Nanoparticles

Axel Dreyer,[a] Michael Peter,[b] Jochen Mattay,[b] Katrin Eckstädt,[c] Andreas Hütten,[c] and Peter Jutzi*[a]

Keywords: Cobalt / Nanoparticles / Synthetic methods / Surfactants / Magnetic properties

In the presence of ionic compounds, the thermal decomposition of octacarbonyldicobalt, $Co_2(CO)_8$, in an inert solvent leads exclusively to ε-Co nanocubes. The ionic species can be added directly or generated in situ by a chemical reaction between an additive and the precursor or between two additives. The additional presence of an inhomogeneous magnetic field leads to disc-shaped crystalline nanoparticles, which assemble to chains.

Introduction

Only very recently, we have investigated in detail the thermal decomposition of decamethylstannocene, $(Me_5C_5)_2Sn$, in organic solvents, which resulted in the formation of different morphologies of nanostructured β-tin particles. Surprisingly, the presence of ionic additives during the thermolysis led exclusively to the formation of cubes with controllable size.[1] In the context of our ongoing interest in the investigation of the magnetic properties of cobalt nanoparticles prepared from the thermal decomposition of octacarbonyldicobalt, $Co_2(CO)_8$, in organic solvents,[2–4] we now investigated the influence of ionic additives on the morphology of cobalt nanoparticles. The effect of ionic compounds as additives on the decomposition of $Co_2(CO)_8$ has not been described in the literature so far, though this synthetic strategy represents a classical procedure[5–7] for the preparation of Co nanoparticles,[8–16] together with the decomposition of other organometallic precursors[17] and with the reduction of cobalt salts.[18–22] Very recent studies have shown that changing the shape of cobalt nanoparticles from spherical to cubic can fundamentally change their magnetic behavior.[15,23–25] Here we describe our observation that the decomposition of $Co_2(CO)_8$ in the presence of ionic additives leads exclusively to Co nanocubes with average edge lengths between 35 and 95 nm, depending on the reaction conditions. For shape control, it is not important whether the ionic additive is present already from the beginning or formed only during the thermal decomposition.

The influence of an external magnetic field during the synthesis of cobalt nanoparticles[26–29] and the self-organization of cobalt nanoparticles under the influence of an external magnetic field[15,14] are documented in the literature. One-dimensional assemblies have been observed in all cases, and the resulting physical effects have been studied. To the best of our knowledge, the influence of an external magnetic field applied during the thermal decomposition of $Co_2(CO)_8$ has not been studied so far.[30] Here we describe the effect of an additional weak external field, which leads to a change in the shape of the cobalt nanoparticles from cubes to discs, which are self-organized to chains.

Results and Discussion

An overview of the performed experiments with a schematic representation of the particle shapes obtained together with a collection of TEM images is presented in Figure 1. The respective XRD patterns are collected in Figure 2. The magnetic properties of the Co nanoparticles correspond to those already described in the literature[11,15,20] and will not be discussed.[31]

The influence of the following additives has been investigated: (1) cetyltrimethylammonium bromide (CTAB), (2) benzylpyridine (BPy), and (3) mixtures of oleic acid (OS) and oleylamine (OA).

[a] Bielefeld University, Department of Chemistry, Institute of Inorganic Chemistry,
Universitätsstrasse 25, 33615 Bielefeld, Germany
Fax: +49-521-106 6026
E-mail: peter.jutzi@uni-bielefeld.de
[b] Bielefeld University, Department of Chemistry, Institute of Organic Chemistry,
Universitätsstrasse 25, 33615 Bielefeld, Germany
[c] Bielefeld University, Department of Physics, Institute of Thin Films & Physics of Nanostructures,
Universitätsstrasse 25, 33615 Bielefeld, Germany

Supporting information for this article is available on the WWW under http://dx.doi.org/10.1002/ejic.201100947.

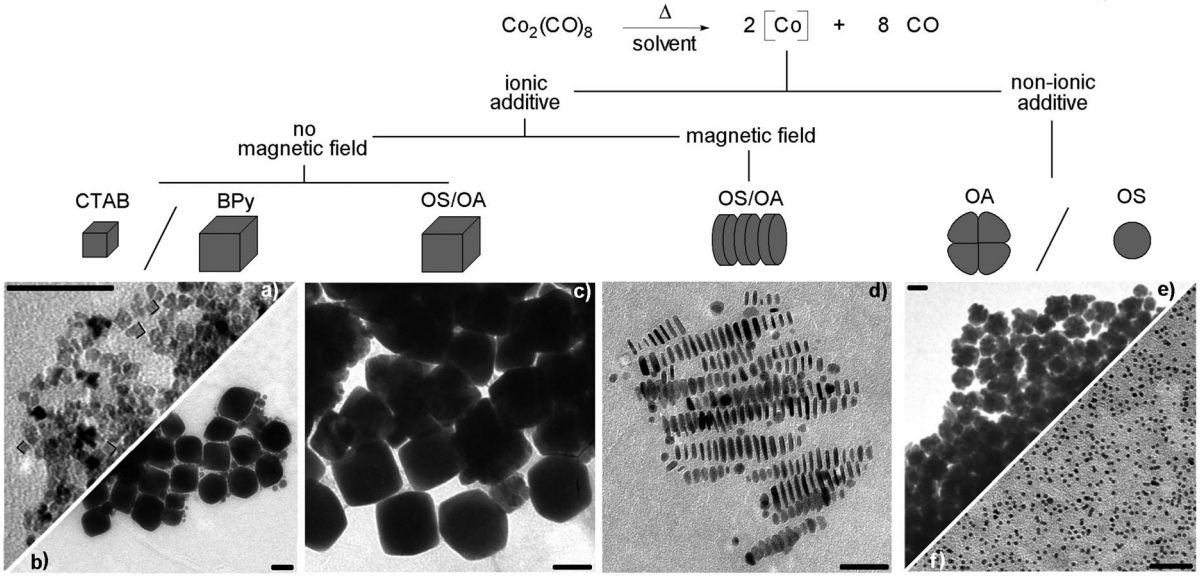

Figure 1. Schematic overview of the morphologies of Co nanoparticles obtained by the thermal decomposition of $Co_2(CO)_8$ under the influence of ionic additives with and without an external magnetic field and under the influence of non-ionic additives. TEM images show the respective morphologies. The chosen additives are: (a) cetyltrimethylammonium bromide (CTAB; the cubic structure of some particles is exemplarily marked), (b) 4-benzylpyridine (BPy), (c and d) an OS/OA mixture in the absence (c) and in the presence of a magnetic field (d), (e) OA, and (f) OS.[8] Scale bar: 50 nm. Additional TEM images with higher magnification are presented in section B of the Supporting Information.

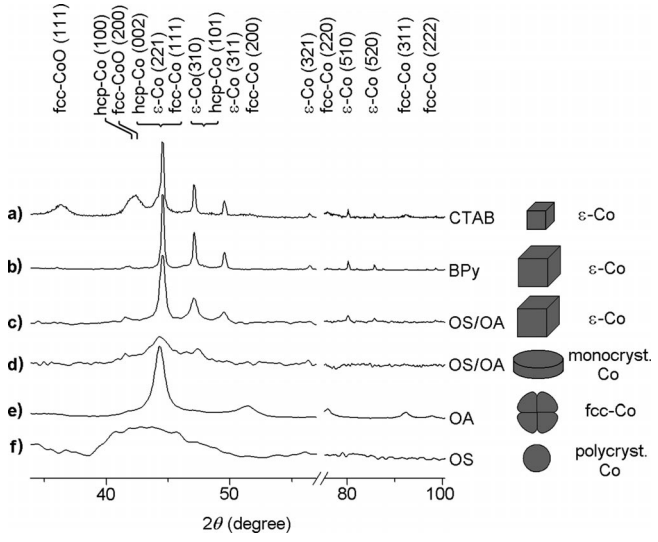

Figure 2. XRD patterns[33] of cobalt nanoparticles with various morphologies synthesized by the thermal decomposition of $Co_2(CO)_8$ in the presence of (a) cetyltrimethylammonium bromide (CTAB), (b) 4-benzylpyridine (BPy), (c and d) an OS/OA mixture () in the absence (c) and in the presence of a magnetic field (d), (e) OA, and (f) OS.

Cetyltrimethylammonium Bromide (CTAB)

The synthesis of Co nanoparticles in the presence of CTAB (0.16 mM) led to the formation of small nanocubes of ε-Co with an edge length of 4.1 ± 1.9 nm (TEM image in Figure 1a and XRD pattern in Figure 2a). The XRD pattern indicates small contributions of fcc cobalt(II) oxide as a result of oxidation at the particle surface during the measurement. The crystallite size was determined as 34.9 nm.[32]

Benzylpyridine (BPy)

The synthesis of Co nanoparticles in the presence of BPy (0.12 mmol) led to the formation of nanocubes of ε-Co with an average edge length of 57.6 ± 21.5 nm (TEM image in Figure 1b and XRD pattern in Figure 2b). The crystallite size of 26.3 nm indicates a polycrystalline texture.

During the usual work-up, a deep green solution was obtained after centrifugation. The conductivity of this solution was measured to be 0.5 $\mu S\,cm^{-1}$. Evaporation of the solvent led to an air-sensitive, viscous, red-brown residue. Its IR spectrum shows absorptions at 1895, 1863 and 1701 cm^{-1}, which can be assigned to the $Co(CO)_4^-$ unit.[34–36] Hieber has reported that $Co_2(CO)_8$ disproportionates with pyridine (Py) already at room temperature to give the red-brown salt $[CoPy_6]^{2+}[Co(CO)_4]^-_2$.[37] We conclude that, during the synthetic procedure (see Experimental Section) the soluble ionic compound $[Co(BPy)_6]^{2+}$-$[Co(CO)_4]^-_2$ is formed in addition to the Co nanocubes (for further details, see section C of the Supporting Information).

Mixtures of Oleic Acid (OS) and Oleylamine (OA)

The synthesis of Co nanoparticles in the presence of a mixture of OS (0.12 mmol) and OA (0.12 mmol) led to the

formation of polycrystalline nanocubes of ε-Co with an average edge-length of 68.6 ± 14.0 nm (TEM image in Figure 1c and XRD pattern in Figure 2c). The average crystallite size was determined to be 22.2 nm (Figure 2c). Other OS/OA ratios also led to the formation of nanocubes. Interestingly, the size of the nanocubes strongly depends on the OS/OA ratio: Figure 3 shows that the average edge-length decreases with an increase of the OA component.

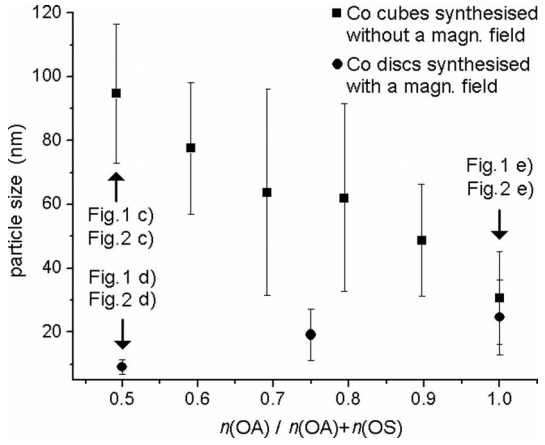

Figure 3. Edge length of Co nanocubes (squares) and diameter of Co nanodiscs (dots) depending on the mixing ratio of the additives (OS/OA). Nanocubes (in the absence of a magnetic field; squares) and nanodiscs (in the presence of a magnetic field; dots) were obtained.

The synthesis of Co nanoparticles in the presence of only a single additive (long-chain amine or carboxylic acid) has already been described in the literature in detail: The use of hexadecylamine (HDA) as additive leads to polycrystalline hcp-Co spheres and that of OS to monocrystalline ε-Co spheres.[11] For comparison, we have performed similar experiments with OA (0.32 mmol) and with OS (0.52 mmol) as single additives. As expected, the formation of spherical nanoparticles was observed. In the presence of OA, small crystallites of fcc-Co are formed, which aggregate to larger particles (27.7 ± 13.1 nm, Figures 1e and 2e). In the presence of OS, polycrystalline Co particles are observed (4.3 ± 1.1 nm, Figures 1f and 2f). The small particles and the resulting broad Bragg reflections do not allow a structure assignment.

In mixtures of organic carboxylic acids and amines, the formation of the corresponding salts is expected ($RCOOH + RNH_2 \rightleftarrows RNH_3^+ + RCOO^-$). The presence of ionic species has been confirmed by IR spectroscopic and conductivity measurements. In IR spectroscopic studies of the system OS/OA, vibrations assignable to the COOH unit appear in pure OS at 1703 and 933 cm^{-1}, whereas vibrations assignable to the COO^- unit in the corresponding salt formed in an OS/OA mixture appear at 1557 and 1396 cm^{-1} (for further details see section D of the Supporting Information). Conductivity measurements in the OS/OA system were not conclusive because of the restricted ion mobility. Alternatively, we have measured the conductivity of the system consisting of hexanoic acid (HS) and hexylamine (HA). A mixture of 3 mmol HS and 3 mmol HA in 12 mL 1.2-dichlorobenzene showed a conductivity of 1.2 ± 0.3 μS cm^{-1} at 30 °C, which increased linearly with increasing temperature up to 2.3 ± 0.3 μS cm^{-1} at 100 °C (see section C of the Supporting Information). As expected, solutions of the pure components did not show any conductivity.

Weak Magnetic Field during Synthesis

The influence of a weak magnetic field on the shape of the Co particles was investigated exemplarily in a system containing an OS/OA mixture as additive. The synthesis was performed in the presence of a heterogeneous magnetic field of 0.03 T. A permanent magnet ($Nd_2Fe_{12}B$, 30 × 5 × 10 mm) was positioned horizontally underneath the reaction flask. Nanodiscs of ε-Co with an average diameter of 9.1 ± 2.3 nm and with an average thickness of 4.5 ± 1.8 nm were formed. The discs are organized in form of chains by magnetic dipole interactions.[10,11] Tilted chain segments confirm the existing disc shape (Figure 1d). The disc size is influenced only to a small extent by the OS/OA ratio; the size increases with the increase of the OA component (Figure 3). XRD investigations prove the presence of monocrystalline Co with a crystallite size of 5.8 nm (Figure 2d). A structure assignment (ε- or hcp-Co) remains uncertain because of broad Bragg reflections.

Conclusions

Our experiments clearly show that the presence of ionic species and of magnetic fields during the thermal decomposition of $Co_2(CO)_8$ allows to control the morphology of the resulting Co nanoparticles. Ionic additives lead exclusively to the formation of nanocubes. The ionic species are added in the form of a stable salt (CTAB) or are formed by a chemical reaction between the additive and the precursor molecule [BPy/$Co_2(CO)_8$] or between additives (OS/OA). In the OS/OA additive system, the additional presence of a weak inhomogeneous magnetic field leads to the formation of nanodiscs, which assemble to chains.

Only very recently, Scariot et al. have observed that nanocubes are formed in the thermal decomposition of $Co_2(CO)_8$ performed in an ionic liquid as solvent.[16] Our experiments demonstrate that an inert organic solvent and the presence of ionic additives is sufficient to initiate a comparable selectivity in particle formation. Puntes et al. have reported that the thermal decomposition of $Co_2(CO)_8$ in the presence of the additive mixture OS/HDA leads to hcp-Co nanodiscs.[11] We assume that a magnetic stirring bar has been used in these experiments.[38] According to our observations, the weak inhomogeneous magnetic field of a stirring bar is sufficient to induce a change in shape from nanocubes to nanodiscs.

In future work, the mechanisms that are responsible for the influence of electric charges and heterogeneous magnetic fields on the formation of anisotropic nanoparticles have to be investigated in detail. With regard to the influence of electric charges, we suppose that a mechanism sim-

ilar to that observed for the formation of tin cubes in the presence of ionic additives is operative.[1] Concerning the influence of magnetic fields, the underlying effect is not yet understood. The presence of paramagnetic intermediates during the formation of the particles is indicated. In the literature, there are hints for the existence of paramagnetic species in the thermal decomposition of $Co_2(CO)_8$.[39,40]

In a more general context, investigations need to be carried out to determine whether our results on the control of the shape of tin and cobalt particles formed can be transformed to other chemical systems used for the preparation of nanoparticles.[41]

Experimental Section

Synthesis and Characterization of the Cobalt Nanoparticles and the Additive Mixtures

In an argon atmosphere, a solution (3 mL) containing 1,2-dichlorobenzene and the respective additive were heated to 182 °C by a hemispherical heating mantle while stirring with a sealed mechanical stirrer. Then, a solution of $Co_2(CO)_8$ in 1,2-dichlorobenzene (1 mL, 0.28 mmol) was quickly injected. After a reaction time of 15 minutes, the black colloidal particle suspension obtained was treated by following a usual work-up procedure: addition of acetonitrile (6 mL), centrifugation [3 min relative centrifugal force (RCF) 7500 $m\,s^{-2}$], substitution of the supernatant solution by pure 1.2-dichlorobenzene and redispersion. Transmission electron microscopy (Philips CM 200 TWIN) was used to characterize the morphology of the as-prepared nanoparticles, while X-ray diffraction (Philips X'pert) was used to characterize their crystalline structure and to determine the crystallite size with the help of the Scherrer equation.

The TEM samples were prepared by applying a drop of the particle solution (0.1 μL) on the carbon-coated copper grid, removing parts of the particle solution by a filter paper, and drying the remaining liquid film under vacuum. The XRD samples were prepared by applying the particle solution (250 μL) on a Si-111 wafer (10 × 10 mm) and removing the solvent in the vacuum.

IR spectroscopy (Bruker Vektor 22) and conductivity measurements (Schott CG853) were used to characterize the additive mixtures. Further experimental and analytical details are given in the Supporting Information.

Supporting Information (see footnote on the first page of this article): Preparation of the cobalt particles, transmission electron microscopy of the cobalt particles, identification of hexa(4-benzylpyridine)cobalt(II) bis(tetracarbonylcobaltate), and IR spectroscopy and conductivity measurements of the additive mixtures.

Acknowledgments

We wish to thank the University of Bielefeld and the Faculties of Chemistry and Physics for support with experiments and analyses, and the Deutsche Forschungsgemeinschaft (DFG) for financial support within the framework of the FOR 945 project 3. We are indebted to Nadine Mill for her experimental work.

[1] A. Dreyer, I. Ennen, T. Koop, A. Hütten, P. Jutzi, *Small* **2011**, *7*, 3075–3086.
[2] D. Sudfeld, K. Wojczykowski, W. Hachmann, P. Jutzi, G. Reiss, A. Hütten, *J. Appl. Phys.* **2003**, *93*, 7328.
[3] A. Hütten, D. Sudfeld, K. Wojczykowski, P. Jutzi, G. Reiss, *J. Magn. Magn. Mater.* **2003**, *262*, 23.
[4] A. Hütten, D. Sudfeld, I. Ennen, G. Reiss, K. Wojczykowski, P. Jutzi, *J. Magn. Magn. Mater.* **2005**, *293*, 93.
[5] A.-H. Lu, E. L. Salabas, F. Schüth, *Angew. Chem.* **2007**, *119*, 1242–1266; *Angew. Chem. Int. Ed.* **2007**, *46*, 1222–1244.
[6] Y. Xia, Y. Xiong, B. Lim, S. K. Skrabalak, *Angew. Chem.* **2009**, *121*, 62–92; *Angew. Chem. Int. Ed.* **2009**, *48*, 60–103.
[7] N. A. Frey, S. Peng, K. Cheng, S. Sun, *Chem. Soc. Rev.* **2009**, *38*, 2532.
[8] J. R. Thomas, *J. Appl. Phys.* **1966**, *37*, 2914.
[9] V. F. Puntes, K. M. Krishnan, A. P. Alivisatos, *Top. Catal.* **2002**, *19*, 145.
[10] V. F. Puntes, K. M. Krishnan, A. P. Alivisatos, *Science* **2001**, *291*, 2115.
[11] V. F. Puntes, D. Zanchet, C. Erdonmenz, A. P. Alivisatos, *J. Am. Chem. Soc.* **2002**, *124*, 12874.
[12] G. Cheng, J. D. Carter, T. Guo, *Chem. Phys. Lett.* **2004**, *400*, 122.
[13] G. Cheng, D. Romero, G. T. Fraser, A. R. Hight Walker, *Langmuir* **2005**, *21*, 12055.
[14] G. Cheng, C. L. Dennis, R. D. Shull, A. R. Hight Walker, *Langmuir* **2007**, *23*, 11740.
[15] G. Cheng, R. D. Shull, A. R. Hight Walker, *J. Magn. Magn. Mater.* **2009**, *321*, 1351–1355.
[16] M. Scariot, D. O. Silva, J. D. Scholten, G. Giovanna Machado, S. R. Teixeira, M. A. Novak, G. Ebeling, J. Dupont, *Angew. Chem.* **2008**, *120*, 9215–9218; *Angew. Chem. Int. Ed.* **2008**, *47*, 9075–9078.
[17] F. Dumestre, B. Chaudret, C. Amiens, M. C. Fromen, M.-J. Casanove, P. Renaud, P. Zurcher, *Angew. Chem.* **2002**, *114*, 4462–4465; *Angew. Chem. Int. Ed.* **2002**, *41*, 4286–4289.
[18] J. P. Chen, C. M. Sorensen, K. J. Klabunde, G. C. Hadjipanayis, *Phys. Rev. B* **1995**, *51*, 11527.
[19] C. Petit, A. Taleb, M. P. Pileni, *J. Phys. Chem. B* **1999**, *103*, 1805–1810.
[20] S. Sun, C. B. Murray, *J. Appl. Phys.* **1999**, *85*, 4325.
[21] C. B. Murray, S. Sun, H. Doyle, T. Betley, *MRS Bull.* **2001**, 985.
[22] C. B. Murray, S. Sun, W. Gaschler, H. Doyle, T. A. Betley, C. R. Kagan, *IBM J. Res. Dev.* **2001**, *45*, 47–56.
[23] N. A. Frey, S. Peng, K. Cheng, S. Sun, *Chem. Soc. Rev.* **2009**, *38*, 2532.
[24] S. A. Majetich, M. Sachan, *J. Phys. D: Appl. Phys.* **2006**, *39*, R407.
[25] S. Yamamuro, K. Sumiyama, *Chem. Phys. Lett.* **2006**, *418*, 166.
[26] X. Yang, F.-y. Lai, J.-z. Zhang, Q.-w. Chen, *J. Phys. Chem. C* **2009**, *113*, 7123–7128.
[27] F. Wang, H. Gu, Z. Zhang, *MRS Bull.* **2003**, *38*, 347–351.
[28] R. Abu-Much, A. Gedanken, *Chem. Eur. J.* **2008**, *14*, 10115–10122.
[29] E. K. Athanassiou, P. Grossmann, R. N. Grass, W. J. Stark, *Nanotechnology* **2007**, *18*, 165606(7pp).
[30] Concluded from the information given in the literature for the experimental details.
[31] B. Vogel, PhD Thesis, University of Bielefeld, **2011**.
[32] The larger size of the crystallites might be caused by a self-organization induced by the magnetic moment of the cubes to iso-oriented crystals during the evaporation of the solvent in the process of XRD sample preparation. A self-organization of small Co dics (4 × 25 nm) has already been observed in the literature and is documented by XRD data.[10,11]
[33] The diffractograms were measured with a copper X-ray source (K_α1: 1.54056 Å, K_α2: 1.54439 Å). XRD reference data from X'Pert High Score (hcp-Co 00–005–0727; fcc-Co 00–015–0806; fcc-CoO 00–048–1719) and from the literature (ε-Co).[15]
[34] G. Fachinetti, G. Fochi, T. Funaioli, P. F. Zanazzi, *J. Chem. Soc., Chem. Commun.* **1987**, 89.

[35] A. Sisak, L. Markó, *J. Organomet. Chem.* **1987**, *330*, 201–206.
[36] G. Fachinetti, G. Fochi, T. Funaioli, *J. Organomet. Chem.* **1986**, *301*, 91–97.
[37] W. Hieber, J. Sedlmeier, *Chem. Ber.* **1954**, *87*, 25–34.
[38] The authors[11] give no experimental details with regard to the stirring equipment.
[39] R. M. de Silva, V. Palshin, K. M. Nalin de Silva, L. L. Henry, C. S. S. R. Kumar, *J. Mater. Chem.* **2008**, *18*, 738–747.
[40] A. Lagunas, C. Jimeno, D. Font, L. Solà, M. A. Pericàs, *Langmuir* **2006**, *22*, 3823–3829.
[41] We assume that the formation of hcp-Co rods (ca. 9×40 nm) during the decomposition of $Co(\eta^3\text{-}C_8H_{13})(\eta^4\text{-}C_8H_{12})$ with H_2 in anisole and in the presence of the additive mixture OS/OA[17] is caused by salt formation and by the presence of an inhomogeneous magnetic field generated by a magnetic stirrer.

Received: September 7, 2011
Published Online: November 23, 2011

DOI: 10.1002/ejic.201101009

[Co(μ-ox)(Hpmtz)] – A New Co^{II} Zig-Zag Chain Complex with the In Situ Generated Oxalate Bridging and Hpmtz Chelating Ligands (Hpmtz = 5-pyrimidyltetrazole) Exhibiting Spin-Canted Antiferromagnetism

A. Rodríguez-Diéguez,[a] José Manuel Seco,[b] and E. Colacio*[a]

Keywords: Cobalt / Bridging ligands / N ligands / Spin canting / Magnetic properties

The compound [Co(μ-ox)(Hpmtz)] (Hpmtz = 5-pyrimidyltetrazole, ox = oxalate) has been synthesized under hydrothermal conditions by reacting $CoCl_2·6H_2O$ with 2-cyanopyrimidine and sodium azide. Both ox and Hpmtz ligands were generated in situ during the hydrothermal reaction. The structure of [Co(μ-ox)(Hpmtz)] consists of oxalate-bridged Co^{II} zig-zag chains bearing Hpmtz chelating ligands. These chains form layers in the *ab* plane via π···π stacking interactions involving the pmtz ligands belonging to neighbouring chains. Layers stack along the *c* axis with an ABAB sequence and are glued by cooperative C9–H···O4 interactions leading to a 3D structure. Magnetic susceptibility measurements indicate that this compound shows spin-canted antiferromagnetism (weak ferromagnetism) with T_C = 6.5 K.

Introduction

Oxalate ($C_2O_4^{2-}$, ox) has been extensively used as bridging ligand to construct a great variety of multidimensional polynuclear complexes that exhibit interesting structures and physical properties (magnetic, magneto-optical, magnetic conductor, superconductor, etc).[1,2] Although numerous examples of 2D and 3D oxalate-bridged metal complexes exist, only a few of them are homometallic one-dimensional systems.[3] Most of these 1D systems are copper(II) complexes exhibiting moderate to weak antiferromagnetic and even ferromagnetic intrachain couplings.[3a–3k] Examples of 1D cobalt(II)–ox frameworks are still more limited, and they invariably exhibit antiferromagnetic coupling.[3f–3h,3l–3o] In some of these 1D metal–ox frameworks, interchain interactions mediated by hydrogen-bonding, dipole–dipole, π–π and π–d interactions can lead to 3D magnetic ordering.[3f,3o,4]

As a contribution to this field we report herein the hydrothermal synthesis, crystal structure and magnetic properties of a new neutral cobalt(II)–ox zig-zag chain complex of formula [Co(μ-ox)(Hpmtz)] (Hpmtz = 5-pyrimidyltetrazole), in which the ox ligand connects two Co^{II} ions in a bis(bidentate) bridging coordination mode and the Hpmtz acts as a chelating ancillary ligand.

[a] Departamento de Química Inorgánica, Facultad de Ciencias, Universidad de Granada,
18071 Granada, Spain
E-mail: ecolacio@ugr.es
[b] Departamento de Química Aplicada, Facultad de Química de San Sebastián, Universidad del País Vasco,
Paseo Manuel Lardizábal, 20008 San Sebastián, Spain

Results and Discussion

The hydrothermal reaction between 2-cyanopyrimidine, sodium azide and $CoCl_2·6H_2O$ leads to the formation of three different compounds, $[Co_2(μ\text{-}pymca)_3]OH·H_2O$,[5] $[Co(pmtz)_2]$[6] and [Co(μ-ox)(Hpmtz)] (**1**). In this latter compound, oxalate is formed in situ from the total hydrolysis of 2-cyanopyrimidine. A similar process has been shown to occur for pyrimidine-2-carboxamide-oxime,[7] 5-pyrimidyltetrazole[8] and pyridine-2-carboxylic acid[9] species, which react with metal ions under hydrothermal conditions to afford oxalate-bridged polymeric complexes. Hpmtz is also generated in situ from the reaction between 2-cyanopyrimidine and sodium azide.[6] A far as we know, this is the first time that the Hpmtz ligand is coordinated to a metal ion in a neutral chelating form.

The structure of **1** consists of neutral [Co(μ-ox)(Hpmtz)] zig-zag chains along the *a* axis, which are involved in extensive π–π interactions (Figure 1). Within the chains, Co^{II} ions are bridged by bis-chelating/bridging oxalate anions, and Hpmtz acts as a terminal chelating ligand.

Each unique cobalt(II) ion exhibits a CoO_4N_2 distorted octahedral coordination environment, in which two oxalate bridging ligands adopt a *cis* configuration, while the two remaining positions are occupied by the two nitrogen atoms of the Hpmtz chelating ligand. The $Co–N_{Hpmtz}$ bond lengths are 2.107(10) and 2.132(10) Å, while $Co–O_{oxalate}$ distances have values in the range 2.067(7)–2.148(10) Å. The *cis* and *trans* bond angles in the octahedron are in the ranges 77.5(4)–98.1(4)° and 165.0(3)–171.7(3)°, respectively. These bond lengths and angles are very similar to those previously reported for the analogous complex $[Co(C_2O_4)\{HO(CH_2)_3OH\}]$.[4] Although there is no centre

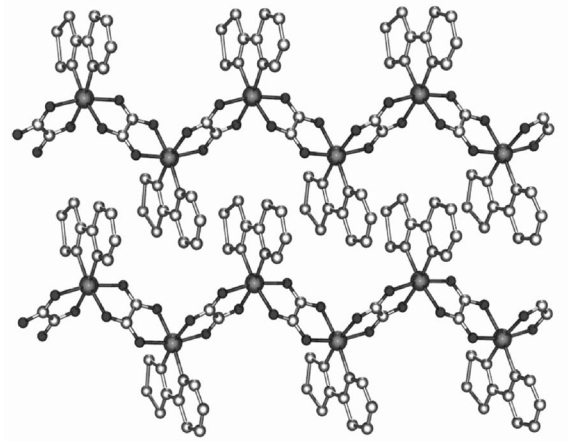

Figure 1. Perspective view of the structure of **1**.

of symmetry at the middle of the C–C bond of each oxalate-bridging ligand, neighbouring metal ions exhibit opposite absolute configurations, resulting in heterochiral ΔΛΔΛΔΛ... zig-zag chains. The dihedral angle between the molecular planes of the two oxalate bridges around the Co^{II} ions is 85.92°, and the intrachain Co···Co distance through the oxalate bridge is 5.423(14) Å. Neighbouring chains are interdigitated to form layers in the *ab* plane and exhibit π–π interchain interactions involving the pyrimidyl ring of the Hpmtz ligand of a chain and the tetrazol ring of the Hpmtz ligand of the neighbouring one, with a centroid–centroid distance of 4.414 Å. The shortest intralayer Co···Co distance is 7.865 Å. Finally, layers stack along the *c* axis with an ABAB sequence and are glued by cooperative C9–H···O4 interactions (C···O distance of 3.342 Å) leading to a 3D structure with a shortest interlayer Co···Co distance of 7.541 Å. Topologies similar to that of compound **1** have been previously observed in complexes $[Co(C_2O_4)\{HO(CH_2)_3OH\}]$[4] and $[Fe(C_2O_4)(phen)]$.[10]

Magnetic Properties

The temperature dependence of χ_M and the $\chi_M T$ product (χ_M is the molar susceptibility per Co atom) for **1** at a magnetic field of 0.5 T is given in Figure 2.

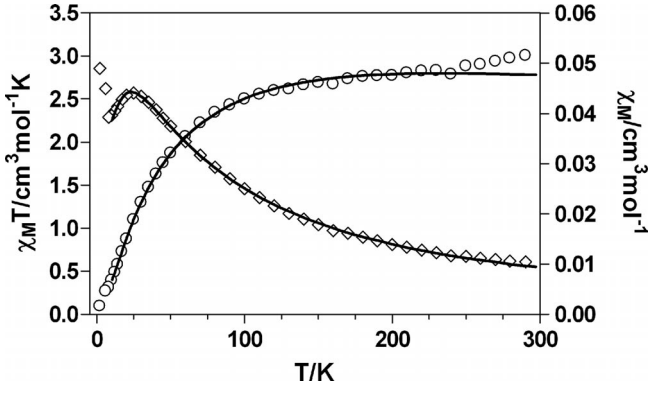

Figure 2. Temperature dependence of χ_M and $\chi_M T$ for compound **1**. The solid lines correspond to the best fit to the empirical model.

The temperature dependence of the magnetic susceptibility values shows a broad maximum at 25 K with a value of 0.044 $cm^3 mol^{-1}$, a minimum at 8 K with a value of 0.036 $cm^3 mol^{-1}$ and a sharp increase below this latter temperature that reaches a value of 0.049 $cm^3 mol^{-1}$ at 2 K. The broad maximum at 25 K is due to a moderate to strong intrachain antiferromagnetic coupling between the Co^{II} ions through the bis-chelating/bridging oxalate ligand, while the sharp rise at very low temperature might be indicative of spin-canted antiferromagnetism (weak ferromagnetism). The room-temperature value of $\chi_M T$, 3.083 $cm^3 mol^{-1}$ K, substantially exceeds the spin-only value of 1.875 $cm^3 mol^{-1}$ K expected for an uncoupled high-spin Co^{II} ($S = 3/2$) ion with $g = 2$, thus indicating that an important orbital contribution due to the distorted octahedral Co^{II} ion exists. The $\chi_M T$ product continuously decreases with the temperature down to a value of 0.1 $cm^3 mol^{-1}$ K at 2 K. This value is much lower than that expected for a magnetically isolated Co^{II} ion with an effective spin doublet and $g_0 \approx 4.3$ ($\chi_M T$ = 1.73 $cm^3 mol^{-1}$ K), thus supporting the existence of an antiferromagnetic exchange interaction. Therefore, the decrease of the $\chi_M T$ product in the 300–2 K temperature range is due to both spin–orbit coupling effects and antiferromagnetic interactions. The $\chi_M T$ vs. T plot shows a kink at about 8 K, which corresponds to the sharp rise below 8 K observed in the χ_M vs. T plot. The susceptibility data above 90 K were fitted to the Curie–Weiss law with Curie and Weiss constants of 3.31 $cm^3 mol^{-1}$ K and θ = –35 K, respectively. The large negative value of the Weiss constant supports the antiferromagnetic interaction between the Co^{II} ions.

Below 8 K, the $\chi_M T$ product becomes field-dependent for applied magnetic fields lower than 0.1 T (Figure 3).

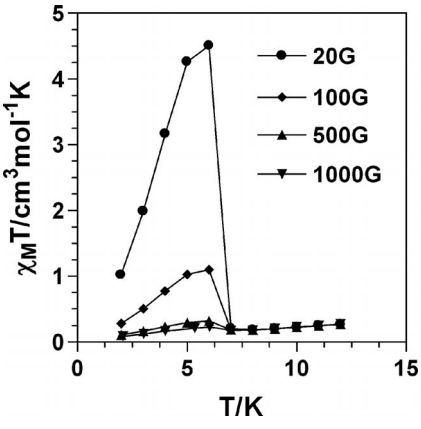

Figure 3. Temperature dependence of $\chi_M T$ for **1** at different applied magnetic fields.

At 20 G, the $\chi_M T$ values rise sharply at around 8 K to reach a maximum of 4.5 $cm^3 mol^{-1}$ K and then decrease rapidly toward 0.90 $cm^3 mol^{-1}$ K at 2 K. This low-temperature behaviour suggests a ferromagnetic phase transition. The field-cooled magnetization (FCM) at 20 G confirms the occurrence of a magnetic ordering below 8 K (Figure 4). The T_C temperature determined from the first derivative of the FCM is 6.5 K.

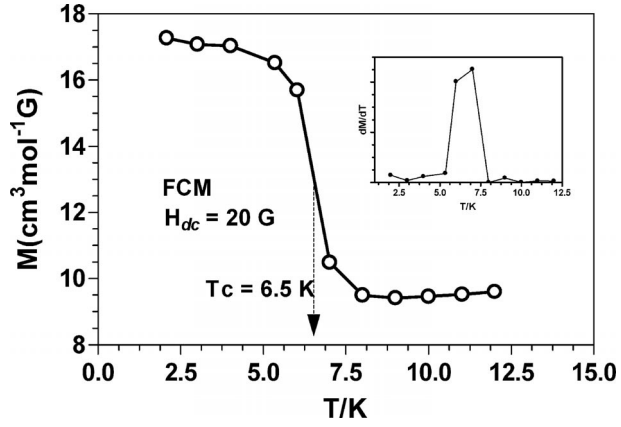

Figure 4. FCM of compound **1** and first derivative of the FCM (inset).

The isothermal magnetization at 2 K shows linear dependence on the field, attaining a value of 1185 $cm^3 Gmol^{-1}$ at 5 T, which is significantly smaller than the theoretical saturation magnetization value (M_s) of 16755 $cm^3 Gmol^{-1}$ with $g = 2$. The compound shows a very thin hysteresis loop with coercive field and remnant magnetization (M_r) values of 390 G and 11 $cm^3 Gmol^{-1}$, respectively, which are typical of a soft magnet (Figure 5).

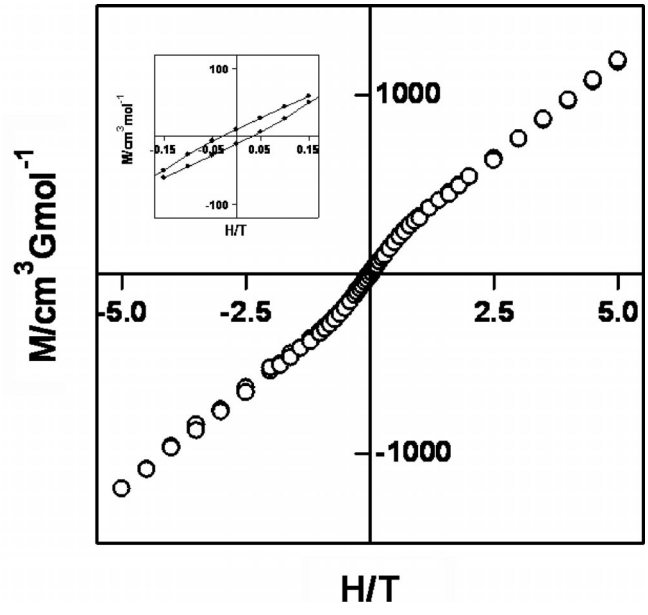

Figure 5. Magnetic hysteresis loop for compound **1**. The central part is highlighted in the inset.

All the magnetic properties described above are characteristics of a canted antiferromagnet, leading to weak ferromagnetism at low temperature. Compound **1** shows no out-of-phase signal (χ_M''), which might be due to the fact that the magnetic moment from canting is so small that the loss of energy related to the out-of-phase signal is negligible. The same *ac* susceptibility behaviour has been observed for other 2D and 3D polynuclear Co^{II} complexes.[5,11]

Two mechanisms have been proposed as sources of canting.[12] The first requires the presence of two equivalent sites in the crystals for the magnetic ions, but the direction of their anisotropy axes should be different. In the presence of near-neighbour antiferromagnetic isotropic exchange, the moments will not be aligned in an exactly parallel fashion, but they will make a small angle to each other. Consequently, there is a small net moment in the antiferromagnetically ordered state. In **1**, the relative orientation of the anisotropic CoN_2O_4 chromophores shows only a slight deviation (4.4°) from the totally antiparallel arrangement, and therefore this mechanism is hardly responsible for the observed spin canting. The second mechanism is known as the antisymmetric exchange, which can be phenomenologically expressed as $\mathbf{d}S_A \times S_B$ and trends to orientate the spins on neighbouring metal ions perpendicular to each other (d being a constant vector). The symmetry requirements for a spin-canting phenomenon exclude the presence of an inversion centre between the interacting magnetic centres. Because there is no centre of symmetry relating neighbouring cobalt(II) ions in **1**, the antisymmetric exchange must be the main mechanism responsible for the spin-canted antiferromagnetism. The 3D long-range order in **1** is only possible through weak π–π and C–H···O interchain interactions, and this is the reason why T_C is relatively low. The same type of interchain interactions have been found to be involved in the 1D spin-canted antiferromagnet [Fe(C_2O_4)(phen)].[10] Similar behaviour has been observed for the linear chain complex [Co(ox)(4-ampy)$_2$] (4-ampy = 4-aminopyridine), in which chains are mainly glued by hydrogen bonds.[3f]

In spite of the similarity between the chain structures of **1** and [Co(C_2O_4){$HO(CH_2)_3OH$}],[4] the former exhibits a lower Curie temperature than the latter (T_C = 10.6 K). This fact may be mainly due to the different magnitude of the interchain interactions leading to the 3D order in both compounds. Thus, in [Co(C_2O_4){$HO(CH_2)_3OH$}] the chains are connected by strong hydrogen bonds, involving the oxygen atom of the hydroxy group of the 1,3-propanediol ligands and oxygen atoms belonging to the oxalato bridging ligand (with a O···O distance of 2.708 Å), and two types of weak C–H···O interactions involving the methylene group and oxalato oxygen atoms (C···O distances in the range 3.20–3.70 Å, the shortest interchain Co···Co distances being 5.244 Å and 6.901 Å). In **1**, however, the interchain interactions are mediated by weak π···π and CH···O contacts and consequently the shortest interchain Co···Co distances (longer than 7.5 Å) are longer than those observed for compound [Co(C_2O_4){$HO(CH_2)_3OH$}]. Therefore, the stronger interchain interactions found for [Co(C_2O_4){$HO(CH_2)_3OH$}] relative to those of **1** leads to a higher T_C value for the former chain compound.

In order to determine the *intrachain* exchange interaction in **1**, we have used the empirical approach proposed recently by Lloret et al.[13] In the framework of this approach, each cobalt(II) ion in the Kramer's ground doublet state arising from spin–orbit coupling is considered to have an effective spin S_{eff} = 1/2, which is related to the real spin (S = 3/2) by a factor of 5/3. The magnetic exchange is assumed to occur between the ground doublets of the Co^{II} ions. The contri-

bution of the excited doublets to the magnetic properties of the ground doublet state is taken into account by a second-order perturbation theory. This introduces a dependence on J, λ, α and Δ in the Landé factor of the ground doublet, g_0, where J is the isotropic exchange interaction, λ is the spin–orbit coupling and α is the orbital reduction factor defined as $\alpha = kA$. The parameter k takes into account the reduction of the spin–orbit coupling due to covalency and A is a measure of the crystal-field strength accounting for the admixture of the upper $^4T_{1g}(^4P)$ state into the $^4T_{1g}(^4F)$ ground state (A assumes a value of 1.5 for a weak crystal field and 1.0 for a strong crystal field),[13] and Δ is the energy gap between the singlet $^4A_2$ and doublet ^4E levels due to the splitting of the orbital triplet $^4T_{1g}$ ground state under an axial distortion. All of these effects are incorporated into a function named $G(T,J)$ which replaces the value of the g_0 Landé factor of the ground Kramer's doublet and is calculated as described.[13] This approach is valid when $|J/\lambda| < 0.1$.

In this context and from the magnetic point of view, complex **1** can be considered as a uniform chain of antiferromagnetically interacting spin doublets. The numerical expression derived by Bonner and Fisher[14] [Equation (1)] can then be used to analyze the magnetic susceptibility of **1**, where $x = (25/9)|J|/kT$ and the g factor is replaced by the $G(T,J)$ function.

$$\chi_M = \frac{N\beta^2[G(T,J)]^2}{kT}\frac{0.25 + 0.074975x + 0.075235x^2}{1.0 + 0.9931x + 0.172135x^2 + 0.757825x^3} \quad (1)$$

The best fit of the data to the empirical model over the 10–300 K temperature range leads to the following set of parameters: J = –7.10(1) cm^{-1}, λ = –110.2(5) cm^{-1}, Δ = 210(5) cm^{-1} and α = 1.25(1), with a temperature-independent paramagnetism of 120×10^{-6} cm^3 mol^{-1}. For the free ion, the value of λ is –170 cm^{-1}. The low value of the $|J/\lambda|$ ratio (0.06) supports the use of the above approach. The J value for **1** falls within the range observed for other cobalt(II) oxalate-bridged complexes (between –4 cm^{-1} and –11 cm^{-1}).[5] The values of the λ, α, k and Δ parameters lie within the range of those observed in other six-coordinate high-spin Co^{II} complexes.[13]

Conclusion

We have succeeded in obtaining under hydrothermal conditions a new Co–ox chain complex, [Co(μ-ox)(Hpmtz)], containing the neutral chelating ligand 5-pyrimidyltetrazol, which was generated in situ from the condensation of 2-cyanopyrimidine and azide. The oxalate ligand was also generated in situ from the hydrolysis of 2-cyanopyrimidine. The compound exhibits a moderate to strong antiferromagnetic interaction between cobalt(II) ions through the symmetric bis-chelating/bridging oxalate ligand. Moreover, this complex displays spin-canting antiferromagnetism (weak ferromagnetism) with T_C = 6.5 K and a very small coercive field and remnant magnetization. The canted structure is mainly due to the antisymmetric exchange, which is compatible with the absence of a centre of symmetry relating neighbouring cobalt(II) ions, and, to a lesser extent, to single-ion local magnetic anisotropy of the Co^{II} ions. The 3D long-range order is caused by weak π–π and C–H···O interchain interactions.

Experimental Section

Materials: Reactions were conducted in oven-dried glassware under aerobic conditions. Cobalt(II) chloride hexahydrate (99.99%), 2-cyanopyrimidine and sodium azide (99.99%) were purchased from Aldrich and were used without further purification.

Physical Measurements: Elemental analyses were carried out at the "Centro de Instrumentación Científica" (University of Granada) on a Fisons-Carlo Erba analyzer model EA 1108. The IR spectra on powdered samples were recorded with a ThermoNicolet IR200FTIR instrument by using KBr pellets.

Magnetization and variable-temperature (1.9–300 K) magnetic susceptibility measurements on polycrystalline samples were carried out with a Quantum Design SQUID MPMS XL-5 device operating at different magnetic fields. The experimental susceptibilities were corrected for the diamagnetism of the constituent atoms by using Pascal's tables.

X-ray Crystallography for [Co(μ-ox)(Hpmtz)]: Suitable crystals of **1** were mounted on glass fibre and used for data collection at 100 K in a Bruker SMART APEX CCD system with Mo-K_α radiation (λ = 0.7107 Å). The data were processed with APEX2 and corrected for absorption by using SADABS.[15] The structures were solved by direct methods with SIR97,[16] revealing positions of all non-hydrogen atoms. These atoms were refined on F^2 by a full-matrix least-squares procedure using anisotropic displacement parameters.[17] An empirical absorption correction was applied. The structures were solved by direct methods and refined with full-matrix least-squares calculations on F^2. Final R, wR_{wp} and goodness-of-fit agreement factors, details on data collection, and analyses can be found in Table 1. The N3 atom was found to be highly disordered.

Table 1. Crystallographic and structure refinement data for [Co(ox)(Hpmtz)] (**1**).

Formula	$C_7H_4N_6O_4Co$
M /g mol^{-1}	295.09
Crystal system	orthorhombic
Space group	$Pna(2_1)$
a /Å	8.9619(19)
b /Å	9.518(2)
c/Å	14.043(3)
β /°	90
V /Å^3	1197.8(4)
Z	4
T /K	293(2)
λ /Å	0.71073
ρ_{calcd} /g cm^{-3}	1.636
μ /mm^{-1}	1.449
GOF on F^2	1.151
$R1^a$ [$I > 2\sigma(I)$]	0.098
$wR2^b$ [$I > 2\sigma(I)$]	0.282

For compound **1**, the best crystallographic data obtained from five attempts are reported. Although we used several experimental crystallization strategies and a rotating anode diffractometer meas-

uring at 100 K, we could not get better crystallographic data because of the extremely small size and the low quality of the crystals. Anisotropic factors were applied to all atoms with the exception of the non-coordinated atoms belonging to the Hpmtz ligand and the hydrogen atoms.

CCDC number 844616 contains the supplementary crystallographic data for this paper. These data can be obtained free of charge from The Cambridge Crystallographic Data Centre via www.ccdc.cam.ac.uk/data_request/cif.

[Co(μ-ox)(Hpmtz)] (1): A mixture of $CoCl_2 \cdot 6H_2O$ (0.118 g, 0.500 mmol), 2-cyanopyirimidine (0.105 g, 1 mmol), sodium azide (0.032 g, 0.5 mmol) and distilled water (10 mL) was sealed in a Teflon-lined acid digestion autoclave and heated hydrothermally at 190 °C under autogenous pressure. After 12 h of heating, the reaction vessel was cooled for 2 h. Three different types of crystals were obtained: orange $[Co_2(\mu\text{-pymca})_3]OH \cdot H_2O$,[5] yellow $[Co(pmtz)_2]$[6] and reddish-orange [Co(μ-ox)(Hpmtz)] (**1**). Reddish-orange cubic crystals of **1** were picked manually in a yield of 30% based on Co. IR (KBr): $\tilde{\nu}(COO^-)$ = 1674 and 1605.56 cm^{-1}. $C_7H_4CoN_6O_4$ (295.08): calcd. C 28.49, H 1.37, N 28.48; found C 28.95, H 1.13, N 28.06.

Acknowledgments

This work was supported by the Ministerio de Educación y Ciencia (MEC) (Spain) (Projects CTQ2008-02269/BQU), the Junta de Andalucía (FQM-195 and Projects of excellence P08-FQM-03705 and FQM-4228) and the University of Granada. We thank Prof. Francesc Lloret, from the Department of Inorganic Chemistry, University of Valencia, for his generous assistance with the fitting of the magnetic susceptibility data.

[1] Some reviews: a) S. Decurtins, R. Pellaux, A. Hauser, M. E. Von Arx in *Magnetism: A Supramolecular Function* (Ed.: O. Kahn), Kluwer, Dordrecht, **1996**, p. 487 and references cited therein; b) M. Pilkington, S. Decurtins in *Comprehensive Coordination Chemistry II. From Biology to Nanaotechnology*, *Vol. 7* (Eds.: J. A. MacCleverty, T. J. Meyer), Elsevier, Amsterdam, **2004**, p. 177; c) M. Pilkington, S. Decurtins, *Perspectives Supramol. Chem.* **2003**, *7*, 275–323; d) R. Clément, S. Decurtins, M. Gruselle, C. Train, *Monastsh. Chem.* **2003**, *134*, 117 and references therein.

[2] a) H. Tamaki, Z. J. Zhong, N. Matsumoto, S. Kida, M. Koikawa, N. Achiwa, I. Hashimoto, H. Okawa, *J. Am. Chem. Soc.* **1992**, *114*, 6974; b) P. J. Day, *J. Chem. Soc., Dalton Trans.* **1997**, 701; c) E. Coronado, J. R. Galán-Mascarós, C. Martí-Gastaldo, *Inorg. Chem.* **2006**, *45*, 1882; d) E. Coronado, J. R. Galán-Mascarós, C. J. Gómez-García, V. Laukhin, *Nature* **2000**, *408*, 447; e) D. Armentano, G. D. Munno, T. F. Mastroprieto, M. Julve, F. Lloret, *J. Am. Chem. Soc.* **2005**, *127*, 10778; f) E. Cariati, R. Macchi, D. Roberto, R. Ugo, S. Galli, N. Casati, P. Macchi, A. Sironi, L. Bogani, A. Caneschi, D. Gatteschi, *J. Am. Chem. Soc.* **2007**, *129*, 9410; g) E. Coronado, J. R. Galán-Mascarós, R. Martí-Gastaldo, *J. Am. Chem. Soc.* **2008**, *130*, 14987; h) C. Train, R. Gheorghe, V. Krstic, L. M. Chamoreau, N. S. Ovanesyan, G. L. J. A. Rikken, M. Gruselle, M. Verdaguer *Nat. Mater.* **2008**, *7*, 729.

[3] a) J. J. Gired, O. Khan, M. Verdaguer, *Inorg. Chem.* **1980**, *19*, 24; b) W. Fitzgerald, J. Foley, D. McSweeney, N. Ray, D. Sheahan, S. Tyagi, *J. Chem. Soc., Dalton Trans.* **1982**, 1117; c) H. Oshio, U. Nagashima, *Inorg. Chem.* **1992**, *31*, 3295; d) J. Suárez-Varela, J. M. Domínguez-Vera, E. Colacio, J. C. Avila-Rosón, M. A. Hidalgo, D. Martín-Ramos, *J. Chem. Soc., Dalton Trans.* **1995**, 2143; e) M. L. Calatayud, I. Castro, J. Sletten, F. Lloret, M. Julve, *Inorg. Chim. Acta* **2000**, *300–302*, 846; f) O. Castillo, A. Luque, P. Román, F. Lloret, M. Julve, *Inorg. Chem.* **2001**, *40*, 5526; g) O. Castillo, A. Luque, M. Julve, F. Lloret, P. Román, *Inorg. Chim. Acta* **2001**, *315*, 9; h) O. Castillo, A. Luque, F. Lloret, P. Román, *Inorg. Chim. Acta* **2001**, *324*, 141; i) J. P. García-Terán, O. Castillo, A. Luque, U. García-Couceiro, P. Román, F. Lloret, *Inorg. Chem.* **2004**, *43*, 5761; j) C. S. Hong, H. Yoon, Y. S. You, *Inorg. Chem. Commun.* **2005**, *8*, 310; k) D. Cangussu, H. O. Stumpf, H. Adams, J. A. Thomas, F. Lloret, M. Julve, *Inorg. Chim. Acta* **2005**, *358*, 2292; l) U. García-Couceiro, O. Castillo, A. Luque, J. P. García-Terán, G. Beobide, P. Román, *Eur. J. Inorg. Chem.* **2005**, 4280; m) J. P. García-Terán, O. Castillo, A. Luque, U. García-Couceiro, G. Beobide, P. Román, *Dalton Trans.* **2006**, 902; n) D. Olea, U. García-Couceiro, O. Castillo, J. Gómez-Herrero, F. Zamora, *Inorg. Chim. Acta* **2007**, *360*, 48–54; o) M. B. Hursthouse, M. E. Light, D. J. Price, *Angew. Chem.* **2004**, *116*, 478; *Angew. Chem. Int. Ed.* **2004**, *43*, 472–475.

[4] Z. Duan, Y. Zhang, B. Zhang, D. Zhu, *Inorg. Chem.* **2008**, *47*, 9152.

[5] A. Rodriguez-Dieguez, J. Cano, R. Kivekäs, A. Debdoubi, E. Colacio, *Inorg. Chem.* **2007**, *46*, 2503.

[6] A. Rodriguez-Dieguez, R. Kivekäs, E. Colacio, *Chem. Commun.* **2005**, *44*, 5228.

[7] A. Rodriguez-Dieguez, R. Kivekäs, H. Sakiyama, A. Debdoubi, E. Colacio, *Dalton Trans.* **2007**, 2145.

[8] A. Rodríguez-Diéguez, E. Colacio, *Chem. Commun.* **2006**, 4140.

[9] J. Y. Lu, J. Macías, J. Lu, J. E. Cmaidalka, *Cryst. Growth Des.* **2002**, *2*, 485.

[10] L. L. Li, K. Lin, C. J. Ho, C. P. Sun, H. D. Yang, *Chem. Commun.* **2006**, 1286.

[11] a) Y.-Q. Tian, C.-X. Cai, X.-M. Ren, C.-Y. Duan, Y. Xu, S. Gao, X.-Z. You, *Chem. Eur. J.* **2003**, *9*, 5673.

[12] F. Palacio, *Molecular Magnetism: From Molecular Assemblies to the Devices*, NATO ASI Series, Kluwer, Dordrecht **1995**, p. 5.

[13] F. Lloret, M. Julve, J. Cano, R. Ruiz-García, E. Pardo, *Inorg. Chim. Acta* **2008**, *361*, 3432.

[14] J. C. Bonner, M. E. Fisher, *Phys. Rev. A: At., Mol. Opt. Phys.* **1964**, *135*, 640.

[15] G. M. Sheldrick, *SADABS*. University of Göttingen, Germany, **2002**.

[16] A. Altomare, M. Cascarano, C. Giacovazzo, A. M. C. Guagliardi, G. Burla, M. Pilodori, J. Camalli, *Appl. Crystallogr.* **1994**, *27*, 435.

[17] G. M. Sheldrick, *SHELXL-97. A Program for Crystal Structure Refinement*, University of Göttingen, Germany, **1997**.

Received: September 22, 2011
Published Online: November 29, 2011

DOI: 10.1002/ejic.201101118

The Structure of $(H_3O)_2B_{12}F_{12}\cdot 6H_2O$ – a CCP Lattice of $B_{12}F_{12}^{2-}$ Anions Intercalated with a Nonplanar Network of O–H···O Connected O_6 Rings

Eric V. Bukovsky,[a] Stephanie R. Fiedler,[a] Dmitry V. Peryshkov,[a] Alexey A. Popov,*[b] and Steven H. Strauss*[a]

Keywords: Water / Boron / Structure elucidation / Thermal analysis / Hydrogen bonds

Hydrates of the dihydronium salt of the superweak anion $B_{12}F_{12}^{2-}$ have been synthesized and structurally characterized. The structure of $(H_3O)_2B_{12}F_{12}\cdot 6H_2O$ consists of a cubic close-packed (CCP) array of $B_{12}F_{12}^{2-}$ anions intercalated with nonplanar, infinite networks of O_6 rings composed of H_3O^+ ions and H_2O molecules. Similar to other salts of $B_{12}F_{12}^{2-}$, $(H_3O)_2B_{12}F_{12}\cdot 6H_2O$ exhibits rapid structural modification, termed latent porosity, and reversibly desorbs water to form other hydrate phases: $(H_3O)_2B_{12}F_{12}\cdot 4H_2O$, $(H_3O)_2B_{12}F_{12}\cdot 2H_2O$, and $(H_3O)_2B_{12}F_{12}$. $(H_3O)_2B_{12}F_{12}\cdot 6H_2O$ is another example of the weak coordinating properties of the $B_{12}F_{12}^{2-}$ anion.

Introduction

We have been studying the structures and physicochemical properties of a variety of metal and nonmetal salts of the icosahedral, superweak anion $B_{12}F_{12}^{2-}$.[1–7] Our hypothesis is that the unique combination of size, shape, high symmetry, thermal stability, and extremely weak Brønsted and Lewis basicity of this anion will lead to unanticipated structures and properties [i.e. unanticipated compared to salts of $B_{12}H_{12}^{2-}$,[8–11] $B_{12}Cl_{12}^{2-}$,[12–14] $B_{12}(OH)_{12}^{2-}$,[15,16] and $B_{12}(CH_3)_{12}^{2-}$[17] on one hand, and of salts of typical fluoroanions, such as BF_4^-, PF_6^-, $Sb_2F_{11}^-$, SiF_6^{2-}, and MnF_6^{2-}, on the other]. For example, $K_2B_{12}H_{12}$ exhibits a common antifluorite structure,[10] but $K_2B_{12}F_{12}$ exhibits an intermetallic Ni_2In structure[3] (the B_{12} centroids occupy the idealized hexagonal close-packed positions of the In atoms[18]), which is the first time that this structure has been observed for an ionic compound with a polyatomic anion at ambient temperatures and pressures.

The nature of hydronium ions (i) in bulk aqueous solutions,[19–21] (ii) on the surface of aqueous solutions (i.e. at the air/water interface, where H_3O^+ ions may be concentrated relative to the bulk solution),[22,23] and (iii) as free H_3O^+ ions[24] or as $[(H_3O)_n(H_2O)_m]^{n+}$ clusters[25–27] within the confines of solid-state structures are of longstanding interest. Furthermore, the acid salts $(H_3O)_2B_{12}Cl_{12}\cdot nH_2O$[28] and $(H_3O)_2B_{12}F_{12}\cdot nH_2O$[29] have been considered as practical alternatives to H_3PO_4 as electrolytes for acid fuel cells[29,30] but have not yet been structurally characterized. For these reasons, we have isolated and determined the structure and thermogravimetric behavior of $(H_3O)_2B_{12}F_{12}\cdot 6H_2O$, and we report our results herein.

Results and Discussion

The structure of $(H_3O)_2B_{12}F_{12}\cdot 6H_2O$ is shown in Figures 1, 2, and 3, and additional drawings can be found in the Supporting Information. Selected interatomic distances and angles are listed in Table 1. The structure of the $B_{12}F_{12}^{2-}$ anion in this compound is normal,[1,3–6] and it is also the most precise structure of any molecular B_{12} species, with B–F and B–B esd values of 0.0005–0.0008 Å (Figure S1). The anions are packed in a cubic close-packed (CCP)-like array, with a network of H_3O^+ ions and H_2O molecules intercalated between the parallel planes of the anions (Figure 1). The B_{12} centroids (⊙) in each of the parallel close-packed planes are rigorously coplanar. The ⊙···⊙ distances are 8.411 and 8.521 Å within the close-packed planes and, because of the presence of the aqueous acid layers, are 8.703 and 8.914 Å between the close-packed planes. The shortest interionic F···F distances are 2.686(1) and 2.780(1) Å (cf. the sum of van der Waals radii of ca. 3 Å).[31]

The $\{H_3O^+/3H_2O\}_\infty$ network consists of O–H···O connected O_6 rings, with each O atom hydrogen bonded to three other O atoms (Figure 2). The network layer is denoted L6(6) using the nomenclature developed for H_2O networks.[32–34] The O···O distances clearly show that the H_3O^+ ions (O1) and H_2O molecules (O2, O3) are ordered: the O1···O2 and O1···O3 distances are 2.590(1) and 2.5739(8) Å, respectively, and the O2···O3 and O3···O3′ distances are 2.8920(8) and 2.911(1) Å, respectively. The three

[a] Department of Chemistry, Colorado State University, Fort Collins, CO 80523, USA
Fax: +1-970-491-1801
E-mail: steven.strauss@colostate.edu
[b] Department of Electrochemistry and Conducting Polymers, Leibniz Institute for Solid State and Materials Research, 01069 Dresden, Germany

Supporting information for this article is available on the WWW under http://dx.doi.org/10.1002/ejic.201101118.

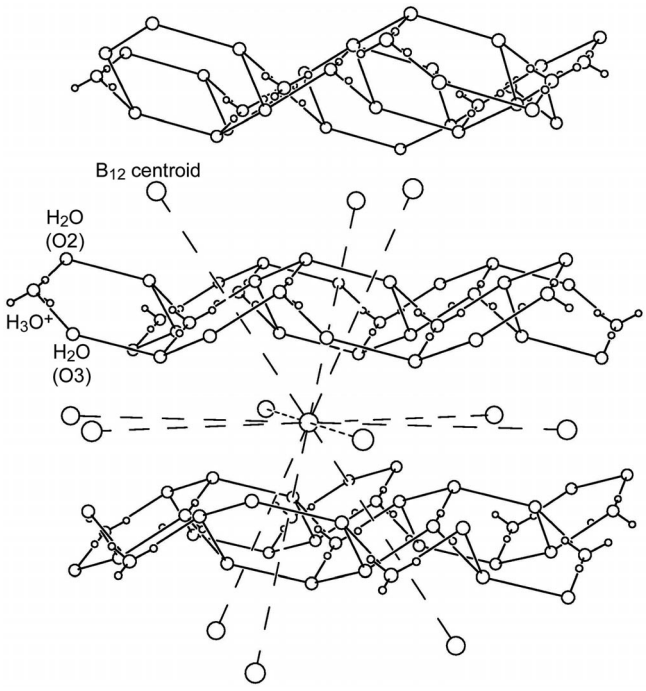

Figure 1. A portion of the $(H_3O)_2B_{12}F_{12}\cdot 6H_2O$ structure that shows only the B_{12} centroids (large spheres), O atoms, and the H atoms of the H_3O^+ cations (O atoms are connected with solid lines for clarity even though they are not directly bonded to one another). The B_{12} centroids are arranged in a CCP array with nonplanar, moguled $\{H_3O^+/3H_2O\}_\infty$ networks intercalated between the close-packed anion layers.

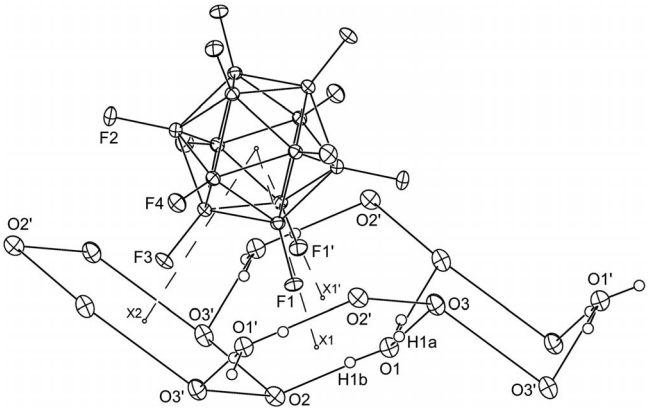

Figure 2. Part of the structure of $(H_3O)_2B_{12}F_{12}\cdot 6H_2O$ that shows the orientation of a $B_{12}F_{12}^{2-}$ anion with respect to a triple-hexagon valley in the moguled $\{H_3O^+/3H_2O\}_\infty$ network (50% ellipsoids for non-hydrogen atoms; only H atoms on the H_3O^+ cations are shown). The circles labeled X1, X1′, and X2 are O_6 ring centroids; the B_{12} centroid is not labeled. Also shown is the chair-configured $[(H_3O)_2(H_2O)_4]^{2+}$ ring.

H_3O^+ H atoms and one H atom from each of the two types of H_2O molecules are also ordered. The second H atoms on O2 and O3 are disordered over two and three positions, respectively. The H_3O^+ H atoms and the disordered H atoms on O2 and O3 are involved in hydrogen bonding

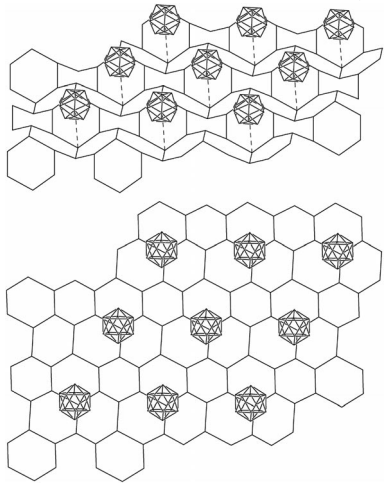

Figure 3. Two views of the moguled $\{H_3O^+/3H_2O\}_\infty$ network and one layer of $B_{12}F_{12}^{2-}$ anions in $(H_3O)_2B_{12}F_{12}\cdot 6H_2O$ (H and F atoms are omitted for clarity; O and B atoms depicted as points). The dotted lines in the upper drawing connect the B_{12} centroids with O2 atoms at the bottom of the triple-hexagon valleys in the network.

Table 1. Selected interatomic distances [Å] and angles [°] for $(H_3O)_2B_{12}F_{12}\cdot 6H_2O$.

B–B	1.787(1)–1.801(1)	O2···O1···O3	125.53(2)
B–F	1.377(1)–1.388(1)	O3···O1···O3′	96.20(4)
O1···O2	2.590(1)	O1···O2···O3	112.72(2)
O1···O3	2.5739(8)	O3···O2···O3′	108.36(3)
O2···O3	2.8920(8)	O1···O3···O2	121.58(3)
O3···O3′	2.911(1)	O1···O3···O3′	89.70(3)
O2···H1b	1.72(1)	O2···O3···O3′	124.89(2)
O2···H3c	2.09(1)		
O3···H1a	1.73(1)	F2···H3a	2.43(1)
O3···H2b	2.04(1)	F3···H3b′	2.67(1)
F1···H1a	2.54(1)	F3···H3b	2.35(1)
F1···H1b	2.68(1)	F3···H3c	2.57(1)
F2···H3a	2.43(1)	F4···H2a	2.55(1)
F3···H3b′	2.67(1)	F4···H3a	2.25(1)

within the L6(6) layers; the ordered H atoms on O2 and O3 each interact with two F atoms in a bifurcated fashion (Figure S3).

There are three types of O_6 rings, two of which are relatively planar and one of which is in a chair configuration. There is an $(H_2O)_6$ hexagon (two O2 and four O3 atoms with an average displacement of ±0.114 Å from the least-squares O_6 plane), the centroid of which is labeled X2 in Figure 2. There is also an $[(H_3O)_2(H_2O)_4]^{2+}$ (or $H_{14}O_6^{2+}$) hexagon (two O1, two O2, and two O3 atoms with an average displacement of ±0.031 Å), which is similar in structure to the discrete $H_{14}O_6^{2+}$ dihydronium hexagon found in the structure of $(H_{14}O_6)_2(FeCl_4)_2Cl_2\cdot C_{36}H_{36}N_{24}O_{12}\cdot 3H_2O$[35,36] and predicted to be as stable as isolated $H_{14}O_6^{2+}$ O_6 hexagons in the gas phase.[37] The centroids of the O_6 hexagons are labeled X1 and X1′ in Figure 2. The X1 and X1′ O_6 hexagons are tilted 53.2° to one another and 59.0° to the X2 hexagon. The ⊙···X1 and ⊙···X2 vectors, which are shown as dashed lines in Figure 2, are nearly coincident with the B–F bonds such that the

$B_{12}F_{12}^{2-}$ anions are located in the triple-hexagon valleys, nearly centered over half of the O2 atoms in each network layer (Figure 3, the other half of the O2 atoms are at triple-hexagon peaks and have $B_{12}F_{12}^{2-}$ anions "beneath" them).

The chair-configured $[(H_3O)_2(H_2O)_4]^{2+}$ O_6 rings have two O1 atoms and four rigorously coplanar O3 atoms. These rings combine with the triple-hexagon peaks and valleys to form $\{H_3O^+/3H_2O\}_n$ L6(6) network layers in $(H_3O)_2B_{12}F_{12}\cdot 6H_2O$. Although L6(6) layers that involve only H_2O molecules are known (see Supporting Information for the refcodes of several structures), there is, as far as we know, only one other example of a structure that may contain an L6(6) layer formed by H_2O molecules and H_3O^+ ions (refcode BIKVIA10).[38] However, the author of that study left open the possibility that none of the H_2O molecules in the L6(6) layer were protonated, which is consistent with the observation that all of the O···O distances in the L6(6) layer are 2.77 Å or longer, and the three O···O distances that involve the putative H_3O^+ ions are 2.83, 2.90, and 3.08 Å. Table S1 lists O···O distances for structures with unambiguous H_3O^+ ions that are hydrogen bonded to two or three H_2O molecules. All of those distances are ≤ 2.69 Å, and in every case at least one O···O distance per H_3O^+ ion is ≤ 2.58 Å.

Thermogravimetric measurements (Figure 4) demonstrate that $(H_3O)_2B_{12}F_{12}\cdot 6H_2O$ undergoes rapid dehydration in three discrete stages to $(H_3O)_2B_{12}F_{12}\cdot 4H_2O$, $(H_3O)_2B_{12}F_{12}\cdot 2H_2O$, and $(H_3O)_2B_{12}F_{12}$, which depends on the temperature and the pressure (P) of water vapor present. The crystalline phase $(H_3O)_2B_{12}F_{12}\cdot 6H_2O$ was stable at 25 °C when $P(H_2O)$ = 6 Torr (i.e. in the presence of dry He that had been bubbled through a saturated aqueous solution of $MgCl_2$ at 20 °C) but was deliquescent at 25 °C when $P(H_2O) > 6$ Torr. The $(H_3O)_2B_{12}F_{12}\cdot 4H_2O$ phase was stable at 55 °C when $P(H_2O)$ = 6 Torr, and the $(H_3O)_2B_{12}F_{12}\cdot 2H_2O$ phase was stable at 120 °C when $P(H_2O)$ = 6 Torr. In the absence of water vapor at 150 °C, the mass of the sample corresponded to $(H_3O)_2B_{12}F_{12}$. The compound was recovered unchanged after prolonged heating at 200 °C, i.e. when cooled to 25 °C, exposed to air, and dissolved in CD_3CN, the ^{11}B and $^{19}F\{^{11}B\}$ NMR spectra each showed the same single resonance observed in the spectra of unheated samples of $(H_3O)_2B_{12}F_{12}\cdot 6H_2O$ in CD_3CN, δ^{11B} = –18 and δ^{19F} = –270 ppm, with slight differences in δ values due to varying amounts of H_2O in the different samples. At higher temperatures, $(H_3O)_2B_{12}F_{12}$ underwent slow decomposition with the formation of $B_{12}F_{12-n}(OH)_n^{2-}$ species. This behavior is the subject of an ongoing study.

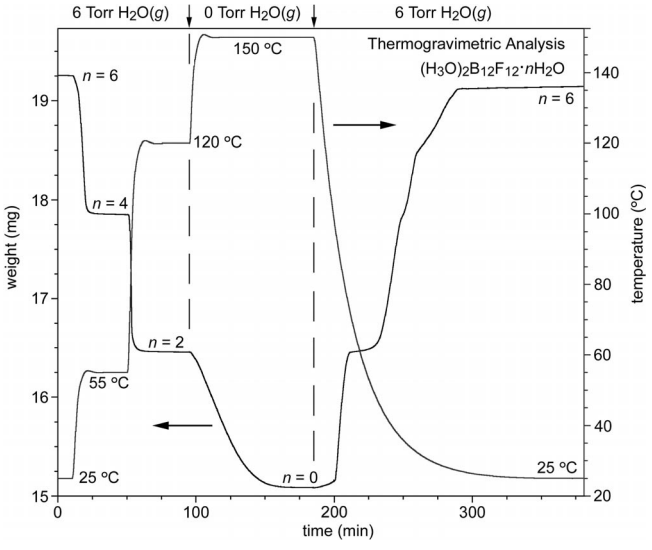

Figure 4. Thermogravimetric behavior of $(H_3O)_2B_{12}F_{12}\cdot 6H_2O$ as a function of temperature and the presence or absence of H_2O vapor.

The IR and Raman spectra of $(H_3O)_2B_{12}F_{12}\cdot 6H_2O$ and $(H_3O)_2B_{12}F_{12}$ are not very diagnostic, and it was not possible to determine whether $(H_3O)_2B_{12}F_{12}$ is molecular or has H_3O^+ ions bridging two or more anions. Tentatively assuming molecularity, the PBE0 DFT-predicted molecular structures of $(H_3O)_2B_{12}F_{12}$ and the putative superacid $H_2B_{12}F_{12}$ are shown in Figure 5, and the relevant interatomic distances are listed in Table S2 (the Supporting Information gives the computational details and sets of orthogonal coordinates). Although the H_3O^+ ions cause lengthening of the B–F bonds (and concomitant shortening of the affected B–B bonds), the isolated $(H_3O)_2B_{12}F_{12}$ molecule appears to be stable. The isolated ion pair (H_3O)-$B_{12}F_{12}^-$ was also found to be stable, in contrast to the $H_3O^+BF_4^-$ ion pair, which has been shown to spontaneously form HF and BF_3OH by MP2 and DFT calculations.[39] $H_2B_{12}F_{12}$ also appears to be stable according to our calculations, and it remains a synthetic target in our ongoing study of $B_{12}F_{12}^{2-}$ chemistry. However, the unusually long B1–B1 bonds of 2.06 Å and the unusually short F1···F2′ distances of 3.02 Å indicate that this compound may be very reactive and therefore difficult to isolate under ambient conditions.

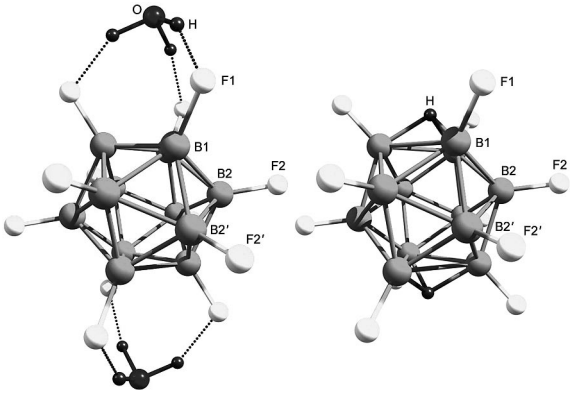

Figure 5. DFT-predicted structures of $(H_3O)_2B_{12}F_{12}$ and $H_2B_{12}F_{12}$.

Conclusions

The structural and physiochemical properties of $(H_3O)_2B_{12}F_{12}\cdot 6H_2O$ are yet another interesting manifestation of the weak coordinating nature of the $B_{12}F_{12}^{2-}$ anion.

The formation of long range order of nonplanar layers consisting of $\{H_3O^+/3H_2O\}_\infty$ is, as far as we can tell, unprecedented in solid-state compounds. Additionally, by way of thermogravimetric characterization, two additional hydrate phases and a purely hydronium salt of $B_{12}F_{12}^{2-}$ have been identified as stable at specific temperature and humidity conditions. The reversible desorption of water from $(H_3O)_2B_{12}F_{12}\cdot nH_2O$ (n = 0, 2, 4) exhibits a latent porosity phenomenon similar to that of $K_2B_{12}F_{12}$. Isolation and characterization of the other hydrate phases and the protic species are the focus of further research.

Experimental Section

Synthesis of $(H_3O)_2B_{12}F_{12}\cdot 6H_2O$: $K_2B_{12}F_{12}$ was prepared as described previously.[2] The $K_2B_{12}F_{12}$ used for synthesis of $(H_3O)_2B_{12}F_{12}\cdot nH_2O$ was at least +99% $B_{12}F_{12}^{2-}$ as determined by ^{19}F and ^{11}B NMR spectroscopy in CD_3CN (CD_3CN was dried by 3 Å sieves for 48 h). An aqueous solution of $(H_3O)_2B_{12}F_{12}$ was prepared by passing an aqueous solution of $K_2B_{12}F_{12}$ through the acid form of a cation-exchange column (Amberlyst® 15; Sigma–Aldrich). Single crystals of $(H_3O)_2B_{12}F_{12}\cdot 6H_2O$ were grown by slow evaporation of an aqueous solution at 25 °C. The water used for ion exchange was distilled and deionized with a Barnstead Nanopure filtration system and had a final resistance of 18 MΩ or greater.

Thermogravimetric Analysis: Thermogravimetric analysis was performed with a TA instruments 2950 Series instrument with a dry helium purge at a flow rate of 55 mL min^{-1}. Samples were contained in an uncovered platinum pan. Humidity conditions inside the furnace were controlled by flowing the purge gas through a gas bubbler that contained water or various aqueous salts to yield the desired humidity. After the thermogravimetric measurement, the samples were collected and analyzed by ^{19}F and ^{11}B NMR spectroscopy to determine if any decomposition had taken place.

XRD: Crystal data for $(H_3O)_2B_{12}F_{12}\cdot 6H_2O$: M_r = 1067.65 g mol^{-1}, monoclinic, $C2/m$, a = 14.504(1), b = 8.5208(7), c = 8.7025(7) Å, β = 122.070(3)°, V = 911.4(1) Å^3, Z = 2, T = 120(2) K, 1479 reflections, 1426 independent reflections, 104 parameters, $R_1[I > 2\sigma(I)]$ = 0.0212, wR_2 = 0.0648, Bruker KappaAPEX II CCD diffractometer (Mo-K_α λ = 0.71073 Å; graphite monochromator). A semiempirical absorption correction was applied using SADABS.[40] The structure was refined using SHELTXL.[41,42] Further details on the crystal structure investigation may be obtained from the Fachinformationszentrum Karlsruhe, 76344 Eggenstein-Leopoldshafen, Germany (fax: +49-7247-808-666; e-mail: crysdata@fiz-karlsruhe.de), on quoting the depository number CSD-423408.

Supporting Information (see footnote on the first page of this article): Additional details of the structure of $(H_3O)_2B_{12}F_{12}\cdot 6H_2O$; computational details, orthogonal coordinates, and the relevant interatomic distances of calculated structures; H bonding interactions in the layers; a discussion of the term "superweak anion"; refcodes of several structures with L6(6) layers.

Acknowledgments

The authors thank Professors O. P. Anderson, I. Bernal, L. Infantes, R. B. King, and I. Goldberg for helpful discussions and Professor L. Dunsch for his continuing support.

[1] S. V. Ivanov, S. M. Miller, O. P. Anderson, K. A. Solntsev, S. H. Strauss, *J. Am. Chem. Soc.* **2003**, *125*, 4694.
[2] D. V. Peryshkov, A. A. Popov, S. H. Strauss, *J. Am. Chem. Soc.* **2009**, *131*, 18393.
[3] D. V. Peryshkov, S. H. Strauss, *J. Fluorine Chem.* **2010**, *131*, 1252.
[4] D. V. Peryshkov, A. A. Popov, S. H. Strauss, *J. Am. Chem. Soc.* **2010**, *132*, 13902.
[5] D. V. Peryshkov, E. Goreshnik, Z. Mazej, S. H. Strauss, *J. Fluorine Chem.* **2010**, *131*, 1225.
[6] S. A. Shackelford, J. L. Belletire, J. A. Boatz, S. Schneider, A. K. Wheaton, B. A. Wight, H. L. Ammon, D. V. Peryshkov, S. H. Strauss, *Org. Lett.* **2010**, *12*, 2714.
[7] See Supporting Information for a discussion of the term "superweak anion".
[8] J. A. Wunderlich, W. H. Lipscomb, *J. Am. Chem. Soc.* **1960**, *82*, 4427.
[9] I. Tiritiris, T. Schleid, K. Muller, W. Preetz, *Z. Anorg. Allg. Chem.* **2000**, *626*, 323.
[10] I. Tiritiris, T. Schleid, *Z. Anorg. Allg. Chem.* **2003**, *629*, 1390.
[11] J.-H. Her, M. Yousufuddin, W. Zhou, S. S. Jalisatgi, J. G. Kulleck, J. A. Zan, S.-J. Hwang, R. C. Bowman Jr., T. J. Udovic, *Inorg. Chem.* **2008**, *47*, 9657.
[12] I. Tiritiris, T. Schleid, *Z. Anorg. Allg. Chem.* **2004**, *630*, 1555.
[13] V. Geis, K. Guttsche, C. Knapp, H. Scherer, R. Uzun, *Dalton Trans.* **2009**, 2687.
[14] J. Derendorf, M. Kessler, C. Knapp, M. Rühle, C. Schulz, *Dalton Trans.* **2010**, *39*, 8671.
[15] T. Peymann, A. Herzog, C. B. Knobler, M. F. Hawthorne, *Angew. Chem.* **1999**, *111*, 1129; *Angew. Chem. Int. Ed.* **1999**, *38*, 1061.
[16] D. J. Stasko, K. J. Perzynski, M. A. Sasil, J. K. Brodbeck, K. Kirschbaum, Y. W. Kim, C. Lind, *Inorg. Chem.* **2004**, *43*, 3786.
[17] T. Peymann, C. B. Knobler, M. F. Hawthorne, *J. Am. Chem. Soc.* **1999**, *121*, 5601.
[18] A. Szytula, J. Leciejewicz, *Handbook of Crystal Structures and Magnetic Properties of Rare Earth Intermetallics*, CRC Press, Boca Raton, **1994**.
[19] E. S. Stoyanov, I. V. Stoyanova, C. A. Reed, *Chem. Sci.* **2011**, *2*, 462, and references therein.
[20] E. S. Stoyanov, I. V. Stoyanova, C. A. Reed, *J. Am. Chem. Soc.* **2010**, *132*, 1484, and references therein.
[21] J. Xu, S. Izvekov, G. A. Voth, *J. Phys. Chem. B* **2010**, *114*, 9555.
[22] B. Jagoda-Cwiklik, L. Cwiklik, P. Jungwirth, *J. Phys. Chem. A* **2011**, *115*, 5881.
[23] H. Takahashi, K. Maruyama, Y. Karino, A. Morita, M. Nakano, P. Jungwirth, N. Matubayasi, *J. Phys. Chem. B* **2011**, *115*, 4745.
[24] E. S. Stoyanov, K.-C. Kim, C. A. Reed, *J. Am. Chem. Soc.* **2006**, *128*, 1948, and references therein.
[25] I. Bernal, *C. R. Chim.* **2006**, *9*, 1454.
[26] I. Bernal, *C. R. Chim.* **2008**, *11*, 942.
[27] Z. Yang, S. Hua, W. Hua, L. Shuhua, *J. Phys. Chem. B* **2011**, *115*, 8249.
[28] W. H. Knoth, H. C. Miller, J. C. Sauer, J. H. Balthis, Y. T. Chia, E. L. Muetterties, *Inorg. Chem.* **1964**, *3*, 159.
[29] S. V. Ivanov, W. J. Casteel Jr., G. P. Pez, Air Products and Chemicals, Inc., European Patent Application EP 1 624 519 A1, **2006**.
[30] M. W. Rupich, J. S. Foos, S. B. Brummer, *J. Electrochem. Soc.* **1985**, *132*, 119.
[31] A. Bondi, *J. Phys. Chem.* **1964**, *68*, 441.
[32] L. Infantes, S. Motherwell, *CrystEngComm* **2002**, *4*, 454.
[33] L. Infantes, J. Chisholm, S. Motherwell, *CrystEngComm* **2003**, *5*, 480.
[34] M. Mascal, L. Infantes, J. Chisholm, *Angew. Chem.* **2006**, *118*, 36; *Angew. Chem. Int. Ed.* **2006**, *45*, 32.
[35] A. V. Virovets, D. G. Samsonenko, D. N. Dybtsev, V. P. Fedin, W. Clegg, *J. Struct. Chem.* **2001**, *42*, 319.

[36] I. Bernal, U. Mukhopadhyay, A. V. Virovets, V. P. Fedin, W. Clegg, *Chem. Commun.* **2005**, 3791.
[37] S. Wallace, L. Huang, L. Massa, U. Mukhopadhyay, I. Bernal, J. Karle, *Proc. Natl. Acad. Sci. USA* **2008**, *105*, 16798.
[38] I. Goldberg, *J. Inclusion Phenom.* **1984**, *1*, 349.
[39] D. Fărcaşiu, P. Lukinskas, *Phys. Chem. Chem. Phys.* **2000**, *2*, 4219.
[40] G. M. Sheldrick, *SADABS*, Bruker AXS, Madison, WI, **1997**.
[41] G. M. Sheldrick, *SHELXTL*, 6.15, Bruker AXS, Madison, WI, **2004**.
[42] G. M. Sheldrick, *Acta Crystallogr.* **2008**, *A64*,112–122.
Received: October 13, 2011
Published Online: December 6, 2011

DOI: 10.1002/ejic.201100838

Thermal Decomposition of Ammonium Paratungstate Tetrahydrate Traced by In Situ UV/Vis Diffuse Reflectance Spectroscopy

Martin J. G. Fait*[a] and Hans-Joachim Lunk[b]

Keywords: In situ spectroscopy / Thermochemistry / Structure elucidation / Tungsten / Polyoxometalates

In situ UV/Vis diffuse reflectance spectra of ammonium paratungstate tetrahydrate at increasing temperatures were recorded in oxidative as well as in reductive atmospheres. From the edge energy of the ligand-to-metal charge transfer transition of tungsten ions, the number of bridging W–O–W bonds, *N*, was determined. The increase of *N* with temperature indicates a stepwise enhancement of the condensation of WO_6 octahedra to finally form WO_3 in an oxidative atmosphere.

Introduction

Monoclinic ammonium paratungstate tetrahydrate, $(NH_4)_{10}[H_2W_{12}O_{42}]\cdot 4H_2O$, which will be referred to as APT-4, is widely used in the industry. It is the feedstock for the production of tungsten carbide, various tungsten heavy alloys, tungsten filaments and ammonium metatungstate, the mostly used starting material in production of tungsten-containing catalysts. The thermal decomposition of APT-4 is still a matter of investigation. Nowadays, in situ techniques are state of the art. A variety of temperature-programmed in situ techniques, such as X-ray diffraction (XRD),[1,2] spectroscopy [infrared (FTIR)[2,3] X-ray absorption (XAS)[1]] and thermoanalytical methods,[4,5] some of which are combined with mass spectrometry, were applied for studying the thermal decomposition of APT-4.[1,2,6,7] However, an in situ study of the decomposition of APT-4 by UV/Vis diffuse reflectance (DR) spectroscopy is still lacking.

UV/Vis DR spectroscopy as an in situ technique has the advantage that the obtained information is structure-related, since the outer-shell electrons are probed.[8] So, this technique is preferred to investigate the local surrounding of ions, in our case of tungsten ions. The band positions of the ligand-to-metal charge transfer (LMCT) transitions act as a fingerprint for the local structure of W^{VI}.[9]

UV/Vis DR spectroscopy at room temperature had been employed to establish a quantitative correlation between the number of bridging W–O–W bonds in polyoxotungstates as bulk materials and their corresponding edge energy, E_g.[9] For the first time, this idea is used to describe the local tungsten structure during the thermal decomposition of APT-4, which is aimed for the present investigation.

In situ UV/Vis DR spectroscopy up to 525 °C is applied in different atmospheres, that is, oxidative and reductive. In oxidative atmospheres (oxygen) the oxidation number of tungsten remains unchanged (W^{+6}), yielding tungsten(VI) oxide, which was demonstrated by other techniques such as ex situ UV/Vis DR spectroscopy on air-calcined samples.[9–11] The usage of a reductive atmosphere (hydrogen) was inspired by the technical process of powder metallurgical manufacturing of tungsten wire from APT-4 as starting material, which, in contrast to the former process, is accompanied by changes in the oxidation number of tungsten ($W^{+6} \rightarrow W^{\pm 0}$). As intermediates, "tungsten blue oxides" [phase mixtures of various suboxides, e.g., $W_{20}O_{58}$ ($W^{+5.8}$) and $W_{18}O_{49}$ ($W^{+5.4}$)] were detected,[12,13] which should be identified by their d–d transitions in UV/Vis DR spectroscopy.[14]

Results and Discussion

The UV/Vis DR spectra of the APT-4 starting material at 50 °C in different atmospheres are depicted in Figures 1a (oxidative) and 1b (reductive). They are characterized by two signals caused by LMCT transitions at 260 and 320 nm, which is in line with previous reports[9] (269, 314 nm). These band positions are typical for iso- (paratungstate: $[H_2W_{12}O_{42}]^{10-}$, metatungstate: $[H_2W_{12}O_{40}]^{6-}$) and heteropolyoxotungstate compounds.[9]

The spectra recorded in oxidative atmospheres at increasing temperature (Figure 1a) are characterized by a systematic, bathochromic shift of the low-energy edge. The evolution of the bands at approximately 400 and 500 nm above 325 °C is caused by the temperature-induced formation of a WO_3 precursor and finally WO_3 (see Figure S1 for com-

[a] Leibniz-Institut für Katalyse,
Albert-Einstein-Strasse 29a, 18059 Rostock, Germany
Fax: +49-381-128151273
E-mail: martin.fait@catalysis.de
[b] Global Tungsten & Powders Corp.,
1 Hawes Street, Towanda, PA 18848, USA

Supporting information for this article is available on the WWW under http://dx.doi.org/10.1002/ejic.201100838.

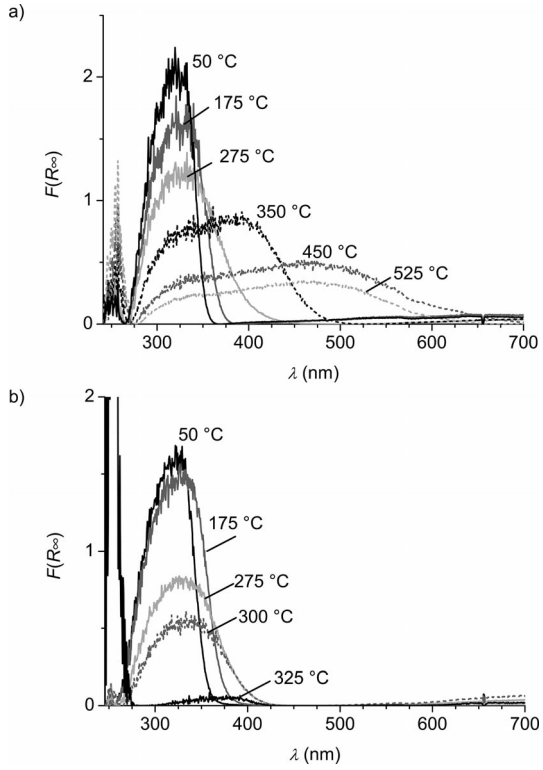

Figure 1. UV/Vis DR spectra of $(NH_4)_{10}[H_2W_{12}O_{42}]\cdot 4H_2O$ while heating in oxidative (a) and reductive (b) atmospheres. The spectra at the "switching temperatures" in correspondence to Figures 2a and 2b are presented.

parison). In reductive atmospheres (Figure 1b) the spectra up to 300 °C are comparable to those taken in oxidative atmosphere. However, at 325 °C the band at 320 nm disappears as a result of the formation of tungsten suboxides. They should be identified by distinct d–d bands in the range 443 (WO_2) to 755 nm ($W_{20}O_{58}$),[14] which, however, could not be proved. The temperature of postulated suboxide formation would agree roughly with the previously reported value[12] (> 350 °C) determined from XRD analysis by the appearance of crystalline phases from an "X-ray amorphous pool", which exists between 250–350 °C.

The edge energies, E_g(meas.), calculated from the UV/Vis DR spectra at the respective temperatures are plotted in Figures 2a (oxidative) and 2b (reductive) (black curves with filled symbols, see Supporting Information, Figures S1 and S2). The E_g(meas.) values at 25 °C for APT-4 (3.6 eV) and WO_3 (2.6 eV) are identical with published data.[9,15] At 525 °C (Figure 2a), the APT-4 and WO_3 curves meet at 2.1 eV, which illustrates the final formation of WO_3 from APT-4 as expected. The observed tendency of E_g(meas.) values to decrease with increasing temperature is caused by two superimposing effects: (I) a direct one due to the thermal expansion of the lattice (dilatation),[16] (II) an indirect one due to structural changes induced by thermal decomposition accompanied by an increased number of nearest tungsten ion neighbours.[9] Effect I is quantified by the linear expansion coefficient. Because of missing data for APT-4, the curve for WO_3 was used (Figure 2a), which is reasonable as: (i) its number of nearest neighbours does not change with temperature (W^{+6} remains constant), and hence, only effect I is active; (ii) WO_3 is a member of the system studied. (The discontinuity at 310 °C is caused by the monoclinic-to-orthorhombic WO_3 modification transition[17] and results in a minor shift of 0.03 eV to higher E_g values.) Indeed, the temperature coefficient of WO_3 is constant up to 290 °C (-11.4×10^{-4} eV/K) in agreement with ref.[17] (WO_3 single crystal: -9.0×10^{-4} eV/K, *a*-polarized light). This value is very similar to that of APT-4, where the paratungstate ion remains unchanged up to 175 °C (i.e., there are no changes in the surrounding tungsten ions, see below) and temperature coefficients result in values of -10.6×10^{-4} (oxidative) and -12.3×10^{-4} eV/K (reductive, see Supporting Information for details of linear fit correlations). In view of the equivalence of the two APT-4 values in different atmospheres, it is likely that the temperature coefficient of WO_3 is independent of the atmosphere, too. A measurement of WO_3 as reference in a reductive atmosphere makes no sense because of changes of the surrounding tungsten ions caused by tungsten ion reduction (see above).

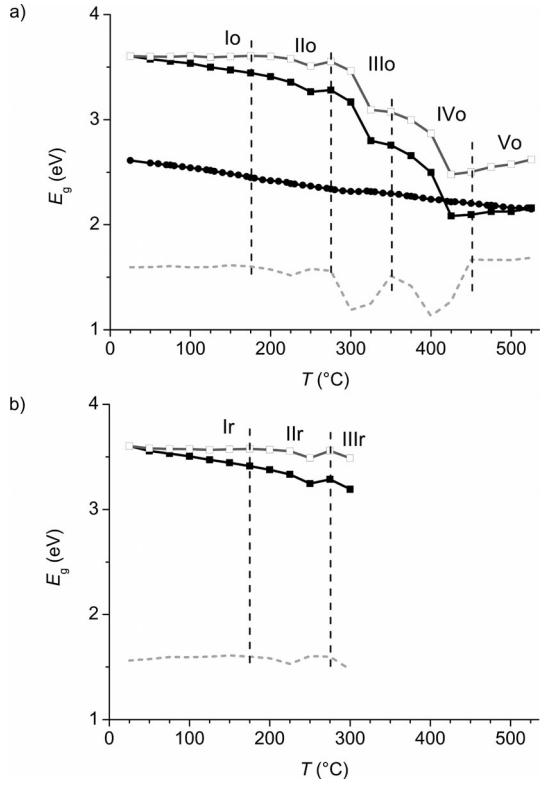

Figure 2. Edge energies (E_g) of $(NH_4)_{10}[H_2W_{12}O_{42}]\cdot 4H_2O$ (APT-4: ■, □) and WO_3 (●) calculated from the UV/Vis DR spectra (filled symbols) and thermal expansion corrected (open symbols) according to dependence on temperature in oxidative (a) and reductive (b) atmospheres. The vertical dashed lines mark the maximum of the first derivative of corrected E_g curves (dashed grey curves). The meaning of the Roman numerals is explained in the text.

To separate effect II from effect I and to quantify the desired contribution caused by changes of the surroundings of the tungsten ion (effect II), the E_g(meas.) values in oxi-

dative and reductive atmospheres must be corrected by using the WO_3 data from the oxidative atmosphere (see Supporting Information). The results [E_g(corr.)] are depicted in Figures 2a and 2b (grey curves with open symbols).

Up to 175 °C, the E_g(corr.) value remains constant. Above 175 °C, all the partial steps are similar in their shape: An exponential decrease in E_g(corr.) is terminated by an increase or a hold, with the exception of range IIIr. The temperature ranges of these steps can be determined best from the derivative curves at their maximum points (vertical lines). In an oxidative atmosphere, these are at 175, 275, 350 and 450 °C (ranges Io to Vo), whereas in a reductive atmosphere they are at 175 and 275 °C (ranges Ir to IIIr). The ranges in the oxidative atmospheres are very similar to the four qualitatively different individual steps, endo-1, endo-2, endo-3 and exo-4, derived from thermogravimetric curves under comparable conditions.[2] Indeed, the ranges Io (50–175 °C) and IIo (175–275 °C) coincide excellently with endo-1 (50–190 °C) and endo-2 (190–250 °C). If endo-3 (250–380 °C) is analyzed in more detail with respect to the NH_4^+/OH^+ ion mass spectrometry curve (m/z = 17),[2] then its shape allows a separation at 350 °C into two distinct steps with different release rates of NH_3/H_2O. In other words, the temperature intervals of the two substeps endo-3a (250–350 °C) and endo-3b (350–380 °C) correspond well to the ranges IIIo (275–350 °C) and IVo at least with the starting temperature of 350 °C. In a reductive atmosphere, both ranges Ir (50–175 °C) and IIr (175–275 °C) are identical with Io and IIo.

The edge energy can be interpreted as a structure-related measure, since the E_g values are primarily determined by the number of bridging W–O–W bonds, N.[9] By using the linear correlation between N and E_g(corr.) for APT-4 and WO_3 deduced from our measurements (see Supporting Information for the explanation and discussion of the reasons why literature data[9] are not suitable), N can be recalculated from the E_g(corr.) values (Figures 2a and 2b). The resulting plots of N vs. T for the thermal decomposition of APT-4 are depicted in Figure 3 for both atmospheres.

In range I up to 175 °C and in both atmospheres, N is constant and equivalent to that of APT-4, which indicates that the anion structure remains intact as a result of the formation of anhydrous ammonium paratungstate by the release of crystal water.[2,6] Above 175 °C (range II) N begins to rise in a similar way in an oxidative as well as in a reductive atmosphere (at 250 °C: N = 4.5), indicating the beginning of the condensation of WO_6 octahedra. In range III a further increase in N is to be noticed, which again seems to be similar in oxidative and reductive atmospheres at least up to 300 °C. This temperature suggests a differentiation with respect to the atmosphere used: While in an oxidative atmosphere the condensation of WO_6 units preserves the tungsten oxidation number W^{+6}, in a reductive atmosphere above 300 °C, the formation of suboxides with reduced tungsten ions is assumed,[12] which unfortunately eludes UV/Vis detection. In an oxidative atmosphere at 425 °C (range IV), a maximum of N is to be found (6.2),

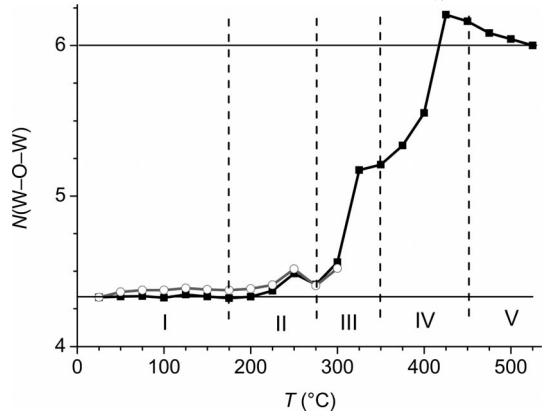

Figure 3. Number of W–O–W bonds, N, during the thermal decomposition of ammonium paratungstate tetrahydrate in oxidative (filled symbols) and reductive atmosphere (open symbols). The positions of the vertical lines correspond to Figures 2a and 2b. The horizontal solid lines at N = 4.33 and 6.00 represent APT-4 and WO_3, respectively.

which can be observed with weakened intensity at 250 and 325 °C in ranges II and III, too. This specific wave form suggests a highly unstable lattice at these temperatures and can be interpreted as enhanced reactivity. This is confirmed by the fact that these temperatures are close to the peak temperatures determined from DTA curves (242, 302, 412).[2] The "overshoot" of N at 425 °C (6.2) over the theoretical value (6.0) occurs exactly at a temperature for which a fragile lattice is proposed. This situation can be attributed to highly distorted WO_6 octahedra and lowered symmetry as shown by XAFS studies.[1] These nonquantifiable phenomena may also affect the edge position of the tungsten ions[18] in addition to N and can be responsible for this behaviour. Above 425 °C N converges to 6.0, which is a characteristic value for WO_3 reached at 525 °C. This means that the decomposition of APT-4 is terminated by the formation of WO_3, which is confirmed also by the fact that the E_g(meas.) values of the APT-4 and WO_3 curves at this temperature are equal (see above).

Conclusions

The detection of stepwise changes of the surroundings of the tungsten ions in the paratungstate anion of APT-4 during its thermal decomposition demonstrates that the in situ UV/Vis spectroscopy is a very sensitive technique to trace transformations in solids.

Experimental Section

Materials Used: The starting chemical ammonium paratungstate tetrahydrate (APT-4), $(NH_4)_{10}[H_2W_{12}O_{42}]\cdot 4H_2O$, was manufactured at Global Tungsten & Powders Corp. (GTP) in Towanda, PA, USA. The mass loss of the starting APT-4 amounted to 10.63%. Due to the fact that any ammonium paratungstate is characterized by a molar ratio (NH_3/WO_3) of 10:12, the formula $(NH_4)_{10}[H_2W_{12}O_{42}]\cdot 2.83H_2O$ was calculated. The relationship of the filled structure with 4 mol H_2O and the "deficit structure" with

2.83 mol H_2O is discussed in ref.[2] The trace element concentrations and the results of characterization by TA-MS, XRD, FTIR and Raman spectroscopy are published.[2] The results of powder characterization techniques are represented in the Supporting Information.

Monoclinic tungsten(VI) oxide, *m*-WO_3, was prepared from APT-4 by heating to 800 °C, holding for 1 h and cooling down to room temperature in an oxygen flow (15 mL min^{-1}). Its powder XRD pattern agrees with PDF [00–043–1035] indicating that the substance is phase-pure.

UV/Vis Diffuse Reflectance Measurements: The experimental details of the UV/Vis DR measurements have been reported previously.[19] The UV/Vis DR probe was kept fixed at the middle position of the reactor bed during the whole experiment. $BaSO_4$ was used as a white reference. The white and black balances were performed at room temperature before registering the spectra. For the oxidative atmosphere, flowing O_2 was used, whereas for the reductive atmosphere H_2 was employed (in each case: 15 mL min^{-1}, supplier: Air Liquide, quality: 5.0). The heating rate was 5 K min^{-1} for all runs in the temperature range from 25 to 525 °C (25 K steps). The UV/Vis DR spectra were calculated from the reflectance (R) according to the Kubelka–Munk function, $F(R_\infty) = (1 - R)^2/2R$.[20]

Supporting Information (see footnote on the first page of this article): Powder characterization of APT-4, UV/Vis DR spectra of WO_3 while heating in air, determination of the edge energy from UV/Vis DR spectra, procedure to correct E_g values, determination of N in the paratungstate anion, discussion of the plot of N vs. E_g from ref.[9] and explanation of reasons for using the current results.

Acknowledgments

The authors thank Mr. L. Knoepke for reference measurements, Mr. E. V. Kondratenko, and the referee for critical and valuable discussion of the manuscript.

[1] O. Kirilenko, F. Girgsdies, R. E. Jentoft, T. Ressler, *Eur. J. Inorg. Chem.* **2005**, 2124–2133.
[2] M. J. G. Fait, H.-J. Lunk, M. Feist, M. Schneider, J. N. Dann, T. A. Frisk, *Thermochim. Acta* **2008**, *469*, 12–22.
[3] J. Madarasz, I. M. Szilagyi, F. Hange, G. Pokol, *J. Anal. Appl. Pyrolysis* **2004**, *72*, 197–201.
[4] N. Fouad, A. Nohman, M. I. Zaki, *Thermochim. Acta* **2000**, *343*, 139–143.
[5] L. Bartha, A. Kiss, J. Neugebauer, T. Nemeth, *High Temp. High Pressures* **1982**, *14*, 1–10.
[6] G. J. French, F. R. Sale, *J. Mater. Sci.* **1981**, *16*, 3427–3436.
[7] A. K. Basu, F. R. Sale, *J. Mater. Sci.* **1977**, *12*, 1115–1124.
[8] B. M. Weckhuysen, R. A. Schoonheydt, *Catal. Today* **1999**, *49*, 441–451.
[9] E. I. Ross-Medgaarden, I. E. Wachs, *J. Phys. Chem. C* **2007**, *111*, 15089–15099.
[10] N. Fouad, A. Nohman, M. Mohamed, M. I. Zaki, *J. Anal. Appl. Pyrolysis* **2000**, *56*, 23–31.
[11] S. Huang, S. Liu, Q. Zhu, X. Zhu, W. Xin, H. Liu, Z. Feng, C. Li, S. Xie, Q. Wang, L. Xu, *Appl. Catal. A* **2007**, *323*, 94–103.
[12] H. J. Lunk, B. Ziemer, M. Salmen, D. Heidemann, *Int. J. Refract. Met. Hard Mater.* **1994**, *12*, 17–26.
[13] J. W. Van Put, T. W. Zegers, *Int. J. Refract. Met. Hard Mater.* **1991**, *10*, 115–122.
[14] V. R. Porter, W. B. White, R. Roy, *J. Solid State Chem.* **1972**, *4*, 250–254.
[15] D. G. Barton, M. Shtein, R. D. Wilson, S. L. Soled, E. Iglesia, *J. Phys. Chem. C* **1999**, *103*, 630–640.
[16] Y. P. Varshni, *Physica* **1967**, *34*, 149–154.
[17] T. Iwai, *J. Phys. Soc. Jpn.* **1960**, *15*, 1596–1600.
[18] X. Gao, S. R. Bare, B. M. Weckhuysen, I. E. Wachs, *J. Phys. Chem. B* **1998**, *102*, 10842–10852.
[19] M. J. G. Fait, R. Abdallah, D. Linke, E. V. Kondratenko, U. Rodemerck, *Catal. Today* **2009**, *142*, 196–201.
[20] G. Kortüm, *Reflexionsspektroskopie*, Springer, Berlin, **1969**.

Received: August 9, 2011
Published Online: December 8, 2011

DOI: 10.1002/ejic.201100953

Synthesis of Rhenium(I) Tricarbonyl Complexes with Carbohydrate-Pendant Tridentate Ligands and Their Cellular Uptake

Yuji Mikata,*[a] Kyoko Takahashi,[b] Yuka Noguchi,[b] Masami Naemura,[b] Anna Ugai,[b] Saori Itami,[c] Keiko Yasuda,[c] Satoshi Tamotsu,[c] Takashi Matsuo,[d] and Tim Storr[e]

Keywords: Sugar–metal hybrid material / Carbohydrates / Glycosides / Rhenium / Ligand effects

Twelve $[Re^{I}\mathbf{L}(CO)_3]^{n+}$ complexes with various carbohydrate-pendant ligands **L** have been prepared and their uptake into HeLa S3 cells were investigated. The ligand library includes: (i) glucose/galactose as the carbohydrate group; (ii) bis(2-pyridylmethyl)amine (DPA), bis(2-quinolylmethyl)amine (DQA), or *N*-(2-pyridylmethyl)glycine (NPG) as the metal binding component; and (iii) an ethylene chain as a linker between the metal binding site and the *O*/*C*-glycosides. Microwave induced plasma mass spectroscopy (MIP-MS) measurements revealed that all complexes were extensively incorporated into the HeLa cells over a 24 h period, and the DQA complexes showed the highest uptake of all the complexes in the series. However, in comparison to the corresponding Re complexes without the pendant carbohydrate functions (prepared with the related ligands $\mathbf{L}^{\mathbf{DPA}}$, $\mathbf{L}^{\mathbf{DQA}}$, and $\mathbf{L}^{\mathbf{NPG}}$), only the NPG complexes exhibited carbohydrate enhanced cellular uptake. Considering their water solubility and cellular uptake properties, the NPG complexes containing an *O*-glycoside group (**L1** and **L′1**) are the best candidates for enhancing cellular uptake of metal ions. Microscopic analysis with PC-12 cells in the presence of the fluorescent complex $[Re(\mathbf{L'7})(CO)_3]Cl$, revealed that the complex stays in the cell cytosol and cannot penetrate into the nucleus.

Introduction

Functionalized carbohydrates are of significant interest as building blocks for high order complex carbohydrate structures, asymmetric catalysts, and sugar-metal hybrid materials.[1] The attachment of carbohydrate moieties to functional molecules provides integrated properties such as water solubility, chirality, and biological recognition elements to those materials. The most convenient and inexpensive strategy to access carbohydrate functionalized materials is a pendant approach in which functional molecules are connected via a linker to commercially available carbohydrates.[2]

The radiopharmaceutical application of group VII metals such as ^{99m}Tc and $^{186/188}$Re is of recent interest. ^{99m}Tc has ideal properties ($t_{1/2}$ = 6.01 h, γ = 142.7 keV) for use in single photon emission computed tomography (SPECT). Convenient isolation from a ^{99}Mo generator justifies the extensive use of ^{99m}Tc in medical imaging methods. ^{186}Re ($t_{1/2}$ = 3.68 d, β = 1.07 MeV, γ = 137 keV) and ^{188}Re ($t_{1/2}$ = 16.98 h, β = 2.12 MeV, γ = 155 keV) have potential use in therapeutic nuclear medicine. The $[M(CO)_3]^+$ (M = Tc, Re) core has received considerable attention due to its small size, inert d^6 low-spin configuration, and simple aqueous chemistry.[3] Tridentate chelates are well suited for binding to the $[M(CO)_3]^+$ core, providing a high level of stability to the resultant complexes due to the chelate effect and by limiting the accessibility of the metal center to endogenous ligands in vivo. The rational design of ligands for radioisotopes with diagnostic/therapeutic properties is highly desirable, especially for use in imaging and therapy. Extensive studies have been accumulated, and several carbohydrate functionalized complexes have been reported that display benefits, in addition to those mentioned above, due to their carbohydrate groups.[2d,4]

In this article, facile synthetic routes to tridentate carbohydrate-pendant ligands (Scheme 1) are reported. The ligand library includes: (i) glucose/galactose as a carbohydrate moiety; (ii) DPA, DQA, or NPG as the metal binding component; and (iii) an ethylene linker between the metal binding site and the *O*/*C*-glycosides. Attachment of carbohydrate functions to the ligands, especially glucose analogs, was hypothesized to enhance the water solubility and more importantly membrane permeability via cellular glucose transporters (GLUT) of the compounds,[5] although some carbohydrate-pendant complexes have been reported

[a] KYOUSEI Science Center, Nara Women's University, Nara 630-8506, Japan
Fax: +81-742-203-095
E-mail: mikata@cc.nara-wu.ac.jp
[b] Department of Chemistry, Nara Women's University, Nara 630-8506, Japan
[c] Department of Biological Sciences, Nara Women's University, Nara 630-8506, Japan
[d] Graduate School of Materials Science, Nara Institute of Science and Technology (NAIST), Takayama, Ikoma, Nara 630-0192, Japan
[e] Department of Chemistry, Simon Fraser University, 8888 University Drive, Burnaby, BC, V5A-1S6, Canada
Supporting information for this article is available on the WWW under http://dx.doi.org/10.1002/ejic.201100953.

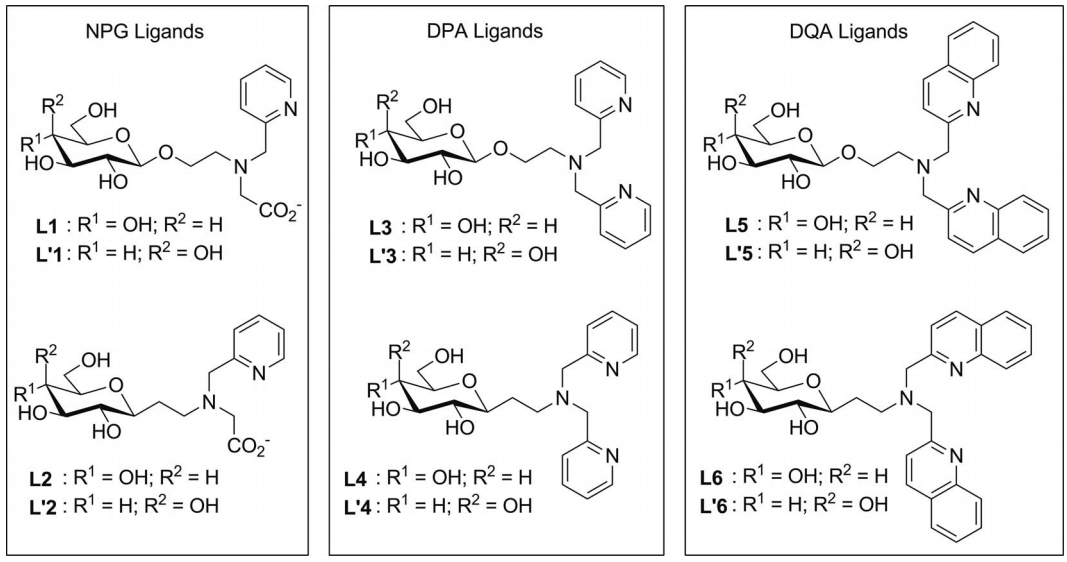

Scheme 1.

to have neither recognition nor transportation ability via the Glut1 transporter.[6] *C*-Glycosides are the carbon analogs of naturally occurring *O*-glycosides and have been extensively studied because of their chemical and enzymatic stability.[7] This paper provides efficient strategies for carbohydrate functionalization of rhenium(I) tricarbonyl complexes, and details of the cellular uptake analyses, performed with HeLa cells, of these complexes.

Results and Discussion

Synthesis of the Ligands

Carbohydrate-pendant ligands **L1**–**6** and **L′1**–**6** were synthesized according to Schemes 2–4. The preparations of **L3** and **L′3** have been reported previously.[8] Ligands **L1H** and **L′1H** were synthesized from 2-bromoethyl 2,3,4,6-tetra-*O*-acetyl-β-D-gluco- or galactopyranoside (**1**/**1′**)[8] that were reacted with *N*-(2-pyridylmethyl)glycine *tert*-butyl ester,[9] a procedure that was then followed by deprotection of the carboxylate and sugar hydroxy groups (Scheme 2). The other ligands, **L2H**, **L′2H L4**–**6** and **L′4**–**6**, were prepared by alkylation of carbohydrate-tethered primary amines **7**/**7′** (Scheme 3) and **11**/**11′**[10] (Scheme 4) with 2 equiv. of an alkylating agent – 2-(chloromethyl)pyridine, 2-(chloromethyl)quinoline, or *tert*-butyl bromoacetate – followed by deprotection. The preparation of *C*-glucosylamine **7** has been reported previously.[11] The *C*-galactosylamine **7′** was obtained by a procedure similar to the one given in that report. During the preparation of **7**/**7′**, the cyanomethyl *C*-glycosides **6**/**6′**[11–12] formed as crystals suitable for X-ray crystallography, and Figures S1 and S2 reveal the molecular structures of **6** and **6′**, including the β-configuration of the carbohydrate groups. It should be mentioned that compounds **8**/**8′** were obtained from a one-pot reaction involving amines **7**/**7′** that were reacted with 1 equiv. of 2-chloromethylpyridine and 1 equiv. of *tert*-butyl bromoacetate; **8**/**8′**

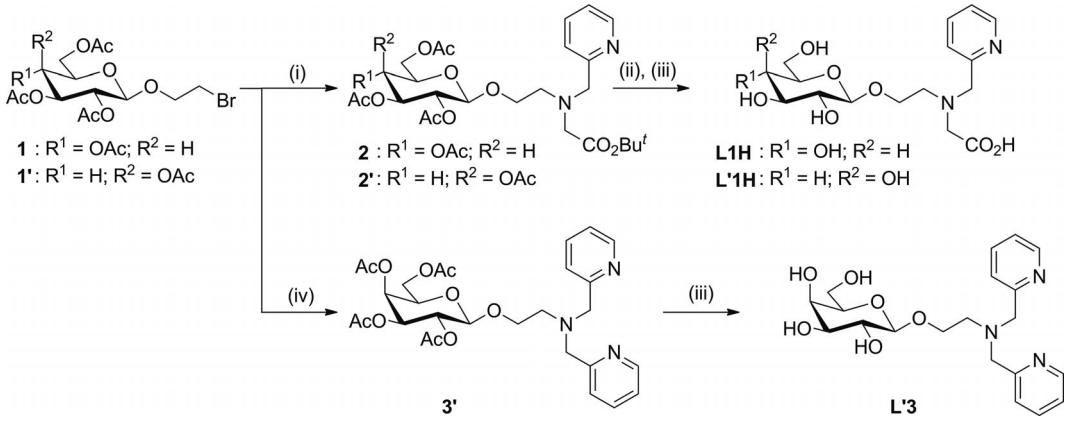

Scheme 2. *Reagents and conditions:* (i) *N*-(2-pyridylmethyl)glycine *tert*-butyl ester, DMF; (ii) formic acid; (iii) NaOMe, MeOH; (iv) bis(2-pyridylmethyl)amine.

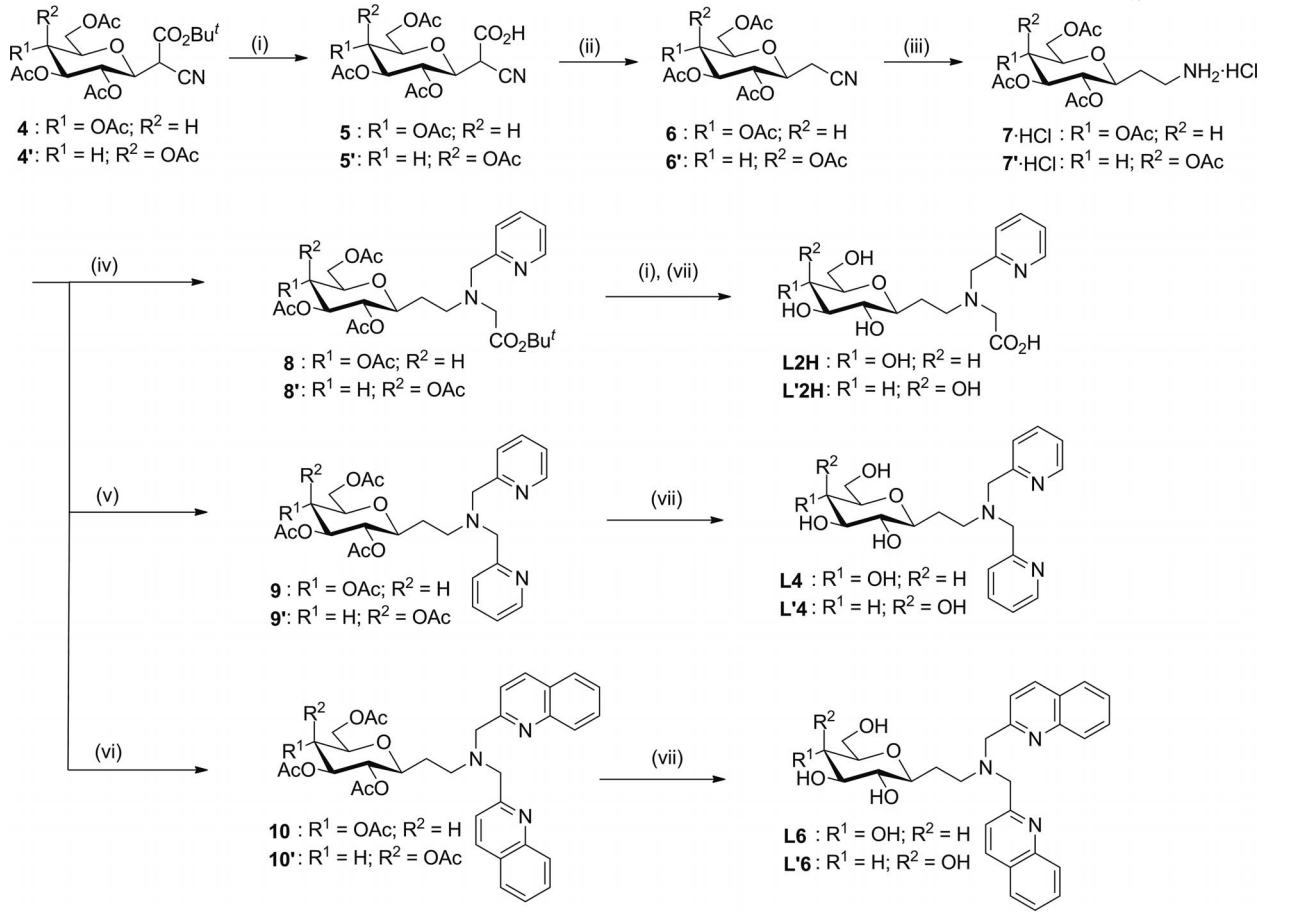

Scheme 3. *Reagents and conditions:* (i) formic acid; (ii) diisopropylethylamine (DIPEA); (iii) H_2, PtO_2, $CHCl_3$/EtOH; (iv) 2-(chloromethyl)-pyridine, *tert*-butyl bromoacetate, dimethylformamide (DMF); (v) 2-(chloromethyl)pyridine, DMF; (vi) 2-(chloromethyl)quinoline, DMF; (vii) NaOMe, MeOH.

were obtained in good yields (69–88%) and no significant amount of side products were isolated. The results of ^{1}H/^{13}C NMR, ESI-MS, and elemental analyses supported the proposed structures for all ligands.

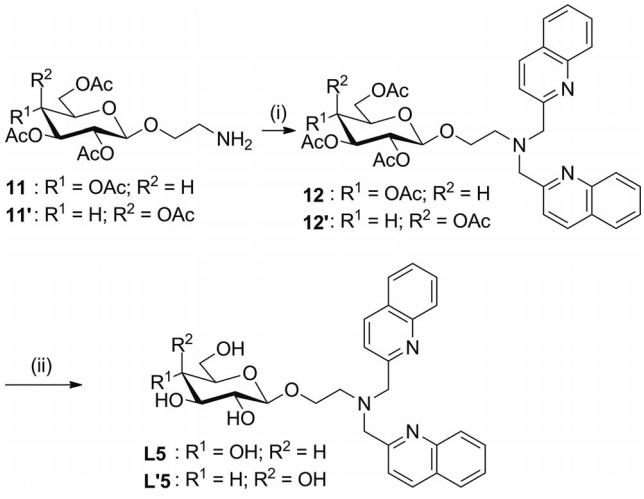

Scheme 4. *Reagents and conditions:* (i) 2-(chloromethyl)quinoline, DMF; (ii) NaOMe, MeOH.

The ethylamine derivatives shown in Scheme 5 that contain the same metal binding sites as **L1**–**6**/**L′1**–**6** but no sugar residues were prepared. $\mathbf{L^{DPA}}$ is a known compound,[13] but the other two ligands ($\mathbf{L^{NPG}H}$ and $\mathbf{L^{DQA}}$) were synthesized for the first time and fully characterized, details of which are provided in this paper. The crystal structure of $\mathbf{L^{DQA}}$ was also determined (see Supporting Information, Table S1 and Figure S3).

Synthesis of the Rhenium(I) Tricarbonyl Complexes

Ligands **L1**–**6** and **L′1**–**6** were refluxed with rhenium pentacarbonyl chloride to afford [Re**L**$(CO)_3$] for **L1**,**2**/**L′1**,**2** or [Re**L**$(CO)_3$]Cl for **L3**–**6**/**L′3**–**6** in 31% to quantitative yield. As represented in the ^{1}H NMR spectrum of [Re(**L4**)$(CO)_3$]Cl shown in Figure 1, distinct chemical shift changes for the protons associated with the metal binding are observed when the ligand binds to the metal. No significant chemical shift changes were observed for the carbohydrate protons. This clearly shows that the rhenium centers in the present complexes coordinate to the tridentate metal binding sites via the nitrogen or oxygen atoms, and confirms that the carbohydrate moieties remain pendant. In

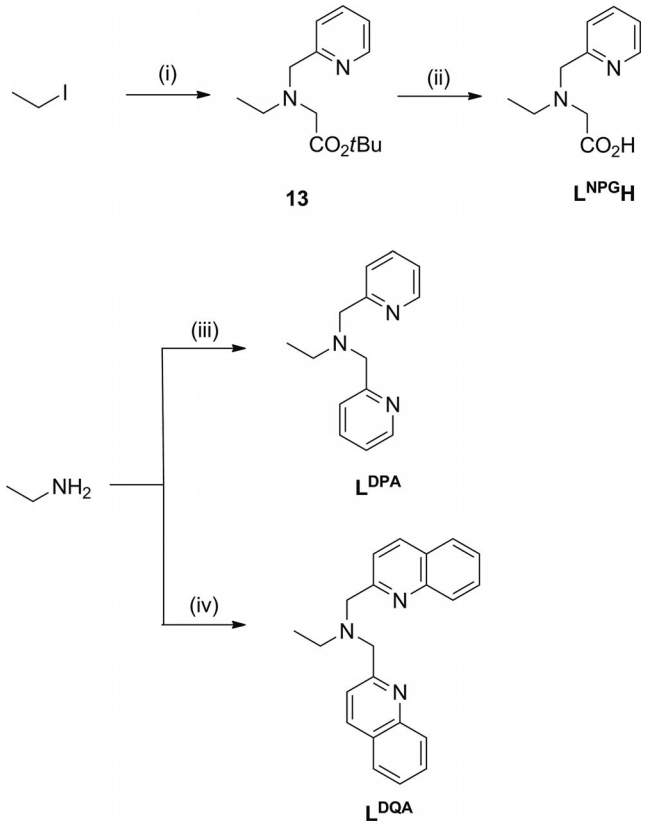

Scheme 5. *Reagents and conditions:* (i) *N*-(2-pyridylmethyl)glycine *tert*-butyl ester, DMF; (ii) trifluroacetic acid (TFA); (iii) 2-(chloromethyl)pyridine, acetonitrile; (iv) 2-(chloromethyl)quinoline, acetonitrile.

Figure 1, the py3 signal, which exhibits a clear doublet in the spectrum of the free ligand, displays further splitting in the spectrum of the complex, this is likely to be due to the long-range effect of the carbohydrate chirality within the more rigid metal chelate. In the NPG complexes, the metal coordinated nitrogen atoms become chiral centers. In this study we did not see any further splitting of the NMR signals, suggesting the exclusive formation of one diastereomer for each of the NPG complexes. But we could not determine the absolute configuration of the complexes. The results from $^{1}H/^{13}C$ NMR, ESI-MS, and elemental analyses supported the proposed structures for all complexes.

Crystal structure elucidation was successfully performed for the *C*-glycoside complex [Re(**L′4**)(CO)$_3$]Cl, and confirmed the above mentioned structure (Figure 2). The Re complex of compound **9** {[Re(**9**)(CO)$_3$]ClO$_4$} with a OH-protected *C*-glucoside group also afforded crystals suitable for X-ray crystallography (Figure 3). These structures exhibit no significant changes from the corresponding *O*-glycoside derivatives, indicating the stable coordination of the tridentate *N*,*O*-ligands that support the rhenium tricarbonyl structure.

The analogous rhenium complexes without the pendant sugar moieties were prepared in a similar way to that employed for the preparation of the **L1**–**6** and **L′1**–**6** complexes detailed above. All complexes were fully characterized by $^{1}H/^{13}C$ NMR, ESI-MS, and elemental analyses, and [Re(**L**^{NPG})(CO)$_3$]Cl and [Re(**L**^{DPA})(CO)$_3$]Cl were also analyzed by X-ray crystallography (Figures S4 and S5, Supporting Information).

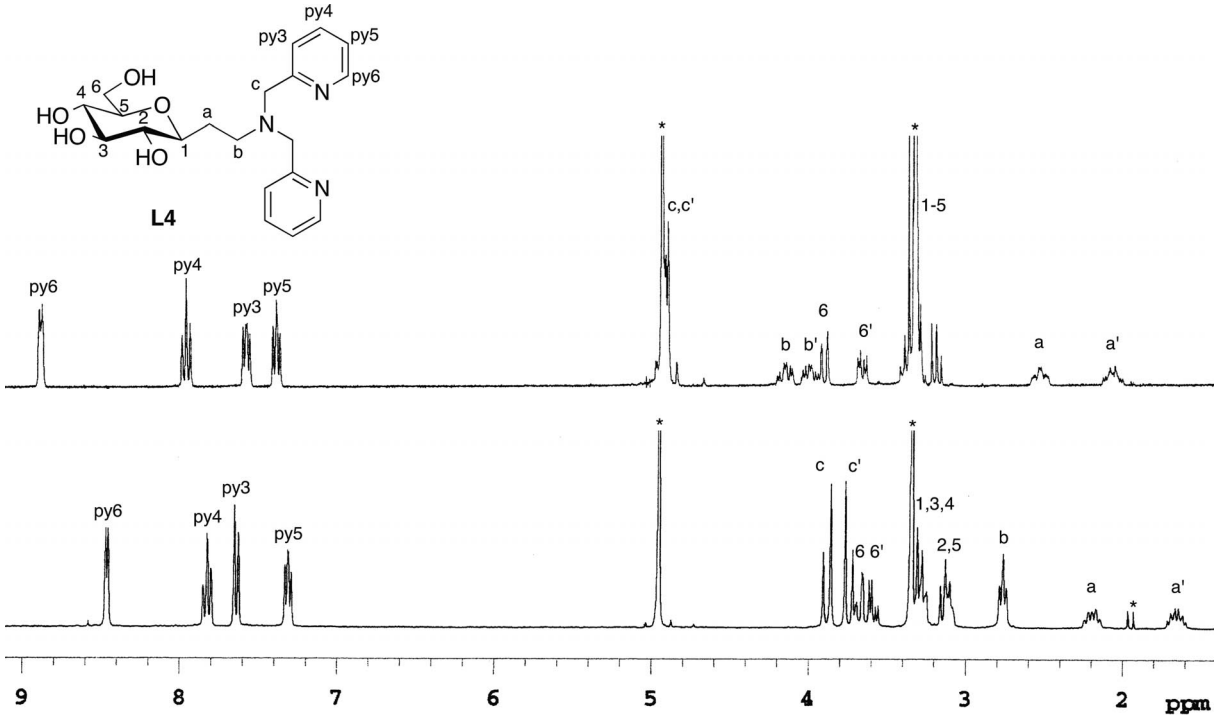

Figure 1. Partial ^{1}H NMR spectra for [Re(**L4**)(CO)$_3$]Cl (top) and **L4** (bottom) in CD_3OD. Asterisks indicate solvent peaks or those associated with small amounts of impurities.

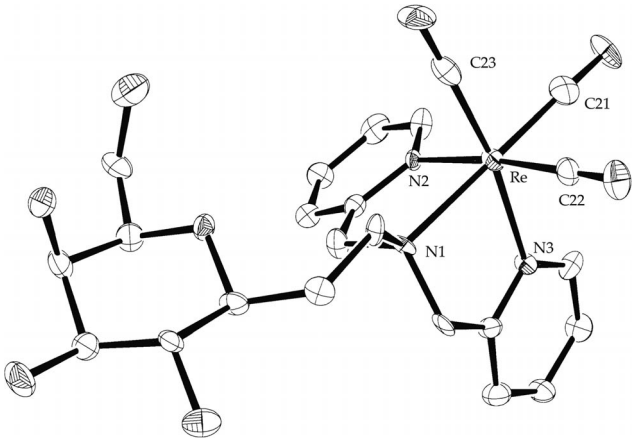

Figure 2. ORTEP diagram of the cationic portion of $[Re(\mathbf{L'4})(CO)_3]$-$Cl{\cdot}0.5CH_3CN{\cdot}0.5C_2H_5OH$ (ellipsoids are drawn at the 50% probability level). The hydrogen atoms, counter anion, and solvent molecules are omitted for clarity.

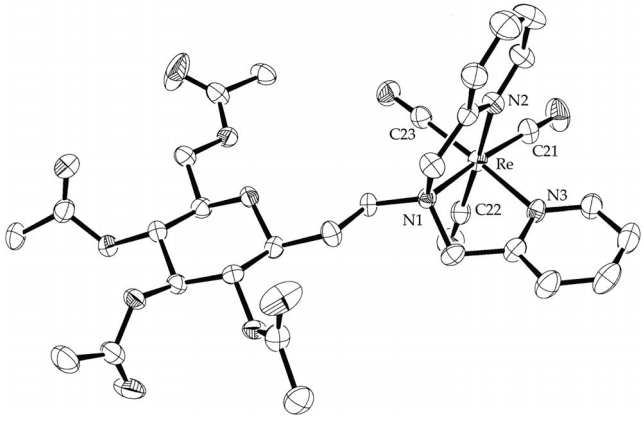

Figure 3. ORTEP diagram of the cationic portion of $[Re(\mathbf{9})(CO)_3]$-$ClO_4{\cdot}H_2O$ (ellipsoids are drawn at the 50% probability level). The hydrogen atoms, counter anion, and solvent molecule are omitted for clarity.

MIP-MS Evaluation of the Uptake of Re Complexes by HeLa S3 Cells

Quantification of rhenium metal uptake into HeLa S3 cells was investigated, allowing for evaluation of the effect of the ligand structure on the uptake process. Fifteen Re complexes with and without pendant carbohydrate moieties were incubated with the cells at 100 μM concentration in growth media for 24 h, and the incorporated metal contents in the cells were quantified by MIP-MS. No detectable cytotoxicity of the complexes was observed under the experimental conditions used. The results of this study are shown in Table 1 and summarized in Figure 4. The cell volume (2.27 pL) was calculated from the mean radius (16.3 μm) of the cells measured by microscopic analysis, and with the assumption that the cells are spherical in shape.

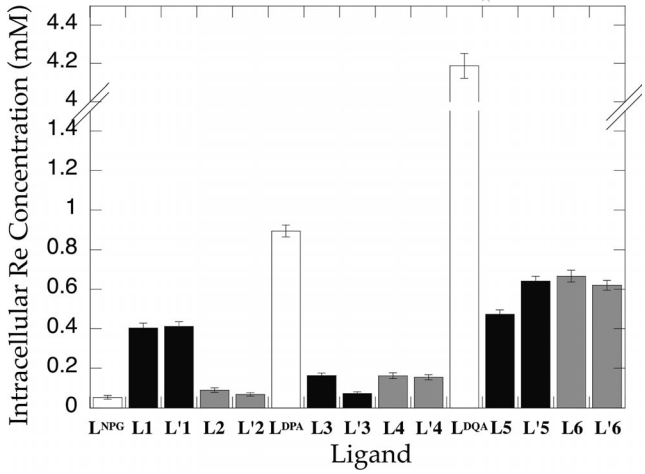

Figure 4. Cellular rhenium concentration (mM) after incubation for 24 h of HeLa S3 cells with the Re^{I} tricarbonyl complexes (100 μM) containing sugar-pendant ligands. Open bars, filled bars, and gray bars represent nonsugar, *O*-glycoside, and *C*-glycoside ligands, respectively.

The rhenium complexes without pendant carbohydrate functions exhibit considerable differences in the amount of cellular uptake when compared to their carbohydrate-appended analogues. The Re complexes of $\mathbf{L^{DPA}}$ and $\mathbf{L^{DQA}}$ exhibit higher uptake values (Figure 4) in comparison to the carbohydrate-attached complexes, probably because of their increased hydrophobicity. It is of significant interest that in the NPG derivatives, for which all complexes have good water solubility, the pendant *O*-glycoside in **L1/L′1** enhances Re incorporation into the cells by a factor of 5–8 compared with the *C*-glycoside and nonsugar analogues. This *O*-glycoside preference was not observed in the DPA and DQA series. Finally, in all cases no significant difference between the glucose and galactose derivatives was observed.

Considering the total charge of the complex, the cell membrane permeability trend would be expected to be as follows: NPG complexes (neutral chelate) > DPA and DQA complexes (cationic metal chelates). However, the present results show that the overall trend in Re complex uptake is DQA > DPA > NPG and there is little difference in the uptake of the the *C*- and *O*-glycosides. Because the DQA complexes exhibit poor water solubility, the high water solubility of the NPG complexes is of significant importance. Interestingly, the NPG *O*-glycoside derivatives (**L1/L′1**) exhibit enhanced uptake in comparison to both the *C*-glycoside analogues (**L2/L′2**) and the carbohydrate-free derivative. The effect of *O*-glycosylation of the ligands in the NPG series causes a deviation from the overall trend observed for metal complex uptake, and provides a potential starting point for further structural modifications aimed at enhancing the cellular uptake of rhenium(I) tricarbonyl complexes. Increased glucose concentration in media did not block the uptake of the **L1** and **L′1** complexes (data not shown), suggesting that the uptake mechanism is different from that for glucose transport.

Table 1. Details of the uptake of Re^{I} tricarbonyl complexes by HeLa S3 Cells.[a]

Ligand	Re [ng L^{-1}], individual	Re [ng L^{-1}], average	Re uptake (nmol/10^5 cells)	Cellular concentration of Re (mM)[b]
$\mathbf{L^{NPG}}$	234.5 ± 37.0 217.0 ± 30.5 233.0 ± 42.0	228.0 ± 36.5	(1.22 ± 0.20) × 10^{-2}	0.054 ± 0.009
L1	1654.0 ± 108.5 1797.5 ± 103.0 1663.0 ± 98.5	1705.0 ± 103.0	(9.16 ± 0.55) × 10^{-2}	0.404 ± 0.024
L′1	1648.0 ± 80.5 1771.0 ± 87.5 1804.0 ± 127.0	1741.0 ± 98.0	(9.35 ± 0.53) × 10^{-2}	0.412 ± 0.023
L2	435.5 ± 50.0 352.0 ± 46.0 338.5 ± 47.5	375.5 ± 48.0	(2.02 ± 0.26) × 10^{-2}	0.089 ± 0.011
L′2	296.0 ± 34.5 298.5 ± 34.5 271.0 ± 33.0	288.5 ± 34.0	(1.55 ± 0.18) × 10^{-2}	0.068 ± 0.008
$\mathbf{L^{DPA}}$	3959.5 ± 131.5 3612.0 ± 117.5 3747.5 ± 122.5	3773.0 ± 124.0	(20.26 ± 0.67) × 10^{-2}	0.893 ± 0.030
L3	702.0 ± 49.5 653.5 ± 53.5 707.5 ± 61.0	687.5 ± 55.0	(3.69 ± 0.30) × 10^{-2}	0.163 ± 0.013
L′3	294.0 ± 36.0 319.0 ± 24.5 303.0 ± 38.5	305.0 ± 33.0	(1.64 ± 0.18) × 10^{-2}	0.072 ± 0.008
L4	616.9 ± 59.0 691.5 ± 61.0 745.5 ± 63.5	684.5 ± 61.0	(3.68 ± 0.33) × 10^{-2}	0.162 ± 0.015
L′4	670.5 ± 65.0 621.0 ± 55.0 673.0 ± 48.5	655.0 ± 56.0	(3.52 ± 0.30) × 10^{-2}	0.155 ± 0.013
$\mathbf{L^{DQA}}$	21303.0 ± 414.0 17067.0 ± 110.0 14723.0 ± 303.5	17698.0 ± 276.0	(95.04 ± 1.48) × 10^{-2}	4.187 ± 0.065
L5	1991.5 ± 87.5 2080.5 ± 93.0 2010.0 ± 115.0	2000.5 ± 98.5	(10.74 ± 0.53) × 10^{-2}	0.473 ± 0.023
L′5	3174.5 ± 108.0 2373.5 ± 105.0 2581.0 ± 100.5	2709.5 ± 104.5	(14.55 ± 0.56) × 10^{-2}	0.641 ± 0.025
L6	2702.0 ± 135.5 2863.5 ± 110.5 2880.0 ± 137.5	2815.0 ± 128.0	(15.12 ± 0.69) × 10^{-2}	0.666 ± 0.030
L′6	2688.5 ± 83.5 2574.5 ± 117.5 2605.0 ± 115.0	2622.5 ± 105.0	(14.08 ± 0.56) × 10^{-2}	0.620 ± 0.025

[a] Recorded after 24 h incubation. [b] The average volume of the cells was estimated to be 2.27 pL (see text).

Evaluation by Fluorescent Microscopy of the Uptake of Re Complexes by PC-12 Cells

The distribution of a representative Re complex inside PC-12 cells was investigated by a fluorescent microscopy measurement[14] performed with a methoxy substituted DQA *O*-galactoside complex, [Re(**L′7**)$(CO)_3$]Cl (Scheme 6), for which superior cell uptake and fluorescence detection was expected. Introduction of the methoxy group on to the quinoline ring enhances the fluorescent intensity and shifts the excitation/emission wavelengths of the ligand relative to the signals for the corresponding ligand devoid of such a group.[15] Considering the "*O*-glycoside effect" observed for the **L1**/**L′1** complexes, the *O*-glycoside linker was chosen for use in this study.

Upon excitation at 330 nm, [Re(**L′7**)$(CO)_3$]Cl exhibited a moderately intense fluorescence signal at around 420 nm (Figure S6), which can be viewed by a fluorescent microscope (excitation 330–385 nm, detection > 420 nm). The fluorescent microscopic analysis was performed with PC-12 rat adrenal pheochromocytoma. Increased fluorescence from the cells was observed after incubation with [Re(**L′7**)$(CO)_3$]Cl (50 μM) for 4 h (Figure 5, b). From this picture we can conclude that the complex penetrates into the cell because the fluorescence was observed from whole cell and not localized in the cell membrane. The fluorescent nuclear stain DAPI (4′,6-diamino-2-phenylindole dihydrochloride) was added during the microscopic analysis and selectively accumulates in the cell nucleus (Figure 5, c). Interestingly, overlaying of parts b and s of Figure 5 demon-

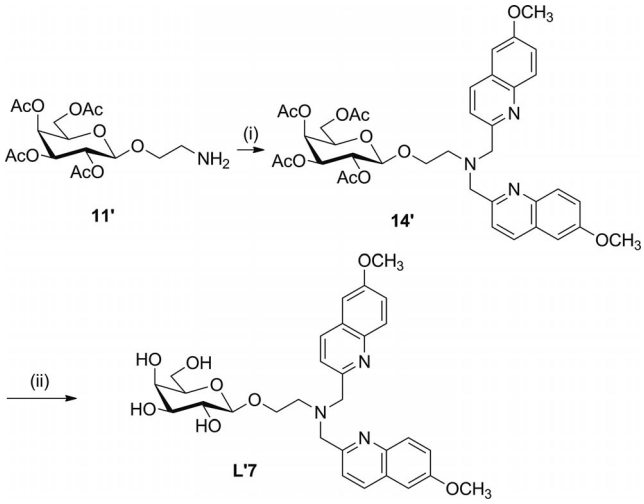

Scheme 6. *Reagents and conditions:* (i) 2-(chloromethyl)-6-methoxyquinoline, DMF; (ii) NaOMe, MeOH.

strates that [Re(**L′7**)(CO)$_3$]Cl is localized in the cytosol and does not penetrate into the nucleus (Figure 5, d). This study clearly demonstrates the cell permeability of [Re(**L′7**)(CO)$_3$]Cl and also the localization of the complex in PC-12 cells.

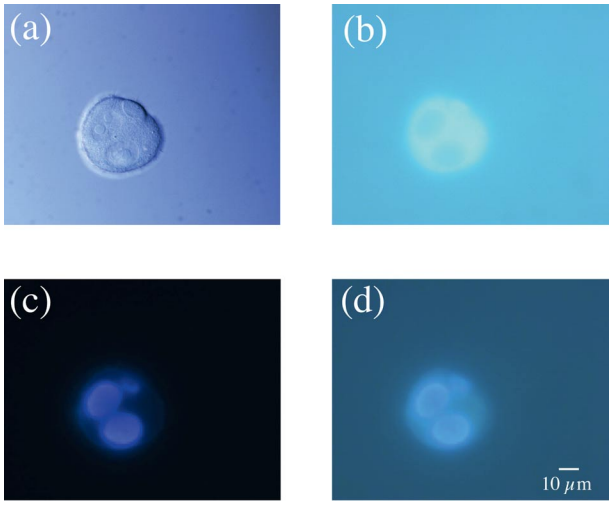

Figure 5. Differential interference contrast and fluorescent micrographs of cultured PC-12 rat adrenal cells incubated in the presence of [Re(**L′7**)(CO)$_3$]Cl (50 μM) for 4 h: (a) differential interference contrast; (b) fluorescent micrograph; (c) fluorescent micrograph in the presence of DAPI; (d) image formed from the merging of images (b) and (c).

Conclusions

Glucose- and galactose-pendant ligands containing DPA, DQA, and NPG as metal binding sites have been prepared. The structures of rhenium(I) tricarbonyl complexes with these ligands were characterized and their uptake into HeLa S3 cells studied. MIP-MS measurements reveal that the DQA complexes show the highest uptake of all the complexes in the series. Microscopic analysis with the fluorescent quinoline derivative [Re(**L′7**)(CO)$_3$]Cl reveals that the complex stays in the cytosol and does not penetrate into the nucleus. The water soluble NPG complexes exhibited carbohydrate enhanced cell uptake; however, no carbohydrate dependent uptake was observed in this study. The NPG complexes with pendant *O*-glycoside groups, **L1** and **L′1**, displayed increased uptake in comparison to both the *C*-glycoside analogues (**L2**/**L′2**) and the carbohydrate-free derivative. This result provides a potential starting point for further structural modifications aimed at enhancing the cellular uptake of rhenium(I) tricarbonyl complexes. We are currently investigating the cellular uptake of the Re complexes in a variety of cell lines to determine the generality of this approach. Biodistribution studies employing radioactive ^{99m}Tc complexes are also currently underway.

Experimental Section

General: All reagents and solvents for the syntheses were obtained from commercial sources and used as received. ^{1}H NMR (300.07 MHz) and ^{13}C NMR (75.00 MHz) spectra were recorded on a Varian GEMINI 2000 spectrometer and referenced to internal tetramethylsilane (TMS) or solvent signals. Elemental analyses were recorded on a J-Science JM-10 Micro Corder. The synthetic and characterization details for all new compounds are described in the Supporting Information.

X-ray Crystallography: Single crystals of **6**, **6′**, **L^{DQA}**, [Re(**L′4**)(CO)$_3$]Cl, [Re(**9**)(CO)$_3$]ClO$_4$, [Re(**L^{NPG}**)(CO)$_3$]Cl, and [Re(**L^{DPA}**)(CO)$_3$]Cl were covered by Paraton-N oil and mounted on glass fibers. All data were collected at 123 or 223 K on a Rigaku Mercury charge coupled device (CCD) detector, with monochromatic Mo-K_α radiation generated from an X-ray tube operating at 50 kV/40 mA. Data were processed on a PC with the CrystalClear Software (Rigaku). Structures were solved by direct methods (SIR-92)

Table 2. Crystallographic data for [Re(**L′4**)(CO)$_3$]Cl·0.5CH$_3$CN·0.5C$_2$H$_5$OH and [Re(**9**)(CO)$_3$]ClO$_4$·H$_2$O.

	[Re(**L′4**)(CO)$_3$]Cl·0.5CH$_3$CN·0.5C$_2$H$_5$OH	[Re(**9**)(CO)$_3$]ClO$_4$·H$_2$O
Formula	$C_{25}H_{31.5}ClN_{3.5}O_{8.5}Re$	$C_{31}H_{37}ClN_3O_{17}Re$
FW	738.70	945.30
Crystal system	monoclinic	monoclinic
Space group	*C*2	$P2_1$
a [Å]	36.4467(14)	14.271(2)
b [Å]	9.2658(4)	7.3184(9)
c [Å]	16.1508(7)	19.286(3)
β [deg]	95.546(2)	111.1690(12)
V [Å^3]	5428.7(12)	1878.4(4)
Z	8	2
$D_{calcd.}$ [g cm^{-3}]	1.807	1.671
μ [cm^{-1}]	46.335	33.838
$2\theta_{max}$ [deg]	55.0	55.0
Temperature [K]	123	223
Reflections collected	21484	14746
Reflections used	11713	8649
R_{int}	0.0322	0.0224
Parameters	712	506
Final *R*1[a] [$I > 2\theta(I)$]	0.0399	0.0307
*wR*2[a] (all data)	0.0806	0.0659
GOF	1.067	1.047

[a] $R1 = (\Sigma||F_o| - |F_c||)/(\Sigma|F_o|)$. $wR2 = \{[\Sigma w(F_o^2 - F_c^2)^2]/[\Sigma w(F_o^2)^2]\}^{1/2}$.

and refined by full-matrix least-squares methods on F^2 (SHELXL-97). Crystal data for carbohydrate-pendant rhenium(I) tricarbonyl complexes [Re(**L′4**)(CO)$_3$]Cl and [Re(**9**)(CO)$_3$]ClO$_4$ are summarized in Table 2. Crystallographic data for **6**, **6′**, $\mathbf{L^{DQA}}$, [Re($\mathbf{L^{NPG}}$)(CO)$_3$]Cl, and [Re($\mathbf{L^{DPA}}$)(CO)$_3$]Cl are provided in Tables S1 and S2 of the Supporting Information, and their ORTEP drawings are given in Figures S1–5.

CCDC-825160 {for [Re(**9**)(CO)$_3$]ClO$_4$}, -825161 {for [Re(**L′4**)(CO)$_3$]Cl}, -825162 {for [Re($\mathbf{L^{NPG}}$)(CO)$_3$]Cl}, -825163 {for [Re($\mathbf{L^{DPA}}$)(CO)$_3$]Cl}, -825164 (for **6**), -825165 (for **6′**), -825166 (for $\mathbf{L^{DQA}}$) contain the supplementary crystallographic data for this paper. These data can be obtained free of charge from The Cambridge Crystallographic Data Centre via www.ccdc.cam.ac.uk/data_request/cif.request/cif.

Cellular Uptake Analyses with HeLa S3 Cells: HeLa S3 cells (100,000 cells/well) were cultured in Minimum Essential Medium (MEM) supplemented with 10% fetal bovine serum (FBS), penicillin (100 U/mL) and streptomycin (0.1 mg/mL). All cells were maintained in a humidified incubator at 37 °C under 5% CO_2. The media was changed to one containing the Re complexes (100 μM) and the cells incubated for 24 h. The well was treated with trypsin for 10 min at 37 °C, and then the cells were collected by centrifuge (1,200 rpm, 5 min) and washed with Phosphate Buffered Saline (PBS) (1 mL, 3 times). The collected cells were added to mili-Q water (50 μL) and concentrated HNO_3 (100 μL). After being heated at 95 °C for 2 h, the solution was diluted to 10 mL with water, and the rhenium content was analyzed with a Hitachi MIP-MS P-6000 Microwave Induced Plasma Mass Spectrometer (NAIST). The average values of three independent experiments with standard deviations are given in Table 1.

Fluorescent Microscopic Analysis with PC-12 Cells: PC-12 rat adrenal pheochromocytoma cells were cultured in Roswell Park Memorial Institute (RPMI) 1640 supplemented with 5% fetal bovine serum (FBS), 10% horse serum (HS) and 1% penicillin-streptomycin (PS). All cells were maintained in a humidified incubator at 37 °C under 5% CO_2. The media was changed to one containing [Re(**L′7**)(CO)$_3$]Cl (50 μM) and the cells incubated for 4 h. The cells were rinsed with FBS, soaked in the growth media, and then analyzed with a fluorescent microscope (excitation filter: OLYMPUS BP330–385, detection filter: BA420). DAPI was added to the cells during the microscopic analysis to enable identification of the nucleus.

Supporting Information (see footnote on the first page of this article): Experimental procedures for the synthesis of the compounds, Tables S1 and S2 containing crystal data for **6**, **6′**, $\mathbf{L^{DQA}}$, [Re($\mathbf{L^{NPG}}$)(CO)$_3$]Cl, and [Re($\mathbf{L^{DPA}}$)(CO)$_3$]Cl, and Figures S1–S98.

Acknowledgments

This work was supported by the Nara Women's University Intramural Grant for Project Research, Grant-in Aid for Scientific Research from the Ministry of Education, Culture, Sports, Science and Technology (MEXT), Japan, and the Research for Promoting Technological Seeds and the A-STEP FS Stage, JST.

[1] a) K. J. Jensen, J. Brask, *Biopolymers (Peptide Sci.)* **2005**, *80*, 747–761; b) J. J. Reina, J. Rojo, *Tetrahedron Lett.* **2006**, *47*, 2475–2478; c) M. Diéguez, O. Pamies, C. Claver, *Chem. Rev.* **2004**, *104*, 3189–3216; d) S. Yano, Y. Mikata, *Bull. Chem. Soc. Jpn.* **2002**, *75*, 2097–2113; e) M. Diéguez, O. Pamies, A. Ruiz, Y. Diaz, S. Castillon, C. Claver, *Coord. Chem. Rev.* **2004**, *248*, 2165–2192; f) M. Diéguez, C. Claver, O. Pamies, *Eur. J. Org. Chem.* **2007**, 4621–4634.

[2] a) M. Gottschaldt, U. Schubert, *Chem. Eur. J.* **2009**, *15*, 1548–1557; b) V. Ladmiral, E. Melia, D. M. Haddleton, *Eur. Polym. J.* **2004**, *40*, 431–449; c) Y. Mikata, Y. Onchi, K. Tabata, S. Ogura, I. Okura, H. Ono, S. Yano, *Tetrahedron Lett.* **1998**, *39*, 4505–4508; d) Y. Mikata, Y. Shinohara, K. Yoneda, Y. Nakamura, K. Esaki, M. Tanahashi, I. Brudziñska, S. Hirohara, M. Yokoyama, K. Mogami, T. Tanase, T. Kitayama, K. Takashiba, K. Nabeshima, R. Takagi, M. Takatani, T. Okamoto, I. Kinoshita, M. Doe, A. Hamazawa, M. Morita, F. Nishida, T. Sakakibara, C. Orvig, S. Yano, *J. Org. Chem.* **2001**, *66*, 3783–3789; e) T. Storr, Y. Sugai, C. A. Barta, Y. Mikata, M. J. Adam, S. Yano, C. Orvig, *Inorg. Chem.* **2005**, *44*, 2698–2705.

[3] R. Alberto, R. Schibli, R. Waibel, U. Abram, A. P. Schubiger, *Coord. Chem. Rev.* **1999**, *190–192*, 901–919.

[4] a) M. L. Bowen, C. Orvig, *Chem. Commun.* **2008**, 5077–5091; b) M. Gottschaldt, D. Koth, D. Müller, I. Klette, S. Rau, H. Görls, B. Schäfer, R. P. Baum, S. Yano, *Chem. Eur. J.* **2007**, *13*, 10273–10280; c) M. Gottschaldt, C. Bohlender, D. Müller, I. Klette, R. P. Baum, S. Yano, U. S. Schubert, *Dalton Trans.* **2009**, 5148–5154; d) D. J. Yang, C.-G. Kim, N. R. Schechter, A. Azhdarinia, D.-F. Yu, C.-S. Oh, J. L. Bryant, J.-J. Won, E. E. Kim, D. A. Podoloff, *Radiology* **2003**, *226*, 465–473; e) T. Storr, M. Obata, C. L. Fisher, S. R. Bayly, D. E. Green, I. Brudziñska, Y. Mikata, B. O. Patrick, M. J. Adam, S. Yano, C. Orvig, *Chem. Eur. J.* **2005**, *11*, 195–203; f) T. Storr, C. L. Fisher, Y. Mikata, S. Yano, M. J. Adam, C. Orvig, *Dalton Trans.* **2005**, 654–655; g) C. L. Ferreira, F. L. N. Marques, M. R. Y. Okamoto, A. H. Otake, Y. Sugai, Y. Mikata, T. Storr, M. L. Bowen, S. Yano, M. J. Adam, R. Chammas, C. Orvig, *Appl. Radiat. Isot.* **2010**, *68*, 1087–1093; h) M. L. Bowen, N. C. Lim, C. B. Ewart, R. Misri, C. L. Ferreira, U. Häfeli, M. J. Adam, C. Orvig, *Dalton Trans.* **2009**, 9216–9227; i) C. L. Ferreira, C. B. Ewart, S. R. Bayly, B. O. Patrick, J. Steele, M. J. Adam, C. Orvig, *Inorg. Chem.* **2006**, *45*, 6979–6987; j) M. L. Bowen, Z.-F. Chen, A. M. Roos, R. Misri, U. Häfeli, M. J. Adam, C. Orvig, *Dalton Trans.* **2009**, 9228–9236; k) E. Benoist, Y. Coulais, M. Almant, J. Kovensky, V. Moreau, D. Lesur, M. Artigau, C. Picard, C. Galaup, S. G. Gouin, *Carbohydr. Res.* **2011**, *346*, 26–34.

[5] A. Salas-Burgos, P. Iserovich, F. Zuniga, J. C. Vera, J. Fischbarg, *Biophys. J.* **2004**, *87*, 2990–2999.

[6] R. Schibli, C. Dumas, J. Petrig, L. Spadola, L. Scapozza, E. Garcia-Garayoa, A. P. Schubiger, *Bioconjugate Chem.* **2005**, *16*, 105–112.

[7] Y. Du, R. J. Linhardt, *Tetrahedron* **1998**, *54*, 9913–9959.

[8] Y. Mikata, Y. Sugai, M. Obata, M. Harada, S. Yano, *Inorg. Chem.* **2006**, *45*, 1543–1551.

[9] S. Tzanopoulou, I. C. Pirmettis, G. Patsis, M. Paravatou-Petsotas, E. Livaniou, M. Papadopoulos, M. Pelecanou, *J. Med. Chem.* **2006**, *49*, 5408–5410.

[10] a) J. Petrig, R. Schibli, C. Dumas, R. Alberto, P. A. Schubiger, *Chem. Eur. J.* **2001**, *7*, 1868–1873; b) S. Orlandi, R. Annunziata, M. Benaglia, F. Cozzi, L. Manzoni, *Tetrahedron* **2005**, *61*, 10048–10060.

[11] Y. Mikata, S. Fujii, M. Naemura, K. Takahashi, Y. Noguchi, *Dalton Trans.* **2009**, 10305–10310.

[12] M. L. Sinnott, G. T. Tzotzos, S. E. Marshall, *J. Chem. Soc. Perkin Trans. 2* **1982**, 1665–1670.

[13] S. Pal, M. K. Chan, W. H. Armstrong, *J. Am. Chem. Soc.* **1992**, *114*, 6398–6406.

[14] K. A. Stephenson, S. R. Banerjee, T. Besanger, O. O. Sogbein, M. K. Levadala, N. McFarlane, J. A. Lemon, D. R. Boreham, K. P. Maresca, J. D. Brennan, J. W. Babich, J. Zubieta, J. F. Valliant, *J. Am. Chem. Soc.* **2004**, *126*, 8598–8599.

[15] a) Y. Mikata, M. Wakamatsu, A. Kawamura, N. Yamanaka, S. Yano, A. Odani, K. Morihiro, S. Tamotsu, *Inorg. Chem.* **2006**, *45*, 9262–9268; b) Y. Mikata, A. Yamashita, A. Kawamura, H. Konno, Y. Miyamoto, S. Tamotsu, *Dalton Trans.* **2009**, 3800–3806; c) Y. Mikata, A. Yamashita, K. Kawata, H. Konno, S. Itami, K. Yasuda, S. Tamotsu, *Dalton Trans.* **2011**, *40*, 4059–4066; d) Y. Mikata, A. Yamashita, K. Kawata, H. Konno, S. Itami, K. Yasuda, S. Tamotsu, *Dalton Trans.* **2011**, *40*, 4976–4981.

Received: September 8, 2011
Published Online: December 7, 2011

DOI: 10.1002/ejic.201100874

Hydrophobic, Photoactive Titania–Alumina Nanocrystallites and Coatings by an Aqueous Sol–Gel Process

Venu Sreekala Smitha,[a] Kizhakkekilikoodayil Vijayan Baiju,[b] Petchimuthu Perumal,[a] Swapankumar Ghosh,[a] and Krishna Gopakumar Warrier*[a]

Keywords: Titania / Sol–gel processes / Heterogeneous catalysis / Nanoparticles / Self cleaning

Hydrophobic coatings of titania–alumina nanocrystallites showing enhanced photocatalytic activity under sunlight were synthesized by an aqueous sol–gel route from titanyl sulfate. The influence of the addition of alumina in the range 5–30 mol-% on the phase transition and grain growth of nanocrystalline titania was investigated. A titania–alumina composition containing 5 mol-% Al_2O_3 (TA-5), annealed at 700 °C, showed the highest photocatalytic activity among all investigated compositions. While pure titania in the present study started to transform to rutile at 700 °C, all the titania–alumina compositions retained 100 % anatase phase up to 800 °C. The specific surface area was measured as 73 $m^2 g^{-1}$ for the titania containing 5 mol-% alumina annealed at 700 °C, whereas pure titania had 38 $m^2 g^{-1}$ under identical conditions. By photon correlation spectroscopy, the particle size of pure titania sol was measured as 29 nm, while that of titania sol containing 5 mol-% alumina was 43 nm. Nanocoatings applied over glazed ceramic surfaces indicated its hydrophobic character though the composition did not contain any hydrophobic material, which produces a high water contact angle. The uniformly roughened surface, preferably with nanostructured morphology that lowers the surface energy, is proposed to be the reason for the observed hydrophobicity.

Introduction

Crystalline anatase titanium dioxide is a material with high potential applicability in different fields such as solar cells,[1] self-cleaning coatings,[2] photocatalysts and ceramic membranes for water treatment.[3,4] A highly porous surface structure has great influence on photocatalytic activity, since it offers a larger number of catalytic sites than a dense surface.[5] In order to increase the photocatalytic activity of titania, several approaches for modification in the synthesis of porous nanostructured TiO_2 have been proposed, including doping with metals and nonmetals.[6,7] The synthesis of mixed metal oxides with titania has been another approach.[8] Among the various synthesis methods, the sol–gel method has attracted great attention, because of the simple experimental procedures and easy control of the composition.[9]

Some of the recent research shows that binary or ternary mixed-oxide sol–gel coatings exhibit superior mechanical, thermal, and photocatalytic properties.[10,3] Important issues that need attention during the preparation of such coatings are improving the surface structure and extending the anatase-to-rutile transformation to higher temperatures, in addition to enhancing the catalytic activity. Alumina has been reported to be one of the most promising additives for improving the surface features of titania, in view of its high temperature stability, chemical inertness, and resistance to abrasion.[11–13] An even distribution of the second phase in such nanocomposites is most desirable, and this depends primarily on the synthesis route. Titania–alumina catalytic supports were synthesized through an alkoxide-derived sol–gel method by Linacero et al., who found that the surface area increased up to 20 mol-% added titania and decreased for added amounts above 20 mol-%.[14] In the case of coatings, the photocatalytic reaction rate increases with increasing roughness of the TiO_2 thin film on a glass substrate, since an increase in roughness will increase the surface area available for photocatalytic decomposition of organic pollutants.[15,16] Such photoactive nanotitania coatings can further be made multifunctional by introducing non-wetting features.[17] An increased surface roughness, preferably with a nanostructured morphology that lowers the surface energy, is needed for obtaining a hydrophobic surface.[18] Such surface phenomena are the result of entrapped air in the pockets of a hierarchically textured surface, leading to the formation of a large water–air interface below the water droplet. Superhydrophobic surfaces are obtained by using various hydrophilic nanoparticles like Al_2O_3, SiO_2, and SnO_2 when embedded in a polymer matrix.[19] Recently, superhydrophobic nanostructured Boehmite coatings were prepared by hydrolysis of aluminum nitride powder.[20]

[a] Materials Division, National Institute for Interdisciplinary Science and Technology, CSIR,
Trivandrum, 695019, India
Fax: +91-471-2491712
E-mail: wwarrierkgk@yahoo.co.in
[b] Department of Civil and Environmental Engineering, Northwestern University,
Evanston, IL 60208, USA

Superhydrophobic PET fabric was prepared from Al_2O_3–SiO_2 hybrids very recently.[21] So far, except for light-induced TiO_2 amphiphilic surfaces with reversible superhydrophobicity and superhydrophilicity,[22] no study is available that reports sol–gel titania–alumina composite coatings exhibiting hydrophobic properties.

Composite precursors of TiO_2 and Al_2O_3 that induce multifunctionality are reported in this work. The synthesis of the composite is carried out by an aqueous sol–gel route starting from titanyl sulfate. The mixed precursor is coated over commercially available glazed ceramic substrates and annealed at different temperatures. A completely water-based titania–alumina composite sol coating on glazed ceramic substrate and resultant functional applications are not yet reported. The hydrophobicity of the coated surface was evaluated by measuring the water contact angle. The excellent photocatalytic activity along with the moderate hydrophobicity arising from the increased surface roughness imparts self-cleaning ability to the prepared nanocomposite coating. Even though the composites prepared in the present work are mainly intended for coating on glazed ceramic tiles, other applications like self-cleaning glass, porcelain insulators, or even tableware can be considered as applications with a definite advantage.

Results and Discussion

The powder X-ray diffraction (PXRD) patterns of pure titania and titania–alumina nanocomposites calcined at 600, 700, and 800 °C for one hour each are presented in Figure 1. While pure titania starts to transform to rutile at 700 °C, all the titania–alumina composites retained 100% anatase phase up to 800 °C. However, peak broadening appears to be taking place in titania due to reduction in crystallite size with the addition of increasing amounts of alumina.

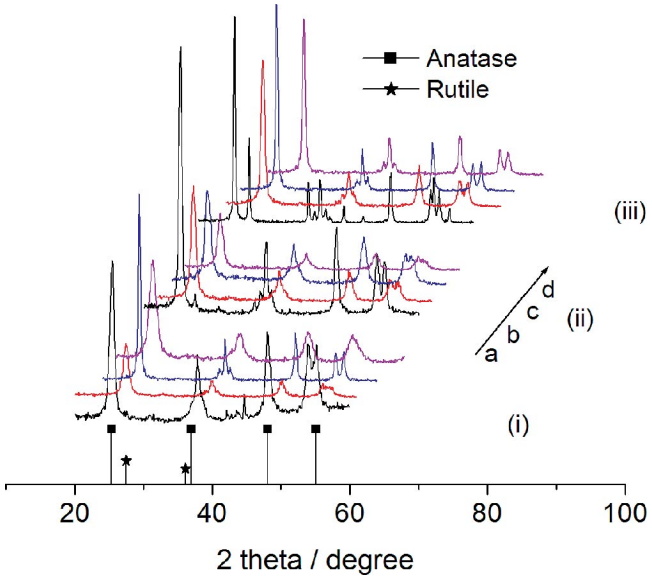

Figure 1. PXRD patterns of (a) pure titania, (b) TA-5, (c) TA-15, and (d) TA-30, calcined at (i) 600, (ii) 700, and (iii) 800 °C.

The average crystallite size measured by using the Scherrer equation was found to decrease from 9.02 nm in pure titania to 6.98 nm in titania containing 30 mol-% alumina (TA-30), which indicates a decreasing trend in crystallite size as a result of the addition of increasing amounts of alumina as presented in Figure 2. This is attributed to the retardation of crystallite growth upon addition of Al_2O_3.[23] The Al^{3+} ions present in alumina may enter the titania lattice and decrease the concentration of oxygen vacancies.[24] Since any decrease in the oxygen vacancy concentration will retard the nucleation rate of anatase titania,[24] the presence of alumina in the titania matrix enhances the phase stability of anatase titania. Furthermore, the reduction in the crystallite size, as shown in Figure 2, is only marginal beyond an addition of 15 mol-% Al_2O_3. The minimum amount of Al_2O_3 required for obtaining an even distribution of the second phase in the titania matrix was calculated to be around 17 mol-%, since the average particle sizes of titania and alumina precursor sols measured by using photon correlation spectroscopy were 29 and 147 nm, respectively. Addition of Al_2O_3 beyond 17 mol-% does not seem to result in size reduction. At higher calcination temperatures (above 700 °C) the crystallite size increased considerably. This grain growth of the titania (matrix) phase can be attributed to the enhanced mass transport prior to the anatase-to-rutile phase transformation.[11]

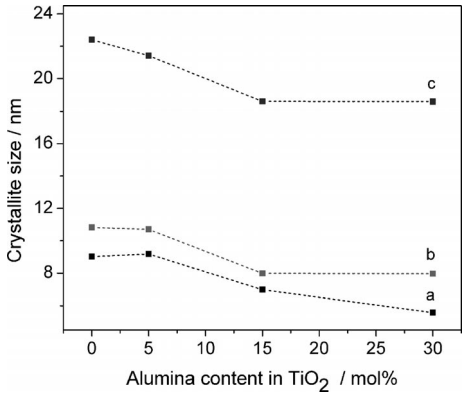

Figure 2. Crystallite size of TiO_2–Al_2O_3 gels as a function of added alumina at calcination temperatures of (a) 600, (b) 700, and (c) 800 °C.

Moreover, samples calcined at 600 °C contain traces of brookite. Since the crystallite size and the presence of the pure anatase phase are important factors affecting photocatalytic activity,[25] nanocomposites calcined at 700 °C were characterized further.

The adsorption/desorption isotherms of titania containing alumina and pure titania calcined at 700 °C are presented in Figure 3. The isotherms showed typical type IV behavior with a hysteresis loop, characteristic of mesoporous materials.[26] Specific surface area (S_{BET}), total pore volume calculated at P/P_0 = 0.9 and average pore radius values are presented in Table 1.

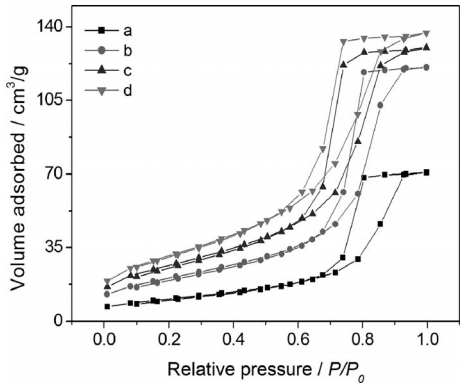

Figure 3. Adsorption/desorption isotherms of (a) pure titania, (b) TA-5, (c) TA-15, and (d) TA-30, calcined at 700 °C.

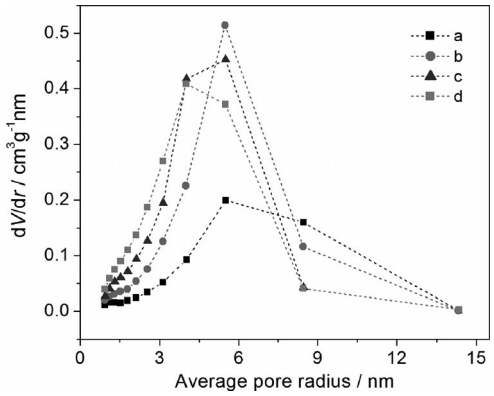

Figure 4. Pore size distribution curves for (a) pure titania, (b) TA-5, (c) TA-15, and (d) TA-30, calcined at 700 °C.

Pure titania calcined at 700 °C has a specific surface area of 38.62 $m^2 g^{-1}$, and TA-30 calcined at the same temperature has a value of 112.38 $m^2 g^{-1}$, which is approximately three times that of pure titania. The higher amount of alumina going to the matrix will increase the defects in the titania matrix, and this further results in an increase in the surface area. The total pore volume is nearly equal to the mesopore volume for all the titania–alumina samples, which indicates that a major contribution to the total surface area is due to the presence of mesopores. Also, the total pore volume and the mesopore volume increased as the alumina content in the titania matrix was increased. This can be explained by the crystallite size reduction achieved by alumina incorporation (as confirmed by the XRD data), which will sustain the mesoporous structure while resulting in a larger surface area.[26] The average pore radius was found to decrease with increasing Al_2O_3 incorporation, in accordance with the previous studies by Padmaja et al.,[27] where the maximum pore size is for high titania content and the pore size decreases with the decrease in the amount of titania at a higher calcination temperature of 1000 °C. The pore size distribution of the samples calcined at 700 °C, obtained by the Barrett–Joyner–Halenda (BJH) method, is shown in Figure 4.

All the samples show a unimodal distribution of pores in the meso range. As alumina content increases, the pore size shifts further to the lower region, which indicates that the alumina added to the titania matrix effectively reduces the pore size.[28,29]

The photocatalytic property of titania is known to depend on several factors like crystallinity, phase assemblage, surface area, and the electronic structure of surface states.[30] The photocatalytic activity of nanocomposites with different alumina content calcined at 700 °C was evaluated by degradation studies of a standard dye such as methylene blue. The degradation of dye solution by the samples upon sunlight irradiation (2 h) is presented in Figure 5.

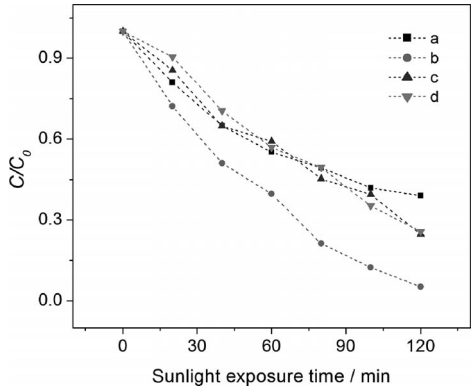

Figure 5. Degradation of methylene blue by (a) titania, (b) TA-5, (c) TA-15, and (d) TA-30, calcined at 700 °C, under exposure to sunlight.

All the samples showed higher photocatalytic activity than that of pure titania, and a higher photocatalytic activity was obtained by adding less (5 mol-%) alumina. This enhancement of photocatalytic activity by adding alumina can be attributed to the presence of nearly 100% anatase, optimum crystallite size, and increased surface area achieved by adding alumina.[31–33] In general, the increase in surface area by particle size reduction is supposed to in-

Table 1. N_2 adsorption characteristics of TiO_2–Al_2O_3 samples calcined at 700 °C.

Sample	Surface area /$m^2 g^{-1}$	Total pore volume /$cm^3 g^{-1}$	Mesopore volume /$cm^3 g^{-1}$	Average pore radius /nm	Crystallite size /nm
Titania	38.62	0.109543	0.109485	5.67	10.82
TA-5	73.94	0.186792	0.186949	5.05	10.70
TA-15	95.08	0.201375	0.200292	4.24	7.99
TA-30	112.38	0.212118	0.212178	3.77	7.96

crease the photocatalytic activity, since the number of active sites on which the electron-acceptor and -donor are adsorbed and participate in the redox reaction will be increased. However, it is reported that photocatalytic efficiency does not increase monotonically with increasing surface area, since surface recombination of charge carriers also plays an important role in photocatalytic reactions in ultrafine particles.[34] In other words, decreasing the nanocrystallite size continuously will never result in continuously higher photocatalytic activity, since a critical size (D^*) exists below which the photocatalytic activity begins to decrease.[33] The existence of a critical size of approximately 10 to 12 nm has been experimentally demonstrated in the literature.[35,36] Baiju et al. proposed that, for optimum photocatalytic activity, the rate of volume and surface charge-carrier recombination processes should be minimum, while that of the interfacial charge-transfer process should be maximum. Below D^*, although the rate of the volume charge-carrier recombination decreases, the rate of the surface charge-carrier recombination increases, which in turn reduces the rate of the interfacial charge-transfer process.[32] Therefore, the photocatalytic activity decreases. This dependence of the photocatalytic activity on the average nanocrystallite size is presented in Figure 6.

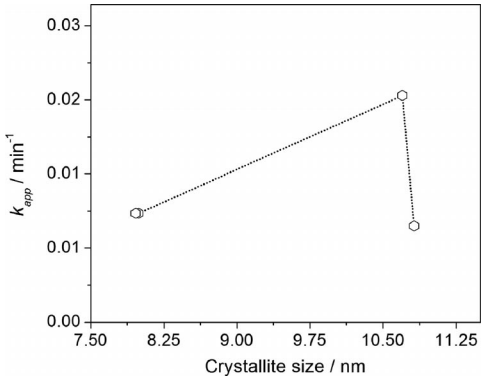

Figure 6. Variation in k_{app} as a function of the average nanocrystallite size of anatase titania for the samples calcined at 700 °C.

The rate constant value obtained for TA-5, calcined at 700 °C, is 0.0214 m^{-1}, whereas the same is only 0.0091 m^{-1} for pure titania treated under identical conditions. Thus, TA-5 synthesized in the present work shows a relatively higher photocatalytic activity because of the critical size, D^*, of anatase titania.

The photocatalytic activity of the same compositions were further investigated under irradiation by a constant indoor source (UV-A; intensity: 0.404 mW cm^{-2}) by using identical concentrations of an aqueous solution of methylene blue: the nanocomposite TA-5 showed the higher activity. The photoactivity results are presented in Figure 7, which shows that better photocatalytic activity is observed for TA-5 under irradiation by the UV-A source also.

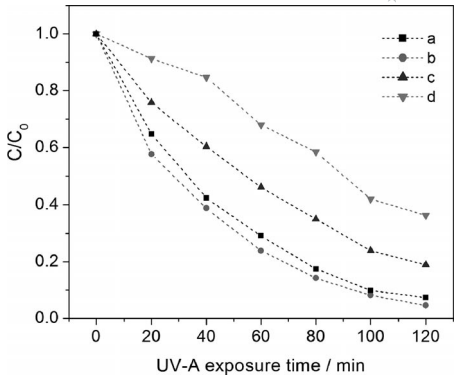

Figure 7. Degradation of methylene blue by (a) titania, (b) TA-5, (c) TA-15, and (d) TA-30, calcined at 700 °C, under exposure to UV-A.

Under exposure to sunlight, the degradation of methylene blue was 60.9 and 94.8% for titania and TA-5, respectively (nearly 34% difference in efficiency), whereas under UV-A light the efficiencies were 92.7 and 95.4 for titania and TA-5, respectively. The increased efficiency for the pure titania under UV light can be attributed to the band gap effect. Addition of alumina (5 mol-%) modified the band gap in such a way that the prepared titania–alumina composite was more active under sunlight than under UV light. The band gap energy calculated by using the diffuse reflectance data were 3.33 and 3.24 eV for pure titania and TA-5, respectively. The band gap energy decreased for the nanocomposite TA-5, and hence the activity was shifted slightly from the UV to the visible region (redshift), and that is the reason for the very good activity under sunlight.

The size of anatase titania particles were calculated from high-resolution transmission electron micrographs. The HR-TEM images of pure titania powder and titania powder containing 5 mol-% alumina, calcined at 700 °C, are shown in Figure 8. Pure titania has an average particle size of approximately 23 nm, whereas the same in TA-5 is approximately 12 nm.

TA-5 calcined at 700 °C shows lattice fringes corresponding to (101) planes of anatase with an interplanar spacing of 0.35 nm. Therefore, it is confirmed from the above observation that addition of alumina inhibits the crystal growth of titania by providing a barrier between titania grains, and a critical size is reached at an amount of 5 mol-% added alumina, leading to the better photocatalytic activity of the sample.[37]

Since surface morphology plays an important role in functional coatings, the coatings were characterized by field emission scanning electron microscopy (FESEM). The FESEM images of glazed ceramics coated with titania and TA-5 calcined at 700 °C are presented in Figure 9, which show that addition of 5 mol-% alumina results in a slight reduction in the particle size. Pure titania coating contains particles of size 24 nm, whereas TA-5 coating has particles of size 20 nm.

Uniformly sized particles having more spherical morphology were observed for the TA-5 sample, which indicates

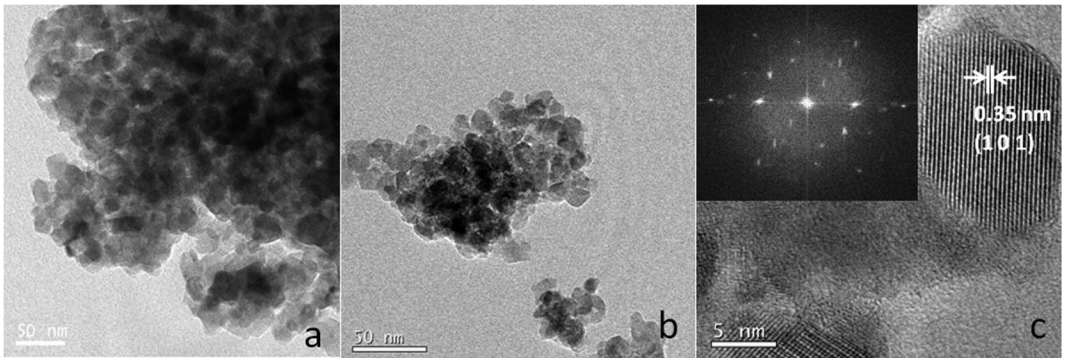

Figure 8. TEM images of (a) pure titania, (b) TA-5, and (c) TA-5 at high resolution, calcined at 700 °C.

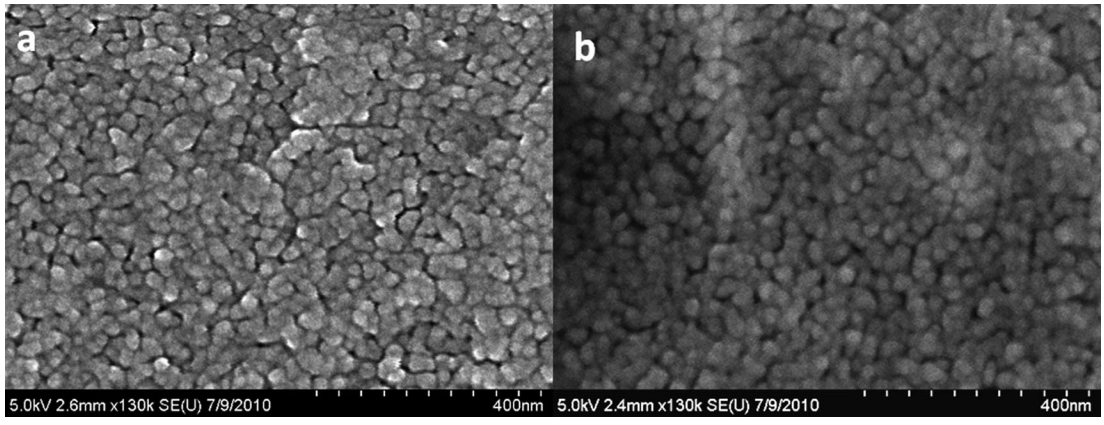

Figure 9. FESEM images of glazed ceramics, coated and annealed at 700 °C, containing (a) pure titania and (b) TA-5.

that the addition of 5 mol-% alumina results in providing a more homogeneous distribution of the second phase in the titania matrix. The wetting properties of the as-prepared coatings were investigated by measuring contact angles (CA) of water on the surfaces by the sessile drop method. The contact angle of an uncoated ceramic was 17.2°, whereas it was 40 and 51.7° after coating with pure titania and pure alumina, respectively. However, the contact angles of tiles coated with TA-5, TA-15, and TA-30, calcined at 700 °C, were 97.6, 98.8, and 101.2°, respectively. The contact angle values are presented in Figure 10.

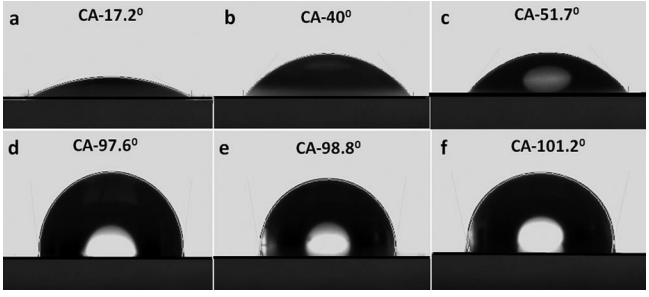

Figure 10. Nature of a water droplet on the surface of tiles coated with (a) nothing, (b) pure titania, (c) pure alumina, (d) TA-5, (e) TA-15, and (f) TA-30, annealed at 700 °C (CA: contact angle).

The hydrophobicity of the coating can be attributed to the increased surface roughness achieved by the addition of alumina, since it is reported that the surface orientations might alter the surface O–H concentrations and surface free energy, thus altering the surface wettability.[13,38] The increased water contact angle for the composite coatings in this work is ascribed to the geometry effect of the surface.[21] The surface roughness analysis of the prepared coatings, carried out by AFM, is provided in Figure 11, which shows that the surface roughness increases with addition of alumina.

It is reported that the uniformly roughened structure of a surface will trap air in its valleys, which allows water droplets to sit on its protuberances and the air, which leads to a hydrophobic surface.[21] The average surface roughness for the pure titania coating was 26.1 nm, whereas that for the titania–alumina coating was 84.9 nm, which rendered the surface hydrophobic, regardless of the absence of high-contact-angle materials. Thus, the current hydrophobic coatings of titania–alumina nanocrystallites showing enhanced photocatalytic activity under sunlight can have possible outdoor applications on a large scale basis.

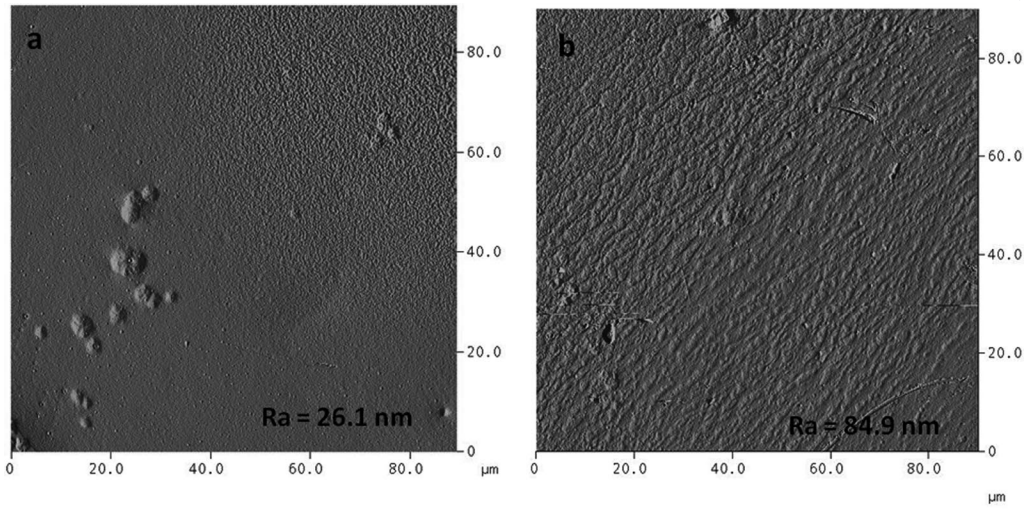

Figure 11. AFM surface image of (a) pure titania and (b) TA-5 coating on a glazed ceramic substrate.

Conclusions

Addition of alumina increases the stability of the anatase phase of nanotitania up to temperatures as high as 800 °C. The crystallite size decreases with the addition of alumina and increases with an increase in the calcination temperature. BET surface area results showed that alumina in the titania matrix effectively reduces the pore size. A higher photocatalytic activity was obtained for the TA-5 nanocomposite, and it was found that the photocatalytic activity depended on the average nanocrystallite size. TEM investigations revealed that pure titania has an average particle size (D_{TEM}) of approximately 23 nm, whereas TA-5 has a D_{TEM} of approximately 12 nm. SEM images showed that adding alumina resulted in particle size reduction and better homogeneity for the prepared coating. The as-prepared homogeneously mixed nanocrystalline TiO_2–Al_2O_3 system had a surface roughness which led to specific hydrophobicity. Thus the present investigation on photoactive and hydrophobic titania–alumina nanocrystallites may result in the development of coatings with multifunctional properties like photoactivity and hydrophobicity.

Experimental Section

The titanium dioxide nanoparticles were prepared by an already reported sol–gel method from titanyl sulfate[39] ($TiOSO_4$, 98% purity), procured from M/s. Travancore Titanium Products, Trivandrum, India. In a typical experiment, titanyl sulfate (15.996 g) was dissolved in distilled water (500 mL) to yield a 0.2 M solution, which was hydrolyzed with constant stirring at room temperature (32 °C) by slow addition of ammonium hydroxide solution (25%, S. D. FINE-CHEM Ltd., India). At this point, the pH was adjusted to 7.5 and kept constant. The precipitate obtained was separated by filtration, washed with distilled water to free it of sulfate ions (as was confirmed by the $BaCl_2$ test). The washed precipitate was then redispersed in distilled water (500 mL) and was then peptized by the dropwise addition of HNO_3 (2 M, Merck, India) solution, till the pH decreased to 1.8–2 to obtain a stable titania sol. The stable sol was then aged for 24 h at room temperature. Similarly, Al $(NO_3)_3 \cdot 9H_2O$ (50 g, S. D. FINE-CHEM Ltd., India) was dissolved in distilled water (500 mL) and hydrolyzed at 80 °C by the controlled addition of NH_4OH solution (25%). The precipitate obtained at pH 7–8 was filtered, washed repeatedly with distilled water, and then converted into a stable sol by peptization with the addition of HNO_3 solution (10%). The stable sol at pH 3–4 was aged for 24 h at room temperature. Alumina (5, 15, and 30 mol-%) was added to the stable titania sol in the form of prepared Boehmite sol (AlOOH). The prepared compositions of titania and alumina were named TA-5, TA-15, and TA-30 to indicate 5, 15, and 30 mol-% alumina content, respectively. The mixed sol was then coated on commercially available glazed ceramic substrates (by the dip coating method) by using a Dip coater (KSV Dip Coater, KSV Instruments Ltd., Finland).

In a typical dip coating experiment, about 150 mL of the prepared sol was transferred into a beaker, and the glazed ceramic substrate (size 5 cm × 5 cm) was slowly immersed into the beaker at a speed of 20 mm min^{-1}. A residing time of 4 min was then allowed for the substrate, after which it was withdrawn at a speed of 20 mm min^{-1}. The coated ceramic samples were dried at 50 °C and then heated to 600, 700, and 800 °C at a heating rate of 1 °C min^{-1} with 1 h of soaking for further studies. A portion of the prepared nanocomposite sols was subsequently dried, powdered, and calcined at the same temperatures for further characterization.

Powder X-ray diffraction (PXRD) patterns of the calcined gels were obtained by using a Philips X′pert Pro Diffractometer in the 2θ range 20–60° by using Cu-K_α radiation (λ = 1.5406 Å). The crystallite sizes of the calcined gels were calculated by using the Scherrer equation [Equation (1)].

$$D_{XRD} = 0.9\lambda/\beta\cos\theta \quad (1)$$

where D_{XRD} is the average crystal diameter (in nm), 0.9 is the shape factor, λ is the X-ray wavelength (Cu-K_α, 1.5406 Å), β is the full width at half maximum intensity (in radians), and θ is the Bragg angle. The Brunauer–Emmett–Teller (BET) surface area measurements and pore size analysis were carried out by nitrogen adsorption at liquid nitrogen temperature with a Micromeritics Gemini

2375 surface area analyzer after degassing each sample at 200 °C for 2 h. The photocatalytic activity of the nanocomposites was studied by monitoring the degradation of methylene blue (MB, AR Grade, Qualigens Fine Chemicals, India) dye in an aqueous suspension under exposure to solar irradiation with continuous magnetic stirring. Although the intensity of solar radiation could not be measured, in order to make correct comparisons, the experiments were conducted for all the samples at the same time (11:00 AM–1:00 PM) on a sunny day during the month of September in Trivandrum city (8.5°N and 76.9°E), which is about 2800 km south of New Delhi, the capital of India.

The prepared nanocomposite (0.1 g) was dispersed in an aqueous solution of MB (100 mL, 1.25×10^{-5} M). The suspension was stirred in the dark for 1 h before irradiating with sunlight for equilibration. The concentration of the dye was measured at different time intervals by using a UV/Visible spectrometer (Shimadzu, Japan, UV-2401PC). A blank dye solution was also irradiated for about 2 h to confirm that the dye was not photobleached by exposure to sunlight. The dye concentration remained unchanged even after irradiation for 2 h. The maximum intensity absorbance peak at 663.2 nm of the MB solution was taken for measuring the degradation. The absorbance (A_0) measured after stirring in the dark was taken as corresponding to the initial concentration (C_0) of the dye. The absorbance (A) of MB solutions, after irradiation time intervals of 20, 40, 60, 80, 100 and 120 min was taken as a measure of the residual concentration, C, of MB dye. The degradation of MB was calculated by using Equation (2).

$$C/C_0 = A/A_0 \quad (2)$$

The photocatalytic decomposition of the organic molecules follows first-order kinetics,[40] which may be represented by Equation (3).

$$dC/dt = k_{app}C \quad (3)$$

where "dC/dt" represents the rate of change in the concentration of the MB dye with respect to the time of exposure to sunlight "t", "k_{app}" is the apparent first-order reaction rate constant, and "C" is the concentration of the MB dye. On plotting $\ln(C_0/C)$ against times of exposure to sunlight, the slope of the linear fit gives k_{app}.

The reflectance spectra of the samples were recorded with a Shimadzu UV 2401 PC Spectrophotometer (spectral range 200–800 nm) equipped with an integration sphere for recording reflectance spectra. The Kubelka–Munk function, $F(R)$, was considered proportional to the absorption of radiation, and the band gap energy, "E_g", of the semiconductor TiO_2 was evaluated from the diffuse reflectance spectra by plotting $[F(R)hv]^2$ against hv.[24] The extrapolation of the linear region of the $F(R)$ spectrum to the energy axis was used for determining the E_g values. The function $F(R)$ was calculated by using the equation $F(R) = (1 - R)^2/2R$.

The surface morphology of the coated glazed ceramic was observed with a field emission scanning electron microscope (FESEM, Hitachi S-4800-II, Japan). The static contact angle measurements of the coated samples were performed by the sessile drop method with a Data Physics OCA 40 micro automatic contact angle meter. The surface roughness analysis of the optimized titania–alumina composition (TA-5) and the glazed ceramic substrates coated with pure titania were done with an AFM machine (Digital instruments nanoscope).

Acknowledgments

The authors are grateful to the Director of the National Institute for Interdisciplinary Science and Technology (NIIST), Council of Scientific and Industrial Research (CSIR), Trivandrum, for providing the necessary facilities. The authors acknowledge Dr. B. M. Jaffer Ali for the AFM analysis and Mr. M. Kiran for the HRTEM images. One of the authors (V. S. S.) thanks CSIR for the Senior Research Fellowship and the Department of Science and Technology, India.

[1] G. K. Mor, K. Shankar, M. Paulose, O. K. Varghese, C. A. Grimes, *Nano Lett.* **2006**, *6*, 215–218.
[2] N. S. Allen, M. Edge, J. Verran, J. Stratton, J. Maltby, C. Bygott, *Polym. Degrad. Stab.* **2008**, *93*, 1632–1646.
[3] V. S. Smitha, K. A. Manjumol, K. V. Baiju, S. Ghosh, P. Perumal, K. G. K. Warrier, *J. Sol–Gel Sci. Technol.* **2010**, *54*, 203–211.
[4] K. A. Manjumol, V. S. Smitha, P. Shajesh, K. V. Baiju, K. G. K. Warrier, *J. Sol–Gel Sci. Technol.* **2010**, *53*, 353–358.
[5] X. C. Wang, J. C. Yu, C. M. Ho, Y. D. Hou, X. Z. Fu, *Langmuir* **2005**, *21*, 2552–2559.
[6] D. Dvoranova, V. Brezova, M. Mazur, M. A. Malati, *Appl. Catal. B* **2002**, *37*, 91–105.
[7] Y. C. Tang, X. H. Huang, H. Q. Yu, C. Hu, *Prog. Chem.* **2007**, *19*, 225–233.
[8] J. A. Rodriguez, D. Stacchiola, *Phys. Chem. Chem. Phys.* **2010**, *12*, 9557–9565.
[9] D. Y. Chen, E. H. Jordan, *J. Sol–Gel Sci. Technol.* **2009**, *50*, 44–47.
[10] Y. Wang, D. S. Zhang, L. Y. Shi, L. Li, J. P. Zhang, *Mater. Chem. Phys.* **2008**, *110*, 463–470.
[11] P. Nair, F. Mizukami, T. Okubo, J. Nair, K. Keizer, A. J. Burggraaf, *AIChE J.* **1997**, *43*, 2710–2714.
[12] R. Connelly, A. K. Pattanaik, V. K. Sarin, *Int. J. Refract. Met. Hard Mater.* **2005**, *23*, 317–321.
[13] W. Tian, Y. Wang, Y. Yang, *Tribol. Int.* **2010**, *43*, 876–881.
[14] R. Linacero, M. L. Rojas-Cervantes, J. D. D. Lopez-Gonzalez, *J. Mater. Sci.* **2000**, *35*, 3279–3287.
[15] Y. Sakatani, D. Grosso, L. Nicole, C. Boissiere, G. Soler-Illia, C. Sanchez, *J. Mater. Chem.* **2006**, *16*, 77–82.
[16] W. X. Huang, H. Huang, H. Li, Z. H. Zhou, H. Chen, *Mater. Res. Innovations* **2009**, *13*, 459–463.
[17] W. X. Hou, Q. H. Wang, *Langmuir* **2009**, *25*, 6875–6879.
[18] A. Nakajima, K. Hashimoto, T. Watanabe, *Monatsh. Chem.* **2001**, *132*, 31–41.
[19] P. N. Manoudis, I. Karapanagiotis, A. Tsakalof, I. Zuburtikudis, C. Panayiotou, *Langmuir* **2008**, *24*, 11225–11232.
[20] A. Kocjan, A. Dakskobler, T. Kosmac, *Int. J. Appl. Ceram. Technol.* **2010**, *8*, 848–853.
[21] N. P. Damayanti, *J. Sol–Gel Sci. Technol.* **2010**, *56*, 47–52.
[22] Z. W. Niu, D. Li, J. Ma, Z. L. Yang, Z. Z. Yang, *Chem. J. Chin. U.* **2004**, *25*, 2390–2392.
[23] K. N. P. Kumar, *Scripta Metall. Mater.* **1995**, *32*, 873–877.
[24] R. D. Shannon, J. A. Pask, *J. Am. Ceram. Soc.* **1965**, *48*, 391–398.
[25] K. Y. Jung, S. B. Park, *Mater. Lett.* **2004**, *58*, 2897–2900.
[26] J. Y. Kim, S. H. Kang, H. S. Kim, Y. E. Sung, *Langmuir* **2010**, *26*, 2864–2870.
[27] P. Padmaja, K. G. K. Warrier, M. Padmanabhan, W. Wunderlich, *J. Sol–Gel Sci. Technol.* **2009**, *52*, 88–96.
[28] S. Sivakumar, C. P. Sibu, P. Mukundan, P. K. Pillai, K. G. K. Warrier, *Mater. Lett.* **2004**, *58*, 2664–2669.
[29] J. Kim, K. C. Song, S. Foncillas, S. E. Pratsinis, *J. Eur. Ceram. Soc.* **2001**, *21*, 2863–2872.
[30] M. S. Vohra, K. Tanaka, *Environ. Sci. Technol.* **2001**, *35*, 411–415.
[31] K. V. Baiju, P. Periyat, P. K. Pillai, P. Mukundan, K. G. K. Warrier, W. Wunderlich, *Mater. Lett.* **2007**, *61*, 1751–1755.

[32] K. V. Baiju, S. Shukla, K. S. Sandhya, J. James, K. G. K. Warrier, *J. Phys. Chem. C* **2007**, *111*, 7612–7622.
[33] L. Q. Mao, Q. L. Li, H. X. Dang, Z. J. Zhang, *Mater. Res. Bull.* **2005**, *40*, 201–208.
[34] A. Alem, H. Sarpoolaky, M. Keshmiri, *Ceram. Int.* **2009**, *35*, 1837–1843.
[35] Z. B. Zhang, C. C. Wang, R. Zakaria, J. Y. Ying, *J. Phys. Chem. B* **1998**, *102*, 10871–10878.
[36] M. Inagaki, T. Imai, T. Yoshikawa, B. Tryba, *Appl. Catal. B* **2004**, *51*, 247–254.
[37] S. Rajesh Kumar, S. C. Pillai, U. S. Hareesh, P. Mukundan, K. G. K. Warrier, *Mater. Lett.* **2000**, *43*, 286–290.
[38] K. J. Tang, J. H. Yu, Y. Y. Zhao, Y. Liu, X. F. Wang, R. R. Xu, *J. Mater. Chem.* **2006**, *16*, 1741–1745.
[39] S. Sivakumar, P. K. Pillai, P. Mukundan, K. G. K. Warrier, *Mater. Lett.* **2002**, *57*, 330–335.
[40] D. F. Ollis, E. Pelizzetti, N. Serpone, *Environ. Sci. Technol.* **1991**, *25*, 1522–1529.

Received: August 22, 2011
Published Online: December 8, 2011

DOI: 10.1002/ejic.201101022

Metal Complexes Based on Tetrathiafulvalene-Fused π-Extended Schiff Base Ligands – Syntheses, Characterization, and Properties

Jie Qin,[a] Chen-Xi Qian,[a] Nan Zhou,[a] Rong-Mei Zhu,[a] Yi-Zhi Li,[a] Jing-Lin Zuo,*[a] and Xiao-Zeng You[a]

Keywords: Redox chemistry / Materials science / Schiff bases / N ligands / Tetrathiafulvalene

π-Conjugated tetrathiafulvalene (TTF)-based donors with a monoamine moiety, 2-[4,5-bis(methylthio)-1,3-dithiol-2-ylidene]-1,3-benzodithiol-5-amine (**L_a**) and 2-(5,6-dihydro[1,3]dithiolo[4,5-*b*][1,4]dithiin-2-ylidene)-1,3-benzodithiol-5-amine (**L_b**), have been synthesized. Condensation of the TTF amines with different pyridinecarbaldehydes afforded new TTF-fused π-extended Schiff base ligands, L_a-imine-4-pyridyl (**L_1**), L_a-imine-3-pyridyl (**L_2**), and L_b-imine-2-pyridyl (**L_3**). Four metal complexes based on these Schiff base pyridine ligands, $M(hfac)_2(L)_2$ (M = Cu^{II}, L = **L_1**, **4**; M = Mn^{II}, L = **L_1**, **5**; M = Cu^{II}, L = **L_2**, **6**; hfac = hexafluoroacetylacetonate) and $[Re(CO)_4(L_3)][Re_2(CO)_6Cl_3]$ (**7**), have been synthesized and structurally characterized. The ligands in all of the complexes show a near planar structure, and the different coordination modes of the metal ions and relative orientation of the terminal N donors result in a different crystalline organization in the solid state. The absorption spectra and redox behavior of these new compounds have been studied. These paramagnetic complexes are promising building blocks for the construction of multifunctional materials due to their planar structures and inherent redox properties.

Introduction

Tetrathiafulvalene (TTF) and its derivatives have received much attention because of their strongly electron-donating and attractive reversible redox properties. With these advantages, they can be used as building blocks for molecular conductors,[1–2] molecular switches,[3] and solar energy systems.[4] However, the preparation of materials that exhibit synergy between two or more properties (multifunctional materials) is still a challenge. In consequence, much effort has been devoted to associate the TTF core with spin-carrier centers through π-conjugated linkages, which may improve the electron mobility along the molecule as well as enhance the stacking interaction by π-orbital overlap.[5–8] This approach combines the electrochemically active properties of TTF donors with the optical or magnetic properties of transitional metal ions to obtain interesting multifunctional molecular materials. The appropriate linkages or effective bridges are important to link the paramagnetic centers and conduct electrons. A variety of mono- or polydentate organic ligands for metal coordination have been attached to the TTF moiety, and their corresponding electroactive complexes have been reported.[9–14] Among them, pyridine and bipyridine groups have attracted the most attention due to their well-known coordination ability to different metal ions.[15–21]

In order to obtain new electroactive complexes with intriguing structures and interesting properties, we have studied several new π-extended Schiff base pyridine ligands with different coordinated orientations. The TTF-based donors with monoamine moieties, 2-[4,5-bis(methylthio)-1,3-dithiol-2-ylidene]-1,3-benzodithiol-5-amine (**L_a**) and 2-(5,6-dihydro[1,3]dithiolo[4,5-*b*][1,4]dithiin-2-ylidene)-1,3-benzodithiol-5-amine (**L_b**), were chosen for condensation reactions with different pyridylaldehydes. Three TTF–Schiff base ligands, in which the TTF fragment is covalently linked to 4-pyridyl (**L_1**), 3-pyridyl (**L_2**), and 2-pyridyl (**L_3**, Scheme 1), have been synthesized. The coordination abilities of monodentate ligands **L_1** and **L_2** have been demonstrated. Their reactions with Cu^{II} or Mn^{II} in the presence of hexafluoroacetylacetonate ($hfac^-$) afforded three new metal complexes, $M(hfac)_2(L)_2$ (M = Cu^{II}, L = **L_1**, **4**; M = Mn^{II}, L = **L_1**, **5**; M = Cu^{II}, L = **L_2**, **6**). Unlike **L_1** and **L_2**, **L_3** can adopt a chelating coordination mode. Our previous reports show that chelating ligands based on TTF derivatives are good for the formation of Re^I complexes.[22] The reaction between **L_3** and $Re(CO)_5Cl$ afforded the new Re^I complex $[Re(CO)_4(L_3)][Re_2(CO)_6Cl_3]$ (**7**). This paper describes the full characterization of all of the ligands and complexes, and their spectroscopic and electrochemical properties.

[a] State Key Laboratory of Coordination Chemistry, School of Chemistry and Chemical Engineering, Nanjing National Laboratory of Microstructures, Nanjing University, Nanjing 210093, P. R. China
Fax: +86-25-83314502
E-mail: zuojl@nju.edu.cn

Supporting information for this article is available on the WWW under http://dx.doi.org/10.1002/ejic.201101022.

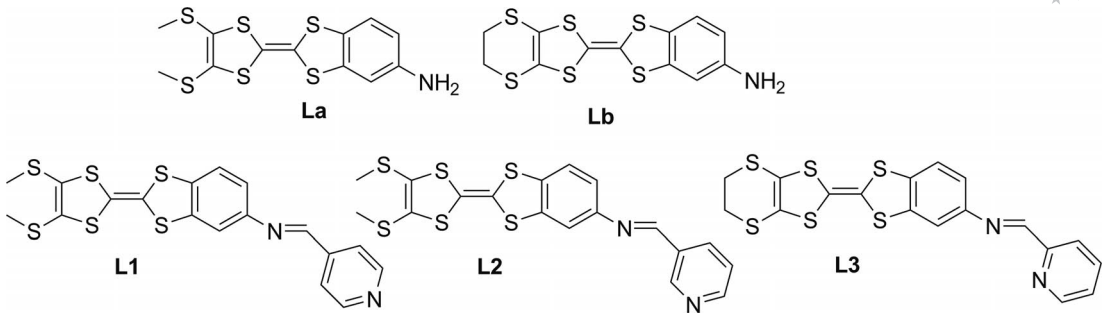

Scheme 1. Structures of $\mathbf{L_a}$–$\mathbf{L_3}$.

Results and Discussion

Synthesis and Characterization

The synthetic pathway is outlined in Scheme 2. The nitro-substituted 1,3-dithiole-2-thione **1** is the key starting material. Although it has been synthesized by a nucleophilic reaction in moderate yield,[23–24] we describe here a facile approach for the synthesis of **1** in high yield starting from 1,2-dibromo-4-nitrobenzene and potassium trithiocarbonate. Compound **2** was synthesized by a literature method.[25] The cross-coupling reactions of **2** with **3a** and **3b** in the presence of triethyl phosphite afforded $\mathbf{L_a}$ and $\mathbf{L_b}$, respectively. The Schiff bases $\mathbf{L_1}$–$\mathbf{L_3}$ were prepared by the direct condensation of $\mathbf{L_a}$ and $\mathbf{L_b}$ with the corresponding pyridinecarbaldehyde in moderate yield. Three mononuclear complexes **4**–**6** were obtained by the coordination of $\mathbf{L_1}$ or $\mathbf{L_2}$ with $M(hfac)_2$ (M = Cu or Mn), whereas the reaction of $Re(CO)_5Cl$ with 1 equiv. of $\mathbf{L_3}$ afforded **7**. All of the new ligands and complexes show good solubility in common polar organic solvents such as CH_2Cl_2, $CHCl_3$, and CH_3CN.

The compounds were characterized by IR, ^{1}H NMR, and UV/Vis spectroscopy and MS. In their IR spectra, $\mathbf{L_a}$ and $\mathbf{L_b}$ display typical NH_2 stretching bands at 3328 and 3362 cm^{-1}, whereas in those of $\mathbf{L_1}$–$\mathbf{L_3}$, the NH_2 stretching band disappeared and a new band at around 1620 cm^{-1}, which results from the C=N stretching vibration, is observed. For **4**–**6**, a sharp absorption band of hfac is clearly visible at around 1645 cm^{-1}, and the coordinated C≡O stretching bands in **7** are found in the 2100–1880 cm^{-1} region.

In their ^{1}H NMR spectra, $\mathbf{L_a}$ and $\mathbf{L_b}$ exhibit resonances at about 3.65 ppm for the NH_2 proton, and $\mathbf{L_1}$–$\mathbf{L_3}$ show singlets at around 8.56 ppm, which are assigned to the imine C*H* proton. Compared with $\mathbf{L_3}$, all of the H signals in the aromatic rings of **7** are shifted by ca. 0.22–0.27 ppm to lower field, which is in agreement with the decrease of electron density around the pyridyl and phenyl units caused by chelation to Re^I.

Crystal Structures

The solid-state structures of $\mathbf{L_a}$, $\mathbf{L_b}$, $\mathbf{L_1}$, $\mathbf{L_2}$, and **4**–**7** were determined by single-crystal X-ray diffraction. The crystallographic and data collection parameters are given in Tables 1 and 2; selected bond lengths and angles are listed in Tables 3, 4, 5, 6, and S1.

Orange crystals of $\mathbf{L_a}$ and $\mathbf{L_b}$, suitable for X-ray structure analysis, were obtained by slow evaporation of solutions of a mixture of dichloromethane and hexane. Both compounds crystallize in monoclinic systems ($P2_1$ and $P2_1/c$, respectively). $\mathbf{L_a}$ has an approximately planar structure except one of the methyl group stretches out of the plane (Fig-

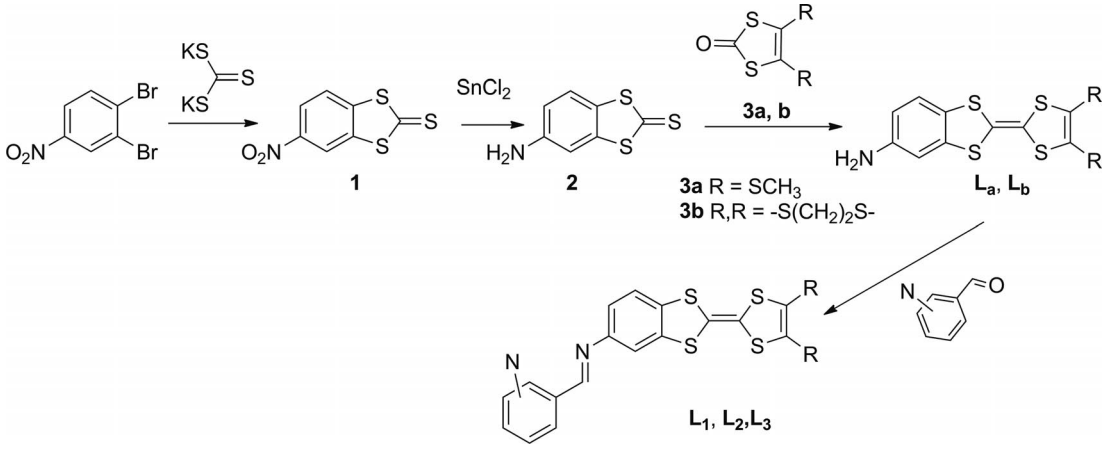

Scheme 2. Synthetic routes to $\mathbf{L_1}$–$\mathbf{L_3}$.

Table 1. Crystallographic data for $\mathbf{L_a}$–$\mathbf{L_2}$.

	$\mathbf{L_a}$	$\mathbf{L_b}$	$\mathbf{L_1}$	$\mathbf{L_2}$
Empirical formula	$C_{12}H_{11}NS_6$	$C_{12}H_9NS_6$	$C_{18}H_{14}N_2S_6$	$C_{18}H_{14}N_2S_6$
M_r	361.58	359.56	450.67	450.67
Crystal system	monoclinic	monoclinic	monoclinic	monoclinic
Space group	$P2_1$	$P2_1/c$	$P2_1/c$	$P2_1/c$
a [Å]	7.8668(13)	6.5417(10)	5.8316(7)	5.0109(8)
b [Å]	5.1367(8)	14.206(2)	10.6633(12)	26.163(4)
c [Å]	18.488(3)	16.4475(19)	31.467(4)	15.370(2)
α [°]	90.00	90.00	90.00	90.00
β [°]	94.667(2)	109.515(5)	90.593(2)	97.556(3)
γ [°]	90.00	90.00	90.00	90.00
V [Å^3]	744.6(2)	1440.7(3)	1956.6(4)	1997.6(5)
Z	2	4	4	4
ρ_c [g cm^{-3}]	1.613	1.658	1.530	1.499
$F(000)$	372	736	928	928
T [K]	291(2)	291(2)	291(2)	291(2)
μ(Mo-K_α) [mm^{-1}]	0.902	0.932	0.705	0.690
Index ranges	$-10 \le h \le 10$, $-6 \le k \le 6$, $-20 \le l \le 23$	$-7 \le h \le 7$, $-13 \le k \le 17$, $-20 \le l \le 17$	$-7 \le h \le 7$, $-12 \le k \le 13$ $-38 \le l \le 21$	$-5 \le h \le 6$, $-32 \le k \le 27$ $-18 \le l \le 18$
GOF (F^2)	1.055	1.069	1.059	1.045
Flack parameters	0.02(15)	–	–	–
R_1[a], wR_2[b] [$I > 2\sigma(I)$]	0.0460, 0.0902	0.0624, 0.1188	0.0451, 0.0891	0.0573, 0.1076

[a] $R_1 = \Sigma||C| - |F_c||/\Sigma F_o|$. [b] $wR_2 = [\Sigma w(F_o^2 - F_c^2)^2/\Sigma w(F_o^2)]^{1/2}$.

Table 2. Crystallographic data for **4**–**7**.

	4	**5**	**6**	**7**
Empirical formula	$C_{46}H_{30}CuF_{12}N_4O_4S_{12}$	$C_{46}H_{30}F_{12}MnN_4O_4S_{12}$	$C_{46}H_{30}CuF_{12}N_4O_4S_{12}$	$C_{28}H_{12}Cl_3N_2O_{10}Re_3S_6$
M_r	1379.00	1370.40	1379.00	1393.71
Crystal system	monoclinic	triclinic	triclinic	orthorhombic
Space group	$P2_1/c$	$P\bar{1}$	$P\bar{1}$	$Pbca$
a [Å]	20.982(13)	9.2030(10)	8.8546(14)	13.8540(11)
b [Å]	8.271(5)	9.8087(10)	9.9736(15)	11.7330(10)
c [Å]	16.794(11)	34.192(4)	16.136(2)	47.050(4)
α [°]	90.00	93.633(2)	78.023(3)	90.00
β [°]	99.442(12)	93.477(2)	78.905(3)	90.00
γ [°]	90.00	114.3620(10)	89.499(3)	90.00
V [Å^3]	2875(3)	2793.2(5)	1367.3(4)	7647.9(11)
Z	2	2	1	8
ρ_c [g cm^{-3}]	1.593	1.629	1.675	2.421
$F(000)$	1390	1382	695	5168
T [K]	291(2)	296(2)	296(2)	296(2)
μ(Mo-K_α) [mm^{-1}]	0.900	0.772	0.946	10.065
Index ranges	$-25 \le h \le 24$, $-10 \le k \le 7$, $-20 \le l \le 20$	$-10 \le h \le 10$, $-11 \le k \le 8$, $-38 \le l \le 40$	$-10 \le h \le 8$, $-12 \le k \le 7$, $-17 \le l \le 19$	$-17 \le h \le 17$, $-14 \le k \le 14$, $-58 \le l \le 57$
GOF (F^2)	1.042	1.087	1.175	1.166
R_1[a], wR_2[b] [$I > 2\sigma(I)$]	0.0514, 0.0903	0.0578, 0.1554	0.0834, 0.2199	0.0457, 0.1122

[a] $R_1 = \Sigma||C| - |F_c||/\Sigma F_o|$. [b] $wR_2 = [\Sigma w(F_o^2 - F_c^2)^2/\Sigma w(F_o^2)]^{1/2}$.

Table 3. Selected bond lengths [Å] and angles [°] for **4**.

Cu(1)–N(2)	2.012(3)	Cu(1)–O(1)	2.098(3)
Cu(1)–O(2)	2.161(2)	C(3)–C(4)	1.347(5)
C(5)–C(6)	1.299(4)	C(7)–C(8)	1.378(5)
C(10)–N(1)	1.450(4)	C(13)–N(1)	1.241(4)
O(1)–Cu(1)–O(2)	85.64(10)	N(2)–Cu(1)–O(1)	90.41(11)
N(2)–Cu(1)–O(1)$^{\#1}$	89.59(11)	N(2)–Cu(1)–O(2)	87.12(11)
N(2)–Cu(1)–O(2)$^{\#1}$	92.88(11)	N(2)–Cu(1)–N(2)$^{\#1}$	180.00(15)
C(10)–N(1)–C(13)	124.0(3)	C(14)–C(13)–N(1)	125.2(3)

Symmetry transformations used to generate equivalent atoms: #1: $-x$, $-y + 2$, $-z + 1$.

Table 4. Selected bond lengths [Å] and angles [°] for **5**.

Mn(1)–N(3)	2.273(3)	Mn(1)–N(4)	2.245(4)
Mn (1)–O(1)	2.151(3)	Mn (1)–O(2)	2.171(3)
Mn (1)–O(3)	2.206(3)	Mn (1)–O(4)	2.152(3)
C(1)–C(2)	1.332(7)	C(3)–C(4)	1.328(8)
C(5)–C(6)	1.382(6)	C(11)–N(2)	1.134(7)
C(17)–C(18)	1.350(6)	C(19)–C(20)	1.339(6)
C(21)–C(22)	1.391(6)	C(27)–N(1)	1.246(6)
O(1)–Mn (1)–O(2)	82.21(11)	O(1)–Mn (1)–O(4)	177.59(12)
O(2)–Mn (1)–O(3)	82.20(12)	O(2)–Mn (1)–O(4)	99.05(12)
O(3)–Mn (1)–O(4)	80.97(11)	N(3)–Mn(1)–O(3)	164.09(13)
N(3)–Mn(1)–N(4)	97.13(13)	N(4)–Mn(1)–O(2)	166.61(13)
C(12)–C(11)–N(2)	124.0(6)	C(28)–C(27)–N(1)	120.9(5)

Table 5. Selected bond lengths [Å] and angles [°] for **6**.

Cu(1)–N(2)	2.046(6)	Cu(1)–O(1)	2.004(5)
Cu(1)–O(2)	2.282(5)	C(3)–C(4)	1.331(10)
C(5)–C(6)	1.330(9)	C(7)–C(8)	1.393(9)
C(13)–C(14)	1.471(10)	C(12)–N(1)	1.426(8)
C(13)–N(1)	1.238(9)		
O(1)–Cu(1)–O(2)	94.03(19)	N(2)–Cu(1)–O(1)	90.0(2)
N(2)–Cu(1)–O(1) #1	90.0(2)	N(2)–Cu(1)–O(2)	91.3(2)
N(2)–Cu(1)–O(2) #1	88.7(2)	N(2)–Cu(1)–N(2)#1	180.000(1)
C(12)–N(1)–C(13)	122.1(7)	C(14)–C(13)–N(1)	121.4(7)

Symmetry transformations used to generate equivalent atoms: #1: $-x, -y + 1, -z$.

Table 6. Selected bond lengths [Å] and angles [°] for **7**.

Re(1)–N(1)	2.164(8)	Re(1)–N(2)	2.191(7)
Re(1)–C(1)	1.933(8)	Re(1)–C(2)	2.006(10)
Re(1)–C(3)	1.917(12)	Re(1)–C(4)	2.038(12)
Re(2)–Cl(1)	2.524(2)	Re(2)–Cl(2)	2.510(3)
Re(2)–Cl(3)	2.509(2)	Re(3)–Cl(1)	2.537(3)
Re(3)–Cl(2)	2.501(2)	Re(3)–Cl(3)	2.508(2)
Re(2)–C(26)	1.894(12)	Re(2)–C(27)	1.891(12)
Re(2)–C(28)	1.888(10)	Re(3)–C(23)	1.881(13)
Re(3)–C(24)	1.892(11)	Re(3)–C(25)	1.898(11)
C(9)–C(10)	1.453(14)	C(14)–C(15)	1.393(13)
C(17)–C(18)	1.352(15)	C(19)–C(20)	1.342(15)
C(10)–N(2)	1.283(12)	C(11)–N(2)	1.444(12)
N(1)–Re(1)–N(2)	74.8(3)	N(1)–Re(1)–C(3)	173.4(4)
N(2)–Re(1)–C(1)	174.2(4)	C(2)–Re(1)–C(4)	178.1(5)
Cl(1)–Re(2)–Cl(3)	78.68(8)	C(27)–Re(2)–C(28)	87.6(4)
Cl(1)–Re(2)–C(28)	170.9(3)	Cl(2)–Re(2)–C(26)	174.9(4)
Cl(3)–Re(2)–C(27)	174.4(3)	Cl(1)–Re(3)–Cl(2)	79.88(8)
C(24)–Re(3)–C(25)	89.6(5)	Cl(1)–Re(3)–C(25)	171.6(3)
Cl(2)–Re(3)–C(24)	174.2(3)	Cl(3)–Re(3)–C(23)	174.9(3)
Re(2)–Cl(1)–Re(3)	83.93(8)	Re(2)–Cl(2)–Re(3)	84.96(8)
Re(2)–Cl(3)–Re(3)	84.84(8)		

ure S1). The average deviation from a least-squares plane through the remaining atoms is 0.0591 Å, whereas for the TTF core alone, it amounts to 0.0441 Å. For $\mathbf{L_b}$ (Figure S2), the average deviation from a least-squares plane through all the atoms is 0.1601 Å, and 0.0898 Å for the TTF core alone, which reflects its almost coplanar conformation.

Figures 1 and 2 show the molecular structure of $\mathbf{L_1}$ and $\mathbf{L_2}$, respectively. For $\mathbf{L_1}$, the TTF skeleton has a nonplanar boat-like conformation, and the average deviation from the least-squares plane is 0.1669 Å. The dihedral angle between the two five-membered rings (containing S1, S2, S3, and S4) is 20.81(1)°. For $\mathbf{L_2}$, the TTF backbone is nearly planar with a dihedral angle of 2.61(1)° between the two five-membered rings (containing S1, S2, S3, and S4), and the average deviation from a least-squares plane is only 0.0190 Å. The pyridyl ring and phenyl group are not coplanar and the dihedral angles between them are 12.83(1) and 35.49(1)° in $\mathbf{L_1}$ and $\mathbf{L_2}$, respectively. Due to crystal packing effects, the methyl substituents in the two ligands are arranged in a distinctly out-of-plane conformation. In $\mathbf{L_1}$, the two methyl groups point in opposite positions, whereas in $\mathbf{L_2}$, they are on the same side.

The asymmetric unit of **4** contains one molecule. As shown in Figure 3, the central Cu^{2+} ion lies on the inversion center and adopts a pseudooctahedral coordination environment, which is defined by four oxygen donors from two hfac anions in the equatorial plane. The Cu1–O1 and Cu1–O2 distances are 2.098(3) and 2.161(2) Å, respectively. The *trans* pyridine nitrogen atoms of $\mathbf{L_1}$ occupy the axial positions with a short Cu1–N2 bond length of 2.012(3) Å. The dihedral angle between the pyridyl plane and the acac plane is 80.77(1)°. The Cu–O and Cu–N bond lengths are comparable to those found in the similar complex, *trans*-$Cu(hfac)_2(TTF–Py)_2$.[26]

The central C=C bond length of the TTF core is 1.299(4) Å, which is within the normal range for a neutral molecule.[26–27] In **4**, $\mathbf{L_1}$ is not planar, and the TTF backbone is more bent than in the free ligand, which is evidenced by the dihedral angle of 33.33(1)° between the two five-membered rings (containing S3, S4, S5, and S6). The dihedral angle between the coordinated pyridyl unit and phenyl group is 12.01(1)°, which indicates that they are not coplanar. The adjacent molecules are stacked in an overlapping arrangement in a palisade fashion (Figure 4). The shortest intermolecular S···S distance is 3.844 Å (S1···S6).

The ORTEP diagram of **5** is depicted in Figure 5. The Mn^{II} ion lies on a two-fold axis and adopts a distorted octa-

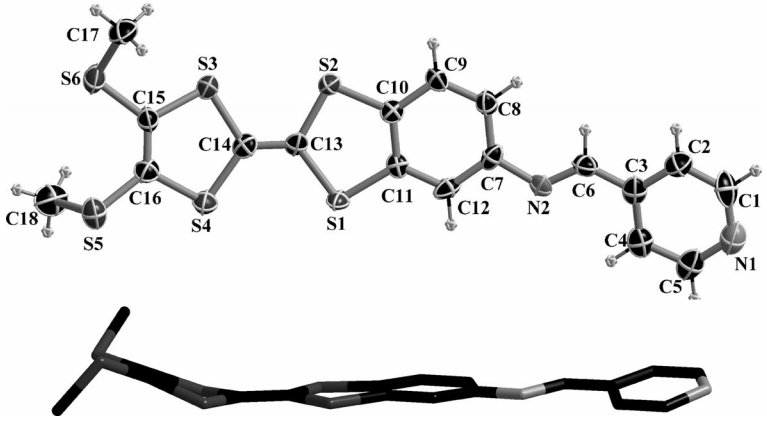

Figure 1. Molecular structure of $\mathbf{L_1}$ (50% probability displacement ellipsoids), front and side views are presented.

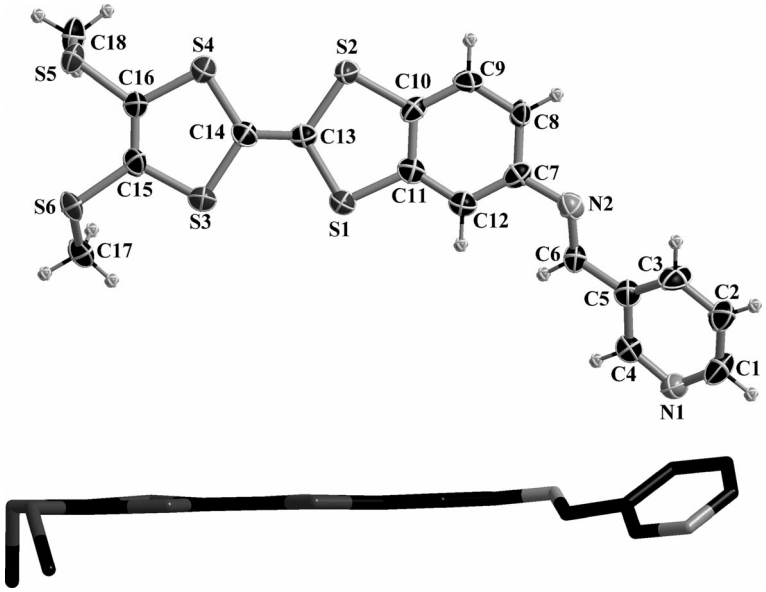

Figure 2. Molecular structure of $\mathbf{L_2}$ (50% probability displacement ellipsoids), front and side views are presented.

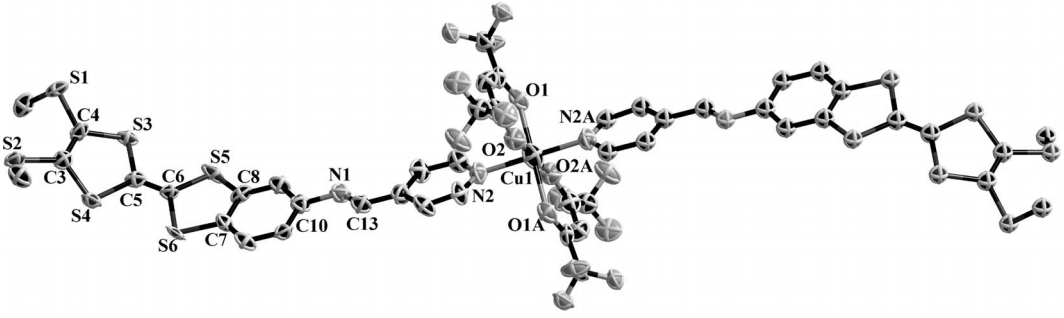

Figure 3. ORTEP view of **4** with the atom numbering scheme (50% probability displacement ellipsoids, H atoms are omitted for clarity).

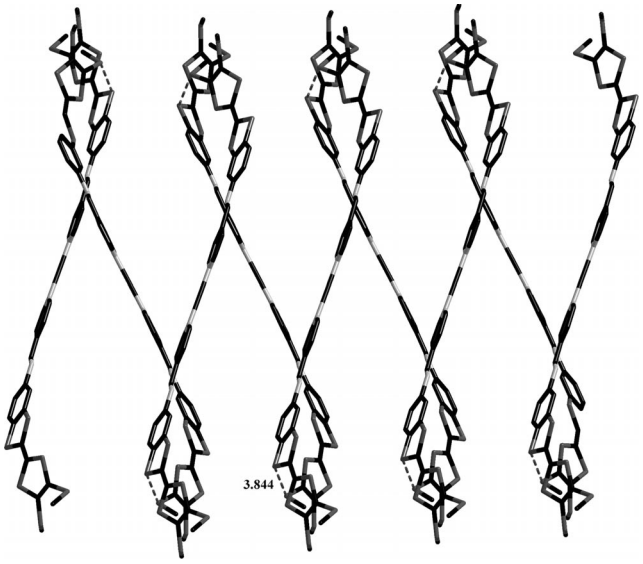

Figure 4. Crystal packing of **4** viewed along the *c* axis (H atoms and $hfac^-$ units are omitted for clarity).

hedral coordination geometry. $\mathbf{L_1}$ has a *cis* coordination mode with an N3–Mn1–N4 bond angle of 97.13(13)°, which is different to that in **4**. The Mn–N bond lengths range from 2.245(4)–2.273(3) Å. The average central C=C bond length of the TTF core is 1.341 Å, which is longer than that in **4**. In contrast to **4**, $\mathbf{L_1}$ is almost planar in **5**. The average dihedral angle between the two five-membered rings is 6.43(1)°, and the average dihedral angle between the coordinated pyridyl ring and the phenyl group is 10.26(1)°.

In the solid state, the molecules are stacked in a head-to-tail fashion. The shortest intermolecular S···S contact is 3.642 Å ($S12\cdots S12^{\#2}$, symmetry code: #2 $-x$-1, $-y-2$, $-z$), which is slightly shorter than the sum of the van der Waals radii (3.70 Å) and leads to the formation of dimers. The dimers are aligned side by side along the *c* axis and further connected through S6···S11 contacts (3.633 Å) to give a 1D zigzag chain structure (Figure 6).

The use of 3-pyridine-type $\mathbf{L_2}$ is to control the supramolecular motifs as the relative orientations of the nitrogen donors on the pyridyl rings might result in different building blocks. Crystallization of $\mathbf{L_2}$ with $Cu(hfac)_2$ from the

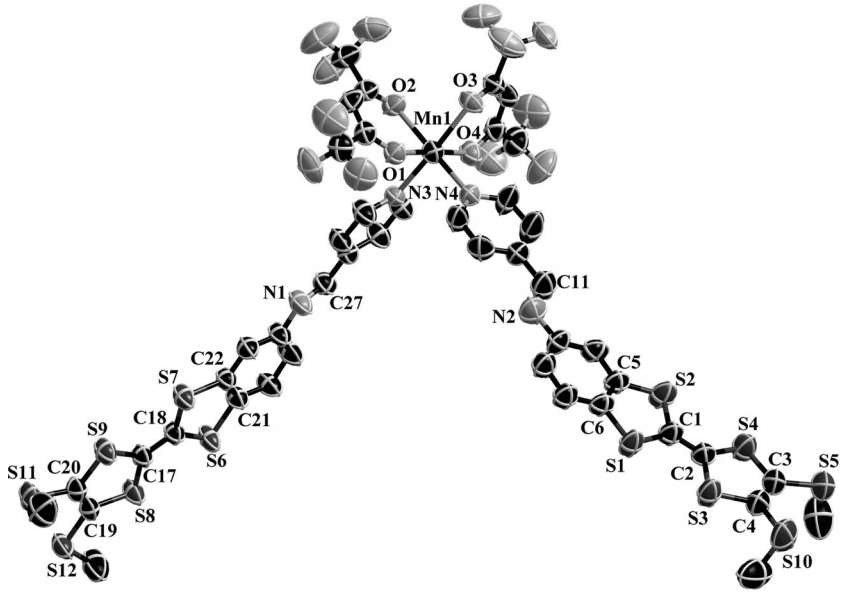

Figure 5. ORTEP view of **5** with the atom numbering scheme (50% probability displacement ellipsoids, H atoms are omitted for clarity).

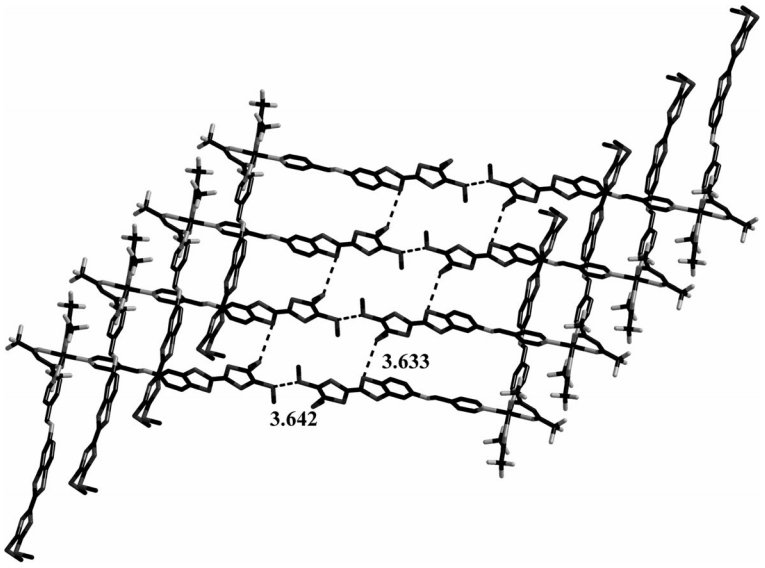

Figure 6. The 1D zigzag chain of **5** formed by short intermolecular S···S interactions (H atoms are omitted for clarity).

same solvent system as **4** afforded **6**. As shown Figure 7, the central Cu^{2+} ion in **6** lies on the inversion center and adopts a pseudooctahedral coordination environment, surrounded by four oxygen atoms from two $hfac^-$ ligands and two nitrogen atoms from the pyridine moiety of $\mathbf{L_2}$. The central C=C bond length of the TTF core is 1.330(9) Å. $\mathbf{L_2}$ is almost planar in **6**. In the TTF skeleton, the dihedral angle between the two five-membered rings (containing S3, S4, S5, and S6) is 2.70(1)°. In the solid state, unlike **4**, the molecules of **6** are face-to-face self-assembled to form a 1D chain-like structure along the *c* axis through short π–π stacking interactions [the centroid···centroid distance between benzene rings of adjacent molecules is 3.663(6) Å, Figure 8].

Different from $\mathbf{L_1}$ and $\mathbf{L_2}$, $\mathbf{L_3}$ prefers a bidentate binding mode for the chelation of transition metal ions. The reaction of $\mathbf{L_3}$ with 1 equiv. of $Re(CO)_5Cl$ afforded **7** in high yield. In previous reports, the common products of reactions between $Re(CO)_5Cl$ and N^N ligands (such as 2-pyridinylimine and its derivatives) are Re^I tricarbonyl complexes.[28–31] As shown in Figure 9, the asymmetric unit in **7** consists of cationic $[Re(CO)_4(\mathbf{L_3})]^+$ with $[Re_2Cl_3(CO)_6]^-$ [tri-μ-halogenohexacarbonyldirhenate(I)] as the counterion.

In the cation, $\mathbf{L_3}$ coordinates Re(1) by two nitrogen atoms to form a strained five-membered metallacycle. As a result, the pyridyl ring forms a large dihedral angle of 51.70(1)° with the phenyl ring. The average Re1–N bond length is 2.177 Å. The N1–Re1–N2 angle of 74.8(3)° is sig-

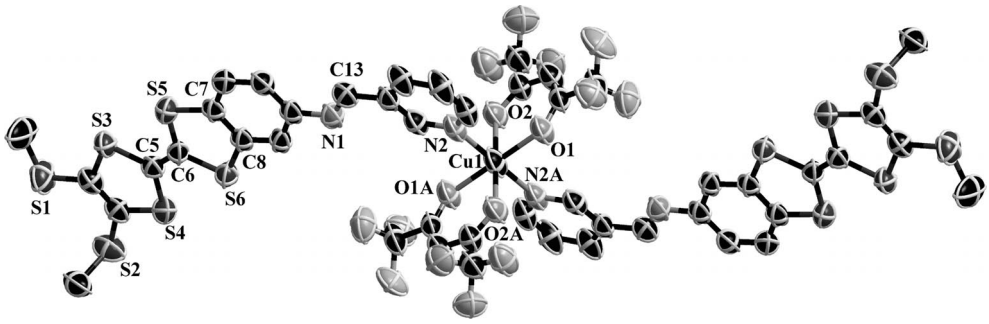

Figure 7. ORTEP view of **6** with the atom numbering scheme (50% probability displacement ellipsoids, H atoms are omitted for clarity).

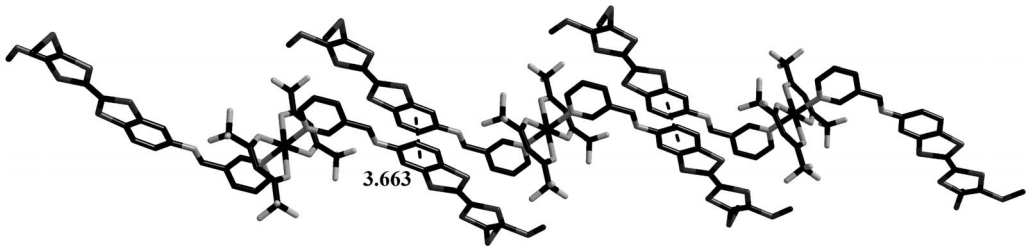

Figure 8. π–π stacking interactions in **6** viewed along the *a* axis (H atoms are omitted for clarity).

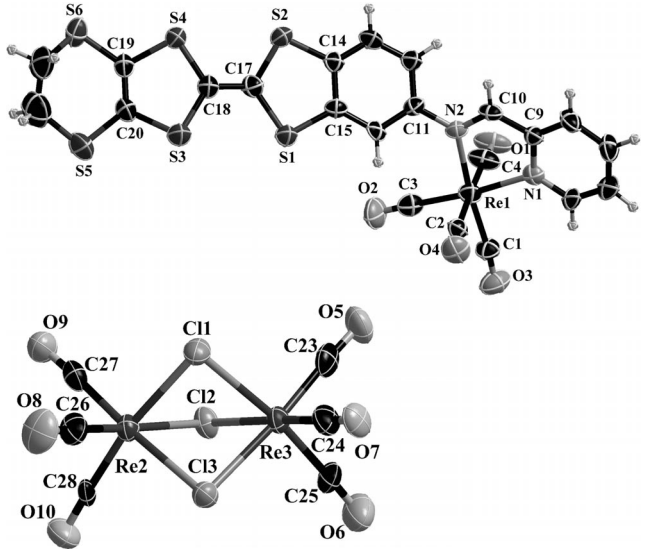

Figure 9. ORTEP view of **7** with the atom numbering scheme (50% probability displacement ellipsoids).

nificantly smaller than the ideal value of 90°, which is due to the steric requirement of $\mathbf{L_3}$. The average Re–C (C1 and C3) bond length for the terminal CO groups in the equatorial plane that includes the pyridine–imine ligand is 1.925 Å, which is shorter than the average value for the Re–C (C2 and C4) bond (2.022 Å) in the axial position. All other bond lengths and angles are in good agreement with the related complexes $[Re(bpy)(CO)_4](PF_6)$[32] and $[Re(bpy)(CO)_4](OSO_2CF_3)$[33] (bpy = 2,2′-bipyridine or its derivatives).

The anion consists of two rhenium atoms bridged by three chlorine atoms, and three terminal carbonyl groups complete the octahedral coordination for each rhenium atom. The average Re–Cl distance is 2.515 Å, and the average Re–C distance is 1.891 Å, which is shorter than that in the cation. The Re–C≡O bond angles of 176.5(9)–177.1(10)° are slightly distorted from linearity. The average angle of Re2–Cl–Re3 is 84.58°. These values agree well with those found in similar complexes.[34] The Re(2)–Re(3) distance of 3.384(1) Å is too long to postulate a direct metal–metal interaction.

Shorter intermolecular S···S contacts are observed between the cations [S4···S5 3.672(5) Å], which form a 1D chain motif along the *a* axis. The dinuclear rhenium(I) anions are located between the cations (Figure 10).

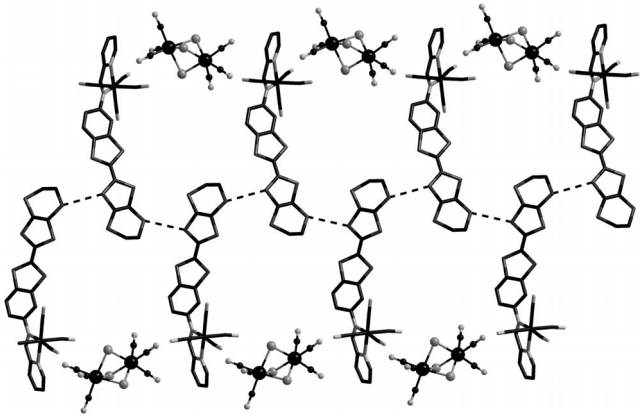

Figure 10. View of the crystal packing arrangement of **7**. The dashed lines represent S···S nonbonded contacts.

Spectroscopic Properties

The absorption spectra of all of the reported compounds were measured in dichloromethane/acetonitrile (1:1) solution at room temperature (Figure 11). The absorption data are summarized in Table 7.

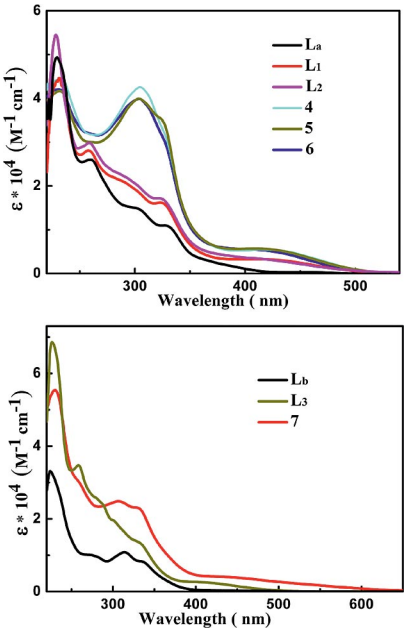

Figure 11. Absorption spectra of $\mathbf{L_a}$, $\mathbf{L_b}$, $\mathbf{L_1}$–$\mathbf{L_3}$, and **4**–**7** in CH_2Cl_2/CH_3CN (1:1, v/v; $c = 2.0 \times 10^{-5}$ M).

All the ligands exhibit a strong absorption band at high energy ($\lambda < 400$ nm), which is assigned to the intraligand π→π* transition. Compared with $\mathbf{L_a}$ and $\mathbf{L_b}$, $\mathbf{L_1}$–$\mathbf{L_3}$ show an additional weak broad absorption band at lower energy (400–500 nm), which corresponds to the intramolecular charge-transfer transition from the highest occupied molecular orbital in TTF to the lowest unoccupied molecular orbital in the electron-accepting pyridyl unit.[35] However, for mononuclear **4**–**6**, no obvious bands with metal-to-ligand charge transfer (MLCT) character are observed, whereas **7** shows a weak MLCT [dπ(Re)→π*(L)] band at around 500–600 nm.

Table 7. Electronic absorption data for $\mathbf{L_a}$–$\mathbf{L_3}$ and **4**–**7**.

	Absorption, λ_{abs} [nm] (ε /M^{-1} cm^{-1})			
$\mathbf{L_a}$	229 (49293)	261 (25959)	328 (10903)	
$\mathbf{L_b}$	225 (32948)	315 (10876)	336 (8307)	
$\mathbf{L_1}$	231 (44649)	258 (28066)	325 (16110)	425 (3408)
$\mathbf{L_2}$	228 (54468)	259 (29895)	325 (17239)	412 (3217)
$\mathbf{L_3}$	226 (68213)	258 (34659)	332 (13777)	410 (2544)
4	235 (44387)	305 (42416)	422 (5412)	
5	233 (41869)	304 (39744)	417 (5674)	
6	232 (41755)	304 (39744)	410 (5506)	
7	230 (55542)	305 (24911)	436 (4021)	

The UV/Vis/NIR spectra of **4**–**7** were investigated upon addition of the oxidant $NOPF_6$ in dichloromethane/acetonitrile (1:1) solution (Figure 12). In **4**, a characteristic absorption band of TTF is exhibited at 305 nm. Upon the addition of $NOPF_6$, two characteristic absorption bands of the $TTF^{\cdot+}$ species at around 450 and 950 nm are observed.[36] After further oxidation with $NOPF_6$, the characteristic band of the dicationic TTF species at around 600 nm is no longer observed. The oxidation experiments were also performed in different solvents, and the results are similar, which suggests that the oxidized compounds can be obtained chemically. Similar phenomena were also observed for **5**–**7**.

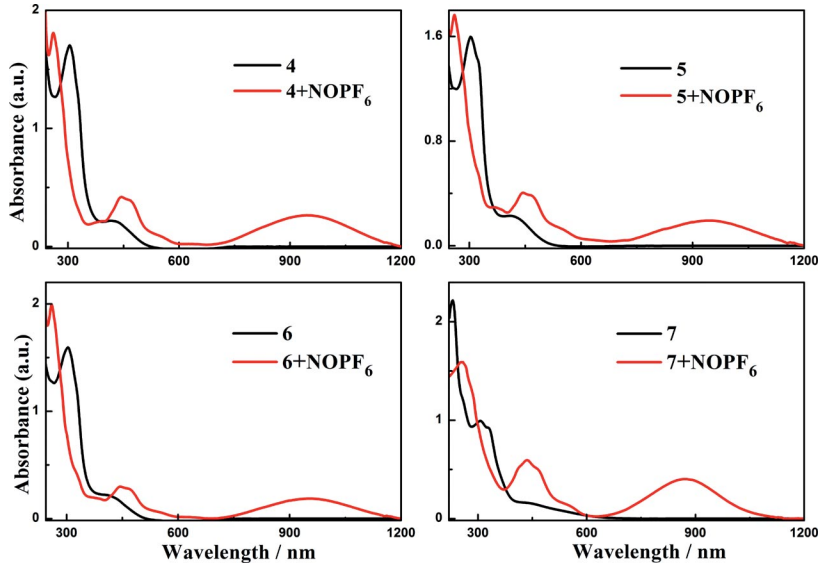

Figure 12. UV/Vis/NIR absorption spectra of **4**–**7** upon the addition of $NOPF_6$.

Electrochemical Properties

The electrochemical properties were studied by cyclic voltammetry, and the data are collected in Table 8.

Table 8. Summary of redox potentials [V] for $\mathbf{L_a}$–$\mathbf{L_3}$ and **4**–**7** (vs. $Ag/AgNO_3$).

	$E_{1/2}{}^1$	$E_{1/2}{}^2$	$E_p{}^{ox}$
$\mathbf{L_a}$	0.32	0.60	–
$\mathbf{L_b}$	034	0.63	–
$\mathbf{L_1}$	0.43	0.72	–
$\mathbf{L_2}$	0.42	0.71	–
$\mathbf{L_3}$	0.41	0.71	–
4	0.42	0.72	
5	0.42	0.72	
6	0.41	0.74	
7	0.47	0.79	1.38

As shown in Figure 13, $\mathbf{L_a}$, $\mathbf{L_b}$, and $\mathbf{L_1}$–$\mathbf{L_3}$ exhibit the usual two-step reversible single-electron oxidations of TTF derivatives, which are derived from the successive oxidation of the TTF unit to TTF^+ and TTF^{2+}, respectively. The $E^1{}_{ox}$ and $E^2{}_{ox}$ values for $\mathbf{L_a}$ and $\mathbf{L_b}$ are around 0.33 and 0.61 V, respectively. Compared with the precursors, the electron-withdrawing nature of the pyridine ring through the conjugated bridge makes the oxidation of the TTF core more difficult for $\mathbf{L_1}$–$\mathbf{L_3}$.[4a,37] The two redox peaks are positively shifted by 90 and 100 mV, respectively, which also confirms the conjugation through the imine junction.[38]

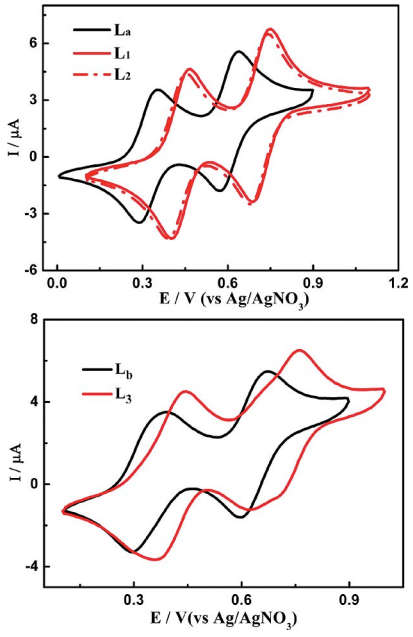

Figure 13. Cyclic voltammograms of $\mathbf{L_a}$, $\mathbf{L_b}$, and $\mathbf{L_1}$–$\mathbf{L_3}$ (5×10^{-4} M) in CH_2Cl_2/CH_3CN (1:1, v/v) with nBu$_4$NClO$_4$ (0.1 M) at a sweep rate of 100 mV/s.

In **4**–**6**, the two observed redox potentials for the TTF core remain almost unchanged (Figure 14). The small effect of complexation on the oxidation potentials can be ascribed to the large separation between the TTF core and the metallic fragment.[39]

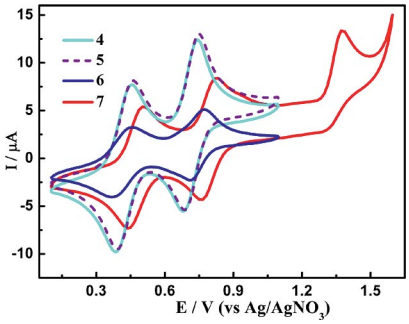

Figure 14. Cyclic voltammograms of **4**–**7** (5×10^{-4} M) in CH_2Cl_2/CH_3CN (1:1, v/v) with nBu$_4$NClO$_4$ (0.1 M) at a sweep rate of 100 mV/s.

In **7**, chelation to the Re^I ion enhances the electron-withdrawing ability of the 2-pyridine ring even further, which causes a decrease of the electron density at the TTF core and results in the large positive shifts of $E^1{}_{ox}$ and $E^2{}_{ox}$ (about 60 and 75 mV, respectively) compared to $\mathbf{L_3}$.[40] The third irreversible oxidation peak at about 1.36 V is assigned to the Re^I-centered one-electron oxidation process.[22,41]

Conclusions

A useful synthetic approach for π-extended TTF–Schiff base ligands has been reported. Four coordination complexes based on these redox active ligands have been prepared and structurally characterized. The different coordination modes of the metal ions and relative orientation of the terminal N donors result in the different crystalline organization of the complexes in the solid state. Electrochemical studies confirmed π-electron conjugated structures and interesting redox active properties for all compounds. The results demonstrate that these new imine-bridged TTF ligands that bear diverse substitution patterns are useful for the synthesis and design of new metal complexes. Further work to obtain oxidized complexes that combine magnetic and conducting properties is in progress.

Experimental Section

General Procedures: IR spectra were recorded with a Vector22 Bruker spectrophotometer (400–4000 cm^{-1}) as KBr pellets. UV/Vis spectra were measured with a UV-3100 spectrophotometer. Elemental analyses were performed with a Perkin–Elmer 240C analyzer. NMR spectra were measured with a Bruker AM 500 spectrometer. Mass spectra were determined with an Autoflex II TM instrument for MALDI-TOF-MS, GC-TOF instrument for EI-MS and an LCQ Fleet instrument for ESI-MS. Absorption spectra were measured with a Shimadzu UV-3100 spectrophotometer. Cyclic voltammograms were recorded with an Im6eX electrochemical analytical instrument, with glassy carbon as the working electrode, platinum as the counter electrode, $Ag/AgNO_3$ as the reference electrode, and 0.1 M nBu$_4$NClO$_4$ as the supporting electrolyte. All the potentials were run at a scan rate of 100 mV/s. 4,5-Bis(methylthio)-1,3-dithiol-2-thione (**3a**) and 4,5-ethylenedithio-1,3-dithiol-2-thione (**3b**) were synthesized according to literature procedures.[41b]

5-Nitro-1,3-benzodithiole-2-thione (1): A mixture of potassium sulfide (43%, 2.06 g, 8.03 mmol), carbon disulfide (1 mL), and *N*,*N*-dimethylformamide (5 mL) was stirred for 2 h at room temperature. To the red suspension of potassium trithiocarbonate was added 1,2-dibromo-4-nitro benzene (2.10 g, 7.40 mmol), and the mixture was stirred for 32 h at 85 °C. The mixture was poured into water (100 mL), and the precipitate was collected by filtration. The solid was purified by chromatography on silica gel with dichloromethane/petroleum ether (v/v = 1:1) to obtain **1** as a pure yellow solid; yield 1.53 g (93%). IR (KBr): $\tilde{\nu}$ = 1564, 1511, 1338, 1306, 1067, 891, 767, 736 cm^{-1}. ^{1}H NMR (500 MHz, $CDCl_3$): δ = 8.35 (d, J = 1.5 Hz, 1 H), 8.24 (dd, J = 9.0, 2.0 Hz, 1 H), 7.62 (d, J = 9.0 Hz, 1 H) ppm. EI-MS: m/z (%) = 229.0 (100) $[M]^+$, 185.0 (30) $[M - CS]^+$. $C_7H_3NO_2S_3$ (229.29): calcd. C 36.67, H 1.32, N 6.11; found C 36.71, H 1.28, N 6.14.

5-Amino-1,3-benzodithiole-2-thione (2): A solution of $SnCl_2{\cdot}2H_2O$ (7.80 g, 34.57 mmol) in ethanol (10 mL) was added to a stirring solution of **1** (2.00 g, 8.73 mmol) in HCl (90 mL, 12 M) and ethanol (45 mL), and the mixture was heated to reflux for 13 h. The precipitate was collected by filtration and washed with water. The crude product was purified by silica gel chromatography with dichloromethane/petroleum ether (v/v = 2:1) as an eluent to obtain **2** as a light yellow solid; yield 0.69 g (40%). IR (KBr): $\tilde{\nu}$ = 3364, 1635, 1583, 1464, 1423, 1297, 1242, 1062, 833, 809, 568, 446 cm^{-1}. ^{1}H NMR (500 MHz, $CDCl_3$): δ = 7.22 (d, J = 8.5 Hz, 1 H), 6.77 (d, J = 1.9 Hz, 1 H), 6.72 (dd, J = 8.5, 2.0 Hz, 1 H), 3.88 (s, 2 H) ppm. EI-MS: m/z (%) = 199.0 (100) $[M]^+$, 155.0 (42) $[M - CS]^+$. $C_7H_5NS_3$ (199.30): calcd. C 42.18, H 2.53, N 7.03; found C 42.38, H 2.61, N 7.08.

2-[4,5-Bis(methylthio)-1,3-dithiol-2-ylidene]-1,3-benzodithiol-5-amine (L_a): Under an argon atmosphere, a solution of **2** (0.40 g, 2.01 mmol), **3a** (0.48 g, 2.28 mmol), and $P(OEt)_3$ (4.10 mL) in toluene (15 mL) was heated to 120 °C for 4 h. After the reaction, excess solvent was removed under vacuum to afford a red oily residue, which was subjected to silica gel column chromatography with dichloromethane/petroleum ether (v/v = 1:1) as the eluent; yield 26%. Orange crystals suitable for X-ray diffraction were obtained from evaporation of a solution of L_a in dichloromethane and hexane. IR (KBr): $\tilde{\nu}$ = 3328, 2914, 1584, 1460, 1422, 1298, 1242, 1061, 897, 836, 811, 772, 568, 444 cm^{-1}. ^{1}H NMR (500 MHz, $CDCl_3$): δ = 6.99 (d, J = 7.5 Hz, 1 H), 6.61 (s, 1 H), 6.46 (d, J = 8.0 Hz, 1 H), 3.66 (s, 2 H), 2.43 (s, 6 H) ppm. MS (MALDI-TOF): m/z = 361.1 $[M]^+$. $C_{12}H_{11}NS_6$ (361.61): calcd. C 39.86, H 3.07, N 3.87; found C 39.82, H 3.09, N 3.94.

2-(5,6-Dihydro[1,3]dithiolo[4,5-*b*][1,4]dithiin-2-ylidene)-1,3-benzodithiol-5-amine (L_b): L_b was obtained according to the procedure reported above for L_a by using **3b** instead of **3a**. Orange crystals suitable for X-ray diffraction were obtained from evaporation of a solution of L_b in dichloromethane and hexane; yield 34%. IR (KBr): $\tilde{\nu}$ = 3362, 2919, 1609, 1586, 1463, 1283, 1120, 884, 840, 802, 771, 421 cm^{-1}. ^{1}H NMR (500 MHz, $CDCl_3$): δ = 6.98 (d, J = 8.5 Hz, 1 H), 6.60 (s, 1 H), 6.46 (d, J = 8.5 Hz, 1 H), 3.64 (s, 2 H),3.27 (s, 4 H) ppm. MS (MALDI-TOF): m/z = 359.1 $[M]^+$. $C_{12}H_9NS_6$ (359.60): calcd. C 40.08, H 2.52, N 3.89; found C 40.12, H 2.47, N 3.93.

L_a-Imine-4-pyridyl (L_1): A mixture of L_a (0.12 g, 0.33 mmol), pyridine-4-carbaldehyde (32 μL), and a catalytic amount of formic acid in distilled ethanol (15 mL) was heated to reflux. After stirring for 5 h, a red precipitate was collected by filtration, washed with ethanol, and dried under vacuum. Red crystals suitable for X-ray diffraction were obtained from evaporation of a solution of L_1 in dichloromethane and ethanol; yield 65%. IR (KBr): $\tilde{\nu}$ = 2916, 1623, 1598, 1551, 1457, 1411, 1242, 988, 886, 819, 772, 586, 502 cm^{-1}. ^{1}H NMR (500 MHz, $CDCl_3$): δ = 8.86 (d, J = 5.0 Hz, 2 H), 8.54 (s, 1 H), 7.84 (d, J = 5.5 Hz, 2 H), 7.37 (s, 1 H), 7.35 (s, 1 H), 7.14 (d, J = 8.0 Hz, 1 H), 2.53 (s, 6 H) ppm. MS (MALDI-TOF): m/z = 449.9 $[M]^+$. $C_{18}H_{14}N_2S_6$ (450.71): calcd. C 47.97, H 3.13, N 6.21; found C 48.02, H 3.10, N 6.27.

L_a-Imine-3-pyridyl (L_2): L_2 was obtained from L_a and pyridine-3-carbaldehyde according to a similar procedure to that described above for L_1.Red crystals suitable for X-ray diffraction were obtained from evaporation of a solution of L_2 in chloroform; yield 62%. IR (KBr): $\tilde{\nu}$ = 2919, 1615, 1454, 1417, 1324, 1203, 1125, 1024, 891, 810, 772, 706, 467 cm^{-1}. ^{1}H NMR (500 MHz, $CDCl_3$): δ = 9.01 (s, 1 H), 8.72 (d, J = 4.5 Hz, 1 H), 8.50 (s, 1 H), 8.30 (d, J = 8.0 Hz, 1 H), 7.45 (dd, J = 8.0, 5.0 Hz, 1 H), 7.27 (s, 1 H), 7.16 (d, J = 1.0 Hz, 1 H), 7.03 (d, J = 8.0 Hz, 1 H), 2.44 (s, 6 H) ppm. MS (MALDI-TOF): m/z = 450.1 $[M]^+$. $C_{18}H_{14}N_2S_6$ (450.71): calcd. C 47.97, H 3.13, N 6.21; found C 48.02, H 3.10, N 6.27.

L_b-Imine-2-pyridyl (L_3): L_3 was obtained according to a similar procedure to that described above for L_1 starting from L_b and pyridine-2-carbaldehyde; yield 59%. IR (KBr): $\tilde{\nu}$ = 2911, 1626, 1584, 1562, 1466, 1408, 1259, 1113, 996, 876, 805, 773, 740, 584, 893 cm^{-1}. ^{1}H NMR (500 MHz, $CDCl_3$): δ = 8.76 (d, J = 3.5 Hz, 1 H), 8.63 (s, 1 H), 8.21 (d, J = 8.0 Hz, 1 H), 7.87 (t, 1 H), 7.43 (q, 1 H), 7.31 (s, 2 H), 7.13 (d, J = 8.0 Hz, 1 H), 3.35 (s, 4 H) ppm. MS (MALDI-TOF): m/z = 448.1 $[M]^+$. $C_{18}H_{12}N_2S_6$ (448.69): calcd. C 48.18, H 2.69, N 6.24; found C 48.14, H 2.63, N 6.27.

$[Cu(hfac)_2(L_1)_2]$ (4): A solution of L_1 (9.0 mg, 0.02 mmol) in dichloromethane (5 mL) was added to a hot solution of $Cu(hfac)_2{\cdot}2H_2O$ (10.4 mg, 0.02 mmol) in hexane (6 mL). The dark red mixture was stirred at room temperature for 15 min. Slow evaporation of the resulting solution in the dark gave wine-colored platelets of **4**, which were suitable for single-crystal X-ray diffraction; yield 70%. IR (KBr): $\tilde{\nu}$ = 2924, 1642, 1615, 1555, 1525, 1482, 1427, 1322, 1258, 1202, 1140, 1030, 870, 825, 790, 773, 688, 668, 587 cm^{-1}.

$[Mn(hfac)_2(L_1)_2]$ (5): Dark red crystals **5** were obtained according to a similar procedure to that described for **4** with $Mn(hfac)_2{\cdot}2H_2O$ instead of $Cu(hfac)_2{\cdot}2H_2O$; yield 81%. IR (KBr): $\tilde{\nu}$ = 2906, 2359, 1645, 1610, 1555, 1522, 1490, 1455, 1421, 1323, 1254, 1191, 1142, 1012, 969, 884, 823, 789, 771, 687, 663, 583 cm^{-1}.

$[Cu(hfac)_2(L_2)_2]$ (6): Dark red crystals **6** were obtained according to a similar procedure to that described for **4** with L_2 instead of L_1; yield 63%. IR (KBr): $\tilde{\nu}$ = 2920, 1645, 1616, 1557, 1531, 1463, 1422, 1344, 1258, 1208, 1138, 1087, 868, 824, 800, 774, 744, 669, 582 cm^{-1}.

$[Re(CO)_4(L_3)][Re_2(CO)_6Cl_3]$ (7): Under a nitrogen atmosphere, a mixture of $Re(CO)_5Cl$ (37 mg, 0.1 mmol) and L_3 (49 mg, 0.1 mmol) in toluene (8 mL) was heated to reflux for 2 h to give a black suspension, which was cooled to room temperature, and the resulting precipitate was collected by filtration. The crude solid was purified by flash chromatography using dichloromethane as the eluent; yield 84%. Black crystals were obtained by diffusing diethyl ether into a dichloromethane solution of **7**. IR (KBr): $\tilde{\nu}$ = 2020, 1959, 1927, 1886, 1474, 1453, 1355, 1302, 1236, 1114, 809, 770, 643, 530 cm^{-1}. ^{1}H NMR (500 MHz, DMSO): δ = 9.34 (s, 1 H), 9.06 (d, J = 5.5 Hz, 1 H), 8.35 (t, 2 H), 7.85 (m, 1 H), 7.74 (d, J = 8.5 Hz, 1 H), 7.72 (d, J = 2.0 Hz, 1 H), 7.44 (dd, J = 8.5, 6.5 Hz, 1 H), 3.40 (s, 4 H) ppm. ESI-MS: m/z = 747.00 $[Re(CO)_4(L_3)]^+$, 646.92 $[Re_2(CO)_6Cl_3]^-$, 341.33 $[Re(CO)_3Cl_2]^-$.

Crystal Structure Determination: The data were collected with a Bruker Smart Apex CCD diffractometer equipped with graphite monochromated Mo-K_a radiation (λ = 0.71073 Å) using a ω-2θ

scan mode at 293 K. The highly redundant data sets were reduced with SAINT[42] and corrected for Lorentz and polarization effects. Absorption corrections were applied using SADABS[43] supplied by Bruker. The structure was solved by direct methods and refined by full-matrix least-squares methods on F^2 using SHELXTL-97.[44] All non-hydrogen atoms were found by alternating difference Fourier syntheses and least-squares refinement cycles and, during the final cycles, refined anisotropically. Hydrogen atoms were placed in calculated positions and refined as riding atoms with a uniform value of U_{iso}.

CCDC-831433 (for $\mathbf{L_a}$), -831434 (for $\mathbf{L_b}$), -831435 (for $\mathbf{L_1}$), -831436 (for $\mathbf{L_2}$), -831437 (for **4**), -831438 (for **5**), -831439 (for **6**), and -831440 (for **7**) contain the supplementary crystallographic data for this paper. These data can be obtained free of charge from The Cambridge Crystallographic Data Centre via www.ccdc.cam.ac.uk/data_request/cif.

Supporting Information (see footnote on the first page of this article): Selected bond lengths and angles of the ligands, the structures of $\mathbf{L_a}$ and $\mathbf{L_b}$.

Acknowledgments

This work was supported by the Major State Basic Research Development Program (grant number 2011CB808704), the National Science Fund for Distinguished Young Scholars of China (grant number 20725104), and the National Natural Science Foundation of China (NSFC) (grant numbers 21021062 and 51173075).

[1] a) M. R. Bryce, *Adv. Mater.* **1999**, *11*, 11–23; b) J. Yamada, T. Sugimoto, *TTF Chemistry: Fundamentals and applications of Tetrathiafulvalene*, Springer, Berlin, **2004**; c) T. Otsubo, K. Takimiya, *Bull. Chem. Soc. Jpn.* **2004**, *77*, 43–58.

[2] a) A. Kobayashi, E. Fujiwara, H. Kobayashi, *Chem. Rev.* **2004**, *104*, 5243–5264; b) D. Lorcy, N. Bellec, M. Fourmigué, N. Avarvari, *Coord. Chem. Rev.* **2009**, *253*, 1398–1438; c) M. Shatruk, L. Ray, *Dalton Trans.* **2010**, *39*, 11105–11121.

[3] a) T. K. Hansen, T. Jørgensen, P. C. Stein, J. Becher, *J. Org. Chem.* **1992**, *57*, 6403–6409; b) P. D. Beer, P. A. Gale, G. Z. Chen, *J. Chem. Soc., Dalton Trans.* **1999**, 1897–1910; c) P. V. Bernhardt, E. G. Moore, *Aust. J. Chem.* **2003**, *56*, 239–258; d) H. Y. Lu, W. Xu, D. Q. Zhang, C. F. Chen, D. B. Zhu, *Org. Lett.* **2005**, *7*, 4629–4632.

[4] a) K. L. McCall, A. Morandeira, J. Durrant, L. J. Yellowlees, N. Robertson, *Dalton Trans.* **2010**, *39*, 4138–4145; b) S. Wenger, P.-A. Bouit, Q. L. Chen, J. Teuscher, D. D. Censo, R. Humphry-Baker, J.-E. Moser, J. L. Delgado, N. Martín, S. M. Zakeeruddin, M. Grätzel, *J. Am. Chem. Soc.* **2010**, *132*, 5164–5169.

[5] L. Huchet, S. Akoudad, J. Roncali, *Adv. Mater.* **1998**, *10*, 541–545.

[6] J. L. Segura, N. Martín, *Angew. Chem.* **2001**, *113*, 1416; *Angew. Chem. Int. Ed.* **2001**, *40*, 1372–1409.

[7] S. X. Liu, S. Dolder, M. Pilkington, S. Decurtins, *J. Org. Chem.* **2002**, *67*, 3160–3162.

[8] a) A. M. Madalan, C. Réthoré, N. Avarvari, *Inorg. Chim. Acta* **2007**, *360*, 233–240; b) G. Cosquer, F. Pointillart, Y. L. Gal, S. Golhen, O. Cador, L. Ouahab, *Dalton Trans.* **2009**, 3495–3502.

[9] B. Chesneau, M. Hardouin-Lerouge, P. Hudhomme, *Org. Lett.* **2010**, *12*, 4868–4871.

[10] a) T. Devic, N. Avarvari, P. Batail, *Chem. Eur. J.* **2004**, *10*, 3697–3707; b) Z. J. Lu, J. P. Wang, Q. Y. Zhu, L. B. Huo, Y. R. Qin, J. Dai, *Dalton Trans.* **2010**, *39*, 2798–2803.

[11] a) J. Massue, N. Bellec, S. Chopin, E. Levillain, T. Roisnel, R. Clérac, D. Lorcy, *Inorg. Chem.* **2005**, *44*, 8740–8748; b) N. Bellec, J. Massue, T. Roisnel, D. Lorcy, *Inorg. Chem. Commun.* **2007**, *10*, 1172–1176.

[12] a) H. Tanaka, M. Tokumoto, S. Ishibashi, D. Graf, E. S. Choi, J. S. Brooks, S. Yasuzuka, Y. Okano, H. Kobayashi, A. Kobayashi, *J. Am. Chem. Soc.* **2004**, *126*, 10518–10519; b) H. R. Wen, C. H. Li, Y. Song, J. L. Zuo, B. Zhang, X. Z. You, *Inorg. Chem.* **2007**, *46*, 6837–6839.

[13] a) J. Baffreau, F. Dumur, P. Hudhomme, *Org. Lett.* **2006**, *8*, 1307–1310; b) J. P. Wang, Z. J. Lu, Q. Y. Zhu, Y. P. Zhang, Y. R. Qin, G. Q. Bian, J. Dai, *Crys. Growth Des.* **2010**, *10*, 2090–2095.

[14] a) N. Avarvari, M. Fourmigué, *Chem. Commun.* **2004**, 1300–1301; b) C. Réthoré, M. Fourmigué, N. Avarvari, *Chem. Commun.* **2004**, 1384–1385; c) N. Avarvari, M. Fourmigué, *Chem. Commun.* **2004**, 2794–2795.

[15] S. X. Liu, S. Dolder, P. Franz, A. Neels, H. Stoeckli-Evans, S. Decurtins, *Inorg. Chem.* **2003**, *42*, 4801–4803.

[16] E. Isomura, K. Tokuyama, T. Nishinaga, M. Iyoda, *Tetrahedron Lett.* **2007**, *48*, 5895–5898.

[17] a) N. Benbellat, K. S. Gavrilenko, Y. L. Gal, O. Cador, S. Golhen, A. Gouasmia, J.-M. Fabre, L. Ouahab, *Inorg. Chem.* **2006**, *45*, 10440–10442; b) K. S. Gavrilenko, Y. L. Gal, O. Cador, S. Golhen, L. Ouahab, *Chem. Commun.* **2007**, 280–282.

[18] Q. Y. Zhu, Y. Liu, W. Lu, Y. Zhang, G. Q. Bian, G. Y. Niu, J. Dai, *Inorg. Chem.* **2007**, *46*, 10065–10070.

[19] a) F. Setifi, L. Ouahab, S. Golhen, Y. Yoshida, G. Saito, *Inorg. Chem.* **2003**, *42*, 1791–1793; b) K. Hervé, Y. L. Gal, L. Ouahab, S. Golhen, O. Cador, *Synth. Met.* **2005**, *153*, 461–464.

[20] Y. P. Zhao, L. Z. Wu, G. Si, Y. Liu, H. Xue, L. P. Zhang, C. H. Tung, *J. Org. Chem.* **2007**, *72*, 3632–3639.

[21] a) K. Sako, Y. Misaki, M. Fujiwara, T. Maitani, K. Tanaka, H. Tatemitsu, *Chem. Lett.* **2002**, 592–593; b) S. Campagna, S. Serroni, F. Puntoriero, F. Loiseau, L. D. Cola, C. J. Kleverlaan, J. Becher, A. P. Sørensen, P. Hascoat, N. Thorup, *Chem. Eur. J.* **2002**, *8*, 4461–4469; c) T. Devic, D. Rondeau, Y. Şahin, E. Levillain, R. Clérac, P. Betail, N. Avarvari, *Dalton Trans.* **2006**, 1331–1337; d) L. K. Keniley Jr., L. Ray, K. Kovnir, L. A. Dellinger, J. M. Hoyt, M. Shatruk, *Inorg. Chem.* **2010**, *49*, 1307–1309.

[22] a) W. Liu, R. Wang, X. H. Zhou, J. L. Zuo, X. Z. You, *Organometallics* **2008**, *27*, 126–134; b) Y. Chen, W. Liu, J. S. Jin, B. Liu, Z. G. Zou, J. L. Zuo, X. Z. You, *J. Organomet. Chem.* **2009**, *694*, 763–770; c) G. N. Li, D. Wen, T. Jin, Y. Liao, J. L. Zuo, X. Z. You, *Tetrahedron Lett.* **2011**, *52*, 675–678; d) G. N. Li, T. Jin, L. Sun, J. Qin, D. Wen, J. L. Zuo, X. Z. You, *J. Organomet. Chem.* **2011**, *696*, 3076–3085.

[23] J. Nakayama, E. Seki, M. Hoshino, *J. Chem. Soc. Perkin Trans. 1* **1978**, 468–471.

[24] a) J. Nakayama, H. Sugiura, M. Hoshino, *Tetrahedron Lett.* **1983**, *24*, 2585–2588; b) Y. Morita, E. Miyazaki, K. Fukui, S. Maki, K. Nakasuji, *Synth. Met.* **2005**, *152*, 433–436.

[25] M. Nihei, M. Kurihara, J. Mizutani, H. Nishihara, *J. Am. Chem. Soc.* **2003**, *125*, 2964–2973.

[26] a) F. Iwahori, S. Golhen, L. Ouahab, R. Carlier, J. P. Sutter, *Inorg. Chem.* **2001**, *40*, 6541–6542; b) F. Pointillart, T. Cauchy, Y. L. Gal, S. Golhen, O. Cador, L. Ouahab, *Inorg. Chem.* **2010**, *49*, 1947–1960.

[27] P. Guionneau, C. J. Kepert, G. Bravic, D. Chasseau, M. R. Truter, M. Kurmoo, P. Day, *Synth. Met.* **1997**, *86*, 1973–1974.

[28] R. N. Dominey, B. Hauser, J. Hubbard, J. Dunham, *Inorg. Chem.* **1991**, *30*, 4754–4758.

[29] V. W.-W. Yam, K. M.-C. Wong, V. W.-M. Lee, K. K.-W. Lo, K.-K. Cheung, *Organometallics* **1995**, *14*, 4034–4036.

[30] W. Wang, B. Spingler, R. Alberto, *Inorg. Chim. Acta* **2003**, *355*, 386–393.

[31] J. Zhang, W. Li, W. F. Bu, L. X. Wu, L. Ye, G. D. Yang, *Inorg. Chim. Acta* **2005**, *358*, 964–970.

[32] a) G. F. Strouse, H. U. Güdel, V. Bertolasi, V. Ferretti, *Inorg. Chem.* **1995**, *34*, 5578–5587; b) F. W. M. Vanhelmont, M. V. Rajasekharan, H. U. Güdel, S. C. Capelli, J. Hauser, H.-B. Bürgi, *J. Chem. Soc., Dalton Trans.* **1998**, 2893–2900.

[33] T. Scheiring, W. Kaim, J. Fiedler, *J. Organomet. Chem.* **2000**, *598*, 136–141.
[34] a) C. P. Hrung, M. Tsutsui, D. L. Cullen, E. F. Meyer Jr., C. N. Morimoto, *J. Am. Chem. Soc.* **1978**, *100*, 6068–6076; b) M. Harmjanz, B. L. Scott, C. J. Burns, *Chem. Commun.* **2002**, 1386–1387; c) F. A. Cotton, E. V. Dikarev, M. A. Petrukhina, *Inorg. Chem.* **2001**, *40*, 6825–6831.
[35] a) R. Andreu, I. Malfant, P. G. Lacroix, P. Cassoux, *Eur. J. Org. Chem.* **2000**, 737–741; b) H. Xue, X. J. Tang, L. Z. Wu, L. P. Zhang, C. H. Tung, *J. Org. Chem.* **2005**, *70*, 9727–9734.
[36] a) C, J. Fang, Z. Zhu, W. Sun, C. H. Xu, C. H. Yan, *New J. Chem.* **2007**, *31*, 580–586; b) C. H. Xu, W. Sun, C. Zhang, C. Zhou, C. J. Fang, C. H. Yan, *Chem. Eur. J.* **2009**, *15*, 8717–8721; c) J. Bigot, B. Charleux, G. Cooke, F. Delattre, D. Fournier, J. Lyskawa, L. Sambe, F. Stoffelbach, P. Woisel, *J. Am. Chem. Soc.* **2010**, *132*, 10796–10801.
[37] C. Goze, C. Leiggener, S. X. Liu, L. Sanguient, E. Levillain, A. Hauser, S. Decurtins, *ChemPhysChem* **2007**, *8*, 1504–1512.
[38] J.-Y. Balandier, A. Belyasmine, M. Sallé, *Eur. J. Org. Chem.* **2008**, 269–276.
[39] a) R. Wang, L. C. Kang, J. Xiong, X. W. Dou, X. Y. Chen, J. L. Zuo, X. Z. You, *Dalton Trans.* **2011**, *40*, 919–926; b) J. C. Wu, S. X. Liu, T. D. Keene, A. Neels, V. Mereacre, A. K. Powell, S. Decurtins, *Inorg. Chem.* **2008**, *47*, 3452–3459.
[40] M. Chahma, N. Hassan, A. Alberola, H. Stoeckli-Evans, M. Pilkington, *Inorg. Chem.* **2007**, *46*, 3807–3809.
[41] a) W. Liu, J. Xiong, Y. Wang, X. H. Zhou, R. Wang, J. L. Zuo, X. Z. You, *Organometallics* **2009**, *28*, 755–762; b) J. Qin, L. Hu, G. N. Li, X. S. Wang, Y. Xu, J. L. Zuo, X. Z. You, *Organometallics* **2011**, *30*, 2173–2179.
[42] *SAINT-Plus*, version 6.02, Bruker Analytical X-ray System, Madison, WI, **1999**.
[43] G. M. Sheldrick, *SADABS – An empirical absorption correction program*, Bruker Analytical X-ray Systems, Madison, WI, **1996**.
[44] G. M. Sheldrick, *SHELXTL-97*, University of Göttingen, Germany, **1997**.

Received: September 26, 2011
Published Online: December 7, 2011

DOI: 10.1002/ejic.201100885

New Organocadmium Hydrazine Adducts and Hydrazide Complexes

Andrew L Johnson,[a] Nathan Hollingsworth,[a] Andrew Kingsley,[b] Gabriele Kociok-Köhn,[a] and Kieran C. Molloy*[a]

Keywords: Cadmium / Hydrazine / Hydrazide / X-ray diffraction / NMR spectroscopy

The synthesis of $(Me_2CdL)_n$ [L = $H_2NN(H)tBu$, n = 2 (**1**); L = $H_2NN(CH_2CH_2)_2NMe$, $n = \infty$ (**2**)] and the conversion of **2** to $MeCdN(H)N(CH_2CH_2)_2NMe$ (**4**) are reported. In the solid state, **1** is a dimer in which each $H_2NN(H)tBu$ bridges two metal centres to generate discrete, isolated Cd_2N_4 rings, whereas **2** is a 1D polymer in which Me_2Cd units are bridged by H_2N and MeN moieties; the chains in **2** are further reinforced by NH···N hydrogen bonds. Hydrazide **4** is tetrameric and isostructural with the known aminomorpholine analogue; it forms a Cd_4N_8 cage structure that embodies both five-membered Cd_2N_3 and six-membered Cd_2N_4 rings. In addition to X-ray crystallography, **1**, **2** and **4** have been characterised by ^1H, ^{13}C, and ^{113}Cd NMR spectroscopy.

Introduction

Recent years have seen an increasing interest in the preparation of metal hydrazine adducts and hydrazides for use as precursors for the deposition of metal nitride thin films.[1] In particular, there has been significant interest in the derivatives of Group 13 (Al, Ga, In) and Group 12 (Zn).[2] Our interest in cadmium chemistry[3] has prompted us to explore the extent to which this chemistry can be extended to cadmium, and we have previously reported the first example of a dimethylcadmium hydrazine adduct and its conversion to a methylcadmium hydrazide.[4] The only other contributions in this area are much older reports that concern hydrazine (N_2H_4) adducts of various Cd^{II} salts.[5] Moreover, the structural chemistry of adducts of Me_2Cd is generally scarce, despite interest in this class of compounds with regard to chemical vapour deposition processes. Thus, crystallographic data have only been reported for the adducts Me_2CdL_2 {L_2 = bipy,[6] TMEDA,[7] dabco,[8] 1,4-dioxane;[9] bipy = 2,2′-bipyridyl; TMEDA = tetramethylethylenediamine, dabco = dimethyl-(μ-2,1,4-diazabicyclo[2.2.2]-octane)}.

We now wish to report the synthesis of two new hydrazine adducts of Me_2Cd, both of which reveal new structural motifs, and the conversion of one of them to only the second reported methylcadmium hydrazide.

Results and Discussion

A 1:1 reaction of $CdMe_2$ with *tert*-butylhydrazine or 1-amino-4-methylpiperazine leads to the formation of adducts $[Me_2CdH_2NN(H)tBu]_2$ (**1**) and $[Me_2CdH_2NN-(CH_2CH_2)_2NMe]_\infty$ (**2**), respectively, in a similar manner to that previously reported for $(Me_2Cd)_3[H_2NN-(CH_2CH_2)_2O]_2$ (**3**).[4]

$$CdMe_2 + H_2NNR^1R^2 \xrightarrow{\text{hexane, r.t.}} Me_2Cd{\cdot}H_2NX$$

1: X = N(H)*t*Bu

2: X = 

Both **1** and **2** are air-sensitive, and crystals of **1** redissolve readily in hexane above –20 °C.

The ^{113}Cd NMR spectrum of **2** shows a much larger high-field shift (δ = –39.3 ppm) than that of **1** (δ = –0.56 ppm) or **3** (δ = –1.7 ppm),[4] which is possibly due to the hydrogen bonding in **2** (see below) reducing dissociation of Lewis acid and Lewis base components at 298 K. At 218 K, the ^{113}Cd NMR spectrum of **1** shows a shift to δ = –12.3 ppm, which is consistent with enhanced metal coordination and reduced metal–ligand dissociation at this temperature.

At room temperature, the broad nature of the methylcadmium signal in the ^1H NMR spectra of both **1** and **2** suggests that dynamic processes are operative at this temperature. Signals for both the *tert*-butyl and piperazine units are also broad, especially the CH_2 units of the piperazine ring. However, cooling of a solution of **1** or **2** to ca. 250 K results in resolution of the Me_2Cd satellites [$^2J(^{113,111}CdH)$ = 49.4 (**1**), 50.4 Hz (**2**), unresolved], which are close to those of **3** (49.4 Hz, unresolved),[4] although no resolution of the other proton resonances in **1** occurs down to 218 K. As with **3**,[4] the NH_2 protons of **1** show little temperature dependence; however, the signal of the NH protons shows a shift from δ = 1.92 ppm to δ = 2.48 ppm on cooling to 218 K, which is consistent with an enhanced HN:→M interaction.

[a] Department of Chemistry, University of Bath,
Claverton Down, Bath BA2 7AY, UK
Fax: +44-1225-386231
E-mail: k.c.molloy@bath.ac.uk
[b] SAFC Hitech,
Power Road, Bromborough, Wirral CH62 3QF, UK

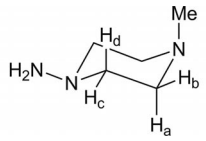

In contrast to **1**, on cooling a sample of **2** to 248 K, the signals of the CH_2 protons of the piperazine ring resolve such that each pair of environments are evident as either a doublet of doublets (H_a, H_d; $^2J \approx 10.5$, $^3J \approx 11$ Hz) or a doublet (H_b, H_c; $^2J \approx 10.5$ Hz). The solid-state structure of **2** (see below) shows that all other ^3J couplings involve dihedral angles of ca. 95° and, as such, ^3J nears 0 Hz, which is consistent with the Karplus equation.[10] The broad singlet due to NH_2 in **2** remains unresolved, which is analogous to that of **3**, and shows only a small temperature dependence (298 K, δ = 2.93 ppm; 248 K, δ = 3.07 ppm), which is surprising, because one of these hydrogen atoms participates in hydrogen bonding.

There is no evidence for further reaction of the NH_2 hydrogen atoms of **1** or **2** at room temperature, and a broad signal of appropriate intensity for 2 H is present in the ^{1}H NMR spectra of both compounds (δ = 2.20 and 2.93 ppm, respectively).

The synthesis of the hydrazide $[MeCdN(H)N(CH_2)_4NMe]_4$ (**4**) was effected by heating a solution of **2**. However, this also resulted in the formation of an additional metallic residue. A more successful approach involved stirring a solution of **2** in tetrahydrofuran (THF) for 1 week with exposure to daylight, which resulted in the clean synthesis of **4**. Interestingly, performing the same reaction in the dark resulted in no reaction; as such, it appears that the hydrazide formation maybe photochemical in some way. Indeed, early work has suggested that the photochemical decomposition of hydrazine involves the initial formation of N_2H_3 and H radicals,[11] though the possibility that the reaction is photoinitiated by Cd–C cleavage is also plausible. The singlet at δ = 2.93 ppm in the ^{1}H NMR spectrum of **2**, which integrates to two protons (H_2N:→Cd), halves in intensity and shifts to δ = 3.42 ppm on reaction, which confirms the formation of **4**.

Unfortunately, neither approach provided a clean way to generate the hydrazide MeCdN(H)N(H)*t*Bu from **1**.

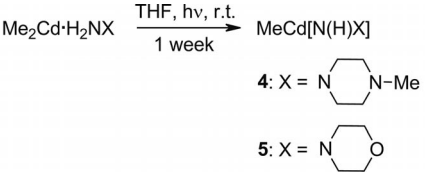

Complex **4** is a tetramer (see below) and is insufficiently soluble to allow low-temperature NMR spectra to be recorded and to make direct comparisons with spectra of **2**. At 298 K the NMR spectra of **4** are simple and show only a single environment for the four $CdCH_3$ units in each of the ^{1}H, ^{13}C and ^{113}Cd NMR spectra; this could be due to either fluxionality or dissociation of **4** into monomeric units, although the low solubility seems less consistent with this latter possibility. In each case the lines are broad, and only the ^2J(CdH) couplings are discernible [$^2J(^{113,111}$CdH) = 61.7 Hz, unresolved]. There is approximate C_2 symmetry about an axis that runs through the centres of the two six-membered Cd_2N_4 rings, but there must also be additional flexibility within the conformations of the two five-membered Cd_2N_3 faces of the polygon to render the metal atoms equivalent. In the ^{1}H NMR spectrum, the CH_2 protons in the piperizine ring are split into a broad 4 H doublet [δ = 2.41 ppm, ^3J(HH) = 6.2 Hz], which corresponds to the CH_2 protons of CH_2NMe ($H_{a,c}$), whereas the assignment of protons $H_{b,d}$ can be tentatively made to resonances at δ = 3.02 and 2.21 ppm. The doublet at δ = 3.02 ppm (H_b) displays a ^2J(HH) coupling (10.3 Hz), and the broad peak observed at δ = 2.21 ppm is consistent with an unresolved doublet of doublets as predicted by the Karplus equation.[10]

The structures of **1**, **2** and **4** are shown in Figures 1, 2 and 3, respectively. The structure of **1** comprises a six-membered Cd_2N_4 ring in a chair conformation where both nitrogen atoms (α and β) of the hydrazine bridge Me_2Cd groups. The six-membered ring is comparable with the $[Cd_2N_4]$ portion of **3**.[4] However, in **1** the interaction from the β-donor nitrogen atom [Cd–N(1) 2.640(3) Å] is weaker than that of the α-donor [Cd–N(2) 2.552(3) Å]. The reverse situation is true of **3**, which is possibly a consequence of the steric bulk of the *tert*-butyl group in **1**. The geometry about the metal centre in **1** is highly distorted and, as with **3**, is best described as disphenoidal, where methyl groups occupy the axial positions [C(1)–Cd–C(2) 156.84(14)°], which is comparable to that observed in **3** [C(1)–Cd(1)–C(2) 156.26(14)°]. The angle between the donor atoms at each metal atom in **1** is much less acute [N(2)′–Cd–N(1) 97.24(9)°] than that in **3** [N(1)–Cd(1)–N(2) 88.11(9)°].[4]

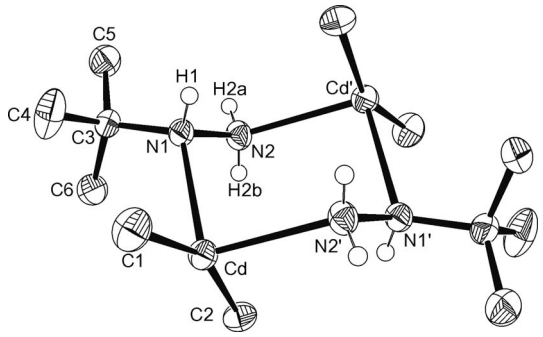

Figure 1. The asymmetric unit of **1** and symmetry-related atoms showing the labelling scheme used; thermal ellipsoids are at the 50% probability level. Only the hydrogen atoms of the hydrazine are shown for clarity. Selected bond lengths [Å] and angles [°]: Cd–C(1) 2.155(3), Cd–C(2) 2.164(3), Cd–N(1) 2.640(3), Cd–N(2′) 2.552(3), N(1)–N(2) 1.439(4); C(1)–Cd–C(2) 156.84(14), C(1)–Cd–N(1) 101.81(11), C(1)–Cd–N(2′) 97.02(12), C(2)–Cd–N(1) 94.65(11), C(2)–Cd–N(2′) 96.94(12), N(1)1–Cd–N(2′) 97.24(9), N(2)–N(1)–Cd 104.79(18), N(1)–N(2)–Cd′ 116.61(19). Symmetry operation: 1 – *x*, 1 – *y*, 1 – *z*.

The structure of **2** (Figure 2) consists of a folded polymeric chain, in which each Me_2Cd is bridged by the NH_2 [N(3), N(6)] and the NCH_3 of the piperazine ring [N(1) or N(4)]. Large estimated standard deviations in the data for **2** mean that all the Cd–N bonds are the same length within

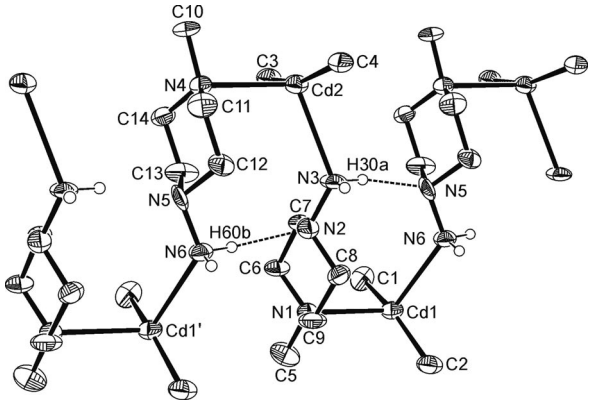

Figure 2. The asymmetric unit of **2** and symmetry-related atoms showing the labelling scheme used; thermal ellipsoids are at the 40% probability level. Only the hydrogen atoms of the hydrazine involved in hydrogen bonding are shown for clarity. Selected bond lengths [Å] and angles [°] for Cd(1), which are typical of both metal environments: Cd(1)–C(2) 2.138(18), Cd(1)–C(1) 2.153(18), Cd(1)–N(1) 2.636(14), Cd(1)–N(6) 2.677(14), N(2)–N(3) 1.445(19); C(1)–Cd(1)–C(2) 158.6(8), C(1)–Cd(1)–N(1) 93.5(7), C(1)–Cd(1)–N(6) 104.6(7), C(2)–Cd(1)–N(1) 96.9(6), C(2)–Cd(1)–N(6) 90.5(6), N(1)–Cd(1)–N(6) 106.0(4), N(2)–N(3)–Cd(2′) 129.0(10). Hydrogen bonds: N(3)–H(30A) 0.92, H(30A)···N(5) 2.33, N(3)···N(5) 3.24(2), N(3)–H(30A)···N(5) 169; N(6)–H(60B) 0.92, H(60B)···N(2) 2.39, N(6)···N(2) 3.30(2), N(6)–H(60B)···N(2) 176. Symmetry operations: ′: $x - 1, y, z$; ″: $1 + x, y, z$.

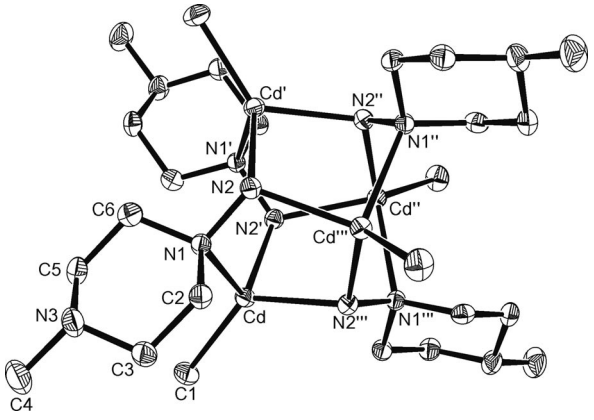

Figure 3. The asymmetric unit of **4** and symmetry-related atoms showing the labelling scheme used; thermal ellipsoids are at the 40% probability level. THF and hydrogen atoms have been omitted for clarity. Selected bond lengths [Å] and angles [°]: Cd–C(1) 2.182(3), Cd–N(1) 2.436(2), Cd–N(2′) 2.260(2), Cd–N(2‴) 2.283(2), N(1)–N(2) 1.465(4); C(1)–Cd–N(1) 115.42(11), C(1)–Cd–N(2′) 128.65(11), C(1)–Cd–N(2‴) 117.49(12), N(1)1–Cd–N(2′) 90.21(8), N(1)–Cd–N(2″) 107.47(9), N(2′)1–Cd–N(2‴) 92.66(9). Symmetry operations: ′: $y - 1/2, 1/2 - x, -z - 1/2$; ″: $-x, 1 - y, z$; ‴: $y - 1/2, 1/2 + x, -z - 1/2$.

error. However, a similar trend for the Cd–N bond lengths to that seen previously in **3** appears to emerge, in which the bond to the terminal NH_2 [Cd(1)–N(6) 2.677(14), Cd(2)–N(3) 2.682(13) Å] appears to be longer than that to the cyclic donor [Cd(1)–N(1) 2.636(14), Cd(2)–N(4) 2.644(13) Å] and also longer than the terminal NH_2 donor bond in **3** [Cd(1)–N(1) 2.613(3) Å]. The Cd–N bond lengths of **2** compare well with those of the dabco adduct [2.588(4), 2.669(4) Å].[8] Compound **2** also contains NH_2···N hydrogen bonds [N(5)···H(30A) 2.33, N(2)···H(60B) 2.39 Å], which effectively prevent the formation of Cd_2N_4 rings seen in **1** and explain the highly folded structure of **2** over the linear nature of **3**. The geometries about the two unique metal atoms in **2** are highly distorted, although less so than those in **3**. Although the coordination number about each cadmium centre is four, it can be best described as disphenoidal, much like **3**, with methyl groups in the axial positions [C(1)–Cd(1)–C(2) 158.6(8)°, C(3)–Cd(2)–C(4)″ 158.6(7)°], two equatorial nitrogen atoms and one vacant equatorial site. The open C–Cd–C angle is consistent with that of **3** and other Me_2CdL_2 adducts.[6–9] The angle between the donor atoms is, however, much less acute in **2** [N(1)–Cd(1)–N(2) 106.0(4)°, N(4)–Cd(2)–N(3) 107.1(4)°] than in **3** [N(1)–Cd(1)–N(2) 88.11(9)°, O–Cd(2)–O″ 65.82(10)°].

$[MeCdN(H)N(CH_2)_4N(CH_3)]_4$ (**4**) adopts a tetrameric Cd_4N_8 cage (Figure 3), which is isostructural to that of the morpholine analogue **5**; all bond lengths and bond angles are identical within error to those in **5**. The only notable difference between the structures of **4** and **5** is in the role of the NH unit. In **4**, each of the four N–H groups is involved in hydrogen bonding to a THF molecule [Figure 4; H(2)···O(1) 2.26(3) Å, N(2)–H(2)···O(1) 164(3)°], whereas in **5** they point to the centroids of lattice toluene molecules.[4]

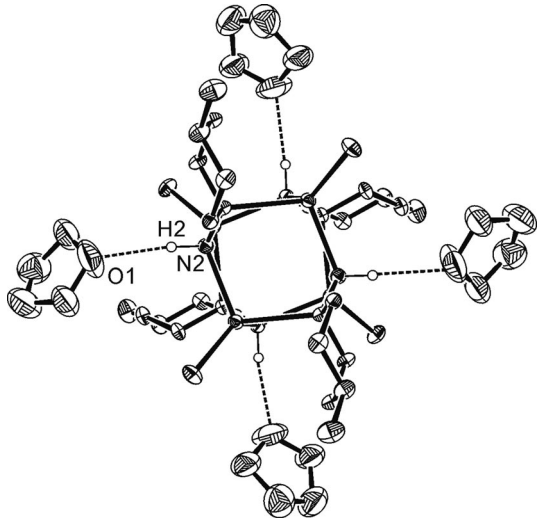

Figure 4. Hydrogen bonding between THF and the N–H hydrazide units in **4**.

The tetrameric cage structure of **4** is also adopted by several zinc,[2] aluminium and gallium hydrazides.[1,12]

Conclusions

Two new organocadmium hydrazine adducts have been identified, which incorporate either a discrete six-membered Cd_2N_4 ring (**1**) or a polymeric chain reinforced by hydrogen bonds (**2**). Compound **2** was photolytically converted into the tetrameric hydrazide **4**, which is only the second reported example of an organocadmium hydrazide.

Experimental Section

General Procedures: Elemental analyses were performed with an Exeter Analytical CE 440 analyser. ^{1}H, ^{13}C and ^{113}Cd NMR spectra were recorded with either a Bruker Avance 500 MHz or 300 MHz FT-NMR spectrometer as saturated solutions in $CDCl_3$ or [D_8]toluene; chemical shifts are in ppm with respect to either Me_4Si (^{1}H, ^{13}C) or Me_2Cd (^{113}Cd); coupling constants are in Hz. All reactions were carried out under an inert gas by using standard Schlenk techniques. Solvents were dried and degassed under argon with activated alumina columns by using an Innovative Technology solvent purification system. *tert*-Butylhydrazine and 1-amino-4-methylpiperazine were purchased from Aldrich and dried with molecular sieves (4 Å); $CdMe_2$ was a gift from SAFC Hitech.

Synthesis of $[Me_2CdNH_2NHC(CH_3)_3]_2$ (1): Dimethylcadmium (2 mL, 2 M solution in toluene, 4 mmol) was added to hexane (5 mL). *tert*-Butylhydrazine was added (0.37 mL, 4 mmol), and the mixture was stirred. Crystals of **1** appeared on cooling to –20 °C (0.62 g, 71%). M.p. 45 °C, 80 °C bubbled, 115 °C decomposed. $C_6H_{18}CdN_2$ (230.56): calcd. C 31.0, H 7.8, N 12.1; found C 31.0, H 7.4, N 11.7. ^{1}H NMR (500 MHz, [D_8]THF, 298 K): δ = –0.80 (br., s, 6 H, $CdCH_3$), 0.58 (s, 9 H, CH_3), 1.92 (br., s, 1 H, NH), 2.20 (br., s, 2 H, NH_2) ppm. ^{13}C NMR (125.76 MHz, [D_8]THF, 298 K): δ = –4.0 (br., $CdCH_3$), 26.3 (CH_3), 52.7 (NHC) ppm. ^{113}Cd NMR (110.99 MHz, [D_8]THF, 298 K): δ = –0.56 ppm. ^{1}H NMR (500 MHz, [D_8]THF, 218 K): δ = –0.63 [br., s, $^{2}J(^{113,111}CdH)$ = 49.4 Hz, 6 H, $CdCH_3$, unresolved], 0.40 (s, 12 H, CH_3), 2.15 (br., s, 2 H, NH_2), 2.42 (br., s, 1 H, NH) ppm. ^{13}C NMR (125.76 MHz, [D_8]THF, 218 K): δ = –5.9 [$CdCH_3$, $^{1}J(^{113,111}CdC)$ = 578, 534 Hz], 25.9 (CH_3), 51.3 (NHC) ppm. ^{113}Cd NMR (110.99 MHz, [D_8]THF, 218 K): δ = –12.3 ppm.

Synthesis of $[Me_2CdNH_2N(CH_2)_4NCH_3]_\infty$ (2): Dimethylcadmium (2 mL, 2 M solution in hexane, 4 mmol) was added to hexane (5 mL). 1-Amino-4-methylpiperazine was added (0.47 mL, 4 mmol), and the mixture was stirred. Crystals of **2** precipitated out of solution (0.98 g, 94%). M.p. 60 °C started to sublime, 85 °C started to bubble, 150 °C violently released gas and decomposed. $C_7H_{19}CdN_3$ (257.57): calcd. C 32.4, H 7.4, N 16.2; found C 32.1, H 7.5, N 15.1. ^{1}H NMR (300 MHz, [D_8]THF, 298 K): δ = –0.85 (br., s, 6 H, $CdCH_3$), 1.97 (s, 3 H, NCH_3), 2.17 (br., s, 4 H, NCH_2), 2.34 (br., s, 4 H, NCH_2), 2.93 (br., s, 2 H, NH_2) ppm. ^{13}C NMR (74.49 MHz, [D_8]THF, 298 K): δ = –7.7 (br., $CdCH_3$), 45.5 (NCH_3), 55.5 (NCH_2), 59.6 (NCH_2) ppm. ^{113}Cd NMR (110.99 MHz, [D_8]THF, 298 K): δ = –39.3 ppm. ^{1}H NMR (500 MHz, [D_8]THF, 248 K): δ = –0.92 [s, 6 H, $CdCH_3$, $^{2}J(^{113,111}CdH)$ = 50.4 Hz, unresolved], 1.88 (br., m, 2 H, NCH_2), 1.96 (s, 3 H, NCH_3), 1.99 (br., m, 2 H, NCH_2), 2.43 (br., m, 2 H, NCH_2), 2.69 (br., m, 2 H, NCH_2) 3.07 (br., s, 2 H, NH_2) ppm. ^{13}C NMR (125.76 MHz, [D_8]THF, 248 K): δ = –10.6 (br., $CdCH_3$), 43.0 (NCH_3), 52.6 (NCH_2), 57.0 (NCH_2) ppm.

Synthesis of $[MeCdN(H)N(CH_2)_4NMe]_4$ (4): Dimethylcadmium (2 mL, 2 M solution in hexane, 4 mmol) was added to THF (10 mL) and cooled to –78 °C. 1-Amino-4-methylpiperazine (0.47 mL, 4 mmol) was added, and the mixture was warmed to room temperature and stirred for 1 week with exposure to daylight. The solution was then stored at –20 °C, and crystals of **4** formed (0.64 g, 70%). M.p. 147 °C. After drying in vacuo, the product was analysed as **4**·THF. $C_{28}H_{68}Cd_4N_{12}O$ (1038.6): calcd. C 32.4, H 6.6, N 16.2; found C 32.8, H 7.4, N 15.8. ^{1}H NMR (300 MHz, [D_8]THF, 298 K): δ = –0.69 [s, $^{2}J(^{113,111}CdH)$ = 61.7 Hz, 3 H, $CdCH_3$, unresolved], 2.06 (s, 3 H, NCH_3), 2.21 (br., s, 2 H, NCH_2), 2.41 (br., m, 4 H, NCH_2), 3.02 (br., m, 2 H, NCH_2), 3.42 (br., s, 1 H, NH) ppm. ^{13}C NMR (74.49 MHz, [D_8]THF, 298 K): δ = –11.2 (br., $CdCH_3$), 45.0 (NCH_3), 53.1 (NCH_2), 65.7 (NCH_2) ppm. ^{113}Cd NMR (110.99 MHz, [D_8]THF, 298 K): δ = –155.3 ppm.

Crystallography: Experimental details relating to the single-crystal X-ray crystallographic studies are summarised in Table 1. For all structures, data were collected with a Nonius Kappa CCD dif-

Table 1. Crystallographic data for **1**–**3**.

	1	**2**	**4**·4THF
Empirical formula	$C_{12}H_{36}Cd_2N_4$	$C_{14}H_{38}Cd_2N_6$	$C_{40}H_{92}Cd_4N_{12}O_4$
Formula mass	461.25	515.30	1254.86
Crystal system	monoclinic	triclinic	tetragonal
Space group	$P2_1/n$	$P\bar{1}$	$I\bar{4}$
a [Å]	11.9337(3)	7.3703(7)	16.2997(2)
b [Å]	6.7285(2)	11.2981(13)	16.2997(2)
c [Å]	13.2770(4)	13.0952(12)	10.4058(2)
α [°]		78.614(6)	
β [°]	112.887(1)	83.606(6)	
γ [°]		88.649(6)	
V [Å^3]	982.16(5)	1062.33(19)	2764.62(7)
Z	2	2	2
$\rho_{calcd.}$ [Mg m^{-3}]	1.560	1.611	1.507
μ(Mo-K_α) [mm^{-1}]	2.158	2.007	1.563
F(000)	464	520	1280
Crystal size [mm]	0.25 × 0.20 × 0.05	0.30 × 0.10 × 0.01	0.40 × 0.30 × 0.20
θ range [°]	3.71–30.07	4.79–25.11	3.41–27.46
Reflections collected	15217	10020	21535
Independent reflections [R(int)]	2868 [0.0648]	3656 [0.1150]	3177 [0.0492]
Reflections observed (> 2σ)	2047	2660	3086
Data completeness	0.994	0.965	0.998
Max., min. transmission	0.8998, 0.6145	0.9802, 0.5842	0.7303, 0.5622
Goodness-of-fit	1.042	1.136	1.102
Final R_1, wR_2 [I > 2σ(I)]	0.0363, 0.0711	0.1036, 0.2574	0.0248, 0.0584
Final R_1, wR_2 (all data)	0.0671, 0.0810	0.1320, 0.2774	0.0260, 0.0592
Largest diff. peak, hole [e Å^{-3}]	1.853, –1.017	3.002, –1.409	0.478, –1.132
Flack parameter			0.35(3)

fractometer at 150(2) K by using Mo-K_α radiation (λ = 0.71073 Å). Structure solution was followed by full-matrix least-squares refinement, which was performed by using the WinGX-1.70 suite of programmes.[13] A semiempirical absorption correction from equivalents was made in all cases. For **1**, **2** and **4**, hydrogen atoms were included at calculated positions, although for **1** and **4** hydrogen atoms attached to nitrogen atoms were located in the difference map and refined; in the case of **2**, the data were of too low quality to allow this. The asymmetric unit of **2** consists of two essentially equivalent molecules, whereas that of **4** incorporates one solvent molecule (THF) per formula unit; analytical data after pumping dry are consistent with retention of one THF per tetrameric unit. CCDC-835247 (for **4**), -835248 (for **1**) and -835249 (for **2**) contain the supplementary crystallographic data for this paper. These data can be obtained free of charge from The Cambridge Crystallographic Data Centre via www.ccdc.cam.ac.uk/data_request/cif.

Acknowledgments

We thank the Engineering and Physical Sciences Research Council (EPSRC) for a doctoral training award (to N. H.).

[1] W. Uhl, *Aluminium and Gallium Hydrazides*, Springer-Verlag, Berlin, **2003**, vol. 105.
[2] a) S. Jana, R. Fröhlich, N. W. Mitzel, *Chem. Eur. J.* **2006**, *12*, 592; b) C. Redshaw, M. R. J. Elsegood, *Chem. Commun.* **2006**, 523; c) S. Jana, R. Fröhlich, N. W. Mitzel, *Chem. Eur. J.* **2006**, *12*, 3936; d) S. Jana, R. Fröhlich, N. W. Mitzel, *Z. Anorg. Allg. Chem.* **2008**, *634*, 1477.
[3] A. L. Johnson, N. Hollingsworth, G. Kociok-Köhn, K. C. Molloy, *Inorg. Chem.* **2008**, *47*, 9706.
[4] A. L. Johnson, N. Hollingsworth, A. Kingsley, G. Kociok-Köhn, K. C. Molloy, *Organometallics* **2009**, *28*, 2650–2653.
[5] a) J. E. House Jr., A. J. Vandenbrook, *Thermochim. Acta* **1990**, *161*, 85–88; b) J. E. House Jr., A. J. Vandenbrook, *Thermochim. Acta* **1989**, *150*, 79–86; c) B. Banerjee, N. R. Chaudhuri, *Thermochim. Acta* **1983**, *71*, 93–105; d) K. C. Patil, C. Nesamani, V. R. P. Verneker, *Synth. React. Inorg. Met.-Org. Chem.* **1982**, *12*, 383–395; e) R. Y. Aliev, M. N. Guseinov, G. Gasanov, *Tezisy Resp. Nauchn. Konf. Molodykh Uch.-Khim. Azerb.* **1974**, 111–112; f) N. A. Aliev, G. K. Abdullaev, R. Y. Aliev, N. M. Guseinov, A. D. Kuliev, *Zh. Neorg. Khim.* **1973**, *18*, 844–845.
[6] M. J. Almond, M. P. Beer, M. G. B. Drew, D. A. Rice, *Organometallics* **1991**, *10*, 2072.
[7] P. O'Brien, M. B. Hursthouse, M. Motevalli, J. R. Walsh, A. C. Jones, *J. Organomet. Chem.* **1993**, *449*, 1.
[8] X. Wang, H. Sun, X. Sun, X. You, X. Huang, *Acta Crystallogr., Sect. C: Cryst. Struct. Commun.* **1995**, *51*, 1754.
[9] M. J. Almond, M. P. Beer, M. G. B. Drew, D. A. Rice, *J. Organomet. Chem.* **1991**, *421*, 129.
[10] M. Karplus, *J. Am. Chem. Soc.* **1963**, *85*, 2870.
[11] R. R. Wenner, A. O. Beckman, *J. Am. Chem. Soc.* **1932**, *54*, 2787.
[12] a) W. Uhl, T. Abel, E. Hagemeier, A. Hepp, M. Layh, B. Rezaeirad, H. Luftmann, *Inorg. Chem.* **2011**, *50*, 325–335; b) W. Uhl, T. Abel, A. Hepp, S. Grimme, M. Steinmetz, *Eur. J. Inorg. Chem.* **2008**, 543–551; c) W. Uhl, T. Abel, J. Koster, B. Rezaeirad, *Z. Anorg. Allg. Chem.* **2009**, *635*, 1014–1022; d) W. Uhl, E. Hagemeier, M. Layh, B. Rezaeirad, J. Kosters, E. U. Wurthwein, N. Ghavtadze, W. Massa, *Eur. J. Inorg. Chem.* **2011**, 1733–1743.
[13] L. J. Farrugia, *J. Appl. Crystallogr.* **1999**, *32*, 837.

Received: August 23, 2011
Published Online: November 4, 2011

DOI: 10.1002/ejic.201101000

Atomic Layer Deposition of Titanium and Vanadium Oxide on Mesoporous Silica and Phenol/Formaldehyde Resins – the Effect of the Support on the Liquid Phase Epoxidation of Cyclohexene

Ilke Muylaert,[a] Jan Musschoot,[b] Karen Leus,[a] Jolien Dendooven,[b] Christophe Detavernier,[b] and Pascal Van Der Voort*[a]

Keywords: Mesoporous materials / Heterogeneous catalysis / Epoxidation / Atomic layer deposition / Supported metal oxides

Titanium and vanadium oxide layers have been grown in the pores of two 2D hexagonal ordered mesoporous materials: SBA-15 (silica) and FDU-15 (phenol/formaldehyde resin). The deposition of the layers was controlled by the self-limiting reaction of the metal oxide precursor with the hydroxyl surface. Single, multiple and mixed titanium and vanadium oxide layers have been synthesised, and the influence of the layer type on the catalytic performance in the liquid phase epoxidation of cyclohexene has been evaluated. The effect of the support on the catalytic behaviour is discussed, and a reaction mechanism is proposed. The support–oxygen–metal bond is assumed to be critical for catalytic epoxidation.

Introduction

Supported titanium and vanadium oxide catalysts are widely used in modern heterogeneous catalysis.[1] In this field, ordered mesoporous materials have become increasingly attractive as supports due to their high surface areas, large pore volumes and uniform pore sizes. Since the discovery of the M41S materials, a huge number of mesoporous materials with different morphologies and surface properties have been developed, from inorganic materials to hybrid inorganic–organic and purely organic structures.[2]

Catalyst preparation generally involves the liquid phase impregnation of these mesoporous supports with a metal salt solution. Although catalysts with high metal loadings can be prepared by liquid phase impregnation, monolayers of highly dispersed and isolated sites are not easily achieved. In particular oligo- and polymerisation of the dispersed metal sites, coalescence, clustering and crystallisation of the metal oxide particles are the main drawbacks.[3–6]

Atomic layer deposition (ALD) is a powerful technique that allows controlled gas phase deposition of metal oxide monolayers on the surface of ordered mesoporous materials.[7] The method is based on the sequential exposure of the mesoporous support to a volatile metal-containing precursor and a reactive gas. During an ALD pulse, the gas reacts with the substrate in a self-limiting fashion, which results in excellent step coverage. A single ALD cycle includes four steps: (1) exposure of the hydroxyl surface of the support to the titanium or vanadium oxide precursor in the gas phase. The self-limiting nature of the reaction between the surface hydroxyl groups and the metal oxide precursor avoids metal oxide clustering, and well dispersed monomer particles are obtained, (2) a degassing stage to remove the excess metal precursor and reacted side groups, (3) a water pulse to hydrolyse the side groups and regenerate a new reactive hydroxyl surface and (4) a second degassing step. The metal oxide loading can be controlled from submonolayer to monolayer loading. Moreover, multiple oxide layers can be deposited by additional ALD cycles. Finally, ALD allows the controlled deposition of mixed metal oxide layers by performing consecutive cycles with different metal oxide precursors. The application of ALD to nanoporous materials, can lead to the modification of both the pore size[8,9] and the catalytic activity[10,11] in a controlled way. Several groups have published the successful synthesis of catalysts by ALD for different catalytic reactions.[12–15]

In this study, vanadium and titanium oxide layers were deposited by ALD on the surface of two mesoporous materials: mesoporous silica (SBA-15) and mesoporous phenol/formaldehyde resin (FDU-15). Three different types of catalysts were synthesised: (1) single titanium and vanadium oxide layers with submonolayer to monolayer loadings, (2) multiple (mono, double and triple) titanium or vanadium oxide layers and (3) mixed titanium and vanadium oxide layers. An overview of the supported SBA-15 and FDU-15 catalysts with the different layer types is given in Table 4.

[a] Ghent University, Department of Inorganic and Physiscal Chemistry, Centre for Ordered Materials, Organometallics and Catalysis,
Krijgslaan 281 – S3, 9000 Ghent, Belgium
Fax: +32-92644983
E-mail: Pascal.VandDerVoort@UGent.be
[b] Ghent University, Department of Solid State Sciences, Krijgslaan 281 – S1, 9000 Ghent, Belgium

All of the catalysts were evaluated in the epoxidation of cyclohexene and their influence on the catalytic activity and selectivity towards the epoxide was examined. Furthermore, the stability and regeneration capacity were evaluated in consecutive catalytic runs. The effect of the support is discussed, and a reaction mechanism is proposed.

Results and Discussion

SBA-15 and FDU-15 were functionalised with titanium and vanadium oxide layers using ALD. These materials, both developed by Zhao et al., exhibit high specific surface areas and contain uniform mesopores, which are interconnected by irregular micropores. In contrast to the siloxane based walls of the inorganic SBA-15 support, the FDU-15 support consists of a porous 3D cross-linked polymer network of aromatic rings and phenolic hydroxyl groups. We have previously shown that FDU-15 is much more stable than SBA-15, both mechanically and hydrothermally.[16] Moreover, these mesoporous resins exhibit a strong degree of leaching resistance as the support–oxygen–metal bond is not sensitive to hydrolysis.[16] This is explained by the more hydrophobic nature of the polymer surface and the more basic character of the phenol group (phenol pK_a = 10 vs. silanol pK_a = 2.2), which shows a strong affinity to the acidic metal centres. Due to these unique features, FDU-type solids have attracted intensive attention as porous supports in catalysis.[17–23]

The nitrogen isotherms and pore size distributions of SBA-15 and FDU-15 are shown in Figure 1. For both materials, a distinct capillary condensation step in the adsorption branch is observed, which indicates a narrow pore size distribution. However, FDU-15 shows a slightly broader distribution. The textural properties of the mesoporous catalysts are summarised in Table 1.

The catalysts were evaluated for their catalytic performance in the liquid phase oxidation of cyclohexene (**1**). The major reaction products are shown in Scheme 1. Three pathways are apparent: (a) epoxidation, (b) a radical pathway between the substrate and the oxidant, *tert*-butyl hydroperoxide, and (c) allylic oxidation. In the presence of water, the epoxide ring can open due to the nucleophilic attack of water on the electrophilic carbon centre of the epoxide to form the *trans*-diol isomer **3**. Usually, the products of pathways (b) and (c) are not considered to be useful

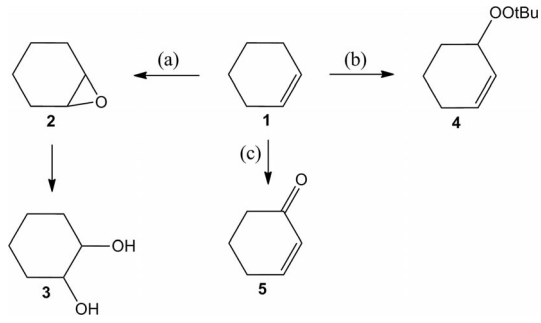

Scheme 1. Oxidation of **1** towards the main reaction products: (a) epoxidation to cyclohexene oxide (**2**) and consecutive ring opening to cyclohexane-1,2-diol (**3**), (b) a radical pathway to *tert*-butyl 2-cyclohexen-1-yl peroxide (**4**) and (c) allylic oxidation to 2-cyclohexene-1-one (**5**).

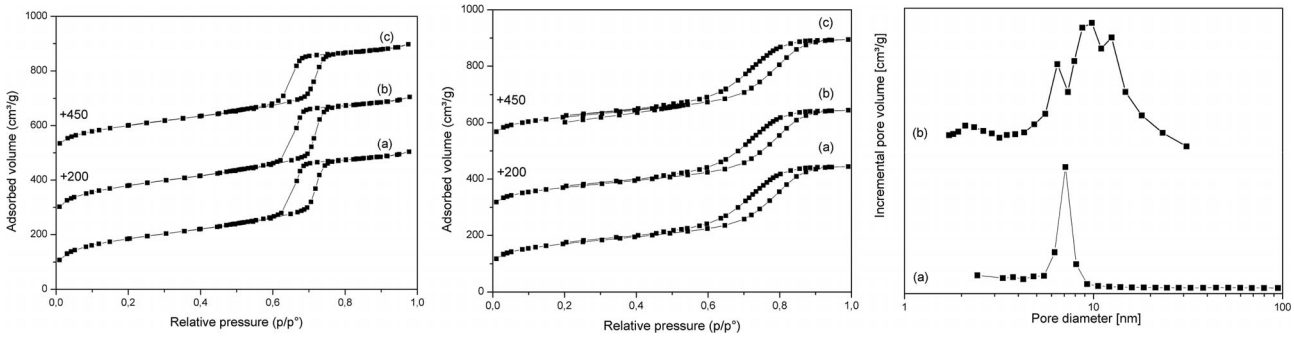

Figure 1. Left: Nitrogen sorption isotherms of (a) SBA-15, (b) TiO_2/SBA-15 (1.08 Ti/nm^2) and (c) TiO_2/SBA-15 after the catalytic run. Middle: Nitrogen sorptions isotherms of (a) FDU-15, (b) TiO_2/FDU-15 (0.59 Ti/nm^2) and (c) TiO_2/FDU-15 after the catalytic run. Right: Pore size distributions of (a) SBA-15 and (b) FDU-15.

Table 1. Textural properties of the titanium and vanadium oxide monolayer SBA-15 and FDU-15 catalysts.

SBA-15	Ti/V Loading [nm^{-2}]	S_{BET}[a] [m^2/g]	Pore size[b] [nm]	Pore volume[c] [cm^3/g]	FDU-15	Ti/V Loading [nm^{-2}]	S_{BET}[a] [m^2/g]	Pore size[b] [nm]	Pore volume[c] [cm^3/g]
SBA-15	–	654	6.40	0.74	FDU-15	–	731	9.31	0.67
TiO_2/SBA-15	1.08	670	6.42	0.73	TiO_2/FDU-15	0.59	722	9.31	0.65
TiO_2/SBA-15, after run I)	0.67	547	6.39	0.69	TiO_2/FDU-15, after run I)	0.59	610	9.30	0.58
VO_x/SBA-15	0.97	648	6.39	0.71	VO_x/FDU-15	0.56	732	9.29	0.68
VO_x/SBA-15, after run I)	0.68	598	6.40	0.70	VO_x/FDU-15, after run I)	0.53	633	9.30	0.61

[a] Specific surface area. [b] Mean pore size calculated from the adsorption branch. [c] Total pore volume.

byproducts, however, they can give very useful, diagnostic insights into the catalytic pathway.

A blank experiment was performed prior to the catalytic tests, and the results are summarised in Tables 2 and 3. The blank test was carried out in dry chloroform with *tert*-butyl hydroperoxide as the oxidant at 80 °C. In the presence of the support, a relatively high conversion of **1** (≈ 20%) was observed. Only a very small amount of **2** was detected (≈ 2%), and the main product formed was **4** (≈ 85%). In order to investigate whether the support itself is responsible for this relatively high conversion, an additional blank experiment without catalyst support was performed and similar conversion values were observed. For these reasons, the catalyst support is not thought to be critical for the reaction towards **4**.

The proposed reaction mechanism towards **4** occurs by a radical pathway as shown in Scheme 2. Initially, a *tert*-butoxy radical is formed by breaking the peroxide bond in *tert*-butyl hydroperoxide. These radicals react with **1** and *tert*-butyl hydroperoxide to form the corresponding radicals in the propagation stage. Finally, the cyclohexene and peroxide radicals react to form the peroxide adduct in the termination step. In addition, very small quantities of other radical products were formed, for instance 2-cyclohexen-1-ol, which was due to the reaction between $^{\cdot}$OH and CH$^{\cdot}$ radicals.

Initiation:	tBuOOH → tBuO$^{\bullet}$ + $^{\bullet}$OH	(1)
Propagation:	tBuO$^{\bullet}$ + CH → CH$^{\bullet}$ + tBuOH	(2)
	tBuO$^{\bullet}$ + TBHP → tBuOH + tBuOO$^{\bullet}$	(3)
Termination:	CH$^{\bullet}$ + tBuOO$^{\bullet}$ → CHOOtBu	(4)
	CH$^{\bullet}$ + $^{\bullet}$OH → CH-OH	(5)

Scheme 2. Proposed reaction mechanism for the formation of **4** by a radical pathway (tBuOOH = **4**, CH = cyclohexene, CH–OH = 2-cyclohexen-1-ol).

In the following sections, the influence of the layer type on the catalytic behaviour in the liquid phase epoxidation of **1** is discussed in terms of activity and selectivity for both the SBA-15- and FDU-15-supported catalysts.

Titanium and Vanadium Oxide (Sub)monolayers on SBA-15 and FDU-15

The hydroxyl surface of the mesoporous SBA-15 and FDU-15 supports was functionalised by performing one ALD cycle with titanium or vanadium oxide. By variation

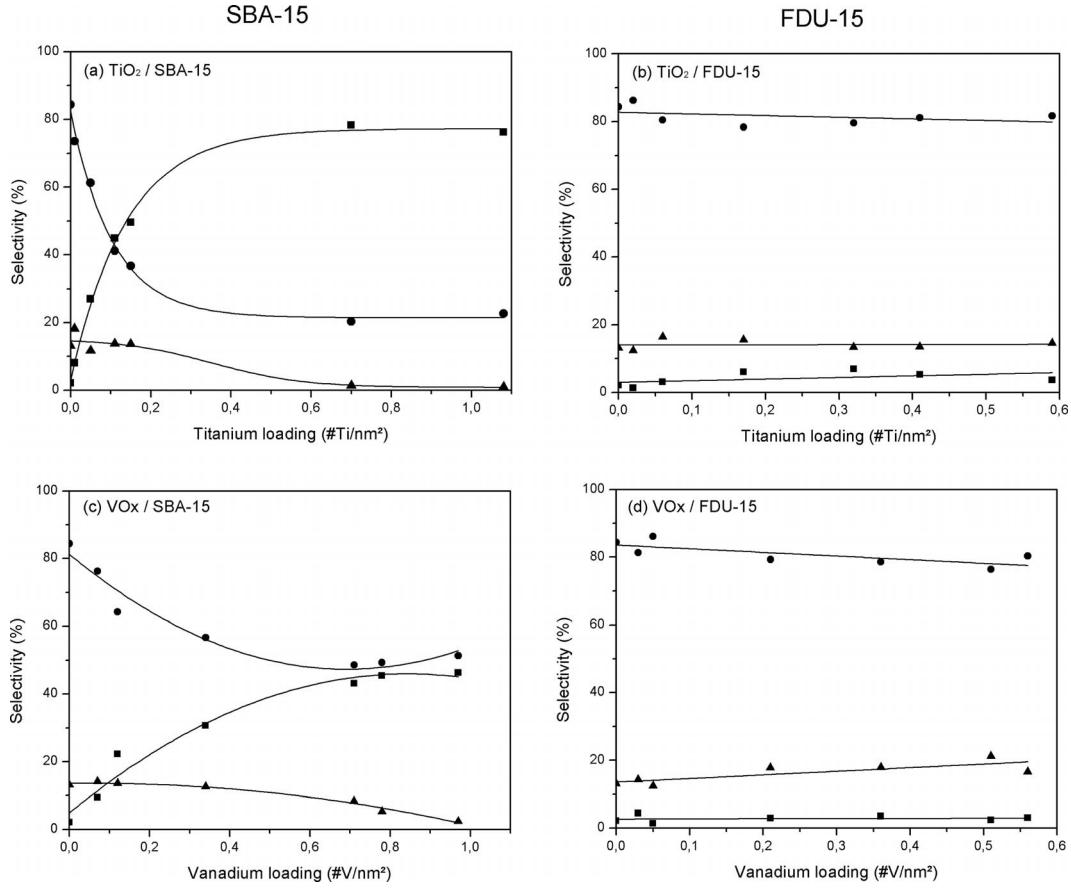

Figure 2. Overview of the selectivity of cyclohexene epoxidation for the SBA-15- and FDU-15-supported catalysts: (a,b) influence of the titanium oxide loading and (c,d) influence of the vanadium oxide loading (■ = **2**, ● = **4**, ▲= **5**). The selectivity was determined after 8 h.

of the exposure time to the metal oxide precursor, the metal oxide loading was controlled with loadings from submonolayer to monolayer. The saturation of the monolayer was determined by the observation of a plateau at 1.08 Ti/nm^2 and 0.98 V/nm^2 for SBA-15. For the FDU-15 support, the maximum loading was estimated at 0.59 Ti/nm^2 and 0.53 V/nm^2.

The nature of the deposited catalytically active species was investigated by X-ray diffraction and spectroscopic measurements (see Supporting Information). For all the supported catalysts, no crystalline TiO_2 (anatase or rutile) or V_2O_5 peaks were observed in the XRD patterns. For the SBA-15 materials, additional Raman and UV/Vis spectroscopic measurements confirmed the presence of unsaturated four-coordinate vanadium and titanium oxide centres, which correspond to amorphous tetrahedral and highly dispersed metal oxide sites. For the FDU-15 catalysts, the covalent support–oxygen–metal bonding was determined by the presence of a new absorption peak at 1010 cm^{-1} in the diffuse reflection IR Fourier transform (DRIFT) spectrum.[16]

The catalytic activity and selectivity of the supported SBA-15 and FDU-15 catalysts with different metal oxide loadings are summarised in Table 2 (a) and Figure 2. The activity of the SBA-15-supported titanium catalyst increased with increasing titanium loading. Determined after 8 h of reaction, the conversion increased from 20–54% for the 0.01 Ti/nm^2 and the 1.08 Ti/nm^2 samples, respectively. In contrast to the conversion of **1**, the catalytic selectivity changed drastically with increasing titanium loading. Figure 2 (a) shows the selectivity towards the three main reaction products vs. titanium loading. Other byproducts account for less than 1%. Herein, the selectivity is calculated as the percentage of the reactant converted into the specific reaction product after 8 h. Figure 2 (a) clearly shows that, with increasing titanium loading, the radical pathway towards **4** is significantly suppressed advantageously to the formation of **2**, which are both expressed in absolute

Table 2. Catalytic properties of (a) SBA-15- and (b) FDU-15-supported catalysts with submonolayer to monolayer loading: influence of the titanium and vanadium oxide loading in oxidation of **1**.

(a) SBA-15 catalysts

Ti loading [Ti/nm^2]	Conversion[a] [%]	**2**[b] [%]	**5**[b] [%]	**4**[b] [%]	TON[c]	TOF[d] [h^{-1}]
–	18.3 (2.7)	2.1 (0.1)	13.1 (0.4)	84.4 (2.3)	61	17
0.01	20.9 (3.1)	8.1 (0.3)	18.2 (0.6)	73.6 (2.3)	52	12
0.05	17.4 (2.6)	27.0 (0.7)	11.7 (0.3)	61.3 (1.6)	53	11
0.11	24.7 (3.7)	44.9 (1.7)	13.8 (0.5)	41.2 (1.5)	45	9
0.15	28.4 (4.3)	49.6 (2.1)	13.7 (0.6)	36.7 (1.6)	24	5
0.70	43.9 (6.5)	78.3 (5.1)	1.4 (0.1)	20.3 (1.3)	20	6
1.08	53.8 (8.0)	76.3 (6.1)	1.0 (0.1)	22.7 (1.8)	15	4
V loading [V/nm^2]	Conversion[a] [%]	**2**[b] [%]	**5**[b] [%]	**4**[b] [%]	TON[c]	TOF[d] [h^{-1}]
0.07	19.6 (2.9)	9.5 (0.3)	14.2 (0.4)	76.3 (2.2)	16	12
0.12	20.6 (3.1)	22.2 (0.7)	13.6 (0.4)	64.2 (2.0)	11	11
0.34	33.4 (5.0)	30.7 (1.5)	12.6 (0.6)	56.7 (2.8)	13	8
0.71	48.7 (7.3)	43.1 (3.1)	8.3 (0.6)	48.6 (3.5)	7	4
0.78	49.6 (7.4)	45.4 (3.4)	5.3 (0.4)	49.3 (3.6)	13	3
0.97	55.2 (8.2)	46.3 (3.8)	2.4 (0.2)	51.3 (4.2)	12	4

(b) FDU-15 catalysts

Ti loading [Ti/nm^2]	Conversion[a] [%]	**2**[b] [%]	**5**[b] [%]	**4**[b] [%]	TON[c]	TOF[d] [h^{-1}]
0.02	17.2 (2.6)	1.3 (0.0)	12.4 (0.3)	86.3 (2.2)	0	0
0.06	21.6 (3.2)	3.1 (0.1)	16.4 (0.5)	80.5 (2.6)	0	0
0.17	23.5 (3.5)	6.1 (0.2)	15.5 (0.5)	78.4 (2.7)	5	2
0.32	26.1 (3.9)	7.0 (0.3)	13.4 (0.5)	79.6 (3.1)	5	3
0.41	25.7 (3.9)	5.3 (0.2)	13.5 (0.5)	81.2 (3.2)	4	2
0.59	24.6 (3.7)	3.7 (0.1)	14.6 (0.5)	81.7 (3.0)	3	2
V loading [V/nm^2]	Conversion[a] [%]	**2**[b] [%]	**5**[b] [%]	**4**[b] [%]	TON[c]	TOF[d] [h^{-1}]
0.03	22.3 (3.3)	4.4 (0.1)	14.3 (0.5)	81.3 (2.7)	2	1
0.05	24.1 (3.6)	1.4 (0.1)	12.4 (0.4)	86.2 (3.1)	2	3
0.21	21.9 (3.3)	2.9 (0.1)	17.8 (0.6)	79.3 (2.6)	3	2
0.36	22.4 (3.4)	3.5 (0.1)	17.9 (0.6)	78.6 (2.7)	3	2
0.51	26.5 (4.0)	2.4 (0.1)	21.2 (0.8)	76.4 (3.1)	2	1
0.56	27.0 (4.0)	3.0 (0.1)	16.6 (0.7)	80.4 (3.2)	2	1

[a] Total conversion of **1** after 8 h. [b] The numbers in brackets represent the absolute amount of the product [mmol]. [c] TON = turn over number as the amount of **2** [mmol] formed per mmol Ti or V (after 8 h). [d] TOF = turn over frequency as the amount of **2** [mmol] formed per mmol Ti or V per hour (after 1 h).

amounts. In addition, the allylic oxidation towards **5** remained initially constant (13%) and then decreased with increasing titanium loading.

By comparison of the SBA-15-supported titanium oxide catalysts (Figure 2, a) with the vanadium oxide catalysts (Figure 2, c), a trend can be observed: the selectivity towards the epoxide product increases with increasing vanadium loading. In addition, there are two main differences between the titanium- and vanadium-based catalysts: (1) for similar metal oxide loadings, the vanadium oxide catalysts show higher conversions of **1**, which is clearly represented by the higher turnover numbers (calculated as the number of molecules of **1** converted per metal oxide centre) for the vanadium catalysts (Table 2, a) and (2) for monolayer loadings, the selectivity towards the epoxide is significantly lower for the vanadium oxide catalysts. The selectivity towards **2** reaches a plateau at 50% epoxide vs. the plateau at 80% epoxide for the titanium-based catalysts.

To compare the effect of the support on the catalytic activity, titanium and vanadium oxide submonolayers and monolayers were also deposited on the FDU-15 support. The results of the performance of these catalysts are summarised in Table 2 (b) and Figure 2 (b and d). From these data, an interesting trend can be observed for both the FDU-15-supported titanium and vanadium oxide catalysts. Relatively high total conversions of **1** were obtained, however, the main product formed was **4**. In contrast to the SBA-15-supported catalysts, the metal oxide loading on the FDU-15 support did not influence the selectivity. Moreover, the yield of **2** does not exceed that of the blank test, which indicates that the FDU-15-supported metal oxide centres are (nearly) not catalytically active in the epoxidation of **1** with *tert*-butyl hydroperoxide.

Titanium and Vanadium Oxide Multilayers and Mixed Layers on SBA-15 and FDU-15

SBA-15 and FDU-15 were functionalised with multiple metal oxide layers (mono-, double and triple) and with mixed titanium/vanadium oxide layers. Table 3 and Figure 3 summarise the influence of the support and the layer type on the catalytic performance in the liquid phase oxidation of **1**.

Figure 3 (a) shows that the total conversion and the selectivity towards **2** is only slightly influenced by additional layers. This trend is also observed for the SBA-15-supported vanadium oxide catalyst in Figure 3 (c): a second or third oxide layer did not alter the product selectivity distribution significantly. For the mixed titanium/vanadium oxide layers supported on SBA-15, however, the selectivity towards **2** drastically increased for the titanium oxide catalysts with a vanadium oxide interlayer. This catalyst shows a maximum selectivity of ca. 85% for **2**. No significant change in catalytic performance was observed for the catalyst with titanium oxide as the interlayer and vanadium oxide as the top layer, which is in agreement with the general trend, i.e. the vanadium-based catalysts show generally lower selectivity for **2** than the titanium-based catalysts.

The results of the multiple and mixed metal oxide layers on FDU-15 are shown in Figure 3 (b, d and f). In contrast to the SBA-15 catalyst, the type of metal oxide layer does not influence the catalytic activity, which indicates that the FDU-15 catalyst is not active in the epoxidation of **1**. An explanation of these results is given below.

Catalyst Stability and Regeneration Capability

To examine the morphology and stability of the support during ALD and the catalytic oxidation cycles, the catalysts were studied by nitrogen sorption measurements. Figure 1 depicts the nitrogen sorption isotherms of the original SBA-15 and FDU-15 supports, the supports after metal oxide deposition and after the first catalytic run. The porosity properties are summarised in Table 1. Concerning the ALD process, from these data it can be concluded that the deposition process has no significant influence on the porosity characteristics of the mesoporous support. Additionally, the H1-type hysteresis loop was preserved, which indicates that the pores were not blocked. These properties indicate that the metal precursors do not clog the pore opening with longer deposition times but diffuse uniformly through the pores. After the first catalytic cycle, the specific surface area and the total pore volume of the catalysts were slightly reduced.

In case of the titanium (1.08 Ti/nm^2) and vanadium (0.97 V/nm^2) monolayer SBA-15 catalysts, leaching after

Table 3. Catalytic properties of SBA-15- and FDU-15-supported catalysts with multiple oxide layers and mixed oxide layers.

SBA-15 Layer type	Conversion[a] [%]	**2** [%]	**5** [%]	**4** [%]	FDU-15 Conversion[a] [%]	**2** [%]	**5** [%]	**4** [%]
–O–Ti–O–Ti–OH	60.3 (9.0)	78.1 (7.0)	3.8 (0.3)	18.1 (1.6)	23.1 (3.5)	3.3 (0.1)	2.9 (0.1)	93.8 (3.3)
–O–Ti–O–Ti–O–Ti–OH	55.7 (8.4)	76.5 (6.4)	2.6 (0.2)	20.9 (1.8)	22.2 (3.3)	7.4 (0.2)	6.9 (0.2)	85.7 (2.8)
–O–V–O–V–OH	62.4 (9.4)	52.1 (4.9)	4.6 (0.4)	43.3 (4.1)	25.6 (3.8)	3.3 (0.1)	5.1 (0.2)	91.6 (3.5)
–O–V–O–V–O–V–OH	63.2 (9.5)	53.7 (8.0)	3.2 (0.3)	43.1 (1.2)	24.8 (3.7)	4.1 (0.2)	5.0 (0.2)	90.9 (3.4)
–O–Ti–O–V–OH	52.6 (6.8)	72.9 (5.0)	0.7 (0.0)	26.4 (1.8)	23.9 (3.6)	3.2 (0.1)	4.3 (0.2)	92.5 (3.3)
–O–V–O–Ti–OH	60.2 (9.0)	84.4 (7.6)	0.9 (0.1)	14.7 (1.3)	21.6 (3.2)	4.8 (0.2)	3.5 (0.1)	91.7 (2.9)

[a] Total cyclohexene conversion after 8 h.

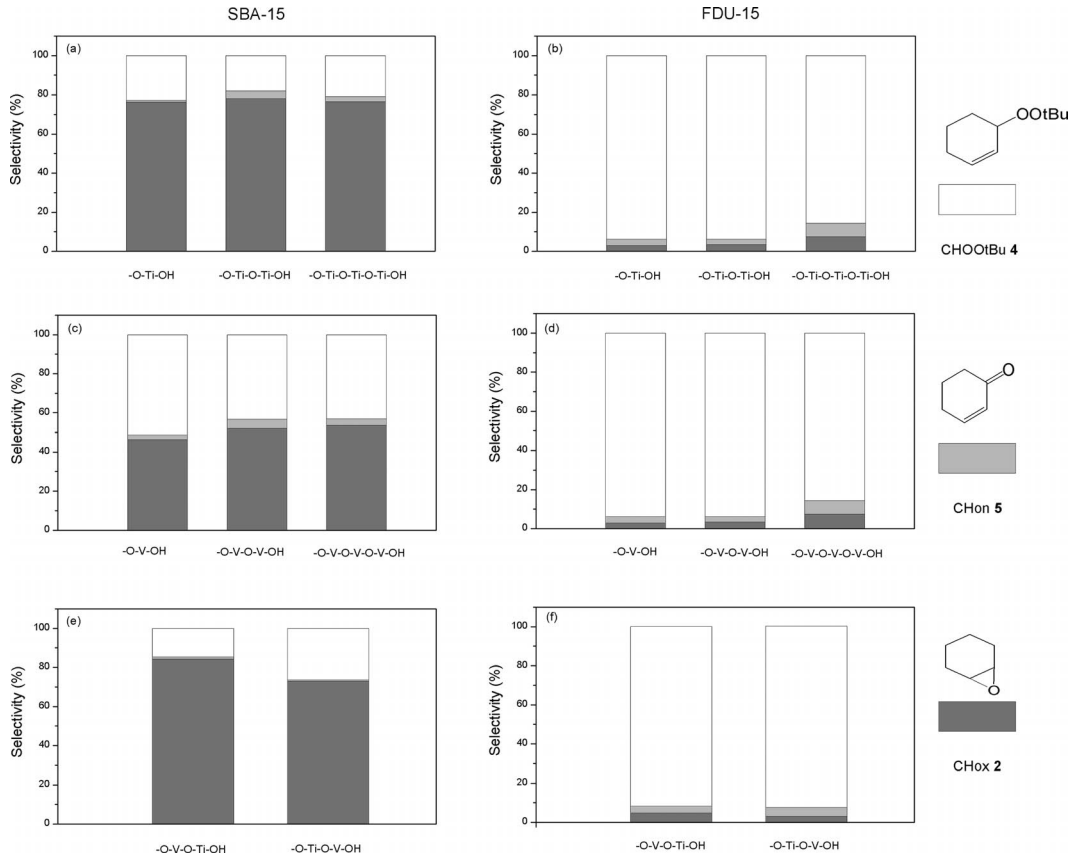

Figure 3. Overview of selectivity in the epoxidation of **1** for the SBA-15- and FDU-15-supported catalysts: (a,b) influence of the number of titanium oxide layers, (c, d) influence of the number of vanadium oxide layers and (e, f) influence of mixed metal oxide layers. The selectivity was determined after 8 h.

4 h (calculated as the percentage of titanium and vanadium atoms lost during the catalytic run) was determined to be 38.2 and 29.6%, respectively. In contrast, no significant leaching was observed for the FDU-15 catalysts, which illustrates the strong surface–oxygen–metal bonds.

To evaluate the regeneration of the catalysts in successive runs, the catalysts were tested in a second catalytic run under identical reaction conditions. The catalysts were recovered from the reaction mixture by filtration and were repeatedly washed with acetone to remove the organic molecules adsorbed onto the catalyst surface. Finally, the catalysts were dried under vacuum prior to reuse. For all the FDU-15-supported catalysts, amounts of epoxidation product that exceeded the blank test were not found. This is similar to the first run and indicates that the FDU-15-supported catalysts are not catalytically active in the epoxidation of **1**. For the SBA-15-supported catalysts, the product selectivity for two successive runs for the titanium monolayer catalyst is illustrated in Figure 4 (a). This graph shows a drastic decrease in the selectivity towards **2** in favour of the radical pathway. This can be explained by taking into account that nearly 40% of the titanium atoms were leached during the first catalytic run (vide supra). A similar reduction in selectivity was observed for all the silica-supported catalysts in the second catalytic run.

Reaction Mechanism

In summary, the SBA-15-supported catalysts have a relatively high catalytic activity in the epoxidation of **1**, but some metal oxide particles are sensitive to leaching, and the FDU-15 catalysts are (nearly) not catalytically active in the epoxidation. As a certain amount of the metal oxide particles were leached from the SBA-15 surface, the question is whether or not the epoxidation reaction proceeds heterogeneously.

In order to examine if the catalytic reaction occurs heterogeneously in the case of the SBA-15-supported catalysts, a hot filtration experiment was performed. After 4 h, the titanium oxide SBA-15 catalyst was filtered from the hot reaction mixture and the conversion was followed without the catalyst. Figure 4 shows the total conversion of **1** and the formation of **2**. Although the total conversion of **1** continued due to the progressive radical formation of **4**, this reaction profile clearly shows that the formation of **2** instantly ends after filtration. Although a considerable amount of the metal oxide centres were leached, the stagnation of the epoxide formation indicates that the leached metal centres were not responsible for the catalytic epoxidation, and that the epoxidation reaction occurs heterogeneously at the supported oxide centres.

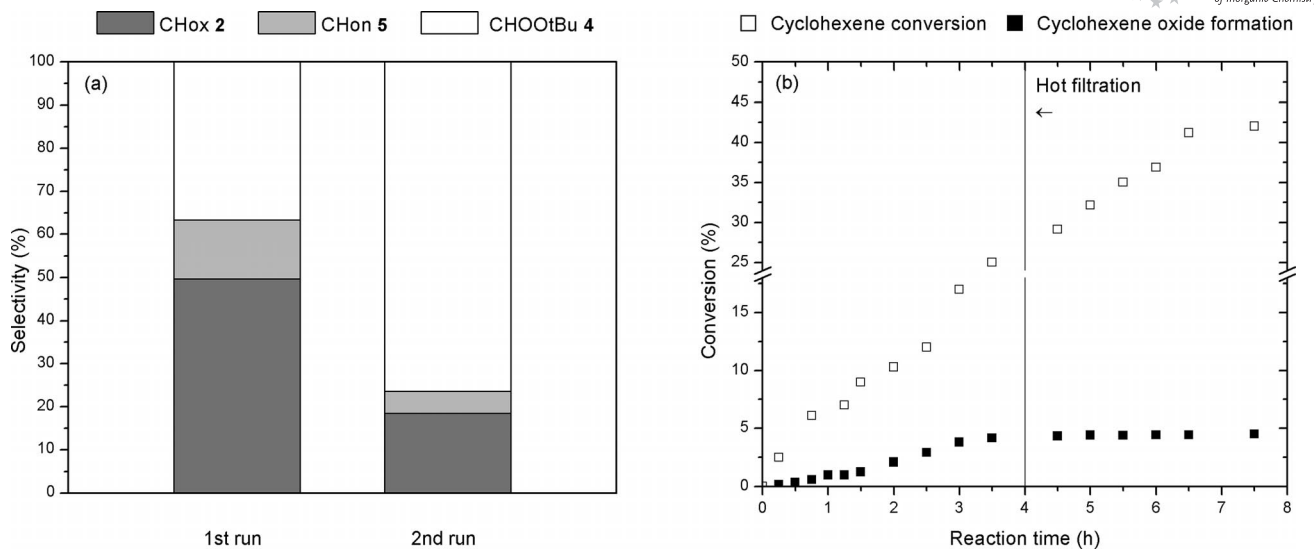

Figure 4. (a) Regeneration capacity of the TiO_2/SBA-15 catalyst and influence on the selectivity and (b) hot filtration experiment of the TiO_2/SBA-15 catalyst.

The hot filtration experiment showed that the epoxidation reaction occured heterogeneously: the supported metal oxide centres were responsible for the epoxidation of **1** and the leached metal centres were not catalytically active (SBA-15 catalysts). However, the metal oxide centres that are strongly bound to the surface were not able to epoxidise **1** (FDU-15 catalysts). These results give more insight in the reaction mechanism of the epoxidation of **1** at a supported metal oxide site, and the proposed reaction cycle is shown in Scheme 3. A similar pathway can be considered for the supported titanium and vanadium oxide catalysts.

In the ideal case, when the hydroxyl-group density on the SBA-15 surface is high, the unsaturated metal centre is triply bound to the surface in a tetrahedral coordination (Scheme 3, a). Initially, the metal centre coordinates to a *tert*-butyl hydroperoxide molecule (step 1). In the next step, the support–oxygen–metal (S–O–M) bond weakens and proton transfer from *tert*-butyl hydroperoxide to the support takes places with the formation of a peroxocomplex (step 2). Subsequently, the olefin enters the reaction cycle (step 3) and coordinates to the metal complex, and the peroxocomplex transfers an oxygen atom to the hydrocarbon

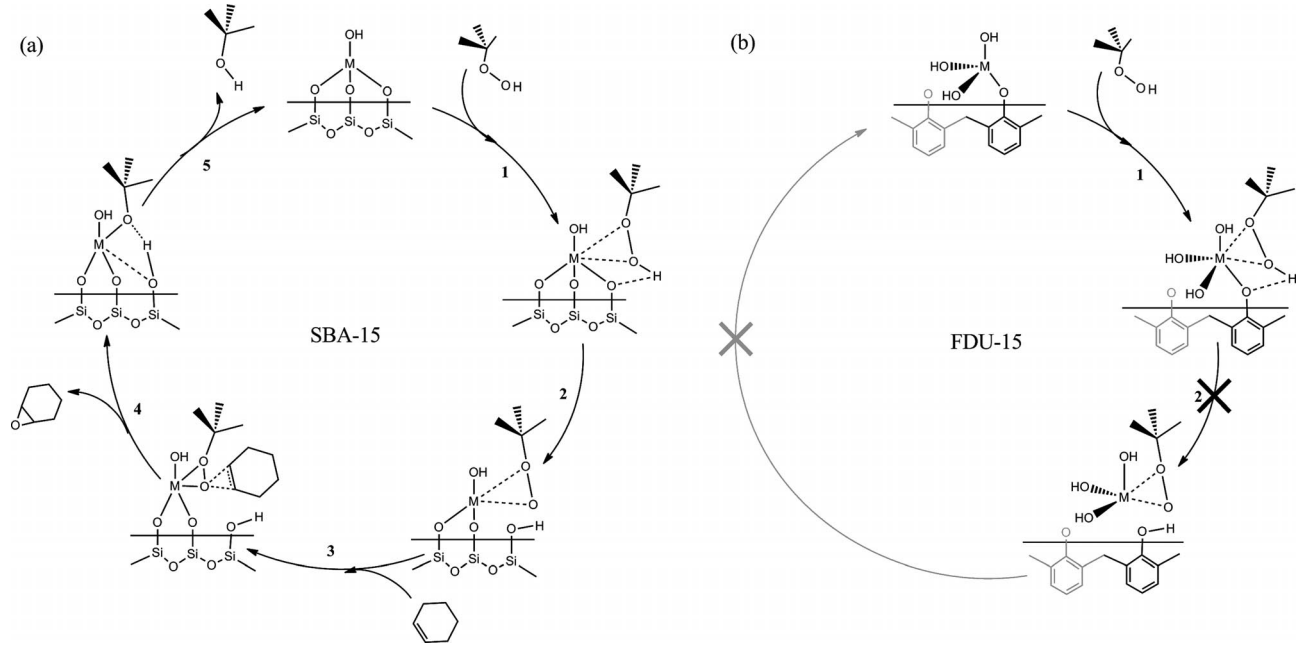

Scheme 3. Proposed reaction mechanism of the cyclohexene epoxidation for (a) SBA-15 catalyst and (b) FDU-15 catalyst. Breaking the S–O–M bond in step 2 is assumed to be critical for the epoxidation of **1** (M = Ti or V).

substrate. The mechanism of this oxygen transfer from the peroxometal complex to the nucleophilic substrate is still a matter of considerable debate.[24] Next, **2** desorbs from the metal centre and the epoxide product exits the catalytic cycle (step 4). Finally, a new proton transfer occurs for the recovery of the original metal complex triply bound to the support together with the exit of the decomposition product *tert*-butyl alcohol. The reaction cycle is closed when the metal centre recondenses with a free hydroxyl group on the substrate surface. This final step in the reaction cycle is extremely important in the regeneration of the catalyst: the initial configuration is only obtained when the recondensation takes place. If not, the metal centre, which was initially triply bound to the support, is only double bound to the surface. Now, the catalyst can run through the catalytic cycle twice more before it leaches from the support. In this reaction pathway, the support–oxygen bond is assumed to be critical in the epoxidation reaction. This observation is in agreement with general perspectives about supported metal oxide catalysts.[25,26]

The reaction mechanism for the FDU-15-supported catalysts is depicted in Scheme 3 (b). Here, the metal oxide centres are supposed to be covalently bound by one single bond (or a double bond at most) as the hydroxyl-group density is lower than on the hydrophilic silica surface. *tert*-Butyl hydroperoxide enters the reaction cycle, however, the support–O–M bond is hard to break and, as a consequence, the active peroxide complex is not formed. This reaction mechanism, where the surface oxygen bond has to break in order to form a peroxocentre provides an answer to why the strongly bonded and leached metal centres are not catalytically active in the epoxidation of **1**.

From the viewpoint of ideal catalyst design for epoxidation reactions at supported metal oxide sites, two main conclusions can be drawn: (1) the catalyst has to be able to form an active metal peroxide complex by breaking the S–O–M bond so this bond should not be too strong, (2) full regeneration can only be accomplished when a recondensation step is completed by recondensation of the S–O–M bond and leaching is reduced.

Conclusions

Titanium and vanadium oxide layers were deposited on the surface of SBA-15 and FDU-15 by atomic layer deposition. This deposition method is a powerful technique to control the growth of (sub)monolayers on the surface of mesoporous supports. The self-limiting nature of the precursor to react with the surface provides uniform layers with well-dispersed single metal centres. The catalytic performance of these catalysts was evaluated in the liquid phase oxidation of cyclohexene. The metal oxide loading had a significant impact on the selectivity. Furthermore, hot filtration experiments and support effects showed that the epoxidation reaction occurs truly heterogeneously. Here, the support–oxygen bond is assumed to be critical for catalytic activity. A recondensation step of the metal centre with a free hydroxyl group on the substrate surface is essential for regeneration and to avoid leaching.

Experimental Section

Chemicals: Pluronic P123 (EO_{20}-PO_{70}-EO_{20}, MW = 5820), tetraethylorthosilicate (TEOS), HCl, phenol, formaline (37 wt.-% formaldehyde solution in H_2O), sodium hydroxide, ethanol, Pluronic F127 (MW = 12600), tetrakis(dimethylamido)titanium (TDMAT), vanadium isopropoxide [VO(*i*PrO)$_3$], chloroform, cyclohexene, toluene and *tert*-butyl hydroperoxide (TBHP, 5.5 M in decane) were purchased from Sigma–Aldrich.

Synthesis of SBA-15: The SBA-15 materials were synthesised by using P123 as the surfactant and TEOS as the silica source.[27] In a typical synthesis, P123 (4 g) was dissolved in HCl (120 mL, 2 M) and distilled water (30 mL). TEOS (9.1 mL) was added, and the mixture was stirred vigorously at 45 °C for 5 h followed by an aging step at 90 °C for 20 h. Finally, the white precipitated product was collected by filtration, washed with distilled water, dried and calcined in air at 550 °C for 6 h (heating rate: 1 °C/min).

Synthesis of FDU-15: Ordered mesoporous FDU-15 resins were synthesised using the evaporation induced self-assembly method reported by Zhao et al.[28] Phenol (1.2 g) was melted at 45 °C before NaOH solution (10 mL, 6.25 M) was added slowly with stirring. Formaline solution (2.4 mL, 37 wt.-% formaldehyde in water) was added dropwise. The reaction mixture was stirred at 70 °C for 1 h. After cooling to room temperature, the pH of the reaction mixture was neutralised with HCl (0.6 M). Water was removed under vacuum at 45 °C. The product was dissolved in ethanol (20 mL) and added to Pluronic F127 (3.2 g) dissolved in ethanol (30 mL). The solution was stirred for 10 min at room temperature and transferred to a dish to evaporate the ethanol. The membrane was thermopolymerised at 100 °C in air. Finally, the mesoporous structure was calcined under a nitrogen flow at 350 °C for 6 h (heating rate: 1 °C/min).

ALD: Titanium and vanadium oxide were deposited on the surface of mesoporous SBA-15 and FDU-15 by ALD in the gas phase. Prior to the deposition, the powders were stored at elevated temperature under vacuum in the ALD reactor. The reactor was slowly vacuum pumped through a needle valve during sample loading and slowly vented during unloading to prevent loss of the powders. A base pressure of 5×10^{-7} mbar was measured. Titanium and vanadium oxide were deposited from TDMAT and VO(*i*PrO)$_3$ respectively.[29–31] TDMAT and VO(*i*PrO)$_3$ were heated to 40 °C, and water was stored at room temperature. The gases entered the reactor through heated lines (45 °C) to prevent condensation, and a turbomolecular pump continually evacuated the reactor. The depo-

Table 4. Overview of the layer type on SBA-15 and FDU-15 (M = Ti or V).

Catalyst	Layer type	Surface
1. Submonolayer		–O–M–OH
2. Multiple layers	monolayer	–O–M–OH
	double layer	–O–M–O–M–OH
	triple layer	–O–M–O–M–O–M–OH
3. Mixed catalysts	interlayer	–O–M_1–O–M_2–OH
		–O–M_2–O–M_1–OH

sition temperature was 150 °C. The reactant pulses were automated by computer controlled pneumatic valves. Both SBA-15 and FDU-15 were functionalised with: (1) a (sub)monolayer of titanium or vanadium oxide with different loadings, (2) multiple (mono, double and triple) titanium or vanadium oxide layers and (3) mixed titanium and vanadium oxide layers. An overview of the different catalysts is given in Table 4.

Catalysis Experiments: The catalytic performance of the catalysts were evaluated in the liquid phase epoxidation of **1**.[32] In a typical catalytic run, chloroform (10.0 mL, 124 mmol), **1** (1.5 mL, 15 mmol), *tert*-butyl hydroperoxide (5.5 M in decane, 5.5 mL, 30 mmol) and 1,2,4-trichlorobenzaldehyde (internal standard, 1.8 mL, 15 mmol) were heated to reflux in a two-necked round-bottomed flask with vigorous stirring under argon at 80 °C and the dried catalyst (30 mg) was added. The conversion of **1** was followed by sampling 0.1 mL of the reaction medium several times. The sample was immediately diluted with ethyl acetate (0.5 mL) and injected in the GC.

Regeneration: at the end of the reaction, the catalyst was filtered from the hot reaction mixture through a membrane filter, washed with acetone, dried and reused in a second catalytic run under the same reaction conditions.

Characterisation: Nitrogen gas sorption experiments were conducted at 77 K with a Micromeritics Tristar 3000. Samples were vacuum dried at 120 °C prior to analysis. The pore size distribution was calculated from the adsorption branch, and the micropore volume was calculated using the *t*-plot method. X-ray powder diffraction patterns were collected with an ARL X′TRA Diffractometer with Cu-K_α radiation with 0.15418 nm wavelength. GC was performed with a Thermo/Interscience Ultra Fast GC equipped with a flame ionisation detector and a 5% diphenyl/95% polydimethylsiloxane column (10 m length and 0.10 mm internal diameter). Helium was used as carrier gas and the flow rate was programmed at 0.8 mL/min. X-ray fluorescence (XRF) spectroscopy measurements were performed with a Bruker system with molybdenum X-rays. The titanium and vanadium loadings on SBA-15 were verified by XRF spectroscopy. The surface area of the silicon, titanium and vanadium was determined at 1.74 keV, 4.51 keV and 4.95 keV, respectively. For the FDU-15 samples, the titanium and vanadium loadings were quantified colorimetrically by UV/Vis spectroscopy with a UV/Vis Varian spectrophotometer following the procedure described by Vogel.[33]

Supporting Information (see footnote on the first page of this article): XRD patterns and spectroscopic analyses (Raman, UV/Vis, DRIFT, XPS) of the supported catalysts.

Acknowledgments

This research was cofunded by Ghent University. I. M. acknowledges the Flemish Agentschap voor Innovatie door Wetenschap en Technologie (IWT) (grant number IWT/SB/71325) for financial support. K. L. is grateful to the Flemish Government for funding (Long Term Structural Methusalem, grant number 01M00409) and to the Geconcerteerde Onderzoeksactie (GOA) (grant number 01G00710). J. M. and C. D. acknowledge the Flemish IWT for financial support through the SBO-METACEL project. J. D. acknowledges the Flemish Fonds voor Wetenschappelijk Onderzoek (FWO) for a PhD fellowship. The research leading to these results has received funding from the European Research Council under the European Union's Seventh Framework Programme (FP7/2007-2013)/ERC, grant number 239865).

[1] N. F. Zheng, G. D. Stucky, *J. Am. Chem. Soc.* **2006**, *128*, 14278–14280.
[2] P. Van Der Voort, C. Vercaemst, D. Schaubroeck, F. Verpoort, *Phys. Chem. Chem. Phys.* **2008**, *10*, 347–360.
[3] O. Collart, P. Van Der Voort, E. F. Vansant, E. Gustin, A. Bouwen, D. Schoemaker, R. R. Rao, B. M. Weckhuysen, R. A. Schoonheydt, *Phys. Chem. Chem. Phys.* **1999**, *1*, 4099–4104.
[4] C. Wang, S. Y. Lim, G. A. Du, C. Z. Loebicki, N. Li, S. Derrouiche, G. L. Haller, *J. Phys. Chem. C* **2009**, *113*, 14863–14871.
[5] M. Baltes, A. Kytokivi, B. M. Weckhuysen, R. A. Schoonheydt, P. Van Der Voort, E. F. Vansant, *J. Phys. Chem. B* **2001**, *105*, 6211–6220.
[6] P. Van Der Voort, M. B. Mitchell, E. F. Vansant, M. G. White, *Interface Sci.* **1997**, *5*, 169–197.
[7] R. L. Puurunen, *J. Appl. Phys.* **2005**, *97*, 000–000.
[8] J. Dendooven, S. P. Sree, K. De Keyser, D. Deduytsche, J. A. Martens, K. F. Ludwig, C. Detavernier, *J. Phys. Chem. C* **2011**, *115*, 6605–6610.
[9] H. Feng, J. W. Elam, J. A. Libera, M. J. Pellin, P. C. Stair, *Chem. Eng. Sci.* **2009**, *64*, 560–567.
[10] M. Lindblad, S. Haukka, A. Kytokivi, E. L. Lakomaa, A. Rautiainen, T. Suntola, *Appl. Surf. Sci.* **1997**, *121*, 286–291.
[11] J. E. Herrera, J. H. Kwak, J. Z. Hu, Y. Wang, C. H. F. Peden, *Top. Catal.* **2006**, *39*, 245–255.
[12] J. Keranen, P. Carniti, A. Gervasini, E. Iiskola, A. Auroux, L. Niinisto, *Catal. Today* **2004**, *91–92*, 67–71.
[13] H. Feng, J. L. Lu, P. C. Stair, J. W. Elam, *Catal. Lett.* **2011**, *141*, 512–517.
[14] J. H. Li, X. H. Liang, D. M. King, Y. B. Jiang, A. W. Weimer, *Appl. Catal. B-Environ.* **2010**, *97*, 220–226.
[15] J. D. S. Sree, T. Korányi, G. Vanbutsele, K. Houthoofd, D. Deduytsche, C. Detavernier, J. Martens, *Catal. Sci. Technol.* **2011**, *1*, 218–221.
[16] I. Muylaert, M. Borgers, E. Bruneel, J. Schaubroeck, F. Verpoort, P. Van Der Voort, *Chem. Commun.* **2008**, 4475–4477.
[17] Z. H. Ji, S. G. Liang, Y. B. Jiang, H. Li, Z. M. Liu, T. Zhao, *Carbon* **2009**, *47*, 2194–2199.
[18] P. Gao, A. Wang, X. Wang, T. Zhang, *Chem. Mater.* **2008**, *20*, 1881–1888.
[19] Y. Wan, X. Qian, N. Q. Jia, Z. Y. Wang, H. X. Li, D. Y. Zhao, *Chem. Mater.* **2008**, *20*, 1012–1018.
[20] R. Xing, N. Liu, Y. M. Liu, H. W. Wu, Y. W. Jiang, L. Chen, M. Y. He, P. Wu, *Adv. Funct. Mater.* **2007**, *17*, 2455–2461.
[21] Y. Wan, H. Y. Wang, Q. F. Zhao, M. Klingstedt, O. Terasaki, D. Y. Zhao, *J. Am. Chem. Soc.* **2009**, *131*, 4541–4550.
[22] S. Y. Yan, Y. Gao, R. Xing, Y. L. Shen, Y. M. Liu, P. Wu, H. H. Wu, *Tetrahedron* **2008**, *64*, 6294–6299.
[23] H. Wang, A. Q. Wang, X. D. Wang, T. Zhang, *Chem. Commun.* **2008**, 2565–2567.
[24] V. Conte, F. DiFuria, G. Licini, *Appl. Catal. A: Gen.* **1997**, *157*, 335–361.
[25] I. Muylaert, P. Van Der Voort, *Phys. Chem. Chem. Phys.* **2009**, *11*, 2826–2832.
[26] B. M. Weckhuysen, D. E. Keller, *Catal. Today* **2003**, *78*, 25–46.
[27] D. Y. Zhao, J. L. Feng, Q. S. Huo, N. Melosh, G. H. Fredrickson, B. F. Chmelka, G. D. Stucky, *Science* **1998**, *279*, 548–552.
[28] Y. Meng, D. Gu, F. Q. Zhang, Y. F. Shi, H. F. Yang, Z. Li, C. Z. Yu, B. Tu, D. Y. Zhao, *Angew. Chem.* **2005**, *117*, 7215; *Angew. Chem. Int. Ed.* **2005**, *44*, 7053–7059.
[29] M. Ritala, M. Leskela, L. Niinisto, P. Haussalo, *Chem. Mater.* **1993**, *5*, 1174–1181.
[30] J. Aarik, A. Aidla, T. Uustare, M. Ritala, M. Leskela, *Appl. Surf. Sci.* **2000**, *161*, 385–395.

[31] Q. Xie, Y. L. Jiang, C. Detavernier, D. Deduytsche, R. L. Van Meirhaeghe, G. P. Ru, B. Z. Li, X. P. Qu, *J. Appl. Phys.* **2007**, *102*, 000–000.
[32] K. Leus, I. Muylaert, M. Vandichel, G. B. Marin, M. Waroquier, V. Van Speybroeck, P. Van Der Voort, *Chem. Commun.* **2010**, *46*, 5085–5087.
[33] A. I. Vogel, *Quantitative Inorganic Analysis*, Longmans, London, 3rd ed., **1961**, pp. 790–791.

Received: September 20, 2011
Published Online: December 9, 2011

DOI: 10.1002/ejic.201100978

The *N*,*N*-Bis(terphenyl)aminophosphenium Cation – A Sensitive Probe for Interactions with Different Anions

Fabian Reiß,[a] Axel Schulz,*[a,b] and Alexander Villinger[a]

Keywords: Sensors / Cations / Anions / Phosphorus / Weakly coordinating anions / Bonding

A series of salts that contain the terphenyl-substituted bis(amino)phosphenium cation with different anions (F^-, Cl^-, $[CF_3CO_2]^-$, $[CF_3SO_3]^-$, $[B(C_6F_5)_4]^-$, $[GaCl_4]^-$, $[SbF_6]^-$, $[Al\{OCH(CF_3)_2\}_4]^-$ and $[CHB_{11}H_5Br_6]^-$) has been prepared by different synthetic protocols. All of the products have been characterised spectroscopically and by single-crystal X-ray diffraction studies. A detailed analysis of the interionic interactions and their influence on the molecular structure of the phosphenium cation reveals a strong dependence on the capability of the anion to enter the pocket generated by the bulky terphenyl substituents.

Introduction

The first dicoordinate phosphorus cation, observed in phosphamethine cyanines, was reported by Dimroth and Hoffmann in 1964.[1] The term "phosphenium ion" was introduced to indicate a positive charge at the two-coordinate phosphorus centre with a formally vacant 3p orbital.[2] Phosphenium cations are related to carbenes of the type R^1–C–R^2 where electronically isovalent P^+ replaces the central carbon atom. Carbenes are best stabilised when R^1 and R^2 are atoms or groups such as NR_2, which can serve as π-electron donors to the carbon atom.[3] The same holds true for electronically isovalent phosphenium analogs (Scheme 1).

Parry et al. reported the first examples of acyclic phosphenium ions $[(Me_2N)_2P]^+$ and $[(Me_2N)(Cl)P]^+$, which were obtained by chloride abstraction from the corresponding amino(chloro)phosphanes by employing Lewis acids such as ECl_3 (E = Fe, Al, Ga).[4] Structural data for acyclic phosphenium ions are still limited to only a few amino-substituted examples: $[(i\mathrm{Pr}_2N)_2P]^+[X]^-$ (X = $[AlCl_4]^-$, $[GaCl_4]^-$, $[B(C_6F_5)_4]^-$).[5,6]

Niecke and Kröher showed that the electrophilic attack of $AlCl_3$ on the P=N double bond of the amino(imino)phosphane R_2N–P=NR (R = Me_3Si) generates the internal salt R_2N–$P^{(+)}$– $N(Al^{(-)}Cl_3)R$ with a formal positive charge at the phosphorus atom and a negative charge at the aluminium atom.[7] This internal salt readily eliminates Me_3Si–Cl upon heating to give a four-membered $(Cl_2)Al^{(-)}$–$N(Me_3Si)$–$P^{(+)}$–$N(SiMe_3)$ heterocycle. Moreover, it was shown that the reaction of the chloro(imino)phosphane 2,4,6-$t\mathrm{Bu}_3C_6H_2$–N=P–Cl with $AlCl_3$ led to the stable salt $[2,4,6\text{-}t\mathrm{Bu}_3C_6H_2\text{–}N{\equiv}P]^+[AlCl_4]^-$, which bears a formal P≡N triple bond,[8] instead of the expected phosphanylium adduct, 2,4,6-$t\mathrm{Bu}_3C_6H_2$–$N(Al^{(-)}Cl_3)$–$P^{(+)}$–Cl.

The only known aryl-substituted bis(amino)phosphenium cation **3** (E = Al, Scheme 2) was introduced by Niecke[9] and coworkers and further studied by Burford et al.[10] As shown in Scheme 2, the phosphadiazonium cation $[Mes^*NP]^+$ (**2**) reacts quantitatively with Mes^*NH_2 (Mes* = 2,4,6-tri-*tert*-butylphenyl) to yield ECl_4^- salts with the bis(amino)phosphenium cation (Mes***3**). The solid-state structures of Mes***3**$[GaCl_4]$ and Mes***3**$[AlCl_4]$ have been confirmed by X-ray crystallography and the structural parameters of the cation are essentially identical.

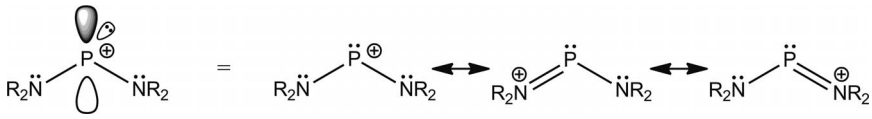

Scheme 1. Stabilisation of phosphenium ions by π-electron donors in $[R_2N\text{–}P\text{–}NR_2]^+$.

Salts that contain a five-membered heterocyclic cation with a formal bis(amino)phosphenium fragment (R_2N–$P^{(+)}$–NR_2) are called 1,3,2-diazaphospholenium ions.[11,12] They are isoelectronic with imidazoyl carbenes,[13] stabilised by similar electronic factors and can be obtained by chlo-

[a] Institut für Chemie, Universität Rostock,
Albert-Einstein-Str. 3a, 18059 Rostock, Germany
Fax: +49-381-498-6381
E-mail: axel.schulz@uni-rostock.de
[b] Leibniz Institut für Katalyse,
Albert-Einstein-Str. 29a, 18059 Rostock, Germany
Fax: +49-381/498-6381

Supporting information for this article is available on the WWW under http://dx.doi.org/10.1002/ejic.201100978.

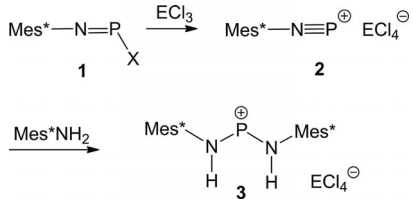

Scheme 2. Synthesis of Mes***3**[ECl_4] (E = Al, Ga).[9,10]

ride abstraction with Lewis acids in 2-chloro-1,3,2-diazaphospholenes (Scheme 3).[12] Chloride abstraction was also successfully applied in the isolation of salts that bear cyclo-1,3-diphospha-2,4-diazenium ions, which can also be regarded as carbene analogs (Scheme 3).[14]

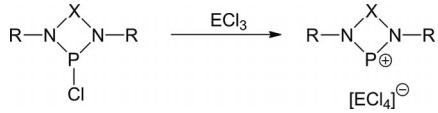

Scheme 3. Synthesis of phosphorus carbene analogs by chloride abstraction. (i) X = $(CH)_2$ 1,3,2-diazaphospholenium ion (R = alkyl, aryl, E = Al, Ga); (ii) X = P–Cl chlorocyclo-1,3-diphospha-2,4-diazenium ions (R = Ter, E = Ga).[12,14]

The structure and bonding of bis(amino)phosphenium ions has been intensively studied.[2b,9,10] In solution, ^{31}P NMR spectroscopy is a powerful tool for the identification of phosphenium ions. As might be anticipated from the low coordination number and the presence of a formal positive charge at phosphorus, the ^{31}P chemical shifts of phosphenium ions are rather deshielded and fall in the range 100–520 ppm.[2b] For instance in $[(Me_2N)(tBu)P]^+$, a strongly deshielded ^{31}P chemical shift is observed at 513 ppm,[15] which can be ascribed to the inability of the *t*Bu group to donate π electrons. Steric effects also play a role in determining the ^{31}P chemical shifts. Interestingly, ^{31}P chemical shifts of bis(amido)-substituted cations increase with increasing ligand size.[2b] This trend has been interpreted on the basis of progressive twisting of the R_2N groups with respect to the P^+ centre, which reduces the N(2p)–P(3p) overlap with increasing steric strain.[15]

Cation–anion interactions that involve phosphenium ions have previously been investigated in some detail.[3] Burford et al. reported the anionic protection of phosphenium ions in solution,[6] Kee et al. described phosphenium–triflate interactions[16] and Dahl investigated equilibria that involve covalent and ionic phosphenium triflates.[17]

To the best of our knowledge, the influence of the anion with respect to the cation structure and physical properties has not been studied comprehensively. As a model system, we have chosen the *N*,*N*-bis[2,6-bis(2,4,6-trimethylphenyl)-phenyl]aminophosphenium ion ($[(TerNH)_2P]^+$, Ter**3**, Schemes 4–6) as its salts are usually easily obtained and allow hydrogen bonding despite the sterically demanding terphenyl group. To gain further insight into the influence of the anion we prepared Ter**3** with the following formal counterions: F^-, Cl^-, $[CF_3CO_2]^-$,[18] $[CF_3SO_3]^-$,[19] $[B(C_6F_5)_4]^-$,[20,21,22] $[GaCl_4]^-$,[10,20,23] $[SbF_6]^-$,[24] $[Al\{OCH(CF_3)_2\}_4]^-$ [20] and the carborate $[CHB_{11}H_5Br_6]^-$.[20,25] Here, we report the anion influence that results in small differences in the solid-state structures but may have an influence on physical properties such as melting points and NMR chemical shifts.

Results and Discussion

Synthesis and Spectroscopic Studies

Convenient synthetic routes[2,3,5,6] to salts that bear Ter**3** include salt-elimination reactions of $(TerNH)_2P$–Cl with Ag[X] (X = weakly coordinating anion,[20] Scheme 4), halogen abstraction by a Lewis acid such as $GaCl_3$ or $SbCl_5$ (Scheme 5) or protonation of imino(amino)phosphane (TerN(H)P=NTer, Scheme 6). A synthetic protocol analogous to the generation of Mes***3** salts illustrated in Scheme 2 cannot be applied to obtain Ter**3** salts as the Ter–N=P–Cl starting material is not accessible.

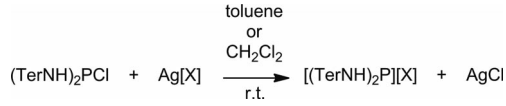

Scheme 4. Synthesis of Ter**3**[X] by salt elimination (X = $[CF_3CO_2]^-$, $[CF_3SO_3]^-$, $[B(C_6F_5)_4]^-$, $[Al\{OCH(CF_3)_2\}_4]^-$, $[CHB_{11}H_5Br_6]^-$ and $[SbF_6]^-$).

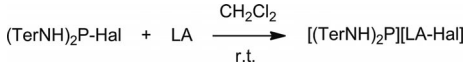

Scheme 5. Synthesis of Ter**3**[X] by halide abstraction ([LA-Hal] = $[GaCl_4]^-$).

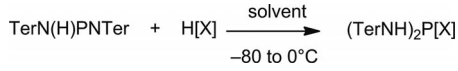

Scheme 6. Synthesis of Ter**3**[X] salts by protonation of terphenyl-substituted imino(amino)phosphane (X = Cl^-, $[CF_3CO_2]^-$, $[CF_3SO_3]^-$, $[B(C_6F_5)_4]^-$).[26]

Silver salts were usually used for the salt-elimination reactions, which were carried out either in toluene or CH_2Cl_2 at ambient temperatures. The formation of Ter**3** was easily followed by UV/Vis due to its prominent orange colour (Table 1). The application of this method was restricted to the synthesis of salts that contain the weakly coordinating anions $[CF_3CO_2]^-$, $[CF_3SO_3]^-$, $[B(C_6F_5)_4]^-$, $[Al\{OCH(CF_3)_2\}_4]^-$ and $[CHB_{11}H_5Br_6]^-$. Interestingly, although this reaction works well with $Ag[B(C_6F_5)_4]$, no reaction was observed with the nonfluorinated species, $Ag[B(C_6H_5)_4]$. In the cases of the fluoridometallate anions $[SbF_6]^-$ and $[BF_4]^-$, the synthesis was not successful even when temperatures below –80 °C were applied. Initially, the formation of Ter**3** was indicated by an orange colour, which quickly diminished when the temperature was raised to ambient temperatures. Only a few orange crystals of Ter**3**[SbF_6] were isolated in addition to the major product, which was identified as 2,6-bis(2,4,6-trimethylphenyl)anilinium hexafluoroantimonate, $[TerNH_3][SbF_6]$.[27a] The synthesis of Ter**3**-[BF_4] did not proceed due to a rapid Cl–F exchange reac-

Table 1. Characterisation data [decomposition temperature (T_{dec}), ^{31}P NMR, ^{1}H NMR, IR (ν_{NH} and ν_{PN}) and UV/Vis spectroscopic data] for Ter**3**[X] (X = F^-, Cl^-, $[CF_3CO_2]^-$, $[CF_3SO_3]^-$, $[B(C_6F_5)_4]^-$, $[GaCl_4]^-$, $[SbF_6]^-$, $[Al\{OCH(CF_3)_2\}_4]^-$ and $[CHB_{11}H_5Br_6]^-$) with TerN(H)PNTer and Mes**3**[Y] (Y = $[GaCl_4]^-$, $[CF_3SO_3]^-$) for comparison.

	T_{dec} [°C]	$^{31}P\{^{1}H\}$ NMR [ppm]	^{1}H (NH) NMR [ppm]	ν_{NH} [cm^{-1}]		ν_{PN} [cm^{-1}]	Vis [nm]		UV [nm]	
TerN(H)PNTer	311	278.0	6.34	3364	3289	1412	406	336	289	247
Ter**3**F	225	119.7[a]	3.79	3334	3292	1418	–	–	292	249
Ter**3**Cl	265[e]	129.9	4.08	3309	3285	1419	–	–	297	248
Ter**3**$[CF_3CO_2]$	190[f]	116.7	4.38	3314	3298	1422	–	–	290	250
Ter**3**$[CF_3SO_3]$	255	261.0	9.67	3341	3234	1426	438	363	292	246
Ter**3**$[B(C_6F_5)_4]$	244	249.1	7.31	–	3287	1419	422	358	296	260
Ter**3**$[GaCl_4]$	215	250.0	7.38	3333	3261	1416	438	361	–	255
Ter**3**$[SbF_6]$[d]	–	249.0	7.39	–	–	–	–	–	–	–
Ter**3**$[Al\{OCH(CF_3)_2\}_4]$	273	249.0	7.2	3319	3255	1426	435	360	297	246
Ter**3**$[CHB_{11}H_5Br_6]$	225	249.6	7.41	3330	3173	1428	435	358	296	245
Mes**3**$[GaCl_4]$[b]	152	272.0	9.94	–	3175	1419	–	–	–	–
Mes**3**$[CF_3SO_3]$[c]	–	279.7	11.6	–	–	–	–	–	–	–

[a] Doublet due to $^{31}P,^{19}F$ coupling. [b] Taken from ref.[11] [c] Taken from ref.[9e] [d] Characterised by X-ray and NMR spectroscopic studies because of fast decomposition. [e] T_{dec} = m.p. [f] M.p. 177 °C.

tion (Scheme 7) even at low temperatures, although Ter**3** was observed initially. Ter**3** is a stronger Lewis acid than BF_3, which is why fluoride-ion exchange was observed.

$$(TerNH)_2PCl + Ag[BF_4] \xrightarrow[-80\ °C]{CH_2Cl_2} (TerNH)_2PF + AgCl + BF_3$$

Scheme 7. Reaction of Ter**3**Cl with $Ag[BF_4]$.

Halide abstraction was attempted with $GaCl_3$ and $SbCl_5$ starting from Ter**3**Cl as well as with SbF_5 in the reaction with Ter**3**F. Only the reaction with $GaCl_3$ gave good yields of the desired product, Ter**3**$[GaCl_4]$, whereas, for SbF_5 and $SbCl_5$, only Ter–N(H)–PF_2 and Ter–N(H)–PCl_2, respectively, were identified as the major products. The protonation reaction of terphenyl-substituted imino(amino)phosphane was successfully applied to the preparation of Ter**3**[X] (X = Cl^-, $[CF_3CO_2]^-$, $[CF_3SO_3]^-$, $[B(C_6F_5)_4]^-$). A large excess of acid during protonation or hydrolysis led to the formation of the ammonium salts $[TerNH_3][X]$ for all Ter**3**[X].

Very pure Ter**3**Cl was obtained in the silyl ether elimination reaction of Ter**3**[X] (X = $[CF_3CO_2]^-$ and $[CF_3SO_3]^-$) with Me_3SiCl. Here the driving force was the formation of $Me_3SiOC(O)CF_3$ and $Me_3SiOS(O_2)CF_3$, respectively. Ter**3**[Cl] is not directly accessible from $TerNH_2$ and PCl_3 in the presence of bases, such as Et_3N, 1,8-diazabicyclo[5.4.0]-undec-7-ene and *n*BuLi, due to the formation of byproducts (e.g. TerN(H)–PCl_2, $[TerN–PCl]_2$, TerN(H)–P=N–Ter). Thus the best way to Ter**3**Cl was through TerN(H)–PCl_2 and 2 equiv. of Ter–NHLi, which led to TerN(H)–P=N–Ter (60% yield). Protonation with HCl yielded Ter**3**[Cl] (Scheme 6).

Ter**3**[X] were all characterised by elemental analysis, ^{31}P and ^{1}H NMR, IR and UV/Vis spectroscopy and single-crystal X-ray structure analysis. Table 1 summarises the spectroscopic data.

According to UV/Vis spectroscopy, all of the ionic Ter**3**[X] species are orange at ambient temperatures, which is due to an $n_{NPN} \rightarrow \pi_{NPN}^*$ excitation. In addition to this strong excitation, which is not observed for the covalently bound species, several other $\pi_{Ter} \rightarrow \pi^*_{Ter}$ excitations were observed. In the IR spectra, the P–N stretching mode, which is influenced by the substituent, structural situation around the NPN unit and the extent of hydrogen bonding, was typically found from 1400–1500 cm^{-1} (cf. $[Mes*NP]^+[GaCl_4]^-$ 1494, Mes*N=P–Cl 1437 cm^{-1}).[28]

Ter**3**[X] were all astonishingly thermally stable and moisture sensitive but stable under an argon atmosphere over a long period as solids and in solvents such as CH_2Cl_2, benzene or toluene at ambient temperature. They could be prepared in bulk and were stable when stored in sealed tubes. Although covalently bound Ter**3**[X] (X = F^-, Cl^-, $[CF_3CO_2]^-$) could be handled in air for a short time, the Ter**3**[X] salts all decomposed quickly as indicated by the colour change from orange to colourless. For example, it was shown that Ter**3**$[Al\{OCH(CF_3)_2\}_4]$ slowly hydrolysed over a period of 7 d in the freezer (–25 °C) to yield the internal salt $(TerNH)_2P^{(+)}(H)–O–Al^{(-)}[OCH(CF_3)_2]_3$.[27b]

Apart from Ter**3**Cl and Ter**3**$[CF_3CO_2]$, for which true melting points were found (265 and 177 °C, respectively), differential scanning calorimetry (DSC) displayed only decomposition points ranging between 190 °C (Ter**3**-$[CF_3CO_2]$) and 273 °C (Ter**3**$[Al\{OCH(CF_3)_2\}_4]$). It is interesting to note that Mes**3**$[GaCl_4]$ is significantly less thermally stable than its terphenyl-substituted counterpart (152 vs. 215 °C). It can be assumed that the terphenyl group provides better kinetic protection.

X-ray studies (see below) and calculations revealed dominant polar-covalent bonding in Ter**3**[X] (X = F^-, Cl^-, $[CF_3CO_2]^-$) and ion-pair formation in the other species. Solution NMR spectroscopy displayed a similar picture. Although a strong upfield shift was observed for Ter**3**[X] (X = F^-, Cl^-, $[CF_3CO_2]^-$) in the ^{1}H (3.8–4.4 ppm) and ^{31}P NMR spectra (117–130 ppm), for the other species, except Ter**3**$[CF_3SO_3]$, the corresponding resonances are found in the downfield region expected for phosphenium ions[2b] at δ^{31P} = 249–250 and δ^{1H} = 7.2–7.4 ppm. As almost the same chemical shifts are observed for all of the ionic species, it

can be assumed that solvated ions are present in solution, with the exception of Ter**3**[CF_3SO_3] for which ion pairing was indicated. In the ^1H NMR spectrum of Ter**3**[CF_3SO_3] a signal is found at 9.67 ppm, which can be attributed to strong NH···O(O_2)SCF_3 hydrogen bonds that are responsible for the ion pairing. In addition, the considerable downfield shift in the ^{31}P NMR spectrum (261 vs. 250 ppm, Table 1) supports this argument along with the X-ray data for the solid-state structure. In contrast to Ter**3**[$GaCl_4$], which forms separated ions in solution, analogous Mes*-**3**[$GaCl_4$] forms ion pairs as indicated by the ^1H and ^{31}P NMR spectra (Table 1, δ^{1H} = 7.38 vs. 9.94 ppm). As shown below, stronger hydrogen bonds were observed in Mes*-**3**[$GaCl_4$] than Ter**3**[$GaCl_4$]. In agreement with ion pairing in Ter**3**[CF_3SO_3], Mes*-**3**[CF_3SO_3] displays an even stronger downfield shift (δ^{1H} = 9.67 vs. 11.60 ppm).

Structural Elucidation

Crystals suitable for single-crystal X-ray diffraction studies of Ter**3**[X] ([X] = F^-, Cl^-, $[CF_3CO_2]^-$, $[CF_3SO_3]^-$, $[B(C_6F_5)_4]^-$, $[GaCl_4]^-$, $[SbF_6]^-$, $[Al\{OCH(CF_3)_2\}_4]^-$ and $[CHB_{11}H_5Br_6]^-$), Mes*-**3**[$GaCl_4$] and $(TerNH)_2P(H)OAl[OCH(CF_3)_2]_3$.[27b] were obtained by crystallisation of saturated solutions at low temperature. We have abstained from a detailed discussion of the structure of TerN(H)PNTer due to a strong disorder problem.

Although Ter**3**[$B(C_6F_5)_4$] crystallised as a solvate with one molecule of CH_2Cl_2 per formula unit, Ter**3**[Al{$OCH(CF_3)_2$}$_4$] with 0.5 molecules of fluorobenzene and Ter**3**[$CHB_{11}H_5Br_6$] with 1.5 molecules of benzene, the other Ter**3**[X] compounds crystallised without the inclusion of solvent. The molecular structures of all Ter**3**[X] species and Mes*-**3**[$GaCl_4$] and $(TerNH)_2P(H)OAl[OCH(CF_3)_2]_3$ are shown in Figures 1, 2, 3 and S1 (see Supporting Information). Selected bond lengths and angles are summarised in Table 2 together with the previously reported data for Mes*-**3**[ECl_4] (E = Al, Ga).[9,10] We have repeated the structural analysis of Mes*-**3**[$GaCl_4$] to get a consistent set of data of comparable quality.

For all Ter**3**[X] species, the central phenyl rings of the terphenyl group attached to the nitrogen atom try to form an almost orthogonal arrangement (torsion angles between 54–90°, Table 2) that forms a pocket generated by four aryl substituents (in 2- and 6-positions), in which the N(H)-PN(H) moiety is embedded and sterically protected (Figure 2). Thus dimerisation of e.g. TerN(H)PNTer and the formation of cyclodiphosphadiazanes is impossible. The N(H)PN(H) moiety is not coplanar to the central aryl rings of the terphenyl group located but twisted (e.g. the $C1_{aryl}$–$C2_{aryl}$–N–P dihedral angles in Ter**3**[$GaCl_4$] are between 29 and 38°). Thus, delocalisation of the NPN π-electron density into the central aryl substituents is limited.

As displayed in Table 2 and Figure 1, the phosphorus atom adopts a trigonal pyramidal environment in all of the covalently bound Ter**3**[X] (X = F^-, Cl^-, $[CF_3CO_2]^-$) species. In all other species the structure consists of separated

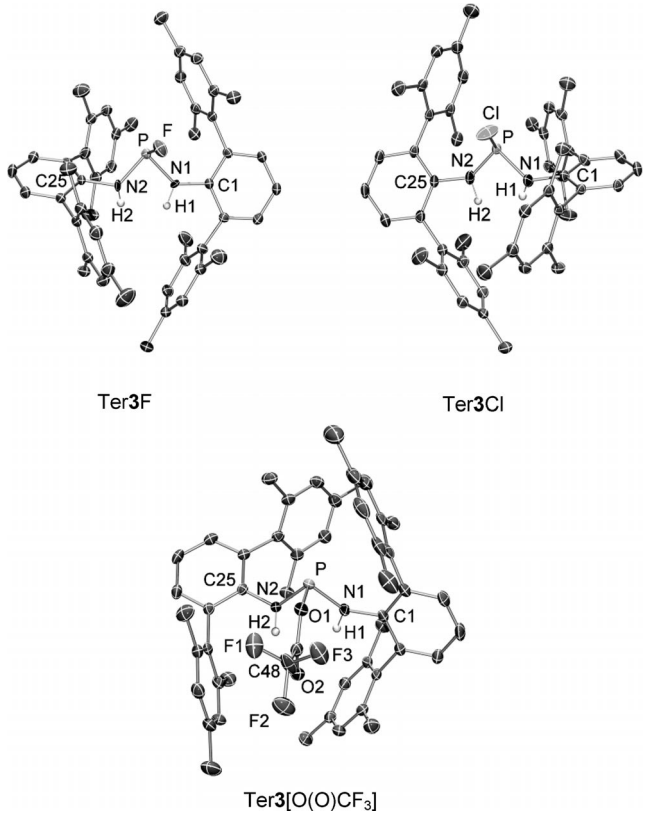

Figure 1. ORTEP drawing of covalently bound Ter**3**[X] species (X = F^-, Cl^-, $[CF_3CO_2]^-$). Thermal ellipsoids with 30% probability at 173 K (hydrogen atoms of the terphenyl group are omitted).

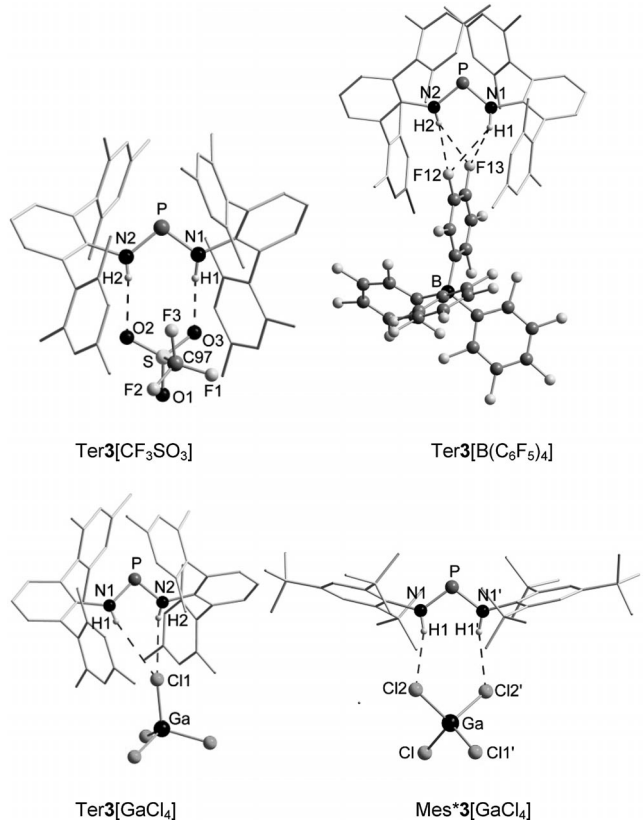

Figure 2. Hydrogen bonds in R**3**[X] (R = Ter, Mes*).

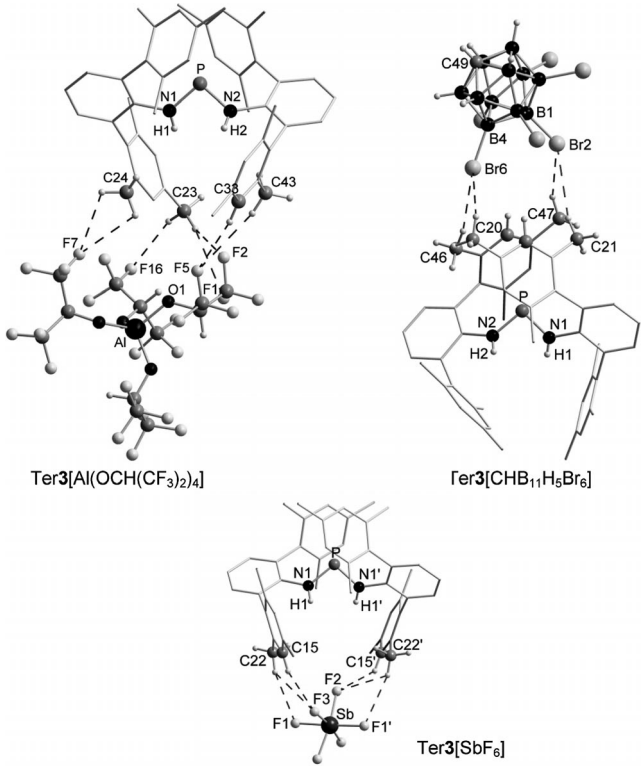

Figure 3. Weak, interionic van der Waals interactions in Ter**3**[X]. Only the interactions of one ion pair are depicted.

[Ter**3**]$^+$ and [X]$^-$ ions with several different interionic contacts (see below). Here, both the nitrogen atoms and the dicoordinated phosphorus atom of the N(H)PN(H) moiety sit in a trigonal planar environment with P–N bond lengths ranging from 1.619–1.635 Å, which are significantly shorter than those found in the covalently bound Ter**3**[X] species [cf. Ter**3**[F], P–N 1.704(6) and 1.663(1) Å, Table 2]. In Ter**3**[CF_3SO_3], a slightly shorter P–N bond length was found [1.609(3) Å] along with a considerably larger N–P–N angle, which can be attributed to strong NH···O hydrogen bonds (see below). The short P–N bond lengths (average 1.628 Å) of the ionic Ter**3**[X] species indicate partial double bond character and lie in the expected range for amino(imino)phosphanes, for example P=N 1.545(6) and P–N 1.632(6) Å in MeN(H)–P=N–Mes* [Σr_{cov}(P–N) = 1.82 and Σr_{cov}(P=N) = 1.62 Å, where r_{cov} = covalent radii].[9d,29,30] Partial P–N double bond character due to hyperconjugation can be discussed for the covalently bound Ter**3**[X] species.[31] As expected for the covalently bound Ter**3**[X] species, small N–P–N angles between 91 and 95° were observed, whereas significantly larger N–P–N angles were measured for the ionic Ter**3**[X] compounds (N–P–N 96–100°), except for Ter**3**[CF_3SO_3] in which a larger angle was measured (104.9°).

Three types of interaction were found between the formal fragments [Ter**3**]$^+$ and [X]$^-$ in Ter**3**[X]: (i) polar covalent bonding with the phosphorus atom of [Ter**3**]$^+$ was found for small nucleophilic anions such as F^-, Cl^-, and [CF_3CO_2]$^-$ (Figure 1), (ii) NH···Y hydrogen bonding (Y = F, Cl, O, where Y is the donor atom of [X]$^-$) was found for medium sized anions that are small enough to enter the pocket generated by the terphenyl groups ([CF_3SO_3]$^-$) and larger complex anions ([$B(C_6F_5)_4$]$^-$, [$GaCl_4$]$^-$) that are capable of partially entering the terphenyl pocket (Figure 2), (iii) weak van der Waals interactions with peripheral H–C_{aryl} atoms were observed for large, weakly coordinating anions ([$Al\{OCH(CF_3)_2\}_4$]$^-$, [SbF_6]$^-$ and [$CHB_{11}H_5Br_6$]$^-$), which are simply too big to gain access to the terphenyl pocket and thus the formation of hydrogen bonds is impossible (Figure 3, Scheme 8).

As depicted in Scheme 8, the P–Y distances (where Y is the atom of [X]$^-$ closest to P) are found in the range between 1.634 (Y = F, Ter**3**F) and 2.008 Å (Y = Cl, Ter**3**Cl) for the covalent species with a typical P–Y single bond (cf. d(P–F) = 1.634(3) vs. Σr_{cov} = 1.66 Å; d(P–Cl) = 2.008(2) vs. Σr_{cov} = 2.04 Å; d(P–O1) = 1.789(2) vs. Σr_{cov} = 1.72 Å), 3.833 (Y = F, Ter**3**[$B(C_6F_5)_4$]) to 4.455 Å (Y = Cl, Ter**3**-[$GaCl_4$]) for species with strong NH···Y hydrogen bonds, and 5.478 (Y = F, Ter**3**[SbF_6]) and 6.445 (Y = Br, Ter**3**[$CHB_{11}H_5Br_6$]) for weak van der Waals interaction with peripheral H_{Ter} atoms.

Table 2. Selected structural data for Ter**3**[X] (X = F^-, Cl^-, [CF_3CO_2]$^-$, [CF_3SO_3]$^-$, [$B(C_6F_5)_4$]$^-$, [$GaCl_4$]$^-$, [SbF_6]$^-$, [$Al\{OCH(CF_3)_2\}_4$]$^-$ and [$CHB_{11}H_5Br_6$]$^-$) and Mes*-**3**[ECl_4] (E = Ga, Al) and $(TerNH)_2P(H)OAl[OCH(CF_3)_2]_3$ for comparison.

	N1–P [Å]	N2–P [Å]	N1–C1 [Å]	∠N–P–N [°]	τ_{aryl} [°][c]
Ter**3**F	1.704(6)	1.663(1)	1.38(2)	91.6(4)	54.3
Ter**3**Cl	1.697(2)	1.591(2)	1.412(2)	94.6(1)	56.3
Ter**3**[CF_3CO_2]	1.675(2)	1.687(2)	1.423(3)	94.84(9)	65.4
Ter**3**[CF_3SO_3]	1.623(3)	1.609(3)	1.443(4)	104.9(1)	89.3
Ter**3**[$B(C_6F_5)_4$]	1.630(3)	1.623(3)	1.440(4)	99.6(2)	87.4
Ter**3**[$GaCl_4$]	1.635(1)	1.626(1)	1.428(2)	99.61(6)	74.5
Ter**3**[SbF_6]	1.635(2)	1.635(2)	1.426(3)	98.0(2)	79.3
Ter**3**[$Al\{OCH(CF_3)_2\}_4$][a]	1.628(3)	1.635(3)	1.431(4)	98.5(2)	89.9
	1.619(3)	1.637(3)	1.435(4)	96.9(2)	89.9
Ter**3**[$CHB_{11}H_5Br_6$]	1.625(3)	1.630(3)	1.426(4)	96.3(1)	69.4
$(TerNH)_2P(H)OAl[OCH(CF_3)_2]_3$	1.625(2)	1.627(2)	1.435(2)	115.09(9)	35.3
Mes*-**3**[$GaCl_4$]	1.601(3)	1.601(3)	1.469(4)	105.2(2)	37.0
Mes*-**3**[$AlCl_4$] [b]	1.611	1.611	1.474	103.7	–

[a] Two independent molecules. [b] No standard deviations available, see ref.[9] [c] τ_{aryl} = torsion angle between the two planes composed of the central aryl of the terphenyl or Mes* group.

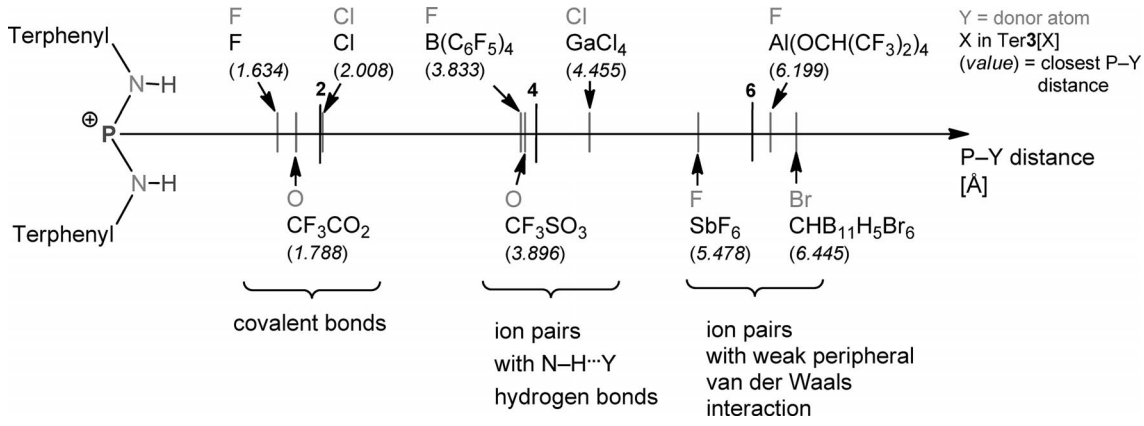

Scheme 8. Interactions between [Ter**3**]$^+$ and [X]$^-$ fragments.

Although the PN distances exhibit only insignificant deviations for all ionic Ter**3**[X] species (besides slightly smaller values for Ter**3**[CF_3SO_3]), the N–P–N angle is a sensitive measure for the magnitude of NH···Y hydrogen bonds (Y = halogen, O). The stronger these hydrogen bonds, the larger the N–P–N angle e.g. 96.3(1)° in Ter**3**[$CHB_{11}H_5Br_6$] with no hydrogen bonds vs. 104.9(1)° in Ter**3**[CF_3SO_3] with the strongest hydrogen bond found in the series. The comparison between Ter**3**[$GaCl_4$] (99.6°) and Mes***3**[$GaCl_4$] (105.2°) supports this argument as significantly shorter NH···Cl contacts are found in Mes***3**[$GaCl_4$] (see below, Table 2, Figure 2), which might be the reason for their different behaviour in solution (ion paring vs. solvated ions, see above).

The hydrogen bond may be generally considered as a three-centre four-electron interaction that stabilises and is associated with spectroscopic and structure-defining effects.[32] Their classification into weak, strong and very strong is somewhat subjective. However, it is their directionality that makes hydrogen bonds important as crystal-structure directors (Figure 2). In the three Ter**3**[X] species (X = $[CF_3SO_3]^-$, $[B(C_6F_5)_4]^-$, and $[GaCl_4]^-$) the NH···Y hydrogen bonds can be classified as strong as they dominate the interionic interaction. The strongest hydrogen bonds are found in Ter**3**[CF_3SO_3] with N···O distances of 2.746 (N1–O3) and 2.830 Å (N2–O2), which result in other structural changes such as a larger N–P–N angle (see above). Especially interesting are the hydrogen bonds in Ter**3**[$B(C_6F_5)_4$] with N···F–C_{aryl} distances of 3.075 (N1–F13) and 3.228 (N2–F12) Å as only one C_6F_5 ring of the anion is inside the terphenyl pocket which is reminiscent of the key–lock principle known in biology. Due to the parallel arrangement of this C_6F_5 ring with one aryl substituent of both terphenyl groups, further weak van der Waals interactions between C_{aryl}···F–C_{anion} (shortest distance 3.547 Å) and C_{aryl}···C–F_{anion} (shortest distance 3.457 Å) and weak C_{methyl}–H···F–C_{anion} hydrogen bonds (shortest C_{methyl}···F–C_{anion} 3.327 Å) can be assumed. In Ter**3**[$GaCl_4$], it is interesting to compare the N–H···Cl–$GaCl_3$ hydrogen bond and with that in Mes***3**[$GaCl_4$] with respect to steric strain. Although in Ter**3**[$GaCl_4$] only one Cl atom forms two N–H···Cl bonds (N1–Cl1 3.796 and N2–Cl1 3.505 Å), in Mes***3**[$GaCl_4$] two Cl atoms form one N–H···Cl bond each in a bidentate fashion, which are identical due to symmetry (3.430 Å, Figure 2). The shorter N–H···Cl distances and the increase of the N–P–N angle (Table 2) indicate stronger hydrogen bonds in Mes***3**[$GaCl_4$]. In Ter**3**[$GaCl_4$], the terphenyl pocket provides less space compared to the situation in Mes***3**[$GaCl_4$] and only one Cl atom fits into the pocket. The strong N–H···Cl–$GaCl_3$ hydrogen bond in Ter**3**[$GaCl_4$] is also manifested by considerable Ga–Cl bond lengthening for the Cl1 atom that is involved in the hydrogen bond [cf. Ga1–Cl1 2.1928(4) vs. Ga1–Cl3 2.1632(5), Ga1–Cl4 2.1652(4), Ga1–Cl2 2.1743(4) Å, Figure 2]. Also in Mes***3**-[$GaCl_4$], two significantly different Ga–Cl bond lengths are found for Ga1–Cl1 2.155(1) and Ga1–Cl2 2.1872(9) Å, where Cl2 and Cl2′ are also involved in hydrogen bonds. The essence of this comparison is the fact that the Mes* group provides more steric protection for the α-atom attached to the Mes* group (e.g. a larger Tolman angle for Mes* 228° vs. Ter 206°),[33] whereas the terphenyl group is capable of embedding a larger moiety and thus better protecting the β-atom such as in the N(H)PN(H) unit in R**3**[X] (R = Mes*, Ter) compounds.

In addition to the interionic hydrogen bonds that have been discussed, short O2···N1 (3.046) and O2···N2 (2.885 Å) distances are present in Ter**3**[CF_3CO_2], which suggest intramolecular NH···O2 hydrogen bonds (Figure 1).

Finally, Ter**3**[X] (X = $[SbF_6]^-$, $[Al\{OCH(CF_3)_2\}_4]^-$ and $[CHB_{11}H_5Br_6]^-$) are poorly crystalline, [34] which indicates the presence of only very weak interionic interactions. It is known that cations with C–H bonds in the presence of fluorido-containing anions usually crystallise better, which is likely to be through the formation of many assisting H–F contacts (e.g. $[Ag(C_2H_4)][Al(OR^F)_4]$[35] and $[H(OEt_2)_2][Al(OR^F)_4]$,[36] where R^F = $C(CF_3)_3$). For all three Ter**3**[X] species, many assisting C_{methyl}–H···Y (Y = F, Br) contacts were detected ($< \Sigma r_{vdW}$(H···Y) = 2.9 for Y = F and 3.3 Å for Y = Br, where r_{vdW} = van der Waals radii),[37] of which only a few (shortest contacts) are shown for the ion pairs in Figure 3. However, these dispersive interactions are weak and not structure determining. Therefore, the structural parameters of Ter**3** within the framework of an ensemble of large and weakly coordinating anions such as $[SbF_6]^-$,

$[Al\{OCH(CF_3)_2\}_4]^-$ and $[CHB_{11}H_5Br_6]^-$ are almost identical (Table 2).

Conclusions

Different synthetic routes to salts that bear the *N*,*N*-bis(terphenyl)aminophosphenium cation (Ter**3**) have been studied. Simple salt-elimination reactions of $(TerNH)_2P–Cl$ with Ag[X] (X = weakly coordinating anion) or the protonation of TerN(H)PNTer with strong acids offer a generally applicable and economic access to Ter**3**[X] compounds with a wide range of anions. Most Ter**3**[X] compounds were obtained in good yields and purity and are suitable starting materials for further synthesis.

Systematic single-crystal X-ray diffraction studies of Ter**3**[X] with focus on the cation–anion interaction revealed that, depending on the size of the anion, the pocket formed by the terphenyl can be entered to some degree, which resulted in strong, structure-defining interionic hydrogen bonds ($[X]^-$ = $[CF_3SO_3]^-$, $[B(C_6F_5)_4]^-$ and $[GaCl_4]^-$). For the ions ($[SbF_6]^-$, $[Al\{OCH(CF_3)_2\}_4]^-$ and $[CHB_{11}H_5Br_6]^-$) that are too big to fit into the terphenyl pocket, many $C_{methyl}–H\cdots Y$ (Y = F, Br) contacts were detected, which can be described as weak dispersive interactions that are not structure determining.

Solution NMR spectroscopic data suggest the dissociation of ionic Ter**3**[X] in contrast to analogous Mes* species, in which ion pairing is observed. This different solution behaviour can be attributed to the better steric protection provided by the terphenyl substituent, which prevents stronger hydrogen bonds. The only exception in the series of ionic Ter**3**[X] species is Ter**3**$[CF_3SO_3]$, for which ion pairing in solution was found to be due to very strong hydrogen bonding.

We have shown that Ter**3** can be used as sensitive probe for the examination of anion properties as well as the type and degree of cation–anion interactions.

Experimental Section

General Information: All manipulations were carried out under oxygen- and moisture-free conditions under argon using standard Schlenk or drybox techniques.

Dichloromethane was purified according to a literature procedure[38] by drying with P_4O_{10} followed by CaH_2 and was freshly distilled and degassed prior to use. Diethyl ether, tetrahydrofuran (THF), toluene and benzene were dried with Na/benzophenone, *n*-hexane was dried with Na/benzophenone/tetraglyme. All solvents were freshly distilled prior to use. *n*BuLi (Acros, 2.5 M), $AgBF_4$ (Acros, 99%), $GaCl_3$ (abcr, 99.9%), SbF_5 (Acros, 99%), $SbCl_5$ (Acros, 99%), $Na[B(C_6H_5)_4]$ (Acros, 99.5%) and $AgSbF_6$ (abcr, 98%) were used as received. PCl_3 (Acros, 97%), CF_3SO_3H (Merck, 98%) and CF_3CO_2H (Solvay, 99%) were freshly distilled prior to use. 2,6-Bis(2,4,6-trimethylphenyl)aniline ($TerNH_2$), 2,6-bis(2,4,6-trimethylphenyl)phenylamino(dichloro)phosphane ($TerN(H)PCl_2$), $Ag[CHB_{11}H_5Br_6]$, silver triflate $Ag[CF_3SO_3]$, $Ag[CF_3CO_2]$, $Ag[Al\{OCH(CF_3)_2\}_4]$ and $Ag(toluene)_3[B(C_6F_5)_4]$ were prepared according to literature procedures.[39,40,41,42,22c] $[(Et_2O)_2H][B(C_6F_5)_4]$ and $Ag[B(C_6H_5)_4]$ were prepared according to modified procedures.[43,44] $^{31}P\{^1H\}$, $^{19}F\{^1H\}$, $^{11}B\{^1H\}$, $^{13}C\{^1H\}$, ^{13}C DEPT and ^1H NMR spectra were obtained with a Bruker AVANCE 250, 300 or 500 spectrometer and were referenced internally to the deuterated solvent (^{13}C, CD_2Cl_2: $\delta_{reference}$ = 54 ppm, $[D_6]$DMSO $\delta_{reference}$ = 40 ppm) or to protic impurities in the deuterated solvent (^1H, $CDHCl_2$: $\delta_{reference}$ = 5.31 ppm, $[D_5]$DMSO = 2.5 ppm). CD_2Cl_2 was dried with P_4O_{10} and freshly distilled prior to use. $[D_6]$DMSO was dried with CaH_2 and freshly distilled prior to use. IR spectra were recorded with a Nicolet 6700 FTIR spectrometer with a Smart Endurance ATR device. Raman spectra were recorded with a Bruker VERTEX 70 FTIR with RAM II FT-Raman module equipped with a Nd:YAG laser (1064 nm). Elemental analyses were measured with an Analysator Flash EA 1112 instrument from Thermo Quest. MS were recorded with a Finnigan MAT 95-XP instrument from Thermo Electron. Melting points were measured on an EZ-Melt instrument from Stanford Research Systems at a heating rate of 20 °C/min (clearing-points are reported). DSC measurements were performed with a DSC 823e instrument from Mettler-Toledo (Heating rate 5 °C/min). UV/Vis spectra were measured with a Lambda 19 instrument from Perkin–Elmer with Lambda-SPX 1 software. Samples were measured in CH_2Cl_2 at ambient temperature. Settings: Scan: 200–800 nm, Interval 0.5 nm, Scan speed 120 nm/min, Smooth 1, Slit 1 nm.

Ter3F: To a stirred suspension of $(TerNH)_2PCl$ (0.500 g, 0.69 mmol) in CH_2Cl_2 (5 mL) was added $AgBF_4$ powder (0.136 g, 0,70 mmol) in small portions at –80 °C over 20 min. The orange solution was warmed to ambient temperature for 30 min, which resulted in the precipitation of silver chloride. The mixture was degassed three times by a freeze–pump–thaw procedure. The precipitate was removed by filtration (F4), and the solvent was removed in vacuo. The resulting yellow residue was washed four times with *n*-hexane (4 mL), dried in vacuo and dissolved in toluene (4 mL). The second fraction of a fractional crystallisation, with storage at –25 °C over 12 h, was collected and washed with toluene (0.5 mL). Removal of the solvent by syringe and drying in vacuo yielded Ter**3**F as a colourless powder (0.098 g, 0.14 mmol, 20%); m.p. 225 °C (dec.). $C_{48}H_{52}FN_2P$ (706.91): calcd. C 81.55, H 7.41, N 3.96; found C 80.43, H 7.46, N 3.90. $^{31}P\{^1H\}$ NMR (121.5 MHz, CD_2Cl_2, 25 °C): δ = 119.70 [d, $^1J(^{19}F,^{31}P)$ = 1084 Hz] ppm. $^{19}F\{^1H\}$ NMR (282.4 MHz, CD_2Cl_2, 25 °C): δ = –63.15 [d, $^1J(^{19}F,^{31}P)$ = 1084 Hz] ppm. ^1H NMR (300.13 MHz, CD_2Cl_2, 25 °C): δ = 1.57 (s, 12 H, *o*-CH_3), 1.73 (s, 12 H, *o*-CH_3), 2.28 (s, 12 H, *p*-CH_3), 3.79 (br. s, 2 H, NH), 6.70–6.84 (m, 12 H, *m*-CH), 6.85–6.91 (m, 2 H, *p*-CH) ppm. $^{13}C\{^1H\}$ NMR (62.9 MHz, CD_2Cl_2, 25 °C): δ = 20.0 (s, *o*-CH_3), 20.43 (br. s, *o*-CH_3), 21.56 (s, *o*-CH_3), 122.0 (s, CH), 128.8 [d, $J(^{13}C,^{31}P)$ = 10.1 Hz], 129.7 (s, CH), 130.9 (m, CH), 135.6 (s, CH), 137.2–137.5 (m), 137.5 (s) ppm. IR (ATR, 25 °C): $\tilde{\nu}$ = 3334 (m), 3292 (m), 3000 (m), 2945 (m), 2915 (m), 2853 (m), 2731 (w), 1611 (m), 1583 (m), 1553 (w), 1530 (w), 1513 (w), 1486 (m), 1418 (s), 1373 (s), 1305 (m), 1265 (m), 1225 (s), 1183 (m), 1097 (w), 1073 (m), 1031 (m), 1006 (m), 946 (m), 928 (m), 889 (s), 861 (m), 846 (s), 836 (s), 796 (m), 751 (s), 697 (s), 662 (m), 650 (m), 637 (m), 597 (m), 563 (m), 549 (m) cm^{-1}. Raman (400 mW, 25 °C, 3 accumulations): 3049 (1), 3012 (1), 2949 (1), 2917 (1), 2856 (1), 2732 (1), 1613 (3), 1587 (3), 1484 (3), 1449 (3), 1379 (4), 1305 (5), 1288 (3), 1182 (3), 1165 (3), 1159 (3), 1078 (3), 1007 (3), 947 (3), 892 (2), 837 (3), 752 (3), 740 (3), 699 (3), 662 (3), 636 (3), 579 (4), 560 (3), 522 (3), 414 (3), 395 (3), 369 (3), 336 (3), 275 (3) cm^{-1}. CI-MS: *m*/*z* (%) = 329 (11) $[TerNH_2]^+$, 330 (60) $[TerNH_3]^+$, 705 (14) $[M + F – H]^+$, 706 (19) $[M + F]^+$, 707 (100) $[M + F + H]^+$. UV/Vis (25 °C, CH_2Cl_2): λ = 292 (s), 249 (s) nm. Crystals suitable for X-ray crystallographic analysis were obtained by concentration of a dichloro-

methane solution of Ter**3**F to incipient crystallisation and storage at –25 °C overnight.

Ter3Cl: An excess of gaseous HCl was passed through a stirred suspension of TerN(H)PNTer (1.31 g, 1.90 mmol) in Et_2O (80 mL) at 0 °C over one hour. The solution was warmed to ambient temperature and stirred for one hour. The solvent was removed in vacuo, and the yellow residue was extracted four times into toluene (40 mL) and filtered (F4). The resulting light yellow solution was concentrated to incipient crystallisation and stored at –1 °C for two days, which resulted in the deposition of colourless crystals. Removal of solvent by syringe and drying in vacuo yielded Ter**3**Cl as a colourless crystalline solid (0.77 g, 1.10 mmol, 58%); m.p. 265 °C. $C_{48}H_{52}ClN_2P$ (723.37): calcd. C 79.70, H 7.25, N 3.87; found C 79.26, H 6.84, N 4.07. $^{31}P\{^1H\}$ NMR (121.5 MHz, CD_2Cl_2, 25 °C): δ = 129.9 ppm. ^1H NMR (300.13 MHz, CD_2Cl_2, 25 °C): δ = 1.68 (s, 12 H, *o*-CH_3), 1.85 (s, 12 H, *o*-CH_3), 2.39 (s, 12 H, *p*-CH_3), 4.08 [d, 2 H, NH, $^2J(^1H,^{31}P)$ = 3.6 Hz], 6.80–6.94 (m, 12 H, *m*-CH), 6.95–7.01 (m, 2 H, *p*-CH) ppm. $^{13}C\{^1H\}$ NMR (75.5 MHz, CD_2Cl_2, 25 °C): δ = 20.30 (s, *o*-CH_3), 20.68 [d, *o*-CH_3, $J(^{13}C,^{31}P)$ = 2.2 Hz], 21.61 (s, *p*-CH_3), 122.68 [d, *p*-CH, $J(^{13}C,^{31}P)$ = 2.2 Hz], 129.00 [d, *m*-C*H*-Mes, $J(^{13}C,^{31}P)$ = 2.8 Hz], 131.64 [d, $J(^{13}C,^{31}P)$ = 3.3 Hz], 135.08 (s), 137.34 [d, $J(^{13}C,^{31}P)$ = 1.7 Hz], 137.25 [d, $J(^{13}C,^{31}P)$ = 3.9 Hz], 137.67 (s), 137.75 [d, $J(^{13}C,^{31}P)$ = 2.2 Hz] ppm. IR (ATR, 25 °C): $\tilde{\nu}$ = 3309 (m), 3285 (m), 2971 (w), 2945 (w), 2914 (m), 2853 (w), 2731 (w), 1610 (m), 1582 (w), 1486 (w), 1419 (s), 1373 (s), 1303 (m), 1284 (m), 1260 (m), 1254 (m), 1242 (m), 1222 (s), 1183 (m), 1098 (w), 1073 (m), 1031 (m), 1006 (m), 931 (m), 895 (s), 861 (m), 846 (s), 797 (m), 770 (s), 752 (s), 664 (m), 639 (m), 597 (m), 563 (m), 549 (m) cm^{-1}. Raman (500 mW, 25 °C, 750 scans): 3312 (1), 3286 (1), 3052 (2), 3015 (2), 2917 (3), 2857 (2), 2731 (1), 1613 (3), 1586 (2), 1482 (2), 1443 (2), 1380 (2), 1304 (3), 1232 (1), 1183 (2), 1162 (1), 1079 (2), 1007 (2), 948 (1), 838 (1), 741 (1), 664 (1), 579 (2), 561 (2), 523 (2), 415 (2), 386 (2), 336 (2), 275 (2), 240 (2) cm^{-1}. CI-MS: *m*/*z* (%) = 330 (15) $[TerNH_3]^+$, 687 (100) $[M – Cl]^+$, 743 (20) [isobutene + M]$^+$. UV/Vis (25 °C, CH_2Cl_2): λ = 297 (s), 248 (s) nm. Crystals of Ter**3**Cl suitable for X-ray crystallographic analysis were obtained in moderate yield by prolonged storage of dichloromethane solutions at –1 °C.

Ter3[B(C_6F_5)$_4$]: To a stirred solution of $(TerNH)_2PCl$ (0.180 g, 0.25 mmol) in toluene (15 mL) was added a solution of Ag[B(C_6F_5)$_4$]·2toluene (0.243 g, 0.25 mmol) in toluene (15 mL) dropwise at ambient temperature over 15 min. The orange solution was stirred for 1 h. The solvent was removed in vacuo, and the orange residue was dissolved in CH_2Cl_2 (10 mL) and filtered (F4). The resulting orange solution was concentrated to incipient crystallisation and stored at –1 °C overnight, which resulted in the deposition of orange crystals. Removal of solvent by syringe and drying in vacuo yielded the dichloromethane solvate Ter**3**[B(C_6F_5)$_4$] as an orange crystalline solid (0.125 g, 0.092 mmol, 37%); m.p. 244 °C (dec.). $C_{73}H_{54}BCl_2F_{20}N_2P$ (1451.88): calcd. C 60.39, H 3.75, N 1.93; found C 60.40, H 3.68, N 1.86. $^{31}P\{^1H\}$ NMR (121.5 MHz, CD_2Cl_2, 25 °C): δ = 249.1 ppm. ^1H NMR (300.13 MHz, CD_2Cl_2, 25 °C): δ = 1.76 (s, 24 H, *o*-CH_3), 2.25 (s, 12 H, *p*-CH_3), 6.94 (s, 8 H, *m*-CH-Mes), 7.14 [d, 4 H, *m*-CH, $^3J(^1H,^1H)$ = 7.74 Hz], 7.31 [d, 2 H, NH, $^2J(^1H,^{31}P)$ = 12.3 Hz], 7.36–743 (m, 2 H, *p*-CH) ppm. $^{11}B\{^1H\}$ NMR (96.29 MHz, CD_2Cl_2, 25 °C): δ = –16.60 ppm. $^{19}F\{^1H\}$ NMR (282.38 MHz, CD_2Cl_2, 25 °C): δ = –132.78 (m), –163.75 (m), –167.49 (m) ppm. $^{13}C\{^1H\}$ NMR (75.5 MHz, CD_2Cl_2, 25 °C): δ = 20.65 (s, *o*-CH_3), 21.32 (s, *p*-CH_3), 129.08 (s, *p*-CH), 130.61 (s, *m*-CH-Mes), 131.08 (s, *m*-CH), 132.26 [d, $J(^{13}C,^{31}P)$ = 3.3 Hz], 132.59 [d, $J(^{13}C,^{31}P)$ = 4.4 Hz], 132.76 [d, $J(^{13}C,^{31}P)$ = 3.0 Hz], 137.52 [d, $J(^{13}C,^{31}P)$ = 6.0 Hz], 141.23 (s), 148.7 [d, *o*-CF, $^1J(^{13}C,^{19}F)$ = 238 Hz], 138.8 [d, *p*-CF, $^1J(^{13}C,^{19}F)$ = 240 Hz], 136.9 [d, *m*-CF, $^1J(^{13}C,^{19}F)$ = 241 Hz], 125 (*ipso*-C) ppm. IR (ATR, 25 °C): $\tilde{\nu}$ = 3287 (w), 2974 (w), 2919 (w), 2859 (w), 2738 (w), 1642 (w), 1611 (w), 1558 (w), 1511 (s), 1461 (s), 1419 (m), 1379 (m), 1340 (m), 1308 (m), 1239 (s), 1203 (m), 1154 (m), 1081 (s), 1033 (m), 977 (s), 954 (s), 857 (m), 806 (m), 774 (m), 756 (s), 738 (s), 681 (m), 660 (s), 630 (m), 610 (m), 600 (m), 572 (m), 556 (m) cm^{-1}. Raman (1500 mW, 25 °C, 700 scans): 3065 (1), 3019 (1), 2922 (2), 2861 (1), 2739 (1), 1644 (1), 1611 (3), 1584 (3), 1480 (2), 1422 (3), 1381 (2), 1301 (3), 1260 (2), 1216 (4), 1187 (3), 1079 (3), 1009 (2), 968 (5), 843 (2), 732 (1), 658 (1), 598 (2), 583 (3), 556 (2), 521 (2), 491 (2), 448 (2), 267 (2) cm^{-1}. MS (ESI-TOF): *m*/*z* (%) = 679 (100) $[B(C_6F_5)_4]^-$. CI-MS: *m*/*z* (%) = 330 (100) $[TerNH_3]^+$, 526 (40) $[TerNP(C_6F_5)]^+$, 687 (41) $[M]^+$, 855 (35) $[M + C_6F_5]^+$. UV/Vis (25 °C, CH_2Cl_2): λ = 422 (w), 358 (m), 296 (m), 260 (s) nm. Crystals of Ter**3**[B(C_6F_5)$_4$] suitable for X-ray crystallographic analysis were obtained in moderate yield by prolonged storage of a saturated dichloromethane solution at ambient temperature.

Ter3[CF_3CO_2]: To a stirred solution of TerN(H)PNTer (0.343 g, 0.50 mmol) in toluene (10 mL) was added a solution of trifluoroacetic acid (0.057 g, 0.50 mmol) in toluene (1 mL) dropwise at –80 °C over five minutes. The solution was warmed to ambient temperature and stirred for one hour. The solvent was removed in vacuo, and the yellow residue was dissolved in dichloromethane (5 mL). The resulting yellow solution was concentrated to incipient crystallisation and stored at ambient temperature overnight, which resulted in the deposition of pale yellow crystals. The supernatant was removed, and the crystalline residue was washed with dichloromethane (0.5 mL) and dried in vacuo to yield Ter**3**[CF_3CO_2] (0.196 g, 0.24 mmol, 48%); m.p. 177 °C (dec. 190 °C). $C_{50}H_{52}F_3N_2O_2P$ (800.93): calcd. C 74.98, H 6.54, N 3.50; found C 74.89, H 6.54, N 3.36. $^{31}P\{^1H\}$ NMR (121.5 MHz, CD_2Cl_2, 25 °C): δ = 116.7 ppm. ^1H NMR (300.13 MHz, CD_2Cl_2, 25 °C): δ = 1.75 (m, 24 H, *o*-CH_3), 2.36 (s, 12 H, *p*-CH_3), 4.38 [d, 2 H, NH, $^2J(^1H,^{31}P)$ = 4.5 Hz], 6.78–6.92 (m, 12 H, *m*-CH), 6.93–7.00 (m, 2 H, *p*-CH) ppm. $^{19}F\{^1H\}$ NMR (282.4 MHz, CD_2Cl_2, 25 °C): δ = –75.25 (s) ppm. $^{13}C\{^1H\}$ NMR (75.5 MHz, CD_2Cl_2, 25 °C): δ = 20.35 (m, *o*-CH_3), 21.56 (s, *p*-CH_3), 122.52 (s, *p*-CH), 129.10 (s, *m*-CH-Mes), 130.19 (*m*-CH), 130.81 (d), 135.24 (d), 137.17 (br. s), 137.58 (s), 137.67 (s), 137.93 (s) ppm. IR (ATR, 25 °C): $\tilde{\nu}$ = 3354 (w), 3314 (w), 3298 (w), 3250 (w), 2946 (w), 2917 (m), 2856 (w), 1875 (w), 1756 (m), 1611 (m), 1487 (w), 1434 (m), 1422 (s), 1368 (m), 1288 (w), 1264 (m), 1241 (w), 1209 (s), 1157 (s), 1142 (s), 1133 (s), 1075 (m), 1031 (m), 1007 (m), 949 (m), 933 (m), 899 (s), 848 (s), 798 (m), 777 (m), 754 (s), 731 (m), 704 (m), 696 (m), 661 (m), 648 (m), 629 (m), 614 (m), 596 (m), 550 (m) cm^{-1}. Raman (1500 mW, 25 °C, 700 scans): 3316 (1), 3300 (1), 3048 (3), 3011 (3), 2915 (3), 2859 (2), 2733 (2), 2550 (1), 1759 (1), 1611 (4), 1588 (3), 1484 (2), 1445 (2), 1381 (3), 1306 (5), 1229 (3), 1185 (1), 1164 (1), 1077 (2), 1007 (2), 949 (1), 824 (1), 739 (1), 662 (2), 577 (3), 554 (2), 521 (2), 489 (1), 415 (1), 330 (2), 276 (2), 249 (2), 234 (2) cm^{-1}. CI-MS *m*/*z* (%) = 330 (100) $[TerNH_3]^+$, 358 (26) $[TerNP]^+$, 671 (15) $[M – CH_4]^+$, 687 (77) $[M]^+$, 705 (21) $[M + F – H]^+$. UV/Vis (25 °C, CH_2Cl_2): λ = 290 (s), 250 (s) nm. Crystals suitable for X-ray crystallographic analysis were obtained by concentration of a dichloromethane solution of Ter**3**[CF_3CO_2] to incipient crystallisation and storage at ambient temperature overnight.

Ter3[$GaCl_4$]: To a stirred suspension of $(TerNH)_2PCl$ (0.180 g, 0.25 mmol) in dichloromethane (6 mL) was added a solution of $GaCl_3$ (0.053 g, 0.30 mmol) in dichloromethane (2 mL) dropwise at ambient temperature over ten minutes. The pale yellow suspension was stirred for one hour, which resulted in an orange solution. This solution was concentrated to incipient crystallisation and stored at –1 °C overnight, which resulted in the deposition of orange crystals.

The supernatant was removed, and the crystalline residue was washed with dichloromethane (0.5 mL) and dried in vacuo to yield Ter**3**[$GaCl_4$] as a orange crystalline solid (0.105 g, 0.12 mmol, 47%); m.p. 215 °C (dec.). $C_{48}H_{52}Cl_4GaN_2P$ (899.45): calcd. C 64.10, H 5.92, N 3.11; found C (measured with lead oxide) 64.53, H 5.92, N 3.14. $^{31}P\{^1H\}$ NMR (121.5 MHz, CD_2Cl_2, 25 °C): δ = 250 ppm. ^1H NMR (300.13 MHz, CD_2Cl_2, 25 °C): δ = 1.80 (s, 24 H, *o*-CH_3), 2.32 (s, 12 H, *p*-CH_3), 7.04 (br. s, 8 H, *m*-CH-Mes), 7.15 [d, 4 H, *m*-CH, $^3J(^1H,^1H)$ = 7.6 Hz], 7.38[d, 2 H, NH, $^2J(^1H,^{31}P)$ = 12.5 Hz], 7.39–7.44 (m, 2 H, *p*-CH) ppm. $^{13}C\{^1H\}$ NMR (75.5 MHz, CD_2Cl_2, 25 °C): δ = 20.83 (br. s, *o*-CH_3), 21.53 (s, *p*-CH_3), 129.12 (s, *p*-CH), 130.64 (s, *m*-CH-Mes), 131.14 (s, *m*-CH), 132.23 [d, $J(^{13}C,^{31}P)$ = 3.3 Hz], 132.72 [d, $J(^{13}C,^{31}P)$ = 4.4 Hz], 132.86 [d, $J(^{13}C,^{31}P)$ = 2.8 Hz], 137.57 [d, $J(^{13}C,^{31}P)$ = 3.9 Hz], 141.21 (s) ppm. IR (ATR, 25 °C): $\tilde{\nu}$ = 3333 (w), 3261 (m), 3052 (w), 2975 (m), 2945 (m), 2916 (m), 2844 (m), 2737 (w), 1609 (m), 1573 (m), 1557 (m), 1478 (m), 1436 (s), 1416 (m), 1380 (m), 1342 (m), 1300 (m), 1292 (m), 1254 (m), 1201 (m), 1164 (m), 1129 (m), 1068 (m), 1032 (m), 1007 (m), 950 (s), 939 (s), 852 (s), 800 (s), 780 (m), 753 (s), 737 (m), 652 (m), 627 (m), 598 (m), 571 (m), 562 (m), 544 (m) cm^{-1}. Raman (1500 mW, 25 °C, 669 scans): 3264 (1), 3057 (1), 3023 (1), 2917 (3), 2857 (1), 2737 (1), 1611 (3), 1582 (3), 1480 (2), 1420 (3), 1380 (2), 1310 (3), 1268 (2), 1216 (5), 1187 (3), 1073 (3), 1007 (2), 963 (4), 840 (2), 730 (2), 658 (2), 598 (2), 583 (3), 521 (2), 489 (2), 415 (2), 361 (2), 269 (2), 230 (1), 207 (1) cm^{-1}. CI-MS: *m*/*z* (%) = 358 (16) $[TerNP]^+$, 671 (21) $[M - CH_4]^+$, 687 (100) $[M]^+$. UV/Vis (25 °C, CH_2Cl_2): λ = 438 (m), 361 (m), 255 (s) nm. Crystals suitable for X-ray crystallographic analysis were obtained by concentration of a dichloromethane solution of Ter**3**[$GaCl_4$] to incipient crystallisation and storage at ambient temperature overnight.

Ter3[CF_3SO_3]: To a stirred solution of TerN(H)PNTer (0.342 g, 0.50 mmol) in toluene (22 mL) was added a solution of CF_3SO_3H (0.075 g, 0.50 mmol) in toluene (4 mL) dropwise at –80 °C over ten minutes. The resulting yellow solution was warmed to ambient temperature and stirred for 30 min. The solvent was removed in vacuo, and the yellow residue was dissolved in dichloromethane (5 mL). This solution was concentrated to incipient crystallisation and stored at –25 °C overnight, which resulted in the deposition of orange crystals. The supernatant was removed, and the crystalline residue was washed with dichloromethane (0.5 mL) and dried in vacuo to yield Ter**3**[CF_3SO_3] as an orange crystalline solid (0.08 g, 0.10 mmol, 20%); m.p. 255 °C (dec.). $C_{49}H_{52}F_3N_2O_3PS$ (836.98): calcd. C 70.31, H 6.26, N 3.35; found C 70.44, H 6.80, N 3.32. $^{31}P\{^1H\}$ NMR (121.5 MHz, CD_2Cl_2, 25 °C): δ = 261 (br. s) ppm. ^1H NMR (300.13 MHz, CD_2Cl_2, 25 °C): δ = 1.74 (s, 24 H, *o*-CH_3), 2.33 (s, 12 H, *p*-CH_3), 6.94 (s, 8 H, *m*-CH-Mes), 7.01 [d, 4 H, *m*-CH, $^3J(^1H,^1H)$ = 7.7 Hz], 7.34 (m, 2 H, *p*-CH), 9.67 [d, 2 H, NH, $^2J(^1H,^{31}P)$ = 12.3 Hz] ppm. $^{13}C\{^1H\}$ NMR (75.5 MHz, CD_2Cl_2, 25 °C): δ = 20.86 [d, *o*-CH_3, $J(^{13}C,^{31}P)$ = 2.2 Hz], 21.56 (s, *p*-CH_3), 128.66 (s, *p*-CH), 129.66 (s, *m*-CH-Mes), 131.34 (s, *m*-CH), 132.90 [d, $J(^{13}C,^{31}P)$ = 8.8 Hz], 133.64 (br. s), 135.46 [d, $J(^{13}C,^{31}P)$ = 5.5 Hz], 137.55 [d, $J(^{13}C,^{31}P)$ = 2.8 Hz], 139.60 (s) ppm. $^{19}F\{^1H\}$ NMR (282.38 MHz, CD_2Cl_2, 25 °C): δ = –78.67 (s) ppm. IR (ATR, 25 °C): $\tilde{\nu}$ = 3341 (w), 3234 (w), 2917 (m), 2857 (w), 2734 (w), 1612 (w), 1575 (w), 1566 (w), 1506 (w), 1441 (m), 1426 (m), 1379 (m), 1293 (m), 1269 (m), 1223 (s), 1168 (s), 1077 (w), 1024 (s), 1010 (s), 969 (m), 850 (s), 803 (m), 754 (m), 744 (m), 636 (s), 596 (m), 563 (m), 551 (m), 541 (m) cm^{-1}. Raman (400 mW, 25 °C, 750 scans): 3055 (3), 3017 (2), 2919 (4), 2858 (2), 2733 (1), 1613 (4), 1682 (3), 1582 (3), 1484 (2), 1435 (3), 1378 (2), 1306 (1), 1214 (5), 1189 (2), 1083 (3), 1031 (2), 1009 (2), 982 (5), 855 (2), 797 (1), 739 (2), 654 (2), 579 (2), 554 (2), 523 (2), 415 (2), 384 (2), 330 (2), 265 (2), 232 (2) cm^{-1}. CI-MS: *m*/*z* (%) = 330 (100) $[TerNH_3]^+$, 687 (13) $[M]^+$. UV/Vis (25 °C, CH_2Cl_2): λ = 438 (w), 363 (m), 292 (s), 246(s) nm. Crystals suitable for X-ray crystallographic analysis were obtained by concentration of a dichloromethane solution of Ter**3**[CF_3SO_3] to incipient crystallisation and storage at –25 °C overnight.

Ter3[Al{$OCH(CF_3)_2$}$_4$]: To a stirred solution of $(TerNH)_2PCl$ (0.175 g, 0.24 mmol) in dichloromethane (4 mL) was added a solution of Ag[Al{$OCH(CF_3)_2$}$_4$] (0.200 g, 0.25 mmol) in dichloromethane (2 mL) dropwise at ambient temperature over ten minutes. The orange solution was stirred for 30 min and filtered (F4). The solvent was removed in vacuo, and the orange precipitate was washed four times with *n*-hexane (4 mL). This precipitate was dissolved in dichloromethane (2 mL) and filtered (F4). Removal of solvent by syringe and drying in vacuo yielded Ter**3**[Al{$OCH(CF_3)_2$}$_4$] (0.232 g, 0.17 mmol, 70%) as a shiny orange mircocrystalline solid; m.p. 273 °C (dec.). $C_{60}H_{56}AlF_{24}N_2O_4P$ (1383.01): calcd. C 52.11, H 4.08, 2.03; found C 52.74, H 4.08, N 1.97. $^{31}P\{^1H\}$ NMR (121.5 MHz, CD_2Cl_2, 25 °C): δ = 249 (br. s) ppm. ^1H NMR (300.13 MHz, CD_2Cl_2, 25 °C): δ = 1.79 (s, 24 H, *o*-CH_3), 2.31 (s, 12 H, *p*-CH_3), 4.51 (m, 4 H, isopropoxy), 7.02 (s, 8 H, *m*-CH-Mes), 7.15 [d, 4 H, *m*-CH, $^3J(^1H,^1H)$ = 7.7 Hz], 7.29 [br. d, 2 H, NH, $^2J(^1H,^{31}P)$ = 12.3 Hz] ppm. 7.42 [t, 2 H, *p*-CH, $^3J(^1H,^1H)$ = 7.7 Hz]. $^{13}C\{^1H\}$ NMR (75.5 MHz, CD_2Cl_2, 25 °C): δ = 20.75 (s, *o*-CH_3), 21.47 (s, *p*-CH_3), 71.47 (m, isopropoxy), 121.71 (s, CF_3), 125.51 (s, CF_3) 129.16 (s, *p*-CH), 130.70 (s, *m*-CH-Mes), 131.14 (s, *m*-CH), 132.25 [d, $J(^{13}C,^{31}P)$ = 3.3 Hz], 132.52 46 [d, $J(^{13}C,^{31}P)$ = 4.4 Hz], 132.90 [d, $J(^{13}C,^{31}P)$ = 2.8 Hz], 137.60 [d, $J(^{13}C,^{31}P)$ = 3.9 Hz], 141.33 (s) ppm. $^{19}F\{^1H\}$ NMR (282.38 MHz, CD_2Cl_2, 25 °C): δ = –77.38 (s) ppm. IR (ATR, 25 °C): $\tilde{\nu}$ = 3479 (w), 3378 (w), 3319 (w), 3255 (w), 2948 (w), 2919 (w), 2860 (w), 2737 (w), 1610 (w), 1603 (w), 1574 (w), 1488 (w), 1441 (m), 1426 (m), 1375 (m), 1290 (m), 1261 (m), 1211 (s), 1178 (s), 1099 (s), 1034 (m), 1009 (m), 957 (m), 890 (m), 852 (s), 798 (m), 754 (m), 736 (m), 727 (m), 685 (s), 650 (m), 630 (m), 597 (m), 566 (m), 550 (m) cm^{-1}. Raman (1500 mW, 25 °C, 700 scans): 3067 (2), 3021 (1), 2920 (2), 2866 (2), 2743 (1), 1611 (3), 1586 (3), 1480 (2), 1428 (5), 1383 (2), 1380 (4), 1289 (3), 1270 (3), 1221 (5), 1185 (3), 1073 (3), 1009 (3), 978 (4), 842 (2), 784 (1), 759 (1), 730 (2), 658 (2), 597 (2), 577 (2), 556 (2), 519 (2), 489 (2), 415 (2), 361 (2), 330 (2), 271 (2), 236 (1) cm^{-1}. CI-MS *m*/*z* (%) = 329 (32) $[TerNH_2]^+$, 330 (20) $[TerNH_3]^+$, 705 (100) $[M + F - H]^+$. UV/Vis (25 °C, CH_2Cl_2): λ = 435 (w), 360 (m), 297 (m), 271 (s), 246 (s) nm. Crystals suitable for X-ray crystallographic analysis were obtained by concentration of a fluorobenzene solution of Ter**3**[Al{$OCH(CF_3)_2$}$_4$] to incipient crystallisation and storage at –25 °C for two days. Longer storage also produced additional crystals of $(TerNH)_2P(H)OAl[OCH(CF_3)_2]_3$ as a result of hydrolysis.

Ter3[$CHB_{11}H_5Br_6$]: To a stirred suspension of $(TerNH)_2PCl$ (0.180 g, 0.25 mmol) in CH_2Cl_2 (5 mL) was added $Ag[CHB_{11}H_5Br_6]$ powder (0.230 g, 0.32 mmol) in one portion at ambient temperature. The orange suspension was stirred for one hour and filtered (F4). The solvent was removed in vacuo, and the resulting orange precipitate was washed four times with benzene (2 mL). The resulting deep orange oil was covered with a layer of benzene and stored at ambient temperature overnight, which resulted in the deposition of orange crystals. Removal of the solvent by syringe and drying in vacuo yielded Ter**3**[$CHB_{11}H_5Br_6$] (0.129 g, 0.10 mmol, 40%); m.p. 225 °C (dec.). $C_{49}H_{58}B_{11}Br_6N_2P$ (1304.32): calcd. C 45.12, H 4.48, N 2.15; found C 45.65, H 4.61, N 1.84. $^{31}P\{^1H\}$ NMR (121.5 MHz, CD_2Cl_2, 25 °C): δ = 249.6 (br. s) ppm. ^1H NMR (300.13 MHz, CD_2Cl_2, 25 °C): δ = 1.80 (s, 24 H, *o*-CH_3), 2.31 (s, 12 H, *p*-CH_3), 1.00–3.50 (m, carboranate-BH/CH), 7.03 (s, 8 H, *m*-CH-Mes), 7.15 [d, 4 H, *m*-CH, $^3J(^1H,^1H)$ = 7.74 Hz], 7.41 (d, 2 H, NH), 7.42 [t, 2 H, *p*-CH, $^3J(^1H,^1H)$ = 7.65 Hz] ppm. ^{11}B

NMR (96.3 MHz, CD_2Cl_2, 25 °C): δ = –1.90 (s, 1B), –9.92 (s, 5B), –20.1 [d, 5B, $^1J(^1H,^{11}B)$ = 167 Hz] ppm. $^{13}C\{^1H\}$ NMR (75.5 MHz, CD_2Cl_2, 25 °C): δ = 20.82 (br. s, *o*-CH_3), 21.55 (s, *p*-CH_3), 129.16 (s, *p*-CH), 130.68 (s, *m*-CH-Mes), 131.17 (s, *m*-CH), 132.25 [d, $J(^{13}C,^{31}P)$ = 3.3 Hz], 132.55 [d, $J(^{13}C,^{31}P)$ = 4.4 Hz], 132.90 [d, $J(^{13}C,^{31}P)$ = 2.8 Hz], 137.58 [d, $J(^{13}C,^{31}P)$ = 3.9 Hz], 141.26 (s) ppm. IR (ATR, 25 °C): $\tilde{\nu}$ = 3330 (w), 3173 (w), 3052 (w), 2946 (w), 2916 (m), 2855 (w), 2601 (m), 1611 (m), 1556 (w), 1510 (m), 1435 (s), 1428 (m), 1378 (m), 1290 (w), 1240 (m), 1199 (m), 1176 (m), 1126 (m), 1076 (w), 1002 (s), 990 (s), 952 (s), 932 (s), 857 (s), 805 (s), 744 (s), 679 (m), 633 (s), 596 (m), 563 (m), 549 (m) cm^{-1}. A Raman spectrum was not measured because of fluorescence behaviour. CI-MS: *m*/*z* (%) = 330 (100) $[TerNH_3]^+$, 386 (15) [isobutene + $TerNH_3$]$^+$. UV/Vis (25 °C, CH_2Cl_2): λ = 435 (w), 358 (m), 296 (w), 245 (s) nm. Crystals suitable for X-ray crystallographic analysis were obtained by concentration of a benzene solution of Ter**3**[$CHB_{11}H_5Br_6$] to a deep orange oil and storage at ambient temperature overnight.

Ter[SbF_6]: To a stirred suspension of $(TerNH)_2PCl$ (0.180 g, 0.25 mmol) in CH_2Cl_2 (5 mL) was added a suspension of Ag[SbF_6] (0.103 g, 0.30 mmol) in dichloromethane (10 mL) over 20 min at –80 °C. The orange solution was warmed to ambient temperature for 30 min, which resulted in the precipitation of silver chloride. The solvent was removed in vacuo, and the residue was dissolved in CH_2Cl_2 (3 mL) and filtered (F4). The resulting solution was concentrated to incipient crystallisation and stored at –1 °C overnight, which resulted in the deposition of colourless crystals and a few orange crystals. The colourless crystals were identified as [$TerNH_3$][SbF_6] and the orange crystals were identified as Ter**3**[SbF_6] by X-ray structure determinations.

CCDC-832970 (for Ter**3**F), -832971 (for Ter**3**Cl), -832972 (for Ter**3**[CF_3CO_2]), -832973 (for Ter**3**[CF_3SO_3]), -832974 (for Ter**3**[$GaCl_4$]), -832975 (for Ter**3**[SbF_6]), -832976 (for Ter**3**-[$B(C_6F_5)_4$]), -832977 (for Mes***3**[$GaCl_4$]), -832978 (for Ter**3**-[$Al(OCH(CF_3)_2)_4$]), -832979 (for $(TerNH)_2P(H)OAl(OCH(CF_3)_2)_3$), -832980 (for Ter**3**[$CHB_{11}H_5Br_6$]), and -832981 (for [$TerNH_3$][SbF_6]) contain the supplementary crystallographic data for this paper. These data can be obtained free of charge from The Cambridge Crystallographic Data Centre via www.ccdc.cam.ac.uk/data_request/cif.

Supporting Information (see footnote on the first page of this article): Crystallographic and further details.

Acknowledgments

Financial support by the Deutsche Forschungsgemeinschaft (DFG) (SCHU 1170/6-1) is gratefully acknowledged.

[1] a) K. Dimroth, P. Hoffmann, *Angew. Chem.* **1964**, *76*, 433–434; *Angew. Chem. Int. Ed. Engl.* **1964**, *3*, 384–385; b) K. Dimroth, P. Hoffmann, *Chem. Ber.* **1966**, *99*, 1325–1331.
[2] a) E. Fluck, *Top. Phosphorus Chem.* **1980**, *10*, 193–284; b) A. H. Cowley, R. A. Kemp, *Chem. Rev.* **1985**, *85*, 367–382.
[3] D. Gudat, *Coord. Chem. Rev.* **1997**, *163*, 71–106.
[4] a) R. W. Kopp, A. C. Bond, R. W. Parry, *Z. Anorg. Chem.* **1976**, *15*, 3042–3046; b) C. W. Schultz, R. W. Parry, *Z. Anorg. Chem.* **1976**, *15*, 3046–3050; c) M. G. Thomas, C. W. Schultz, R. W. Parry, *Inorg. Chem.* **1977**, *16*, 994–1002.
[5] a) A. H. Cowley, M. C. Cushner, J. S. Szobota, *J. Am. Chem. Soc.* **1978**, *100*, 7784–7786; b) A. H. Cowley, C. Cushner, M. Lattman, H. L. McKee, J. S. Szobota, J. C. Wilburn, *Pure Appl. Chem.* **1980**, *52*, 789–797.
[6] N. Burford, P. Losier, C. Macdonald, V. Kyrimis, P. K. Bakshi, T. S. Cameron, *Inorg. Chem.* **1994**, *33*, 1434–1439.
[7] a) E. Niecke, R. Kroher, *Angew. Chem.* **1976**, *88*, 758–759; *Angew. Chem. Int. Ed. Engl.* **1976**, *15*, 692–693; b) see also M. Sanchez, M. R. Mazieres, L. Lamande, R. Wolf, in: *Multiple Bonds and Low Coordination in Phosphorus Chemistry* (Eds.: M. Regitz, O. J. Scherer), Thieme, Stuttgart, Germany, **1990**, p. 129.
[8] a) E. Niecke, M. Nieger, F. Reichert, *Angew. Chem.* **1988**, *100*, 1779–1780; *Angew. Chem. Int. Ed. Engl.* **1988**, *27*, 1715–1717; b) E. Niecke, M. Nieger, F. Reichert, W. W. Schoeller, *Angew. Chem.* **1988**, *100*, 1781–1782; *Angew. Chem. Int. Ed. Engl.* **1988**, *27*, 1713–1715.
[9] M. Nieger, E. Niecke, R. Detsch, *Z. Kristallogr.* **1995**, *210*, 971–972.
[10] N. Burford, T. S. Cameron, J. A. C. Clyburne, K. Eichele, K. N. Robertson, S. Sereda, R. E. Wasylishen, W. A. Whitla, *Inorg. Chem.* **1996**, *35*, 5460–5467.
[11] M. Denk, S. Gupta, R. Ramachandran, *Tetrahedron Lett.* **1996**, *37*, 9025–9028.
[12] a) S. Burck, D. Gudat, K. Nättinen, M. Nieger, M. Niemeyer, D. Schmid, *Eur. J. Inorg. Chem.* **2007**, 5112–5119; b) S. Burck, D. Gudat, M. Nieger, W.-W. du Mont, *J. Am. Chem. Soc.* **2006**, *128*, 3946–3955; c) D. Gudat, A. Haghverdi, M. Nieger, *Angew. Chem.* **2000**, *112*, 3211–3214; *Angew. Chem. Int. Ed.* **2000**, *39*, 3084–3087; d) D. Gudat, A. Haghverdi, H. Hupfer, M. Nieger, *Chem. Eur. J.* **2000**, *6*, 3414–3425.
[13] A. J. Arduengo III, R. L. Harlow, M. Kline, *J. Am. Chem. Soc.* **1991**, *113*, 361–363.
[14] D. Michalik, A. Schulz, A. Villinger, N. Weding, *Angew. Chem.* **2008**, *120*, 6565; *Angew. Chem. Int. Ed.* **2008**, *47*, 6465–6468.
[15] A. H. Cowley, M. Lattman, J. C. Wilburn, *Inorg. Chem.* **1981**, *20*, 2916–2919.
[16] V. A. Jones, S. Sriprang, H. G. Butler, M. Thornton-Pett, T. P. Kee, *J. Organomet. Chem.* **1998**, *567*, 199.
[17] O. Dahl, *Tetrahedron Lett.* **1982**, *23*, 1493.
[18] See, for example: a) M. D. R. Gomes da Silva, M. Manuela, A. Pereira, *Carbohydr. Res.* **2011**, *346*, 197–202; b) N. Yanagihara, T. Gotoh, T. Ogura, *Polyhedron* **1996**, *15*, 4349–4354; c) K. Hubner, H. W. Roesky, M. Noltemeyer, R. Bohra, *Chem. Ber.* **1991**, *124*, 515–517.
[19] a) G. A. Lawrance, *Chem. Rev.* **1986**, *86*, 17–33; b) G. M. Whitesides, F. D. Gutowski, *J. Org. Chem.* **1976**, *41*, 2882–2825.
[20] A. G. Massey, A. J. Park, *J. Organomet. Chem.* **1964**, *2*, 245–250.
[21] For reviews, see: a) I. Krossing, I. Raabe, *Angew. Chem.* **2004**, *116*, 2116–2142; *Angew. Chem. Int. Ed.* **2004**, *43*, 2066–2090; b) C. Reed, *Acc. Chem. Res.* **1998**, *31*, 133–139; c) S. H. Strauss, *Chem. Rev.* **1993**, *93*, 927–942, and references cited therein.
[22] a) A. Schulz, A. Villinger, *Chem. Commun.* **2010**, *46*, 3696–3698; b) A. Schulz, A. Villinger, *Chem. Eur. J.* **2010**, *16*, 7276–7281; c) M. Kuprat, M. Lehmann, A. Schulz, A. Villinger, *Organometallics* **2010**, *29*, 1421–1427.
[23] See, for example: a) W. Baumann, A. Schulz, A. Villinger, *Angew. Chem.* **2008**, *120*, 9672–9675; *Angew. Chem. Int. Ed.* **2008**, *47*, 9530–9532; b) A. Schulz, A. Villinger, *Inorg. Chem.* **2009**, *48*, 7359–7367; c) D. Michalik, A. Schulz, A. Villinger, N. Weding, *Angew. Chem.* **2008**, *120*, 6565–6568; *Angew. Chem. Int. Ed.* **2008**, *47*, 6465–6468; d) N. Burford, J. Clyburne, P. K. Bakshi, T. S. Cameron, *J. Am. Chem. Soc.* **1993**, *115*, 8829–8830.
[24] See, for example: a) R. V. Honeychuck, W. H. Hersh, *Inorg. Chem.* **1989**, *28*, 2869–2886; b) W. H. Hersh, *J. Am. Chem. Soc.* **1985**, *107*, 4599–4601; c) T. Drews, K. Seppelt, *Angew. Chem.* **1997**, *109*, 264; *Angew. Chem. Int. Ed. Engl.* **1997**, *36*, 273; d) A. J. Edwards, G. R. Jones, R. J. Sills, *J. Chem. Soc., Chem. Commun.* **1968**, 1527; e) S. Seidel, K. Seppelt, *Science* **2000**, *290*, 117; f) T. Drews, S. Seidel, K. Seppelt, *Angew. Chem.* **2002**, *114*, 470; *Angew. Chem. Int. Ed.* **2002**, *41*, 454.
[25] J. Plesek, T. Jelinek, S. Hermanek, B. Stibr, *Collect. Czech. Chem. Commun.* **1986**, *51*, 819–829.

[26] $[H(Et_2O)]^+[B(C_6F_5)_4]^-$ was used as a proton source.
[27] a) $[TerNH_3][SbF_6]$ and b) $(TerNH)_2P^{(+)}(H)–O–Al^{(-)}[OCH(CF_3)_2]_3$ were characterised by XRD. The full data set can be found in the Supporting Information.
[28] N. Burford, J. A. C. Clyburne, D. Silvert, S. Warner, W. A. Whitla, *Inorg. Chem.* **1997**, *36*, 482–484.
[29] R. Detsch, E. Niecke, M. Nieger, F. Reichert, *Chem. Ber.* **1992**, *125*, 321–330.
[30] P. Pyykkö, M. Atsumi, *Chem. Eur. J.* **2009**, *15*, 12770–12779.
[31] G. Fischer, S. Herler, P. Mayer, A. Schulz, A. Villinger, J. J. Weigand, *Inorg. Chem.* **2005**, *44*, 1740–1751.
[32] G. R. Desiraju, *J. Chem. Soc., Dalton Trans.* **2000**, 3745–3751.
[33] C. A. Tolman, *Chem. Rev.* **1977**, *77*, 313–348.
[34] I. Krossing, A. Reisinger, *Coord. Chem. Rev.* **2006**, *250*, 2721–2744.
[35] I. Krossing, A. Reisinger, *Angew. Chem.* **2003**, *115*, 5903–5906; *Angew. Chem. Int. Ed.* **2003**, *42*, 5725–5728.
[36] I. Krossing, A. Reisinger, *Eur. J. Inorg. Chem.* **2005**, *10*, 1979–1989.
[37] A. F. Holleman, E. Wiberg, *Lehrbuch der Anorganischen Chemie*, 102nd ed., de Gruyter, Berlin, **2007**, Anhang IV.
[38] C. B. Fischer, S. Xu, H. Zipse, *Chem. Eur. J.* **2006**, *12*, 5779–5784.
[39] F. Reiß, A. Schulz, A. Villinger, N. Weding, *Dalton Trans.* **2010**, *39*, 9962–9972, and references cited therein.
[40] a) G. B. Dunks, K. Palmer-Ordonez, *Inorg. Chem.* **1978**, *17*, 1514–1516; b) G. B. Dunks, K. Barker, E. Hedaya, C. Hefner, K. Palmer-Ordonez, P. Remec, *Inorg. Chem.* **1981**, *20*, 1692–1697; c) A. Franken, B. T. King, J. Rudolph, P. Rao, B. C. Noll, J. Michl, *Collect. Czech. Chem. Commun.* **2001**, *66*, 1238–1249; d) Z. Xie, T. Jelinek, R. Bau, C. A. Ree, *J. Am. Chem. Soc.* **1994**, *116*, 1907–1913.
[41] G. M. Whitesides, F. D. Gutowski, *J. Org. Chem.* **1976**, *41*, 2882–2825.
[42] I. Krossing, *Chem. Eur. J.* **2001**, *7*, 490–502.
[43] P. Jutzi, *Organometallics* **2000**, *19*, 1442–1444.
[44] O. Popovych, *Anal. Chem.* **1966**, *38*, 117–119.

Received: September 14, 2011
Published Online: December 8, 2011

DOI: 10.1002/ejic.201100939

Theoretical Investigations of Mechanisms of Thermal Cleavage of E=E Bonds in Heavy Butadiene Systems (E = C, Si, Ge, Sn, and Pb)

Jeng-Horng Sheu[a] and Ming-Der Su*[a]

Keywords: Reaction mechanisms / Density functional calculations / Cleavage reactions / Cycloaddition

The potential energy surfaces for the intramolecular reactions of heavy 1,3-butadiene have been explored using DFT. All the stationary points, which include the heavy 1,3-butadienes ($R_2E{=}ER{-}ER{=}ER_2$, E = group 14 element), intramolecular fragments, transition states, and the products, were completely optimized at the B3LYP/LANL2DZ level of theory. Five 1,3-butadiene species, which include carbon, silicon, germanium, tin, and lead, were chosen as model reactants. Our theoretical findings suggest the following: (1) both sterically bulky substituents attached to the heavy butadiene and the weakness of the E=E double bond lead to the easy cleavage of one E=E double bond in heavy 1,3-butadiene and (2) for two intramolecular reactions (cycloaddition and 1,2-migration) of the heavy 1,3-butadienes with sterically overcrowded substituents, the lighter the E atoms involved in the 1,3-butadiene molecule, the smaller the intramolecular barrier, the lower the reaction enthalpy, and the more facile its intramolecular reaction at room temperature. Furthermore, a configuration-mixing model has been used to rationalize the computational results, and the results obtained allow a number of predictions to be made.

Introduction

Since the first successful isolation of a stable, doubly bonded silicon compound,[1] there has been considerable effort devoted in this area of chemistry. Many types of stable disilenes ($R_2Si{=}SiR_2$) have been reported and many of their fundamental reactions have been described.[2] Nevertheless, very few studies have focused on the syntheses of stable, conjugated tetrasilabutadienes ($R_2Si{=}SiR{-}SiR{=}SiR_2$). As far as we are aware, only two stable tetrasila-1,3-dienes (**1** and **2**) have been prepared and structurally characterized over the last twenty years.[3] Another kinetically stable tetrasilabutadiene derivative **3** has been synthesized by Iwamoto, Kira, and coworkers.[4] Unlike the conformations of **1** and **2**, which adopt the s-*cis* form in the solid state and in solution,[3] **3** has an anticlinal conformation with an $Si_1{-}Si_2{-}Si_3{-}Si_4$ dihedral angle of 122.56(7)° in the solid state.[4] Apparently, the substituent R has a significant influence on the geometric structure of $R_2Si{=}SiR{-}SiR{=}SiR_2$.

The successful syntheses of these new conjugated tetrasilabutadienes will broaden the category of disilenes. According to the experimental studies of Iwamoto, Kira, and coworkers,[4] it was found that the thermolysis of **3** at 80 °C in benzene for three hours gave cyclotrisilene **4** and cyclic silene **5** in high yields. However, only a very limited amount of information is available about the mechanisms of such reactions. Furthermore, if one can thermally cleave a Si=Si double bond in **3** and rearrange the fragment species to produce the intriguing final products, would it be possible to extend this phenomenon to other conjugated π systems with group 14 elements? Attempts to prepare other heavy butadiene analogues using group 14 elements (such as Sn and Pb) have not been reported to date.[5] As the synthesis of isolable tetrasilabutadiene species such as **3** is both unusual and useful, we were curious about the chemical and physical properties of such species and wanted detailed mechanistic knowledge in order to exercise greater control over their synthesis. To the best of our knowledge, neither experimental nor theoretical studies have been devoted to the study of the reaction mechanisms of heavy butadiene systems. It is astonishing how little is known about the intramolecular reaction mechanisms of **3** considering the importance of tetrasilabutadiene in heavy group 14 synthetic chemistry and the extensive research on the corresponding butadiene species.[6]

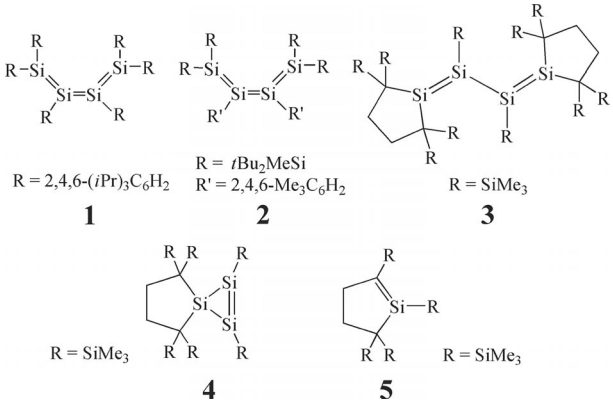

1 **2** **3** **4** **5**

[a] Department of Applied Chemistry, National Chiayi University, Chiayi 60004, Taiwan
E-mail: midesu@mail.ncyu.edu.tw

Supporting information for this article is available on the WWW under http://dx.doi.org/10.1002/ejic.201100939.

We report the results of DFT calculations for the mechanisms of the reactions shown in Scheme 1.

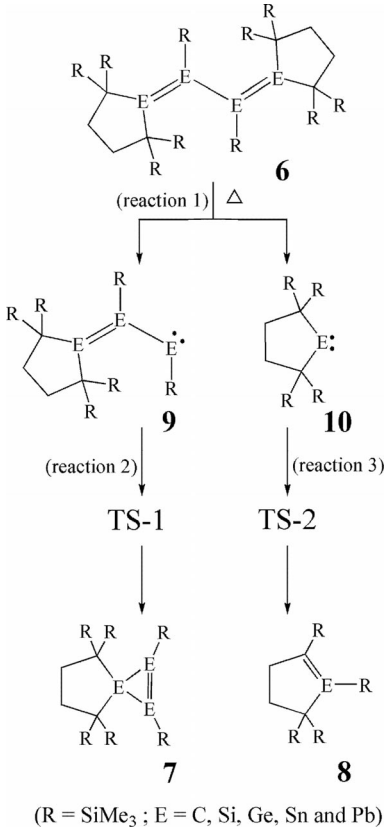

Scheme 1.

We have considered the reaction pathways of two kinds of intramolecular model reactions, which afford the spiro product **7** and the five-membered cyclic species **8**, respectively, and involve a series of heavy butadiene systems with group 14 elements E (E = C, Si, Ge, Sn, Pb). Each of these pathways was examined computationally and is described in detail. Moreover, Gibbs free energies (ΔG) of the thermal reactions are presented and discussed, which should be useful for further experimental observations. In view of recent dramatic developments in group 14 heavy carbenes,[2] analogous studies of group 14 heavy butadienes that bear sterically bulky substituents should be forthcoming and will open up new areas.

Results and Discussion

Geometries of Heavy Butadiene Systems with Group 14 Elements

Before discussing the geometric optimizations and potential energy surfaces (Reactions 1–3) for the intramolecular reactions of the group 14 butadiene systems, we first examined the geometry of **3**. As the structure of **3** (i.e. **6-Si**) has been determined by X-ray crystal analysis, its geometry optimization was first carried out to calibrate the B3LYP calculations. As shown in Figure 1, the calculated Si_1–Si_2, Si_2–Si_3, and Si_3–Si_4 distances are 2.230, 2.376, and 2.230 Å, respectively. These values are very close to those of 2.198, 2.340, and 2.217 Å observed in the X-ray crystal structure.[4] Additionally, our calculated Si_1–Si_2–Si_3–Si_4 dihedral angle is 122.4°, which is in excellent agreement with the experimental value (122.6°).[4] These results strongly suggest that the B3LYP calculations are reliable enough for the present purpose.

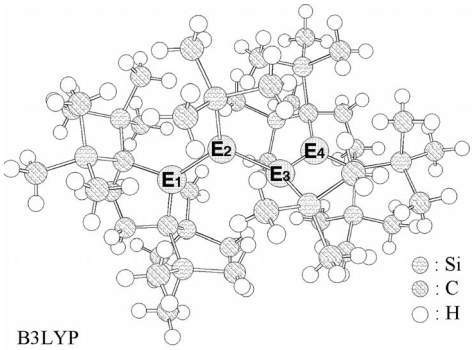

Reactant 6

6-E	E1-E2(Å)	E2-E3(Å)	E3-E4(Å)	∠E1-E2-E3-E4
6-C	1.423	1.573	1.425	113.5°
6-Si	2.230 (2.198)	2.376 (2.340)	2.230 (2.217)	122.4° (122.6°)
6-Ge	2.384	2.525	2.385	133.4°
6-Sn	2.817	2.969	2.816	153.5°
6-Pb	2.964	3.087	2.963	156.6°

Figure 1. B3LYP/LANL2DZ optimized geometries [Å and °] of singlet **6** (E = C, Si, Ge, Sn, Pb). The experimental values are in parenthesis. Hydrogen atoms are omitted for clarity.

We also examined the other heavy butadiene reactants **6** (E = C, Si, Ge, Sn, Pb) in the singlet state, which were calculated at the B3LYP/LANL2DZ level of theory. The key geometric parameters for **6** are collected in Figure 1.

The average E=E double bond lengths of 1.424, 2.230, 2.384, 2.816, and 2.963 Å calculated for **6-C**, **6-Si**, **6-Ge**, **6-Sn**, and **6-Pb**, respectively, agree with the available experimental data. For example, the B3LYP E=E bond lengths are in reasonable agreement with 1.356,[12] 2.140–2.160,[13] 2.213–2.247,[14] 2.768,[15] and 3.354–3.370 Å[16] normally observed for C=C, Si=Si, Ge=Ge, Sn=Sn, and Pb=Pb double bonds, respectively. Moreover, our calculated E–E single bond lengths in the heavy butadiene systems are 1.573 (**6-C**), 2.376 (**3**, **6-Si**), 2.525 (**6-Ge**), 2.969 (**6-Sn**), and 3.087 Å (**6-Pb**), respectively. These values are somewhat longer than those observed experimentally, which are 1.545 (C–C),[12] 2.352 (Si–Si),[13] 2.445–2.663 (Ge–Ge),[14,17] 2.810 (Sn–Sn),[15] and 2.844–3.188 Å (Pb–Pb),[18,19] respectively. The calculation of somewhat longer bond lengths may be attributed to the steric effects caused by the larger size of the five-membered ring substituents attached to the terminal E atoms of **6**. In any event, the consistent agreement between our computational results and the available experimental data is encouraging. We therefore believe that the models (B3LYP/LANL2DZ) employed in this study should

provide reliable information for the discussion of the reaction mechanisms, for which experimental data are still not available.

Additionally, an interesting trend that can be observed in Figure 1 is the increase in the bond lengths (E=E and E–E) and the dihedral angles (E–E=E–E) on going from carbon to lead. For instance, the E–E=E–E dihedral angle in **6** increases in the order of C (113.5°) < Si (122.4°) < Ge (133.4°) < Sn (153.5°) < Pb (156.6°). Again, the reason for these phenomena can be attributed to avoiding steric congestion that results from the bulkier five-membered ring substituents.

Thermal Dissociation of an E=E Double Bond in Heavy Butadienes

The formation of **7** and **8** can most likely be interpreted in terms of the initial formation of **9** and **10** by E=E double bond dissociation (Reaction 1, Schemes 1 and 2), i.e. heavy, conjugated **6** undergo dissociation into heavy carbene **9** and five-membered cyclic heavy carbene **10** intermediates because of the steric repulsions between two bulky five-membered-ring substituents attached to the terminal E atoms in **6**, where large ring strains further promote the dissociation. As a result, the formation of **7** can be explained by the addition of facile intramolecular carbene (>E:) into the E=E double bond of **9** via **TS-1** (Reaction 2, TS = transition state). On the other hand, **10** undergo intramolecular 1,2-silyl-group migration to yield **8** via **TS-2** (Reaction 3). In order to verify the existence of **9** and **10**, we first performed DFT calculations on the dissociation of an E=E double bond in **6** using the B3LYP/LANL2DZ level of theory. The optimized geometries that involve **9** and **10** at both singlet and triplet states with selected structural parameters are collected in Figures 2 and 3, respectively, and the corresponding energies are summarized in Table 1. The major conclusions drawn from the current study can be summarized as follows.

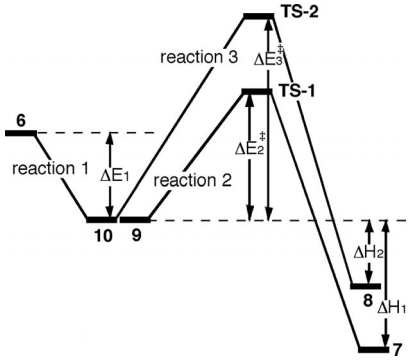

Scheme 2.

As seen in Table 1, it is intriguing to find that the dissociation of heavy 1,3-butadiene **6** into the singlet ground state of **9** and **10** is predicted to be a slightly endothermic process, except for **6-C**. For instance, for **6-C**, **6-Si**, **6-Ge**, **6-Sn**, and **6-Pb** the dissociation energies are calculated to be –44, 27, 13, 10, and 5.1 kcal mol^{-1}, respectively. After consideration of the Gibbs free energy, the dissociation energy of these molecular systems is anticipated to be –61, +8.0. –2.0,

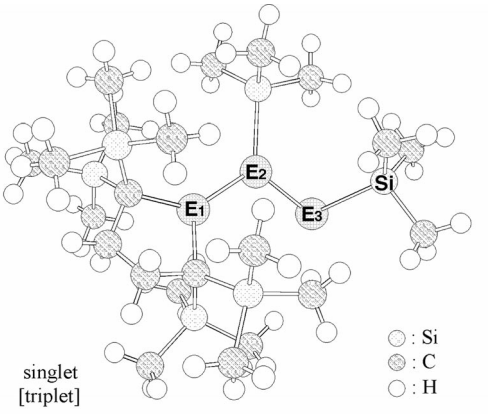

9

9-E	E1-E2(Å)	E2-E3(Å)	E1-E3(Å)	∠E1-E2-E3	∠E2-E3-Si
9-C	1.459 [1.452]	1.450 [1.379]	2.476 [2.482]	119.7° [122.5°]	138.0° [157.8°]
9-Si	2.240 [2.229]	2.323 [2.261]	3.780 [3.806]	111.8° [115.9°]	105.8° [128.9°]
9-Ge	2.428 [2.412]	2.472 [2.436]	3.699 [3.974]	99.46° [108.4°]	102.8° [102.4°]
9-Sn	2.858 [2.779]	2.862 [2.837]	4.312 [4.621]	97.93° [107.7°]	97.87° [120.6°]
9-Pb	3.191 [3.007]	3.030 [3.017]	4.491 [4.622]	96.14° [96.17°]	93.39° [112.8°]

Figure 2. B3LYP/LANL2DZ optimized geometries [Å and °] of both singlet and triplet intermediate **9** (E = C, Si, Ge, Sn, Pb). Hydrogen atoms are omitted for clarity.

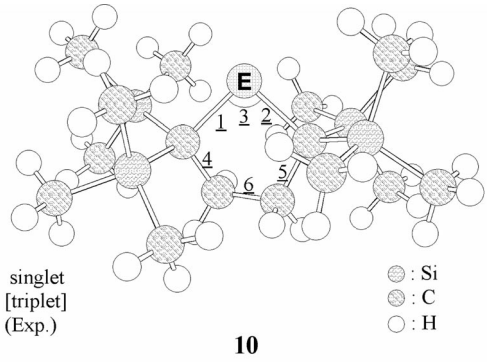

10

10-E	1	2	3	4	5	6
10-C	1.508 [1.521]	1.508 [1.520]	108.1° [119.0°]	1.588 [1.594]	1.585 [1.591]	1.547 [1.562]
10-Si	1.946 [1.963] (1.911)	1.942 [1.963] (1.904)	94.43° [102.8°] (93.88°)	1.583 [1.587] (1.569)	1.579 [1.585] (1.568)	1.555 [1.573] (1.530)
10-Ge	2.043 [2.073] (2.010)	2.041 [2.075] (2.020)	91.79° [99.54°] (90.97°)	1.581 [1.577] (1.562)	1.577 [1.577] (1.560)	1.556 [1.579] (1.529)
10-Sn	2.225 [2.263] (2.220)	2.226 [2.267] (2.220)	87.91° [93.86°] (86.70°)	1.583 [1.574] (1.583)	1.579 [1.574]	1.558 [1.586] (1.482)
10-Pb	2.301 [2.398]	2.301 [2.398]	86.10° [90.56°]	1.581 [1.559]	1.577 [1.558]	1.559 [1.599]

Figure 3. B3LYP/LANL2DZ optimized geometries [Å and °] of both singlet and triplet intermediate **10** (E = C, Si, Ge, Sn, Pb). The experimental values (ref.[24]) are in round parenthesis. Hydrogen atoms are omitted for clarity.

Table 1. Relative energies for the processes: Reaction 1: **6**→**9** + **10**, Reaction 2: **9**→**TS-1**→**7**, and Reaction 3: **10**→**TS-2**→**8** (Schemes 1 and 2).[a]

System	C	Si	Ge	Sn	Pb
Reaction 1					
6	0.0	0.0	0.0	0.0	0.0
9 + **10**	–44.2	+26.9	+13.3	+10.4	+5.1
($\Delta E1$)	(–61.3)	(+8.0)	(–2.0)	(–6.5)	(–12.7)
Reaction 2					
9	0.0	0.0	0.0	0.0	0.0
	(0.0)	(0.0)	(0.0)	(0.0)	(0.0)
$\Delta E_{st,\ 9}$[b]	–31.8	+1.3	+7.7	+12.0	+12.5
	(–31.2)	(+0.26)	(+6.1)	(+10.8)	(+11.6)
TS-1[c]	–5.9	+9.2	+13.5	+17.7	+19.7
($\Delta E2^{\ddagger}$)	(–6.5)	(+7.6)	(+14.0)	(+19.7)	(+23.3)
7	–51.4	–22.6	–4.1	+1.7	+12.4
($\Delta H1$)	(–50.3)	(–23.8)	(–6.7)	(–0.40)	(+14.6)
Reaction 3					
10	0.0	0.0	0.0	0.0	0.0
	(0.0)	(0.0)	(0.0)	(0.0)	(0.0)
$\Delta E_{st,\ 10}$	12.2	+27.3	+30.6	+31.4	+35.0
	(+12.5)	(+25.8)	(+29.8)	(+31.2)	(+34.9)
TS-2[d]	0.23	+20.9	+26.7	+31.4	+40.2
($\Delta E3^{\ddagger}$)	(+1.8)	(+20.6)	(+26.2)	(+34.2)	(+39.4)
8	–57.4	–8.5	+3.9	+18.6	+32.2
($\Delta H2$)	(–56.3)	(–10.5)	(+2.1)	(+15.6)	(+28.0)

[a] At the B3LYP/LANL2DZ levels of theory. The B3LYP optimized structures of the stationary points are shown in Figures 1, 2, 3, 4, 5, 6, and 7. Energy differences have been zero-point corrected. The Gibbs free energy (at 298 K) is in round parentheses. All units are in kcal mol^{-1}. [b] Singlet–triplet energy splitting (ΔE_{st} = $E_{triplet} - E_{singlet}$). [c] Our computational data indicate that the relative entropy of **TS-1** ($\Delta S^{\ddagger}$) was predicted to be 3.9, 5.2, 8.2, –9.8, and –18.2 cal mol^{-1} K^{-1} for **TS-1-C**, **TS-1-Si**, **TS-1-Ge**, **TS-1-Sn**, and **TS-1-Pb**, respectively. [d] Our computational data indicate that the relative entropy of **TS-2** was predicted to be –6.4, 1.9, 2.3, 1.3, and 3.9 cal mol^{-1} K^{-1} for **TS-2-C**, **TS-2-Si**, **TS-2-Ge**, **TS-2-Sn**, and **TS-2-Pb**, respectively.

–6.5, and –13 kcal mol^{-1}, respectively. This strongly implies that **6** (**6-C**, **6-Ge**, **6-Sn**, and **6-Pb**) are kinetically unstable and may dissociate spontaneously to the more stable **9** and **10** at room temperature if they are produced. This can be attributed to two reasons: (1) the drop in bond dissociation energy on going from **6-C** to heavier, homonuclear systems[20] and (2) the steric hindrance of the substituents attached to the heavy butadienes. Many experimental findings strongly indicate that the double bonding between the heavy group 14 elements (E = Si, Ge, Sn, Pb) is relatively weak.[21] Our theoretical results also show that the bond strength of the E=E double bond decreases with the increasing atomic number of E.[22] Additionally, to consider the steric effect, we choose H_2E=EH–EH=EH_2 (E = C, Si, Ge, Sn, Pb) as models to examine the dissociation reaction H_2E=EH–EH=EH_2→H_2E=EH–HE: + :EH_2. The B3LYP/LANL2DZ results indicate that the dissociation energy is 183, 56.7, 35.5, 24.4, and 12.6 kcal mol^{-1} for C, Si, Ge, Sn, and Pb, respectively. These values are much larger than those of **6** with bulkier substituents (Table 1). Again, these calculations show that the effect of severe steric congestion can readily cleave one E=E double bond of the heavy 1,3-butadienes by utilizing a smaller dissociation energy. In combination, all these important factors led to the conclusion that both the sterically bulky substituents attached to the heavy butadiene and the weakness of the E=E double bond lead to the easy cleavage of one E=E double bond in the heavy 1,3-butadiene. This is in accord with the experimental data[4] and the computational results (Table 1).

Moreover, as represented in Figure 1, the relatively small C=C and C–C bond lengths in **6-C** (1.42 and 1.64 Å, respectively), may result in the severely sterically overcrowded bulky substituents attached to **6-C**. This would result in the spontaneous dissociation of one C=C bond in **6-C** without any difficulty, which was confirmed by our computational results. That is, the dissociation of singlet **6-C** into the singlet ground state of **9-C** and the lowest singlet state of **10-C** is predicted to be highly exothermic by 44 kcal mol^{-1}. Accordingly, the large energy difference that favors **9-C** and **10-C** over **6-C**, compared with the other reactants (**6-Si**, **6-Ge**, **6-Sn**, and **6-Pb**), strongly indicates that C is more reluctant to form a 1,3-butadiene with bulkier substituents than a fragment carbene species (**9-C** or **10-C**). In particular, for **6-Si**, the total energy of **9-Si** and **10-Si** is somewhat higher than that of **6-Si** by only 8.0 kcal mol^{-1} (ΔG).[23] This computational result strongly implies that if the temperature is raised above room temperature the small energy barrier could be easily overcome, which could readily lead to the dissociation of one Si=Si bond in **6-Si** molecule to yield **9-Si** and **10-Si**. Again, this theoretical finding is consistent with the available experimental observations.[4]

Furthermore, as shown in Figure 2, we also calculated the geometries of **9** at both singlet and triplet states. The DFT frequency calculations reveal that all these species (**9-C**, **9-Si**, **9-Ge**, **9-Sn**, and **9-Pb**) have no imaginary frequency and are true minima on the potential energy surfaces. The B3LYP results indicate that all of the species **9** studied here, which are analogous to other substituted heavy carbenes,[9] have singlet ground states. Moreover, no matter what multiplicity E adopts, our computations suggest that both the E_1–E_2 and E_2–E_3 bond lengths show a monotonic increase on going from C to Pb. This is mainly due to the increase of the atomic radius of E on going from carbon to lead. Additionally, our theoretical investigations also indicate that, irrespective of its multiplicity, the E_1–E_2–E_3 bond angle decreases uniformly as E goes from C to Pb. It appears that as E becomes heavier, a more acute E_1–E_2–E_3 bond angle is preferred in **9**, which may be due to relativistic effects.[24] When E changes from carbon to lead, the valence s orbital is more strongly contracted than the corresponding p orbitals,[24] i.e. the size difference between the valence s and p orbitals increases from C to Pb. Consequently, the valence s and p orbitals of the heavier members of the group overlap less to form strong hybrid orbitals.[24] Therefore, we expect that **9** with a heavier E center favors a smaller E_1–E_2–E_3 bond angle.

From our DFT calculations, the stability of the singlet state increases with decreasing electronegativity of E in **9**. That is to say, the singlet–triplet energy splitting (ΔE_{st} = $E_{triplet} - E_{singlet}$) generally increases as the atomic number of E increases. The reason for this may be partially due to the fact that the relativistic effect[24] on a heavier E atom

stabilizes the s orbital relative to the p orbital, which favors the singlet state relative to the triplet. This prediction is confirmed by our theoretical results (Table 1), i.e. an increasing trend in ΔE_{st} for **9-C** (–31) < **9-Si** (1.3) < **9-Ge** (7.7) < **9-Sn** (12) < **9-Pb** (13 kcal mol^{-1}) at the B3LYP level of theory. We will use ΔE_{st} to predict the reactivity of **9** in a later section.

We also calculated the geometry of **10** at both singlet and triplet states (Figure 3). Fortunately, several stable five-membered cyclic heavy carbenes have been isolated and characterized unequivocally, i.e. silylene **10-Si**,[25a] germylene **10-Ge**,[25b] and stannylene **10-Sn**.[25c] Selected experimental geometric parameters for **10-Si**, **10-Ge**, and **10-Sn** are given in Figure 3. In principle, the agreement of bond lengths and angles in **10-Si**, **10-Ge**, and **10-Sn** between the experimental and B3LYP results for the singlet state is quite good, with the agreement between bond lengths and angles of within 0.076 Å and 1.2°. Again, as a result of this encouraging agreement, it is believed that the B3LYP calculations provide an adequate theoretical level for further investigations of the molecular geometries of **10** and the physical features of their reactions.[26]

Moreover, the computational results in Figure 3 demonstrate that the calculated E–C single bond lengths in singlet **10** increase in the order of 1.508 (**10-C**) < 1.946 (**10-Si**) < 2.043 (**10-Ge**) < 2.225 (**10-Sn**) < 2.301 Å (**10-Pb**). The same trend for the triplet **10** species is also shown in Figure 3. The C–E–C bond angle (where E is the heavy carbene center) follows the opposite trend to that of the E–E bond length, i.e. 108° (**10-C**) > 94.4° (**10-Si**) > 91.8° (**10-Ge**) > 87.9° (**10-Sn**) > 86.1° (**10-Pb**). Likewise, the same phenomenon is also shown for triplet **10** in Figure 3. Additionally, it is apparent that, as the E atom becomes heavier, a C–E–C bond angle that approaches 90° is preferred. Again, the reason for this may be attributed to the relativistic effect.[24]

Furthermore, the ΔE_{st} values of **10** are the most important parameters in this study. As shown in Table 1, our theoretical results show an increasing trend in ΔE_{st} for **10-C** (12.2) < **10-Si** (27.3) < **10-Ge** (30.6) < **10-Sn** (31.4) < **10-Pb** (35.0 kcal mol^{-1}) at the B3LYP/LANL2DZ level of theory. This trend is analogous to the ΔE_{st} results observed for **9**. Consequently, our results (Table 1 and Figure 3) demonstrate that the heavier the E atom in **10**, the smaller its C–E–C bond angle, and the larger the ΔE_{st} becomes. Again, these results can be ascribed to the relativistic effect.[24] We shall use the above conclusions to explain the origins of the energy barriers for cycloadditions and 1,2-migrations in later sections.

Reaction 2: Intramolecular Cycloaddition Reactions

We then considered the mechanism for Reaction 2 with focus on the transition states and the cycloaddition products. The chemical reactions considered were: **9** → **TS-1** → **7** (Scheme 1). The optimized geometries for the stationary points (**TS-1** and **7**) calculated at the B3LYP/LANL2DZ level of theory and selected geometric parameters are collected in Figures 4 and 5, respectively. The relative energies of the stationary points for these mechanisms are summarized in Table 1. There are several important conclusions from these results to which attention should be drawn.

For Reaction 2, we located **TS-1** for each of the group 14 elements, along with the imaginary frequency eigen vector. These reactions appear to be concerted because we have only been able to locate one TS for each reaction and have confirmed that it is a true TS on the basis of frequency analysis. The DFT frequency calculations for **TS-1-C**, **TS-1-Si**, **TS-1-Ge**, **TS-1-Sn**, and **TS-1-Pb** suggest that the single imaginary frequency values are 227*i*, 156*i*, 96.6*i*, 66.2*i*, and 60.1*i* cm^{-1}, respectively. As shown in Figure 4, vibrational motion for the cycloaddition involves bond formation between E_1 and E_3. Thus, our theoretical investigations suggest that the intramolecular cycloaddition **9** proceeds by a one-step process. The fact that such cycloadditions follow a concerted pathway is also supported by the geometries of the TSs (Figure 4). For instance, the E_1–E_2 bond length in these TSs increases in the following order: **TS-1-C** (2.189)[27] < **TS-1-Si** (2.266) < **TS-1-Ge** (2.425) < **TS-1-Sn** (2.816) < **TS-1-Pb** (2.918 Å). Likewise, our B3LYP calculations show that the E_2–E_3 bond length increases in the order: **TS-1-C** (1.276) < **TS-1-Si** (2.189) < **TS-1-Ge** (2.437) < **TS-1-Sn** (2.893) < **TS-1-Pb** (2.980 Å). These structural features indicate that the transition structures for the cycloaddition reaction of **9** that contain lighter E atoms are more reactive.[28] This is consistent with the Hammond postulate,[29] which associates an earlier transition state with a smaller reaction barrier and a larger exothermicity. Indeed,

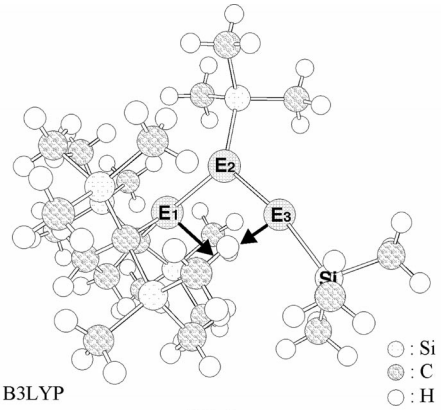

TS-1

TS-1-E	E1-E2(Å)	E2-E3(Å)	E1-E3(Å)	∠E1-E2-E3	∠E2-E3-Si
TS-1-C	2.189	1.276	2.892	110.4°	150.9°
TS-1-Si	2.266	2.189	3.381	98.74°	153.4°
TS-1-Ge	2.425	2.437	3.312	85.87°	139.5°
TS-1-Sn	2.816	2.893	3.518	76.07°	143.6°
TS-1-Pb	2.918	2.980	3.287	67.74°	149.9°

Figure 4. B3LYP/LANL2DZ optimized geometries [Å and °] of **TS-1** (E = C, Si, Ge, Sn, Pb). The relative energies for each species are shown in Table 1. The heavy arrows indicate the main atomic motions in the transition state eigen vector. Hydrogen atoms are omitted for clarity.

the barrier height for Reaction 2 is predicted to increase on going from carbon to lead (Table 1). In consequence, our calculations indicate that the lighter and more electronegative the E in **9**, the lower the activation barrier for Reaction 2.

As shown in Scheme 1, Reaction 2 can produce five cycloaddition products, **7-C**, **7-Si** (i.e. **4**), **7-Ge**, **7-Sn**, and **7-Pb** (Figure 5). To the best of our knowledge, only one crystallographic investigation on substituted **7-Si** has been carried out over the last three years, and no theoretical calculations are available for **7**. Our B3LYP calculations predict that the average E_1–E_2 (E_1–E_3), and E_2=E_3 bond lengths in **7-Si** are 2.369 and 2.168 Å, respectively, which are consistent with the experimental values of 2.301 and 2.143 Å.[4] Similarly, the calculated E_1–E_2–E_3 and E_2–E_1–E_3 bond angles in **7-Si** are 62.85° and 54.45°, respectively, which compare favorably with the corresponding bond angles determined from the X-ray data of 62.46° and 55.42°.[4] Again, due to the agreement between the B3LYP theory and the experimental data, we are confident that the same relative accuracy should also apply to the geometries and energies predicted for the other species of **7**.

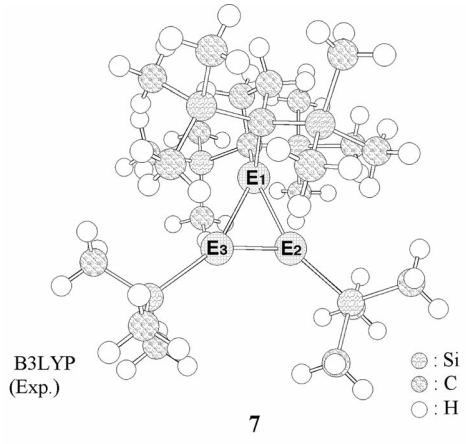

7

7-E	E1-E2(Å)	E2-E3(Å)	E1-E3(Å)	∠E1-E2-E3	∠E2-E1-E3
7-C	1.567	1.346	1.566	64.51°	50.89°
7-Si	2.369 (2.301)	2.168 (2.143)	2.372 (2.301)	62.85° (62.46°)	54.45° (55.42°)
7-Ge	2.529	2.312	2.531	63.01°	54.36°
7-Sn	2.925	2.736	2.921	64.82°	55.68°
7-Pb	3.110	2.825	3.157	64.64°	53.96°

Figure 5. B3LYP/LANL2DZ optimized geometries [Å and °] of **7** (E = C, Si, Ge, Sn, Pb). The experimental values are in round parenthesis. Hydrogen atoms are omitted for clarity.

Additionally, the DFT computations show that the E_2=E_3 double bond length and the average E_1–E_2 and E_1–E_3 bond lengths follow the same trend as the atomic weight of E changes (Figure 5). As presented earlier, **9** with a lighter but more electronegative E atom reaches the TS relatively early, whereas a heavier, less electronegative E atom arrives at the TS relatively late. The former is therefore predicted to undergo a more exothermic abstraction, which is borne out by our DFT calculations. The order of free energy (ΔG) follows the same trend as the activation energy (Table 1). The energy of **7-Pb** is greater than that of the corresponding starting material, which strongly implies that the intramolecular cycloaddition reaction of **9-Pb** is energetically unfavorable and would be endothermic at room temperature. Thus, from consideration of both the kinetics and the thermodynamics of Reaction 2, one may conclude that the lighter, more electronegative E atoms involved in **9**, the more facile its intramolecular cycloaddition reaction becomes at room temperature. In addition, our theoretical findings suggest that the intramolecular cycloaddition reactions of **9** should proceed in a concerted manner. In other words, such cycloadditions of **9** should be favored to produce stereoretention products. Our DFT observations are in accordance with the conclusion as given in Figures 4 and 5.

Reaction 3: Intramolecular Migration Reactions

Next, we considered the other mechanism of Reaction 3. To maintain consistency with our previous work, we used the following reaction mechanism to explore the 1,2-silyl-group migration reactions of **10**: **10**→**TS-2**→**8**. The geometries and energies of **10** (E = C, Si, Ge, Sn, Pb) were calculated using the B3LYP/LANL2DZ level of theory. Selected geometric parameters and relative energies of stationary points for Reaction 3 are collected in Figures 6 and 7 and Table 1, and several noteworthy features were revealed.

As expected,[25] **10** can undergo an intramolecular 1,2-silyl-group migration with an energy barrier to form a five-membered cyclic product with a double bond (**8**). As can be seen in Figure 6, it is evident that these TSs (**TS-2-C**, **TS-2-Si**, **TS-2-Ge**, **TS-2-Sn**, and **TS-2-Pb**), which are all at the first-order saddle point as determined by frequency calculations at the B3LYP level, proceed in a three-center pattern involving one E, one carbon, and one silicon atom. Our DFT frequency calculations for **TS-2-C**, **TS-2-Si**, **TS-2-Ge**, **TS-2-Sn**, and **TS-2-Pb** indicate that the single imaginary frequency values are 211*i*, 164*i*, 119*i*, 76.8*i*, and 63.1*i* cm^{-1}, respectively. Their normal modes associated with the single imaginary frequency are consistent with the 1,2-silyl-group shift process. From Figure 6, it is apparent that the length of the E–C bond for the migration transition structure follows the same trend as the central atom E radius. One of the interesting points that emerged from the calculations of the TS geometries are the extent to which the migrating Si–C bond is formed in the TS. Compared to its value in the reactant, the migrating Si–C bond length in **TS-2-C**, **TS-2-Si**, **TS-2-Ge**, **TS-2-Sn**, and **TS-2-Pb** is 7.0, 35, 45, 58, and 70% longer than that of the corresponding **10**, respectively. These data indicate that the **10-C** intramolecular migration arrives at the TS relatively early, whereas the **10-Pb** intramolecular migration reaches the TS relatively late. According to the Hammond postulate,[29] the energy barriers are encountered earlier in the intramolecular migration of the former than that of the latter. Indeed, from Table 1 one can easily see that the migration energy barrier

of the TS increases on going from carbon to lead. That is to say, the heavier the central E atom involved in **10**, the larger its 1,2-shift barrier, which hinders its migration reaction.

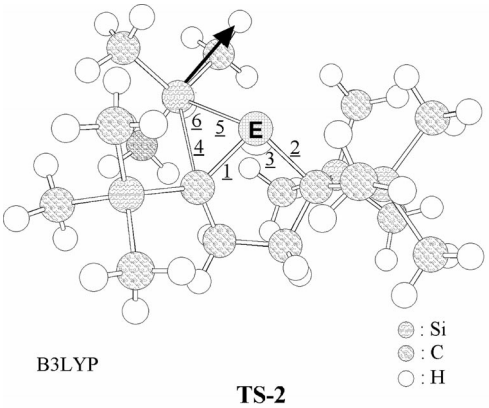

TS-2

TS-2-E	1	2	3	4	5	6
TS-2-C	1.444	1.531	108.7°	2.122	2.288	37.98°
TS-2-Si	1.829	1.985	94.44°	2.655	2.586	40.82°
TS-2-Ge	1.915	2.093	91.59°	2.824	2.639	40.86°
TS-2-Sn	2.100	2.280	86.67°	3.064	2.807	41.63°
TS-2-Pb	2.172	2.383	84.24°	3.288	2.855	40.65°

Figure 6. B3LYP/LANL2DZ optimized geometries [Å and °] of **TS-2** (E = C, Si, Ge, Sn, Pb). The relative energies for each species are given in Table 1. The heavy arrows indicate the main atomic motions in the TS eigen vector. Hydrogen atoms are omitted for clarity.

To the best of our knowledge, experimental structures for such migration products **8** are not yet known.[4b] Nevertheless, as seen in Figure 7, our DFT calculations anticipate that all the C=E double bond and C–E single bond lengths increase in the same order as the atomic radius of the central E atom. Moreover, compared with the geometric features shown in Figures 6 (**TS-2**) and 7 (**8**), it can be seen that the length of the migrating E–Si bond in **TS-2** is 19, 8.9, 8.1, 7.4, and 7.3% longer than that of the corresponding **8**, respectively. Again, our DFT results demonstrate that the lighter the E atom, the more reactive the TS, which would encounter a lower energy barrier and a more exothermic reaction.[29] As shown in Table 1, the B3LYP results indicate that the order of free energy (ΔG) of the 1,2-silyl-group migration follows the same trend as its activation barrier. It is evident that the energies of **8-Ge**, **8-Sn**, and **8-Pb** are all above those of the corresponding reactants. Namely, our computational results suggest that the 1,2-silyl-group migration products **8-Ge**, **8-Sn**, and **8-Pb** are not produced from the 1,2-shift reaction as in Reaction 3, but may exist if these migration products are produced through other reaction pathways. Our theoretical reports are in line with the experimental evidence. It was found experimentally that the most intriguing reactivity of **10-Si** is the facile 1,2-migration of one neighboring trimethylsilyl group that gives a corresponding silaethene derivative **8-Si** (**5**; Reaction 3) in stark contrast to the corresponding stable **10-Ge** and **10-Sn**, which show no such 1,2-shift isomerization even at 100 °C.[4]

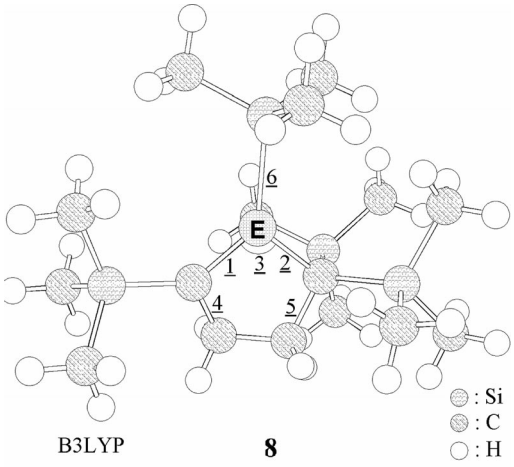

8

8-E	1	2	3	4	5	6
8-C	1.377	1.574	111.2°	1.542	1.589	1.925
8-Si	1.751	1.944	100.6°	1.548	1.595	2.375
8-Ge	1.822	2.029	98.12°	1.544	1.591	2.442
8-Sn	1.990	2.200	92.97°	1.541	1.588	2.614
8-Pb	2.040	2.282	90.21°	1.534	1.578	2.662

Figure 7. B3LYP/LANL2DZ optimized geometries [Å and °] of **8** (E = C, Si, Ge, Sn, Pb). Hydrogen atoms are omitted for clarity.

The Origin of the Energy Barrier and the Reaction Enthalpy for Intramolecular Reactions of Heavy Butadienes

In order to understand the key factors that determine the general features of the intramolecular reactions of these heavy 1,3-butadienes, a configuration mixing (CM) model[30,31] has been used to gain a better understanding of the reactivity of the various species. According to this model, the intramolecular stabilization of both cycloaddition and migration TSs depends on ΔE_{st} in the corresponding reactants (**9** and **10**), i.e. a smaller ΔE_{st} results in a more stable TS, a lower activation energy, and faster cycloaddition or migration. These results are also consistent with the prediction that the activation barrier should be correlated to the reaction enthalpy for chemical reactions, as illustrated earlier. We refer readers to several review articles on the subject of CM model theory for further, more detailed information.[30,31]

With the above conclusions in mind, we shall explain the origin of the theoretically observed trends shown previously.

*(1) Why are the intramolecular cycloaddition reactions of **9** with lighter E atoms more facile than those of **9** with heavier E atoms?*

The reason for this can be traced back to ΔE_{st} of the **9** species. As discussed earlier, our calculations (Table 1) suggest an increasing trend in ΔE_{st}: **9-C** (–31) < **9-Si** (1.3) < **9-**

Ge (7.7) < **9-Sn** (12) < **9-Pb** (13 kcal mol^{-1}). Consequently, it can be seen that this result is in good agreement with the trend in activation energies as well as the reaction enthalpies for **9** discussed earlier. That is, our theoretical work indicates that the lower the atomic weight of E in **9**, the lower its barrier to intramolecular cycloaddition, and the larger the exothermicity of this reaction.

*(2) Why does the ease of intramolecular 1,2-shift reaction of **10** decrease in the order of C > Si > Ge > Sn > Pb?*

According to the CM model discussed above, it is clear that the magnitude of ΔE_{st} for **10** should play a decisive role in the determination of its reactivity for 1,2-silyl-group migration reactions. As shown in Table 1, our theoretical results indicate an increasing trend in ΔE_{st}: **10-C** (12.2) < **10-Si** (27.3) < **10-Ge** (30.6) < **10-Sn** (31.4) < **10-Pb** (35.0 kcal mol^{-1}) at the B3LYP level of theory. This correlates well with the trends in both barrier height and reaction enthalpy as discussed in the previous section.

Accordingly, our theoretical findings strongly suggest that the ΔE_{st} values of **9** and **10** can be used to predict the reactivities of intramolecular reactions, such as cycloaddition and 1,2-migration.

One may wonder why the ΔE_{st} value of **9** or **10** increases monotonically from carbon to lead. The reason for this can be easily understood by the relativistic effect.[24] That is, the size difference between the valence s and p orbitals increases from C to Pb (the so-called "inert s-pair effect" or "nonhybridization effect").[24] Therefore, the valence s and p orbitals differ in spatial extension and subsequently overlap less to form strong hybrid orbitals. Also, the valence orbital energy between s and p increases from carbon to lead. This, in turn, enlarges ΔE_{st} as E goes from C to Pb.[24]

Conclusion

From our survey of the intramolecular reaction mechanisms of heavy 1,3-butadiene systems, we have come to the following conclusions:

(a) As demonstrated previously,[21] from a binding energy point of view, it is well known that the π bond strength of E=E decreases on going from carbon to lead. As a consequence, the greater the atomic weight of E, the longer the E=E bond length, the weaker the π bond strength of E=E, the lower its π bond dissociation energy, and the more facile the dissociation reaction of heavy 1,3-butadiene, which was indeed observed in this study.

(b) In addition to the weakness of the E=E double bond, the severely sterically demanding and bulky five-membered cyclic substituents attached to the heavy 1,3-butadiene can greatly promote the dissociation of one E=E double bond in **6**. That is to say, steric strain affects the bond energy, and the latter is not independent of the former. Thus, the easy thermal cleavage of one E=E double bond in a heavy 1,3-butadiene that possesses severely overcrowded substituents is attributed to both the E=E bond strength and the steric effects of the substituents.

(c) In light of our theoretical results, we are confident that the most reasonable mechanism for the thermal dissociation of **6** to **7** and **8** takes place according to the routes shown in Scheme 1. In principle, the thermal cleavage of one E=E double bond in **6** can subsequently lead to two kinds of intramolecular reactions. One is cycloaddition (Reaction 2; **6**→**9**→**TS-1**→**7**) and the other is 1,2-silyl-group migration (Reaction 3; **6**→**10**→**TS-2**→**8**).

(d) Our theoretical findings suggest that these heavy 1,3-butadienes (**6-C**, **6-Ge**, **6-Sn**, and **6-Pb**) can spontaneously dissociate one E=E double bond at room temperature. However, our DFT results indicate that **6-Si** does not easily break one Si=Si double bond at room temperature. Nevertheless, adding more thermal energy to the **6-Si** system can overcome the dissociation barrier to perform further reactions. This finding is in agreement with experimental observations.[4]

(e) As our analysis demonstrates, the CM approach adds additional facets and insights to this relatively poorly understood area of mechanistic study for heavy 1,3-butadienes such as **6**. Our theoretical evidence indicates that the ΔE_{st} value of a heavy carbene (such as **9** and **10**) can serve as a diagnostic tool to better understand and predict its chemical reactivity, both kinetically and thermodynamically.

(f) No matter what the intramolecular reaction (Reaction 2 or 3) the heavy 1,3-butadiene with the sterically overcrowded substituents adopts, our present theoretical investigations demonstrate that the lighter the E atom involved in the intermediate carbene species (**9** or **10**), the smaller its ΔE_{st} value, and, in turn, the more facile its intramolecular cycloaddition or 1,2-migration reaction.

(g) The reason that the ΔE_{st} value of heavy carbene species increases monotonically as E changes from carbon to lead can be ascribed to the relativistic effect.[24]

We encourage experimentalists to carry out further experiments to confirm our predictions.

Theoretical Methods

General: All geometries were fully optimized without symmetry constraints, although in some instances the resulting structure showed various elements of symmetry. For our DFT calculations, we used the hybrid gradient-corrected exchange functional proposed by Becke,[7] combined with the gradient-corrected correlation functional of Lee, Yang, and Parr.[8] This functional is commonly known as B3LYP and has been shown to be reliable both for geometries and energies.[9] The B3LYP calculations were carried out with relativistic effective core potentials on group 14 elements modeled using the double-zeta (DZ) basis sets.[10] The DZ basis set for hydrogen was augmented by a set of p-type polarization functions (p exponents 0.356). Accordingly, we denote our B3LYP calculations as B3LYP/LANL2DZ. Thus, model reactants **6** have 654 (390 electrons) basis functions.

The spin-unrestricted (UB3LYP) formalism was used for the open-shell (triplet) species. The S^2 expectation values of these species all showed an ideal value (2.002) after spin annihilation so that their geometries and energies are reliable for this study. Frequency calculations were performed on all structures to confirm that the reactants and products had no imaginary frequencies, and that TSs possessed only one imaginary frequency. The relative energies were

thus corrected for vibrational zero-point energies (ZPE, not scaled). Thermodynamic corrections at 298 K, ZPE corrections, heat capacity corrections, and entropy corrections (ΔS) were applied at the B3LYP/LANL2DZ level. Thus, the relative Gibbs free energy (ΔG) at 298 K was also calculated at the same level of theory. All of the DFT calculations were performed using the GAUSSIAN 03 package of programs.[11]

Supporting Information (see footnote on the first page of this article): Cartesian coordinates calculated for all the stationary points at the B3LYP level.

Acknowledgments

The authors are grateful to the National Center for High-Performance Computing of Taiwan for generous amounts of computing time and to the National Science Council of Taiwan for the financial support. Special thanks are also due to the peer reviewers of this article for their helpful suggestions and comments.

[1] R. West, M. Fink, J. Michl, *Science* **1981**, *214*, 1343–1344.
[2] For recent reviews, see: a) M. Weidenbruch, *Eur. J. Inorg. Chem.* **1999**, 373–381; b) M. Haaf, T. A. Schmedake, R. West, *Acc. Chem. Res.* **2000**, *33*, 704–741; c) M. Kira, T. Iwamoto, *J. Organomet. Chem.* **2000**, *611*, 236–247; d) B. Gehrhus, M. F. Lappert, *J. Organomet. Chem.* **2001**, *617*, 209–223; e) M. Weidenbruch, *J. Organomet. Chem.* **2002**, *646*, 39–52; f) M. Weidenbruch, *Organometallics* **2003**, *22*, 4348–4360; g) N. J. Hill, R. West, *J. Organomet. Chem.* **2004**, *689*, 4165–4183; h) M. Kira, *J. Organomet. Chem.* **2004**, *689*, 4475–4488; i) M. Kira, T. Iwamoto, S. Ishida, in: *Organosilicon Chemistry VI – From Molecules to Materials* (Eds.: N. Auner, J. Weis), Wiley-VCH, Weinheim, **2005**, pp. 25–32; j) M. Kira, T. Iwamoto, *Adv. Organomet. Chem.* **2006**, *54*, 73–148; k) B. Gehrhus, P. B. Hitchcock, R. Pongtavornpinyo, L. Zhang, *Dalton Trans.* **2006**, *15*, 1847–1857; l) A. Sekiguchi, M. Ichinohe, R. Kinjo, *Bull. Chem. Soc. Jpn.* **2006**, *79*, 825–832; m) V. Y. Lee, A. Sekiguchi, *Angew. Chem.* **2007**, *119*, 6716; *Angew. Chem. Int. Ed.* **2007**, *46*, 6596–6620; n) M. Kira, T. Iwamoto, S. Ishida, *Bull. Chem. Soc. Jpn.* **2007**, *80*, 258–275; o) M. Kira, *Chem. Commun.* **2010**, *46*, 2893–2903.
[3] a) M. Weidenbruch, S. Willms, W. Saak, G. Henkel, *Angew. Chem.* **1997**, *109*, 2612; *Angew. Chem. Int. Ed. Engl.* **1997**, *36*, 2503–2504; b) A. Grybat, S. Boomgaarden, W. Saak, H. Marsmann, M. Weidenbruch, *Angew. Chem.* **1999**, *111*, 2161; *Angew. Chem. Int. Ed.* **1999**, *38*, 2010–2012; c) S. Willms, A. Grybat, W. Saak, M. Weidenbruch, *Z. Anorg. Allg. Chem.* **2000**, *626*, 1148–1152; d) S. Boomgaarden, W. Saak, M. Weidenbruch, H. Marsmann, *Z. Anorg. Allg. Chem.* **2001**, *627*, 349–352; e) S. Boomgaarden, W. Saak, M. Weidenbruch, H. Marsmann, *Organometallics* **2001**, *20*, 2451–2453; f) S. Boomgaarden, W. Saak, H. Marsmann, M. Weidenbruch, *Z. Anorg. Allg. Chem.* **2002**, *628*, 1745–1748; g) M. Ichinohe, K. Sanuki, S. Inoue, A. Sekiguchi, *Organometallics* **2004**, *23*, 3088–3090.
[4] a) K. Uchiyama, S. Nagendran, S. Ishida, T. Iwamoto, M. Kira, *J. Am. Chem. Soc.* **2007**, *129*, 10638–10639; b) S. Ishida, T. Iwamoto, M. Kira, *Organometallics* **2009**, *28*, 919–921.
[5] For $R_2Ge{=}GeR{-}GeR{=}GeR_2$, see: H. Schäfer, W. Saak, M. Weidenbruch, H. Marsmann, *Angew. Chem. Int. Ed.* **2000**, *39*, 3702–3705.
[6] For instance, see: a) M. Weidenbruch, L. Kirmaier, H. Marsmann, P. J. Jones, *Organometallics* **1997**, *16*, 3080–3082; b) D. Ostendorf, L. Kirmaier, W. Saak, H. Marsmann, M. Weidenbruch, *Eur. J. Inorg. Chem.* **1999**, 2301–2307; c) S. Boomgaarden, W. Saak, H. Marsmann, M. Weidenbruch, *Z. Anorg. Allg. Chem.* **2001**, *627*, 805–806; d) M. Weidenbruch, *Organometallics* **2003**, *22*, 4348–4360; e) and Refs.[3b,3c,3d,3e]
[7] a) A. D. Becke, *Phys. Rev. A* **1988**, *38*, 3098–3100; b) A. D. Becke, *J. Chem. Phys.* **1993**, *98*, 5648–5652.
[8] C. Lee, W. Yang, R. G. Parr, *Phys. Rev. B* **1988**, *37*, 785–789.
[9] a) M.-D. Su, *J. Phys. Chem. A* **2004**, *108*, 823–832; b) M.-D. Su, *Inorg. Chem.* **2004**, *43*, 4846–4861; c) M.-D. Su, *Chem. Eur. J.* **2004**, *10*, 6073–6084; and references therein.
[10] a) T. H. Dunning Jr., P. J. Hay, in: *Modern Theoretical Chemistry* (Ed.: H. F. Schaefer, III), Plenum, New York, **1976**; pp. 1–28; b) P. J. Hay, W. R. Wadt, *J. Chem. Phys.* **1985**, *82*, 270–283; c) P. J. Hay, W. R. Wadt, *J. Chem. Phys.* **1985**, *82*, 284–298; d) P. J. Hay, W. R. Wadt, *J. Chem. Phys.* **1985**, *82*, 299–310; e) C. E. Check, T. O. Faust, J. M. Bailey, B. J. Wright, T. M. Gilbert, L. S. Sunderlin, *J. Phys. Chem. A* **2001**, *105*, 8111–8116.
[11] M. J. Frisch, G. W. Trucks, H. B. Schlegel, G. E. Scuseria, M. A. Robb, J. R. Cheeseman, V. G. Zakrzewski, J. A. Montgomery Jr., T. Vreven, K. N. Kudin, J. C. Burant, J. M. Millam, S. S. Iyengar, J. Tomasi, V. Barone, B. Mennucci, M. Cossi, G. Scalmani, N. Rega, G. A. Petersson, H. Nakatsuji, M. Hada, M. Ehara, K. Toyota, R. Fukuda, J. Hasegawa, M. Ishida, T. Nakajima, Y. Honda, O. Kitao, H. Nakai, M. Klene, X. Li, J. E. Knox, H. P. Hratchian, J. B. Cross, C. Adamo, J. Jaramillo, R. Gomperts, R. E. Stratmann, O. Yazyev, A. J. Austin, R. Cammi, C. Pomelli, J. W. Ochterski, P. Y. Ayala, K. Morokuma, G. A. Voth, P. Salvador, J. J. Dannenberg, V. G. Zakrzewski, S. Dapprich, A. D. Daniels, M. C. Strain, O. Farkas, D. K. Malick, A. D. Rabuck, K. Raghavachari, J. B. Foresman, J. V. Ortiz, Q. Cui, A. G. Baboul, S. Clifford, J. Cioslowski, B. B. Stefanov, G. Liu, A. Liashenko, P. Piskorz, I. Komaromi, R. L. Martin, D. J. Fox, T. Keith, M. A. Al-Laham, C. Y. Peng, A. Nanayakkara, M. Challacombe, P. M. W. Gill, B. Johnson, W. Chen, M. W. Wong, C. Gonzalez, J. A. Pople, *Gaussian03*, Gaussian, Inc., Wallingford CT, **2003**.
[12] a) G. Raabe, J. Michl, *Chem. Rev.* **1985**, *85*, 419–509; b) A. G. Brook, K. M. Baines, *Adv. Organomet. Chem.* **1986**, *25*, 1–44; c) R. West, *Angew. Chem.* **1987**, *99*, 1231; *Angew. Chem. Int. Ed. Engl.* **1987**, *26*, 1201–1211; d) T. Tsumuraya, S. A. Batcheller, A. Masamune, *Angew. Chem.* **1991**, *103*, 916; *Angew. Chem. Int. Ed. Engl.* **1991**, *30*, 902–930.
[13] a) A. Sekiguchi, H. Sakurai, *Adv. Organomet. Chem.* **1995**, *37*, 1–38; b) M. Driess, H. Grützmacher, *Angew. Chem.* **1996**, *108*, 900; *Angew. Chem. Int. Ed. Engl.* **1996**, *35*, 828–856.
[14] E. W. Abel, F. G. A. Stone, G. Wilkinson (Eds.), *Comprehensive Organometallic Chemistry II*, Elsevier, Oxford, UK, **1995**, Vol. 2.
[15] S. Masamune, in: *Silicon Chemistry* (Eds.: E. R. Corey, J. Y. Corey, P. P. Gaspar), Ellis Horwood Ltd., Chichester, UK, **1988**, pp. 257–268.
[16] a) M. Stürmann, M. Weidenbruch, K. W. Klinkhammer, F. Lissner, H. Marsmann, *Organometallics* **1998**, *17*, 4425–4428; b) see also ref.[2a] However, the authors cannot yet decide with certainty if these reported compounds are really diplumbenes with a formal lead–lead double bond.
[17] G. H. Spikes, P. P. Power, *Chem. Commun.* **2007**, 85–87.
[18] a) H. Preut, F. Huber, *Z. Anorg. Allg. Chem.* **1976**, *419*, 92–96; b) J. Kapp, M. Remko, P. v. R. Schleyer, *Inorg. Chem.* **1997**, *36*, 4241–4246.
[19] L. Lu, B. Twamley, P. P. Power, *J. Am. Chem. Soc.* **2000**, *122*, 3524–3525.
[20] H. Jacobsen, T. Ziegler, *J. Am. Chem. Soc.* **1994**, *116*, 3667–3679.
[21] Further supporting experimental evidence comes from the fact that many variously substituted R_2EER_2 (E = Si, Ge, Sn, Pb) compounds have E=E bonded dimeric structures in the solid state but dissociate in solution to yield monomeric R_2E; see: a) S. Masamune, Y. Eriyama, T. Kawase, *Angew. Chem.* **1987**, *99*, 601; *Angew. Chem. Int. Ed. Engl.* **1987**, *26*, 584–585; b) K. W. Zilm, G. A. Lawless, R. M. Merrill, J. M. Miller, G. G. Webb, *J. Am. Chem. Soc.* **1987**, *109*, 7236–7238; c) N. Tokitoh, H. Suzuki, R. Okazaki, *J. Am. Chem. Soc.* **1993**, *115*, 10428–10429; d) H. Suzuki, N. Tokitoh, R. Okazaki, *Bull. Chem. Soc.*

Jpn. **1995**, *68*, 2471–2481; e) M. A. Bona, M. C. Cassani, J. M. Keates, G. A. Lawless, M. F. Lappert, M. Sturmann, M. Weidenbruch, *J. Chem. Soc., Dalton Trans.* **1998**, 1187–1190; f) K. Kishikawa, N. Tokitoh, R. Okazaki, *Chem. Lett.* **1998**, 239–240; g) M.-L. Tsai, M.-D. Su, *J. Phys. Chem. A* **2006**, *110*, 6216–6223, and references cited therein.

[22] a) G. Trinquier, *J. Am. Chem. Soc.* **1990**, *112*, 2130–2137; b) P. P. Power, *Chem. Rev.* **1999**, *99*, 3463–3504.

[23] For comparison, as suggested by one reviewer, we also performed DFT with an all electron basis set and the (MP2) ab initio level of theory to confirm the relative energies obtained in this work. As a result, three computational methods, B3LYP/6-31G(d), MP2/LANL2DZ, and MP2/6-31G(d), have been applied to the study of the dissociation reaction of **6-Si**→**9-Si** and **10-Si**. Our computations showed that the dissociation energy (ZPE, not scaled) was predicted to be 37.6, 34.8, and 38.1 kcal mol^{-1}, respectively, compared with 26.9 kcal mol^{-1} (B3LYP/LANL2DZ, Table 1). Although these recalculated values are somewhat larger than those obtained from the B3LYP/LANL2DZ method, it is believed the qualitative trend, which our present theoretical observations show, would not be changed even using the more sophisticated theories.

[24] a) P. Pyykkö, J.-P. Desclaux, *Acc. Chem. Res.* **1979**, *12*, 276–281; b) W. Kutzelnigg, *Angew. Chem.* **1984**, *96*, 262; *Angew. Chem. Int. Ed. Engl.* **1984**, *23*, 272–295; c) P. Pyykkö, *Chem. Rev.* **1988**, *88*, 563–594; d) P. Pyykkö, *Chem. Rev.* **1997**, *97*, 597–636.

[25] a) M. Kira, R. Yauchibara, R. Hirano, C. Kabuto, H. Sakurai, *J. Am. Chem. Soc.* **1991**, *113*, 7785–7787; b) M. Kira, S. Ishida, T. Iwamoto, C. Kabuto, *J. Am. Chem. Soc.* **1999**, *121*, 9722–9723; c) M. Kira, S. Ishida, T. Iwamoto, M. Ichinohe, C. Kabuto, L. Ignatovich, H. Sakurai, *Chem. Lett.* **1999**, 263–264.

[26] The thermodynamic parameters for an analog of **10** with E = Si, Ge, Sn and R = SiH_3 have been reported by Kira et al.[4b]

[27] One reviewer mentioned that although we showed the geometric parameters of the **TS-1** they are more like those of the reactant. However, it is not valid for E = C. For instance, in the **TS-1-C** structure, the C_1–C_2 bond elongates beyond its corresponding length in the product, and the C_1–C_3 bond length becomes longer than that in **9**. One may question whether this is indeed the TS for the cycloaddition? We thus rechecked this TS point. Repeated attempts to search for the TS for a cycloaddition reaction always led to the **TS-1-C** structure given in Figure 4, although we did not use the IRC method to confirm that it is the real TS that connects **9-C** and **7-C** due to the large size of the system. It is believed that using the more sophisticated method as well as the bigger basis sets can greatly refine the structural data, but the trends for their reactivities are still the same.

[28] As seen in Figure 4, the TS for light E atoms being like the reactant seems to be invalid for E = C. The C_1–C_2 bond length in **TS-1-C** elongates beyond its corresponding length in the **7**, and C_1–C_3 becomes longer than that in **9**. The reason for this is presumably because the attached substituents are sterically bulky and the atomic radius of carbon is too small compared with the other group 14 elements. These two effects force their C–C bonds to be longer than usual.

[29] G. S. Hammond, *J. Am. Chem. Soc.* **1955**, *77*, 334–338.

[30] For details, see: a) S. Shaik, H. B. Schlegel, S. Wolfe, in: *Theoretical Aspects of Physical Organic Chemistry*, John Wiley & Sons Inc., New York, **1992**; b) A. Pross, in: *Theoretical and Physical principles of Organic Reactivity*, John Wiley & Sons Inc., New York, **1995**; c) S. Shaik, *Prog. Phys. Org. Chem.* **1985**, *15*, 197–337; d) S. Shaik, P. C. Hiberty, in: *A Chemist's Guide to Valence Bond Theory*, Wiley Interscience, Hoboken, **2008**.

[31] a) For the first paper that originated the CM model, see: S. Shaik, *J. Am. Chem. Soc.* **1981**, *103*, 3692–3701; b) For the most up to date review of the CM model, see: S. Shaik, A. Shurki, *Angew. Chem.* **1999**, *111*, 616; *Angew. Chem. Int. Ed.* **1999**, *38*, 586–625.

Received: September 6, 2011
Published Online: December 12, 2011

DOI: 10.1002/ejic.201100943

Platinum(II) Complexes Bearing a Thiolate/Thioether Ligand – Hemilability vs. Dealkylation

Fabrice Guyon,*[a] Michael Knorr,[a] Aurélie Garillon,[b] and Carsten Strohmann[c]

Keywords: Platinum / S ligands / Coordination modes / C–S activation

Substitution of the chloro ligands of *cis*-[Pt(PEt$_3$)$_2$Cl$_2$] by 4-methylthio-2-thioxo-1,3-dithiole-5-thiolate (**L**) leads to the thiolato complexes *trans*-[Pt(PEt$_3$)$_2$Cl**L**] (**2**) and *trans*-[Pt(PEt$_3$)$_2$**L**$_2$] (**1**), which have been characterised by X-ray crystallography. In the solid state, the square planar arrangement is capped by an endocyclic sulfur atom of **L**, which gives rise to distorted square-pyramidal and pseudooctahedral geometries for **2** and **1**, respectively. Complex **1** coexists in solution with [Pt(PEt$_3$)(η^1-**L**)(η^2-**L**)] (**3**), which results from the reversible dissociation of one phosphane ligand. The combination of η^1-(thiolato) and η^2-(thiolato/thioether) **L** in **3** has been established by variable-temperature ^{1}H NMR spectroscopy and crystal structure determination. The η^2-coordination mode of **L** is also observed in *cis*-[Pt(PEt$_3$)$_2$**L**]$^+$ (**4**), which results from the abstraction of the chloro ligand of **2** by excess TlPF$_6$. An *S*-demethylation reaction occurs when **1** is heated in acetonitrile to yield the structurally-characterised dithiolene complex [Pt(PEt$_3$)$_2$(dmit)] (**5**) (dmit^{2-} = 2-thioxo-1,3-dithiole-4,5-dithiolate) and Me**L**. Treatment of *cis*-[Pt(PPh$_3$)$_2$Cl$_2$] with 2 equiv. of **L** leads to a mixture of [Pt(PPh$_3$)$_2$(dmit)] (**6**) and [Pt(PPh$_3$)(η^1-**L**)(η^2-**L**)] (**7**). Complex **7** predominates in solution over its parent compound, [Pt(PPh$_3$)$_2$**L**$_2$]. The identification of CH$_3$Cl by ^{1}H NMR spectroscopy proves that [Pt(PPh$_3$)$_2$Cl**L**] is involved as an intermediate in the demethylation process. The reaction of **L** with platinum precursors that are blocked in a *cis* arrangement by chelation of 1,1-bis(diphenylphosphanyl)methane (dppm) and 1,1-bis(diphenylphosphanyl)ethane (dppe) leads to the formation of the thiolato complexes *cis*-[Pt(η^2-dppm)**L**$_2$] (**8**) and *cis*-[Pt(η^2-dppe)**L**$_2$] (**9**). The solid-state structure of **8** reveals the occurrence of an additional weak interaction between a thiomethyl group and the platinum centre (Pt–S 3.073 Å).

Introduction

Hemilabile ligands are polydentate ligands that contain one or several donor functionalities, which firmly bind to the metal centre, and at least one substitutionally-labile donor functionality, which allows a reversible opening–closing mechanism upon addition of a substrate. This class of ligands has found increasing use in the design of catalysts and chemosensors.[1] For this purpose, ligands that combine hard and soft donor atoms, such as P∩O and P∩N, have been studied extensively. However, the combination of identical atoms that lie in different environments, such as the thiolate/thioether association, may also confer hemilabile properties. For example, this behaviour has been studied for an oxorhenium(V) complex coordinated by edtMe (edtH_2 = 1,2-ethanedithiol).[2] In continuation of our previous studies that concerned the coordination chemistry of dithiolene and dithioether ligands,[3] we are interested in mixed thioether/thiolate derivatives with a tetrathioethylene skeleton as potential hemilabile ligands (Scheme 1). Although these systems exhibit attractive features, the literature on this family of ligands is limited.[4] Compared to the properties of edtMe, their chelating ability is expected to be strengthened due to the entropic factors that result from the use of a rigid ethylene bridge between the thiolate and the thioether groups. Moreover, multiple accessible oxidation states are expected in sulfur-rich ligands with the tetrathiafulvalene framework.[5] In these redox-active thiolate/thioether ligands, the binding properties could change as a function of their oxidation state. Ligands that allow electrochemical control over the binding properties have been termed redox-switchable hemilabile ligands.[6] With potential applications in catalysis or materials science in mind, we have undertaken a study of the synthesis and properties of square-planar complexes with mixed thiolate/thioether ligands that possess a tetrathioethylene core. This paper reports the preparation and reactivity of platinum(II) complexes with hemilabile 4-methylthio-2-thioxo-1,3-dithiole-5-thiolate (Medmit$^-$ = **L**). The parent dithiolene ligand, 2-thioxo-1,3-dithiole-4,5-dithiolate (dmit^{2-}), is one of the most studied dithiolene ligands and has applications in conducting materials.[7] The coordinating ability and structural aspects of **L** have been studied by Olk et al. with several other transition metals.[4a,4b] Its coordination mode has been identified as monodentate through the thiolate sulfur atom in (Ph$_3$P)$_3$-

[a] Institut UTINAM, UMR CNRS 6213, Université de Franche-Comté, Faculté des Sciences et des Techniques, 16 Route de Gray, 25030 Besançon, France
E-mail: fabrice.guyon@univ-fcomte.fr
[b] SERAC – UT Spectro, Technopole Temis, 18 rue Alain Savary, 25000 Besançon, France
[c] Anorganische Chemie, Technische Universität Dortmund, Otto-Hahn-Strasse 6, 44227 Dortmund, Germany

AgL, $(Ph_3P)_2$AuL, Cp_2TiL$_2$, (tmeda)ZnL$_2$ [tmeda = 1,2-bis(dimethylamino)ethane] and (dppe)PdL$_2$ [dppe = 1,2-bis(diphenylphosphanyl)ethane], whereas the mixed thiolate/thioether ligand acts as a bidentate ligand in $(Ph_3P)_2$CuL. Interestingly, both coordination modes coexist in (dppe)NiL$_2$. To develop this topic further, our contribution focuses on the complexation of **L** with platinum(II). We investigated the reactivity of the coordinated ligand and the influence of the nature of the ancillary ligand on the coordination mode.

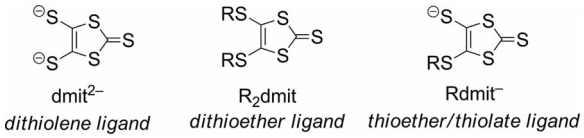

Scheme 1.

Results and Discussion

Substitution of Chlorine by L in *cis*-[Pt(PEt$_3$)$_2$Cl$_2$]

The reaction of *cis*-[Pt(PEt$_3$)$_2$Cl$_2$] with 2 equiv. of CsL in dichloromethane yielded *trans*-[Pt(PEt$_3$)$_2$L$_2$] (**1**) as an ochre, air-stable powder (Scheme 2). Complex **1** is highly soluble in halogenated solvents, but poorly soluble in acetone and methanol. A cyclic voltammetry study performed in CH_2Cl_2 showed that **1** is irreversibly oxidised at ca. 0.8 V vs. $AgClO_4$/Ag (0.1 M in MeCN). The hydrogen atoms of the thiomethyl groups appear as a singlet at 2.44 ppm in the ^{1}H NMR spectrum, which excludes any coupling in solution between these protons and the metal. The ^{31}P{^{1}H} NMR spectrum of **1** displays a singlet at 12.5 ppm, and the coupling constant $^1J_{P,Pt}$ of 2372 Hz is consistent with the *trans* configuration of the ligands around the platinum centre.[8] Modification of the nature of the solvent, for example MeOH or acetone, had no influence on the configuration of the resulting material. Monomeric complexes of the type [Pt(PR$_3$)$_2$(SR)$_2$] have already been studied in the context of *cis–trans* isomerisation.[9] The formation of *trans* species has been observed during the substitution of chloro ligands by thiolate[8a,10] and in solution for an isolated *cis*-[Pt(PR$_3$)$_2$(SR)$_2$] complex.[11] To gain more information about the isomerisation process that occurs during the formation of **1**, we reacted **L** with an equimolar amount of *cis*-[Pt(PEt$_3$)$_2$Cl$_2$], which was solubilised in acetone with a relatively high dilution. After 1 h of reaction at ambient temperature, *trans*-[Pt(PEt$_3$)$_2$LCl] (**2**) was extracted into hexane from the unreacted starting material along with a small amount of **1**. Upon cooling, **2** was isolated as yellow crystals. The ^{31}P{^{1}H} NMR spectrum of **2** shows an unique signal at 14.5 ppm, which is flanked by two satellites with $^1J_{P,Pt}$ of 2387 Hz. These data are in agreement with two magnetically equivalent phosphorus ligands in a *trans* arrangement. ^{1}H NMR analysis reveals the presence of a singlet at 2.41 ppm. The integration ratio between this signal and those of the ethyl groups fits with the stoichiometry of **2**. The *cis–trans* isomerisation may occur at the first stage of the substitution to minimise the steric hindrance between the two PEt$_3$ ligands. The five-coordinate intermediate that results from the associative activation in square-planar substitution reactions favours the rearrangement, which takes place at ambient temperature. In contrast, in the reaction of PtCl$_2$ with 2 equiv. of tri-*n*-butylphosphane, which has approximately the same basicity and cone angle as PEt$_3$, isomerisation from the kinetic product, *cis*-[Pt(PBu$_3$)$_2$Cl$_2$],

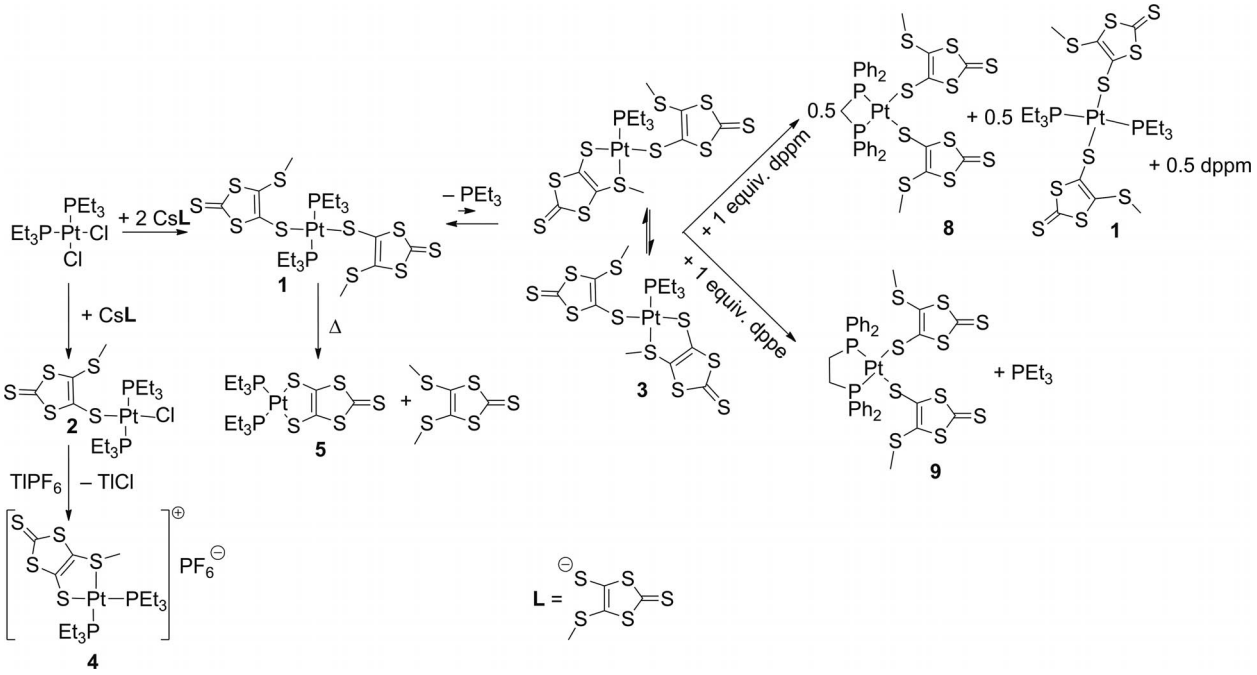

Scheme 2.

to the thermodynamic product, *trans*-[Pt(PBu$_3$)$_2$Cl$_2$], requires a much higher temperature.[12] Moreover, ^{31}P NMR monitoring of the substitution evidences a singlet at 12.1 ppm ($^1J_{Pt,P}$ 2895 Hz), the intensity of which decreases with time. This signal is tentatively assigned to a square-pyramidal intermediate of the type *cis*-[Pt(PEt$_3$)$_2$Cl$_2$**L**] (Scheme 2).

Crystallographic analysis of **1** confirms a centrosymmetric, *trans*-bis(thiolato) structure (Figure 1). The Pt atom displays a slightly distorted square-planar coordination with P–Pt–S angles of 86.415(15) and 93.585(15)°. The tetrathioethylene unit is perpendicular to the coordination sphere of Pt with a P–Pt–S(1)–C(1) dihedral angle of 100.5°. The Pt–P distance of 2.3339(5) Å and the Pt–S distance of 2.3345(5) Å are similar to those reported for other *trans*-[Pt(PEt$_3$)$_2$(thiolate)$_2$] compounds.[8b,13] No interaction between the thiomethyl groups and the Pt atom is obvious in the solid state. In contrast, the Pt···S(2) contacts of 3.328 Å, which are slightly shorter than the sum of the corresponding Van der Waals radii, suggest an incipient octahedral geometry for this complex, which is corroborated by the Pt–S(1)–C(1)–S(2) dihedral angle of 0.657°.

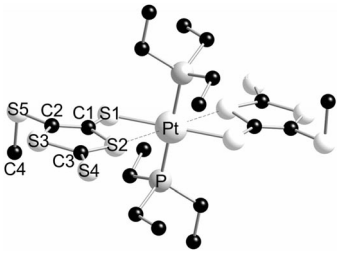

Figure 1. Molecular structure of **1**. H atoms are omitted for clarity. Selected bond lengths [Å] and angles [°]: Pt–S(1) 2.3345(5), Pt–P 2.3339(5), C(1)–S(1) 1.7377(18), C(1)–C(2) 1.352(2), C(2)–S(5) 1.7521(18), S(5)–C(4) 1.806(2), S(1)–Pt–P 86.415(15), S(1)–Pt–P# 93.585(15), Pt–S(1)–C(1) 106.00(6), C(2)–S(5)–C(4) 99.73(9).

The structure of **2** is shown in Figure 2. The thiolate ligand lies *trans* to the chloro ligand. The Pt–S(1) distance of 2.3011(15) Å is similar to that in **1** and is in accord with the weak thermodynamic *trans* influence exerted by the chloro ligand. In contrast, due to the more pronounced *trans* influence of the thiolato ligand, the Pt–Cl bond length of 2.3619(15) Å is significantly longer than that in *trans*-[Pt(PEt$_3$)$_3$Cl$_2$] (2.294 Å).[14] The Pt–P bond lengths of 2.3279(16) and 2.3179(16) Å are in the same range as those of *trans*-[Pt(PEt)$_3$Cl$_2$] [2.300(19) Å] and **1**. The coordination sphere of Pt involves two phosphorus atoms, a chloro ligand and a thiolato sulfur atom with *cis* angles lying between 87.48(6) and 92.35(6)°. Similar to the situation described in **1**, the square-planar arrangement is capped by an endocyclic sulfur atom of **L**. However, the interaction is more pronounced in **2** as the Pt···S contact is shortened to 3.193 Å. Therefore, the coordination environment around the Pt centre in the solid state is best described as distorted square-pyramidal. In addition, molecules of **2** are organised in centrosymmetric dimers within the unit cell with a parallel orientation of the dmit core. The plane-to-plane separation is 3.45 Å, and the shortest S···S distance is 3.601 Å. This supramolecular assembly is not surprising as the ability of dmit to develop a network of intermolecular interactions through short S···S contacts is well documented.[15]

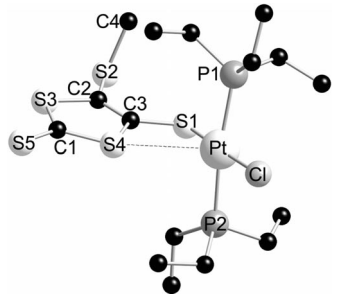

Figure 2. Molecular structure of **2**. H atoms are omitted for clarity. Selected bond lengths [Å] and angles [°]: Cl–Pt 2.3619(15), P(1)–Pt 2.3279(16), P(2)–Pt 2.3179(16), Pt–S(1) 2.3011(15), C(3)–S(1) 1.737(6), C(2)–C(3) 1.350(8), C(2)–S(2) 1.748(6), C(4)–S(2) 1.790(8), S(1)–Pt–P(2) 92.35(6), S(1)–Pt–P(1) 87.48(6), P(2)–Pt–P(1) 172.50(6), S(1)–Pt–Cl 176.73(6), P(2)–Pt–Cl 87.52(5), P(1)–Pt–Cl 92.23(5), C(3)–S(1)–Pt 103.1(2), C(2)–S(2)–C(4) 102.0(4).

Evolution of 1 in Solution – Hemilability vs. Demethylation

An additional weak peak with two satellites is observed at 16.5 ppm ($^1J_{P,Pt}$ = 3348 Hz) in the ^{31}P{^{1}H} NMR spectrum of **1** (Figure 3). This signal, and another singlet at 54.7 ppm, became more intense after the sample was stored for several days at 278 K. Concomitantly, the peak due to the phosphane ligands disappears. The nature of [Pt(PEt$_3$)(η^1-**L**)(η^2-**L**)] (**3**), which results from the transformation of **1**, was established unambiguously by crystal structure determination after crystallisation by addition of hexane to a CDCl$_3$ solution (Figure 4).

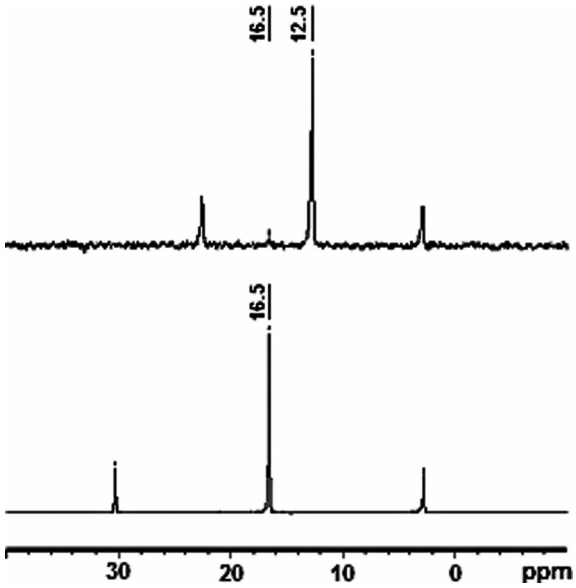

Figure 3. ^{31}P{^{1}H} NMR spectra (CDCl$_3$ solution) of **1** (top) and **3** (bottom).

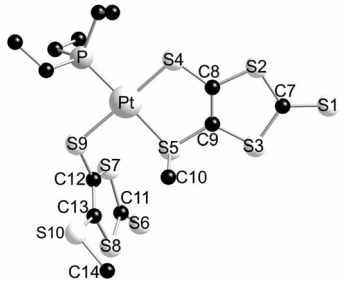

Figure 4. Molecular structure of **3**. H atoms are omitted for clarity. Selected bond lengths [Å] and angles [°]: Pt–S(4) 2.3052(10), Pt–S(9) 2.3278(10), Pt–S(5) 2.3418(10), Pt–P 2.2593(11), S(4)–C(8) 1.723(4), C(8)–C(9) 1.332(5), C(9)–S(5) 1.755(4),S(5)–C(10),1.806(4), S(9)–C(12) 1.751(4), C(12)–C(13) 1.341(5), C(13)–S(10) 1.738(4), S(10)–C(14) 1.784(4), P–Pt–S(4) 92.40(4), P–Pt–S(9) 86.47(4), S(4)–Pt–S(9) 178.65(4), P–Pt–S(5) 177.89(3), S(4)–Pt–S(5) 89.51(4), S(9)–Pt–S(5), 91.63(5), Pt–S(4)–C(8) 101.10(13), S(4)–C(8)–C(9) 126.6(3), C(8)–C(9)–S(5) 121.2(3), C(9)–S(5)–Pt 101.51(14), C(9)–S(5)–C(10) 102.77(18), C(10)–S(5)–Pt 104.38(15), Pt–S(9)–C(12) 106.67(13), S(9)–C(12)–C(13) 125.2(3), C(12)–C(13)–S(10) 122.7(3), C(13)–S(10)–S(14) 102.7(2).

Compound **3** bears only one phosphane ligand and the coordination demand of the Pt^{II} atom is satisfied by a supplementary strong dative interaction with one thiomethyl group. In solution, the two thiomethyl groups are equivalent at 293 K as only one signal is observed for these substituents in the ^{1}H NMR spectrum at 2.68 ppm (a poorly resolved doublet with $^4J_{P,H}$ = 1.4 Hz) with satellites due to $^3J_{Pt,H}$ of 14 Hz. In contrast, the exchange of the coordinated thiomethyl groups on platinum is slow at 223 K, and at this temperature, two singlets are found at 2.89 and 2.46 ppm (Figure 5). The evaluation of the coalescence temperature (T_c = 240 K) and $\Delta\nu$ value in the low exchange limit allows the calculation of an activation energy $\Delta G^{\ddagger}$ of 47 kJ mol^{-1} with the Eyring equation.

In the solid state, two types of **L** are clearly identified. The first is ligated to the platinum through a covalent Pt–S(thiolate) bond of 2.3278(10) Å. The second ligand chelates the metal with Pt–S(thiolate) and Pt–S(thioether) distances of 2.3052(10) and 2.3418(10) Å, respectively. As mentioned in the introduction, such a combination of η^1- and η^2-**L** ligands has already been observed in [Ni(dppe)-**L**$_2$]. However, in this case, the difference in strength of the interactions between the metal centre and the two types of sulfur atoms is much more pronounced.[4b] Compared to the value measured in centrosymmetric **1**, the Pt–P bond in **3**, *trans* to Pt–$S_{thioether}$, is significantly stronger [2.2593(11) vs. 2.3339(5) Å]. The distances measured for the *trans* Pt–P and Pt–$S_{thioether}$ bonds compare well with those reported for *cis*-[(Et$_3$P)ClPt^1{S(MeS^2)=C(S^{3}Me)S}Pt^{2}Cl(PEt$_3$)*(Pt^1–S^3)(S^2–Pt^2)*] [Pt–S 2.311(9) and 2.335(10) Å; Pt–P 2.267(10) and 2.249(10) Å].[4c] Due to the hemilability of **L**, **1** and **3** coexist in solution in the equilibrium mixture **1** ⇆ **3** + PEt$_3$ with a small equilibrium constant (Scheme 2). Indeed, from the integration of the signals at 2.68 (**3**) and 2.44 ppm (**1**) in the ^{1}H NMR spectrum of a pure sample of **1** in $CDCl_3$, the [**1**] to [**3**] ratio can be estimated to be 17:1. The complete transformation of **1** is a consequence of the oxidation of the triethylphosphane to its corresponding weakly-coordinating phosphane oxide (responsible for the signal at δ = 54.7 ppm in the $^{31}P\{^1H\}$ NMR spectrum, see above), which displaces the balance in favour of **3**. No reaction is observed when **3** is treated with excess Cs**L**.

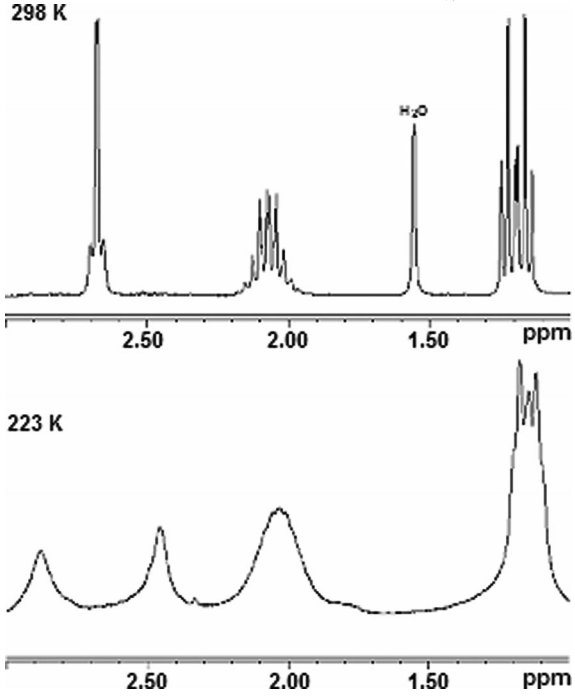

Figure 5. ^{1}H NMR spectra of **3** ($CDCl_3$ solution) recorded at 298 and 223 K.

The η^2-coordination mode of **L** is also observed in [Pt(PEt$_3$)$_2$(η^2-**L**)]$^+$ (**4**), which resulted from the abstraction of the chloro ligand of **2** by excess $TlPF_6$ (Scheme 2). This reaction was monitored by $^{31}P\{^1H\}$ and ^{1}H NMR spectroscopy. The spectra prove unambiguously that the vacant coordination site on platinum is electronically saturated by a strong interaction with the thiomethyl group, which provides a 16 electron count. Indeed, the $^{31}P\{^1H\}$ NMR spectrum consists of two mutually coupled doublets at 13.3 and 9.4 ppm ($^2J_{P,P}$ = 22 Hz), which indicates the nonequivalence of the two phosphanes. The high-field resonance exhibits a ^1J coupling of 2702 Hz to the ^{195}Pt nucleus, whereas the low-field resonance displays a $^1J_{Pt,P}$ coupling of 3048 Hz. In the ^{1}H NMR spectrum, the thiomethyl protons resonate at 2.95 ppm, which is similar to that observed in **3**. The coupling constants $^4J_{P,H}$ and $^3J_{Pt,H}$ of 3.1 and 33 Hz, respectively, are significantly stronger in **4**. These observations corroborate a strong η^2-coordination mode of **L** and the rearrangement of the phosphane ligands from a *trans* to a *cis* conformation.

Heating a solution of **1** in acetonitrile overnight led to the formation of [Pt(PEt$_3$)$_2$(dmit)] (**5**) and liberation of 4,5-bis(methylthio)-1,3-dithiole-2-thione, which indicates that a methyl migration from one sulfur ligand to the other occurs at high temperature (Scheme 2). The $^{31}P\{^1H\}$ NMR spectrum of **5** consists of a singlet at 6.5 ppm, which is coupled to platinum ($^1J_{P,Pt}$ = 2798 Hz). An X-ray structure analysis

of **5** confirmed unambiguously that the demethylation reaction occurred. The coordination sphere of the Pt^{II} complex is square planar and consists of a chelating dithiolene and two *cis* PEt_3 ligands. The structure depicted in Figure 6 is very similar to those of other structurally characterised heteroleptic phosphane(dithiolene)platinum(II) complexes, particularly $[Pt(PPh_3)_2(dmit)]$.[16] In **5**, the Pt–S bond lengths of 2.3408(16) and 2.3314(17) Å are also similar to those in **1**. Great attention has been paid to metal-assisted C–S bond activation from synthetic, catalytic and bioinorganic standpoints. The C–S bond cleavage evidenced in **1** is not without precedent. The conversion of thioether complexes into thiolato compounds by dealkylation has been observed in numerous group VIII metal complexes of N∩S, P∩S, As∩S and S∩S donor chelates.[17] Such alkyl extrusion may result from photoreactions,[18] electrochemical reductions,[19] reactions with nucleophiles[20] or under high-temperature conditions.[21] It should, however, be mentioned that boiling an acetone solution of trigonal-planar $[Au(PPh_3)_2\mathbf{L}]$ resulted not in C–S bond activation but in the dissociation of one of the phosphane ligands, which led to a linear, two-coordinate gold(I) centre in $[Au(PPh_3)\mathbf{L}]$.[4a]

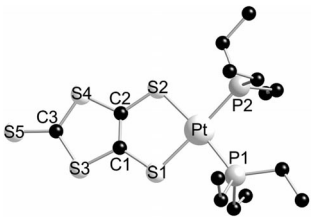

Figure 6. Molecular structure of **5**. H atoms are omitted for clarity. Selected bond lengths [Å] and angles [°]: P(1)–Pt 2.2971(18), P(2)–Pt 2.2931(16), Pt–S(2) 2.3314(17), Pt–S(1) 2.3408(16), C(1)–S(1) 1.748(6), C(2)–S(2) 1.735(6), C(1)–C(2) 1.349(9), P(2)–Pt–P(1) 98.60(5), P(2)–Pt–S(2) 88.28(5), P(1)–Pt–S(2) 173.10(5), P(2)–Pt–S(1) 176.36(5), P(1)–Pt–S(1) 83.84(5), S(2)–Pt–S(1) 89.33(5), C(1)–S(1)–Pt 101.7(2), C(2)–S(2)–Pt 101.4(2), C(2)–C(1)–S(1) 122.6(5), C(1)–C(2)–S(2) 124.9(5).

Influence of the Nature of the Phosphane Ligand

i) PPh_3 vs. PEt_3

In order to evaluate the influence of the nature of the phosphane ligand on the reactivity described above, Cs**L** was also reacted with the *cis*-$[Pt(PPh_3)_2Cl_2]$. The reaction was first studied in dichloromethane at ambient temperature using a 2:1 ligand-to-metal ratio. The $^{31}P\{^1H\}$ NMR spectrum of the crude product mixture showed the formation of two complexes, which are characterised by singlets at 18.4 and 17.3 ppm with $J_{P,Pt}$ couplings of 2961 and 3585 Hz, respectively. The two complexes were separated by chromatography on silica gel. On the basis of the NMR spectroscopic data reported by Bereman et al., the low-field resonance is attributed to $[Pt(PPh_3)_2(dmit)]$ (**6**).[16,22] Concerning the species responsible of the chemical shift at 17.3 ppm, the strong value of the associated coupling constant compares well with that observed for **3** and suggests the formation of $[Pt(PPh_3)(\eta^1\text{-}\mathbf{L})(\eta^2\text{-}\mathbf{L})]$ (**7**). This hypothesis is confirmed by the detection of the signal of free triphenylphosphane at –3.7 ppm in the ^{31}P NMR spectrum of the crude product. Moreover, dynamic behaviour similar to that reported for **3** was observed in solution. The ^1H NMR spectrum recorded at 293 K displays one broad resonance at 2.61 ppm, which is split into two singlets at 2.95 and 2.27 ppm at low temperature. In contrast, heating the sample to 320 K gives rise to a sharp singlet with a $^3J_{Pt,H}$ coupling of 15 Hz. As in **3**, the two sulfur ligands mutually exchange their coordination mode from η^1-thiolato to a chelating one that involves both Pt–S(thiolate) and Pt–S(thioether) interactions (Scheme 3) with an activation energy $\Delta G^{\ddagger}$ of 46.1 kJ mol^{-1} (at T_c = 241 K). By adding a large excess of triphenylphosphane to a $CDCl_3$ solution of **7**, the resonance due to compound **7** disappears in the $^{31}P\{^1H\}$ NMR spectrum, and a new singlet at 19.8 ppm with a $J_{Pt,P}$ coupling of 3054 Hz arises. This signal, and that observed in the ^1H NMR spectrum at 2.23 ppm, indicates the formation of $[Pt(PPh_3)_2(\eta^1\text{-}\mathbf{L})_2]$. From these observations, we can conclude that the monophosphane complex is the main product in the equilibrium $[Pt(PR_3)_2(\eta^1\text{-}\mathbf{L})_2] \leftrightarrows [Pt(PR_3)(\eta^1\text{-}\mathbf{L})(\eta^2\text{-}\mathbf{L})] + PR_3$ (R = Ph), whereas the use of the more basic triethylphosphane stabilises the diphosphane complex. Complex **7** is not sensitive to the presence of acetonitrile even in excess. Single crystals of **7** were grown from $CHCl_3/CH_3CN$. Two independent $[Pt(PPh_3)(\eta^1\text{-}\mathbf{L})(\eta^2\text{-}\mathbf{L})]$ molecules are located in general positions in the unit cell, which differ mainly in the orientation of the sulfur ligand that is coordinated in the η^1 mode. The molecular structure

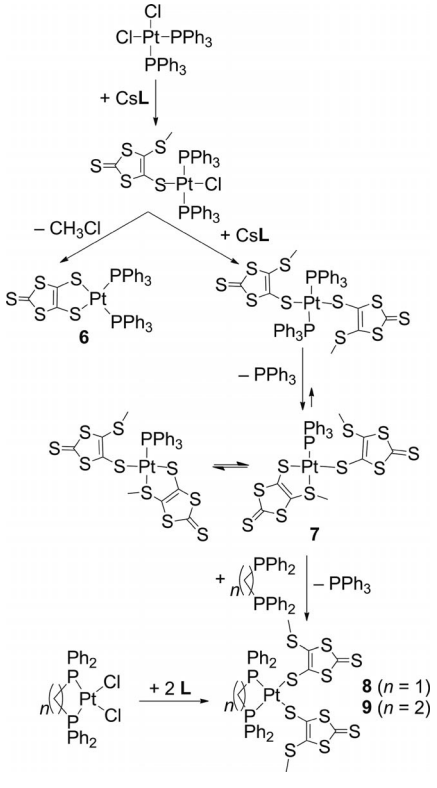

Scheme 3.

Table 1. Pt–P and Pt–S bond lengths [Å] in the molecular structures determined in this work.

	1	**2**	**3**	**5**	**7**[a]		**8**
Pt–P	2.3339(5)	2.3279(16)	2.2593(11)	2.2971(18)	2.2459(10)	2.2504(10)	2.2504(10)
		2.3179(16)		2.2931(16)			2.2415(10)
$Pt–S_{thiolate}$	2.3345	2.3011(15)	2.3052(10)	2.3314(17)	2.2892(9)	2.2937(9)	2.3622(10)
			2.3278(10)	2.3408(16)	2.3379(9)	2.3359(9)	2.3689(10)
$Pt–S_{thioether}$			2.3418(10)		2.3303(9)	2.3217(9)	

[a] Two independent molecules in the unit cell.

of **7** is similar to that of **3** with a square-planar environment around the platinum centre composed of one phosphorus atom, two thiolate sulfur atoms and one thioether sulfur atom (Figure 7). The nature of the phosphane (PPh_3 vs. PEt_3) does not significantly affect the Pt–P and Pt–S bond lengths (Table 1). The $Pt–S_{thioether}$ bond *trans* to the phosphane is only slightly stronger with PPh_3 [2.3303(9) and 2.3217(9) vs. 2.3418(10) Å].

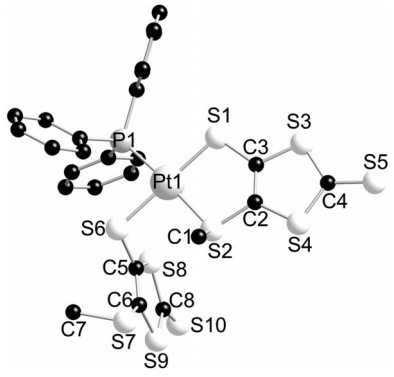

Figure 7. Molecular structure of **7** (only one of the two independent molecules of the unit cell is depicted). H atoms are omitted for clarity. Selected bond lengths [Å] and angles [°]: P(1)–Pt(1) 2.2459(10), Pt(1)–S(1) 2.2892(9), Pt(1)–S(1) 2.3303(9), Pt(1)–S(6) 2.3379(9), P(1)–Pt(1)–S(1) 93.41(3), P(1)–Pt(1)–S(2) 175.50(3), S(1)–Pt(1)–S(2) 90.55(3), P(1)–Pt(1)–S(6) 87.20(3), S(1)–Pt(1)–S(6) 178.54(4), S(2)–Pt(1)–S(6) 88.89(3). For the second molecule: Selected bond lengths [Å] and angles [°]: P(2)–Pt(2) 2.2504(10), Pt(2)–S(11) 2.2937(9), Pt(2)–S(12) 2.3217(9), Pt(1)–S(16) 2.3359(9), P(2)–Pt(2)–S(11) 91.95(3), P(2)–Pt(2)–S(12) 174.81(3), S(11)–Pt(2)–S(12) 90.26(3), P(2)–Pt(2)–S(16) 90.73(3), S(11)–Pt(2)–S(16) 176.98(3), S(12)–Pt(2)–S(16) 86.95(3).

The nature of the phosphane donor plays also a role in the rate of the demethylation reaction. As mentioned above, the formation of **7** was always accompanied by **6**, even when the substitution reaction was performed at 273 K. At first glance, the increase of the rate of formation of the dithiolene compound on going from PEt_3 to PPh_3 ancillary ligands is surprising because of the predominant species in solution (diphosphane vs. monophosphane complex). Indeed, we have shown above that [$Pt(PEt_3)_2$(dmit)] was formed by heating a solution of [$Pt(PEt_3)_2\mathbf{L}_2$]. In order to gain more information on the species involved in the dealkylation process when triphenylphosphane is coordinated to the platinum centre, we reacted Cs**L** with an equimolar amount of *cis*-[$Pt(PPh_3)_2Cl_2$] solubilised in acetone in high dilution. The mixture immediately turned yellow, and, an ochre powder was isolated after workup. The ^{31}P NMR spectrum revealed signals arising from **6** and **7** as well as a singlet at 15.5 ppm with $J_{Pt,P}$ equal to 3130 Hz, which is tentatively assigned to the complex resulting from the monosubstitution of a chloro ligand, [$Pt(PPh_3)_2$Cl**L**] (Scheme 3). More informative is the evolution of the sample. After storage for one week at 278 K, only the resonance due to **6** was detected in the ^{31}P NMR spectrum. The ^1H NMR spectrum exhibits an intense singlet at 3.01 ppm, which indicates the formation of CH_3Cl. Based on this observation, a mechanism for the demethylation reaction is proposed starting from [$Pt(PPh_3)_2$Cl**L**]. The first step is the oxidative addition of the S–CH_3 bond, which leads to a labile hexacoordinate Pt^{IV} species, [$Pt(PPh_3)_2$(dmit)ClMe]. This intermediate evolves to **6** by the reductive elimination of chloromethane. Thus, the reactivity and the coordinating mode of **L** in platinum complexes can be tuned by the nature of the ancillary phosphane ligands.

ii) Using Chelating Diphosphanes

The reaction of Cs**L** with platinum precursors blocked in a *cis* arrangement with the chelating diphosphanes 1,1-bis(diphenylphosphanyl)methane (dppm) and dppe allows the formation of the air-stable complexes *cis*-[$Pt(\eta^2$-dppm)$\mathbf{L}_2$] (**8**) and *cis*-[$Pt(\eta^2$-dppe)$\mathbf{L}_2$] (**9**) (Scheme 3). The $^{31}P\{^1H\}$ NMR spectra for **8** and **9** display singlet resonances with platinum satellites at –48.1 ($^1J_{P,Pt}$ = 2585 Hz) and 47.1 ppm ($^1J_{P,Pt}$ = 2974 Hz), respectively. In the ^1H NMR spectra, the resonance of the S–CH_3 groups gives rise to singlets at 2.34 ppm for **8** and 2.26 ppm for **9**. Again, no interaction seems to occur in solution between the platinum centre and thiomethyl group(s). Complexes **8** and **9** were also isolated quantitatively by adding one equivalent of dppm or dppe to **7** (Scheme 3). The reactivity is somewhat different starting from **3**. Indeed, addition of one equivalent of dppm to **3** resulted in the formation of an equimolar mixture of **8**, [$Pt(PEt_3)_2\mathbf{L}_2$] and unreacted dppm (see Supporting Information), whereas dppe displaces the triethylphosphane to give **9** almost quantitatively (Scheme 2). This example illustrates the higher stability of the five-membered metallacycle compared to the four-membered one. The molecular structure of **8** was determined by a single-crystal X-ray diffraction study. The *cis* arrangement of the **L** ligands in **8** with a S(1)–Pt–S(6) angle of 88.59(4)° is shown in Figure 8. The

P(1)–Pt–P(2) angle of 74.05(4)° and the Pt–P distances of 2.2504(10) and 2.2415(10) Å are typical of dppm chelated to platinum.[23] Compared to the situation described above for *trans* **1** and **2**, the platinum–thiolato bonds are slightly elongated to 2.3622(10) and 2.3689(10) Å (Table 1). Again, the coordination environment around the platinum centre is best described as distorted square-pyramidal as an additional short Pt···S contact of 3.073 Å is observed. In this case, the S(2) sulfur atom involved belongs to a thiomethyl group; for the other **L** ligand, the sulfur thiomethyl atom S(7) is located at 3.692 Å. The apical Pt···S distance of **8** approaches the values reported in platinum(II)–1,4,7-trithiacyclononane complexes (2.84–2.97 Å).[24] The molecular structure of **8** compares well with that reported for the analogous compound *cis*-[Pd(η^2-dppe)**L**$_2$], in which a close Pd···S(thiomethyl) contact of 3.11 Å was pointed out.[4b] The intermolecular interactions observed in the solid-state packing diagram of **8** along the *bc* plane are worth mentioning; the S···S contacts of 3.416 Å (S4···S8) and 3.421 Å (S3···S3) fall below the sum of the Van der Waals radii of two S atoms (3.70 Å) and give rise to a 2D supramolecular network (see Supporting Information).

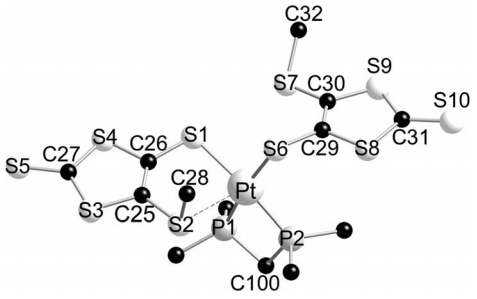

Figure 8. Molecular structure of complex **8**. For clarity, H atoms are omitted and only C_{ipso} of the phenyl groups are represented. Selected bond lengths [Å] and angles [°]: P(1)–Pt 2.2504(10), P(2)–Pt 2.2415(10), Pt–S(1) 2.3622(10), Pt–S(6) 2.3689(10), S(2)–C(28) 1.794(5), C(25)–S(2) 1.743(4), C(25)–C(26) 1.354(5), C(26)–S(1) 1.726(4), C(29)–S(6) 1.737(4), C(29)–C(30) 1.331(6), C(30)–S(7) 1.753(4), C(32)–S(7) 1.788(4), P(2)–Pt–P(1) 74.05(4), P(2)–Pt–S(1) 172.75(4), P(1)–Pt–S(1) 98.69(4), P(2)–Pt–S(6) 98.66(4), P(1)–Pt–S(6) 172.65(4), S(1)–Pt–S(6) 88.59(4), C(26)–S(1)–Pt 105.48(14), C(25)–C(26)–S(1) 130.3(3), C(26)–C(25)–S(2) 125.6(3), C(25)–S(2)–C(28) 100.9(2), C(29)–S(6)–Pt 106.74(14), C(30)–C(29)–S(6) 127.2(3), C(29)–C(30)–S(7) 121.9(3), C(30)–S(7)–C(32) 102.9(2).

Complex **8** is also sensitive to demethylation upon heating. Indeed, after heating an acetonitrile solution of **8** overnight, NMR spectroscopy revealed the partial evolution of the bis(thiolate) complex to the dithiolene complex [Pt(η^2-dppm)(dmit)] (δ = 47.0 ppm with $J_{Pt,P}$ = 2429 Hz in the $^{31}P\{^1H\}$ NMR spectrum) and formation of Me_2dmit (δ = 2.49 ppm in the ^1H NMR spectrum).

Conclusions

We have shown that thiolate/thioether **L** coordinates to diphosphane platinum(II) centres by a firm metal–thiolate link and an incipient metal–thioether interaction in [PtP_2**L**$_2$]-type complexes. The dative interaction leads to the displacement of a phosphane ligand (hemilabile behaviour) or to the activation of the C–SMe bond on the platinum centre to generate a dithiolene complex. These results are very encouraging for the purpose of extending our research to other thiolate/thioether–platinum complexes, especially by introducing a reversibly oxidisable ligand with a coordination mode determined by its oxidation state. In light of the reactivity of the Pt–H bond towards insertion reactions, we are currently probing the synthesis of platinum–hydride complexes that bear this thiolate/thioether ligand system.

Experimental Section

General: All manipulations were performed using Schlenk techniques in an atmosphere of dry oxygen-free argon. Elemental analyses were performed with a Leco Elemental Analyser CHN 900. $^{31}P\{^1H\}$ NMR spectra were recorded at 300.13 MHz with a Bruker DRX 300 spectrometer. Cs**L**,[4b] *cis*-[Pt(PEt_3)$_2$Cl$_2$],[25] *cis*-[Pt(PPh_3)$_2$Cl$_2$],[26] [Pt(dppm)Cl$_2$][27] and [Pt(dppe)Cl$_2$][28] were prepared according to literature procedures.

***trans*-[Pt(PEt_3)$_2$(L_1)$_2$] (1):** A CH_2Cl_2 (20 mL) solution of *cis*-[Pt(PEt_3)$_2$Cl$_2$] (0.240 g, 0.48 mmol) and caesium 4-methylthio-2-thioxo-1,3-dithiole-5-thiolate (Cs**L**, 2 equiv., 0.330 g, 0.96 mmol) was stirred overnight at room temperature. After filtration, the solution was concentrated under reduced pressure. Ochre single crystals were grown by the addition of hexane (245 mg, 60%). $C_{20}H_{36}P_2PtS_{10}$ (854.12): calcd. C 28.12, H 4.25, S 37.54; found C 27.84, H 4.05, S 37.20. ^1H NMR ($CDCl_3$, 298 K): δ = 2.44 (6 H, S–CH_3), 2.02 (m, 12 H, P–CH_2–), 1.16 (m, 18 H, CH_2–CH_3) ppm. $^{31}P\{^1H\}$ NMR ($CDCl_3$, 298 K): δ = 12.5 (s, $^1J_{^{195}Pt,^{31}P}$ = 2372 Hz) ppm. IR (KBr): $\tilde{\nu}$ = 2961, 2930, 1437, 1059 (C=S), 1032 (C=S), 1007, 890, 760, 729 cm^{-1}.

***trans*-[Pt(PEt_3)$_2$ClL] (2):** To an acetone (30 mL) solution of *cis*-[Pt(PEt_3)$_2$Cl$_2$] (0.200 g, 0.40 mmol) was added dropwise Cs**L** (0.135 g, 0.39 mmol) dissolved in acetone (10 mL). After stirring the mixture at room temperature for 3 h, the solution was filtered, and the filtrate was evaporated to dryness. The residue was then extracted into hexane (4 × 10 mL), and the combined extracts were concentrated in vacuo. Cooling the solution to 253 K precipitated yellow needles of **2** (95 mg, 36%). $C_{16}H_{33}ClP_2PtS_5$ (678.24): calcd. C 28.33, H 4.90, S 37.54; found C 28.58, H 5.03, S 36.87. ^1H NMR ($CDCl_3$, 298 K): δ = 2.41 (3 H, S–CH_3), 1.98 (m, 12 H, P–CH_2–), 1.16 (m, 18 H, CH_2–CH_3) ppm. $^{31}P\{^1H\}$ NMR ($CDCl_3$, 298 K): δ = 14.5 (s, $^1J_{^{195}Pt,^{31}P}$ = 2387 Hz) ppm.

[Pt(PEt_3)(η^1-L)(η^2-L)] (3): Complex **1** (0.043 g, 0.05 mmol) was dissolved in oxygenated CH_2Cl_2 (10 mL) and let for two weeks at 278 K. A layer of hexane was added, and **3** was afforded as dark crystals after a few days (30 mg, 82%). $C_{14}H_{21}PPtS_{10}$ (736.05): calcd. C 22.84, H 2.88, S 43.56; found C 22.48, H 2.65, S 43.07. ^1H ($CDCl_3$, 298 K): δ = 2.68 (d, $^4J_{P,H}$ = 1.4, $^3J_{Pt,H}$ = 14 Hz, 6 H, S–CH_3), 2.08 (s, 6 H, P–CH_2–), 1.19 (m, 9 H, CH_2–CH_3) ppm. $^{31}P\{^1H\}$ NMR ($CDCl_3$, 298 K): δ = 16.5 (s, $^1J_{^{195}Pt,^{31}P}$ = 3348 Hz) ppm.

cis*-[Pt(PEt_3)$_2$L]$^+$ (4):** Complex **2** (13.5 mg, 0.02 mmol), $TlPF_6$ (9 mg, 0.026 mmol) and $CDCl_3$ (0.5 mL) were mixed in a NMR tube (Caution:*** *Thallium and its compounds are extremely toxic and should be handled with great care*). The reaction was monitored by $^{31}P\{^1H\}$ and ^1H NMR spectroscopy. After a few minutes the $^{31}P\{^1H\}$ NMR spectrum showed the quantitative transformation

of **2** into **4**. ^{1}H NMR ($CDCl_3$, 298 K): δ = 2.95 (d, $^4J_{P,H}$ = 3.1, $^3J_{Pt,H}$ = 33 Hz, 3 H, S–CH_3), 2.16 (s, 12 H, P–CH_2–), 1.20 (m, 18 H, CH_2–CH_3) ppm. ^{31}P{^{1}H} NMR ($CDCl_3$, 298 K): δ = 13.5 (d, $^2J_{P,P}$ = 22, $^1J_{^{195}Pt,^{31}P}$ = 3048 Hz), 9.4 (d, $^2J_{P,P}$ = 22, $^1J_{^{195}Pt,^{31}P}$ = 2702 Hz) ppm.

[Pt(PEt$_3$)$_2$(dmit)] (5): Heating a solution of **1** (0.100 g, 0.12 mmol) in acetonitrile (10 mL) to reflux overnight led to an equimolar mixture of **5** and Me_2dmit. A pure sample of **5** was synthesised according the following procedure: equimolar quantities (0.5 mmol) of *cis*-[Pt(PEt$_3$)$_2$Cl$_2$] and Na_2dmit[29] were heated to reflux in CH_2Cl_2 (20 mL) overnight under argon. After filtration, hexane was added to the red solution, which resulted in the precipitation of **5** as a red-brown powder (170 mg, 54%). $C_{15}H_{30}P_2PtS_5$ (627.76): calcd. C 28.70, H 4.82, S 25.54; found C 28.91, H 4.89, S 25.02. ^{1}H NMR ($CDCl_3$, 298 K): δ = 2.09 (12 H, P–CH_2–), 1.18 (t, 18 H, CH_2–CH_3) ppm. ^{31}P{^{1}H} NMR ($CDCl_3$, 298 K): δ = 6.5 (s, $^1J_{^{195}Pt,^{31}P}$ = 2798 Hz) ppm. IR (KBr): $\tilde{\nu}$ = 2924, 2853, 1470, 1052 (C=S), 1027(C=S) cm^{-1}.

[Pt(PPh$_3$)(η^1-L)(η^2-L)] (7): A CH_2Cl_2 (10 mL) solution of *cis*-[Pt(PPh$_3$)$_2$Cl$_2$] (0.126 g, 0.16 mmol) and Cs**L** (2 equiv., 0.110 g, 0.32 mmol) was stirred at room temperature for 3 h. After filtration, the solvent was removed under reduced pressure. The resulting orange powder was washed with ethanol to afford a solid (0.105 mg), which was identified as a mixture of **6**[16] and **7**. Complexes **6** and **7** were separated by chromatography (SiO_2, $CHCl_3$), and pure **7** (50 mg) was recovered in the first fraction. $C_{26}H_{21}PPtS_{10}$ (880.22): calcd. C 35.48, H 2.41, S 36.43; found C 35.71, H 2.69, S 35.87. ^{1}H NMR ($CDCl_3$, 320 K): δ = 7.70–7.44 (m, 15 H, *Ph*), 2.60 ($^3J_{Pt,H}$ = 15 Hz, 6 H, S–CH_3) ppm. ^{31}P{^{1}H} NMR ($CDCl_3$, 298 K): δ = 17.3 (s, $^1J_{^{195}Pt,^{31}P}$ = 3585 Hz) ppm.

[Pt(dppm)L$_2$] (8): An MeOH (10 mL) solution of [Pt(dppm)Cl$_2$] (0.085 g, 0.13 mmol) and Cs**L** (2 equiv., 0.090 g, 0.26 mmol) was stirred 4 h. at 40 °C. After filtration, the solid was extracted into CH_2Cl_2 (10 mL). Evaporation under reduced pressure afforded an orange powder (60 mg, 46%). $C_{33}H_{28}P_2PtS_{10}$ (1002.24): calcd. C 39.54, H 2.82, S 31.99; found C 39.42; H 2.70, S 31.67. ^{1}H NMR ($CDCl_3$, 298 K): δ = 7.75–7.47 (20 H, Ph), 4.41(m, 2 H, P–CH_2–P), 2.35 (s, 6 H, S–CH_3) ppm. ^{31}P{^{1}H} NMR ($CDCl_3$, 298 K): δ = –48.1 (s, $^1J_{^{195}Pt,^{31}P}$ = 2585 Hz) ppm. IR (KBr): $\tilde{\nu}$ = 3053, 2963, 1435, 1261, 1099, 1063 (C=S), 1028 (C=S), 874, 800 cm^{-1}.

[Pt(dppe)L$_2$] (9): Complex **9** was prepared in an analogous manner to **8** starting from [Pt(dppm)Cl$_2$] and Cs**L** (50% yield). $C_{34}H_{30}P_2PtS_{10}$ (1016.27): calcd. C 40.18, H 2.98, S 31.55; found C 40.05, H 2.77, S 30.97. ^{1}H NMR ($CDCl_3$, 298 K): δ = 7.76–7.52 (20 H, Ph), 2.38 (m, 4 H, PCH_2–CH_2P), 2.26 (s, 6 H, S–CH_3) ppm. ^{31}P{^{1}H} NMR ($CDCl_3$, 298 K): δ = 47.0 (s, $^1J_{^{195}Pt,^{31}P}$ = 2974 Hz) ppm. IR (KBr): $\tilde{\nu}$ = 2959, 2914, 1435, 1103, 1049 (C=S), 1028 (C=S), 878, 818, 750, 715 cm^{-1}.

Crystal Structure Determinations: Compounds **1** and **5**: Stoe IPDS diffractometer; data collection: Expose in IPDS (Stoe & Cie, 1999), cell determination and refinement: Cell in IPDS (Stoe & Cie, 1999), integration: Integrate in IPDS (Stoe & Cie, 1999); numerical absorption correction: Faceit in IPDS (Stoe & Cie, 1999). Compounds **2**, **3**, **7** and **8**: Bruker APEX diffractometer (D8 three-circle goniometer) (Bruker AXS); data collection, cell determination and refinement: Smart version 5.622 (Bruker AXS, 2011); integration: SaintPlus version 6.02 (Bruker AXS, 1999); empirical absorption correction: Sadabs version 2.01 (Bruker AXS, 1999).

A suitable crystal of each complex was mounted in an inert oil (perfluoropolyalkylether); the crystal structure determination was

Table 2. Crystallographic refinement data for **1**, **2** and **3**.

	1	**2**	**3**
Formula	$C_{20}H_{36}P_2PtS_{10}$	$C_{16}H_{33}ClP_2PtS_5$	$C_{14}H_{21}PPtS_{10}$
Formula weight	854.12	678.24	736.06
Temperature [K]	173(2)	173(2)	173(2)
Wavelength [Å]	0.71073	0.71073	0.71073
Crystal system	monoclinic	monoclinic	monoclinic
Space group	$P\bar{1}$	$P2_1/n$	$P2_1/c$
a [Å]	8.6626(9),	10.4688(9)	10.7909(6)
b [Å]	10.5196(11)	22.4622(10)	29.2394(11)
c [Å]	10.8651(11)	11.2344(7)	7.6003(2)
α [°]	61.1180(10)		
β [°]	87.101(2)	108.792(8)	98.731(3)
γ [°]	69.5280(10)		
Volume [Å^3]	803.70(14)	2501.0(3)	2370.25(17)
Z	1	4	4
Density (calculated) [g cm^{-3}]	1.765	1.801	2.096
Absorption coefficient [mm^{-1}]	5.125	6.264	6.287
F(000)	424	1336	592
Crystal size [mm]	0.30 × 0.30 × 0.20	0.30 × 0.20 × 0.10	0.40 × 0.20 × 0.20
Theta range for data collection [°]	2.16 to 27.00	2.25 to 27.00	2.03 to 27.00
Index ranges	–11 ≤ *h* ≤ 11, –13 ≤ *k* ≤ 13, –13 ≤ *l* ≤ 13	–13 ≤ *h* ≤ 13, –28 ≤ *k* ≤ 28, –14 ≤ *l* ≤ 14	–12 ≤ *h* ≤ 13, –36 ≤ *k* ≤ 37, –9 ≤ *l* ≤ 9
Reflections collected	19653	17987	23207
Independent reflections	3506 [*R*(int) = 0.0295]	5421 [*R*(int) = 0.0627]	5041 [*R*(int) = 0.0411]
Refinement method		Full-matrix least-squares on F^2	
Data/restraints/parameters	3506/0/156	5421/0/233	5041/0/240
Goodness-of-fit on F^2	1.025	1.013	0.990
Final *R* indices [$I > 2\sigma(I)$]	*R*1 = 0.0123, *wR*2 = 0.0338	*R*1 = 0.0409, *wR*2 = 0.1063	*R*1 = 0.0272, *wR*2 = 0.0506
R indices (all data)	*R*1 = 0.0123, *wR*2 = 0.0338	*R*1 = 0.0530, *wR*2 = 0.1094	*R*1 = 0.0396, *wR*2 = 0.0522
Largest diff. peak and hole [e Å^{-3}]	0.925 and –0.883	4.170 and –1.734	0.988 and –2.435

Table 3. Crystallographic refinement data for **5**, **7** and **8**.

	5	**7**	**8**
Formula	$C_{15}H_{30}P_2PtS_5$, CH_2Cl_2	$C_{26}H_{21}PPtS_{10}$, 0.5 $CHCl_3$	$C_{33}H_{28}P_2PtS_{10}$
Formula weight	712.65	880.22	1002.18
Temperature [K]	173(2)	173(2)	173(2)
Wavelength [Å]	0.71073	0.71073	0.71073
Crystal system	monoclinic	monoclinic	monoclinic
Space group	$P2_1/n$	$P\bar{1}$	$P\bar{1}$
a [Å]	11.075(4)	13.3850(2)	7.9483(2)
b [Å]	17.921(6)	13.8880(2)	11.3708(3)
c [Å]	13.330(5)	19.6274(3)	20.6496(6)
α [°]		90.5060(10)	103.175(2)
β [°]	102.422(6)	97.8530(10)	94.626(2)
γ [°]		113.727(2)	91.375(2)
Volume [Å^3]	2593.7(16)	3300.63(9)	1809.51(8)
Z	4	4	2
Density (calculated) [g cm^{-3}]	1.832	1.891	1.839
Absorption coefficient [mm^{-1}]	6.168	5.074	4.569
F(000)	1400	1836	988
Crystal size [mm]	$0.30 \times 0.30 \times 0.20$	$0.20 \times 0.20 \times 0.20$	$0.40 \times 0.20 \times 0.10$
Theta range for data collection [°]	1.93 to 26.63	2.15 to 27.00	2.30 to 27.00
Index ranges	$-13 \le h \le 13$, $-22 \le k \le 22$, $-16 \le l \le 16$	$-17 \le h \le 17$, $-17 \le k \le 17$, $-25 \le l \le 25$	$-10 \le h \le 10$, $-14 \le k \le 14$, $-26 \le l \le 26$
Reflections collected	47856	140362	26543
Independent reflections	5394 [R(int) = 0.0552]	14385[R(int) = 0.0519]	7854 [R(int) = 0.0382]
Refinement method		Full-matrix least-squares on F^2	
Data/restraints/parameters	5394/0/241	14385/0/725	7854/ 0/417
Goodness-of-fit on F^2	1.070	1.009	1.007
Final R indices [$I > 2\sigma(I)$]	$R1$ = 0.0378, $wR2$ = 0.1043	$R1$ = 0.0242, $wR2$ = 0.0567	$R1$ = 0.0279, $wR2$ = 0.0593
R indices (all data)	$R1$ = 0.0399, $wR2$ = 0.1057	$R1$ = 0.0357, $wR2$ = 0.0580	$R1$ = 0.0366, $wR2$ = 0.0603
Largest diff. peak and hole [e Å^{-3}]	2.454 and –1.240	1.445 and –1.494	4.138 and –0.764

effected at 173(2) K. All structures were solved by applying direct and Fourier methods using SHELXS-97 and SHELXL-97.[30,31] For each structure, the non-hydrogen atoms were refined anisotropically. All of the H atoms were placed in geometrically calculated positions and each was assigned a fixed isotropic displacement parameter based on a riding model. The crystallographic parameters are listed in Tables 2 and 3.

CCDC-842700 (for **1**), -842701 (for **2**), -842702 (for **3**), -842703 (for **5**), -842704 (for **7**) and -842705 (for **8**) contain the supplementary crystallographic data for this paper. These data can be obtained free of charge from The Cambridge Crystallographic Data Centre via www.ccdc.cam.ac.uk/data_request/cif.

Supporting Information (see footnote on the first page of this article): $^{31}P\{^1H\}$ NMR spectrum of the result of the reaction between **3** and dppm, view of the 2D supramolecular network of **8**.

[1] a) A. Bader, E. Lindner, *Coord. Chem. Rev.* **1991**, *108*, 27–110; b) C. S. Slone, D. A. Weinberger, C. A. Mirkin, *Prog. Inorg. Chem.* **1999**, *48*, 233–350; c) P. Braunstein, F. Naud, *Angew. Chem.* **2001**, *113*, 702; *Angew. Chem. Int. Ed.* **2001**, *40*, 680–699; d) Z. Weng, S. Teo, T. S. A. Hor, *Acc. Chem. Res.* **2007**, *40*, 676–684; e) H. V. Huynh, C. H. Yeo, Y. X. Chew, *Organometallics* **2010**, *29*, 1479–1486; f) S. E. Angell, C. W. Rogers, Y. Zhang, M. O. Wolf, W. E. Jones Jr, *Coord. Chem. Rev.* **2006**, *250*, 1829–1841; g) S. M. Thompson, F. Stöhr, D. Sturmayr, G. Kickelbick, U. Schubert, *J. Organomet. Chem.* **2003**, *686*, 183–191; h) For a discussion of the reactivity of heterobimetallic Fe–Pd complexes that bear a hemilabile μ_2-η^2-bound $Si(OR)_3$ ligand see: P. Braunstein, M. Knorr, T. Stährfeldt, *J. Chem. Soc., Chem. Commun.* **1994**, 1913–1914.

[2] X. Shan, J. H. Espenson, *Organometallics* **2003**, *22*, 1250–1254.

[3] a) F. Guyon, A. Hameau, A. Khatyr, M. Knorr, H. Amrouche, D. Fortin, P. D. Harvey, C. Strohmann, A. L. Ndiaye, V. Huch, M. Veith, N. Avarvari, *Inorg. Chem.* **2008**, *47*, 7483–7492; b) A. Hameau, F. Guyon, M. Knorr, M. Enescu, C. Strohmann, *Monatsh. Chem.* **2006**, *137*, 545–555; c) F. Guyon, D. Lucas, I. V. Jourdain, M. Fourmigué, Y. Mugnier, H. Cattey, *Organometallics* **2001**, *20*, 2421–2424; d) I. V. Jourdain, M. Fourmigué, F. Guyon, J. Amaudrut, *Organometallics* **1999**, *18*, 1834–1839; e) A. L. Ndiaye, F. Guyon, M. Knorr, V. Huch, M. Veith, *Z. Anorg. Allg. Chem.* **2007**, *633*, 1959–1963.

[4] a) S. Zeltner, S. Jelonek, J. Sieler, R.-M. Olk, *Eur. J. Inorg. Chem.* **2001**, 1535–1541; b) S. Zeltner, R.-M. Olk, P. Joerchel, J. Sieler, *Z. Anorg. Allg. Chem.* **1999**, *625*, 368–373; c) B. Cetinkaya, P. B. Hitchcook, M. F. Lappert, P. L. Pye, D. B. Shaw, *J. Chem. Soc., Dalton Trans.* **1979**, 434–440; d) D. W. Allen, R. Berridge, N. Bricklebank, E. Cerrada, M. E. Light, M. B. Hursthouse, M. Laguna, A. Moreno, P. J. Skabara, *J. Chem. Soc., Dalton Trans.* **2002**, 2654–2659.

[5] a) D. Lorcy, N. Bellec, M. Fourmigué, N. Avarvari, *Coord. Chem. Rev.* **2009**, *253*, 1398–1438; b) I. V. Jourdain, F. Guyon, *Can. J. Chem.* **2000**, *78*, 1570–1574; c) M. Nomura, T. Fujii, M. Kajitani, *Organometallics* **2009**, *28*, 3776–3784.

[6] T. B. Higgins, C. A. Mirkin, *Inorg. Chim. Acta* **1995**, *240*, 347–353.

[7] a) N. Sevenstrup, J. Becher, *Synthesis* **1995**, 215–235; b) A. E. Pullen, R.-M. Olk, *Coord. Chem. Rev.* **1999**, *188*, 211–262; c) P. Cassoux, L. Valade, H. Kobayashi, A. Kobayashi, R. A. Clark, A. E. Underhill, *Coord. Chem. Rev.* **1991**, *110*, 115–160; d) R.-M. Olk, B. Olk, W. Dietzsch, R. Kirmse, E. Hoyer, *Coord. Chem. Rev.* **1992**, *117*, 99–131; e) M. Fourmigué, *Coord. Chem. Rev.* **1998**, *178–180*, 823–864.

[8] a) W. Henderson, B. K. Nicholson, C. E. F. Rickard, *Inorg. Chim. Acta* **2001**, *320*, 101–109; b) S. Kato, O. Niyomura, Y. Kawahara, T. Kanda, *J. Chem. Soc., Dalton Trans.* **1999**, 1677–

1686; c) F. Estudiante-Negrete, R. Redon, S. Hernandez-Ortega, R. A. Toscano, D. Morales-Morales, *Inorg. Chim. Acta* **2007**, *360*, 1651–1660.
[9] a) R. D. Lai, A. Shaver, *Inorg. Chem.* **1981**, *20*, 477–480; b) Q. Chen, F. Boeheim, J. Dabrowiak, J. Zubieta, *Inorg. Chim. Acta* **1994**, *216*, 83–87.
[10] a) V. Cordero-Pensado, V. Gomez-Benitez, S. Hernandez-Ortega, R. A. Toscano, D. Morales-Morales, *Inorg. Chim. Acta* **2006**, *359*, 4007–4018; b) S. Miranda, E. Vergara, F. Mohr, D. De Vos, E. Cerrada, A. Mendia, M. Laguna, *Inorg. Chem.* **2008**, *47*, 5641–5648.
[11] M. Alesi, S. Fantasia, M. Manassero, A. Pasini, *Eur. J. Inorg. Chem.* **2006**, 1429–1435.
[12] G. B. Kauffman, L. A. Teter, in: *Inorganic Syntheses*, **1963**, vol. VII (Ed.: J. Kleinberg), McGraw-Hill Book Company, Inc., p. 245.
[13] X. Chang, K.-E. Lee, Y.-J. Kim, S. W. Lee, *Inorg. Chim. Acta* **2006**, *359*, 4436–4440.
[14] G. G. Messmer, E. L. Amma, *Inorg. Chem.* **1966**, *5*, 1775–1781.
[15] See, for example, M. Fourmigué, B. Domercq, I. V. Jourdain, P. Molinié, F. Guyon, J. Amaudrut, *Chem. Eur. J.* **1998**, *4*, 1714–1723.
[16] C. E. Keefer, S. T. Purrington, R. D. Bereman, B. W. Knight, D. R. Bedgood Jr, P. D. Boyle, *Inorg. Chim. Acta* **1998**, *282*, 200–208.
[17] a) P. G. Eller, J. M. Riker, D. W. Meek, *J. Am. Chem. Soc.* **1973**, *95*, 3540–3548; b) L. F. Lindoy, S. E. Livingstone, T. N. Lockyer, *Inorg. Chem.* **1967**, *6*, 652–656; c) J. S. Kim, J. H. Reibenspies, M. Y. Darensbourg, *J. Am. Chem. Soc.* **1996**, *118*, 4115–4123; d) C. Huang, S. Gou, H. Zhu, W. Huang, *Inorg. Chem.* **2007**, *46*, 5537–5543; e) G. N. Schrauzer, H. N. Rabinowiz, *J. Am. Chem. Soc.* **1968**, *90*, 4297–4302; f) K. Wang, E. I. Stiefel, *Science* **2001**, *291*, 106–109.
[18] S.-I. Ohkoshi, Y. Ohba, M. Iwaizumi, S. Yamauchi, M. Ohkoshi-Ohtnai, K. Tokuhisa, M. Kajitani, T. Akiyama, A. Sugimori, *Inorg. Chem.* **1996**, *35*, 4569–4574.
[19] S. K. Ibrahim, C. J. Pickett, *J. Chem. Soc., Chem. Commun.* **1991**, 246–249.
[20] D. M. Roundhill, S. G. N. Roundhill, W. B. Beaulieu, U. Bagchi, *Inorg. Chem.* **1980**, *19*, 3365–3373.
[21] S. Mandal, N. Paul, P. Banerjee, T. K. Mondal, S. Goswani, *Dalton Trans.* **2010**, *39*, 2717–2726.
[22] C. E. Keefer, R. D. Bereman, S. T. Purrington, B. W. Knight, P. D. Doyle, *Inorg. Chem.* **1999**, *38*, 2294–2302.
[23] a) C. Albrecht, C. Bruhn, C. Wagner, D. Steinborn, *Z. Anorg. Allg. Chem.* **2008**, *634*, 1301–1308; b) T. S. Lobana, P. Kaur, G. Hundal, R. J. Butcher, A. Castineiras, *Z. Anorg. Allg. Chem.* **2008**, *634*, 747–753.
[24] T. W. Green, R. Lieberman, N. Mitchell, J. A. Krause Bauer, W. B. Connick, *Inorg. Chem.* **2005**, *44*, 1955–1965.
[25] G. W. Parshall, in: *Inorganic Syntheses* (Ed.: R. W. Parry), **1970**, vol. XII, McGraw-Hill Book Company, Inc., p. 27.
[26] U. Nagel, *Chem. Ber.* **1982**, *115*, 1998–1999.
[27] M. P. Brown, R. J. Puddephatt, M. Rashidi, K. R. Seddon, *J. Chem. Soc., Dalton Trans.* **1977**, 951–955.
[28] E. G. Hope, W. Lewason, N. A. Powell, *Inorg. Chim. Acta* **1986**, *115*, 187–192.
[29] K. S. Varma, A. Bury, N. J. Harris, A. E. Underhill, *Synthesis* **1987**, 837–838.
[30] G. M. Sheldrick, *SHELXS-90*, University of Göttingen, Germany, **1990**.
[31] G. M. Sheldrick, *SHELXL-97*, University of Göttingen, Germany, **1997**.

Received: September 6, 2011
Published Online: December 7, 2011

DOI: 10.1002/ejic.201100948

Synthesis and Structure of Lead(II) Complexes of (η^6-Benzenecarboxylato)-tricarbonylchromium

Balasubramanian Murugesapandian[a] and Peter W. Roesky*[a]

Keywords: Carbonyl ligands / Chromium / Coordination polymers / Lead / N ligands

Treatment of (η^6-benzoic acid)tricarbonylchromium with lead(II) acetate in the presence of *trans*-1,2-bis(4-pyridyl)ethene (bpe) afforded the one-dimensional coordination polymer $[Pb\{(\eta^6\text{-}C_6H_5COO)Cr(CO)_3\}_2bpe]_n$ (**1**). In contrast, the reaction of (η^6-benzoic acid)tricarbonylchromium with lead(II) acetate in the presence of 1,10-phenanthroline (1,10-phen) or 2,2′-bipyridine (2,2′-bipy) gave the lead(II) compounds $[Pb\{(\eta^6\text{-}C_6H_5COO)Cr(CO)_3\}_2(1,10\text{-phen})]$ (**2**) and $[Pb\{(\eta^6\text{-}C_6H_5COO)Cr(CO)_3\}_2(2,2'\text{-bipy})]$ (**3**). The solid-state structures of all compounds were determined by single-crystal X-ray diffraction.

Introduction

Recently, metal–organic frameworks (MOFs) and infinite coordination polymers (ICPs) have been studied extensively.[1] This kind of chemistry is based on the early work of Robson[1e,2] on net-based coordination polymers around 1990[1c,1d] and the concept of reticular design initiated by Yaghi et al.,[3,4] in the late 1990s. These compounds show fascinating structures, which originate from a broad variety of molecule-based topologies. Moreover, there are promising applications[5] such as the storage of gases,[1k,6] catalysis,[7] and sensors for special classes of molecules.[1k,8] Some of these materials also show interesting physical properties such as magnetism,[9] luminescence,[10] and optoelectronic effects.[11] The construction of MOFs and ICPs is often based on organic carboxylates. MOF5 consists of cationic secondary building units (SBUs) that are linked by benzenedicarboxylate (bdc) anions to form a continuous cubic neutral framework of composition $Zn_4O(bdc)_3$.[12] In contrast to these investigations, the use of metal–organic carboxylates for the construction of coordination oligomers, ICPs, and MOFs is still rare.[9a,13] Most of the used compounds are based on ferrocene derivatives as organometallic ligands.[14] Recently, we became interested in the synthesis of coordination polymers based on (η^6-benzenecarboxylato)-tricarbonylchromium. Although (η^6-benzoic acid)tricarbonylchromium was already reported in 1958 by E. O. Fischer,[15] to the best of our knowledge only the group 4-metal η^6-benzenecarboxylate complexes $[(\eta^5\text{-}C_5H_5)_2TiX\{(\mu\text{-}O_2CC_6H_5)Cr(CO)_3\}]$ (X = Cl, Br, CH_3) and $[(\eta^5\text{-}C_5H_5)_2M\{(\mu\text{-}O_2CC_6H_5)Cr(CO)_3\}_2]$ (M = Ti, Zr)[16] were structurally characterized before we started our investigation last year.[17] Moreover, Long and co-workers used an (η^6-1,4-benzenedicarboxylic acid)tricarbonylchromium building block for the construction of a porous metal–organic framework that had a $[Zn_4O\{(\eta^6\text{-}1,4\text{-benzenedicarboxylato})Cr(CO)_3\}_3]$ scaffold.[18] Under photolysis conditions, replacement of a single CO ligand per metal atom by N_2 and H_2 was observed. This kind of reactivity was also seen in the discrete complexes.[19]

We recently started to investigate the application of [(η^6-benzenecarboxylato)$Cr(CO)_3$] and [(η^6-1,4-benzenedicarboxylato)$Cr(CO)_3$] as metalloligands for the construction of molecular and polymer compounds based on the alkaline metals, zinc, and cadmium. We want to study the influence of the organometallic compound on the formation process and the structure of the coordination compound. Further derivatization of the tricarbonylchromium unit by classical thermal or photolytic activation methods seems to be possible. Now we are interested in using lead(II), which has an additional lone pair, as a node for the metalloligand. Due to the stereochemically active lone pair of lead(II), it can form interesting structures, and the compounds sometimes show luminescence properties. The coordination chemistry of lead(II) and lead(II)-based coordination polymers often shows a flexible coordination environment that leads to interesting structures.[20] Divalent lead compounds are known to form different coordination polymers and oligomers that show interesting structural features as a consequence of the large radius, adoption of different coordination numbers, and a variable stereochemical activity.[20a,21]

Herein we report on the reaction of $[\{\eta^6\text{-}C_6H_5COOH\}Cr(CO)_3]$ with lead(II) acetate in the presence of *trans*-1,2-bis(4-pyridyl)ethene, 1,10-phenanthroline, and 2,2′-bipyridine, which gave a one-dimensional coordination polymer and mononuclear complexes.

[a] Institut für Anorganische Chemie, Karlsruher Institut für Technologie (KIT),
Engesserstr. 15, 76128 Karlsruhe, Germany
Fax: +49-721-6084-4854
E-mail: roesky@kit.edu

Results and Discussion

To explore the coordination chemistry of (η^6-benzenecarboxylato)tricarbonylchromium as a metalloligand in lead(II) chemistry, nitrogen-based ligands have been used as ancillary ligands. Lead(II) coordination polymers with N-donor ligands in the absence of a metalloligand have been studied in some detail.[22] Treatment of (η^6-benzoic acid)tricarbonylchromium with lead(II) acetate in the presence of *trans*-1,2-bis(4-pyridyl)ethene (bpe) afforded the one-dimensional coordination polymer $[Pb\{(\eta^6\text{-}C_6H_5COO)Cr(CO)_3\}_2(bpe)]_n$ (**1**) (Scheme 1). In contrast, the reaction of (η^6-benzoic acid)tricarbonylchromium with lead(II) acetate in the presence of 1,10-phenanthroline (1,10-phen) or 2,2′-bipyridine (2,2′-bipy) gave the lead(II) compounds $[Pb\{(\eta^6\text{-}C_6H_5COO)Cr(CO)_3\}_2(1,10\text{-phen})]$ (**2**) and $[Pb\{(\eta^6\text{-}C_6H_5COO)Cr(CO)_3\}_2(2,2'\text{-bipy})]$ (**3**) (Scheme 2). All new complexes were characterized by standard analytical/spectroscopic techniques, and the solid-state structures were determined by single-crystal X-ray diffraction.

The ^{1}H NMR spectrum of compound **1** shows two signals for the pyridine rings [$\delta(^1H)$ = 8.60 and 7.61 ppm], one singlet for the CH=CH protons, and three signals for the benzenecarboxylate unit at $\delta(^1H)$ = 6.20, 5.86, and 5.66 ppm. For compound **2**, four signals for the 1,10-phenanthroline ligand and three signals for the benzenecarboxylate unit at δ = 6.15, 5.80, and 5.61 ppm were observed in the ^{1}H NMR spectrum. The ^{1}H NMR spectrum of compound **3** shows four signals for the 2,2′-bipyridine ligand and three signals for the benzenecarboxylate unit at δ = 6.15, 5.80, and 5.61 ppm. The $^{13}C\{^1H\}$ NMR spectra of all compounds show the expected sets of signals. The characteristic signals of the carbonyl groups were seen at δ = 233.3 ppm for all compounds. The signals of the carboxylate groups were observed at $\delta \approx$ 169.7 (**1**), 169.0 (**2**), and 169.5 ppm (**3**). In the IR spectra, the νCO stretching frequencies were measured in the expected range.

All three compounds are light-sensitive in solution. They change color from yellow to blue upon decomposition. Thus, crystals of compounds **1**–**3** were grown in the dark. Compound **1** crystallizes in the triclinic space group $P\bar{1}$. Data-collection parameters and selected bond lengths and angles are given in the Experimental Section and in the caption of Figure 1. The asymmetric unit consists of one lead atom, two carboxylate anions (Cr1 and Cr2), and one *trans*-

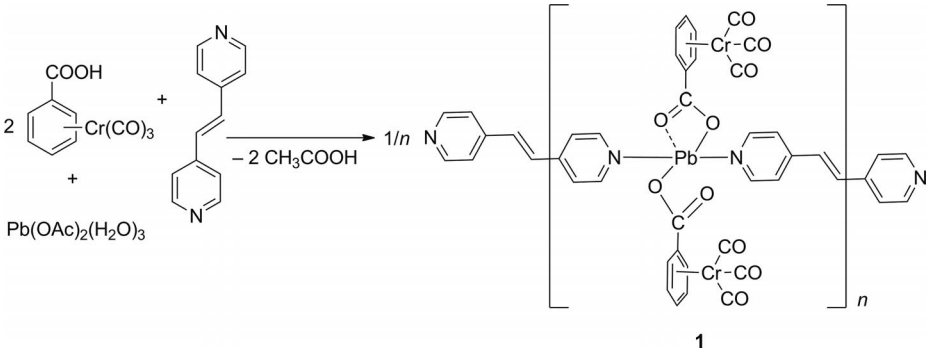

Scheme 1. Synthesis of compound **1**.

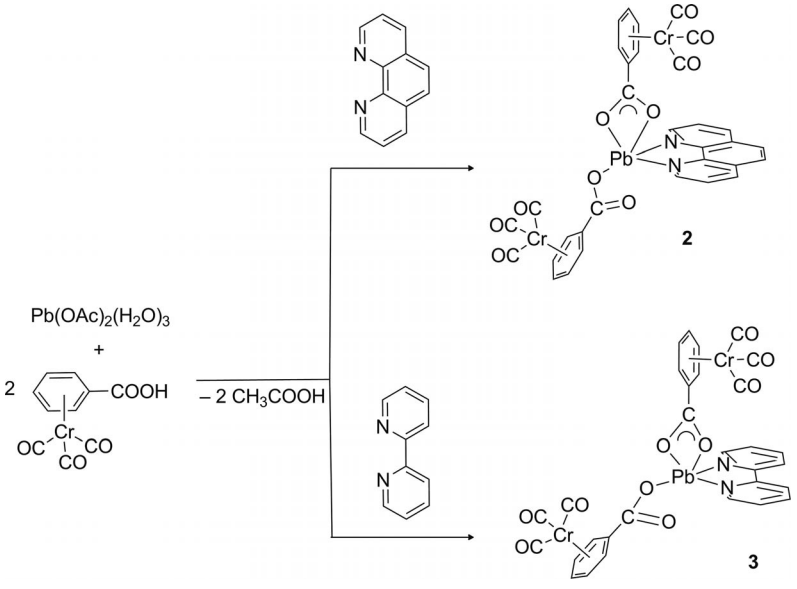

Scheme 2. Synthesis of compounds **2** and **3**.

1,2-bis(4-pyridyl)ethene ligand (Figure 1). The structure consists of a one-dimensional polymer in which the $[Pb\{(\eta^6\text{-}C_6H_5COO)Cr(CO)_3\}_2]$ nodes are connected by *trans*-1,2-bis(4-pyridyl)ethene ligands. The lead atom is fivefold coordinated by two nitrogen atoms of two *trans*-1,2-bis(4-pyridyl)ethene ligands [Pb–N1 2.597(6) Å and Pb–N2 2.541 Å] and three oxygen atoms from two (η^6-benzenecarboxylato)tricarbonylchromium units. Thus, the carboxylate $[\{\eta^6\text{-}C_6H_5COO\}Cr(CO)_3]$ anions display two different coordination modes (κ^1 and κ^2) to result in pentacoordinated lead atoms. The Pb–O bond lengths are Pb–O1 2.314(5) Å, Pb–O6 2.323(5) Å, and Pb–O7 2.735(7) Å. This clearly shows that the κ^2-coordinated carboxylate unit (O6 and O7) is asymmetrically coordinated with a weak Pb–O interaction. Additionally, the C–O bond lengths within this carboxylate unit are also different [O6–C17 1.283(9) Å and O7–C17 1.241(9) Å], thus indicating that the O6–C17–O7 unit is not forming a complete delocalized heteroallyl system. Intermolecular π–π stacking interactions[23] of the pyridyl rings of adjacent chains were observed.

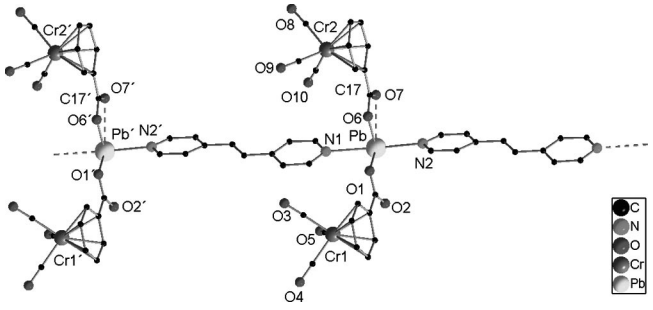

Figure 1. Molecular structure of compound **1**. Hydrogen atoms are omitted for clarity. Selected bond lengths [Å] and angles [°]: Pb–N1 2.597(6), Pb–N2 2.541(6), Pb–O1 2.314(5), Pb–O6 2.323(5), Pb–O7 2.735(7), O6–C17 1.283(9), O7–C17 1.241(9); O1–Pb–O6 75.15(2), O1–Pb–N2 84.98(2), O6–Pb–N2 83.42(2), O1–Pb–N1 80.7(2), O6–Pb–N1 83.3(2), N2–Pb–N1 162.5(2), O1–Pb–O7 125.92(2), O6–Pb–O7 50.82(2), N2–Pb–O7 86.6(3), N1–Pb–O7 93.7(3).

The structure on the corresponding ferrocenyl-based compound $[Pb(FcCOO)(\mu_2\text{-}FcCOO)(bpe)]_n$ [Fc = $(\eta^5\text{-}C_5H_5)Fe(\eta^5\text{-}C_5H_4)$] is significantly different. This compound forms a one-dimensional ladderlike structure. The $FcCOO^-$ units coordinate in two different modes to the lead atom. One coordination mode is a monodentate one, whereas the other $FcCOO^-$ unit acts as a bridging bidentate ligand, which binds to two lead atoms.[14a] This shows that the nature of the organometallic compound has a significant influence on the structure of the polymer.[17b]

Compound **2** crystallizes in the triclinic space group $P\bar{1}$. Data collection parameters and selected bond lengths and angles are given in the Experimental Section and in the caption of Figure 2. The asymmetric unit consists of one lead atom, two carboxylate anions (Cr1 and Cr2), and one 1,10-phenanthroline ligand (Figure 2). The lead atom is fivefold coordinated by two nitrogen atoms of the 1,10-phenanthroline ligand [Pb–N1 2.585(4) Å and Pb–N2 2.591 Å] and three oxygen atoms from two (η^6-benzenecarboxylato)-tricarbonylchromium units. The Pb–O bond lengths are Pb–O1 2.390(3) Å, Pb–O6 2.624(3) Å, and Pb–O7 2.273(3) Å. Thus, one carboxylate unit (Cr2) coordinates in a chelating κ^2-coordination mode to the lead atom, whereas the carboxylate unit that corresponds to Cr1 binds in a monodentate mode. As observed for compound **1**, the chelating κ^2-coordinated carboxylate unit is asymmetrically bound to the metal atom. The difference between the two Pb–O distances of 0.351 Å is about 0.05 Å shorter compared to the same unit of compound **1**. In the solid state, two molecules of compound **2** are arranged face-to-face, thus forming a four-membered Pb–O2–Pb′–O2′ ring, but the Pb–O2′ distance of 3.209(4) Å is too long to be considered bonding. A crystallographic inversion center is observed in the middle of the Pb–O2–Pb′–O2′ ring. A comparable situation is found in the lead(II) acetate $[Pb(CH_3COO)_2(1,10\text{-phen})\cdot 2H_2O]$, which also forms a loose dimer in the solid state.[24] In contrast, by using β-ferrocenylacrylate as metalloligand, the one-dimensional chain polymer $[Pb(\eta^1\text{-}\mu_2\text{-}OOCCH{=}CHFc)_2(phen)]_n$ [Fc = $(\eta^5\text{-}C_5H_5)Fe(\eta^5\text{-}C_5H_4)$] is obtained. This shows the significant influence of the carboxylate group on the structure of the formed product.[25]

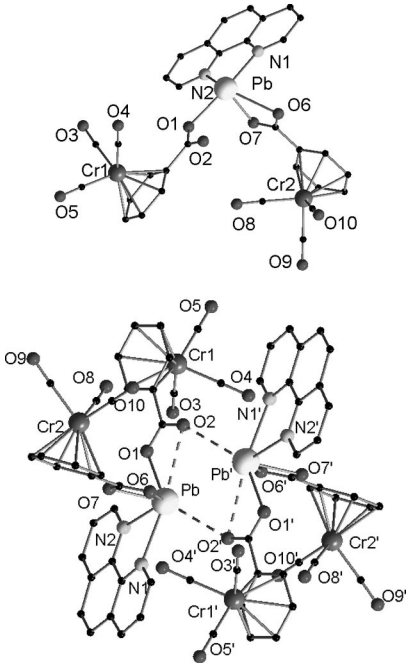

Figure 2. Top: Molecular structure of compound **2**. Hydrogen atoms are omitted for clarity. Bottom: Face-to-face setup of two molecules in the unit cell. Selected bond lengths [Å] and angles [°]: Pb–N1 2.585(4), Pb–N2 2.591(3), Pb–O1 2.390(3), Pb–O6 2.624(3), Pb–O7 2.372(3); O7–Pb–O1 78.26(13), O7–Pb–N1 79.08(11), O1–Pb–N1 136.26(12), O7–Pb–N2 79.63(10), O1–Pb–N2 75.68(12), N1–Pb–N2 63.72(12), O7–Pb–O6 52.10(9), O1–Pb–O6 110.15(13), N1–Pb–O6 83.50(11), N2–Pb–O6 126.45(10).

Compound **3** crystallizes in the monoclinic space group $P2_1/c$. Data-collection parameters and selected bond lengths and angles are given in the Experimental Section and in the caption of Figure 3. The asymmetric unit consists of one lead atom, two carboxylate anions (Cr1 and Cr2), and one 2,2′-bipyridine ligand (Figure 3). As observed for compound **2**, the lead atom in compound **3** is

thus fivefold coordinated by two nitrogen atoms of the ligand [Pb–N1 2.585(3) Å and Pb–N2 2.554(3) Å] and three oxygen atoms from two (η^6-benzenecarboxylato)tricarbonylchromium units [Pb–O1 2.755(2) Å, Pb–O2 2.317(2) Å, and Pb–O6 2.451(3) Å]. The carboxylate unit that corresponds to Cr1 is involved in a chelating κ^2-coordination mode to the lead atom, whereas the carboxylate unit that corresponds to Cr2 coordinates in a monodentate fashion. Similarly to compound **2** in the solid state, two molecules of compound **3** are arranged face-to-face, thus forming a four-membered Pb–O1–Pb′–O1′ ring.

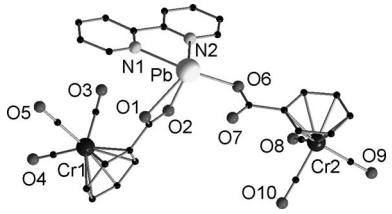

Figure 3. Molecular structure of compound **3**. Hydrogen atoms are omitted for clarity. Selected bond lengths [Å] and angles [°]: Pb–N1 2.585(3), Pb–N2 2.554(3), Pb–O1 2.755(2), Pb–O2 2.317(2), Pb–O6 2.451(3); O2–Pb–O6 82.42(9), O2–Pb–N2 84.96(9), O6–Pb–N2 76.44(9), O2–Pb–N1 77.39(10), O6–Pb–N1 136.30(9), N2–Pb–N1 63.59(9), O2–Pb–O1 50.61(7), O6–Pb–O1 118.06(8), N2–Pb–O1 126.00(9), N1–Pb–O1 76.42(9).

The stereochemical influence of the lone pair of lead(II) compounds has been investigated by Shimoni-Livny et al.[21c] On the basis of a Cambridge Structural Database (CSD) search, they classified lead coordination compounds as "holodirected" or "hemidirected." By using this definition, complexes are holodirected if the lead–ligand bonds are directed throughout the surface of the encompassing sphere. In contrast, hemidirected compounds are complexes in which the lead–ligand bonds are directed throughout only part of the globe. Thus, a void (or gap) in the distribution of the lead–ligand bonds is observed in hemidirected compounds.[21c] On the basis of this definition, we consider compounds **1**–**3** to be hemidirected.

Thermogravimetric analysis (TGA) measurements were performed for the polymeric compound **1** (Figure 4). Compound **1** is thermally relatively robust as shown by TGA. Decomposition starts at 166 °C. The first three CO molecules (calculated for the asymmetric unit) were lost in the temperature range between 166 and 186 °C (obsd. 9.5%, calcd. 9.3%). Then the product further decomposes slowly up to 423 °C with a weight loss of 42%, which is a result of the decomposition of the other three CO molecules and almost the complete organic shell. The remaining product is stable up to 1000 °C, at which point the next thermal degradation starts.

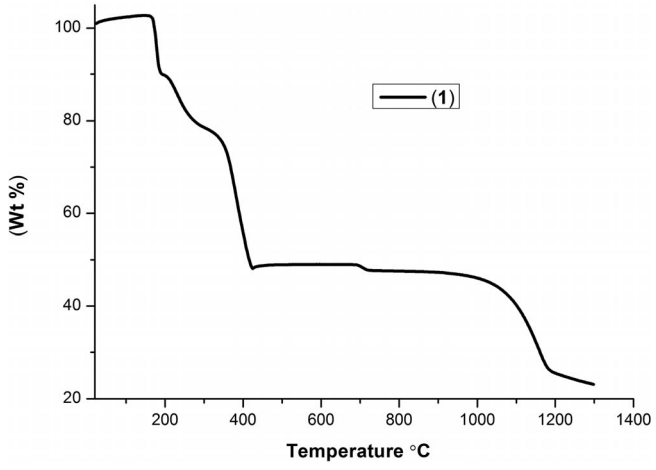

Figure 4. TGA curves for **1** in the temperature range between 25 and 1300 °C at a heating rate of 5 °C min^{-1} under N_2.

Conclusion

A coordination polymer of lead(II) with the organometallic ligand [{η^6-C_6H_5COO}$Cr(CO)_3$] was obtained by the reaction of [{η^6-C_6H_5COOH}$Cr(CO)_3$] with lead(II) acetate in the presence of *trans*-1,2-bis(4-pyridyl)ethene. In contrast, by using the chelating ancillary ligands 1,10-phenanthroline or 2,2′-bipyridine, mononculear complexes that form loose dimers in the solid state were obtained. The carboxylate [{η^6-C_6H_5COO}$Cr(CO)_3$] anion coordinates either in a κ^1 or a κ^2 mode, thereby resulting in fivefold-coordinated lead atoms. The reported structures differ in comparison to coordination polymers of lead(II) with other carboxylate anions. TGA studies of compound **1** show that upon heating some of the carbonyl groups of the [{η^6-C_6H_5COO}$Cr(CO)_3$] anion are lost selectively before the organic ligand sphere is thermally decomposed.

Experimental Section

General: Deuterated solvents were obtained from Aldrich (99 atom-% D). NMR spectra were recorded with a Bruker Avance II 300 MHz NMR spectrometer. Chemical shifts are referenced to internal solvent resonances and are reported relative to tetramethylsilane. IR spectra were obtained with a Bruker FTIR Tensor 37 by using the attenuated total reflection (ATR) method. Elemental analyses were carried out with an Elementar Vario EL. TGA measurements were made with a Netzsch STA 429 instrument. The solvents were used as purchased from commercial sources without further purification. [{η^6-C_6H_5COOH}$Cr(CO)_3$] was prepared according to literature procedures.[26]

[Pb{(η^6-C_6H_5COO)$Cr(CO)_3$}$_2$(bpe)]$_n$ (1): Lead(II) acetate [$Pb(CH_3COO)_2 \cdot 3H_2O$] (76.0 mg; 0.200 mmol) was dissolved in a mixture of methanol/DMF (10 mL:1 mL). [{η^6-C_6H_5COOH}-$Cr(CO)_3$] (101 mg; 0.400 mmol) was added to this solution, and the solution was stirred for 1 h. Then *trans*-1,2-bis(4-pyridyl)ethene (37.0 mg; 0.200 mmol) was added, and the subsequent mixture was stirred for 6 h. While stirring, a yellow precipitate was formed. The precipitate was dissolved by heating and kept for crystallization. After 1 d, yellowish-orange crystals were formed. Yield: 130 mg (72% based on Pb). $C_{32}H_{20}Cr_2N_2O_{10}Pb$ (903.71): calcd. C 42.53, H 2.23, N 3.10; found C 42.30, H 2.45, N 3.10. ^{1}H NMR ([D_6]-DMSO, 300 MHz, 25 °C): δ = 8.60 (d, 4 H, Py), 7.61 (d, 4 H, Py), 7.54 (s, 2 H, CH=CH), 6.20 (d, 4 H, Ar), 5.86 (t, 2 H, Ar), 5.66 (t, 4 H, Ar) ppm. ^{13}C{^{1}H} NMR ([D_6]DMSO, 75 MHz, 25 °C): δ = 233.3 (CO), 169.7 (COO), 150.2 (Py), 143.4 (Py), 130.6 (Py),121.3 (Py), 103.1 (Ar), 97.2 (Ar), 97.1 (Ar), 92.7 (Ar) ppm. IR (ATR): $\tilde{\nu}$ = 3092 (br.), 2928 (br.), 2033 (br.), 1949 (s), 1868 (s), 1667 (sh),

1589 (s), 1522 (sh), 1502 (sh), 1417 (s), 1352 (s), 1218 (sh), 1201 (s), 1142 (s), 1094 (s), 1064 (s), 1044 (sh), 1004 (s), 978 (s), 960 (s), 829 (s), 783 (s), 721 (s), 681 (s), 655 (s) 618(s), 529 (s) cm^{-1}.

[Pb{(η^6-C_6H_5COO)Cr(CO)$_3$}$_2$(1,10-Phen)] (2): Lead(II) acetate [Pb(CH_3COO)$_2$·3H_2O] (76.0 mg; 0.200 mmol) was dissolved in methanol (10 mL). [{η^6-C_6H_5COOH}Cr(CO)$_3$] (101 mg; 0.400 mmol) was added to this solution, and the solution was stirred for 1 h. Then 1,10-phenanthroline (36.0 mg; 0.200 mmol) was added to the mixture, and the subsequent solution was stirred for 6 h. While stirring, a yellow precipitate was formed. The precipitate was dissolved by heating and kept for crystallization. Yield: 140 mg (77.5% based on Pb). $C_{32}H_{18}Cr_2N_2O_{10}Pb$ (901.69): calcd. C 42.63, H 2.01, N 3.11; found C 42.32, H 2.18, N 3.13. ^{1}H NMR ([D$_6$]DMSO, 300 MHz, 25 °C): δ = 9.31 (br., 2 H, Phen), 8.65 (d, 2H Phen), 8.08 (s, 2 H, Phen), 7.94 (m, 2 H, Phen), 6.15 (d, J = 6 Hz, 4 H, Ar), 5.80 (t, J = 6 Hz, 2 H, Ar), 5.61 (t, J = 6 Hz, 4 H, Ar) ppm. ^{13}C{^{1}H} NMR ([D$_6$]DMSO, 75 MHz, 25 °C): δ = 233.3 (CO), 169.1 (COO), 150.0 (Phen), 144.9 (Phen), 137.7 (Phen), 129.3 (Phen), 127.0 (Phen), 124.2 (Phen), 103.4 (Ar), 96.8 (Ar), 96.9 (Ar), 92.7 (Ar) ppm. IR (ATR): $\tilde{\nu}$ = 3079 (br.), 2925 (br.), 2030 (s), 1953 (s), 1864 (s), 1676 (sh), 1582 (s) 1500 (s), 1448 (sh), 1426 (sh), 1360 (s), 1279 (s), 1222 (s), 1147 (s), 1094 (s), 1009 (s), 992 (sh), 962 (s), 919 (s), 891 (s), 853 (s), 827 (s), 783 (s), 725 (s), 681 (s), 656 (s), 624 (s), 530 (s) cm^{-1}.

[Pb{(η^6-C_6H_5COO)Cr(CO)$_3$}$_2$(2,2′-bipy)] (3): Lead(II) acetate [Pb(CH_3COO)$_2$·3H_2O] (76.0 mg; 0.200 mmol) was dissolved in a mixture of methanol/DMF (10 mL:1 mL). [{η^6-C_6H_5COOH}-Cr(CO)$_3$] (101 mg; 0.400 mmol) was added to this solution, and the solution was stirred for 1 h. Then 2,2′-bipyridine (32.0 mg; 0.200 mmol) was added to the mixture, and the subsequent solution was stirred for 6 h. While stirring, a yellow precipitate was formed. The precipitate was dissolved by heating and kept for crystallization. Yield: 130 mg (73.9% based on Pb). $C_{30}H_{18}Cr_2N_2O_{10}Pb$ (877.67): calcd. C 41.06, H 2.07, N 3.19; found C 41.00, H 1.94, N 3.18. ^{1}H NMR ([D$_6$]DMSO, 300 MHz, 25 °C): δ = 8.70 (d, J = 3 Hz, 2 H, Py), 8.39 (d, J = 6 Hz, 2 H, Py), 7.95 (m, J = 9 Hz, 2 H, Py), 7.45 (m, J = 9 Hz, 2 H, Py), 6.21 (d, J = 6 Hz, 4 H, Ar), 5.87 (t, J = 6 Hz, 4 H, Ar), 5.65 (t, J = 6 Hz, 4 H, Ar) ppm. ^{13}C{^{1}H} NMR ([D$_6$]DMSO, 75 MHz, 25 °C): δ = 233.3 (CO), 169.5 (COO), 155.2 (Py), 149.3 (Py), 137.4 (Py), 124.3 (Py), 120.5 (Py), 103.1 (Ar), 97.2 (Ar), 97.0 (Ar), 92.6 (Ar) ppm. IR (ATR): $\tilde{\nu}$ = 3093 (br.), 1949 (s), 1899 (sh), 1872 (s), 1844 (s), 1581 (s) 1521 (s), 1500 (s), 1470 (s), 1432 (s), 1361 (s), 1311 (sh), 1242 (sh), 1152 (s), 1095 (s), 1048 (s), 1007 (s), 974 (sh), 952 (s), 847 (sh), 835 (s), 781 (s), 760 (s), 734 (s), 681 (s), 654 (s), 616 (s), 534 (s) cm^{-1}.

X-ray Crystallographic Studies of 1–3: Single crystals of compounds **1**–**3** were grown from the hot mother solution. A suitable crystal was covered with mineral oil (Aldrich) and mounted on a glass fiber. The crystal was transferred directly to the –73 °C cold stream of a STOE IPDS 2 diffractometer. All structures were solved by using SHELXS-97.[27] The remaining non-hydrogen atoms were located from successive difference Fourier map calculations. The refinements were carried out by using the SHELXL-97 program.[27] The locations of the largest peaks in the final difference Fourier map calculation as well as the magnitude of the residual electron densities in each case were of no chemical significance. CCDC-843114 (**1**), -843115 (**2**), and -843116 (**3**) contain the supplementary crystallographic data for this paper. These data can be obtained free of charge from The Cambridge Crystallographic Data Centre via www.ccdc.cam.ac.uk/data_request/cif.

Crystal Data for 1: $C_{32}H_{20}Cr_2N_2O_{10}Pb$, M_r = 903.69, triclinic, a = 9.7738(4) Å, b = 13.3043(5) Å, c = 13.7563(5) Å, α = 116.268(3)°, β = 90.504(3)°, γ = 104.302(3)°, V = 1539.92(10) Å^3, T = 200(2) K, space group $P\bar{1}$, Z = 2, μ(Mo-K_α) = 6.209 mm^{-1}, 13263 reflections measured, 6425 independent reflections (R_{int} = 0.1101). The final R_1 values were 0.0559 [$I > 2\sigma(I)$]. The final $wR(F^2)$ values were 0.1535 (all data). The goodness of fit on F^2 was 1.048.

Crystal Data for 2: $C_{64}H_{36}Cr_4N_4O_{20}Pb_2$, M_r = 1803.35, triclinic, a = 10.481(2) Å, b = 12.276(3) Å, c = 13.217(3) Å, α = 69.64(3)°, β = 80.86(3)°, γ = 72.15(3)°, V = 1514.9(5) Å^3, T = 200(2) K, space group $P\bar{1}$, Z = 1, μ(Mo-K_α) = 6.311 mm^{-1}, 24787 reflections measured, 8154 independent reflections (R_{int} = 0.0854). The final R_1 values were 0.0331 [$I > 2\sigma(I)$]. The final $wR(F^2)$ values were 0.0847 (all data). The goodness of fit on F^2 was 1.039.

Crystal Data for 3: $C_{60}H_{36}Cr_4N_4O_{20}Pb_2$, M_r = 1755.31, monoclinic, a = 9.9537(3) Å, b = 22.5651(7) Å, c = 13.9019(5) Å, β = 108.273(3)°, V = 2965.0(2) Å^3, T = 200(2) K, space group $P2_1/c$, Z = 2, μ(Mo-K_α) = 6.446 mm^{-1}, 28969 reflections measured, 6271 independent reflections (R_{int} = 0.0464). The final R_1 values were 0.0245 [$I > 2\sigma(I)$]. The final $wR(F^2)$ values were 0.0476 (all data). The goodness of fit on F^2 was 0.943.

Acknowledgments

This work was supported by the Alexander-von-Humboldt-Stiftung (fellowship for B. M.), by the Deutsche Forschungsgemeinschaft (DFG) – Center for Functional Nanostructures (CFN), and by the Landesstiftung Baden-Württemberg GmbH.

[1] a) M. Oh, C. A. Mirkin, *Nature* **2005**, *438*, 651–654; b) A. M. Spokoyny, D. Kim, A. Sumrein, C. A. Mirkin, *Chem. Soc. Rev.* **2009**, *38*, 1218–1227; c) B. F. Hoskins, R. Robson, *J. Am. Chem. Soc.* **1989**, *111*, 5962–5964; d) B. F. Hoskins, R. Robson, *J. Am. Chem. Soc.* **1990**, *112*, 1546–1554; e) R. Robson, *Dalton Trans.* **2008**, 5113–5131; f) O. M. Yaghi, M. O'Keeffe, N. W. Ockwig, H. K. Chae, M. Eddaoudi, J. Kim, *Nature* **2003**, *423*, 705–714; g) D. J. Tranchemontagne, J. L. Mendoza-Cortes, M. O'Keeffe, O. M. Yaghi, *Chem. Soc. Rev.* **2009**, *38*, 1257–1283; h) C. Janiak, *Dalton Trans.* **2003**, 2781–2804; i) C. Janiak, J. K. Vieth, *New J. Chem.* **2010**, *34*, 2366–2388; j) A. U. Czaja, N. Trukhan, U. Müller, *Chem. Soc. Rev.* **2009**, *38*, 1284–1293; k) M. P. Suh, Y. E. Cheon, E. Y. Lee, *Coord. Chem. Rev.* **2008**, *252*, 1007–1026.

[2] R. Robson, *J. Chem. Soc., Dalton Trans.* **2000**, 3735–3744.

[3] M. Eddaoudi, J. Kim, N. Rosi, D. Vodak, J. Wachter, M. O'Keeffe, O. M. Yaghi, *Science* **2002**, *295*, 469–472.

[4] H. K. Chae, D. Y. Siberio-Perez, J. Kim, Y. Go, M. Eddaoudi, A. J. Matzger, M. O'Keeffe, O. M. Yaghi, *Nature* **2004**, *427*, 523–527.

[5] D. Maspoch, D. Ruiz-Molina, J. Veciana, *Chem. Soc. Rev.* **2007**, *36*, 770–818.

[6] M. Dinca, J. R. Long, *Angew. Chem.* **2008**, *120*, 6870; *Angew. Chem. Int. Ed.* **2008**, *47*, 6766–6779.

[7] J. Lee, O. K. Farha, J. Roberts, K. A. Scheidt, S. T. Nguyen, J. T. Hupp, *Chem. Soc. Rev.* **2009**, *38*, 1450–1459.

[8] S. Qiu, G. Zhu, *Coord. Chem. Rev.* **2009**, *253*, 2891–2911.

[9] a) M. Andruh, J.-P. Costes, C. Diaz, S. Gao, *Inorg. Chem.* **2009**, *48*, 3342–3359; b) X.-M. Zhang, Z.-M. Hao, W.-X. Zhang, X.-M. Chen, *Angew. Chem.* **2007**, *119*, 3526; *Angew. Chem. Int. Ed.* **2007**, *46*, 3456–3459.

[10] a) M. D. Allendorf, C. A. Bauer, R. K. Bhakta, R. J. T. Houk, *Chem. Soc. Rev.* **2009**, *38*, 1330–1352; b) Z. Li, G. Zhu, X. Guo, X. Zhao, Z. Jin, S. Qiu, *Inorg. Chem.* **2007**, *46*, 5174–5178.

[11] Q.-R. Fang, G.-S. Zhu, M. Xue, Q.-L. Zhang, J.-Y. Sun, X.-D. Guo, S.-L. Qiu, S.-T. Xu, P. Wang, D.-J. Wang, Y. Wei, *Chem. Eur. J.* **2006**, *12*, 3754–3758.

[12] H. Li, M. Eddaoudi, M. O'Keeffe, O. M. Yaghi, *Nature* **1999**, *402*, 276–279.
[13] a) S.-H. Cho, B. Ma, S. T. Nguyen, J. T. Hupp, T. E. Albrecht-Schmitt, *Chem. Commun.* **2006**, 2563–2565; b) Y.-M. Jeon, J. Heo, C. A. Mirkin, *J. Am. Chem. Soc.* **2007**, *129*, 7480–7481.
[14] a) H. Hou, L. Li, G. Li, Y. Fan, Y. Zhu, *Inorg. Chem.* **2003**, *42*, 3501–3508; b) T. A. Zevaco, H. Görls, E. Dinjus, *Polyhedron* **1998**, *17*, 613–616; c) G. Li, Z. Li, H. Hou, X. Meng, Y. Fan, W. Chen, *J. Mol. Struct.* **2004**, *694*, 179–183; d) R. Costa, C. Lopez, E. Molins, E. Espinosa, *Inorg. Chem.* **1998**, *37*, 5686–5689.
[15] a) E. O. Fischer, K. Öfele, H. Essler, W. Fröhlich, J. P. Mortensen, W. Semmlinger, *Chem. Ber.* **1958**, *91*, 2763–2772; b) B. Nicholls, M. C. Whiting, *J. Chem. Soc.* **1959**, 551–556.
[16] G. Han-Mou, C. Chi-Tain, J. Ting-Ting, C. Mei-Yueh, *J. Organomet. Chem.* **1993**, *448*, 99–106.
[17] a) B. Murugesapandian, P. W. Roesky, *Dalton Trans.* **2010**, *39*, 9598–9603; b) B. Murugesapandian, P. W. Roesky, *Inorg. Chem.* **2011**, *50*, 1698–1704; c) B. Murugesapandian, P. W. Roesky, *Heteroat. Chem.* **2011**, *22*, 294–300; d) B. Murugesapandian, P. W. Roesky, *Eur. J. Inorg. Chem.* **2011**, 4103–4108.
[18] S. S. Kaye, J. R. Long, *J. Am. Chem. Soc.* **2008**, *130*, 806–807.
[19] Y. Zheng, W. Wang, J. Lin, Y. She, K. Fu, *J. Phys. Chem.* **1992**, *96*, 9821–9827.
[20] a) J. Parr, *Polyhedron* **1997**, *16*, 551–566; b) Y.-H. Zhao, H.-B. Xu, Y.-M. Fu, K.-Z. Shao, S.-Y. Yang, Z.-M. Su, X.-R. Hao, D.-X. Zhu, E.-B. Wang, *Cryst. Growth Des.* **2008**, *8*, 3566–3576; c) X.-L. Wang, Y.-Q. Chen, Q. Gao, H.-Y. Lin, G.-C. Liu, J.-X. Zhang, A.-X. Tian, *Cryst. Growth Des.* **2010**, *10*, 2174–2184; d) H. Krautscheid, C. Lode, F. Vielsack, H. Vollmer, *J. Chem. Soc., Dalton Trans.* **2001**, 1099–1104; e) G.-P. Yang, L. Hou, Y.-Y. Wang, Y.-N. Zhang, Q.-Z. Shi, S. R. Batten, *Cryst. Growth Des.* **2011**, *11*, 936–940; f) H.-B. Duan, H.-R. Zhao, X.-M. Ren, H. Zhou, Z.-F. Tian, W.-Q. Jin, *Dalton Trans.* **2011**, *40*, 1672–1683.
[21] a) B. Shaabani, B. Mirtamizdoust, D. Viterbo, G. Croce, H. Hammud, *Z. Anorg. Allg. Chem.* **2010**, *636*, 1596–1600; b) J. Yang, G.-D. Li, J.-J. Cao, Q. Yue, G.-H. Li, J.-S. Chen, *Chem. Eur. J.* **2007**, *13*, 3248–3261; c) L. Shimoni-Livny, J. P. Glusker, C. W. Bock, *Inorg. Chem.* **1998**, *37*, 1853–1867.
[22] a) A. Morsali, M. Payeghader, S. S. Monfared, M. Moradi, *J. Coord. Chem.* **2003**, *56*, 761–770; b) A. Morsali, X.-M. Chen, *J. Coord. Chem.* **2004**, *57*, 1233–1241; c) A. Morsali, A. R. Mahjoub, *Chem. Lett.* **2004**, *33*, 64–65; d) Y. J. Shi, Y. Xu, Y. Zhang, B. Huang, D. R. Zhu, C. M. Jin, H. G. Zhu, Z. Yu, X. T. Chen, X. Z. You, *Chem. Lett.* **2001**, 678–679; e) X.-Y. Wang, Y. He, L.-N. Zhao, Z.-G. Kong, *Inorg. Chem. Commun.* **2011**, *14*, 1186–1189.
[23] S. Grimme, *Angew. Chem.* **2008**, *120*, 3478; *Angew. Chem. Int. Ed.* **2008**, *47*, 3430–3434.
[24] J. Harrowfield, H. Miyamae, B. Skelton, A. Soudi, A. White, *Aust. J. Chem.* **1996**, *49*, 1081–1088.
[25] L. K. Li, Y. L. Song, H. W. Hou, Y. T. Fan, Y. Zhu, *Eur. J. Inorg. Chem.* **2005**, 3238–3249.
[26] a) R. Atencio, L. Brammer, S. Fang, F. C. Pigge, *New J. Chem.* **1999**, *23*, 461; b) L. Brammer, J. C. M. Rivas, R. Atencio, S. Fang, F. C. Pigge, *J. Chem. Soc., Dalton Trans.* **2000**, 3855.
[27] G. M. Sheldrick, *Acta Crystallogr., Sect. A* **2008**, *64*, 112–122.

Received: September 7, 2011
Published Online: December 8, 2011

DOI: 10.1002/ejic.201100952

Synthesis and Structural Characterization of Zinc Complexes that Contain Chelating Phenolate Phosphane Ligands

Lan-Chang Liang,*[a] Huan-Yu Shih,[a] Han-Sheng Chen,[a] and Sheng-Ta Lin[a]

Keywords: Cluster compounds / Zinc / Zincates / O,P ligands / Phosphane ligands

The preparation and characterization of zinc complexes supported by potentially tridentate biphenolate phosphane ligands are reported. The in situ prepared dilithium complexes of 2,2′-*tert*-butylphosphanylbis(4,6-di-*tert*-butylphenolate) ($[\mathbf{L}^{t\mathbf{Bu}}]^{2-}$) and 2,2′-phenylphosphanylbis(4,6-di-*tert*-butylphenolate) ($[\mathbf{L}^{\mathbf{Ph}}]^{2-}$) react with $ZnCl_2$ in tetrahydrofuran (THF) to produce lithium zincates $Zn[\mathbf{L}^{t\mathbf{Bu}}Li(THF)]_2$ and $Zn[\mathbf{L}^{\mathbf{Ph}}Li(THF)]_2$, respectively, regardless of the stoichiometry of the starting materials. Alkane elimination reactions of $ZnEt_2$ with one equiv. of $H_2\mathbf{L}^{t\mathbf{Bu}}$ or $H_2\mathbf{L}^{\mathbf{Ph}}$ in THF generate $Zn_2(\mathbf{L}^{t\mathbf{Bu}})_2(THF)$ or $Zn_2(\mathbf{L}^{\mathbf{Ph}})_2(THF)_2$, whereas those employing two equiv. of the protio ligands afford $Zn(\mathbf{L}^{t\mathbf{Bu}}H)_2$-(MeCN) or $Zn(\mathbf{L}^{\mathbf{Ph}}H)_2(MeCN)$, respectively. The X-ray structures of $Zn[\mathbf{L}^{t\mathbf{Bu}}Li(THF)]_2$, $Zn_2(\mathbf{L}^{t\mathbf{Bu}})_2(THF)$, $Zn_2(\mathbf{L}^{\mathbf{Ph}})_2(THF)_2$, and $Zn(\mathbf{L}^{t\mathbf{Bu}}H)_2(MeCN)$ are presented.

Introduction

Zinc complexes that contain phenol-derived ligands are of interest in view of their important roles in biomimetic models and polymerization catalysis.[1–3] For instance, phenoxyl radical complexes of zinc have been studied as reference compounds in order to assess the inherent properties of tyrosyl radicals in a number of metalloproteins,[4–8] which take advantage of the spectroscopically silent and redox innocent nature of Zn^{II}. In addition, zinc phenolate complexes are known to be active catalyst precursors in the ring-opening polymerization of cyclic molecules.[9–14] We are currently exploring the reactions and structural chemistry of hybrid chelating ligands with main-group and transition metals.[15–24] In particular, a series of group 1 derivatives of the potentially tridentate biphenolate phosphane ligands 2,2′-*tert*-butylphosphanylbis(4,6-di-*tert*-butylphenolate) ($[\mathbf{L}^{t\mathbf{Bu}}]^{2-}$) and 2,2′-phenylphosphanylbis(4,6-di-*tert*-butylphenolate) ($[\mathbf{L}^{\mathbf{Ph}}]^{2-}$) has been prepared and structurally characterized.[25–29] As indicated by X-ray studies, these species tend to form aggregates, whose structural preferences have been found to be a function of several parameters, which include the identity of phosphorus bound substituents, the electrophilicity of the metal, and the coordinating solvent. Herein we report the preparation of zinc cluster compounds that contain $[\mathbf{L}^{t\mathbf{Bu}}]^{2-}$ and $[\mathbf{L}^{\mathbf{Ph}}]^{2-}$ and that the complex constitution also depends dramatically on the synthetic strategy employed. For instance, $Zn_2(\mathbf{L}^{t\mathbf{Bu}})_2$-(THF) and $Zn_2(\mathbf{L}^{\mathbf{Ph}})_2(THF)_2$ are not synthetically accessible by salt metathesis routes but may be prepared by alkane elimination methods. The versatility of the $[\mathbf{L}^{t\mathbf{Bu}}]^{2-}$ and $[\mathbf{L}^{\mathbf{Ph}}]^{2-}$ binding modes is also demonstrated. Scheme 1 summarizes the synthesis of the complexes reported in this study.

[a] Department of Chemistry and Center for Nanoscience & Nanotechnology, National Sun Yat-sen University, Kaohsiung 80424, Taiwan
E-mail: lcliang@mail.nsysu.edu.tw

Results and Discussion

Synthesis and Characterization of $Zn[\mathbf{L}^{t\mathbf{Bu}}Li(THF)]_2$ and $Zn[\mathbf{L}^{\mathbf{Ph}}Li(THF)]_2$

Our initial attempts to prepare $Zn_2(\mathbf{L}^{t\mathbf{Bu}})_2(THF)$ involved the salt metathesis of $\mathbf{L}^{t\mathbf{Bu}}Li_2$[26] with $ZnCl_2$. The reaction of in situ prepared $\mathbf{L}^{t\mathbf{Bu}}Li_2$ with an equimolar amount of $ZnCl_2$ in THF at room temperature generated $Zn[\mathbf{L}^{t\mathbf{Bu}}Li$-$(THF)]_2$ as an off-white solid in 80% isolated yield. Surprisingly, $Zn_2(\mathbf{L}^{t\mathbf{Bu}})_2(THF)$ (vide infra) was not observed from the $^{31}P\{^1H\}$ NMR spectra of reaction aliquots. This suggests that the presumed intermediate, $ZnCl(\mathbf{L}^{t\mathbf{Bu}}Li)(THF)_x$, is more reactive towards intermolecular salt metathesis with $\mathbf{L}^{t\mathbf{Bu}}Li_2$ to give $Zn[\mathbf{L}^{t\mathbf{Bu}}Li(THF)]_2$ than intramolecular salt elimination to give $Zn_2(\mathbf{L}^{t\mathbf{Bu}})_2(THF)$. Such a phenomenon is interesting as intramolecular reactions are usually more kinetically accessible. $Zn[\mathbf{L}^{t\mathbf{Bu}}Li(THF)]_2$ was also prepared in a similar isolated yield from the reaction of $ZnCl_2$ with two equiv. of $\mathbf{L}^{t\mathbf{Bu}}Li_2$ under similar conditions.

Colorless crystals of $Zn[\mathbf{L}^{t\mathbf{Bu}}Li(THF)]_2$ suitable for X-ray diffraction analysis were grown from a concentrated diethyl ether solution at –35 °C. As depicted in Figure 1, this molecule contains two monoanionic $[\mathbf{L}^{t\mathbf{Bu}}Li(THF)]^-$ ligands,

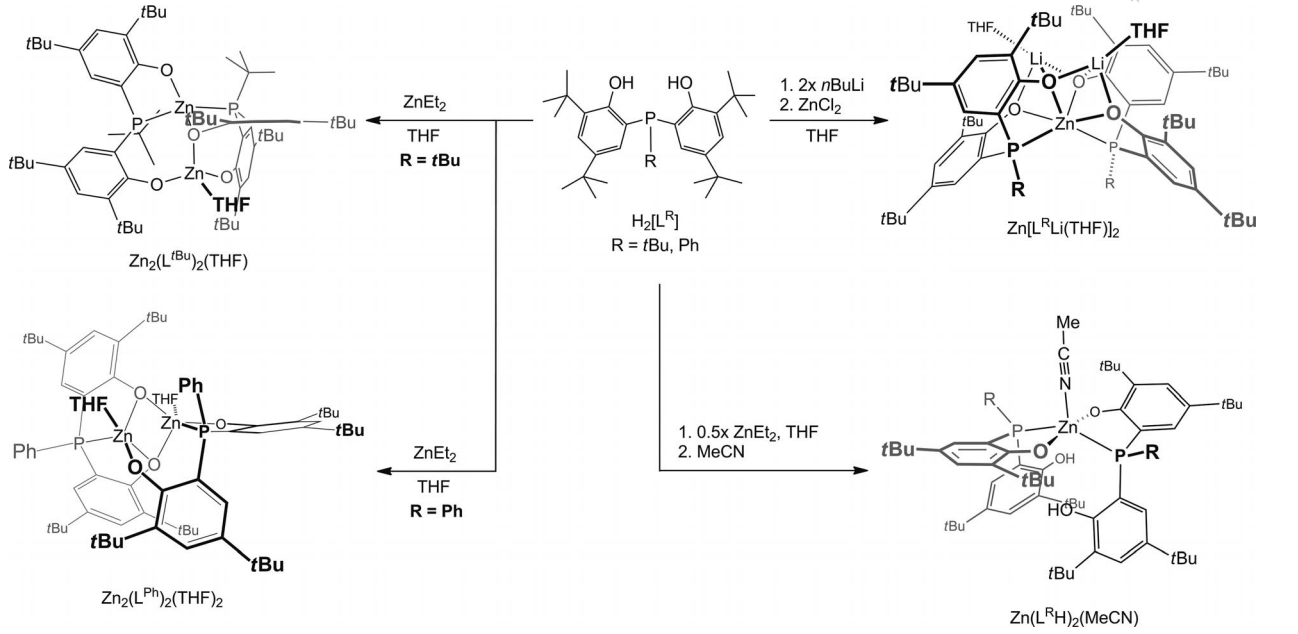

Scheme 1. Synthesis of zinc complexes.

which are both κ^3-O,P,O bound to the zinc center. Zn[$\mathbf{L}^{t\mathbf{Bu}}$Li(THF)]$_2$ is thus a homoleptic compound that contains a six-coordinate zinc core. Alternatively, Zn[$\mathbf{L}^{t\mathbf{Bu}}$Li(THF)]$_2$ may be regarded as a contact ion pair of lithium zincate[30–33] with phenolate oxygen donors bridging the metal centers. With respect to the lithium atoms, the phenolate phosphane ligands, on the other hand, act as a κ^2-O,O donor to one lithium center and as a κ^1-O donor to the other. As a result, the phenolate O1 donor is μ^2-bridged between zinc and one of the lithium atoms, whereas O2 is simultaneously bound to the three metals. With the coordination of an additional THF molecule, each lithium atom is thus four-coordinate with a distorted tetrahedral geometry. Overall, this molecule is C_2 symmetric, and the C_2 axis coincides with the Li1–Zn1–Li1A plane and bisects the Li1–Zn1–Li1A angle. In accordance with the large steric size of [$\mathbf{L}^{t\mathbf{Bu}}$Li(THF)]$^-$, the core geometry of this six-coordinate zinc complex is severely distorted from an ideal octahedron.

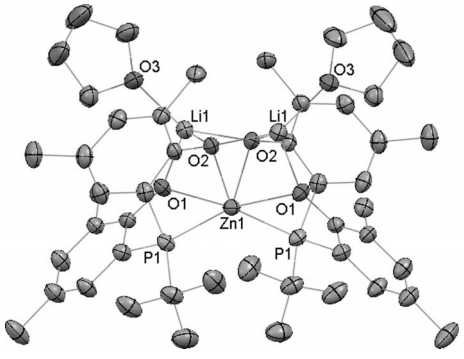

Figure 1. Molecular structure of Zn[$\mathbf{L}^{t\mathbf{Bu}}$Li(THF)]$_2$ with thermal ellipsoids drawn at the 35% probability level. All methyl groups in aryl *tert*-butyl are omitted for clarity.

Table 1 summarizes selected bond lengths and angles. The Zn–O bonds are slightly longer than those of other zinc complexes that contain terminal or bridging phenolate-derived ligands.[13,14,34–37]

The solution NMR spectroscopic data of Zn[$\mathbf{L}^{t\mathbf{Bu}}$Li(THF)]$_2$ are consistent with a structure with C_2 symmetry, reminiscent of that found in the solid state. The ^{1}H NMR spectrum at room temperature exhibits four distinct singlet resonances for aryl *tert*-butyl groups and four well-resolved signals for aromatic protons. The hydrogen atoms in the phosphorus bound *tert*-butyl groups are observed as a doublet resonance with $^3J_{PH}$ of 12 Hz. The ^{31}P{^{1}H} and ^{7}Li{^{1}H} NMR spectra show only one singlet resonance. The ^{31}P NMR chemical shift of Zn[$\mathbf{L}^{t\mathbf{Bu}}$Li(THF)]$_2$ (–39 ppm) measured in THF is notably upfield shifted from that of $\mathbf{L}^{t\mathbf{Bu}}Li_2$ (–22 ppm). The incorporation of two-coordinated THF is also confirmed by upfield chemical shifts (2.96 and 1.15 ppm vs. free THF at 3.57 and 1.40 ppm)[38] and the signal integrals relative to [$\mathbf{L}^{t\mathbf{Bu}}$]$^{2-}$ in the ^{1}H NMR spectrum.

Zn[$\mathbf{L}^{\mathbf{Ph}}$Li(THF)]$_2$ was prepared similarly in nearly quantitative yield. No Zn$_2$($\mathbf{L}^{\mathbf{Ph}}$)$_2$(THF)$_2$ was detected by ^{31}P{^{1}H} NMR spectroscopy even if the reaction was conducted with an equimolar amount of ZnCl$_2$ and $\mathbf{L}^{\mathbf{Ph}}$Li$_2$.[25] The solution NMR spectroscopic data of Zn[$\mathbf{L}^{\mathbf{Ph}}$Li(THF)]$_2$ suggest a C_2-symmetric structure analogous to that of Zn[$\mathbf{L}^{t\mathbf{Bu}}$Li(THF)]$_2$. Both Zn[$\mathbf{L}^{t\mathbf{Bu}}$Li(THF)]$_2$ and Zn[$\mathbf{L}^{\mathbf{Ph}}$Li(THF)]$_2$ are intriguing as alkali-metal-containing zinc complexes often display synergistic effects.[39–44] The solubility of Zn[$\mathbf{L}^{\mathbf{Ph}}$Li(THF)]$_2$ in nonpolar solvents is much lower than that of Zn[$\mathbf{L}^{t\mathbf{Bu}}$Li(THF)]$_2$, which is probably because of the formation of higher aggregates for the former.[45–47] This phenomenon highlights the discrepancy in the identity of the phosphorus substituents in these cluster compounds.

Synthesis and Characterization of $Zn_2(L^{tBu})_2(THF)$

In contrast to the salt metathesis reactions, alkane elimination of $ZnEt_2$ with one equiv. of H_2L^{tBu} in THF produced $Zn_2(L^{tBu})_2(THF)$ in 80% yield as colorless crystals after recrystallization from a concentrated pentane solution at –35 °C. As depicted in Figure 2, $Zn_2(L^{tBu})_2(THF)$ contains two biphenolate phosphane ligands that bridge two zinc atoms in an overall C_1-symmetric fashion. Both $[L^{tBu}]^{2-}$ ligands are κ^2-O,P bound to Zn1 with a "pendant" phenolate κ^1-bound to Zn2. In addition, the O4 donor bridges between both zinc atoms, and Zn2 is further coordinated to one THF molecule. As a result, both Zn1 and Zn2 are four-coordinate, the core geometry of which is best described as distorted tetrahedral. Selected bond lengths and angles are summarized in Table 1.

Table 1. Selected bond lengths [Å] and angles [°] for $Zn[L^{tBu}Li(THF)]_2$, $Zn_2(L^{tBu})_2(THF)$, $Zn_2(L^{Ph})_2(THF)_2$, and $Zn(L^{tBu}H)_2(MeCN)$.

$Zn[L^{tBu}Li(THF)]_2$			
O(1)–Zn(1)	2.357(2)	O(2)–Li(1)	2.112(6)
O(2)–Zn(1)	2.226(2)	O(3)–Li(1)	1.974(6)
P(1)–Zn(1)	2.3402(9)	Li(1)–O(2A)	1.942(6)
O(1)–Li(1)	1.835(6)		
O(2)–Zn(1)–O(1)	85.26(8)	O(2A)–Zn(1)–P(1A)	81.81(6)
O(2A)–Zn(1)–O(2)	72.78(10)	O(2)–Zn(1)–P(1A)	140.56(6)
O(2A)–Zn(1)–P(1)	140.56(6)	P(1A)–Zn(1)–O(1A)	72.61(5)
O(2)–Zn(1)–P(1)	81.81(6)	P(1)–Zn(1)–O(1A)	117.38(6)
P(1A)–Zn(1)–P(1)	133.94(5)	O(1)–Zn(1)–O(1A)	156.27(11)
O(2A)–Zn(1)–O(1)	75.62(7)	O(1)–Li(1)–O(2A)	96.1(3)
P(1A)–Zn(1)–O(1)	117.38(6)	O(1)–Li(1)–O(3)	113.0(3)
P(1)–Zn(1)–O(1)	72.61(5)	O(2A)–Li(1)–O(3)	144.8(3)
O(2A)–Zn(1)–O(1A)	85.26(8)	O(1)–Li(1)–O(2)	103.5(3)
O(2)–Zn(1)–O(1A)	75.62(7)	O(2A)–Li(1)–O(2)	81.2(2)
O(3)–Li(1)–O(2)	109.0(3)		
$Zn_2(L^{tBu})_2(THF)$			
O(1)–Zn(1)	1.919(2)	O(4)–Zn(1)	2.031(2)
O(2)–Zn(2)	1.863(2)	O(5)–Zn(2)	2.079(2)
O(3)–Zn(2)	1.899(2)	P(1)–Zn(1)	2.3217(9)
O(4)–Zn(2)	2.010(2)	P(2)–Zn(1)	2.3434(10)
O(1)–Zn(1)–O(4)	114.14(9)	O(2)–Zn(2)–O(3)	119.47(9)
O(1)–Zn(1)–P(1)	89.11(7)	O(2)–Zn(2)–O(4)	110.91(9)
O(4)–Zn(1)–P(1)	115.98(6)	O(3)–Zn(2)–O(4)	110.58(9)
O(1)–Zn(1)–P(2)	118.05(7)	O(2)–Zn(2)–O(5)	115.04(9)
O(4)–Zn(1)–P(2)	84.41(6)	O(3)–Zn(2)–O(5)	91.08(9)
P(1)–Zn(1)–P(2)	136.90(3)	O(4)–Zn(2)–O(5)	107.94(9)
$Zn_2(L^{Ph})_2(THF)_2$			
Zn(1)–O(4)	1.891(5)	Zn(2)–O(3)	1.905(5)
Zn(1)–O(1)	2.092(5)	Zn(2)–O(2)	1.976(5)
Zn(1)–O(5)	2.193(6)	Zn(2)–O(1)	2.062(5)
Zn(1)–O(2)	2.336(4)	Zn(2)–O(6)	2.173(6)
Zn(1)–P(1)	2.343(2)	Zn(2)–P(2)	2.678(2)
O(4)–Zn(1)–O(1)	148.0(2)	O(3)–Zn(2)–O(2)	130.9(2)
O(4)–Zn(1)–O(5)	86.5(2)	O(3)–Zn(2)–O(1)	134.3(2)
O(1)–Zn(1)–O(5)	95.1(2)	O(2)–Zn(2)–O(1)	92.12(19)
O(4)–Zn(1)–O(2)	99.9(2)	O(3)–Zn(2)–O(6)	89.8(2)
O(1)–Zn(1)–O(2)	81.91(18)	O(2)–Zn(2)–O(6)	99.5(2)
O(5)–Zn(1)–O(2)	172.3(2)	O(1)–Zn(2)–O(6)	98.4(2)
O(4)–Zn(1)–P(1)	128.82(17)	O(3)–Zn(2)–P(2)	80.45(17)
O(1)–Zn(1)–P(1)	82.88(15)	O(2)–Zn(2)–P(2)	87.67(15)
O(5)–Zn(1)–P(1)	96.1(2)	O(1)–Zn(2)–P(2)	87.90(15)
O(2)–Zn(1)–P(1)	76.48(13)	O(6)–Zn(2)–P(2)	170.20(15)
$Zn(L^{tBu}H)_2(MeCN)$			
O(1)–Zn(1)	2.0360(19)	P(2)–Zn(1)	2.4639(10)
O(3)–Zn(1)	2.0090(19)	Zn(1)–N(1)	2.101(3)
P(1)–Zn(1)	2.4631(10)		
O(3)–Zn(1)–O(1)	165.61(8)	O(1)–Zn(1)–P(1)	79.94(6)
O(3)–Zn(1)–N(1)	101.44(9)	N(1)–Zn(1)–P(1)	116.11(8)
O(1)–Zn(1)–N(1)	92.95(9)	O(3)–Zn(1)–P(2)	80.68(6)
O(3)–Zn(1)–P(1)	93.94(6)	O(1)–Zn(1)–P(2)	94.79(6)
N(1)–Zn(1)–P(2)	106.97(8)	P(1)–Zn(1)–P(2)	136.76(3)

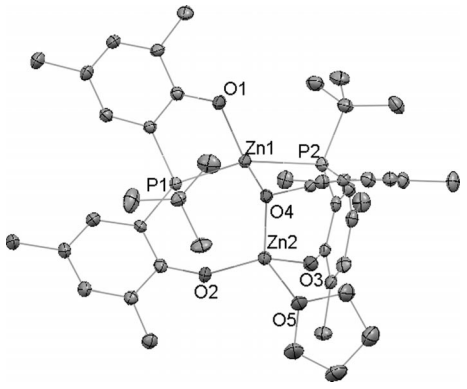

Figure 2. Molecular structure of $Zn_2(L^{tBu})_2(THF)$ with thermal ellipsoids drawn at the 35% probability level. All methyl groups in aryl *tert*-butyl and one unbound THF found in the asymmetric unit cell are omitted for clarity.

The solution NMR spectroscopic data of $Zn_2(L^{tBu})_2(THF)$ at room temperature, however, are indicative of a structure with higher symmetry. For instance, the aryl *tert*-butyl groups are observed as two singlet resonances, and the phosphorus donors as one broad singlet resonance in the ^1H and $^{31}P\{^1H\}$ NMR spectra, respectively. These results suggest that a fluxional exchange process occurs in solution on the NMR timescale. A variable-temperature $^{31}P\{^1H\}$ NMR study revealed that the broad singlet resonance sharpens upon heating and broadens upon cooling to give rise to two resolved broad singlet resonances between –15 and –40 °C. These signals become two doublet resonances centered at –24.2 and –37.6 ppm with $^2J_{pp}$ of 83 Hz at temperatures lower than –45 °C, which is consistent with the X-ray structure wherein the two phosphorus donors are concomitantly coordinated to Zn1.

Synthesis and Characterization of $Zn_2(L^{Ph})_2(THF)_2$

Similar to $Zn_2(L^{tBu})_2(THF)$, the addition of one equiv. of $ZnEt_2$ to a THF solution of H_2L^{Ph} at –35 °C generated $Zn_2(L^{Ph})_2(THF)_2$ in 75% yield as colorless crystals suitable for X-ray diffraction analysis. An X-ray study of $Zn_2(L^{Ph})_2(THF)_2$, however, revealed a distinct structure (Figure 3, Table 1) from that of $Zn_2(L^{tBu})_2(THF)$, which highlights the phosphorus substituent effect. Notably, the two phosphorus donors in $Zn_2(L^{Ph})_2(THF)_2$ are coordinated to two different zinc atoms; the Zn2–P2 bond of 2.678(2) Å is long, whereas

the Zn1–P1 bond length of 2.343(2) Å is typical.[10,48,49] Consistent with the lower electron-releasing nature of the phosphorus substituent, $Zn_2(\mathbf{L^{Ph}})_2(THF)_2$ adopts one more coordinated THF molecule than $Zn_2(\mathbf{L^{tBu}})_2(THF)$. Both zinc atoms in $Zn_2(\mathbf{L^{Ph}})_2(THF)_2$ are five-coordinate; each contains one coordinated THF, and the entire molecule is C_1-symmetric. Although one $[\mathbf{L^{Ph}}]^{2-}$ (containing P2) is κ^2-O,P bound to Zn2 with a "pendant" phenolate κ^1-bound to Zn1, the other (containing P1) is κ^3-O,P,O coordinated to Zn1 with both phenolate oxygen donors bridging the two zinc atoms. Interestingly, these binding modes are similar to those found in $Zn_2(\mathbf{L^{tBu}})_2(THF)$ and $Zn[\mathbf{L^{tBu}}Li(THF)]_2$, respectively. In addition, the latter coordination mode is also reminiscent of those of $\mathbf{L^{Ph}}Li_2(DME)_2$,[25] $[\mathbf{L^{Ph}}Li_2(THF)_2]_2$,[28] and $[\mathbf{L^{tBu}}Li_2(DME)]_2$ (DME = dimethyl ether).[26] This similarity is intriguing, particularly in view of the inherently distinct cationic charges and atomic sizes of Li and Zn.

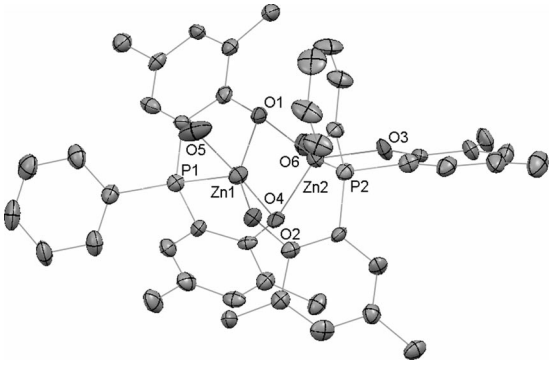

Figure 3. Molecular structure of $Zn_2(\mathbf{L^{Ph}})_2(THF)_2$ with thermal ellipsoids drawn at the 35% probability level. All methyl groups in *tert*-butyl and all methylene groups in THF are omitted for clarity.

Similar to that found for $Zn_2(\mathbf{L^{tBu}})_2(THF)$, variable-temperature solution NMR studies of $Zn_2(\mathbf{L^{Ph}})_2(THF)_2$ are all consistent with a C_1-symmetric static structure that undergoes a fluxional process upon warming in solution to give rise to an averaged structure, which has seemingly higher molecular symmetry at room temperature. In the ^1H NMR spectra, the aryl *tert*-butyl groups are observed as two singlet resonances at room temperature and eight well-resolved signals at temperatures lower than –45 °C. Consistently, the broad singlet resonance observed in the $^{31}P\{^1H\}$ NMR spectrum at room temperature resolves to become two singlets (–52.3 and –54.8 ppm in $[D_8]$toluene) below –5 °C. In good agreement with the X-ray structure, the two phosphorus donors do not show any internuclear coupling even at –80 °C.

Synthesis and Characterization of $Zn(\mathbf{L^{tBu}}H)_2(MeCN)$ and $Zn(\mathbf{L^{Ph}}H)_2(MeCN)$

Given the unexpected results obtained from the salt metathesis routes regardless of the stoichiometry of the starting materials employed, we became interested in whether the formation of $Zn_2(\mathbf{L^{tBu}})_2(THF)$ and $Zn_2(\mathbf{L^{Ph}})_2(THF)_2$ is a function of the relative ratios of $ZnEt_2$ with the corresponding H_2L. The reactions of $ZnEt_2$ with two equiv. of $H_2\mathbf{L^{tBu}}$ or $H_2\mathbf{L^{Ph}}$ in THF generated $Zn(\mathbf{L^{tBu}}H)_2(MeCN)$ or $Zn(\mathbf{L^{Ph}}H)_2(MeCN)$, respectively, after work up with acetonitrile in ca. 80% isolated yield. Acetonitrile facilitates the purification of these zinc complexes, whose $^{31}P\{^1H\}$ NMR spectroscopic data differ negligibly with or without the employment of acetonitrile. These data are, however, notably distinct from those of $Zn_2(\mathbf{L^{tBu}})_2(THF)$ and $Zn_2(\mathbf{L^{Ph}})_2(THF)_2$. In particular, neither $Zn_2(\mathbf{L^{tBu}})_2(THF)$ nor $Zn_2(\mathbf{L^{Ph}})_2(THF)_2$ was detected from the $^{31}P\{^1H\}$ NMR spectra of reaction aliquots in the preparation of $Zn(\mathbf{L^{tBu}}H)_2(MeCN)$ or $Zn(\mathbf{L^{Ph}}H)_2(MeCN)$. The isolation of $Zn(LH)_2(MeCN)$ rather than $Zn(LH)_2(THF)$ seems to reflect the distinct Lewis basic strengths of these coordinating solvents. The formation of $[\mathbf{L^{Ph}}H]^-$ derivatives was also found in previously established lithium chemistry.[27]

The ^1H NMR spectrum of $Zn(\mathbf{L^{tBu}}H)_2(MeCN)$ empirically confirmed the coordination of two $[\mathbf{L^{tBu}}H]^-$ and one acetonitrile molecule to zinc. The hydroxy protons are observed as a broad singlet resonance at 7.59 ppm and the phosphorus donors as one singlet resonance at –32 ppm in the ^1H and $^{31}P\{^1H\}$ NMR spectra, respectively, which indicates the presence of intramolecular symmetry in this molecule. The aryl *tert*-butyl groups, however, are observed in the ^1H NMR spectra as two sharp singlet resonances at room temperature and four well-resolved signals at –75 °C, which is consistent with a fluxional exchange process in solution. The static structure of $Zn(\mathbf{L^{tBu}}H)_2(MeCN)$ is thus C_2 symmetric. The NMR spectroscopic data of $Zn(\mathbf{L^{Ph}}H)_2(MeCN)$ at room temperature also suggest a time-averaged structure similar to that of $Zn(\mathbf{L^{tBu}}H)_2(MeCN)$.

Colorless crystals of $Zn(\mathbf{L^{tBu}}H)_2(MeCN)$ suitable for X-ray diffraction analysis were grown from a concentrated acetonitrile solution at –35 °C. As depicted in Figure 4, this molecule contains two $[\mathbf{L^{tBu}}H]^-$ ligands that are κ^2-O,P bound to zinc. Selected bond lengths and angles are summarized in Table 1. Interestingly, intramolecular hydrogen

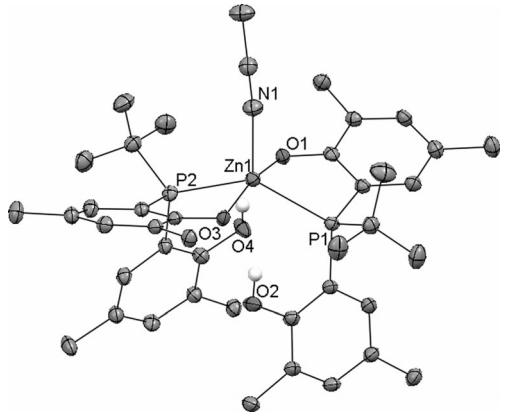

Figure 4. Molecular structure of $Zn(\mathbf{L^{tBu}}H)_2(MeCN)$ with thermal ellipsoids drawn at the 35% probability level. All methyl groups in aryl *tert*-butyl are omitted for clarity.

bonding is present between the [$L^{tBu}H$]$^-$ ligands. The O1–O4 and O2–O3 distances of 2.667 and 2.637 Å, respectively, are comparable to those reported previously.[50] With the coordination of one acetonitrile molecule, this species is thus five-coordinate. The core geometry is best described as approximately halfway (geometric parameter τ = 0.48)[51] between ideal trigonal bipyramidal and square pyramidal. The acetonitrile ligand binds to zinc with an unusually acute C≡N–Zn angle of 155.0(3)°. This phenomenon is rare but not unprecedented.[41,52,53]

Conclusions

We have prepared and structurally characterized a series of phenolate phosphane complexes of zinc. Of particular note are the versatile coordination modes of these hybrid chelating ligands that could be either a κ^3-O,P,O chelate or a κ^2-O,P chelate tethered with a pendant phenolate or phenol. As demonstrated in Zn[L^RLi(THF)]$_2$ and Zn(L^RH)$_2$(MeCN) (R = *t*Bu, Ph), the biphenolate phosphane ligands may be transformed to become monoanionic [L^RLi(THF)]$^-$ or [L^RH]$^-$ by phenolate coordination to lithium or protonation, respectively. The formation of lithium zincates Zn[L^{tBu}Li(THF)]$_2$ and Zn[L^{Ph}Li(THF)]$_2$ instead of Zn$_2$(L^{tBu})$_2$(THF) and Zn$_2$(L^{Ph})$_2$(THF)$_2$ by salt metathesis highlights the significance of the synthetic strategies employed in the complex preparation. A profound phosphorus substituent effect is observed between Zn$_2$(L^{tBu})$_2$(THF) and Zn$_2$(L^{Ph})$_2$(THF)$_2$, wherein both complex conformation and structural connectivity are notably different.

Experimental Section

General Procedures: Unless otherwise specified, all experiments were performed under nitrogen using standard Schlenk or glovebox techniques. All solvents were reagent grade or better and purified by standard methods. H_2L^{tBu} and H_2L^{Ph} were prepared according to literature procedures.[26,54] All other chemicals were obtained from commercial vendors and used as received. The NMR spectra were recorded with Varian Unity or Bruker AV instruments. Chemical shifts (δ) are listed as parts per million downfield from tetramethylsilane and coupling constants (J) are in Hertz. ^{1}H NMR spectra were referenced to the residual solvent peak at 7.16 ppm for C_6D_6 or 7.24 ppm for $CDCl_3$. ^{13}C NMR spectra were referenced to the internal solvent peak at 128.39 ppm for C_6D_6 or 77.23 ppm for $CDCl_3$. The assignment of the carbon atoms is based on DEPT ^{13}C NMR spectroscopy. ^{31}P and ^{7}Li NMR spectra were referenced externally to 85% H_3PO_4 at 0 ppm and LiCl in D_2O at 0 ppm, respectively. Routine coupling constants are not listed. All NMR spectra were recorded at room temperature unless otherwise noted. Elemental analysis was performed with a Heraeus CHN-O Rapid analyzer.

X-ray Crystallography: Crystallographic data are summarized in Table 2. Data were collected with a Bruker-Nonius Kappa CCD diffractometer with graphite-monochromated Mo-K_α radiation (λ = 0.7107 Å). Structures were solved by direct methods and refined by full-matrix least-squares procedures against F^2 using SHELXL-97.[55] All full-weight non-hydrogen atoms were refined anisotropically. Hydrogen atoms were placed in calculated positions. The structures of Zn[L^{tBu}Li(THF)]$_2$, Zn$_2$(L^{tBu})$_2$(THF), and Zn$_2$(L^{Ph})$_2$(THF)$_2$ contain disordered molecules of diethyl ether, THF, and pentane, respectively. Attempts to obtain a suitable disorder model failed. The SQUEEZE procedure of the Platon program[56] was

Table 2. Crystal data and structure refinement for Zn[L^{tBu}Li(THF)]$_2$, Zn$_2$(L^{tBu})$_2$(THF), Zn$_2$(L^{Ph})$_2$(THF)$_2$, and Zn(L^{tBu}H)$_2$(MeCN).

	Zn[L^{tBu}Li(THF)]$_2$	Zn$_2$(L^{tBu})$_2$(THF)	Zn$_2$(L^{Ph})$_2$(THF)$_2$	Zn(L^{tBu}H)$_2$(MeCN)
Formula	$C_{72}H_{114}Li_2O_6P_2Zn$	$C_{72}H_{114}O_6P_2Zn_2$	$C_{76}H_{106}O_6P_2Zn_2$	$C_{66}H_{103}NO_4P_2Zn$
Fw	1216.82	1268.31	1308.29	1101.80
Crystal size [mm^3]	0.28 × 0.14 × 0.04	0.38 × 0.34 × 0.12	0.39 × 0.15 × 0.05	0.37 × 0.31 × 0.27
$D_{calcd.}$ [Mg/m^3]	0.999	1.088	1.106	1.096
Crystal system	orthorhombic	monoclinic	tetragonal	monoclinic
Space group	*Pban*	$P2_1/c$	$P4_2bc$	$P2_1/n$
a [Å]	28.9698(11)	22.5680(15)	29.2014(4)	13.916(3)
b [Å]	11.4748(4)	14.6988(9)	29.2014(4)	33.736(7)
c [Å]	24.3488(8)	23.3554(14)	18.4281(3)	14.975(4)
α [°]	90	90	90	90
β [°]	90	91.162(4)	90	108.302(14)
γ [°]	90	90	90	90
V [Å^3]	8094.1(5)	7745.9(8)	15714.0(4)	6675(3)
Z	4	4	8	4
T [K]	200(2)	200(2)	200(2)	200(2)
2θ range [°]	2.82, 50.06	1.80, 50.04	4.42, 49.98	2.42, 50.06
Index ranges (*h*; *k*; *l*)	–34, 34; –13, 13; –28, 25	–26, 26; –16, 17; –27, 22	–33, 32; –31, 33; –21, 21	–16, 13; –40, 39; –17, 17
Total reflections	45556	44639	81905	43414
Independent reflections	7155	13575	13353	11772
R_{int}	0.0677	0.0617	0.1661	0.0577
Absorption coeff. [mm^{-1}]	0.384	0.704	0.696	0.459
Data/restraints/parameters	7155/0/375	13575/0/713	13353/1/735	11772/0/656
Goodness of fit	1.017	1.010	0.827	1.097
Final *R* indices [$I > 2\sigma(I)$]	*R*1 = 0.0619, *wR*2 = 0.1704	*R*1 = 0.0524, *wR*2 = 0.1211	*R*1 = 0.0741, *wR*2 = 0.1786	*R*1 = 0.0504, *wR*2 = 0.1330
R indices (all data)	*R*1 = 0.0915, *wR*2 = 0.1850	*R*1 = 0.0834, *wR*2 = 0.1308	*R*1 = 0.1319, *wR*2 = 0.2080	*R*1 = 0.0788, *wR*2 = 0.1492
Residual density [e/Å^3]	–0.581 to 0.617	–0.750 to 0.902	–0.488 to 0.521	–0.471 to 0.689

used to obtain a new set of F^2 (hkl) values without the contribution of solvent molecules, which led to the presence of significant voids in these structures. The refinement reduced $R1$ to 0.0619 for $Zn[\mathbf{L}^{t\mathbf{Bu}}Li(THF)]_2$, 0.0524 for $Zn_2(\mathbf{L}^{t\mathbf{Bu}})_2(THF)$, and 0.0741 for $Zn_2(\mathbf{L}^{\mathbf{Ph}})_2(THF)_2$.

CCDC-826002 {for $Zn[\mathbf{L}^{t\mathbf{Bu}}Li(THF)]_2$}, -826003 [for $Zn_2(\mathbf{L}^{t\mathbf{Bu}})_2(THF)$], -826004 [for $Zn_2(\mathbf{L}^{\mathbf{Ph}})_2(THF)_2$], and -826005 [for $Zn(\mathbf{L}^{t\mathbf{Bu}}H)_2(MeCN)$] contain the supplementary crystallographic data for this paper. These data can be obtained free of charge from The Cambridge Crystallographic Data Centre via www.ccdc.cam.ac.uk/data_request/cif.

Synthesis of $Zn[\mathbf{L}^{t\mathbf{Bu}}Li(THF)]_2$. Method 1: To a prechilled THF solution (9 mL) of $H_2\mathbf{L}^{t\mathbf{Bu}}$ (125 mg, 0.25 mmol) at –35 °C was added *n*BuLi (0.2 mL, 2.5 M in hexane, 0.50 mmol). The reaction solution was stirred at room temperature for 1 h. A THF solution (1 mL) of $ZnCl_2$ (17 mg, 0.124 mmol) was added. The solution was stirred at room temperature overnight and the solvents evaporated to dryness under reduced pressure. Diethyl ether (4 mL) was added. The ether solution was filtered through a pad of Celite and the solvents evaporated to dryness under reduced pressure. The solid thus obtained was washed with acetonitrile (6 mL) and dried in vacuo to give the product as an off-white solid; yield 125 mg (82%). **Method 2:** The reaction parameters are similar to those of Method 1 except that 1 equiv. instead of 0.5 equiv. of $ZnCl_2$ with respect to $Li_2\mathbf{L}^{t\mathbf{Bu}}$ was employed to generate an off-white solid in 80% yield. ^{1}H NMR (500 MHz, C_6D_6): δ = 7.83 (dd, 2 H, Ar), 7.63 (dd, 2 H, Ar), 7.55 (d, 2 H, Ar), 7.44 (d, 2 H, Ar), 2.96 (m, 8 H, OCH_2), 1.64 (s, 18 H, ArCMe_3), 1.53 (s, 18 H, ArCMe_3), 1.42 (d, 18 H, $^3J_{PH}$ = 12 Hz, PCMe_3), 1.38 (s, 18 H, ArCMe_3), 1.30 (s, 18 H, ArCMe_3), 1.15 (m, 8 H, OCH_2CH_2) ppm. ^{13}C{^{1}H} NMR (125 MHz, C_6D_6): δ = 167.69 (vt, J_{PC} = 6 Hz, 1 C), 167.32 (vt, J_{PC} = 7.5 Hz, 1 C), 137.35 (s, 1 C), 137.21 (s, 1 C), 135.95 (s, 1 C), 134.78 (s, 1 C), 129.37 (s, CH), 126.36 (s, CH), 126.21 (s, CH), 125.70 (s, CH), 118.39 (t, J_{PC} = 25.7 Hz, 1 C), 117.68 (t, J_{PC} = 24.1 Hz, *1* C), 68.23 (s, OCH_2), 36.07 (s, Ar*C*Me$_3$), 35.96 (s, Ar*C*Me$_3$), 34.66 (s, Ar*C*Me$_3$), 34.50 (s, Ar*C*Me$_3$), 32.57 (s, ArCMe_3), 32.28 (s, ArCMe_3), 31.74 (s, ArCMe_3), 31.15 (s, ArCMe_3), 31.02 (m, P*C*Me$_3$), 30.61 (m, PCMe_3), 25.88 (s, OCH_2CH_2) ppm. ^{31}P{^{1}H} NMR (202 MHz, C_6D_6): δ = –39.79. ^{7}Li{^{1}H} NMR (194 MHz, C_6D_6): δ = 0.58 ppm. $C_{72}H_{114}Li_2O_6P_2Zn\cdot 3MeCN$ (1340.1): calcd. C 69.89, H 9.26; found C 69.97, H 9.03.

Synthesis of $Zn[\mathbf{L}^{\mathbf{Ph}}Li(THF)]_2$: To a THF solution (3 mL) of $H_2\mathbf{L}^{\mathbf{Ph}}$ (104 mg, 0.20 mmol) at –35 °C was added *n*BuLi (0.16 mL, 2.5 M in hexane 0.40 mmol). The reaction solution was stirred at room temperature for 1 h, cooled to –35 °C, and added to a prechilled (–35 °C) THF solution (2 mL) of $ZnCl_2$ (27.3 mg, 0.20 mmol). The reaction mixture was stirred at room temperature for 23 h. All volatiles were removed in vacuo. The solid residue was triturated with pentane (1 mL × 3). Diethyl ether (6 mL) was added. The ether solution was filtered through a pad of Celite, and the solvents evaporated to dryness under reduced pressure to give the product as an off-white solid; yield 120.6 mg (96%). ^{1}H NMR (500 MHz, $CDCl_3$): δ = 7.40 (m, 4 H, Ar), 7.30 (m, 4 H, Ar), 7.23 (m, 6 H, Ar), 7.20 (m, 2 H, Ar), 7.16 (m, 2 H, Ar), 3.10 (m, 8 H, OCH_2), 1.51 (s, 18 H, CMe_3), 1.49 (m, 8 H, OCH_2CH_2), 1.23 (s, 18 H, CMe_3), 1.18 (s, 18 H, CMe_3), 1.15 (s, 18 H, CMe_3) ppm. ^{13}C{^{1}H} NMR (125 MHz, $CDCl_3$): δ = 166.66 (t, J_{PC} = 8.3 Hz, 1 C), 166.08 (t, J_{PC} = 8.3 Hz, 1 C), 136.88 (s, 1 C), 136.82 (s, 1 C), 136.65 (s, 1 C), 136.01 (s, 1 C), 133.30 (t, J_{PC} = 5.9 Hz, *C*H), 130.71 (t, J_{PC} = 20 Hz, 1 C), 128.52 (s, *C*H), 128.43 (s, *C*H), 127.66 (t, J_{PC} = 4.5 Hz, *C*H), 126.03 (s, *C*H), 125.58 (s, *C*H), 124.56 (s, *C*H), 118.34 (t, J_{PC} = 26 Hz, 1 C), 117.76 (t, J_{PC} = 26 Hz, 1 C), 67.61 (s, OCH_2), 35.12 (s, *C*Me$_3$), 34.09 (s, *C*Me$_3$), 31.66 (s, CMe_3), 31.61 (s, CMe_3), 31.14 (s, CMe_3), 29.94 (s, CMe_3), 25.18 (s, OCH_2CH_2) ppm. ^{31}P{^{1}H} NMR (202 MHz, $CDCl_3$): δ = –49.97 ppm. ^{7}Li{^{1}H} NMR (194 MHz, $CDCl_3$): δ = 0.33 ppm. With multiple attempts, we were unable to obtain satisfactory elemental analysis data, which was likely due to incomplete combustion of the samples examined.

Synthesis of $Zn_2(\mathbf{L}^{t\mathbf{Bu}})_2(THF)$: To a THF solution (6 mL) of $H_2\mathbf{L}^{t\mathbf{Bu}}$ (204 mg, 0.40 mmol) at –35 °C was added $ZnEt_2$ (0.40 mL, 1 M in hexane, 0.40 mmol). The solution was stirred at room temperature for 1 h, and the solvents evaporated to dryness under reduced pressure. The solid residue thus obtained was washed with acetonitrile (6 mL) and dried in vacuo to give the product as a colorless crystalline solid; yield 192 mg (80%). Colorless crystals suitable for X-ray diffraction analysis were grown from a concentrated pentane solution at –35 °C. ^{1}H NMR (500 MHz, C_6D_6): δ = 7.83 (br. s, 4 H, Ar), 7.56 (s, 4 H, Ar), 3.35 (br. s, 4 H, OCH_2), 1.55 (s, 36 H, ArCMe_3), 1.46 (m, 18 H, PCMe_3), 1.37 (s, 36 H, ArCMe_3), 1.27 (br. s, 4 H, OCH_2CH_2) ppm. ^{13}C{^{1}H} NMR (125 MHz, C_6D_6): δ = 167.07 (br. s, 1 C), 139.96 (s, CH), 138.34 (br. s, CH), 127.48 (s, 1 C), 116.05 (br. s, 1 C), 69.91 (s, OCH_2), 36.30 (s, Ar*C*Me$_3$), 34.79 (s, Ar*C*Me$_3$), 33.49 (m, P*C*Me$_3$), 32.31 (s, ArCMe_3), 30.93 (s, ArCMe_3), 29.91 (s, PCMe_3), 25.71 (s, OCH_2CH_2) ppm. ^{31}P{^{1}H} NMR (202 MHz, C_6D_6): δ = –35.58 (br) ppm. $C_{68}H_{106}O_5P_2Zn_2\cdot THF\cdot 3MeCN$ (1391.6): calcd. C 67.30, H 8.91; found C 67.60, H 8.36.

Synthesis of $Zn_2(\mathbf{L}^{\mathbf{Ph}})_2(THF)_2$: To a THF solution (6 mL) of $H_2\mathbf{L}^{\mathbf{Ph}}$ (200 mg, 0.38 mmol) at –35 °C was added $ZnEt_2$ (0.38 mL, 1 M in hexane, 0.38 mmol). The solution was stirred at room temperature for 1 h and the solvents evaporated to dryness under reduced pressure. The solid residue thus obtained was washed with acetonitrile (6 mL) and dried in vacuo to give the product as a colorless crystalline solid; yield 186 mg (75%). Colorless crystals suitable for X-ray diffraction analysis were grown from a concentrated pentane solution at –35 °C. ^{1}H NMR (500 MHz, C_6D_6): δ = 7.68 (m, 4 H, Ar), 7.58 (m, 10 H, Ar), 7.02 (m, 4 H, Ar), 3.35 (m, 8 H, OCH_2), 1.53 (br. s, 36 H, CMe_3), 1.28 (s, 36 H, CMe_3), 1.19 (m, 8 H, OCH_2CH_2) ppm. ^{13}C{^{1}H} NMR (125 MHz, C_6D_6): δ = 166.99 (m, 1 C), 139.83 (m, 1 C), 133.94 (s, CH), 133.77 (s, CH), 117.41 (m, 1 C), 116.77 (m, 1 C), 69.48 (s, OCH_2), 36.14 (s, Ar*C*Me$_3$), 34.88 (s, Ar*C*Me$_3$), 32.23 (s, ArCMe_3), 30.80 (s, ArCMe_3), 25.74 (s, OCH_2CH_2) ppm. ^{31}P{^{1}H} NMR (202 MHz, C_6D_6): δ = –51.0 (br) ppm. $C_{76}H_{106}O_6P_2Zn_2$ (1308.38): calcd. C 69.75, H 8.17; found C 69.90, H 8.13.

Synthesis of $Zn(\mathbf{L}^{t\mathbf{Bu}}H)_2(MeCN)$: To a THF solution (5 mL) of $H_2\mathbf{L}^{t\mathbf{Bu}}$ (204 mg, 0.40 mmol) at –35 °C was added $ZnEt_2$ (0.20 mL, 1 M in hexane, 0.20 mmol). The solution was stirred at room temperature for 1 h, and the solvents evaporated to dryness under reduced pressure. The solid residue thus obtained was washed with acetonitrile (6 mL) and dried in vacuo to give the product as an off-white solid; yield 179 mg (81%). ^{1}H NMR (500 MHz, C_6D_6): δ = 7.89 (d, 4 H, Ar), 7.64 (d, 4 H, Ar), 7.59 (br. s, 2 H, OH), 1.51 (s, 36 H, CMe_3), 1.35 (m, 18 H, PCMe_3), 1.32 (s, 36 H, CMe_3), 0.60 (s, 3 H, MeCN) ppm. ^{13}C{^{1}H} NMR (125.7 MHz, C_6D_6): δ = 163.92 (br. s, 1 C), 140.69 (s, CH), 140.37 (s, CH), 125.78 (s, 1 C), 124.72 (s, 1 C), 116.23 (s, CN), 113.50 (br. d, 1 C), 36.28 (s, Ar*C*Me$_3$), 34.86 (s, Ar*C*Me$_3$), 33.80 (m, P*C*Me$_3$), 32.16 (s, ArCMe_3), 31.60 (s, ArCMe_3), 28.10 (t, PCMe_3), 0.42 (s, *Me*CN) ppm. ^{31}P{^{1}H} NMR (121.48 MHz, C_6D_6): δ = –32.4 ppm. $C_{66}H_{103}NO_4P_2Zn$ (1101.87): calcd. C 71.93, H 9.43; found C 71.97, H 9.25.

Synthesis of $Zn(L^{Ph}H)_2(MeCN)$: To a THF solution (6 mL) of H_2L^{Ph} (103 mg, 0.20 mmol) at room temperature was added $ZnEt_2$ (0.10 mL, 1 M in hexane, 0.10 mmol). The solution was stirred at room temperature for 1 h, and the solvents evaporated to dryness under reduced pressure. The solid residue thus obtained was washed with acetonitrile (6 mL) and dried in vacuo to give the product as an off-white solid; yield 92 mg (81%). ^1H NMR (500 MHz, C_6D_6): δ = 7.62 (m, 4 H, Ar), 7.36 (m, 6 H, Ar), 6.99 (br. s, 2 H, OH), 6.92 (m, 4 H, Ar), 6.88 (m, 4 H, Ar), 1.55 (s, 36 H, CMe_3), 1.21 (s, 36 H, CMe_3), 0.62 (s, 3 H, MeCN) ppm. $^{13}C\{^1H\}$ NMR (125.7 MHz, C_6D_6): δ = 163.02 (br. s, 1 C), 141.19 (s, 1 C), 139.31 (s, 1 C), 133.67 (s, CH), 130.32 (s, CH), 129.38 (s, CH), 128.67 (s, CH), 128.45 (s, CH), 116.76 (s, CN), 114.80 (s, 1 C), 36.10 (s, Ar*C*Me$_3$), 34.86 (s, Ar*C*Me$_3$), 32.02 (s, ArC*Me*$_3$), 30.48 (s, ArC*Me*$_3$), 0.42 (s, *Me*CN) ppm. $^{31}P\{^1H\}$ NMR (202.3 MHz, C_6D_6): δ = –45.09 ppm. $C_{70}H_{95}NO_4P_2Zn{\cdot}MeCN$ (1182.9): calcd. C 73.09, H 8.35; found C 72.84, H 7.77.

Acknowledgments

We thank the National Science Council of Taiwan for financial support (NSC 99-2113-M-110-003-MY3 and 99-2119-M-110-002), Mr. Ting-Shen Kuo (NTNU) for assistance with X-ray crystallography, and the National Center for High-performance Computing (NCHC) for accesses to chemical databases.

[1] N. V. Kaminskaia, B. Spingler, S. J. Lippard, *J. Am. Chem. Soc.* **2000**, *122*, 6411–6422.
[2] P. Chaudhuri, M. Hess, J. Müller, K. Hildenbrand, E. Bill, T. Weyhermüller, K. Wieghardt, *J. Am. Chem. Soc.* **1999**, *121*, 9599–9610.
[3] C. A. Wheaton, P. G. Hayes, B. J. Ireland, *Dalton Trans.* **2009**, 4832–4846.
[4] D. P. Goldberg, S. P. Watton, A. Masschelein, L. Wimmer, S. J. Lippard, *J. Am. Chem. Soc.* **1993**, *115*, 5346–5347.
[5] E. Bill, J. Müller, T. Weyhermüller, K. Wieghardt, *Inorg. Chem.* **1999**, *38*, 5795–5802.
[6] A. Sokolowski, J. Müller, T. Weyhermüller, R. Schnepf, P. Hildebrandt, K. Hildenbrand, E. Bothe, K. Wieghardt, *J. Am. Chem. Soc.* **1997**, *119*, 8889–8900.
[7] M. Orio, C. Philouze, O. Jarjayes, F. Neese, F. Thomas, *Inorg. Chem.* **2010**, *49*, 646–658.
[8] K. Ghosh, P. Kumar, N. Tyagi, U. P. Singh, *Inorg. Chem.* **2010**, *49*, 7614–7616.
[9] D. J. Darensbourg, M. W. Holtcamp, G. E. Struck, M. S. Zimmer, S. A. Niezgoda, P. Rainey, J. B. Robertson, J. D. Draper, J. H. Reibenspies, *J. Am. Chem. Soc.* **1999**, *121*, 107–116.
[10] D. J. Darensbourg, J. R. Wildeson, J. C. Yarbrough, J. H. Reibenspies, *J. Am. Chem. Soc.* **2000**, *122*, 12487–12496.
[11] D. J. Darensbourg, M. S. Zimmer, P. Rainey, D. L. Larkins, *Inorg. Chem.* **2000**, *39*, 1578–1585.
[12] C. K. Williams, L. E. Breyfogle, S. K. Choi, W. Nam, V. G. Young, M. A. Hillmyer, W. B. Tolman, *J. Am. Chem. Soc.* **2003**, *125*, 11350–11359.
[13] C. M. Silvernail, L. J. Yao, L. M. R. Hill, M. A. Hillmyer, W. B. Tolman, *Inorg. Chem.* **2007**, *46*, 6565–6574.
[14] G. Labourdette, D. J. Lee, B. O. Patrick, M. B. Ezhova, P. Mehrkhodavandi, *Organometallics* **2009**, *28*, 1309–1319.
[15] L.-C. Liang, *Coord. Chem. Rev.* **2006**, *250*, 1152–1177.
[16] L.-C. Liang, P.-S. Chien, Y.-L. Huang, *J. Am. Chem. Soc.* **2006**, *128*, 15562–15563.
[17] L.-C. Liang, J.-M. Lin, C.-H. Hung, *Organometallics* **2003**, *22*, 3007–3009.
[18] M.-H. Huang, L.-C. Liang, *Organometallics* **2004**, *23*, 2813–2816.
[19] L.-C. Liang, P.-S. Chien, M.-H. Huang, *Organometallics* **2005**, *24*, 353–357.
[20] L.-C. Liang, P.-S. Chien, J.-M. Lin, M.-H. Huang, Y.-L. Huang, J.-H. Liao, *Organometallics* **2006**, *25*, 1399–1411.
[21] L.-C. Liang, Y.-N. Chang, H. M. Lee, *Inorg. Chem.* **2007**, *46*, 2666–2673.
[22] L.-C. Liang, Y.-L. Hsu, S.-T. Lin, *Inorg. Chem.* **2011**, *50*, 3363–3372.
[23] L.-C. Liang, Y.-N. Chang, H.-S. Chen, H. M. Lee, *Inorg. Chem.* **2007**, *46*, 7587–7593.
[24] L.-C. Liang, L.-C. Cheng, T.-L. Tsai, C.-H. Hu, W.-H. Guo, *Inorg. Chem.* **2009**, *48*, 5697–5703.
[25] Y.-N. Chang, L.-C. Liang, *Inorg. Chim. Acta* **2007**, *360*, 136–142.
[26] Y.-L. Hsu, L.-C. Liang, *Organometallics* **2010**, *29*, 6201–6208.
[27] L.-C. Liang, Y.-N. Chang, H.-Y. Shih, S.-T. Lin, H. M. Lee, *Eur. J. Inorg. Chem.* **2011**, 4077–4082.
[28] C. D. Carmichael, M. D. Fryzuk, *Dalton Trans.* **2008**, 800–806.
[29] C. D. Carmichael, M. D. Fryzuk, *Can. J. Chem.* **2010**, *88*, 667–675.
[30] S. Merkel, D. Stern, J. Henn, D. Stalke, *Angew. Chem.* **2009**, *121*, 6468; *Angew. Chem. Int. Ed.* **2009**, *48*, 6350–6353.
[31] M. Uchiyama, Y. Matsumoto, D. Nobuto, T. Furuyama, K. Yamaguchi, K. Morokuma, *J. Am. Chem. Soc.* **2006**, *128*, 8748–8750.
[32] D. V. Graham, E. Hevia, A. R. Kennedy, R. E. Mulvey, *Organometallics* **2006**, *25*, 3297–3300.
[33] J. B. Woods, X. Yu, T. Chen, Z.-L. Xue, *Organometallics* **2004**, *23*, 5910–5912.
[34] G. A. Morris, H. Zhou, C. L. Stern, S. T. Nguyen, *Inorg. Chem.* **2001**, *40*, 3222–3227.
[35] M. B. Dinger, M. J. Scott, *Inorg. Chem.* **2001**, *40*, 1029–1036.
[36] A. Erxleben, *Inorg. Chem.* **2001**, *40*, 208–213.
[37] A. V. Wiznycia, J. Desper, C. J. Levy, *Inorg. Chem.* **2006**, *45*, 10034–10036.
[38] G. R. Fulmer, A. J. M. Miller, N. H. Sherden, H. E. Gottlieb, A. Nudelman, B. M. Stoltz, J. E. Bercaw, K. I. Goldberg, *Organometallics* **2010**, *29*, 2176–2179.
[39] D. R. Armstrong, W. Clegg, P. García-Álvarez, A. R. Kennedy, M. D. McCall, L. Russo, E. Hevia, *Chem. Eur. J.* **2011**, *17*, 8333–8341.
[40] L. Jin, C. Liu, J. Liu, F. Hu, Y. Lan, A. S. Batsanov, J. A. K. Howard, T. B. Marder, A. Lei, *J. Am. Chem. Soc.* **2009**, *131*, 16656–16657.
[41] C. Redshaw, M. R. J. Elsegood, *Angew. Chem.* **2007**, *119*, 7597; *Angew. Chem. Int. Ed.* **2007**, *46*, 7453–7457.
[42] H. R. L. Barley, W. Clegg, S. H. Dale, E. Hevia, G. W. Honeyman, A. R. Kennedy, R. E. Mulvey, *Angew. Chem.* **2005**, *117*, 6172; *Angew. Chem. Int. Ed.* **2005**, *44*, 6018–6021.
[43] Y. Kondo, M. Shilai, M. Uchiyama, T. Sakamoto, *J. Am. Chem. Soc.* **1999**, *121*, 3539–3540.
[44] M. Uchiyama, T. Miyoshi, Y. Kajihara, T. Sakamoto, Y. Otani, T. Ohwada, Y. Kondo, *J. Am. Chem. Soc.* **2002**, *124*, 8514–8515.
[45] L. M. Jackman, D. Çizmeciyan, P. G. Williard, M. A. Nichols, *J. Am. Chem. Soc.* **1993**, *115*, 6262–6267.
[46] L. M. Jackman, B. D. Smith, *J. Am. Chem. Soc.* **1988**, *110*, 3829–3835.
[47] J. F. Allan, R. Nassar, E. Specht, A. Beatty, N. Calin, K. W. Henderson, *J. Am. Chem. Soc.* **2004**, *126*, 484–485.
[48] L.-C. Liang, W.-Y. Lee, T.-L. Tsai, Y.-L. Hsu, T.-Y. Lee, *Dalton Trans.* **2010**, *39*, 8748–8758.
[49] L.-C. Liang, W.-Y. Lee, C.-H. Hung, *Inorg. Chem.* **2003**, *42*, 5471–5473.
[50] P. L. Holland, R. A. Andersen, R. G. Bergman, J. K. Huang, S. P. Nolan, *J. Am. Chem. Soc.* **1997**, *119*, 12800–12814.
[51] A. W. Addison, T. N. Rao, J. Reedijk, J. van Rijn, G. C. Verschoor, *J. Chem. Soc., Dalton Trans.* **1984**, 1349–1356.

[52] A. Petitjean, R. G. Khoury, N. Kyritsakas, J.-M. Lehn, *J. Am. Chem. Soc.* **2004**, *126*, 6637–6647.
[53] R. D. Köhn, M. Haufe, G. Kociok-Köhn, *J. Am. Chem. Soc.* **2006**, *128*, 10682–10683.
[54] R. Siefert, T. Weyhermüller, P. Chaudhuri, *J. Chem. Soc., Dalton Trans.* **2000**, 4656–4663.
[55] G. M. Sheldrick, *SHELXTL*, version 5.1, Bruker AXA Inc., Madison, WI, **1998**.
[56] A. L. Spek, *PLATON - A Multipurpose Crystallographic Tool*, Utrecht University, The Netherlands, **2003**.

Received: September 8, 2011
Published Online: December 6, 2011

DOI: 10.1002/ejic.201100975

Oleum and Sulfuric Acid as Reaction Media: The Actinide Examples $UO_2(S_2O_7)$-lt (low temperature), $UO_2(S_2O_7)$-ht (high temperature), $UO_2(HSO_4)_2$, $An(SO_4)_2$ (An = Th, U), $Th_4(HSO_4)_2(SO_4)_7$ and $Th(HSO_4)_2(SO_4)$

Ulf Betke[a] and Mathias S. Wickleder*[a]

Keywords: Actinides / Uranium / Thorium / Structure elucidation / Oleum / Sulfates

New uranium sulfates have been synthesised by the reaction of $UO_2(CH_3COO)_2{\cdot}2H_2O$ with sulfuric acid/sulfur trioxide mixtures in sealed glass ampoules. Both polymorphs of the disulfate $UO_2(S_2O_7)$ [low temperature (lt): triclinic, $P\bar{1}$, $Z = 2$, $a = 647.8(1)$ pm, $b = 684.2(1)$ pm, $c = 800.1(1)$ pm, $\alpha = 87.31(2)°$, $\beta = 78.37(2)°$, $\gamma = 75.34(2)°$, $V = 0.33605(9)$ nm^3; high temperature (ht): orthorhombic, $Pca2_1$, $Z = 8$, $a = 1080.21(2)$ pm, $b = 814.74(1)$ pm, $c = 1655.63(3)$ pm, $V = 1.45710(4)$ nm^3] and the hydrogensulfate $UO_2(HSO_4)_2$ [monoclinic, $P2_1/n$, $Z = 4$, $a = 779(3)$ pm, $b = 815.39(3)$ pm, $c = 1285.77(5)$ pm, $\beta = 103.700(1)°$, $V = 0.79428(5)$ nm^3] contain hexavalent uranium in the form of the well-known linear $[UO_2]^{2+}$ ion. The pentagonal bipyramidal coordination sphere around U is completed by disulfate and hydrogensulfate ions, which connect the uranyl groups to a three-dimensional network. Reaction of uranyl acetate with sulfuric acid at sufficiently high temperature (300 °C) leads to a reduction of uranium to the tetravalent form under separation of green plates of $U(SO_4)_2$ [orthorhombic, $Pbca$, $Z = 8$, $a = 940.11(2)$ pm, $b = 898.13(2)$ pm, $c = 1349.09(3)$ pm, $V = 1.13909(4)$ nm^3]. The U^{4+} ions in $U(SO_4)_2$ are in a square antiprismatic coordination of eight monodentate sulfate tetrahedra. By treatment of ThO_2 with sulfuric acid, the thorium (hydrogen)sulfates $Th(SO_4)_2$ [orthorhombic, $Pbca$, $Z = 8$, $a = 953.74(3)$ pm, $b = 911.49(3)$ pm, $c = 1365.02(4)$ pm, $V = 1.18665(6)$ nm^3], $Th_4(HSO_4)_2(SO_4)_7$ [tetragonal, $I\bar{4}2d$, $Z = 4$, $a = 1327.7(2)$ pm, $c = 1362.8(2)$ pm, $V = 2.402.3(6)$ nm^3] and $Th(HSO_4)_2(SO_4)$ [triclinic, $P\bar{1}$, $Z = 2$, $a = 576.18(2)$ pm, $b = 896.11(3)$ pm, $c = 948.58(3)$ pm, $\alpha = 65.387(2)°$, $\beta = 87.838(2)°$, $\gamma = 88.917(2)°$, $V = 0.44495(3)$ nm^3] could be obtained. Whereas $Th(SO_4)_2$ is isotypic with the respective uranium compound, both hydrogensulfates contain ninefold-coordinated thorium to form a triple-capped trigonal prism. The structure of $Th(HSO_4)_2(SO_4)$ can be described as a distorted variant of the UCl_3 structure type.

Introduction

The eligibility of highly concentrated mineralic acids as reaction media has been barely explored up to now. In our group, the synthetic techniques to handle reactions in such aggressive media have been developed in the last decade, wherein the main focus has been on sulfuric acid and its derivatives. The most convenient synthetic approach is reactions under solvothermal conditions in sealed glass ampoules or steel autoclaves at elevated temperatures up to 400 °C. Even substrates that were long thought to be inert towards sulfuric acid, like platinum metal, for example, could be reacted to give the unique platinum sulfate $Pt_2(HSO_4)_2(SO_4)_2$, for instance, which contains trivalent platinum and a $[Pt_2]$ dumbbell.[1] By similar reactions in the presence of alkaline metal cations, a series of ternary platinum sulfates that contain the same $[Pt_2]$ fragment as well as the unique $[Pt_{12}O_8(SO_4)_{12}]^{4-}$ cluster anion in $Cs_4[Pt_{12}O_8(SO_4)_{12}]$ could be obtained.[2,3] Furthermore, sulfuric acid has the remarkable potential to stabilise metals in uncommon oxidation states. Besides the Pt^{III} compounds mentioned above, the first sulfate of gold, $Au_2(SO_4)_2$, could be synthesized from H_2SO_4, which is in fact a true Au^{II} compound that features a dumbbell-shaped $[Au_2]^{4+}$ cation.

A closer look at the knowledge of simple sulfate salts of the elements revealed that sulfates of high-valent metals are nearly nonexistent.[4] Therefore, we started a research program to shed some more light on this interesting class of compounds by successfully transferring the synthetic procedures established for precious and other metals towards the d-block metals of group 5 to 7. From the highly acidic media of sulfuric acid, or sulfuric acid in a mixture with the corresponding anhydride SO_3, the sulfates $Nb_2O_2(SO_4)_3$, $WO(SO_4)_2$, $MoO_2(SO_4)$ and two modifications of $Re_2O_5(SO_4)_2$ could be obtained.[5] The potential of H_2SO_4 to stabilise uncommon oxidation states was again demonstrated by the formation of $MoO(HSO_4)(SO_4)$, the first hydrogensulfate of a refractory metal as well as the first sulfate of pentavalent molybdenum.[6] If rare-earth ions are present during the synthesis, the ternary sulfates RE_2-

[a] Carl von Ossietzky University of Oldenburg, Institute of Pure and Applied Chemistry,
Carl-von-Ossietzky Strasse 9–11, 26129 Oldenburg, Germany
Fax: +49-441-798-3352
E-mail: mathias.wickleder@uni-oldenburg.de

$[W_2O_3(SO_4)_6]$ (RE = Sm–Gd, Ho), $RE_2Nb_2O_2(SO_4)_3[H(SO_4)_2]_2$ (RE = Y, Ce–Nd, Sm–Er), $Sm_2Nb_2O_2(SO_4)_5(S_2O_7)$ and $M_2Nb_4O_5(SO_4)_8$ (M = Bi, Eu) can be isolated.[7]

Other typical metals, which are known to exist in high oxidation states, are found for the early actinide elements of Pa to Am. The most common and easily accessible example is uranium that forms the rather stable $[UO_2]^{2+}$ (uranyl) ion, which exists even in aqueous solutions without any hydrolysis. Therefore many simple (solvated) salts that contain this cation are known. However, the better part of research has been done on addition compounds of uranyl nitrate, which play an important role in the waste reprocessing of spent nuclear fuels. The knowledge of simple (solvated) uranyl sulfates is limited to the hydrated species $UO_2(SO_4)\cdot nH_2O$ (n = 2.5, 3.5).[8–10] The only solvent-free sulfate of hexavalent uranium is $UO_2(SO_4)$.[11]

Due to the formal analogy between uranium in its highest oxidation state and the metals of group 6, we started to explore the behaviour of uranyl species in strongly acidic reaction media like sulfuric acid and mixtures of H_2SO_4 and SO_3. This lead to the new disulfate $UO_2(S_2O_7)$ in two modifications as well as the hydrogensulfate $UO_2(HSO_4)_2$, the crystal structures of which are presented here.

Furthermore, the chemistry of uranium in the tetravalent form as well as the reactions of thorium-containing precursors with sulfuric acid have been explored due to the similarities between the tetravalent actinide ions and the chemistry of the rare-earth elements. Furthermore, sulfuric acid as well as sulfates of these elements play an important role in the processing of monazite ores when it comes to the order of isolating the rare-earth elements in this mineral.[12] The first step is the digestion of the respective ores in concentrated sulfuric acid, whereupon the rare-earth elements as well as uranium and thorium dissolve. The separation of the desired rare-earth metals from thorium and uranium is maintained by selective hydrolysation steps and precipitation processes. Despite the high technical relevance of this separation process, the knowledge of tetravalent actinide sulfates is restricted to the hydrates $Th(SO_4)_2\cdot 8H_2O$ and $U(SO_4)_2\cdot 4H_2O$,[13,14] at least if one neglects a number of ternary thorium sulfates that have been reported recently.[15] No solvent-free sulfates or sulfate derivatives of tetravalent actinide elements have been described in the literature up to now.

In the rare-earth-metal–sulfuric acid–sulfur trioxide system, numerous compounds have been synthesised in our group in the last years. Examples are the hydrogensulfates $RE(HSO_4)_3$ (RE = La–Nd, Er),[16,17] hydrogensulfate disulfates of the composition $RE(HSO_4)(S_2O_7)$ (RE = Nd–Lu),[18,19] the simple binary sulfates $RE_2(SO_4)_3$ (RE = Sc, Y)[20] and the disulfates $RE_2(S_2O_7)_3$ (RE = La–Nd).[19] In analogy thereto, the tetravalent thorium and uranium sulfates and hydrogensulfates $An(SO_4)_2$ (An = Th, U), $Th_4(HSO_4)_2(SO_4)_7$ and $Th(HSO_4)_2(SO_4)$ could be obtained by similar reactions. They are the first examples of (hydrogen)sulfates of these elements, and are probably intermediates in the above-mentioned separation process of Th, U and rare-earth elements.

Results

Crystal Structures

$UO_2(S_2O_7)$-lt

The low-temperature (lt) polymorph of uranyl disulfate crystallises in the triclinic space group $P\bar{1}$ with two formula units per unit cell. The asymmetric unit contains one crystallographically independent uranium atom, which is in a distorted pentagonal bipyramidal coordination of two terminal oxide ligands (O11, O12) and five monodentate disulfate ions (Figure 1). The main reason for the pronounced distortion around U are the distances to the oxide ligands, which are short, as expected, at 175 and 176 pm, respectively. The distances to the disulfate ligands that coordinate in the *cis* position towards the oxide ions to uranium fall in the narrow range between 241 and 244 pm. The $[O{=}U{=}O]^{2+}$ moiety is almost linear with an angle O11–U1–O12 of 179.5°. The distortion of the pentagonal bipyramid becomes also apparent in the angles between the oxide ligands and the equatorial disulfate ions, which range between 86 and 95°.

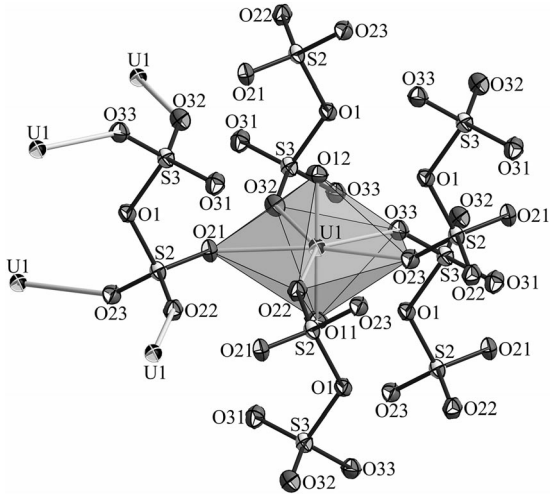

Figure 1. Atom labeling scheme and thermal ellipsoids (50% probability) for $UO_2(S_2O_7)$-lt. Each uranium atom is in a distorted pentagonal bipyramidal coordination of two oxide ligands forming the characteristic linear $[UO_2]^{2+}$ moiety as well as five monodentate disulfate ions coordinating in a *cis* position towards the oxide ligands. Each disulfate ion coordinates towards five different uranium atoms leaving one S–O group uncoordinated.

The asymmetric unit contains one crystallographically unique disulfate ion represented by the sulfur atoms S2 and S3. Interestingly, no chelating coordination of a metal is observed. Clearly, the short distance between two possible coordination sites in the equatorial plane around the $[UO_2]^{2+}$ ion (280 to 290 pm) relative to the distance between two disulfate oxygen atoms (312 pm) renders the chelating attack unfavourable. Instead, the $[S_2O_7]$ group coordinates in a monodentate fashion towards five different uranyl ions, thereby leaving one oxygen atom (O31) uncoordinated. This is easily reflected in the respective S–O distances, which fall in the narrow range between 144 and 145 pm for the coordi-

nating S–O groups, whereas for the S3–O31 bond, a distance of 141 pm is found. For the oxygen bridge in the disulfate ion (O1), no coordination towards the metal is observed.

The S–O–S bridge of the disulfate ion is highly asymmetric, as for the S2–O1 bond a distance of 160 pm is found; but the S3–O1 bond length amounts to 168 pm, respectively. This is in good accord with the different coordination of the $S2O_3$ and $S3O_3$ parts of the disulfate ion, as the former utilises all three oxygen atoms for coordination towards uranium, but the latter leaves one S–O group uncoordinated. Therefore the sulfur atom S2 compensates the loss of electron density due to a more intense coordination towards U by the formation of a stronger bond to the bridging disulfate oxygen atom indicated by the shorter S–O distance. This finding is supported by the bond-valence sums for the respective sulfur atoms, which can be calculated as 5.981 for the sulfur atom S2 and 6.072 for S3 according to Brown and Altermatt.[21]

For simple metal disulfates like the respective disulfates of Na, K and Cd, a symmetric S–O–S bridge is found due to the highly networking $[S_2O_7]$ ions in this class of compounds.[22–24] The only example of a highly asymmetric oxygen bridge in a disulfate ion is reported for $Te(S_2O_7)_2$.[25,26] In this compound, a similar asymmetric coordination of a disulfate ligand towards tellurium is found, this leading to a short (158 pm) and a long (167 pm) S–O bond to the bridging oxide ion.

Finally, the structure of $UO_2(S_2O_7)$-lt is built by networking the uranyl ions through disulfate to a three-dimensional network according to the Niggli formula $^3_\infty[UO_{2/1}(S_2O_7)_{5/5}]$. All uranyl ions are oriented roughly in the [10–1] direction (Figure 2).

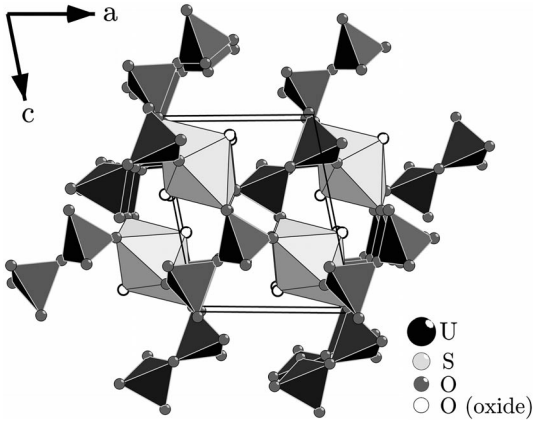

Figure 2. The uranyl ions in $UO_2(S_2O_7)$-lt are connected in a polymeric structure according to the Niggli formula $^3_\infty[UO_{2/1}(S_2O_7)_{5/5}]$. The $[UO_2]^{2+}$ ions are oriented roughly parallel to the [10–1] direction.

$UO_2(S_2O_7)$-ht

The high-temperature (ht) modification of uranyl disulfate crystallises in the acentric orthorhombic space group $Pca2_1$ with eight formula units in the unit cell. The structure of high-temperature $UO_2(S_2O_7)$ is of lower density compared to the low-temperature polymorph (4.068 versus 4.409 $g\,cm^{-3}$). The asymmetric unit contains two crystallographically independent uranium atoms, which are both in a distorted pentagonal bipyramidal coordination of two oxide ligands, one bidentate and three monodentate disulfate ions (Figure 3). The distances U–O to the oxide ions O11, O12, O21 and O22 are 174 and 175 pm, and the angles O=U=O amount to 178 and 180°, respectively. The remaining distances U–O range between 239 and 246 pm. The angles between oxide ions and equatorial disulfate ligands lie in the narrow range between 88 and 92°, therefore the distortion of the coordination polyhedra around uranium is minor compared to the low-temperature uranyl disulfate (87 to 95°). This is probably a consequence of the less dense structure.

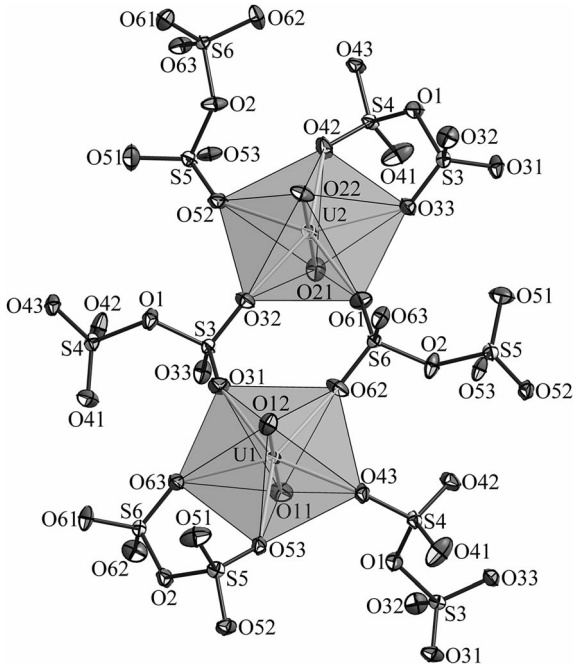

Figure 3. Both uranium atoms in the crystal structure of $UO_2(S_2O_7)$-ht are in a pentagonal bipyramidal coordination of two oxide ions and four disulfate ligands (one chelating and three monodentate $[S_2O_7]$ groups). Apparently, a pseudo-inversion centre is located between both $[UO_2]^{2+}$ ions, which is nearly fulfilled by most disulfate groups as well. Only the $[S_2O_7]$ ions on the top left and the lower right penetrate the centre of symmetry resulting in the acentric space group $Pca2_1$. The thermal ellipsoids are drawn at the 50% probability level.

The asymmetric unit contains two crystallographically unique disulfate ions represented by the sulfur atoms S3 and S4 as well as S5 and S6, respectively. In analogy towards $UO_2(S_2O_7)$-lt, each disulfate group coordinates the uranium atoms by utilisation of five S–O moieties, thus leaving one oxygen atom (O41, O51) uncoordinated (Figure 4). This is easily reflected in the short distances S4–O41 and S5–O51 of 140 and 141 pm, respectively. The asymmetric coordination of the disulfate groups leads again to asymmetric S3–O1–S4 and S5–O2–S6 bridges (160/165 and 158/165 pm). The distances S–O to the coordinating oxygen atoms range between 143 and 145 pm. However, in contrast

to the low-temperature modification of $UO_2(S_2O_7)$ each disulfate ion coordinates only towards four different uranium atoms (one as chelating ligand and three as monodentate ligand).

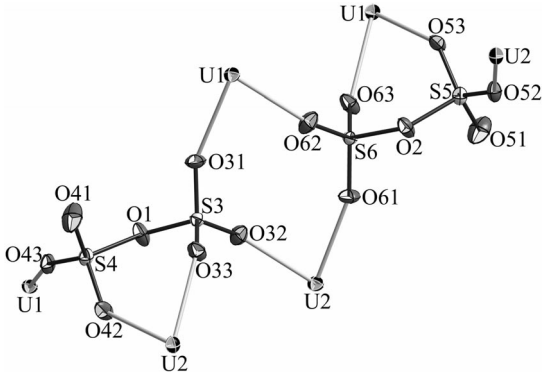

Figure 4. Each disulfate ion in $UO_2(S_2O_7)$-ht coordinates four different uranyl moieties (one chelating, three monodentate) leaving one S–O group uncoordinated. The asymmetric coordination mode leads to asymmetric S–O–S bridges as well. The thermal ellipsoids are drawn at the 50% probability level.

Finally, the disulfate ions connect the uranyl moieties to a polymeric network according to the Niggli formula $^3_\infty[UO_{2/1}(S_2O_7)_{4/4}]$ (Figure 5).

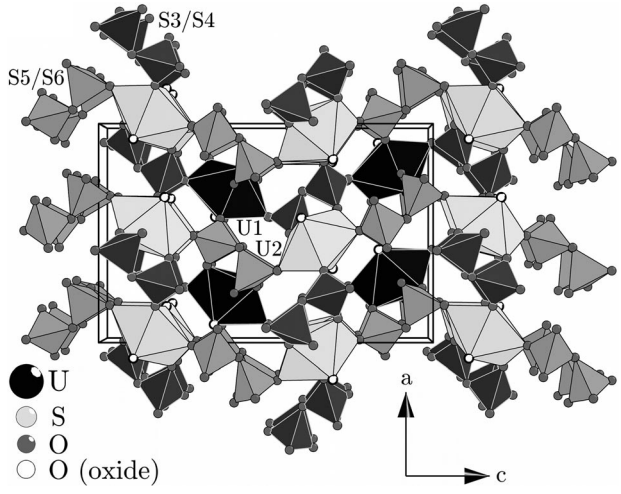

Figure 5. The uranyl ions in $UO_2(S_2O_7)$-ht are connected in a polymeric structure according to the Niggli formula $^3_\infty[UO_{2/1}(S_2O_7)_{4/4}]$.

$UO_2(HSO_4)_2$

Uranyl hydrogensulfate crystallises in the monoclinic space group $P2_1/n$ with four formula units per unit cell. The asymmetric unit contains one crystallographically independent uranium atom, which is in a distorted pentagonal bipyramidal coordination of two terminal oxide ligands represented by the oxygen atoms O11 and O12, as well as five monodentate hydrogensulfate ions (Figure 6). The oxide ligands are oriented in a *trans* position towards each other (angle O11–U1–O12: 179.6°) to form the characteristic linear uranyl ion. The distances U–O in the $[UO_2]^{2+}$ moiety are short, as expected, at 174 and 175 pm, respectively. The hydrogensulfate ligands coordinate the uranium atom in the equatorial plane thereto with distances U–O falling in the narrow range between 238 and 242 pm. The distortion of the pentagonal bipyramid around uranium is less pronounced than in the respective low-temperature uranyl disulfate, most likely due to the less bulky oxo anions. This is clearly visible in the angles between the oxide ligands and the equatorial disulfate ions (87 to 92°), which differ from the right angle to a much lesser degree than in $UO_2(S_2O_7)$-lt (86 to 95°).

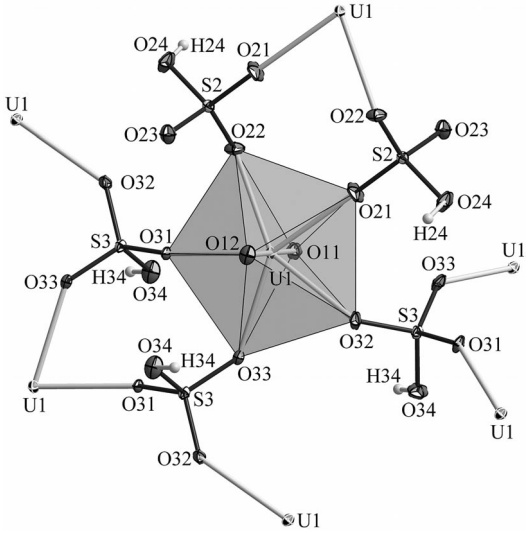

Figure 6. Atom labeling scheme and thermal ellipsoids (50% probability) for $UO_2(HSO_4)_2$. Each uranium atom is in a distorted pentagonal bipyramidal coordination of two oxide ligands forming the characteristic linear $[UO_2]^{2+}$ moiety as well as five monodentate hydrogensulfate ions coordinating in the *cis* position towards the oxide ligands. The $[HS2O_4]$ ion coordinates towards two uranyl moieties, whereas the $[HS3O_4]$ group is bonded to three $[UO_2]^{2+}$ ions.

The asymmetric unit contains two crystallographically unique hydrogensulfate ions represented by the sulfur atoms S2 and S3. First of all, the hydrogensulfate ion $[HS2O_4]$ coordinates two uranyl moieties over the oxygen atoms O21 and O22, whereas $[HS3O_4]$ binds to three $[UO_2]^{2+}$ ions by utilising the respective O31, O32 and O33 oxygen atoms. The bond lengths for the coordinating S–O groups fall in the narrow range between 145 and 146 pm. For the remaining formally noncoordinating S–O groups, short bonds around 140 pm are to be expected, although sulfur oxygen distances between 145 and 154 pm are found. Most likely the oxygen atoms O24 and O34 represent the hydroxy moiety of the hydrogensulfate ions, which is in good accord with the long S–O bonds. The oxygen atom O23 acts as an acceptor moiety in hydrogen bonding towards both the $[O_3S2O24H24]$ and the $[O_3S3O34H34]$ ion, which explains the elongation of the S2–O23 bond. The hydrogen bonds O23···H24–O24 and O23···H34–O34 are rather strong with a donor–acceptor distance of 270 and 273 pm, respectively. The hydrogen-bond network in $UO_2(HSO_4)_2$ is not extended in all three directions, but chains of hydrogen bonded $[HSO_4]$ ions along [010] are formed (Figure 7).

These network consists of zigzag chains of $[HS2O_4]$ ions, which are each flanked by an attached $[HS3O_4]$ moiety, alternatingly in the [100] and [–100] direction, respectively.

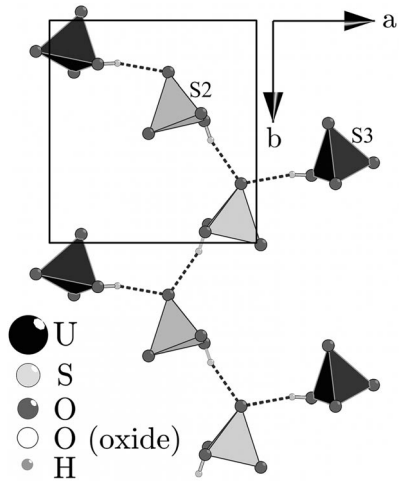

Figure 7. The hydrogensulfate ions in $UO_2(HSO_4)_2$ are networked by hydrogen bonding to chains running in the [010] direction. The chains consist of $[HS2O_4]$ ions (light grey), which are connected through O23···H24–O24 hydrogen bonds to a zigzag chain. Additionally, each $[HS2O_4]$ group is flanked by an attached $[HS3O_4]$ moiety (dark grey) through a O23···H34–O34 hydrogen bond.

Finally, the crystal structure of $UO_2(HSO_4)_2$ is built by stacking the $^1_\infty[HSO_4]_n$ chains one upon each other in the [100] as well as the [001] direction (Figure 8). The uranyl ions are located between these chains.

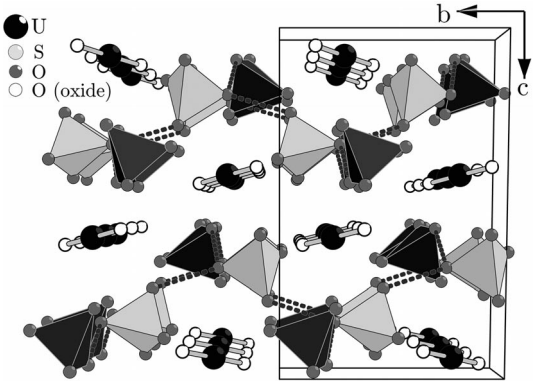

Figure 8. The crystal structure of $UO_2(HSO_4)_2$ is built by stacking the $^1_\infty[HSO_4]_n$ chains in the [100] as well as the [001] direction, whereas the uranyl ions are located between these chains (hydrogen atoms omitted for clarity).

An(SO$_4$)$_2$ (An = Th, U)

Thorium(IV) and uranium(IV) bis-sulfate both crystallise in the orthorhombic space group *Pbca* with four formula units per unit cell. Their structure is isotypic to the respective sulfate of tetravalent cerium, $Ce(SO_4)_2$.[27] The asymmetric unit contains one crystallographically independent An^{4+} ion, which is in a square antiprismatic coordination of eight monodentate sulfate ligands (Figure 9). The Th–O distances range between 236 and 245 pm, whereas for the slightly smaller U^{4+} ion, U–O distances between 231 and 240 pm can be observed.

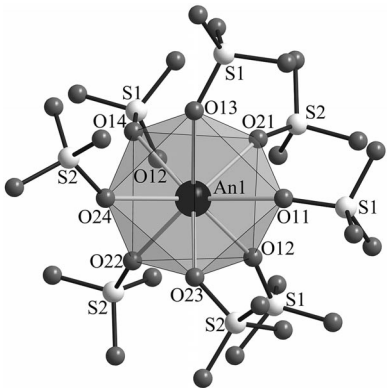

Figure 9. The An^{4+} ions (An = Th, U) in $An(SO_4)_2$ are coordinated by eight monodentate sulfate ligands forming a square antiprism. The distances An–O range between 236 and 245 pm for $Th(SO_4)_2$ and 231 and 240 pm for the respective uranium compound.

The asymmetric unit contains two crystallographically unique sulfate ions represented by the sulfur atoms S1 and S2. Each sulfate group coordinates towards four different actinide ions, therefore all S–O distances are almost equal and amount to 146–147 pm for both compounds (Figure 10). Furthermore, the sulfate tetrahedra are of almost ideal geometry, clearly visible in the angles O–S–O, which fall in the narrow range between 108 and 111°. Finally, the sulfate ions connect the An^{4+} ions to a three-dimensional structure according to the Niggli formula $^3_\infty[An(SO_4)_{8/4}]$ (An = Th, U) (Figure 11).

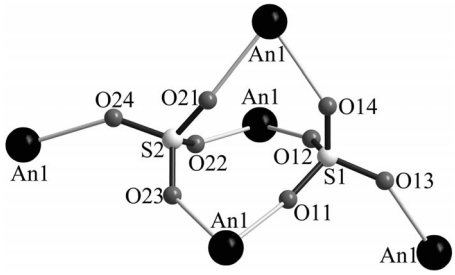

Figure 10. Each sulfate ion in the structure of $An(SO_4)_2$ (An = Th, U) binds towards four different An^{4+} ions leading to $[SO_4]$ groups of almost ideal tetrahedral geometry.

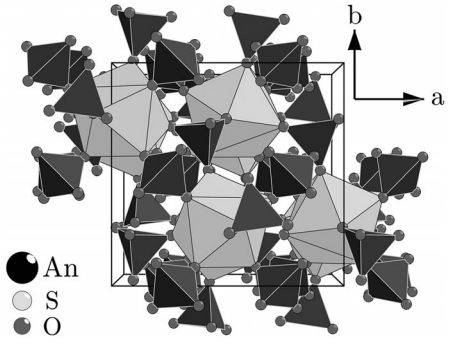

Figure 11. In $An(SO_4)_2$ (An = Th, U) the An^{4+} ions are networked through sulfate tetrahedra to a polymeric structure according with the Niggli formula $^3_\infty[An(SO_4)_{8/4}]$.

$Th_4(HSO_4)_2(SO_4)_7$

Thorium(IV) bis(hydrogensulfate) heptasulfate crystallises in the tetragonal *I*-centered space group $I\bar{4}2d$ and four formula units per unit cell. The only crystallographically independent thorium atom is in ninefold coordination of seven sulfate as well as two hydrogensulfate ions, thus forming a triple-capped trigonal prism (Figure 12). The three caps of the coordination polyhedron are built by the S2–O21/22 and S4–O41 groups, respectively. The Th–O distances range between 237 and 250 pm, whereas the Th1–O51 and Th1–O52 bonds to the hydrogensulfate ligands are the longest at 247 and 250 pm. Furthermore, the comparatively long Th1–O52A distance to the disordered hydrogensulfate ion [$HS5O_4$] of 278 pm should also be noted.

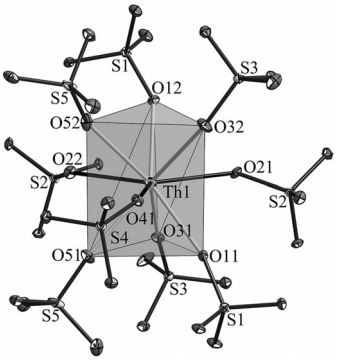

Figure 12. Atom labeling scheme and thermal ellipsoids (50% probability) for $Th_4(HSO_4)_2(SO_4)_7$. Each thorium atom is surrounded by nine monodentate oxo anions forming a triple-capped trigonal prismatic coordination sphere. The distances Th–O range between 237 and 250 pm (hydrogen atoms omitted for clarity).

The asymmetric unit contains at least five crystallographically unique sulfur atoms, which belong to four sulfate ions (S1 to S4) and one hydrogensulfate group (S5). The oxo anions represented by the sulfur atoms S1, S2, S3 and S5 are located on a twofold axis (Wyckoff site 8*c* and 8*d* of space group $I\bar{4}2d$); the [$S4O_4$] ion resides on the –4 axis (site 4a). All four sulfate tetrahedra coordinate with all four oxygen atoms towards thorium, thus leading to [SO_4] groups of nearly perfect tetrahedral symmetry and S–O distances in the narrow range between 146 and 147 pm (Figure 13). The hydrogensulfate ion represented by the sulfur atom S5 exhibits a disorder: one of the two oxygen positions is split equally (O52 and O52A), thereby leading to a long S5–O52 distance of 154 pm, and a shorter one of 150 pm (bond S5–O52A) (Figure 14). With respect to the long S5–O52 bond, the respective S–O group has been interpreted as the hydroxy moiety of the hydrogensulfate ion. From the Fourier map, the positioning of a hydrogen atom was possible, which is also plausible with respect to a hydrogen bond O52–H1···O41 towards an adjacent sulfate ion (distance D–A: 267 pm). Most likely, the S5–O52A group does not carry a hydrogen atom, but should be interpreted as normal coordinating S–O moiety. However, the Th1–O52 and Th1–O52A distances are special, because a shorter Th–O distance (250 pm) can be observed for the hydroxy moiety than for the unprotonated S–O group (Th–O distance: 278 pm). The reason for this behaviour is possibly the strong O52–H1···O41 hydrogen bond. Both remaining oxygen atoms of the [$HS5O_4$] ion represented by the oxygen atom O51 coordinate normally towards thorium, whereas the slightly shorter S5–O51 distance of 143 pm should be noted.

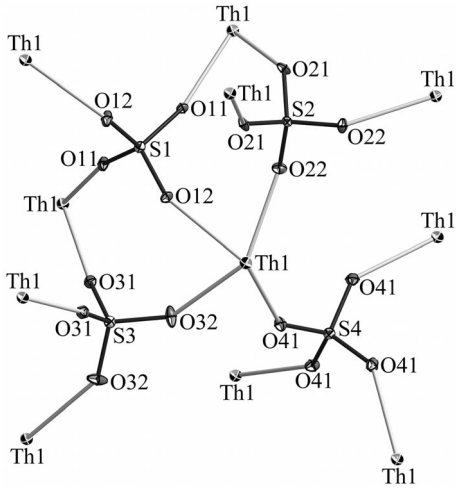

Figure 13. The crystal structure of $Th_4(HSO_4)_2(SO_4)_7$ contains four crystallographically independent sulfate ions, which coordinate four different thorium atoms each. The [SO_4] groups exhibit nearly perfect tetrahedral symmetry with bond lengths S–O between 146 and 147 pm. The thermal ellipsoids are drawn at the 50% probability level.

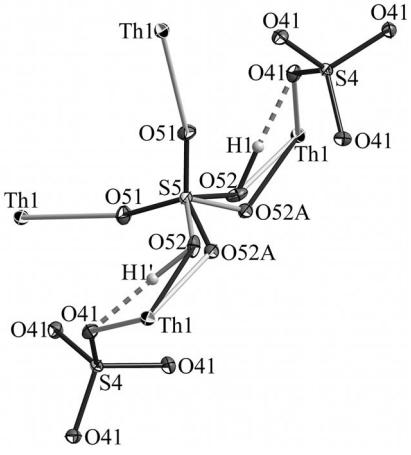

Figure 14. The hydrogensulfate ion in $Th_4(HSO_4)_2(SO_4)_7$ exhibits a disorder leading to a splitting of one oxygen site (O52/O52A), which is caused by a twofold axis. Both orientations are shown (light grey and dark grey bonds). One long distance S–O of 154 pm is found for O52, which can be interpreted as the hydroxy moiety. The position of the hydrogen atom could be refined and is in reasonable accord to the hydrogen bond O52–H1···O41 (distance O52–O41: 267 pm). The thermal ellipsoids are drawn at the 50% probability level.

Finally, a polymeric structure results by networking the Th^{4+} ions according to the Niggli formula $^{3}_{\infty}[Th(HSO_4)_{2/4}(SO_4)_{7/4}]$ (Figure 15).

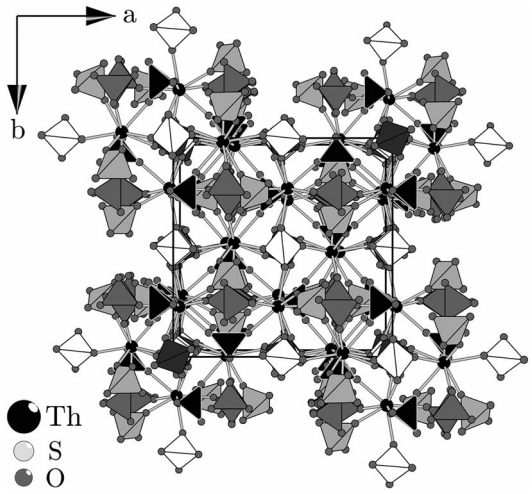

Figure 15. The Th^{4+} ions in $Th_4(HSO_4)_2(SO_4)_7$ are networked in a polymeric structure according to the Niggli formula $^3_\infty[Th(HSO_4)_{2/4}(SO_4)_{7/4}]$ (hydrogen atoms omitted for clarity).

Th(HSO$_4$)$_2$(SO$_4$)

Thorium(IV) bis(hydrogensulfate) sulfate crystallises in the triclinic space group $P\bar{1}$ with two formula units per unit cell. The asymmetric unit contains one crystallographically unique thorium atom, which is in a ninefold coordination of six hydrogensulfate ions and three sulfate groups to form a triple-capped trigonal prism (Figure 16). The Th–O distances range from 236 to 249 pm, whereas the sulfate ligands form stronger bonds (oxygen atoms O12/13/14: 236 to 237 pm) than the hydrogensulfate ions (243 to 249 pm). The three caps of the coordination polyhedron are built by one sulfate ion (Th1–O12 bond) and two hydrogensulfate groups (Th1–O21/31 bonds).

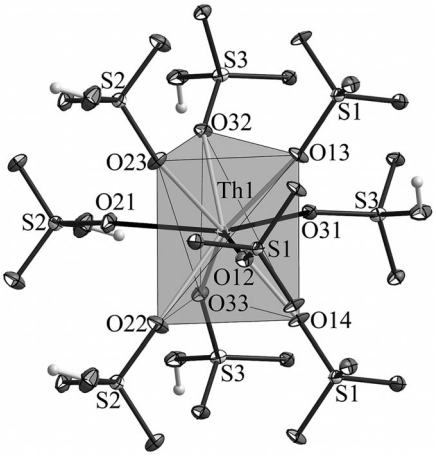

Figure 16. Atom labeling scheme and thermal ellipsoids (50% probability) for $Th(HSO_4)_2(SO_4)$. Each thorium atom is surrounded by nine monodentate oxo anions forming a triple-capped trigonal prismatic coordination sphere. The Th–O distances range between 236 and 249 pm.

The asymmetric unit contains two hydrogensulfate ions represented by the sulfur atoms S2 and S3 as well as one sulfate group (S1). Each oxo anion coordinates three different thorium atoms with correlated S–O distances in the range between 144 and 148 pm (Figure 17). For the noncoordinating S2–O24 and S3–O34 groups, significantly elongated distances are found (154 and 153 pm, respectively), which are in good accord with a hydrogensulfate S–OH moiety. A maximum in electron density could be successfully refined as a hydrogen atom for both oxo anions. Between hydrogensulfate and sulfate ions strong hydrogen bonding can be observed, whereas the noncoordinating S1–O11 moiety of the sulfate group acts as acceptor functionality towards both hydrogensulfate S–OH groups. This is easily reflected in the significantly elongated S1–O11 distance of 146 pm. The hydrogen bonds connect the oxo anions along the [100] direction (O34–H34···O11 bond; D–A distance: 254 pm) as well as in the [001] direction (O24–H24···O11 bond; D–A distance: 278 pm) (Figure 18).

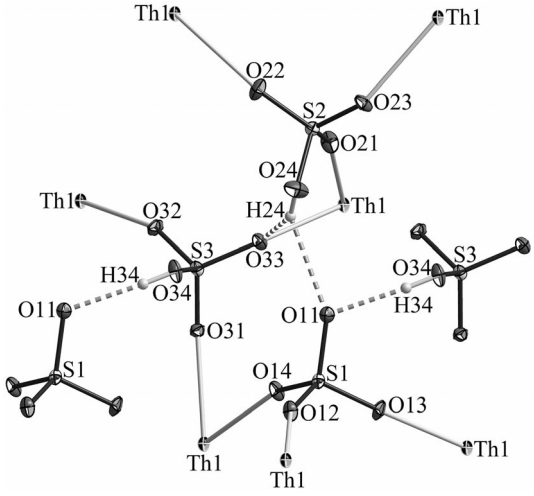

Figure 17. In $Th(HSO_4)_2(SO_4)$, each oxo anion coordinates three different thorium atoms. Furthermore, rather strong hydrogen bridges between the hydrogensulfate S–OH groups and the noncoordinating S–O moiety of the sulfate ion are built (O24–H24···O11 bond; D–A distance: 278 pm and O34–H34···O11 bond; D–A distance: 254 pm). The thermal ellipsoids are drawn at the 50% probability level.

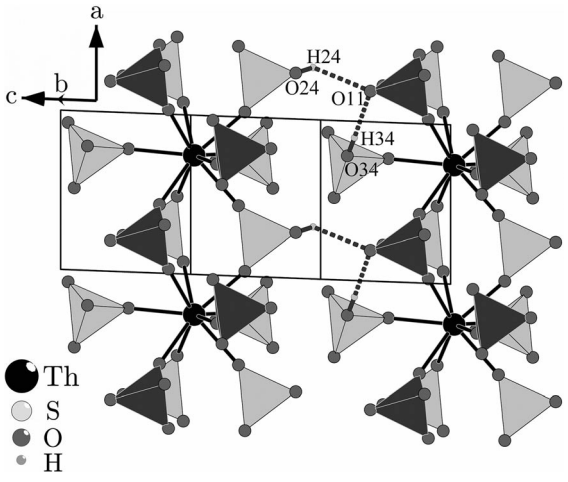

Figure 18. The hydrogen bridges (dashed bonds) in $Th(HSO_4)_2(SO_4)$ connect the oxo anions along [100] and [001], respectively.

Finally, a polymeric network according to the Niggli formula $^{3}_{\infty}[Th(HSO_4)_{6/3}(SO_4)_{3/3}]$ is built that exhibits channels of nearly hexagonal symmetry along [100] in which the noncoordinating S–O as well as the S–OH moieties are oriented.

It is worth mentioning that the crystal structure of $Th(HSO_4)_2(SO_4)$ has a remarkable similarity with the hydrogensulfates of the lighter rare-earth ions La^{3+} to Nd^{3+}, which crystallise in a derivative of the UCl_3 structure type.[16] This is not surprising because the radius of Th^{4+} is nearly the same as Nd^{3+} (Th^{4+} = 123 pm, Nd^{3+} = 125 pm for ninefold coordination)[28] and both compounds are of the formal composition $M(EO_4)_3$. The structural analogy manifests in the same coordination geometry around the metal ions, similar M–O distances and the same coordination behaviour of the $[SO_4]$ moieties, as well as the formation of channels inside which the S–OH groups are oriented (Figure 19).

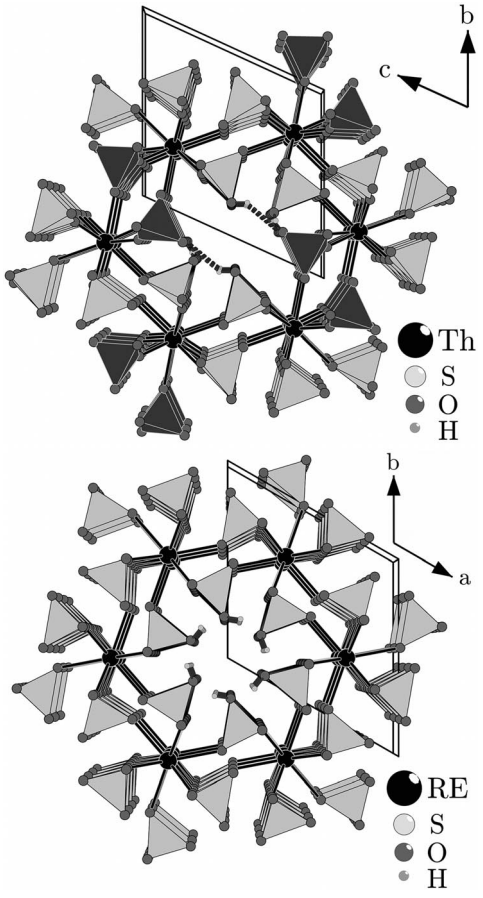

Figure 19. The crystal structure of $Th(HSO_4)_2(SO_4)$ (top) can be derived from the structure of the rare-earth hydrogensulfates $RE(HSO_4)_3$ (RE = La–Nd, below), which crystallise in a derivative of the UCl_3 structure type.[16] The formation of strong hydrogen bonds between sulfate (dark grey) and hydrogensulfate ions (light grey) in the structure of the thorium compound leads to a distortion and a lowering of the symmetry from space group $P6_3/m$ for $RE(HSO_4)_3$ to $P\bar{1}$ for $Th(HSO_4)_2(SO_4)$.

However, the substitution of one hydrogensulfate ion by one sulfate group in $Th(HSO_4)_2(SO_4)$ leads to a distortion of the crystal structure. This results in a lowering of the symmetry from the hexagonal space group $P6_3/m$ found for $RE(HSO_4)_3$ (RE = La–Nd) towards the triclinic space group $P\bar{1}$ for the thorium compound. The main reason for this distortion effect are the hydrogen bonds between the oxo anions. For the rare-earth hydrogensulfates, channels of ideal hexagonal symmetry are formed, inside which only hydrogensulfate hydroxy moieties are oriented. The shortest distances O–H···O range above 300 pm, therefore the hydrogen bridges have only a minor influence on the overall crystal structure. The lack of a potential acceptor functionality in the form of a noncoordinating S–O group inside the channels probably inhibits the formation of strong hydrogen bonds. In $Th(HSO_4)_2(SO_4)$, one hydrogensulfate ion is substituted by a sulfate moiety under preservation of its coordination behaviour. Therefore, the channels now contain both hydroxy moieties and noncoordinating S–O groups, which leads to the formation of rather strong hydrogen bridges between sulfate and hydrogensulfate ions (shortest O–H···O distance: 254 pm) and the above-mentioned distortion of the hexagonal channels.

Discussion

The structural chemistry of the actinide elements thorium und uranium features similarities with structures built by rare-earth elements on the one hand and the high-valent metals of the d block on the other. The latter is especially the case for hexavalent uranium, which forms the uranyl ion $[UO_2]^{2+}$ in formal analogy to the $[MO_2]^{n+}$ moieties found for the metals of group 6 and 7, for example. For both the $[UO_2]$ and $[MO_2]$ arrangements, short U/M–O distances are found, thus indicating a multiple bond between metal and oxygen.[29,30] However, significant differences between uranium and the d-block elements can be found in the arrangement of the oxide ligands. For the d-block metals, a bent geometry of the $[MO_2]^{n+}$ moiety with an angle O=M=O in the narrow range between 100 and 110° is found due to a maximisation of orbital overlap in π bonding between metal and oxide ligands.[31] In contrast thereto, for the uranyl ion a linear geometry with an angle O=U=O of almost 180° is found as a consequence of the interactions between filled uranium 6p orbitals and the orbitals of the oxide ligands.[32,33] In most cases, the uranyl ion is coordinated by five other ligands in the equatorial plane, so that usually a distorted pentagonal bipyramidal coordination is the result. Examples that contain sulfate ions are the respective hydrates of uranyl sulfate, $UO_2(SO_4)\cdot nH_2O$ (n = 2.5, 3.5).[8–10]

Both polymorphs of $UO_2(S_2O_7)$ as well as $UO_2(HSO_4)_2$ are not exceptions here, as they contain the linear $[UO_2]^{2+}$ ion, which is surrounded in the equatorial plane by five other donor atoms that belong to five or four oxo anions, respectively. However, in comparison to the only known unsolvated uranyl compound that contains sulfate ions, $UO_2(SO_4)$, the oxide ligands are terminal and do not coordinate to adjacent uranium atoms. In contrast thereto, one oxide ligand in $UO_2(SO_4)$ binds towards a second uranyl ion, therefore polymeric chains of oxide-connected uranium atoms are built.[11]

In comparison to the refractory metal oxide sulfates, the formation of polymeric structures in all three dimensions should be noted for the respective uranyl compounds. For the d-block metals, a trend towards the reduction in dimensionality with increasing valence can be observed [e.g., in the crystal structures of $Nb_2O_2(SO_4)_3$ and $MoO_2(SO_4)$ (polymeric in all three directions), $WO(SO_4)_2$ and $Re_2O_5(SO_4)_2$ (layer structures) or $Re_2O_5(S_2O_7)(SO_4)$ (chain structure)].[5,34,35]

A significant difference between the systems U^{VI}–H_2SO_4–SO_3 and RM–H_2SO_4–SO_3 (RM = refractory metal) is the inability to substitute oxide ligands of the uranyl moiety by sulfate ions simply by increasing the amount of sulfur trioxide present during the synthesis. For the sulfates of d-block metals, the number of oxide ligands coordinated towards the metal ion is roughly correlated to the SO_3 concentration of the sulfuric acid used during synthesis. This trend is nicely illustrated for molybdenum, which forms the sulfate $MoO_2(SO_4)$ that features the above-mentioned $[MoO_2]^{2+}$ moiety from concentrated sulfuric acid,[5,34] but $MoO(HSO_4)(SO_4)$ from fuming sulfuric acid that contains 65% SO_3, which contains only one oxide ligand in a [Mo=O] fragment.[6] The formal addition reaction of SO_3 to an oxide ion of the uranyl moiety (building a sulfate ligand) is obviously unfavourable, again indicating the distinct stability of the $[UO_2]^{2+}$ fragment. By increasing the concentration of sulfur trioxide in the U^{VI}–H_2SO_4–SO_3 system, a sulfate ion ingests a molecule SO_3 instead, thereby forming the disulfate $UO_2(S_2O_7)$ and not the hypothetical sulfate-richer compound $UO(SO_4)_2$.

For the lower oxidation states of actinide elements, the tetravalent form is worth mentioning, which is the only reasonably stable oxidation state for thorium so far. Furthermore, hexavalent uranium is easily reduced towards the green U^{4+} cation, which becomes apparent in the smooth reduction of $UO_2(CH_3COO)_2{\cdot}2H_2O$ in sulfuric acid to lead to $U(SO_4)_2$. However, a reduction in sulfuric acid is not a typical reaction. The reducing agent in this case is most likely acetic acid, which is oxidised to oxalic acid or further to CO_2 at high temperatures according to the reactions $H_3C–COOH + 3[UO_2]^{2+} + 6H^+ \rightarrow HOOC–COOH + 3U^{4+} + 4H_2O$ and $HOOC–COOH + [UO_2]^{2+} + 2H^+ \rightarrow 2CO_2 + U^{4+} + 2H_2O$. This reduction is not complete, as, besides $U(SO_4)_2$, uranyl hydrogensulfate can also be isolated. The addition of oxalic acid to the reaction mixture also leads to a mixture of $U(SO_4)_2$ and $UO_2(HSO_4)_2$.

The Th^{4+} and U^{4+} are the largest easily accessible tetravalent metal cations, the radii of which (Th^{4+} 119 pm, U^{4+} 114 pm for eightfold coordination) fall in the typical range of ionic radii of the trivalent rare-earth ions (112 to 130 pm) as well as Ce^{4+} (111 pm).[28] Therefore it is not surprising that the bis-sulfates $An(SO_4)_2$ (An = Th, U) are isotypic to the respective cerium compound, $Ce(SO_4)_2$, and exhibit similarities in coordination environment and bond lengths with other rare-earth sulfates. Another example is the thorium bis-hydrogensulfate sulfate $Th(HSO_4)_2(SO_4)$, which is structurally related to the hexagonal rare-earth hydrogensulfates $RE(HSO_4)_3$ (RE = La–Nd). In this context, a phase transition induced by heating $Th(HSO_4)_2(SO_4)$ towards an undistorted hexagonal structure isotypic to $RE(HSO_4)_3$ is thinkable. A very promising point is the potential proton conductivity of $Th(HSO_4)_2(SO_4)$. The protons probably become mobile along the channels parallel to [100] just by hopping from hydrogensulfate to sulfate ions. An accurate examination along these lines could not be performed up to now due to the small crystal size and sample impurities in $Th(HSO_4)_2(SO_4)$. However, the growth of a larger single crystal and a direction-dependent conductivity measurement at elevated temperatures should be of great interest.

Conclusion

The reaction of $UO_2(CH_3COO)_2{\cdot}2H_2O$ and finely divided ThO_2 with sulfuric acid/sulfur trioxide allowed for the accessibility of a class of compounds nearly undescribed in the literature up to now. First of all, two disulfates and a hydrogensulfate of hexavalent uranium could be synthesised in formal analogy to reactions of high-valent d-block metals with H_2SO_4/SO_3. Furthermore, the bis-sulfates of Th and U as well as two hydrogensulfate sulfates of thorium were obtained that exhibit similarities to rare-earth chemistry. The crystal structures of this class of compounds exhibit some expected trends and analogies to rare-earth and refractory metal chemistry on the one hand, but also show interesting possibilities [for example, the potential H^+ conductivity of $Th(HSO_4)_2(SO_4)$], which encourage further investigations. However, the first step must be the preparation of phase-pure samples of the compounds, then further examinations can be performed. In addition to the above-mentioned proton conductivity of $Th(HSO_4)_2(SO_4)$, spectroscopic studies of the U^{4+} cations in $U(SO_4)_2$ and $Th(SO_4)_2$ doped with U^{4+} are of interest due to the lack of spectroscopic data for tetravalent uranium in the literature.

Experimental Section

Synthesis

$UO_2(S_2O_7)$-lt: A mixture of $UO_2(CH_3COO)_2{\cdot}2H_2O$ (0.1 g) (VEB Berlin-Chemie, Berlin, Germany) and fuming sulfuric acid (1.2 mL) that contained 65% SO_3 (puriss., Merck, Darmstadt, Germany) were sealed in a thick-walled glass ampoule (25 cm in length and 1.5 cm in diameter) and were heated to 175 °C in a block thermostat (Gefran 800P, Liebisch, Bielefeld, Germany). The temperature was maintained for three days and then slowly cooled to room temperature (2.5 °C per hour). The mother liquor was separated from the yellow crystals of $UO_2(S_2O_7)$ by decantation inside a glovebox.

$UO_2(S_2O_7)$-ht: A mixture of $UO_2(CH_3COO)_2{\cdot}2H_2O$ (0.1 g) and fuming sulfuric acid (2 mL) that contained 65% SO_3 were sealed in a thick-walled glass ampoule and were heated to 300 °C in a block thermostat. The temperature was maintained for three days and then slowly cooled to room temperature (3.5 °C per hour). The mother liquor was separated from the yellow needle-shaped crystals of $UO_2(S_2O_7)$ by decantation inside a glovebox.

$U(SO_4)_2$: A mixture of $UO_2(CH_3COO)_2{\cdot}2H_2O$ (0.1 g) and 100% H_2SO_4 (2 mL), which was prepared by adding a stoichiometric

amount of SO_3 in the form of 65% Oleum to commercial 95% H_2SO_4 (BüFa, Oldenburg, Germany), was transferred into a thick-walled glass ampoule. After torch-sealing, the ampoule was heated in a block thermostat to 300 °C for three days and then slowly cooled to room temperature (3.5 °C per hour). Green plates of $U(SO_4)_2$ separated together with yellow blocks as a side product. The mother liquor was separated from the crystals by decantation under an inert atmosphere.

$UO_2(HSO_4)_2$: Uranyl hydrogensulfate was formed as a side product during the synthesis of $U(SO_4)_2$ in the form of yellow crystals, which were separated mechanically from the green plates of $U(SO_4)_2$.

Reaction of ThO_2 with H_2SO_4: A suspension of reactive ThO_2 (0.1 g) in 100% H_2SO_4 (2 mL) was heated in a sealed glass ampoule to 300 °C for three days. After cooling to room temperature (3.5 °C per hour) colourless crystals separated. On a closer look the crystalline precipitate contained at least three different sorts of crystals, which were separated mechanically (Figure 20). The best part was made by small hexagonal needles, which could be identified as $Th(HSO_4)_2(SO_4)$. Furthermore, $Th(SO_4)_2$ was isolated in the form of thin plates. The last component was $Th_4(HSO_4)_2(SO_4)_7$, which crystallised in the form of small polyhedra. Unfortunately, the selective synthesis of phase-pure samples of these thorium sulfates has been unsuccessful up to now.

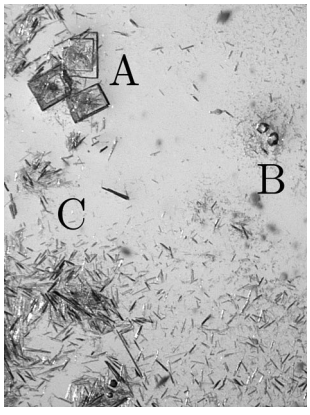

Figure 20. Crystalline product of the reaction between ThO_2 and sulfuric acid. The larger plates (A) are $Th(SO_4)_2$, whereas $Th_4(HSO_4)_2(SO_4)_7$ forms small polyhedral crystals (B). The main product is $Th(HSO_4)_2(SO_4)$, which crystallises in the form of small hexagonal needles (C).

Reactive ThO_2 was prepared by thermal decomposition of the respective thorium oxalate (VEB Laborchemie Apolda, Germany) according to literature procedures.[36]

Structure Determination: The selection of suitable single crystals of all six compounds was performed under inert oil. Afterwards the crystals were mounted inside an oil drop on a glass capillary (0.1 mm in diameter) and were placed into a stream of cold nitrogen (–120 °C) inside the diffractometer (IPDS I, Stoe, Darmstadt, Germany or κ-APEX II, Bruker, Karlsruhe, Germany). After checking the crystal quality and determining the unit-cell parameters, the reflection intensities were collected. A summarisation of the crystallographic data for all compounds can be found in Table 1. Atomic positions and further details of the crystal structure investigations can be obtained from the Fachinformationszentrum Karlsruhe, 76344 Eggenstein-Leopoldshafen, Germany, [fax: +49-7247-808-666; e-mail: crysdata@fiz-karlsruhe.de, http://www.fiz-karlsruhe.de/request_for_deposited_data.html] on quoting the depository numbers given in Table 1.

$UO_2(S_2O_7)$-lt: Structure solution assuming space group $P\bar{1}$ was successful by applying direct methods (SHELXS).[37] Subsequent refinement with SHELXL yielded the complete crystal structure.[38] After introduction of anisotropic displacement parameters, a numerical absorption correction was applied to the reflection data by using the programs X-RED and X-SHAPE.[39,40] Finally, the structure refined to $R_1 = 0.0334$, $wR_2 = 0.0816$ for $F_o > 2\sigma(F_o)$ and $R_1 = 0.0384$, $wR_2 = 0.0825$ for all data. Selected bond lengths for $UO_2(S_2O_7)$-lt are summarised in Table 2.

$UO_2(S_2O_7)$-ht: Structure solution in the acentric space group $Pca2_1$ by using the direct methods of SHELXS was uncomplicated and revealed the position of two uranium atoms. The remaining sulfur and oxygen atoms were located during subsequent refinement cycles with SHELXL. After applying a numerical absorption correc-

Table 1. Crystallographic data for $UO_2(S_2O_7)$-lt and -ht, $UO_2(HSO_4)_2$, $An(SO_4)_2$ (An = Th, U), $Th_4(HSO_4)_2(SO_4)_7$ and $Th(HSO_4)_2(SO_4)$.

	$UO_2(S_2O_7)$	$UO_2(S_2O_7)$	$UO_2(HSO_4)_2$	$U(SO_4)_2$	$Th(SO_4)_2$	$Th_4(HSO_4)_2(SO_4)_7$	$Th(HSO_4)_2(SO_4)$
M_r [g mol^{-1}]	446.15	446.15	464.17	430.15	424.16	1794.72	522.24
a [pm]	647.8(1)	1080.21(2)	779.79(3)	940.11(2)	953.74(3)	1327.7(2)	576.18(2)
b [pm]	684.2(1)	814.74(1)	815.39(3)	898.13(2)	911.49(3)		896.11(3)
c [pm]	800.1(1)	1655.63(3)	1285.77(5)	1349.09(3)	1365.02(4)	1362.8(2)	948.58(3)
α [°]	87.31(2)						65.387(2)
β [°]	78.37(2)		103.700(1)				87.838(2)
γ [°]	75.34(2)						88.917(2)
V [nm^3]	0.33605(9)	1.45710(4)	0.79428(5)	1.13909(4)	1.18665(6)	2.4023(6)	0.44495(3)
Z	2	8	4	8	8	4	2
Space group	$P\bar{1}$	$Pca2_1$	$P2_1/n$	$Pbca$	$Pbca$	$I\bar{4}2d$	$P\bar{1}$
T [°C]	–120	–120	–120	–120	–120	–120	–120
λ [pm]	71.073	71.073	71.073	71.073	71.073	71.073	71.073
$D_{calcd.}$ [g cm^{-3}]	4.409	4.068	3.882	5.016	4.748	4.959	3.898
μ [cm^{-1}]	247.92	228.71	209.95	292.33	258.37	256.35	175.24
R_1[a] [$F_o > 2\sigma(F_o)$]	0.0334	0.0247	0.0226	0.0150	0.0134	0.0220	0.0212
wR_2[b] [$F_o > 2\sigma(F_o)$]	0.0816	0.0564	0.0382	0.0278	0.0300	0.0480	0.0335
R_1[a] (all data)	0.0384	0.0287	0.0287	0.0242	0.0165	0.0243	0.0280
wR_2[b] (all data)	0.0825	0.0574	0.0499	0.0287	0.0306	0.0486	0.0343
Flack-X parameter		0.470(7)				0.02(1)	
CSD number	423493	423494	423492	423491	423489	423490	423488

[a] R_1 is defined as $\Sigma||F_o| - |F_c||/\Sigma|F_o|$ for $I > 2\sigma(I)$. [b] wR_2 is defined as $\{\Sigma w(F_o^2 - F_c^2)^2/\Sigma w(F_o^2)^2\}^{1/2}$.

Table 2. Selected bond lengths for $UO_2(S_2O_7)$-lt.

Bond lengths [pm]			
U1–O11	175.0(6)	S2–O21	143.8(7)
U1–O12	176.1(6)	S2–O22	144.0(8)
U1–O33	241.0(7)	S2–O23	144.7(7)
U1–O32	241.7(7)	S2–O1	159.9(6)
U1–O22	242.0(8)	S3–O31	140.9(8)
U1–O23	243.6(7)	S3–O32	144.6(8)
U1–O21	243.7(6)	S3–O33	145.1(7)
		S3–O1	167.7(7)

tion and introduction of anisotropic displacement parameters, the structure model converged to $R_1 = 0.0247$, $wR_2 = 0.0564$ for $F_o > 2\sigma(F_o)$ and $R_1 = 0.0287$, $wR_2 = 0.0574$ for all data. The Flack-X parameter refined to a value of 0.470(7), so a refinement as racemic twin was applied. However, the structure was searched for a missing centre of symmetry, though only the uranium atoms were found to fulfil a pseudo-inversion symmetry, which is not in accord with any orthorhombic space group. As no correlation between the heavy-atom parameters was found, the choice of the acentric space group $Pca2_1$ in combination with racemic twinning is reasonable. Selected bond lengths for $UO_2(S_2O_7)$-ht are summarised in Table 3.

Table 3. Selected bond lengths for $UO_2(S_2O_7)$-ht.

Bond lengths [pm]			
U1–O11	173.7(5)	S3–O31	142.7(5)
U1–O12	174.2(5)	S3–O32	143.5(5)
U1–O43	238.9(6)	S3–O33	143.8(5)
U1–O62	239.2(5)	S3–O1	159.9(6)
U1–O53	241.4(5)	S4–O41	140.5(7)
U1–O63	242.7(5)	S4–O42	143.5(6)
U1–O21	243.0(5)	S4–O43	144.2(5)
U2–O21	173.6(5)	S4–O1	165.0(5)
U2–O22	175.4(5)	S5–O51	140.5(7)
U2–O32	238.8(5)	S5–O52	143.5(6)
U2–O61	238.8(5)	S5–O53	144.2(5)
U2–O42	240.8(5)	S5–O2	164.9(5)
U2–O52	240.9(6)	S6–O61	143.4(5)
U2–O33	245.8(5)	S6–O62	143.8(5)
		S6–O63	144.5(5)
		S6–O2	164.9(5)

$UO_2(HSO_4)_2$: The structure was easily solved in the monoclinic space group $P2_1/n$ by using SHELXS direct methods. Subsequent refinement with SHELXL revealed the complete crystal structure. After applying a numerical absorption correction to the data and introducing anisotropic displacement parameters the hydrogen atom coordinates could be refined. Finally, the structure model refined to $R_1 = 0.0226$, $wR_2 = 0.0482$ for $F_o > 2\sigma(F_o)$ and $R_1 = 0.0287$, $wR_2 = 0.0499$ for all data. Selected bond lengths for $UO_2(HSO_4)_2$ are summarised in Table 4.

$An(SO_4)_2$ (An = Th, U): Systematic absences suggested the orthorhombic space group *Pbca* and structure solution was easily possible assuming this space group by using direct methods of SHELXS. After a few refinement cycles with SHELXL, the complete crystal structure could be revealed. A numerical absorption correction was applied to the data and anisotropic displacement parameters were introduced. Finally, the structure refined to $R_1 = 0.0134$, $wR_2 = 0.0300$ for $F_o > 2\sigma(F_o)$ and $R_1 = 0.0165$, $wR_2 = 0.0306$ for all data for $Th(SO_4)_2$ and $R_1 = 0.0150$, $wR_2 = 0.0278$ for $F_o > 2\sigma(F_o)$ and $R_1 = 0.0242$, $wR_2 = 0.0287$ for all data for $U(SO_4)_2$. Selected bond lengths for $An(SO_4)_2$ (An = Th, U) are summarised in Table 5.

Table 4. Selected bond lengths for $UO_2(HSO_4)_2$.

Bond lengths [pm]			
U1–O11	174.4(3)	S2–O21	144.5(3)
U1–O12	175.0(3)	S2–O22	145.2(3)
U1–O21	237.8(3)	S2–O23	145.5(3)
U1–O31	238.8(3)	S2–O24	153.6(4)
U1–O32	241.3(3)	S3–O31	144.9(3)
U1–O33	241.4(3)	S3–O32	145.0(3)
U1–O22	242.0(3)	S3–O33	145.4(3)
		S3–O34	153.0(4)
O24–H24	75(3)	O34–H34	75(3)

Table 5. Selected bond lengths for $An(SO_4)_2$ (An = Th, U).

Bond lengths [pm]			
Th1–O14	235.8(2)	U1–O14	230.9(2)
Th1–O11	238.2(2)	U1–O24	232.7(2)
Th1–O23	238.2(2)	U1–O23	232.8(2)
Th1–O24	238.5(2)	U1–O13	233.7(2)
Th1–O13	238.8(2)	U1–O22	234.6(2)
Th1–O22	239.2(2)	U1–O11	235.1(2)
Th1–O21	240.9(2)	U1–O21	237.7(2)
Th1–O12	245.3(2)	U1–O12	240.2(2)

$Th_4(HSO_4)_2(SO_4)_7$: Structure solution in the tetragonal *I*-centered space group $I\bar{4}2d$ by using the direct methods of SHELXS revealed the position of the thorium atom. Missing sulfur and oxygen atoms were located during subsequent refinement cycles with SHELXL. A numerical absorption correction was applied to the data and anisotropic displacement parameters were introduced. The refinement of the hydrogensulfate hydrogen atom could only be performed by applying weak O–H and S–H distance restraints. However, the position of the hydrogen atom is plausible with respect to hydrogen bonding. Finally, the structure refined to $R_1 = 0.0220$, $wR_2 = 0.0480$ for $F_o > 2\sigma(F_o)$ and $R_1 = 0.0243$, $wR_2 = 0.0486$ for all data. The correct absolute structure is indicated by a Flack-X parameter of 0.02(1). Selected bond lengths for $Th_4(HSO_4)_2(SO_4)_7$ are summarised in Table 6.

Table 6. Selected bond lengths for $Th_4(HSO_4)_2(SO_4)_7$.

Bond lengths [pm]			
Th1–O11	236.9(5)	S1–O11	146.7(6)
Th1–O21	238.8(5)	S1–O12	147.3(6)
Th1–O31	240.0(6)	S2–O21	146.6(5)
Th1–O22	240.5(5)	S2–O22	146.8(5)
Th1–O41	242.1(6)	S3–O31	146.1(6)
Th1–O32	246.0(6)	S3–O32	147.4(6)
Th1–O12	246.6(6)	S4–O41	147.3(5)
Th1–O51	247.3(6)	S5–O51	143.1(6)
Th1–O52	250(2)	S5–O52	154(2)
Th1–O52A	278(2)	S5–O52A	150(2)
		O52–H1	105(7)

$Th(HSO_4)_2(SO_4)$: The crystal structure was solved by assuming the space group $P\bar{1}$ by using the direct methods of SHELXS, which allowed us to determine the location of the thorium atom. Subsequent refinement with SHELXL revealed missing sulfur and oxygen atoms. After applying a numerical absorption correction to the data and introduction of anisotropic displacement parameters, the

coordinates of both hydrogensulfate hydrogen atoms could be refined. Finally, the structure model converged to $R_1 = 0.0212$, $wR_2 = 0.0335$ for $F_o > 2\sigma(F_o)$ and $R_1 = 0.0280$, $wR_2 = 0.0343$ for all data. Selected bond lengths for $Th(HSO_4)_2(SO_4)$ are summarised in Table 7.

Table 7. Selected bond lengths for $Th(HSO_4)_2(SO_4)$.

Bond lengths [pm]			
Th1–O13	236.1(3)	S1–O11	145.7(3)
Th1–O12	236.3(3)	S1–O12	146.3(3)
Th1–O14	237.0(3)	S1–O13	147.1(3)
Th1–O22	242.9(3)	S1–O14	147.6(3)
Th1–O23	244.4(3)	S2–O21	144.4(3)
Th1–O32	244.8(3)	S2–O22	144.5(3)
Th1–O31	245.6(3)	S2–O23	145.5(3)
Th1–O21	248.4(3)	S2–O24	154.1(4)
Th1–O33	249.1(3)	S3–O31	144.9(3)
		S3–O32	145.4(3)
O24–H24	76(3)	S3–O33	146.7(3)
O34–H34	76(3)	S3–O34	152.5(3)

Acknowledgments

The authors thank Mr. Wolfgang Saak for the collection of the X-ray data. We also thank the Fonds der Chemischen Industrie and the Heinz-Neumüller-Stiftung for granting a stipend to U. B. Funding through the Deutsche Forschungsgemeinschaft (DFG) is also gratefully acknowledged.

[1] M. Pley, M. S. Wickleder, *Z. Anorg. Allg. Chem.* **2004**, *630*, 1036–1039.
[2] M. Pley, M. S. Wickleder, *Eur. J. Inorg. Chem.* **2005**, 529–535.
[3] M. Pley, M. S. Wickleder, *Angew. Chem.* **2004**, *116*, 4262; *Angew. Chem. Int. Ed.* **2004**, *43*, 4168–4170.
[4] S. S. Pollack, *Inorg. Chem.* **1987**, *26*, 1825–1826.
[5] U. Betke, M. S. Wickleder, *Inorg. Chem.* **2011**, *50*, 858–872.
[6] U. Betke, K. Neuschulz, M. S. Wickleder, *Chem. Eur. J.* **2011**, *17*, 8538–8541.
[7] U. Betke, M. S. Wickleder, *Eur. J. Inorg. Chem.* **2011**, 4400–4413.
[8] N. van der Putten, B. O. Loopstra, *Cryst. Struct. Commun.* **1974**, *3*, 377–380.
[9] N. P. Brandenburg, B. O. Loopstra, *Cryst. Struct. Commun.* **1973**, *2*, 243–246.
[10] A. Zalkin, H. Ruben, D. H. Templeton, *Inorg. Chem.* **1978**, *17*, 3701–3702.
[11] N. P. Brandenburg, B. O. Loopstra, *Acta Crystallogr., Sect. B: Struct. Sci.* **1978**, *34*, 3734–3736.
[12] M. S. Wickleder, B. Fourest, P. K. Dorhout, *The Chemistry of the Actinide and Transactinide Elements*, fourth edition, chapter 3: *Thorium*, Springer, Dordrecht, The Netherlands, **2010**.
[13] J. Habash, A. J. Smith, *Acta Crystallogr., Sect. C: Cryst. Struct. Commun.* **1983**, *39*, 413–415.
[14] P. Kierkegaard, *Acta Chem. Scand.* **1956**, *10*, 599–616.
[15] A. J. Albrecht, G. E. Sigmon, L. Moore-Shay, R. Wei, C. Dawes, J. Szymanowski, P. C. Burns, *J. Solid State Chem.* **2011**, *184*, 1591–1597; K. E. Knope, R. E. Wilson, S. Skanthakumar, L. Soderholm, *Inorg. Chem.* **2011**, *50*, 8621–8629.
[16] M. S. Wickleder, *Z. Anorg. Allg. Chem.* **1998**, *624*, 1583–1587.
[17] M. S. Wickleder, *Z. Anorg. Allg. Chem.* **1998**, *624*, 1347–1354.
[18] M. S. Wickleder, *Z. Anorg. Allg. Chem.* **2000**, *626*, 621–622.
[19] S. Schwarzer, *Neuartige Sulfate der Platin- und Selten-Erd-Metalle*, Dissertation, University of Oldenburg, Germany, **2010**.
[20] M. S. Wickleder, *Z. Anorg. Allg. Chem.* **2000**, *626*, 1468–1472.
[21] I. D. Brown, D. Altermatt, *Acta Crystallogr., Sect. B: Struct. Sci.* **1985**, *41*, 244–247.
[22] K. Ståhl, T. Balic-Zunic, F. da Silva, K. M. Eriksen, R. W. Berg, R. Fehrmann, *J. Solid State Chem.* **2005**, *178*, 1697–1704.
[23] H. Lynton, M. R. Truter, *J. Chem. Soc.* **1960**, 5112–5118.
[24] M. A. Simonov, S. V. Shkovrov, S. I. Troyanov, *Sov. Phys. Crystallogr.* **1988**, *33*, 297–297.
[25] F. W. B. Einstein, A. C. Willis, *Acta Crystallogr., Sect. B: Struct. Sci.* **1981**, *37*, 218–220.
[26] J. Bruns, M. S. Wickleder: unpublished results.
[27] D. L. Rogachev, M. A. Porai-Koshits, V. Y. Kuznetsov, L. M. Dikareva, *J. Struct. Chem.* **1974**, *15*, 397–401.
[28] A. F. Holleman, N. Wiberg, *Lehrbuch der Anorganischen Chemie*, 102nd ed., de Gruyter, Berlin, Germany, **2007**.
[29] C. J. Ballhausen, H. B. Gray, *Inorg. Chem.* **1962**, *1*, 111–122.
[30] H. B. Gray, C. R. Hare, *Inorg. Chem.* **1962**, *1*, 363–368.
[31] K. Tatsumi, R. Hoffmann, *Inorg. Chem.* **1980**, *19*, 2656–2658.
[32] R. G. Denning, *Struct. Bonding (Berlin)* **1992**, *79*, 215–276.
[33] R. G. Denning, *J. Phys. Chem. A* **2007**, *111*, 4125–4143.
[34] A. F. Christiansen, H. Fjellvåg, A. Kjekshus, B. Klewe, *J. Chem. Soc., Dalton Trans.* **2001**, *6*, 806–815.
[35] U. Betke, M. S. Wickleder, *unpublished results.*
[36] G. Brauer, *Handbuch der präparativen anorganischen Chemie*, vol. III, Enke Verlag, Stuttgart, Germany, **1981**.
[37] G. M. Sheldrick, *SHELXS-97 – Program for the Solution of Crystal Structures*, University of Göttingen, Germany, **1997**; A short history of SHELX: G. M. Sheldrick, *Acta Crystallogr., Sect. A: Found. Crystallogr. A* **2008**, *64*, 112–122.
[38] G. M. Sheldrick, *SHELXL-97 – Program for the Refinement of Crystal Structures*, University of Göttingen, Germany, **1997**.
[39] *X-RED 1.22* – Data Reduction for STADI4 and IPDS, Stoe & Cie, Darmstadt, Germany, **2001**.
[40] *X-SHAPE 1.06f* – Crystal Optimization for Numerical Absorption Correction, Stoe & Cie, Darmstadt, Germany, **1999**.

Received: September 13, 2011
Published Online: December 6, 2011

DOI: 10.1002/ejic.201101032

New Approach to [FeFe]-Hydrogenase Models Using Aromatic Thioketones

Ahmad Q. Daraosheb,[a] Ulf-Peter Apfel,[a][‡] Helmar Görls,[a] Christian Friebe,[b] Ulrich S. Schubert,[b] Mohammad El-khateeb,[c][‡‡] Grzegorz Mloston,*[d] and Wolfgang Weigand*[a]

Dedicated to Professor Heinz Heimgartner on the occasion of his 70th birthday

Keywords: Bioinorganic chemistry / Enzyme mimics / Hydrogenase models / Electrochemistry / Sulfur heterocycles / Thioketones / Iron

The reactions of triiron dodecacarbonyl with thiobenzophenone (**2a**) and 9*H*-thioxanthene-9-thione (**2b**) were investigated under different conditions. In the case of a 1:1 molar ratio of triiron dodecacarbonyl and **2a** or **2b**, the *ortho*-metallated complexes $[Fe_2(CO)_6\{\mu,\kappa,S,SCH(C_6H_5)C_6H_4\text{-}\eta^2\}]$ (**3a**) and $[Fe_2(CO)_6\{\mu,\kappa,S,SCH(C_6H_4)\text{–}S\text{–}C_6H_3\text{-}\eta^2\}]$ (**4a**) were obtained as the major products, respectively. In contrast, the treatment of triiron dodecacarbonyl with an excess of **2a** or **2b** afforded $[Fe_2(CO)_6\{\mu\text{-}SCH(C_6H_5)C_6H_4S\text{-}\mu\}]$ (**3b**) and $[Fe_2(CO)_6\{\mu\text{-}SCH(C_6H_4)\text{–}S\text{–}C_6H_3S\text{-}\mu\}]$ (**4b**), respectively, which are both bioinspired models for the active site of [FeFe]-hydrogenase. In addition to these complexes, the two reactions afforded $[Fe_2(CO)_6\{\mu\text{-}SC(C_6H_5)_2S\text{-}\mu\}]$ (**3c**) and $[Fe_2(CO)_6\{\mu\text{-}SC(C_6H_4\text{–}S\text{–}C_6H_4)S\text{-}\mu\}]$ (**4c**). Furthermore, $[\{Fe_2(CO)_6\{\mu\text{-}SCH(C_6H_5)_2\}\}_2(\mu^4\text{-}S)]$ (**3d**) was isolated from the reaction of $Fe_3(CO)_{12}$ with **2a**. The molecular structures of all of the new complexes were determined from the spectroscopic and analytical data and the crystal structures for **3c**, **3d**, **4b**, and **4c** were obtained. A plausible mechanism for the formation of the isolated complexes that involves dithiirane derivatives as the key intermediates is proposed. Herein, thioketones **2a** and **2b** act as sulfur transfer reagents. The electrochemical experiments showed that complex **3b** behaves as a catalyst for the electrochemical reduction of protons from acetic acid.

Introduction

Nature has developed highly efficient enzymes that regulate the generation and depletion of H_2.[1–4] These enzymes are called hydrogenases and can be classified into three major groups according to the metal content of their active sites, namely, [FeFe]-, [NiFe]-, and [Fe]-hydrogenases.[5] The [FeFe]-hydrogenases have a higher hydrogen production ability compared to that of other hydrogenases.[6–8] Microorganisms have used H_2 as a primary fuel source for billions of years and consume an enormous amount of H_2 in different forms as an energy source and as a transporter.[9]

Inspired by the rapid and reversible proton reduction that is catalyzed by these hydrogenase enzymes, considerable research has been devoted to the design and synthesis of model species that mimic the active sites of the hydrogenases.[10]

Recently, we investigated the oxidative addition of the di- or tetra-substituted 1,2,4-trithiolans to iron carbonyl compounds in an attempt to produce [FeFe]-hydrogenase model complexes.[11a]

In an earlier investigation of the reaction of 3,3,5,5-tetraphenyl-1,2,4-trithiolane (**1**) with $Fe_3(CO)_{12}$,[11b] we observed a different reaction pathway to that of the corresponding tetra-alkyl-substituted analogues. The latter react with iron carbonyl complexes to yield the oxidative addition products that result from the cleavage of the S–S bond. In contrast, the former undergoes a [2+3]-cycloreversion reaction[12,13a] and the fragments [e.g., $Ph_2C{=}S$ (**2a**)] react with the iron carbonyl complexes to yield the *ortho*-metallated complex **3a** as the major component of the reaction mixture.[11b–11e] In the same paper, the *ortho*-metallated complexes **3e**, **3f**, and **3g** (Figure 1) were obtained after the aro-

[a] Institut für Anorganische und Analytische Chemie, Friedrich-Schiller-Universität, Humboldtstraße 8, 07743 Jena, Germany
Fax: +49-3641-948102
E-mail: wolfgang.weigand@uni-jena.de
[b] Laboratory of Organic and Macromolecular Chemistry (IOMC) and Jena Center for Soft Matter (JCSM), Friedrich-Schiller-Universität Jena, Humboldtstr. 10, 07743 Jena, Germany
[c] Faculty of Science and Arts at Alkamil, King Abdul Aziz University, P. O. Box 110, Alkamil 21931, Kingdom of Saudi Arabia
[d] University of Lodz, Department of Organic and Applied Chemistry, Tamka 12, 91-403 Lodz, Poland
[‡] Current address: Department of Chemistry, Massachusetts Institute of Technology, Cambridge, MA 02139, USA
[‡‡] Permanent address: Chemistry Department, Jordan University of Science and Technology, P. O. Box 3030, Irbid 22110, Jordan

matic thioketones 4,4′-bis(dimethylamino)-thiobenzophenone, dibenzosuberenethione, and xanthione, respectively, were treated with $Fe_3(CO)_{12}$.

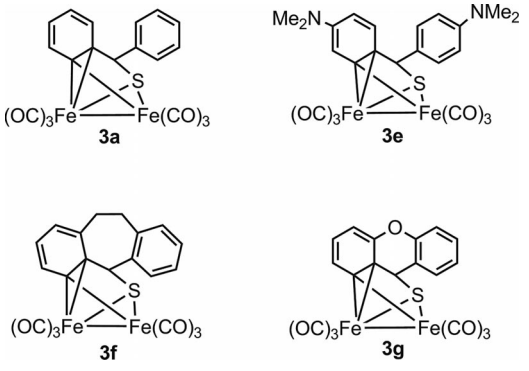

Figure 1. The *ortho*-metallated complexes **3a** and **3e**–**g**.

These observations prompted us to investigate the reaction of **2a** and 9H-thioxanthene-9-thione (**2b**) with $Fe_3(CO)_{12}$, and to examine the reactivity of the complexes of type **3** that were initially obtained under the applied reaction conditions. The structures of the isolated *ortho*-metallated complexes **3a** and **3e**–**g** (Figure 1) suggested that these compounds can play the role of key intermediates in the synthesis of new iron complexes that may be unattainable otherwise.

In the present work we demonstrate the role of the *ortho*-metallated complexes as precursors for the synthesis of the new [FeFe]-hydrogenase model complexes. In addition, the synthesis and the structural characterization of the two synthetic targets **3b** and **4b**, as well as the proposed mechanism (Scheme 3) of their formation, are described. To the best of our knowledge, this is the first study to illustrate the synthesis of the 1,3-dithiolato-diiron complexes from the symmetrical aromatic thioketones.

Results and Discussion

The reaction of $Fe_3(CO)_{12}$ with one equivalent of thiobenzophenone (**2a**) or 9H-thioxanthene-9-thione (**2b**) in thf at reflux for 20 min resulted in the formation of the *ortho*-metallated complexes, [$Fe_2(CO)_6${μ,κ,*S*,SCH(C_6H_5)C_6H_4-η^2}] (**3a**) and [$Fe_2(CO)_6${μ,κ,*S*,SCH(C_6H_4)–S–C_6H_3-η^2}] (**4a**), respectively, as the major products. In addition to **3a**, complexes [$Fe_2(CO)_6${μ-SCH(C_6H_5)C_6H_4S-μ}] (**3b**) and [$Fe_2(CO)_6${μ-SC(C_6H_5)$_2$S-μ}] (**3c**) were produced from the reaction of $Fe_3(CO)_{12}$ with **2a**. Similarly, complexes [$Fe_2(CO)_6${μ-SCH(C_6H_4)–S–C_6H_3S-μ}] (**4b**) and [$Fe_2(CO)_6$-{μ-SC(C_6H_4–S–C_6H_4)S-μ}] (**4c**) were isolated along with **4a** from the reaction of $Fe_3(CO)_{12}$ with **2b** (Schemes 1 and 2).

It must be noted, however, that products **3b**, **3c**, **4b**, and **4c** were obtained in trace amounts in these reactions. In contrast, the treatment of $Fe_3(CO)_{12}$ with an excess of **2a** or **2b** in thf at reflux for ca. 3 h gave the [2Fe2S]-model complexes, **3b**–**c** and **4b**–**c**, respectively, in moderate yields. Unexpectedly, the tetranuclear complex, [{$Fe_2(CO)_6${μ-SCH(C_6H_5)$_2$}}$_2$(μ^4-S)] (**3d**), and known tetraphenylethylene

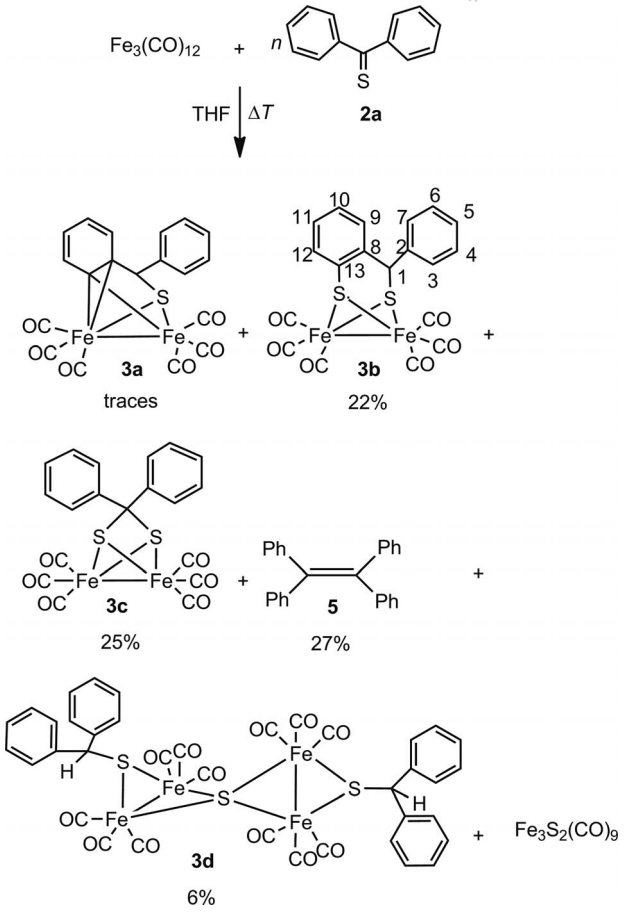

Scheme 1. The reaction of $Fe_3(CO)_{12}$ with **2a** where (a) *n* is 1, the reaction time is 20 min, **3a** (major), **3b** and **3c** (traces), and (b) *n* is 3, the reaction time is 180 min, and the main products are **3b**–**d** and **5**.

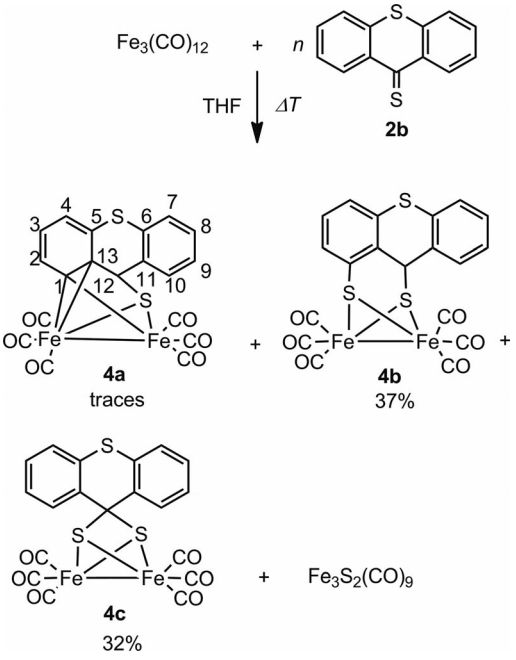

Scheme 2. The reaction of $Fe_3(CO)_{12}$ with **2b** where (a) *n* is 1, the reaction time is 20 min, **4a** (major), **4b** and **4c** (traces) and (b) *n* is 3, the reaction time is 180 min, and the main products are **4b** and **4c**.

(**5**) were obtained from the reaction of **2a** with $Fe_3(CO)_{12}$. Complexes **3b**–**d** and **4a**–**c** are air-stable in the solid state for months and for several hours in solution. It is worth noting that these complexes are fairly soluble in common organic solvents including the hydrocarbons. It is interesting to note that there is only one sulfur atom in the structures of starting thioketones **2a** and **2b**. The reaction of these compounds with $Fe_3(CO)_{12}$, however, furnished the [2Fe2S] complexes, **3b**, **3c**, **4b**, and **4c**, and the [4Fe3S] complex, **3d**. Thus, an important question arose about the source of the additional sulfur atom in these complexes. A possible explanation is based on the assumption that these thioketones act as sulfur transfer reagents. If this assumption is true, then the question arises as to whether or not these thioketones can be used as efficient precursors for [FeFe]-hydrogenase model synthesis. In order to find convincing answers for these questions, we investigated the reaction of **3a** with **2a**. This reaction led to the formation of complex **3b** in a moderate yield, which suggests that **2a** is acting as a sulfur transfer reagent, while **3a** is an important intermediate in the multistep synthesis of the [FeFe]-hydrogenase model complexes of the type **3b**. A plausible mechanism for the formation of complex **3b** from **3a** is shown in Scheme 3. The postulated reactive intermediate **8** plays a key role in the formation of **3b**. A similar reaction pathway has already been described by Eisch et al.[13c]

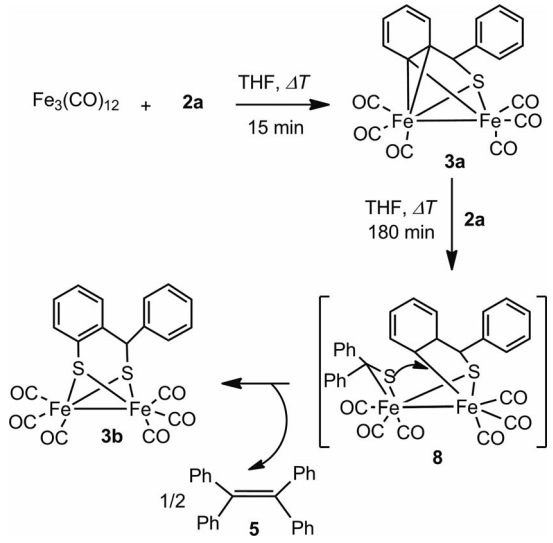

Scheme 3. The proposed mechanism for the formation of **3b** from **3a**.

Complex **3c** is believed to be produced by the oxidative addition of $Fe_3(CO)_{12}$ along the S–S bond of the in situ-generated diphenyldithiirane (**7**). The latter could be formed from **2a** by means of a stepwise mechanism (Scheme 4) under the catalytic influence of the carbonyliron complex that is present in the reaction mixture. Thiobenzophenone *S*-sulfide (thiosulfine) (**6**) is believed to be a reactive intermediate in the formation of **7**. On the other hand, compound **6** could play the role of a sulfur transfer reagent in the process that leads to the formation of complex **3d** (Scheme 5). Saito et al. described the conversion of a special type of thioketone to dithiiranes by means of heating the corresponding thioketone with S_8.[13b] In addition, Huisgen and Rapp have also suggested that "the thioketone itself can be converted to a sulfur donor that is capable of generating the thione *S*-sulfide in an unidentified pathway".[13a]

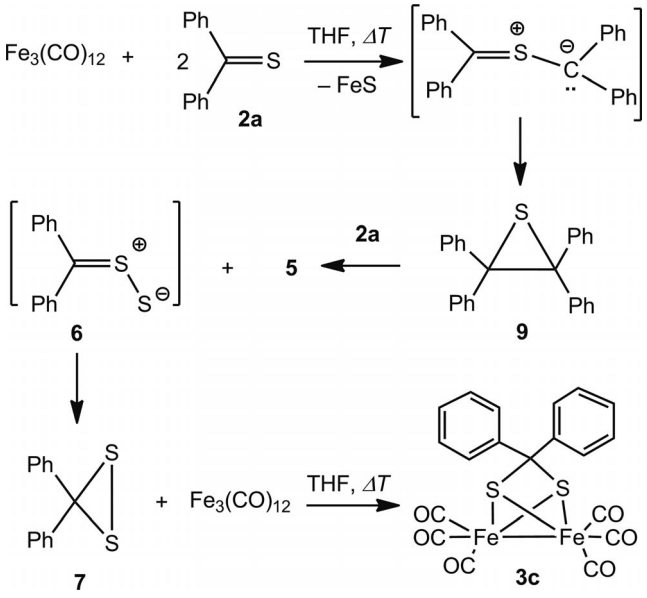

Scheme 4. The reaction pathway for the formation of **3c** via the intermediate diphenyldithiirane (**7**).

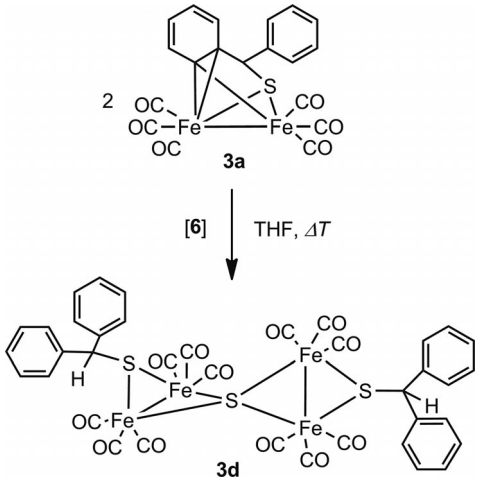

Scheme 5. The proposed mechanism for the conversion of the initially formed **3a** into the dinuclear complex **3d** by means of a sulfur transfer mechanism.

The ^1H and $^{13}C\{^1H\}$ NMR spectra of **4a** exhibit signals at δ = 4.86 and 60.7 ppm, respectively, which were attributed to the methine group. These resonances, as well as the other signals in the ^1H and $^{13}C\{^1H\}$ NMR spectra of **4a**, are in the same range as those observed for the analogue complexes **3a** and **3e**–**g**. The ^1H NMR spectra for **3c** and **4c** show a broad signal at δ = 7.57 ppm (for **3c**) and two broad resonances at δ = 7.42 and 7.74 ppm (for **4c**), which were attributed to the aromatic protons. In addition, there are no signals at $\delta < 6.2$ ppm to indicate the presence of

methine protons in these complexes. The ^{1}H NMR spectra of **3b** and **4b** show a singlet at δ = 5.90 and 5.28 ppm, respectively, which corresponds to the methine protons. These values are shifted downfield compared to those of the analogues **3a** and **4a**, respectively. The ^{1}H NMR spectrum of **3d** reveals the presence of two methine groups and the resonances for these protons are found at δ = 4.21 and 4.66 ppm, respectively. The ^{13}C NMR spectra of **3b**–**d** and **4a**–**c** display the resonances of the C=O groups in the range of 207 to 210 ppm. Finally, the IR spectra of complexes **3b**–**d** and **4a**–**c** display three major absorption bands in the region of 2075 to 1985 cm^{-1}, which are typical for carbonyl groups that are bonded to iron atoms.

The molecular structures of complexes **3c**, **3d**, **4b**, and **4c** were confirmed by X-ray diffraction analysis and are shown in Figures 2, 3, 4, and 5, respectively. The central [2Fe2S] moieties of these complexes are in the "butterfly" arrangement and have a distorted octahedral geometry around the iron center. The thiolato sulfur atoms S(1) and S(2) are μ^2-coordinated to Fe(1) and Fe(2) in the structures of **3c**, **4b**, and **4c**. However, the two sulfur atoms of the bridging dithiolato ligand of complex **4b** are connected to different carbon atoms. One of the sulfur atoms is bonded to an aliphatic carbon while the other one is bonded to an aromatic carbon. In complexes **3c** and **4c**, on the other hand, the sulfur atoms are both bonded to the same aliphatic carbon. All of the iron atoms in tetranuclear complex **3d** are bonded to the same sulfur atom (S3) and, in addition, the thiolato sulfur atoms S(1) and S(2) are μ^2-coordinated to Fe(1), Fe(2) and Fe(3), Fe(4), respectively. The Fe–Fe bond length of **4b** [2.5218(5) Å] is comparable to those reported for the [FeFe]-hydrogenase model complexes[10i,10l,14–20] and to that of **3d** [2.5246 Å (mean)], but it is longer than the corresponding bond lengths in the analogous complexes **3e** [2.4993(6) Å][11b] and **4c** [2.4867(4) Å]. In addition, the Fe–S bond lengths of **4b** [2.2396 Å (mean)] are significantly shorter than those reported for the [FeFe]-hydrogenase model complexes[21–27] and are about 0.02 Å shorter than those of **4c** [2.2694 Å (mean)] and of **3c** [2.2673 Å (mean)]. The Fe–Fe bond length of **3c** [2.4850(5) Å] is similar to that of the reported analogous complex **3a** [2.4986(6) Å].[11b] The angles of S(1)–Fe(1)–S(2) [85.22(2)°] and S(1)–Fe(2)–

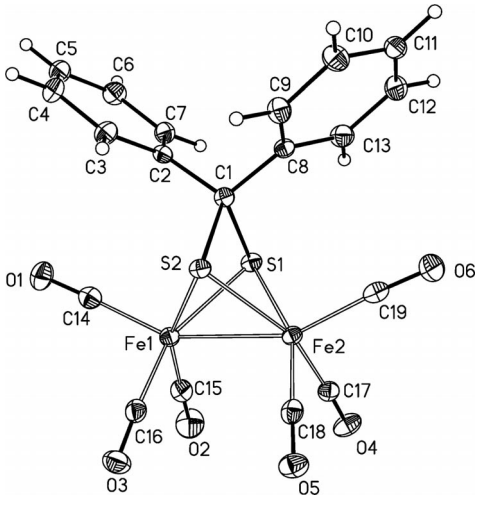

Figure 2. The ORTEP drawing of [$Fe_2(CO)_6${μ-SC(C_6H_5)$_2$S-μ}] (**3c**) with the thermal ellipsoids set at the 50% probability level. The selected distances [Å] and angles [°] are Fe(1)–Fe(2) 2.4867(4), Fe(1)–S(1) 2.2785(6), Fe(1)–S(2) 2.2625(6), Fe(2)–S(1) 2.2757(6), Fe(2)–S(2) 2.2608(6), Fe(1)–S(1)–Fe(2) 66.190(19), Fe(1)–S(2)–Fe(2) 66.699(19), S(1)–Fe(1)–S(2) 72.21(2), and S(1)–Fe(2)–Fe(1) 56.618(17).

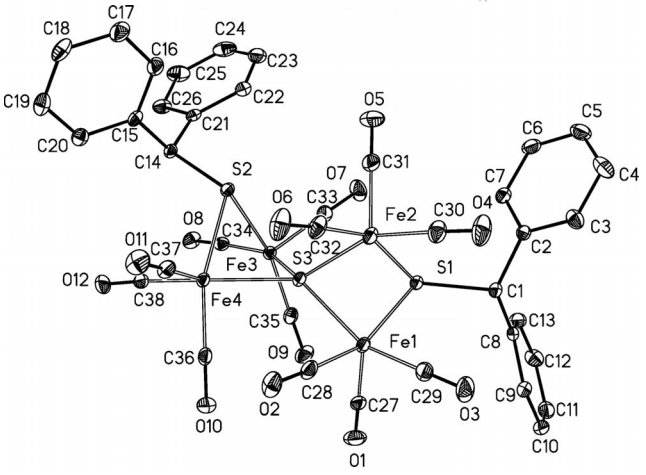

Figure 3. The ORTEP drawing of [{$Fe_2(CO)_6${μ-SCH(C_6H_5)$_2$}}$_2$-(μ^4-S)] (**3d**) with the thermal ellipsoids set at the 50% probability level. The hydrogen atoms were omitted for clarity. The selected distances [Å] and angles [°] are Fe(1)–Fe(2) 2.5195(3), Fe(3)–Fe(4) 2.5297(4), Fe(1)–S(1) 2.2555(5), Fe(2)–S(1) 2.2625(5), Fe(1)–S(3) 2.2321(5), Fe(2)–S(3) 2.2443(4), Fe(3)–S(2) 2.2701(5), Fe(4)–S(2) 2.2637(5), Fe(3)–S(3) 2.2344(5), Fe(4)–S(3) 2.2379(5), Fe(1)–S(1)–Fe(2) 67.789(16), Fe(1)–S(3)–Fe(2) 68.505(15), Fe(3)–S(2)–Fe(4) 67.831(14), Fe(3)–S(3)–Fe(4) 68.849(15), Fe(1)–S(3)–Fe(3) 136(74), S(2)–Fe(4)–S(3) 76.324(17), and S(1)–Fe(2)–Fe(1) 55.974(13).

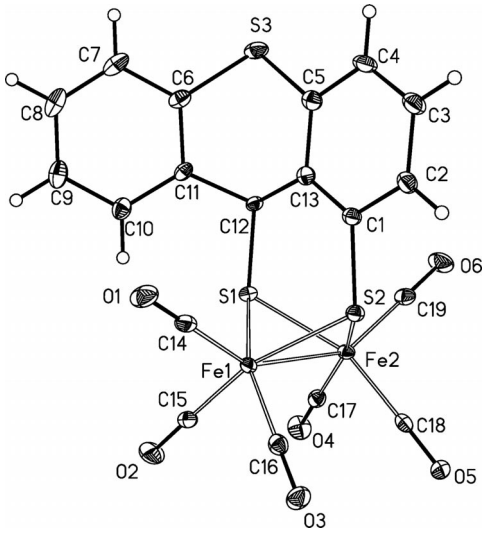

Figure 4. The ORTEP drawing of [$Fe_2(CO)_6${μ-SCH(C_6H_4)–S–C_6H_4S-μ}] (**4b**) with the thermal ellipsoids set at the 50% probability level. The selected distances [Å] and angles [°] are Fe(1)–Fe(2) 2.5218(5), Fe(1)–S(1) 2.2415(6), Fe(1)–S(2) 2.2340(6), Fe(2)–S(1) 2.2417(7), Fe(2)–S(2) 2.2412(7), Fe(1)–S(1)–Fe(2) 68.46(2), Fe(1)–S(2)–Fe(2) 66.60(2), S(1)–Fe(2)–S(2) 85.05(2), and S(1)–Fe(2)–Fe1 55.767(18).

S(2) [85.02(2)°] in **4b** are within the same ranges as those observed for the [FeFe]-hydrogenase model complexes.[14–27] However, these angles are wider than the corresponding angles of S(1)–Fe(1)–S(2) [72.21(2)°] and S(1)–Fe(2)–S(2) [72.29(2)°] in **4c**, and of S(1)–Fe(1)–S(2) [72.26(2)°] and S(1)–Fe(2)–S(2) [72.17(2)°] in **3c**, which is attributed to the bonding of the two sulfur atoms of the dithiolato ligand to the same carbon in **3c** or **4c**.

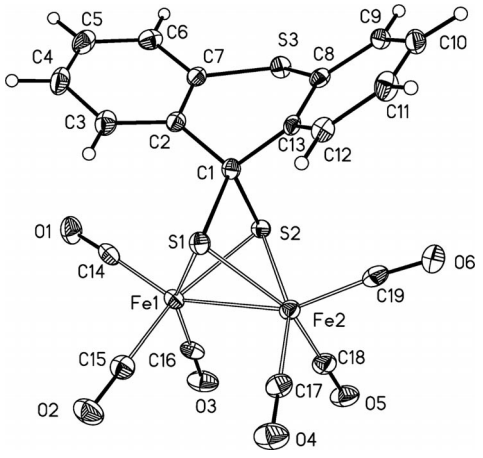

Figure 5. The ORTEP drawing of $[Fe_2(CO)_6\{\mu\text{-}SC(C_6H_4\text{–}S\text{–}C_6H_4)\text{-}S\text{-}\mu\}]$ (**4c**) with the thermal ellipsoids set at the 50% probability level. The selected distances [Å] and angles [°] are Fe(1)–Fe(2) 2.4850(5), Fe(1)–S(1) 2.2693(6), Fe(1)–S(2) 2.2629(6), Fe(2)–S(1) 2.2643(6), Fe(2)–S(2) 2.2728(7), Fe(1)–S(1)–Fe(2) 66.478(19), Fe(1)–S(2)–Fe(2) 66.44(2), S(1)–Fe(1)–S(2) 72.26(2), and S(1)–Fe(1)–Fe(2) 56.666(18).

Electrochemical Investigations

The electrocatalytic dihydrogen formation of the [FeFe]-hydrogenase model compounds has been well established.[28] In order to show the ability of the new complexes to act as catalyst for dihydrogen formation, cyclic voltammetry was performed for compound **3b** in the presence and absence of acetic acid. The cathodic scan of complex **3b** (Figure 6) reveals an irreversible reduction peak at $E_{p,red}$ = –1.58 V. In comparison to the internal standard ferrocene, this signal is most likely a one-electron reduction and was therefore attributed to the $[Fe^IFe^I] \rightarrow [Fe^IFe^0]^-$ process. The signal remained completely irreversible at the different scan rates (1.5, 1.0, 0.8, 0.1, and 0.05 V/s). This behavior suggests an EC mechanism where the $[Fe^IFe^I]$ state is transferred into $[Fe^IFe^0]^-$ by a one-electron reduction, followed by a fast change in the bonding properties within the molecule, which is in good agreement with the literature results.[29,30] This change in the bonding properties can be best described by the cleavage of the Fe–Fe bond and/or the appearance of a bridging carbonyl molecule.[29] At –2.15 V a further reduction of the chemically changed $[Fe^IFe^0]$ species was observed, which was attributed to the $[Fe^IFe^0]^- \rightarrow [Fe^0Fe^0]^{2-}$ process in accordance with $Fe_2(CO)_6(pdt)$ (pdt = propanedithiolato).[31] Two sparsely separated reoxidation signals were observed at –2.07 and –2.00 V. An additional oxidation peak appears at –0.80 V. This signal was only observed upon the initial one-electron reduction of the initial $[Fe^IFe^I]$ species at –1.58 V. According to the literature, this might be the reoxidation of a chemically transformed $[Fe^IFe^0]$ species.[29] At ca. +1.28 V the irreversible oxidation of the $[Fe^IFe^I]$ cluster can be observed. A corresponding reduction signal appeared at –0.67 mV, which suggests that there was structural reorganization after the oxidation and that it was not solely a simple reduction of the obtained $[Fe^{II}Fe^I]$ complex as has been already described for similar reduction processes.

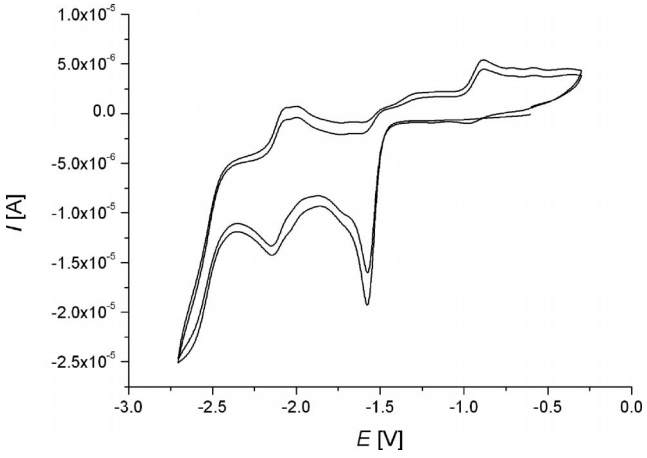

Figure 6. The cyclic voltammetric reduction of $[Fe_2(CO)_6\{\mu\text{-}SCH(C_6H_5)C_6H_4S\text{-}\mu\}]$ (**3b**) in acetonitrile (1.0 mM) on a glassy carbon electrode where Fc/Fc^+ was used as the internal standard and $[nBu_4N][PF_6]$ (0.1 M) was used as the supporting electrolyte.

The influence of compound **3b** towards the electrochemical reduction of protons to dihydrogen was investigated between 0.0 and –2.5 V by the addition of acetic acid (pK_a = 22.3 in CH_3CN) (Figure 7). In the presence of acid, the initial one-electron reduction signal remains unchanged. Neither a significant increase nor a shift of the signal was observed. An acid-dependent increase in the peak current

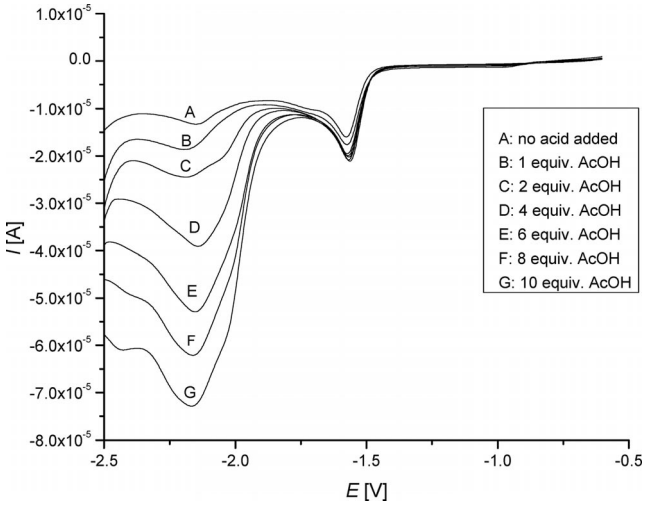

Figure 7. The cyclic voltammograms of $[Fe_2(CO)_6\{\mu\text{-}SCH(C_6H_5)\text{-}C_6H_4S\text{-}\mu\}]$ (**3b**) in acetonitrile (1 mM) in the presence of HOAc (0–10 mM), (potentials vs. Fc/Fc^+).

around –2.0 V was observed when the cathodic scan included more negative potentials. According to the literature, this behavior could be explained by the catalytic reduction of acetic acid by a reduced **3b**.[28] However, a comparison of the peak currents at around –2.0 V and in pure acetic acid reveals only moderate catalytic activity for compound **3b**.

Since compound **3b** revealed the structural properties of $[Fe_2(CO)_6(pdt)]$ (pdt = propanedithiolato) (Fe–S-alkyl bond) and $[Fe_2(CO)_6(bdt)]$ (bdt = benzenedithiolato) (Fe–S-phenyl bond), and since both of the complexes revealed different electrochemical properties, a short comparison between the three complexes will be given here. In contrast to **3b** and $[Fe_2(CO)_6(pdt)]$,[31] $[Fe_2(CO)_6(bdt)]$[10h] shows an initial two-electron reduction to a $[Fe^0Fe^0]$ complex at –1.25 V (Table 1). This reduction, however, appears at two different potentials. The one-electron reduction of $[Fe_2(CO)_6(pdt)]$ and **3b** is observed at –1.34 and –1.58 V, respectively. In contrast to $[Fe_2(CO)_6(bdt)]$, the second one-electron reduction is found at a distinctly lower potential around –2 V for both of the complexes. When acetic acid was added to the complexes, the reduction of the protons to dihydrogen was observed for all of the complexes at around –2 V. Based on these results, complex **3b** should be considered to be a comparable model to the [FeFe]-hydrogenase model complexes with a propanedithiolato backbone.

Table 1. The electrochemical data of the iron complexes **3b**, $[\{Fe_2(CO)_6\}(pdt)]$, and $[\{Fe_2(CO)_6\}(bdt)]$.

	$E_{red\,1}$ [V]	$E_{red\,2}$ [V]	E_{ox} [V]
3b[a]	–1.58	–2.15	+1.28
$[\{Fe_2(CO)_6\}(pdt)]$[31][b]	–1.34	–1.95	+1.14
$[\{Fe_2(CO)_6\}(bdt)]$[10h][c]	–1.27	–1.23	irreversible

[a] Glassy carbon electrode (potentials given in V, ± 0.01) vs. Fc/Fc^+ (0.01 M) in $[nBu_4N][PF_6]/CH_3CN$ (0.1 M) as the supporting electrolyte. [b] CH_3CN solution (0.1 M $[nBu_4N][PF_6]$) with a glassy carbon working electrode standard vs. Fc/Fc^+. [c] First scan, v = 0.1 Vs^{-1}; solution in $[nBu_4N][PF_6]/CH_3CN$.

Conclusions

In summary, we have succeeded in synthesizing two new complexes, **3b** and **4b**, that are bioinspired models for the active site of the [FeFe]-hydrogenases by using the aromatic thioketones, **2a** and **2b**, as the starting materials. The synthesis of **3b** was accomplished by a multistep reaction. A possible mechanism for the formation of **3b** has been proposed. Firstly, thioketone **2a** reacts with $Fe_3(CO)_{12}$ to give the *ortho*-metallated complex, **3a**. Secondly, a further equivalent of **2a**, which is activated by a side-on coordination to an iron atom, serves as a sulfur transfer reagent. Thirdly, complex **3b** is formed by the insertion of sulfur into the Fe–C σ-bond of **3a**. It was found that complex **3b** behaves as a catalyst for the electrochemical production of hydrogen in the presence of a weak acid, for example acetic acid, at a moderate potential.

The most remarkable feature of this investigation, however, is the assembly of a [FeFe]-hydrogenase active-site-core analogue from simple aromatic thioketones. This is of particular interest to prebiotic chemistry since one can envision that in a hydrothermal vent environment that has a higher CO concentration, where reduced hydrothermal fluids pass through the iron-/sulfide-containing crust, significant concentrations of iron carbonyls and thioketones might be formed.[32a] In a slightly different prebiotic reaction that was reported by Cody et al., iron sulfide is consumed in the presence of CO and alkylthiol to produce $[Fe_2(RS)_2(CO)_6]$, sulfur, and hydrogen.[32b] These possible prebiotic reactions that are emerging for the [FeFe]-hydrogenase model systems are of great importance in the context of the iron-sulfur world hypothesis.[32c]

Experimental Section

General Comments: All of the reactions were carried out under an argon atmosphere by using the standard Schlenk techniques. The ^1H and $^{13}C\{^1H\}$ NMR and 2D NMR spectra were recorded with a Bruker AVANCE 200 or 400 MHz spectrometer at room temperature and the solvent was used as the standard. The Mass spectra were obtained with a FINNIGAN MAT SSQ 710 instrument. The infrared spectra were measured with a Perkin–Elmer System 2000 FTIR spectrometer. Thiobenzophenone (**2a**)[12d] and 9*H*-thioxanthene-9-thione (**2b**)[13a] were prepared according to the literature procedures. The solvents and $Fe_3(CO)_{12}$ were purchased from Sigma–Aldrich. All of the solvents were dried and distilled prior to use according to the standard methods. Silica gel 60 (0.015–0.040 mm) was used for the column chromatography. TLC was done with Merck TLC aluminum sheets, silica gel 60 F_{254}. The elemental analyses were performed with a Vario EL III CHNS (Elementaranalysen GmbH Hanau) as single determinations.

$[Fe_2(CO)_6\{\mu\text{-}SCH(C_6H_5)C_6H_4S\text{-}\mu\}]$ (3b), $[Fe_2(CO)_6\{\mu\text{-}SC(C_6H_5)_2\}(S\text{-}\mu)]$ (3c), and $[\{Fe_2(CO)_6\{\mu\text{-}SCH(C_6H_5)_2S\text{-}\mu\}]$ (3d). Method A: $Fe_3(CO)_{12}$ (100 mg, 0.2 mmol) and thiobenzophenone (**2a**) (118 mg, 0.4 mmol) in thf (30 mL) were stirred at 65 °C under argon for a period of 3 to 4 h. The reaction mixture was cooled to room temperature and the solvent was removed under vacuum. The crude product was purified by column chromatography. Elution with hexane gave an orange solution of complex **3c** (R_f = 0.7), elution with hexane/diethyl ether (1:1, v/v) afforded a reddish solution of complex **3b** (R_f = 0.5) and elution with diethyl ether gave a red solution of **3d** (R_f = 0.5). The solutions were evaporated under vacuum. Suitable crystals of **3c** and **3d** for X-ray analysis were obtained by the slow evaporation of a concentrated pentane solution at –25 °C.

3b: Yield 22 mg (22%). $C_{19}H_{10}Fe_2O_6S_2$ (509.9): calcd. C 44.74, H 1.98, S 12.57; found C 45.18, H 1.83, S 12.1. ^1H NMR (400 MHz, $CDCl_3$, 25 °C): δ = 5.90 [s, 1 H, H(1)], 7.03–7.23 (m, 5 H, Ar-H), 7.32 [dd, ^3J = 7.7 Hz, 1 H, H(10)], 7.37 [dd, ^3J = 8.1 Hz, 1 H, H(11)], 7.75 [d, ^3J = 8.0 Hz, 1 H, H(9)], 8.51 [d, ^3J = 8.2 Hz, 1 H, H(12)] ppm. $^{13}C\{^1H\}$ NMR (400 MHz, $CDCl_3$): δ = 70.7 (C1), 123.8, 125.9, 126.7, 127.1, 128.2, 130.8, 138.3, 141.8, 143.7, 144.6, 152.5, 157.8 (2 Ph), 207.3, 208.9, 210.5 (CO) ppm. FTIR (KBr): $\tilde{\nu}_{C\equiv O}$ = 2073 (vs), 2035 (vs), 2008 (w, sh), 1994 (s), 1979 (s) cm^{-1}. MS (DEI = 70 eV): m/z = 510 [M^+], 482 [M^+ – CO], 454 [M^+ – 2CO], 426 [M^+ – 3CO], 398 [M^+ – 4CO], 370 [M^+ – 5CO], 342 [M^+ – 6CO].

3c: Yield 25 mg (25%). $C_{19}H_{10}Fe_2O_6S_2$ (509.9): calcd. C 44.74, H 1.98, S 12.57; found C 44.96, H 1.72, S 12.23. ^{1}H NMR (400 MHz, $CDCl_3$, 25 °C): δ = 7.57 (br. s, 10 H, 2 Ph) ppm. $^{13}C\{^1H\}$ NMR (400 MHz, $CDCl_3$): δ = 95.0 (SCS), 123.6, 127.7, 128.5 (2 Ph), 207.0, 208.2 (CO) ppm. FTIR (KBr): $\tilde{\nu}_{C\equiv O}$ = 2076 (vs), 2035 (vs), 1990 (vs) cm^{-1}. MS (DEI = 70 eV): *m*/*z* = 510 [M$^+$], 482 [M$^+$ – CO], 454 [M$^+$ – 2CO], 426 [M$^+$ – 3CO], 398 [M$^+$ – 4CO], 370 [M$^+$ – 5CO], 342 [M$^+$ – 6CO].

3d: Yield 21 mg (10%). $C_{38}H_{22}Fe_4O_{12}S_3$ (989.8): calcd. C 46.09, H 2.24, S 9.72; found C 46.52, H 2.47, S 9.39. ^{1}H NMR (200 MHz, $CDCl_3$, 25 °C): δ = 4.21, 4.66 (s, 2 H, 2 SCH), 7.06, 7.44, 7.68 (br. s, 20 H, 2 Ph) ppm. $^{13}C\{^1H\}$ NMR (200 MHz, $CDCl_3$): δ = 38.1, 38.9 (2 CS), 121.3, 125.2, 126.5, 127.3 (2 Ph), 206.6, 207.8, 208.1 (CO) ppm. FTIR (KBr): $\tilde{\nu}_{C\equiv O}$ = 2072 (vs), 2059 (w, sh), 2039 (vs), 1998 (vs) cm^{-1}. MS (DEI = 70 eV): *m*/*z* = 990 [M$^+$], 906 [M$^+$ – 3CO], 878 [M$^+$ – 4CO], 822 [M$^+$ – 6CO], 794 [M$^+$ – 7CO], 766 [M$^+$ – 8CO], 738 [M$^+$ – 9CO], 711 [M$^+$ – 10CO], 655 [M$^+$ – 12CO].

[$Fe_2(CO)_6${μ-SCH(C_6H_5)C_6H_4S-μ}] (3b). Method B: Thioketone **2a** (18 mg, 0.1 mmol) was added to a solution of **3a** (46 mg, 0.1 mmol) in thf (30 mL) under argon and the mixture was stirred at 65 °C for 3 h. The solvent was removed under vacuum and the crude product was purified by column chromatography. Elution with hexane/diethyl ether (1:1, v/v) gave a reddish solution (R_f = 0.5), which was identified as complex **3b**. Yield 21 mg (41%).

[$Fe_2(CO)_6${μ,κ,*S*,SCH(C_6H_4)–S–C_6H_4-η^2}] (4a): $Fe_3(CO)_{12}$ (140 mg, 0.28 mmol) was dissolved in thf (40 mL) and 9*H*-thioxanthene-9-thione (**2b**) (64 mg, 0.28 mmol) was added to the solution. The mixture was stirred at 65 °C for 20 min under argon. The solvent was removed in vacuo. The crude product was purified by column chromatography by using hexane as the eluent. The major dark red band (R_f = 0.5) was collected and the solvent was removed. The product was identified as complex **4a**. Yield 92 mg (65%). $C_{19}H_8Fe_2O_6S_2$ (507.8): calcd. C 44.91, H 1.59, S 12.62; found C 44.70, H 1.92, S 12.58. ^{1}H NMR (400 MHz, $CDCl_3$, 25 °C): δ = 4.82 [s, 1 H, H(12)], 6.94 [m, 1 H, H(8)] 7.26 [m, 1 H, H(9)], 7.36 [m, 1 H, H(10)], 7.39 [m, 1 H, H(7)], 7.62 [m, 1 H, H(3)], 7.92 [m, 1 H, H(4)], 8.04 [m, 1 H, H(2)] ppm. $^{13}C\{^1H\}$ NMR (400 MHz, $CDCl_3$): δ = 60.7 (CS), 125.0, 125.8, 126.6, 127.2, 127.5, 128.2, 128.5, 131.0, 135.9, 136.8, 141.8, 154.8 (2Ph), 208.6, 209.4 (CO) ppm. FTIR (C_5H_{12}): $\tilde{\nu}_{C\equiv O}$ = 2071 (vs), 2037 (vs), 2001 (vs), 1984 (w, sh) cm^{-1}. MS (DEI = 70 eV): *m*/*z* = 508 [M$^+$], 480 [M$^+$ – CO], 452 [M$^+$ – 2CO], 424 [M$^+$ – 3CO], 396 [M$^+$ – 4CO], 368 [M$^+$ – 5CO], 340 [M$^+$ – 6CO].

[$Fe_2(CO)_6${μ-SCH(C_6H_4)–S–C_6H_4S-μ}] (4b) and [$Fe_2(CO)_6${μ-SC(C_6H_4–S–C_6H_4)S-μ}] (4c): The ligand, 9*H*-thioxanthene-9-thione (**2b**) (163 mg, 0.48 mmol), was added to a solution of $Fe_3(CO)_{12}$ (120 mg, 0.24 mmol) in thf (40 mL) under argon. The reaction mixture was stirred at 65 °C for a period of 3 to 4 h. After evaporation of the solvent, the residue was purified by coloum chromatography on a silica gel column. Elution with hexane gave an orange-reddish solution of complex **4c** (R_f = 0.6). Elution with hexane/diethyl ether (2:1, v/v) afforded a reddish solution of complex **4b** (R_f = 0.3). The two solutions were evaporated under vacuum. Suitable crystals of **4b** and **4c** for X-ray analysis were obtained by the slow evaporation of a concentrated pentane solution at –25 °C. **4b**. Yield 48 mg (37%). $C_{19}H_8Fe_2O_6S_3$ (540.1): calcd. C 42.25, H 1.49, S 17.80; found C 42.58, H 1.68, S 17.30. ^{1}H NMR (400 MHz, $CDCl_3$, 25 °C, assignment analogous to **4a**): δ = 5.28 ppm. [s, 1 H, H(12)], 7.05 [dd, 1 H, ^3J = 8.0 Hz, H(8)], 7.31 [m, 1 H, H(9)], 7.43[d, 1 H, ^3J = 8.0 Hz, H(10)], 7.56 [d, 1 H, ^3J = 8.0 Hz, H(7)], 7.76 [dd, 1 H, ^3J = 8.0 Hz, H(3)], 8.03 [d, 1 H, ^3J = 8.0 Hz, H(4)], 8.62 [d, 1 H, ^3J = 8.0 Hz, H(2)] ppm. $^{13}C\{^1H\}$ NMR (400 MHz, $CDCl_3$): δ = 69.9 (C12), 125.3, 126.4, 126.5, 126.8, 126.9, 127.1, 127.8, 128.05, 129.3, 132.8, 142.1 158.2 (2 Ph), 207.0, 208.5, 209.2, 212.2 (CO) ppm. FTIR (KBr): $\tilde{\nu}_{C\equiv O}$ = 2075 (vs), 2038 (vs), 2017 (w, sh), 2003 (s), 1985 (s) cm^{-1}. MS (DEI = 70 eV): *m*/*z* = 540 [M$^+$], 512 [M$^+$ – CO], 484 [M$^+$ – 2CO], 456 [M$^+$ – 3CO], 428 [M$^+$ – 4CO], 400 [M$^+$ – 5CO], 372 [M$^+$ – 6CO]. **4c**: Yield 41 mg (32%). $C_{19}H_8Fe_2O_6S_3$ (540.1): calcd. C 42.25, H 1.49, S 17.80; found C 42.73, H 1.58, S 17.62. ^{1}H NMR (400 MHz, $CDCl_3$, 25 °C, assignment analogous to **4a**): δ = 7.42, 7.74 (br. s, 8 H, 2

Table 2. The crystal data and refinement details for the X-ray structure determinations of the compounds **3c**, **3d**, **4b**, and **4c**.

	3c	**3d**	**4b**	**4c**
Formula	$C_{19}H_8Fe_2O_6S_3$	$C_{38}H_{22}Fe_4O_{12}S_3$	$C_{19}H_7Fe_2O_6S_3$	$C_{19}H_{10}Fe_2O_6S_2$
fw [g mol^{-1}]	540.13	990.14	539.13	510.09
T [°C]	–140(2)	–140(2)	–140(2)	–140(2)
Crystal system	monoclinic	triclinic	monoclinic	monoclinic
Space group	$P2_1/n$	$P\bar{1}$	$P2_1/c$	$C2/c$
a [Å]	10.3982(3)	9.1211(2)	7.8592(2)	20.4829(12)
b [Å]	9.6800(2)	13.7459(2)	14.9765(3)	6.4767(5)
c [Å]	19.7021(5)	16.5123(3)	17.2733(3)	30.4653(17)
α [°]	90	89.164(1)	90	90
β [°]	99.020(2)	83.405(1)	92.011(1)	107.121(3)
γ [°]	90	76.626(1)	90	90
V [Å^3]	1958.58(9)	2000.65(6)	2031.87(7)	3862.5(4)
Z	4	2	4	8
ρ [g cm^{-3}]	1.832	1.644	1.762	1.754
μ [cm^{-1}]	18.37	16.39	17.71	17.53
Measured data	12241	21290	12476	6437
Data with $I > 2\sigma(I)$	3895	8546	4262	3780
Unique data/R_{int}	4480/0.0313	10330/0.0197	4595/0.0231	4106/0.0218
wR_2 (all data, on F^2)[a]	0.0727	0.0701	0.0865	0.0733
R_1 [$I > 2\sigma(I)$][a]	0.0306	0.0294	0.0341	0.0311
s[b]	1.027	1.042	1.011	1.065
Residual electron density [e Å^{-3}]	0.475/–0.409	0.485/–0.368	1.765/–0.534	0.466/–0.349
Absorption correction	none	none	none	none

[a] $R_1 = (\Sigma||F_o| - |F_c||)/\Sigma|F_o|$; $wR_2 = \{\Sigma[w(F_o^2 - F_c^2)^2]/\Sigma[w(F_o^2)^2]\}^{1/2}$; $w^{-1} = \sigma^2(F_o^2) + (aP)^2 + bP$; $P = [2F_c^2 + \max(F_o^2)]/3$. [b] $s = \{\Sigma[w(F_o^2 - F_c^2)^2]/(N_o - N_p)\}^{1/2}$.

Ph) ppm. $^{13}C\{^1H\}$ NMR (400 MHz, $CDCl_3$): δ = 93.9 (SCS), 123.8, 126.3, 127.0,129.3, 132.9, 134.3, 137.0 (2 Ph), 207.0, 208.1 (CO) ppm. FTIR (KBr): $\tilde{\nu}_{C\equiv O}$ = 2075 (vs), 2037 (vs), 2001 (vs) cm^{-1}. MS (DEI = 70 eV): *m*/*z* = 540 [M^+], 512 [M^+ – CO], 484 [M^+ – 2CO], 456 [M^+ – 3CO], 428 [M^+ – 4CO], 400 [M^+ – 5CO], 372 [M^+ – 6CO].

Characterization of 1,1,2,2-Tetraphenylethene (5): Colorless crystals, m.p. 222–224 °C (ref.[33] m.p. 222 °C). ^1H NMR (200 MHz, $CDCl_3$, 25 °C): δ = 7.05–7.21 (m, 20 H, Ar-H) ppm. MS (DEI = 70 eV): *m*/*z* = 332 [M^+].

Electrochemistry: The cyclic voltammograms were measured in a three electrode cell with a 1.0 mm diameter glassy carbon disc working electrode, a platinum auxiliary electrode, and Ag/AgCl in CH_3CN as the reference electrode. The solvent contained [nBu$_4$N][PF_6] (0.1 M) as the supporting electrolyte. The measurements were performed at room temperature with a Metrohm 663 VA Standard galvanostat. Deaeration of the sample solutions was accomplished by passing a stream of nitrogen through the solutions for 5 min prior to the measurements, and the solutions were kept under nitrogen for the duration of the measurements. All of the data obtained were corrected against the Fc/Fc^+ couple as an internal standard ($E_{1/2}$ = 503 mV vs. Ag/AgCl in CH_3CN).

Crystal Structure Determination: The intensity data for the compounds were collected with a Nonius KappaCCD diffractometer by using graphite-monochromated Mo-K_α radiation. The data were corrected for Lorentz and polarization effects but not for absorption effects.[34,35] The crystallographic data, as well as the structure solutions and refinement details, are summarized in Table 2. The structures were solved by direct methods (SHELXS)[36] and were refined by full-matrix least-squares techniques against F_o^2 (SHELXL-97).[36] All of the hydrogen atom positions were included at the calculated positions with fixed thermal parameters. All of the non-hydrogen atoms were refined anisotropically.[36] XP (SIEMENS Analytical X-ray Instruments, Inc.) was used for the structure representations.

CCDC-803654 (for **3c**), -803655 (for **3d**), -803656 (for **4b**) and -803657 (for **4c**) contain the supplementary crystallographic data for this paper. These data can be obtained free of charge from The Cambridge Crystallographic Data Centre via www.ccdc.cam.ac.uk/data_request/cif.

Acknowledgments

This work has been funded by the European Union (EU) (SYNTHCELLS project, Approaches to the Bioengineering of Synthetic Minimal Cells), grant number #FP6043359 (to A. D.). U.-P. A. is thankful for a fellowship from the Studienstiftung des deutschen Volkes.

[1] J. Yano, J. Kern, K. Sauer, M. J. Latimer, Y. Pushkar, J. Biesiadka, B. Loll, W. Saenger, J. Messinger, A. Zouni, V. K. Yachandra, *Science* **2006**, *314*, 821–825.
[2] R. E. Blankenship, *Molecular Mechanisms of Photosynthesis*, Blackwell Science Ltd., Oxford, UK, **2002**, pp. 6–10.
[3] G. Renger, A. R. Holzwarth, *Primary Electron Transfer*, in: *Photosystem II: The Light-Driven Water: Plastoquinone Oxidoreductase* (Eds.: T. J. Wydrzynski, K. Satoh), Springer, Dordrecht, **2005**, vol. 22, p. 139.
[4] P. M. Vignais, B. Billoud, J. Meyer, *FEMS Microbiol. Rev.* **2001**, *25*, 455–501.
[5] J. C. Fontecilla-Camps, A. Volbeda, C. Cavazza, Y. Nicolet, *Chem. Rev.* **2007**, *107*, 4273–4303.
[6] a) W. Lubitz, E. Reijerse, M. van Gastel, *Chem. Rev.* **2007**, *107*, 4331–4365; b) C. Tard, C. J. Pickett, *Chem. Rev.* **2009**, *109*, 2245–2274.
[7] M. Y. Darensbourg, E. J. Lyon, J. J. Smee, *Coord. Chem. Rev.* **2000**, *206*, 533–561.
[8] D. J. Evans, C. J. Pickett, *Chem. Soc. Rev.* **2003**, *32*, 268–275.
[9] S. M. Kotay, D. Das, *Int. J. Hydrogen Energy* **2008**, *33*, 258–263.
[10] a) J. F. Capon, F. Gloaguen, F. Y. Pétillon, P. Schollhammer, J. Talarmin, *Eur. J. Inorg. Chem.* **2008**, 4671–4681; b) D. M. Heinekey, *J. Organomet. Chem.* **2009**, *694*, 2671–2680; c) F. Gloaguen, T. B. Rauchfuss, *Chem. Soc. Rev.* **2009**, *38*, 100–108; d) C. Tard, X. Liu, S. K. Ibrahim, M. Bruschi, L. D. Gioia, S. Davies, X. Yang, L.-S. Wang, G. Sawers, C. J. Pickett, *Nature* **2005**, *434*, 610–613; e) F. Gloaguen, J. D. Lawrence, T. B. Rauchfuss, *J. Am. Chem. Soc.* **2001**, *123*, 9476–9477; f) F. Gloaguen, J. D. Lawrence, T. B. Rauchfuss, M. Benard, M.-M. Rohmer, *Inorg. Chem.* **2002**, *41*, 6573–6582; g) R. Mejia-Rodriguez, D. Chong, J. H. Reibenspies, M. P. Soriaga, M. Y. Darensbourg, *J. Am. Chem. Soc.* **2004**, *126*, 12004–12014; h) J.-F. Capon, F. Gloaguen, P. Schollhammer, J. Talarmin, *J. Electroanal. Chem.* **2006**, *595*, 47–52; i) G. A. N. Felton, A. K. Vannucci, J. Chen, L. T. Lockett, N. Okumura, B. J. Petro, U. I. Zakai, D. H. Evans, R. S. Glass, D. L. Lichtenberger, *J. Am. Chem. Soc.* **2007**, *129*, 12521–12530; j) T. Liu, M. Y. Darensbourg, *J. Am. Chem. Soc.* **2007**, *129*, 7008–7009; k) M. Y. Darensbourg, *Nature* **2005**, *433*, 598–591; l) J. Windhager, M. Rudolph, S. Bräutigam, H. Görls, W. Weigand, *Eur. J. Inorg. Chem.* **2007**, *18*, 2748–2760.
[11] a) J. Windhager, H. Gorls, H. Petzold, G. Mloston, G. Linti, W. Weigand, *Eur. J. Inorg. Chem.* **2007**, 4462–4471; b) A. Q. Daraosheh, H. Görls, M. El-khateeb, G. Mloston, W. Weigand, *Eur. J. Inorg. Chem.* **2011**, 349–355; c) H. Alper, *J. Organomet. Chem.* **1975**, *84*, 347–350; d) H. Alper, A. S. K. Chan, *J. Am. Chem. Soc.* **1973**, *95*, 4905–4913; e) H. Alper, A. S. K. Chan, *Inorg. Chem.* **1974**, *13*, 232–236.
[12] a) K. Shimada, K. Kodaki, S. Aoyagi, Y. Takikawa, C. Kabuto, *Chem. Lett.* **1999**, 695–696; b) H. Petzold, S. Bräutigam, H. Görls, W. Weigand, M. Celeda, G. Mloston, *Chem. Eur. J.* **2006**, *12*, 8090–8095; c) G. Mloston, A. Majchrzak, A. Senning, I. Søtofte, *J. Org. Chem.* **2002**, *67*, 5690–5695; d) V. Polshettiwar, M. K. Kaushik, *Tetrahedron Lett.* **2004**, *45*, 6255–6257.
[13] a) R. Huisgen, J. Rapp, *Tetrahedron* **1997**, *53*, 939–960; b) T. Saito, Y. Shundo, S. Kitazawa, S. Motoki, *J. Chem. Soc., Chem. Commun.* **1992**, 600–602; c) J. J. Eisch, Y. Qian, M. Singh, *J. Organomet. Chem.* **1996**, *512*, 207–217.
[14] F. Gloaguen, J. D. Lawrence, M. Schmidt, S. R. Wilson, T. B. Rauchfuss, *J. Am. Chem. Soc.* **2001**, *123*, 12518–12527.
[15] L.-C. Song, Z.-Y. Yang, H.-Z. Bian, Q.-M. Hu, *Organometallics* **2004**, *23*, 3082–3084.
[16] A. Q. Daraosheh, M. K. Harb, J. Windhager, H. Görls, M. El-khateeb, W. Weigand, *Organometallics* **2009**, *28*, 6275–6280.
[17] H. Li, T. B. Rauchfuss, *J. Am. Chem. Soc.* **2002**, *124*, 726–727.
[18] U.-P. Apfel, Y. Halpin, M. Gottschaldt, H. Görls, J. G. Vos, W. Weigand, *Eur. J. Inorg. Chem.* **2008**, 5112–5118.
[19] L.-C. Song, Z.-Y. Yang, Y.-J. Hua, H.-T. Wang, Y. Liu, Q.-M. Hu, *Organometallics* **2007**, *26*, 2106–2110.
[20] E. J. Lyon, I. P. Georgakaki, J. H. Reibenspies, M. Y. Darensbourg, *J. Am. Chem. Soc.* **2001**, *123*, 3268–3278.
[21] S. Ott, M. Kritikos, B. Åkermark, L. Sun, *Angew. Chem.* **2003**, *115*, 3407; *Angew. Chem. Int. Ed.* **2003**, *42*, 3285–3288.
[22] S. Ezzaher, J.-F. Capon, F. Gloaguen, F. Y. Petillon, P. Schollhammer, J. Talarmin, *Inorg. Chem.* **2007**, *46*, 3426–3428.
[23] M. Razavet, S. C. Davies, D. L. Hughes, J. E. Barclay, D. J. Evans, S. A. Fairhurst, X. Liu, C. J. Pickett, *Dalton Trans.* **2003**, 586–595.
[24] Y. Si, K. Charreteur, J.-F. Capon, F. Gloaguen, F. Y. Pétillon, P. Schollhammer, J. Talarmin, *J. Inorg. Biochem.* **2010**, *104*, 1038–1042.

[25] F. Huo, J. Hou, G. Chen, D. Guo, X. Peng, *Eur. J. Inorg. Chem.* **2010**, 3942–3951.
[26] L.-C. Song, Z.-Y. Yang, H.-Z. Bian, Y. Liu, H.-T. Wang, X.-F. Liu, Q.-M. Hu, *Organometallics* **2005**, *24*, 6126–6135.
[27] S. Jiang, J. Liu, Y. Shi, Z. Wang, B. Åkermark, L. Sun, *Dalton Trans.* **2007**, 896–902.
[28] G. A. N. Felton, C. A. Mebi, B. J. Petro, A. K. Vannucci, D. H. Evans, R. S. Glass, D. L. Lichtenberger, *J. Organomet. Chem.* **2009**, *694*, 2681–2699.
[29] M. K. Harb, U.-P. Apfel, J. Kübel, H. Görls, G. A. N. Felton, T. Sakamoto, D. H. Evans, R. S. Glass, D. L. Lichtenberger, M. El-khateeb, W. Weigand, *Organometallics* **2009**, *28*, 6666–6675.
[30] U.-P. Apfel, D. Troegel, Y. Halpin, S. Tschierlei, U. Uhlemann, H. Görls, M. Schmitt, J. Popp, P. Dunne, M. Venkatesan, M. Coey, M. Rudolph, J. G. Vos, R. Tacke, W. Weigand, *Inorg. Chem.* **2010**, *49*, 10117–10132.
[31] a) D. Chong, I. P. Georgakaki, R. Mejia-Rodriguez, J. Sanabria-Chinchilla, M. P. Soriaga, M. Y. Darensbourg, *Dalton Trans.* **2003**, 4158–4163; b) S. J. Borg, T. Behrsing, S. P. Best, M. Razavet, X. Liu, C. J. Pickett, *J. Am. Chem. Soc.* **2004**, *126*, 16988–16999; c) J.-F. Capon, S. Ezzaher, F. Gloaguen, F. Y. Pétillon, P. Schollhammer, J. Talarmin, T. J. Davin, J. E. McGrady, K. W. Muir, *New J. Chem.* **2007**, *31*, 2052–2064.
[32] a) E. T. McGuinness, *Chem. Rev.* **2010**, *110*, 5191–5215; b) G. D. Cody, N. Z. Boctor, T. R. Filley, R. M. Hazen, J. H. Scott, A. Sharma, H. S. Yoder Jr, *Science* **2000**, *289*, 1337–1340; c) G. Wächtershäuser, *Prog. Biophys. Mol. Biol.* **1992**, *58*, 85–201.
[33] W. Schlenk, E. Bergmann, *Justus Liebigs Ann. Chem.* **1928**, *463*, 1–97.
[34] *COLLECT*, Data Collection Software, Nonius B. V., Netherlands, **1998**.
[35] Z. Otwinowski, W. Minor, in: *Methods in Enzymology* (Eds.: C. W. Carter, R. M. Sweet), Academic Press, New York, **1997**, vol. 276, pp. 307–326.
[36] G. M. Sheldrick, *Acta Crystallogr., Sect. A* **2008**, *64*, 112–122.
Received: September 30, 2011
Published Online: December 12, 2011

DOI: 10.1002/ejic.201100804

A Highly Selective Fluorescent and Colorimetric Chemosensor for Zn^{II} and Its Application in Cell Imaging

Guoqiang Xie,[a] Yanjun Shi,[a] Fengping Hou,[a] Hongyan Liu,[a] Liang Huang,[a] Pinxian Xi,[a] Fengjuan Chen,[a] and Zhengzhi Zeng*[a]

Keywords: Fluorescence / Zinc / N ligands / Colorimetric chemosensor / 8-Aminoquinoline / Cell imaging

A fluorescent, colorimetric chemosensor, **L1**, based on 8-aminoquinoline, has been developed as a sensor for Zn^{2+}. **L1** exhibited high selectivity and sensitivity towards Zn^{2+} over other common metal ions in a physiological pH window with a 1:1 binding mode. The ability of **L1** to monitor intracellular Zn^{2+} in living cells has been examined by fluorescence microscopy and indicated that **L1** is cell-permeable and biocompatible. We hope that such Zn^{2+}-selective sensors will find application in biomedical and environmental detection.

Introduction

The development of fluorescent chemosensors that have the capability to selectively recognize and sense metal ions is one of the most challenging fields in organic and supramolecular chemistry.[1] Sensors based on ion-induced changes (e.g. intensity and/or emission wavelength) in fluorescence have many advantages over other techniques, which include their simplicity, high sensitivity, high selectivity, and instantaneous response.[2] So far, a number of excellent metal-ion sensors based on metal–ligand coordination or chemical reaction have been reported to detect transition and heavy metal ions, such as zinc ions.[3] Zinc is the second most abundant transition metal in human body after iron and plays important roles in various pathological processes.[4] Zn^{2+} does not give any spectroscopic or magnetic signals due to its $3d^{10}4s^0$ electronic configuration. However, fluorescence is an effective way to detect zinc in biological systems.

Considerable efforts have been made to design and synthesize fluorescent chemosensors for Zn^{2+}.[5] Among the various fluorescent sensors, 8-aminoquinoline and its derivatives are the first class of probes to have been developed for Zn^{2+}.[6] They exhibit good photostability, high affinity to metal ions, and satisfactory membrane permeability.[7] Despite some commercial fluorescent probes for Zn^{2+},[8] the design of facile, easy to synthesize, nontoxic Zn^{2+}-selective sensors is still a challenging task, and there is a need for the design and synthesis of such chemosensors, which are small molecules and highly sensitive for real-time detection in biological systems at physiological pH.

We have synthesized a new 8-aminoquinoline derivative **L1** as a Zn^{2+} chemosensor, which shows high sensitivity and selectivity for Zn^{2+} over other possible competitive cations based on internal charge transfer (ICT) and chelation-enhanced fluorescence mechanisms. The mode of binding of **L1** with Zn^{2+} was investigated by UV/Vis spectrophotometric titration and fluorescence titration. The ability of **L1** to detect Zn^{2+} in living cells was examined by fluorescence microscopy.

Results and Discussion

L1 was easily prepared from 8-aminoquinoline and rhodamine 6G in high yield (Scheme 1), and its structure was confirmed by ^1H and ^{13}C NMR spectroscopy, ESI-MS (see Supporting Information), and X-ray diffraction (Figure 1).

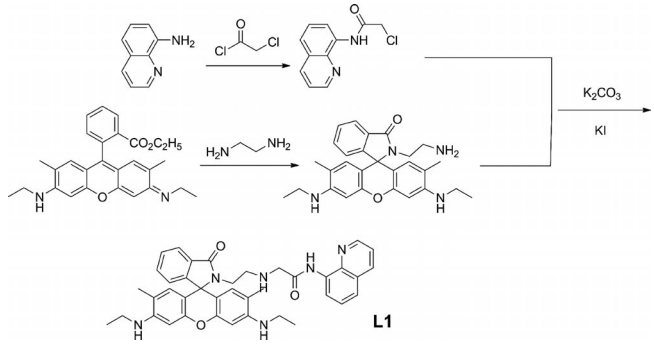

Scheme 1. Synthetic route to **L1**.

[a] Key Laboratory of Nonferrous Metal Chemistry and Resources Utilization of Gansu Province,
Lanzhou 730000, P. R. China
Fax: +86-931-8912582
E-mail: zengzhzh@yahoo.com.cn
zengzhzh@lzu.edu.cn

Supporting information for this article is available on the WWW under http://dx.doi.org/10.1002/ejic.201100804.

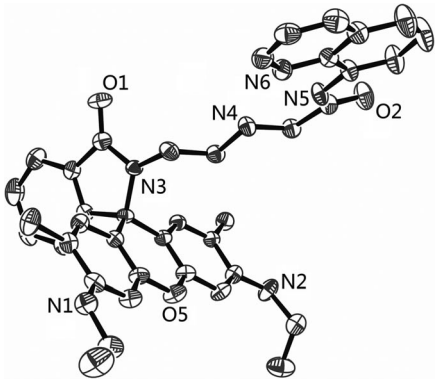

Figure 1. X-ray crystal structure of **L1**. All hydrogen atoms are omitted for clarity (50% probability level for the thermal ellipsoids).

The mode of coordination of **L1** with Zn^{2+} was investigated by spectrophotometric titration in acetonitrile solution. Figure 2a shows the spectral variation of **L1** with the gradual addition of Zn^{2+}. The absorbance of **L1** at 237 and 303 nm decreased linearly with increasing concentration of Zn^{2+}. In addition, two new absorption peaks appeared at 256 and 362 nm, and their intensity increased with the addition of Zn^{2+}, which was accompanied by three isosbestic points at 247, 282, and 340 nm, respectively. These phenomena are expected to correspond to the coordination of **L1** with Zn^{2+}, which extended the conjugated system and resulted in the appearance of the new absorption in the long-wavelength region.[9] According to the linear Benesi–Hildebrand expression,[10] the measured absorbance $[1/(A - A_0)]$ at 362 nm varied as a function of $1/[Zn^{2+}]$ in a linear relationship (R^2 = 0.9980), which indicates a 1:1 stoichiometry between Zn^{2+} and **L1** (Figure 2b). Moreover, there were no absorption peaks between 450 and 700 nm, which indicates that the spirolactam rhodamine was not ring-opened and the N3 atom does not participate in the coordination to Zn^{2+}.

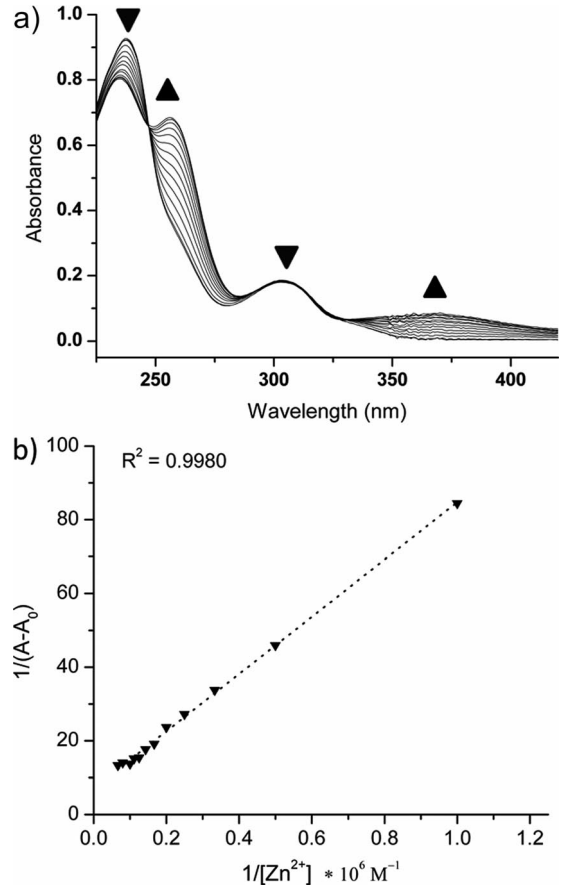

Figure 2. (a) Absorption spectra of **L1** (10 μM) in the presence of Zn^{2+} (0–1 equiv.) in CH_3CN. (b) Plot of $1/(A - A_0)$ at 362 nm as a function of $1/[Zn^{2+}]$.

The spectrum of **L1** (10 μM) showed a weak emission at around 499 nm (λ_{ex} = 365 nm, fluorescence intensity, F_0 = 14.4, quantum yield, Φ_0 = 0.005) in acetonitrile solution. As shown in Figure 3, the addition of Zn^{2+} (0–15 μM) to the solution produced a new emission band centered at 499 nm with an approximately 77-fold enhancement in intensity (Φ = 0.537).

The fluorescence titration profile of **L1** with Zn^{2+} demonstrates that the detection of Zn^{2+} is 1 μM in the range of 0–15 μM of $[Zn^{2+}]$. These results can be explained as follows. After binding with Zn^{2+}, the intramolecular electron-transfer process becomes forbidden, which enhances the fluorescence emission.[11] Simultaneously, the electron transfer from the nitrogen atom of the heterocycle to the metal ion enhances the ICT process.[12] Another reason for enhanced fluorescence could be that a more rigid structure forms when Zn^{2+} binds with **L1**. The association constant for Zn^{2+} was estimated to be 2.9×10^4 M^{-1} on the basis of the linear fit of the titration curve that assumes a 1:1 stoichiometry (Figure S1, Supporting Information). The Job plot (Figure 3, inset) also confirmed that the binding mode had a 1:1 stoichiometry.

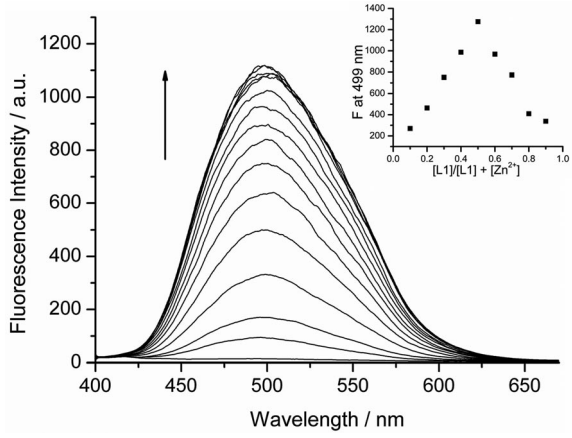

Figure 3. Fluorescence spectra of **L1** (10 μM) in acetonitrile in the presence of different concentrations of Zn^{2+} (0–2 equiv.) excited at 365 nm. Inset: Job plot to determine the stoichiometry of **L1** and Zn^{2+} in acetonitrile (the total concentration of **L1** and Zn^{2+} is 25 μM).

When Zn^{2+} was added to the solution of **L1**, the colorless solution turned pink, and greenish fluorescence was observed by the naked eye. However, the fluorescence did not derive from the fluorophore of rhodamine 6G, because no emission peaks were observed between 530 and 650 nm when we excited the system between 480 and 520 nm. We presumed that the fluorescence of the system originated in the fluorophore of 8-aminoqunoline when excited at 365 nm. Therefore, we can deduce a possible sensing mechanism (Figure 4) in which the spirolactam rhodamine is not ring-opened and three N atoms (labeled N4, N5, and N6 in Figure 1) participate in the coordination to Zn^{2+}.[13] The species that forms in solution has a nearly planar structure. The fourth ligand (X) is NO_3^- by consideration of the charge balance in solution.

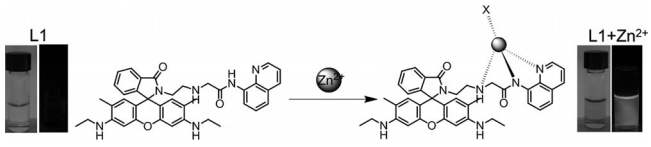

Figure 4. Proposed binding mode of **L1** with Zn^{2+}.

An important property of chemosensors is their high selectivity towards the analyte over the other competitive metal ions. Therefore, we determined the fluorescence intensity of **L1** at 499 nm in the presence of various metal ions. As shown in Figure 5, the addition of Zn^{2+} gave rise to a prominent fluorescence enhancement in an acetonitrile solution of **L1**, whereas the addition of other metal ions, such as K^+, Na^+, Ca^{2+}, and Mg^{2+}, which exist at high concentrations in human cells, did not show any significant color or spectral changes. Fluorescence enhancement of **L1** was observed in the presence of Cd^{2+} because the chemical properties of Cd^{2+} are similar to those of Zn^{2+}. However, the fluorescence intensity of **L1** in the presence of Cd^{2+} is far below that in the presence of Zn^{2+} (F_{Zn}/F_{Cd} = 2.8) under

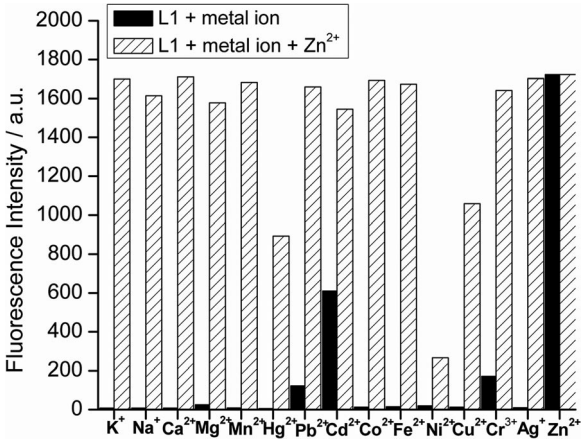

Figure 5. Fluorescence intensities of **L1** (10 μM) in the presence of various metal ions and ion mixtures in acetonitrile. [K^+], [Na^+], [Ca^{2+}], and [Mg^{2+}] = 5 mM, [Zn^{2+}], [Mn^{2+}], [Cr^{3+}], [Pb^{2+}], [Cd^{2+}], [Co^{2+}], [Fe^{2+}], [Ni^{2+}], [Ag^+], [Hg^{2+}], [Cu^{2+}] = 20 μM (λ_{ex} = 365 nm, λ_{em} = 499 nm).

the same conditions, which reflects the lower affinity of **L1** for Cd^{2+}. The fluorescence of the **L1**/Zn^{2+} system was quenched by Ni^{2+}, Cu^{2+}, and Hg^{2+}, which may be due to nonradiative energy transitions or energy transfer between the d orbital of the ions and the fluorophore.[14] These results demonstrate the high selectivity of **L1** towards Zn^{2+}.

For practical applications, the sensing ability of **L1** towards Zn^{2+} at different pH values was investigated (Figure 6). **L1** showed no appreciable fluorescent response to Zn^{2+} in acidic environments due to the more difficult protonation of the imino group (N5) of **L1**, which led to a weak coordination of Zn^{2+}.[15] However, **L1** exhibited satisfactory sensing abilities when the pH was increased from 5.5 to 9.0. These data indicate that **L1** could act as a fluorescent probe for Zn^{2+} under physiological pH conditions.

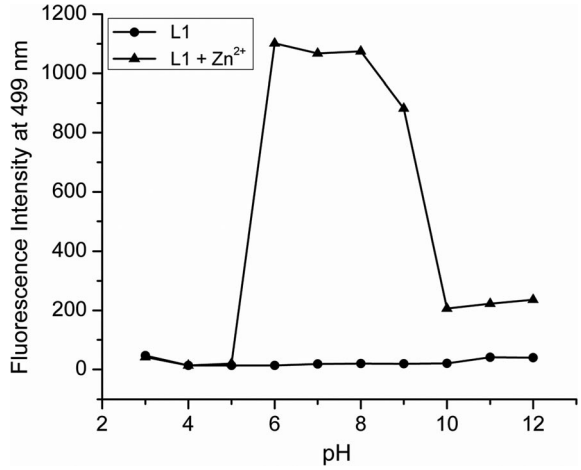

Figure 6. Fluorescence intensities of **L1** (10 μM) in the absence and presence of Zn^{2+} (20 μM) at various pH values in CH_3CN/H_2O (95:5, v/v). (λ_{ex} = 365 nm).

We also investigated the time evolution of the response of **L1** to 2 equiv. of Zn^{2+} in CH_3CN (Figure 7). We found that the interaction of **L1** with Zn^{2+} was completed in less than 2 min. Therefore, this system could be used to track Zn^{2+} in cells and organisms in real-time.

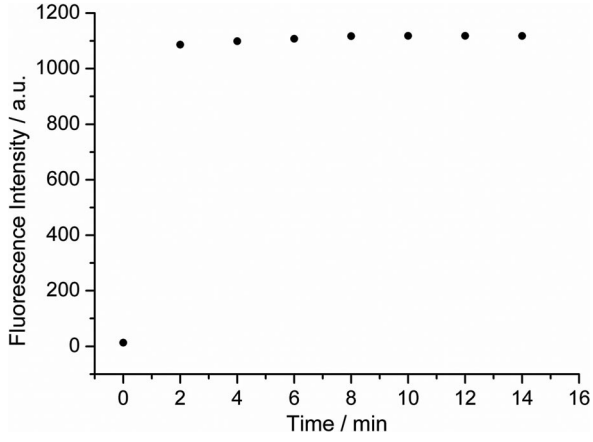

Figure 7. Time evolution of the response of **L1** (10 μM) to 2 equiv. of Zn^{2+} in CH_3CN.

As we developed **L1** to be used with cells, we quantified its effects on the viability of L929 fibroblast cells in vitro. Cell viability was evaluated by using a modified 3-(4,5-dimethylthiazol-2-yl)-2,5-diphenyltetrazolium bromide (MTT) assay. Figure 8 shows the viability of cells treated with **L1** over a range of concentrations for 24, 48, and 72 h. **L1** does not negatively affect cell viability over the full range of concentrations measured, which indicates that they exhibit no cytotoxicity and could be used for intracellular detection.

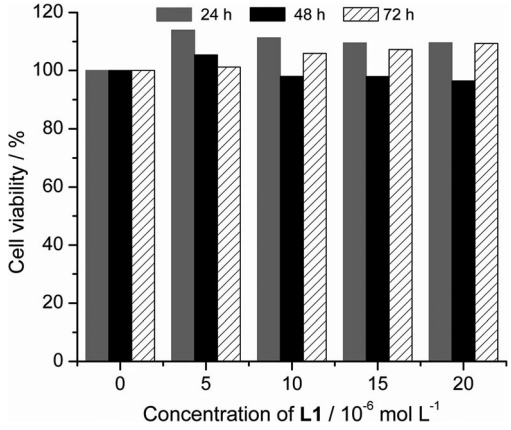

Figure 8. MTT assay of L929 cells cultured for 24, 48, and 72 h in media that contain different amounts of **L1**.

Bright field microscopy images of cells grown in the presence and absence of **L1** confirmed the biocompatibility of **L1** (Figure S2).

The ability of **L1** to detect Zn^{2+} in SCABER (human bladder cancer) cells was also examined. The cells were supplemented with **L1** (10 μM) in Dulbecco's modified Eagle's medium (DMEM) supplemented with 10% fetal bovine serum (FBS) at 37 °C for 3 h and showed very weak intracellular fluorescence as determined by fluorescence microscopy (Figure 9b). With the addition of Zn^{2+} (40 μM) to the treated cells in a culture medium at 37 °C for 0.5 h, a significant increase in fluorescence from the intracellular area was observed (Figure 9d). These results demonstrate that **L1** could be used as a sensor to detect intracellular Zn^{2+} in living cells.

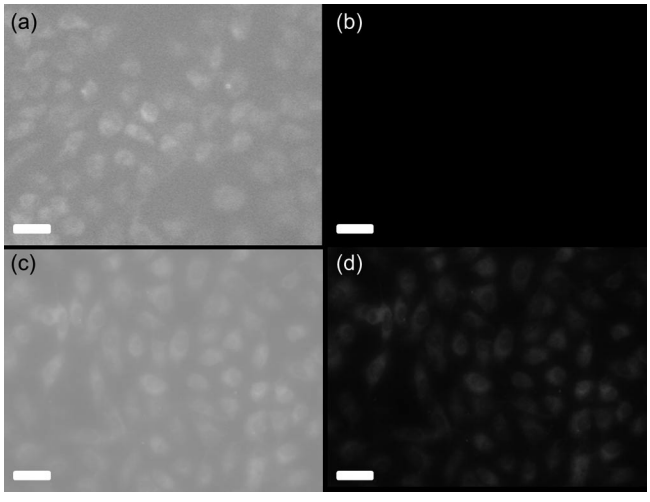

Figure 9. (a) Bright field image and (b) fluorescence microscopy image of SCABER cells loaded with **L1** (10 μM) incubated for 3 h. (c) Bright field image and (d) fluorescence microscope image of SCABER cells loaded with **L1** (10 μM) incubated for 3 h with the addition of Zn^{2+} (2 equiv.). Scale bar = 50 μM.

Conclusions

We have developed a fluorescent, colorimetric chemosensor based on 8-aminoquinoline for the detection of Zn^{2+} in living cells. **L1** displayed high selectivity, sensitivity, and a fast time response to Zn^{2+} in a physiological pH window with a 1:1 binding mode. The ability of **L1** to monitor intracellular Zn^{2+} in living cells was examined by fluorescence microscopy, which indicated that **L1** is cell-permeable and biocompatible. We hope that such Zn^{2+}-selective sensors will find application in biomedical and environmental detection.

Experimental Section

Materials and General Methods: ^1H and ^{13}C NMR spectra were recorded with a Varian Mercury-400 spectrometer with Me_4Si as the internal standard and $CDCl_3$ as the solvent. Mass spectra were performed with an HP-5988A spectrometer (EI at 70 eV). Absorption spectra were determined with a Varian UV-Cary 100 spectrophotometer. Fluorescence measurements were performed with a Hitachi F-4500 spectrofluorimeter. Both excitation and emission slits were 5 nm. Quantum yields were determined by an absolute method by using an integrating sphere with an Edinburgh Instrument FLS920. The pH values were adjusted by the addition of HCl (0.1 M) or NaOH (0.1 M). The volume of the added solutions was less than 20 μL to leave the concentration of **L1** unchanged. All pH measurements were carried with a pH-10C digital pH meter. All titration experiments were run twice for reliable data. All imaging experiments were performed with a fluorescence-inverted microscope (DMI 4000 B, Leica Microsystem) with excitation between 340 and 380 nm. The total magnification was 400×. The cationic solutions were prepared from $NaClO_4$, K_2CO_3, $Mg(ClO_4)_2$, $Ca(NO_3)_2$, $FeSO_4$, $Pb(NO_3)_2$,$Co(NO_3)_2$, $NiCl_2$, $Zn(NO_3)_2$, $Zn(ClO_4)_2$ $AgNO_3$, $CdSO_4$, $HgCl_2$, and $CuSO_4$ in distilled water with a concentration of 0.01 M or 0.001 M. The volume of the cationic solutions added was less than 100 μL to leave the concentration of **L1** unchanged. All synthetic materials were purchased from commercial suppliers and used without further purification. CH_3CN for spectroscopy was of HPLC reagent grade without fluorescent impurities.

Crystal Structure Determination: Single-crystal X-ray diffraction measurements were carried out with a Bruker SMART 1000 CCD diffractometer operating at 50 kV and 30 mA by using Mo-K_α radiation (λ = 0.71073 Å). The selected crystal was mounted inside a Lindemann glass capillary for data collection, which used the SMART and SAINT software.[16a,16b] An empirical absorption correction was applied by using the SADABS program.[16c] The structure was solved by direct methods and refined by full-matrix least squares on F^2 by using the SHELXTL-97 program package.[16d,16e] All non-hydrogen atoms were subjected to aniostropic refinement, and all hydrogen atoms were added in idealized positions and refined isotropically. Crystal data for **L1**: M_r = 640.77, triclinic, space group $P\bar{1}$, a = 10.4814(6) Å, b = 13.0286(7) Å, c = 13.1038(7) Å, α

= 79.464(3)°, β = 80.073(3)°, γ = 81.045(3), V = 1718.62(16) Å^3, Z = 2, $\rho_{calcd.}$ = 1.238 g cm^{-3}, R(reflections) = 0.0591(3051), wR_2(reflections) = 0.0974(6351). CCDC-825020 contains the supplementary crystallographic data for this paper. These data can be obtained free of charge from The Cambridge Crystallographic Data Centre via www.ccdc.cam.ac.uk/data_request/cif.

Preparation of 2-Chloro-*N*-(quinol-8-yl)acetamide: To a cooled, stirred solution of 8-aminoquinoline (288 mg, 2.0 mmol) and pyridine (0.23 mL, 2.8 mmol) was added a chloroform (10 mL) solution of 2-chloroacetyl chloride (0.15 mL, 2.0 mmol) dropwise over 1 h. After 2 h at room temperature, a brown-yellow solid was obtained by removing the solvent under reduced pressure. The crude product was purified by silica gel column chromatography using dichloromethane as eluent to afford 2-chloro-*N*-(quinol-8-yl)acetamide (362 mg, 80%).

Preparation of L1: 2-Chloro-*N*-(quinol-8-yl)acetamide (110 mg, 0.5 mmol), *N*-(rhodamine-6G)lactam-ethylenediamine (228 mg, 0.5 mmol), and potassium iodide (8 mg) were dissolved in acetonitrile (30 mL) with stirring and heated to reflux under nitrogen for 10 h. The mixture was cooled to room temperature, and the solvent was removed under reduced pressure to obtain a pale-yellow solid, which was purified by silica gel column chromatography using dichloromethane/petroleum ether (5:1, v/v) as eluent to afford **L1**. Yield: 83.8%. ^{1}H NMR (400 MHz): δ = 11.234 (s, 1 H), 8.743–8.738 (d, 1 H), 8.726–8.462 (m, 1 H), 8.101–8.076 (m, 1 H), 7.903–7.882 (m, 1 H), 7.505–7.424 (m, 4 H), 7.357–7.326 (m, 1 H), 7.075–7.055 (m, 1 H), 6.356 (s, 2 H), 6.253 (s, 2 H), 3.457 (s, 2 H), 3.402–3.372 (t, 2 H), 3.201 (s, 2 H), 3.126–3.110 (m, 4 H), 2.562–2.532 (t, 2 H), 1.805 (s, 6 H), 1.278–1.242 (t, 6 H) ppm. ^{13}C NMR (100 MHz): δ = 170.40, 168.69, 153.67, 148.39, 147.36, 138.84, 135.80. 134.33, 132.38, 131.13, 128.29, 127.93, 127.84, 127.03, 123.80, 122.75, 121.37, 121.28, 117.90, 116.20, 105.82, 96.42, 65.14, 53.19, 48.23, 40.03, 38.18, 16.41, 14.57 ppm. ESI-MS: 641.1 $[M + 1]^+$.

Cell Incubation and Imaging: The SCABER cells were provided by Cells Bank of the Chinese Academy of Science (Shanghai, China). Cells were grown in H-DMEM (high glucose) supplemented with 10% FBS in an atmosphere of 5% CO_2/95% air at 37 °C. Cells (5×10^8/L) were plated on 18 mm glass coverslips and allowed to adhere for 24 h. Uptake experiments of Zn^{2+} were performed in the same medium supplemented with 20 μM $Zn(NO_3)_2$ for 0.5 h. Before the experiments, cells were washed with phosphate-buffered saline (PBS) and incubated with 10 μM **L1** at 37 °C for 3 h. Cell imaging was carried out after washing the cells with PBS.

Assessment of Biocompatibility: The biocompatibility was determined in L929 mouse fibroblast cell lines. The cell viability was evaluated by using the modified MTT assay. The cells were plated at a density of 1×10^5 in 96-well plates 24 h prior to exposure to the materials. Different concentrations of **L1** with saturated surfaces [by interaction with DMEM/F12 (1:1) for 24 h before use] were added to the wells, and the cells were incubated for 24, 48, and 72 h. After treatment, 10 μL of MTT (5 mg mL^{-1} in PBS) was added into each well. After 4 h of incubation, culture supernatants were aspirated, and purple insoluble MTT product was redissolved in dimethyl sulfoxide (150 μL) over 10 min. The concentration of the reduced MTT in each well was determined spectrophotometrically by subtraction of the absorbance reading at 630 nm from that measured at 570 nm using a microplate reader. All MTT experiments were performed five times, and the maximum and minimum were discounted. The results were expressed as the mean ± standard deviation. Cell viabilities were presented as the percentage of the absorbance of **L1**-treated cells to the absorbance of control cells.

Supporting Information (see footnote on the first page of this article): Materials and general methods; schematic molecular structures; experimental details; additional NMR and ESI-MS data.

Acknowledgments

This study was supported by the Fundamental Research Funds for the Central University (Lzujbky-2011-18), the Foundation of Key Laboratory of Nonferrous Metals Chemistry and Resources Utilization of Gansu Province, and the State Key Laboratory of Applied Organic Chemistry.

[1] a) A. P. De Silva, H. Q. N. Gunaratne, T. Gunnlaugsson, A. J. M. Huxley, C. P. McCoy, J. T. Rademacher, T. E. Rice, *Chem. Rev.* **1997**, *97*, 1515; b) L. Prodi, F. Bolletta, M. Montalti, N. Zaccheroni, *Coord. Chem. Rev.* **2000**, *205*, 59; c) J. S. Kim, D. T. Quang, *Chem. Rev.* **2007**, *107*, 3780; d) H. N. Kim, M. H. Lee, H. J. Kim, J. S. Kim, J. Yoon, *Chem. Soc. Rev.* **2008**, *37*, 1465.

[2] a) B. Valeur, I. Leray, *Coord. Chem. Rev.* **2000**, *205*, 3; b) K. Rurack, U. Resch-Genger, *Chem. Soc. Rev.* **2002**, *31*, 116; c) V. Amendola, L. Fabbrizzi, F. Forti, M. Licchelli, C. Mangano, P. Pallavicini, A. Poggi, D. Sacchi, A. Taglieti, *Coord. Chem. Rev.* **2006**, *250*, 273.

[3] a) A. W. Czarnik, *Fluorescent Chemosensors for Ion and Molecule Recognition*, American Chemical Society, Washington, DC, **1993**; b) A. P. de Silva, D. B. Fox, A. J. M. Huxley, T. S. Moody, *Coord. Chem. Rev.* **2000**, *205*, 41; c) Q. W. He, E. W. Miller, A. P. Wong, C. J. Chang, *J. Am. Chem. Soc.* **2006**, *128*, 9316.

[4] a) T. V. O'Halloran, *Science* **1993**, *261*, 715; b) J. Y. Koh, S. W. Suh, B. J. Gwag, Y. Y. He, C. Y. Hsu, D. W. Choi, *Science* **1996**, *272*, 1013; c) F. Walker, R. E. Black, *Annu. Rev. Nutr.* **2004**, *24*, 255; d) C. J. Frederickson, A. I. Bush, *Biometals* **2001**, *14*, 353.

[5] a) K. Kiyose, H. Kojima, Y. Urano, T. Nagano, *J. Am. Chem. Soc.* **2006**, *128*, 6548; b) K. Komatsu, Y. Urano, H. Kojima, T. Nagano, *J. Am. Chem. Soc.* **2007**, *129*, 13447; c) C. R. Goldsmith, S. J. Lippard, *Inorg. Chem.* **2006**, *45*, 555; d) B. A. Wong, S. Friedle, S. J. Lippard, *J. Am. Chem. Soc.* **2009**, *131*, 7142; e) A. E. Dennis, R. C. Smith, *Chem. Commun.* **2007**, 4641; f) J. F. Zhu, H. Yuan, W. H. Chan, A. W. M. Lee, *Org. Biomol. Chem.* **2010**, *8*, 3957; g) Z. C. Xu, J. Y. Yoon, D. R. Spring, *Chem. Soc. Rev.* **2010**, *39*, 1996; h) Z. C. Xu, K. H. Baek, H. N. Kim, J. N. Cui, X. H. Qian, D. R. Spring, I. Shin, J. Yoon, *J. Am. Chem. Soc.* **2010**, *132*, 601; i) Z. C. Xu, G. H. Kim, S. J. Han, M. J. Jou, C. Lee, I. Shin, J. Yoon, *Tetrahedron* **2009**, *65*, 2307.

[6] K. Rurack, *Spectrochim. Acta, Part A* **2001**, *57*, 2161.

[7] P. Jiang, Z. J. Guo, *Coord. Chem. Rev.* **2004**, *248*, 205.

[8] a) I. B. Mahadevan, M. C. Kimber, S. F. Lincoln, E. R. Tiekink, A. D. Ward, W. H. Betts, I. J. Forbes, P. D. Zalewski, *Aust. J. Chem.* **1996**, *49*, 561; b) P. D. Zalewski, I. J. Forbes, W. H. Betts, *Biochem. J.* **1993**, *296*, 403; c) C. J. Frederickson, E. J. Kasarskis, D. Ringo, R. E. Frederickson, *J. Neurosci. Methods* **1987**, *20*, 91; d) C. J. Frederickson, *J. Int. Rev. Neurobiol.* **1989**, *31*, 145.

[9] Y. Liu, N. Zhang, Y. Chen, L. H. Wang, *Org. Lett.* **2007**, *9*, 315.

[10] a) H. A. Benesi, J. H. Hildebrand, *J. Am. Chem. Soc.* **1949**, *71*, 2703; b) M. Barra, C. Bohne, J. C. Scaiano, *J. Am. Chem. Soc.* **1990**, *112*, 8075.

[11] a) K. Hiratani, T. J. Hirose, K. Kasuga, K. Saito, *J. Org. Chem.* **1992**, *57*, 7083; b) T. Yang, C. Tu, J. Y. Zhang, L. P. Lin, X. M. Zhang, Q. Liu, J. Ding, Q. Xu, Z. J. Guo, *Dalton Trans.* **2003**, 3419.

[12] P. J. Jiang, L. Z. Chen, J. Lin, Q. Liu, J. Ding, X. Gao, Z. J. Guo, *Chem. Commun.* **2002**, 1424.

[13] a) L. Huang, X. Wang, G. Q. Xie, P. X. Xi, Z. P. Li, M. Xu, Y. J. Wu, D. C. Bai, Z. Zeng, *Dalton Trans.* **2010**, *39*, 7894; b) P. X. Xi, L. Huang, H. Liu, P. F. Jia, F. J. Chen, M. Xu, Z. Z. Zeng, *J. Biol. Inorg. Chem.* **2009**, *14*, 815; c) P. X. Xi, L. Huang, G. Q. Xie, F. J. Chen, Z. H. Xu, D. C. Bai, Z. Z. Zeng, *Dalton Trans.* **2011**, *40*, 6382–6384.
[14] K. M. Hendrickson, T. Rodopoulos, P. A. Pittet, I. Mahadevan, S. F. Lincoln, A. D. Ward, T. Kurucsev, P. A. Duckworth, I. J. Forbes, P. D. Zalewski, W. H. Betts, *J. Chem. Soc., Dalton Trans.* **1997**, 3879.
[15] Y. Chen, K. Y. Han, Y. Liu, *Bioorg. Med. Chem.* **2007**, *15*, 4537.
[16] a) Bruker, *SMART*, version 5.622, Bruker AXS Inc., Madison, Wisconsin, USA, **1997**; b) Bruker, *SAINT*, version 6.02, Bruker AXS Inc., Madison, Wisconsin, USA, **1999**; c) G. M. Sheldrick, *SADABS*, version 2.03, University of Göttingen, Germany, **1996**; d) G. M. Sheldrick, *SHELXL-97*, *Program for the Solution of Crystal Structures*, University of Göttingen, Göttingen, Germany, **1997**; e) G. M. Sheldrick, *SHELXL-97*, *Program for the Refinement of Crystal Structures*, University of Göttingen, Göttingen, Germany, **1997**.

Received: August 1, 2011
Published Online: December 8, 2011

